Published in Journals: Applied Sciences, Energies, Materials, Sensors and Designs

Topic Reprint

Advances in Non-Destructive Testing Methods, 2nd Edition

Edited by
Grzegorz Peruń and Tangbin Xia

mdpi.com/topics

MDPI

Advances in Non-Destructive Testing Methods, 2nd Edition

Advances in Non-Destructive Testing Methods, 2nd Edition

Topic Editors

Grzegorz Peruń
Tangbin Xia

MDPI

Basel • Beijing • Wuhan • Barcelona • Belgrade • Novi Sad • Cluj • Manchester

Topic Editors

Grzegorz Peruń
Faculty of Transport and Aviation Engineering
Department of Road Transport
Silesian University of Technology
Katowice
Poland

Tangbin Xia
Department of Industrial Engineering & Management
Shanghai Jiao Tong University
Shanghai
China

Editorial Office

MDPI AG
Grosspeteranlage 5
4052 Basel, Switzerland

This is a reprint of the Topic, published open access by the journals *Applied Sciences* (ISSN 2411-9660), *Energies* (ISSN 1996-1073), *Materials* (ISSN 1996-1944), *Sensors* (ISSN 1424-8220) and *Designs* (ISSN 2411-9660), freely accessible at: https://www.mdpi.com/topics/non_destructive_ii.

For citation purposes, cite each article independently as indicated on the article page online and as indicated below:

Lastname, A.A.; Lastname, B.B. Article Title. *Journal Name* **Year**, *Volume Number*, Page Range.

ISBN 978-3-7258-4293-3 (Hbk)
ISBN 978-3-7258-4294-0 (PDF)
https://doi.org/10.3390/books978-3-7258-4294-0

Contents

About the Editors

Grzegorz Peruń

Grzegorz Peruń obtained his M.Sc. degree from the Silesian University of Technology, Katowice, Poland, in 2004, followed by his Ph.D. degree in 2010. His doctoral thesis was defended with honors at the Silesian University of Technology, and also for which he received an award from the Fiat Group (Gliwice - Turyn 2011). Habilitation "Modeling dynamic of power transmission system with planetary gear in computer-aided design and diagnostics" was obtained from Air Force Institute of Technology, Warsaw, Poland, in 2018.

He is the author of 248 published scientific works—articles, conference papers, and other scientific publications. He is a co-author of two patents, author of a monograph, academic textbook "Engineering design with software HiCAD" (2014), and co-author of two academic textbooks: "Aircraft Airframe" (2014) and "Aircraft Systems" (2015). His research interests include mechanical engineering, construction of machines, especially modeling and simulation of toothed gears, vibroacoustics, gearbox diagnostic, signal processing, transport, GIS, and for several years also non-destructive testing techniques.

Since 2019, he has been a professor SUT in the Faculty of Transport and Aviation Engineering, Department of Road Transport. He is a certified specialist in NDT testing, author of, among others, software for resonance defectoscope. He is a contributor to research grants and an editor of Special Issues of many journals with national and international reach. He is proficient in several programming languages, which he uses effectively in his academic work and research. He has given lectures as a part of the Erasmus program at FH Köln, Fakultät für Fahrzeugsysteme und Produktion, and Technical University of Košice, Faculty of Aeronautics.

Tangbin Xia

Tangbin Xia received a Ph.D. degree in Mechanical Engineering (Industrial Engineering) from Shanghai Jiao Tong University in 2014. He was a Visiting Scholar with WuMRC, University of Michigan, and ISyE, Georgia Institute of Technology. Currently, he is a Tenured Associate Professor and serves as Vice Dean of the School of Mechanical Engineering in SJTU, Deputy Secretary General of The Shanghai Society for Modern Design Theory and Methodology Research, and the Review Expert for the Government Quality Award of Shanghai Municipality. He was awarded Young Chang Jiang Scholar of the Ministry of Education in 2022. His major research interests are Intelligent Manufacturing Systems, Quality and Reliability Engineering, and Big Data and Artificial Intelligence. His research group has published more than 100 SCI papers.

Preface

Non-destructive testing (NDT) methods are a group of tests that allow the detection of external (surface) as well as internal defects of the structure. They enable the determination of the state of micro- and macro-structure without interfering with the structure of the tested object and they provide information about the functional properties of the tested object. This basic feature and the variety of non-destructive testing methods make them applicable in many industries. Despite the numerous advantages, NDT methods also have limitations, one of which may be the economic factor of the cost of purchasing testing equipment. NDT can be carried out at various stages of production, operation, or repair. They are used to carry out quality control of products and to determine the technical condition of an object.

Unlike the well-known destructive testing methods that have been in use for a long time, many of the testing methods classified as nondestructive have been in use recently. At present, a wide variety of nondestructive testing methods, operating on the basis of different phenomena, can be specified. A detailed classification and description can be found in the EN-ISO/ISO standards, among others. The most common group of nondestructive tests includes visual methods, penetrant methods, magnetic-powder methods, methods using eddy currents, thermographic methods, vibration methods, acoustic methods, ultrasonic methods, and radiographic methods. Visual, penetrant, and electromagnetic methods, including eddy current, are ideal for detecting surface discontinuities. The detection of subsurface defects is made possible by eddy current, magnetic particle thermographic methods. Among the methods of non-destructive volumetric testing, acoustic, ultrasonic, and radiographic methods should be listed first.

Grzegorz Peruń and Tangbin Xia
Topic Editors

sensors

MDPI

Communication

Impedance Variation in a Coaxial Coil Encircling a Metal Tube Adapter

Yao Luo [1,2,*] and Xinyi Yang [1,2]

[1] State Key Laboratory of Power Grid Environmental Protection, School of Electrical Engineering and Automation, Wuhan University, Wuhan 430072, China; yangxy@whu.edu.cn
[2] School of Electrical Engineering and Automation, Wuhan University, Wuhan 430072, China
* Correspondence: luoyao@whu.edu.cn

Abstract: The impedance change in an induction coil surrounding a metal tube adapter is investigated using the truncated region eigenfunction expansion (TREE) method. The conventional TREE method is inapplicable to this problem as a consequence of the numerical overflow of the eigenfunctions of the air–metal multi-subdomain regions. The difficulty is surmounted by a normalization procedure for the numerical eigenfunctions obtained from the 1D finite element method (FEM). An efficient algorithm is devised by the Clenshaw–Curtis quadrature rule for integrals involving the numerical eigenfunctions. The numerical results of the TREE and FEM simulation coincide very well in all cases, and the efficiency of the proposed method is also confirmed.

Keywords: tube adapter; eddy current; numerical eigenfunctions; Clenshaw–Curtis quadrature

1. Introduction

A tube adapter is a component connecting two tubes of different diameters. The standard analytical method of Dodd and Deeds [1] is unable to investigate the interaction of an induction coil with a metal tube adapter due to the end effects involved in this problem. The truncated region eigenfunction expansion (TREE) method, pioneered by Hannakam and Tepe [2], and developed by Theodoulidis, Kriezis, and Bowler [3–9] for the modeling of the eddy current nondestructive testing (EC NDT), is capable of analyzing the end effects and establishing analytical models. However, the successful implementation of TREE for the model of end effects depends on the solution of relevant eigenvalue equations, which are transcendental, and complex roots should be determined. Conventionally, the Newton–Raphson algorithm [10–13] or contour integral based on the Cauchy's theorem [14–17] are applied to solve the eigenvalue equations. A novel method based on the Sturm–Liouville theory and Galerkin approach has been proposed recently [18–20], which greatly simplifies the process of locating the complex eigenvalues.

However, the TREE method has hitherto been available only for problem of the air–metal region of two subdomains. For a problem involving the region of three air–metal subdomains, the source should be decomposed into the odd and even parts, if possible, to reduce the problem to the two subdomains [6,8,21–23]. No solutions for the problem involving regions of more subdomains have yet been found in the literature. The difficulty lies in the fact that the symbolic piecewise eigenfunctions for regions of three or more subdomains will become extremely clumsy, and more seriously, they are very prone to numerical overflow with the complex argument, especially when the argument has a relatively large imaginary part. Nevertheless, the issue of numerical overflow should not be superficially ascribed to the multi-subdomain regions but rather to the formally constructed eigenfunctions. By a proper normalization of the eigenfunctions, the overflow could be evaded, and the TREE method should become applicable to problems of multi-subdomain regions. In this work, the normalization of complex eigenfunctions is achieved

based on the approach of [19], and a problem including regions of three subdomains (See Figure 1) is solved with TREE.

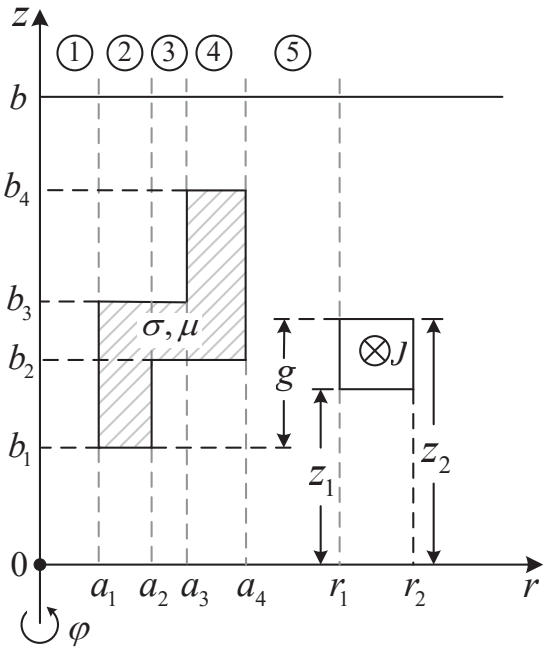

Figure 1. Side view of a metal tube adapter encircled by a coaxial coil.

In Section 2, the TREE solution is given for a metal tube adapter surrounded by a coaxial coil. The permeability of the metal is not restricted to μ_0. In Section 3, a method successful in dealing with the overflow issue is devised. The numerical eigenfunctions are obtained by the 1D FEM solution of the Sturm–Liouville equations and normalized, and the Clenshaw–Curtis quadrature is applied to the computation of the integrals involving the numerical eigenfunctions. By this strategy, efficient computation of the matrix elements can be contrived. In Section 4, the TREE results are compared with those from the FEM simulation.

2. Formulation

A metal tube adapter of conductivity σ and permeability $\mu = \mu_r \mu_0$ (μ_r is supposed to be constant) is encircled by a coaxial induction coil excited by a time harmonic current of frequency ω and amplitude I (See Figure 2). The geometry of the coil and tube adapter is shown in Figure 1. A perfect electric boundary is imposed at $z = 0$ and $z = b$ to discretize the eigenvalues of this boundary value problem (BVP).

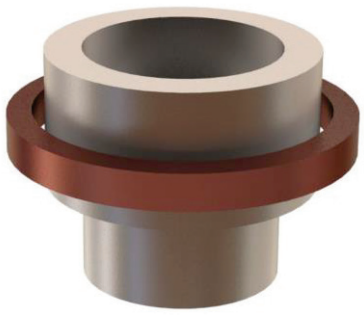

Figure 2. A metal tube adapter encircled by a coaxial coil.

The solution domain is divided into five regions along the r-axis (See Figure 1). The vector potentials $\boldsymbol{A}_1$ to $\boldsymbol{A}_5$ satisfy the Laplace or Helmholtz equations in the corresponding regions:

$$\nabla^2 \boldsymbol{A}_{1,5} = 0 \tag{1}$$

$$\nabla^2 \boldsymbol{A}_{2,3,4} = k^2 \boldsymbol{A}_{2,3,4} \tag{2}$$

where $k = \sqrt{i\omega\sigma\mu_0\mu_r}$ is the wavenumber of the metal.

Only the φ-component of the vector potential exists due to the axisymmetry of the BVP, i.e., $\boldsymbol{A} = A\boldsymbol{e}_\varphi$, and the vector Laplacian of Equations (1) and (2) is reduced to

$$\nabla_\varphi^2 = \frac{\partial^2}{\partial r^2} + \frac{1}{r}\frac{\partial}{\partial r} - \frac{1}{r^2} + \frac{\partial^2}{\partial z^2} \tag{3}$$

2.1. Vector Potential of the Source Coil

The formulation of the source vector potential can be obtained by the source expansion of the Poisson equation [24,25]. The vector potential of the coil can be written in the form outlined in Figure 3,

$$A_I(r,z) = \mathbf{S}^{\mathrm{T}}(z)\mathbf{I}_1(\boldsymbol{\alpha} r)\mathbf{C}_1^{(e)} \tag{4a}$$

$$A_{II}(r,z) = \mathbf{S}^{\mathrm{T}}(z)\left[\mathbf{I}_1(\boldsymbol{\alpha} r)\mathbf{C}_2^{(e)} + \mathbf{K}_1(\boldsymbol{\alpha} r)\mathbf{D}_2^{(e)} + \mathbf{V}(r)\right] \tag{4b}$$

$$A_{III}(r,z) = \mathbf{S}^{\mathrm{T}}(z)\mathbf{K}_1(\boldsymbol{\alpha} r)\mathbf{D}_3^{(e)} \tag{4c}$$

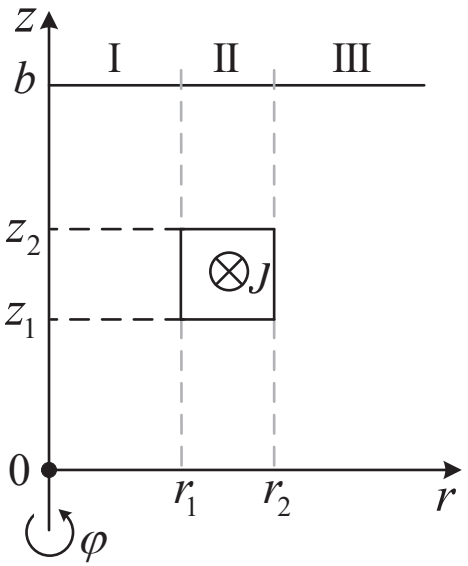

Figure 3. Side view of an isolated coil with truncation boundary.

Where the source vector $\mathbf{V}(r)$ is

$$\mathbf{V}(r) = \begin{bmatrix} v_1(r) \\ v_2(r) \\ \vdots \end{bmatrix}$$

with the elements

$$v_i(r) = \kappa_i \mathbf{L}_1(\alpha_i r) \tag{5}$$

where $\alpha_i = i\pi/b$, and $\mathbf{L}_n(x)$ is the modified Struve function of order n, and

$$\kappa_i = \frac{2\mu_0 J}{i\alpha_i^2} \sin\left[\frac{\alpha_i}{2}(z_1 - z_2)\right] \sin\left[\frac{\alpha_i}{2}(z_1 + z_2)\right] \tag{6}$$

Other matrices and vectors in (4a)–(4c) are

$$\boldsymbol{\alpha} = \begin{bmatrix} \alpha_1 & 0 & \cdots \\ 0 & \alpha_2 & \cdots \\ \vdots & \vdots & \ddots \end{bmatrix}, \mathbf{I}_1(\boldsymbol{\alpha} r) = \begin{bmatrix} I_1(\alpha_1 r) & 0 & \cdots \\ 0 & I_1(\alpha_2 r) & \cdots \\ \vdots & \vdots & \ddots \end{bmatrix}, \mathbf{K}_1(\boldsymbol{\alpha} r) = \begin{bmatrix} K_1(\alpha_1 r) & 0 & \cdots \\ 0 & K_1(\alpha_2 r) & \cdots \\ \vdots & \vdots & \ddots \end{bmatrix}, \mathbf{S}(z) = \begin{bmatrix} \sin(\alpha_1 z) \\ \sin(\alpha_2 z) \\ \vdots \end{bmatrix},$$

where $I_n(x)$ and $K_n(x)$ are the modified Bessel functions of the first and second kinds of order n, respectively, and $\mathbf{C}_1^{(e)}$, $\mathbf{C}_2^{(e)}$, $\mathbf{D}_2^{(e)}$, $\mathbf{D}_3^{(e)}$ are the coefficients to be determined. With the interface conditions of B_r and H_z at $r = r_1$ and $r = r_2$, the coefficients can be found:

$$C_{1,i}^{(e)} = \kappa_i[\chi(\alpha_i r_1) - \chi(\alpha_i r_2)] \tag{7a}$$

$$C_{2,i}^{(e)} = -\kappa_i \chi(\alpha_i r_2) \tag{7b}$$

$$D_{2,i}^{(e)} = \kappa_i \eta(\alpha_i r_1) \tag{7c}$$

$$D_{3,i}^{(e)} = \kappa_i[\eta(\alpha_i r_1) - \eta(\alpha_i r_2)] \tag{7d}$$

where

$$\chi(x) = x[K_1(x)\mathbf{L}_0(x) + K_0(x)\mathbf{L}_1(x)] \tag{8a}$$

$$\eta(x) = x[I_1(x)\mathbf{L}_0(x) - I_0(x)\mathbf{L}_1(x)] \tag{8b}$$

For the function $\chi(x)$ used for the subsequent analysis, it is advisable to adopt an alternative form for the practical evaluations, namely

$$\chi(x) = \begin{cases} \frac{x^2}{2} \sum\limits_{m=0}^{m_0} \frac{(x/2)^{2m}}{\Gamma(m+3/2)} \left[\frac{K_1(x)}{\Gamma(m+3/2)} + \frac{xK_0(x)}{2\Gamma(m+5/2)}\right], x < 15 \\ 1 + \frac{x}{\pi^2} \sum\limits_{m=0}^{m_1} \frac{\Gamma^2(m+1/2)}{(x/2)^{2m}} \left[\frac{K_0(x)}{m-1/2} - \frac{K_1(x)}{x/2}\right], x \geq 15 \end{cases} \tag{9}$$

Expression (9) is obtained by the Maclaurin and asymptotic expansions of $\mathbf{L}_n(x)$ [26], and high accuracy can be achieved by setting $m_0 = 23$ and $m_1 = 10$, respectively.

2.2. Impedance Change in the Coil Encircling the Metal Tube Adapter

The vector potentials in the five regions of Figure 2 are expansible by the separation of variables

$$A_1(r,z) = \mathbf{S}^\mathrm{T}(z)\mathbf{I}_1(\boldsymbol{\alpha} r)\mathbf{C}_1 \tag{10a}$$

$$A_2(r,z) = \mathbf{F}^\mathrm{T}(z)[\mathbf{I}_1(\mathbf{P}_1 r)\mathbf{C}_2 + \mathbf{K}_1(\mathbf{P}_1 r)\mathbf{D}_2] \tag{10b}$$

$$A_3(r,z) = \mathbf{G}^\mathrm{T}(z)[\mathbf{I}_1(\mathbf{P}_2 r)\mathbf{C}_3 + \mathbf{K}_1(\mathbf{P}_2 r)\mathbf{D}_3] \tag{10c}$$

$$A_4(r,z) = \mathbf{H}^\mathrm{T}(z)[\mathbf{I}_1(\mathbf{P}_3 r)\mathbf{C}_4 + \mathbf{K}_1(\mathbf{P}_3 r)\mathbf{D}_4] \tag{10d}$$

$$A_5(r,z) = \mathbf{S}^\mathrm{T}(z)\left[\mathbf{I}_1(\boldsymbol{\alpha} r)\mathbf{C}_1^{(e)} + \mathbf{K}_1(\boldsymbol{\alpha} r)\mathbf{D}^{(s)}\right] \tag{10e}$$

where $\mathbf{P}_1$, $\mathbf{P}_2$, and $\mathbf{P}_3$ are the eigenvalue matrices of regions 2, 3, and 4, respectively,

$$\mathbf{P}_1 = \begin{bmatrix} p_{1,1} & 0 & \cdots \\ 0 & p_{1,2} & \cdots \\ \vdots & \vdots & \ddots \end{bmatrix}, \mathbf{P}_2 = \begin{bmatrix} p_{2,1} & 0 & \cdots \\ 0 & p_{2,2} & \cdots \\ \vdots & \vdots & \ddots \end{bmatrix}, \mathbf{P}_3 = \begin{bmatrix} p_{3,1} & 0 & \cdots \\ 0 & p_{3,2} & \cdots \\ \vdots & \vdots & \ddots \end{bmatrix},$$

and

$$\mathbf{F}(z) = \begin{bmatrix} f_1(p_{1,1}, z) \\ f_2(p_{1,2}, z) \\ \vdots \end{bmatrix}, \mathbf{G}(z) = \begin{bmatrix} g_1(p_{2,1}, z) \\ g_2(p_{2,2}, z) \\ \vdots \end{bmatrix}, \mathbf{H}(z) = \begin{bmatrix} h_1(p_{3,1}, z) \\ h_2(p_{3,2}, z) \\ \vdots \end{bmatrix}$$

are the axial eigenfunctions satisfying the relevant Sturm–Liouville equations:

$$\frac{d^2 f_i(z)}{dz^2} - k_1^2(z) f_i(z) = -p_{1,i}^2 f_i(z),\ f_i(0) = f_i(b) = 0 \tag{11a}$$

$$\frac{d^2 g_i(z)}{dz^2} - k_2^2(z) g_i(z) = -p_{2,i}^2 g_i(z),\ g_i(0) = g_i(b) = 0 \tag{11b}$$

and

$$\frac{d^2 h_i(z)}{dz^2} - k_3^2(z) h_i(z) = -p_{3,i}^2 h_i(z),\ h_i(0) = h_i(b) = 0 \tag{11c}$$

with

$$k_1(z) = \begin{cases} k, b_1 \le z \le b_3 \\ 0, \text{others} \end{cases} \tag{12a}$$

$$k_2(z) = \begin{cases} k, b_2 \le z \le b_3 \\ 0, \text{others} \end{cases} \tag{12b}$$

and

$$k_3(z) = \begin{cases} k, b_2 \le z \le b_4 \\ 0, \text{others} \end{cases} \tag{12c}$$

Taking account of the interface conditions of B_r and H_z at $r = a_1$, $r = a_2$, $r = a_3$, and $r = a_4$, the following equations for the coefficients $\mathbf{C}_2$, $\mathbf{C}_3$, $\mathbf{C}_4$, $\mathbf{D}_1$, $\mathbf{D}_2$, and $\mathbf{D}_3$ can be derived

$$\frac{b}{2}\mathbf{I}_1(\boldsymbol{\alpha} a_1)\mathbf{C}_1 = \mathbf{T_1}[\mathbf{I}_1(\mathbf{P}_1 a_1)\mathbf{C}_2 + \mathbf{K}_1(\mathbf{P}_1 a_1)\mathbf{D}_1] \tag{13a}$$

$$\mathbf{T}_1^{\mathrm{T}}\boldsymbol{\alpha}\mathbf{I}_0(\boldsymbol{\alpha} a_1)\mathbf{C}_1 = \mathbf{P}_1[\mathbf{I}_0(\mathbf{P}_1 a_1)\mathbf{C}_2 - \mathbf{K}_0(\mathbf{P}_1 a_1)\mathbf{D}_2] \tag{13b}$$

$$\mathbf{I}_1(\mathbf{P}_1 a_2)\mathbf{C}_2 + \mathbf{K}_1(\mathbf{P}_1 a_2)\mathbf{D}_2 = \mathbf{T}_2[\mathbf{I}_1(\mathbf{P}_2 a_2)\mathbf{C}_3 + \mathbf{K}_1(\mathbf{P}_2 a_2)\mathbf{D}_3] \tag{13c}$$

$$\mathbf{T}_2^{\mathrm{T}}\mathbf{P}_1[\mathbf{I}_0(\mathbf{P}_1 a_2)\mathbf{C}_2 - \mathbf{K}_0(\mathbf{P}_1 a_2)\mathbf{D}_2] = \mathbf{P}_2[\mathbf{I}_0(\mathbf{P}_2 a_2)\mathbf{C}_3 - \mathbf{K}_0(\mathbf{P}_2 a_2)\mathbf{D}_3] \tag{13d}$$

$$\mathbf{I}_1(\mathbf{P}_2 a_3)\mathbf{C}_3 + \mathbf{K}_1(\mathbf{P}_2 a_3)\mathbf{D}_3 = \mathbf{T}_3[\mathbf{I}_1(\mathbf{P}_3 a_3)\mathbf{C}_4 + \mathbf{K}_1(\mathbf{P}_3 a_3)\mathbf{D}_4] \tag{13e}$$

$$\mathbf{T}_3^{\mathrm{T}}\mathbf{P}_2[\mathbf{I}_0(\mathbf{P}_2 a_3)\mathbf{C}_3 - \mathbf{K}_0(\mathbf{P}_2 a_3)\mathbf{D}_3] = \mathbf{P}_3[\mathbf{I}_0(\mathbf{P}_3 a_3)\mathbf{C}_4 - \mathbf{K}_0(\mathbf{P}_3 a_3)\mathbf{D}_4] \tag{13f}$$

$$\mathbf{T}_4[\mathbf{I}_1(\mathbf{P}_3 a_4)\mathbf{C}_4 + \mathbf{K}_1(\mathbf{P}_3 a_4)\mathbf{D}_4] = \frac{b}{2}\left[\mathbf{I}_1(\boldsymbol{\alpha} a_4)\mathbf{C}_1^{(e)} + \mathbf{K}_1(\boldsymbol{\alpha} a_4)\mathbf{D}^{(s)}\right] \tag{13g}$$

$$\mathbf{P}_3[\mathbf{I}_0(\mathbf{P}_3 a_4)\mathbf{C}_4 - \mathbf{K}_0(\mathbf{P}_3 a_4)\mathbf{D}_4] = \mathbf{T}_4^{\mathrm{T}}\boldsymbol{\alpha}\left[\mathbf{I}_0(\boldsymbol{\alpha} a_4)\mathbf{C}_1^{(e)} - \mathbf{K}_0(\boldsymbol{\alpha} a_4)\mathbf{D}^{(s)}\right] \tag{13h}$$

where

$$\mathbf{T}_1 = \int_0^b \mathbf{S}(z)\mathbf{F}^{\mathrm{T}}(z)dz \tag{14}$$

$$\mathbf{T}_2 = \int_0^b \frac{1}{\mu_r^{(1)}(z)}\mathbf{F}(z)\mathbf{G}^{\mathrm{T}}(z)dz \tag{15}$$

$$\mathbf{T}_3 = \int_0^b \frac{1}{\mu_r^{(2)}(z)}\mathbf{G}(z)\mathbf{H}^{\mathrm{T}}(z)dz \tag{16}$$

$$\mathbf{T}_4 = \int_0^b \mathbf{S}(z)\mathbf{H}^{\mathrm{T}}(z)dz \tag{17}$$

In (13a)–(13h), the orthogonalities of the eigenfunctions

$$\int_0^b \mathbf{S}(z)\mathbf{S}^{\mathrm{T}}(z)dz = \frac{b}{2}\mathbf{I} \tag{18a}$$

$$\int_0^b \frac{1}{\mu_r^{(1)}(z)}\mathbf{F}(z)\mathbf{F}^{\mathrm{T}}(z)dz = \mathbf{I} \tag{18b}$$

$$\int_0^b \frac{1}{\mu_r^{(2)}(z)}\mathbf{G}(z)\mathbf{G}^{\mathrm{T}}(z)dz = \mathbf{I} \tag{18c}$$

$$\int_0^b \frac{1}{\mu_r^{(3)}(z)}\mathbf{H}(z)\mathbf{H}^{\mathrm{T}}(z)dz = \mathbf{I} \tag{18d}$$

have been adopted, where $\mathbf{I}$ is the identity matrix, and

$$\mu_r^{(1)}(z) = \begin{cases} \mu_r, b_1 \le z \le b_3 \\ 1, \text{ others} \end{cases} \tag{19a}$$

$$\mu_r^{(2)}(z) = \begin{cases} \mu_r, b_2 \le z \le b_3 \\ 1, \text{ others} \end{cases} \tag{19b}$$

$$\mu_r^{(3)}(z) = \begin{cases} \mu_r, b_2 \le z \le b_4 \\ 1, \text{ others} \end{cases} \tag{19c}$$

The orthonormalization relations of (18b)–(18d) will be expounded in Section 3. The matrix algebra of (13a)–(13h) yields the equation system

$$\begin{bmatrix} \mathbf{A}_{11} & \mathbf{A}_{12} & \mathbf{0} & \mathbf{0} \\ \mathbf{A}_{21} & \mathbf{A}_{22} & \mathbf{A}_{23} & \mathbf{A}_{42} \\ \mathbf{A}_{31} & \mathbf{A}_{32} & \mathbf{A}_{33} & \mathbf{A}_{34} \\ \mathbf{0} & \mathbf{0} & \mathbf{A}_{43} & \mathbf{A}_{44} \end{bmatrix} \begin{bmatrix} \mathbf{C}_2 \\ \mathbf{D}_2 \\ \mathbf{C}_4 \\ \mathbf{D}_4 \end{bmatrix} = \begin{bmatrix} \mathbf{0} \\ \mathbf{0} \\ \mathbf{0} \\ \mathbf{E} \end{bmatrix} \tag{20}$$

where

$$\mathbf{A}_{11} = \mathbf{U}_1\mathbf{I}_1(\mathbf{P}_1 a_1) - \mathbf{P}_1\mathbf{I}_0(\mathbf{P}_1 a_1) \tag{21a}$$

$$\mathbf{A}_{12} = \mathbf{U}_1\mathbf{K}_1(\mathbf{P}_1 a_1) + \mathbf{P}_1\mathbf{K}_0(\mathbf{P}_1 a_1) \tag{21b}$$

$$\mathbf{A}_{21} = \mathbf{I}_1(\mathbf{P}_2 a_3)\mathbf{M}_3 + \mathbf{K}_1(\mathbf{P}_2 a_3)\mathbf{M}_1 \tag{21c}$$

$$\mathbf{A}_{22} = \mathbf{I}_1(\mathbf{P}_2 a_3)\mathbf{M}_4 + \mathbf{K}_1(\mathbf{P}_2 a_3)\mathbf{M}_2 \tag{21d}$$

$$\mathbf{A}_{23} = -\mathbf{T}_3\mathbf{I}_1(\mathbf{P}_3 a_3) \tag{21e}$$

$$\mathbf{A}_{24} = -\mathbf{T}_3\mathbf{K}_1(\mathbf{P}_3 a_3) \tag{21f}$$

$$\mathbf{A}_{31} = \mathbf{T}_3^{\mathrm{T}}\mathbf{P}_2[\mathbf{I}_0(\mathbf{P}_2 a_3)\mathbf{M}_3 - \mathbf{K}_0(\mathbf{P}_2 a_3)\mathbf{M}_1] \tag{21g}$$

$$\mathbf{A}_{32} = \mathbf{T}_3^{\mathrm{T}}\mathbf{P}_2[\mathbf{I}_0(\mathbf{P}_2 a_3)\mathbf{M}_4 - \mathbf{K}_0(\mathbf{P}_2 a_3)\mathbf{M}_2] \tag{21h}$$

$$\mathbf{A}_{33} = -\mathbf{P}_3\mathbf{I}_0(\mathbf{P}_3a_3) \tag{21i}$$

$$\mathbf{A}_{34} = \mathbf{P}_3\mathbf{K}_0(\mathbf{P}_3a_3) \tag{21j}$$

$$\mathbf{A}_{43} = \mathbf{U}_2\mathbf{I}_1(\mathbf{P}_3a_4) + \mathbf{P}_3\mathbf{I}_0(\mathbf{P}_3a_4) \tag{21k}$$

$$\mathbf{A}_{44} = \mathbf{U}_2\mathbf{K}_1(\mathbf{P}_3a_4) - \mathbf{P}_3\mathbf{K}_0(\mathbf{P}_3a_4) \tag{21l}$$

$$\mathbf{E} = \mathbf{T}_4^{\mathrm{T}}\boldsymbol{\alpha}\Big[\mathbf{I}_0(\boldsymbol{\alpha}a_4) + \mathbf{K}_0(\boldsymbol{\alpha}a_4)\mathbf{K}_1^{-1}(\boldsymbol{\alpha}a_4)\mathbf{I}_1(\boldsymbol{\alpha}a_4)\Big]\mathbf{C}_1^{(e)} \tag{21m}$$

with

$$\mathbf{U}_1 = \frac{2}{b}\mathbf{T}_1^{\mathrm{T}}\boldsymbol{\alpha}\mathbf{I}_0(\boldsymbol{\alpha}a_1)\mathbf{I}_1^{-1}(\boldsymbol{\alpha}a_1)\mathbf{T}_1 \tag{22a}$$

$$\mathbf{U}_2 = \frac{2}{b}\mathbf{T}_4^{\mathrm{T}}\boldsymbol{\alpha}\mathbf{K}_0(\boldsymbol{\alpha}a_4)\mathbf{K}_1^{-1}(\boldsymbol{\alpha}a_4)\mathbf{T}_4 \tag{22b}$$

$$\mathbf{M}_1 = a_2[\mathbf{X}_1\mathbf{I}_1(\mathbf{P}_1a_2) - \mathbf{X}_2\mathbf{I}_0(\mathbf{P}_1a_2)] \tag{22c}$$

$$\mathbf{M}_2 = a_2[\mathbf{X}_1\mathbf{K}_1(\mathbf{P}_1a_2) + \mathbf{X}_2\mathbf{K}_0(\mathbf{P}_1a_2)] \tag{22d}$$

$$\mathbf{M}_3 = a_2[\mathbf{X}_3\mathbf{I}_1(\mathbf{P}_1a_2) + \mathbf{X}_4\mathbf{I}_0(\mathbf{P}_1a_2)] \tag{22e}$$

$$\mathbf{M}_4 = a_2[\mathbf{X}_3\mathbf{K}_1(\mathbf{P}_1a_2) - \mathbf{X}_4\mathbf{K}_0(\mathbf{P}_1a_2)] \tag{22f}$$

$$\mathbf{X}_1 = \mathbf{P}_2\mathbf{I}_0(\mathbf{P}_2a_2)\mathbf{T}_2^{-1} \tag{22g}$$

$$\mathbf{X}_2 = \mathbf{I}_1(\mathbf{P}_2a_2)\mathbf{T}_2^{\mathrm{T}}\mathbf{P}_1 \tag{22h}$$

$$\mathbf{X}_3 = \mathbf{P}_2\mathbf{K}_0(\mathbf{P}_2a_2)\mathbf{T}_2^{-1} \tag{22i}$$

$$\mathbf{X}_4 = \mathbf{K}_1(\mathbf{P}_2a_2)\mathbf{T}_2^{\mathrm{T}}\mathbf{P}_1 \tag{22j}$$

Solving Equation (20) will give the coefficients $\mathbf{C}_2$, $\mathbf{D}_2$, $\mathbf{C}_4$, and $\mathbf{D}_4$, and other coefficients can be found by

$$\mathbf{C}_1 = \frac{2}{b}\mathbf{I}_1^{-1}(\boldsymbol{\alpha}a_1)\mathbf{T}_1[\mathbf{I}_1(\mathbf{P}_1a_1)\mathbf{C}_2 + \mathbf{K}_1(\mathbf{P}_1a_1)\mathbf{D}_2] \tag{23}$$

$$\mathbf{C}_3 = \mathbf{M}_3\mathbf{C}_2 + \mathbf{M}_4\mathbf{D}_2 \tag{24}$$

$$\mathbf{D}_3 = \mathbf{M}_1\mathbf{C}_2 + \mathbf{M}_2\mathbf{D}_2 \tag{25}$$

The coefficient required for the calculation of ΔZ is

$$\mathbf{D}^{(s)} = \mathbf{K}_1^{-1}(\boldsymbol{\alpha}a_4)\left\{-\mathbf{I}_1(\boldsymbol{\alpha}a_4)\mathbf{C}_1^{(e)} + \frac{2}{b}\mathbf{T}_4[\mathbf{I}_1(\mathbf{P}_3a_4)\mathbf{C}_4 + \mathbf{K}_1(\mathbf{P}_3a_4)\mathbf{D}_4]\right\} \tag{26}$$

Accordingly, the coil impedance variation is given by

$$\begin{aligned}\Delta Z &= \tfrac{i\omega}{I^2}\textstyle\int_V \boldsymbol{A}^{(s)}\cdot\boldsymbol{J}dV \\ &= \tfrac{\pi^2 i\omega N^2}{(r_2-r_1)^2(z_2-z_1)^2}\sum\limits_{n=1}^{\infty}\tfrac{\cos(\alpha_n z_1)-\cos(\alpha_n z_2)}{\alpha_n^3}[\chi(\alpha_n r_2)-\chi(\alpha_n r_1)]d_n^{(s)}\end{aligned} \tag{27}$$

where the current density J has been omitted (letting J = 1) to simplify the expression.

3. Eigenfunctions and the Associated Integrals of the Multi-Subdomain Regions

In the conventional TREE models, symbolic piecewise eigenfunctions are used for the air–metal multi-subdomain regions. With this approach, the TREE method is restricted to the two-subdomain problems (apart from certain problems of three subdomains). For problems involving air–metal regions of more subdomains, the overflow of the explicit eigenfunctions is inevitable, which raises serious difficulties in the numerical evaluations. Therefore, the eigenfunctions of (11a)–(11c) cannot be treated by the conventional TREE method.

In [18–20], the eigenvalue problem of (11a)–(11c) is reformulated in terms of a Sturm–Liouville problem. In accordance with [18–20], the eigenvalues of (11a) can be obtained by the solution of a generalized eigenvalue equation

$$\mathbf{K}\mathbf{U}_i = p_{1,i}^2 \mathbf{W}\mathbf{U}_i \tag{28}$$

where $\mathbf{K}$ is the stiffness matrix with the elements

$$\mathbf{K}_{mn} = \int_0^b \frac{1}{\mu_r^{(1)}(z)} \left[\frac{d\varphi_m(z)}{dz} \frac{d\varphi_n(z)}{dz} + k_1^2(z)\varphi_m(z)\varphi_n(z) \right] dz \tag{29}$$

and $\mathbf{W}$ is the damping matrix of the elements

$$\mathbf{W}_{mn} = \int_0^b \frac{\varphi_m(z)\varphi_n(z)}{\mu_r^{(1)}(z)} dz \tag{30}$$

where φ_m and φ_n are the FEM functions consisting of the Lagrange polynomials defined on the reference interval $-1 \leq \xi \leq 1$ (the shape functions).

A sparse matrix $\mathbf{K}$ will be generated from the FEM basis. Hence, Equation (28) can be solved by an efficient algorithm, such as Arnoldi iteration [27]. This solution provides both the eigenvalues $p_{1,i}$ and the eigenvectors $\mathbf{U}_i$, which are the discrete eigenfunctions $f_i(z)$. Moreover, denoting

$$\mathbf{U} = [\mathbf{U}_1, \mathbf{U}_2, \ldots]^{\mathrm{T}} \tag{31}$$

and by virtue of the vector normalization

$$\mathbf{U}' = \frac{\mathbf{U}}{\sqrt{\mathrm{diag}\left(\mathbf{U}\mathbf{W}\mathbf{U}^{\mathrm{T}}\right)}} \tag{32}$$

the eigenfunction normalization

$$\int_0^b \frac{1}{\mu_r^{(1)}} f_i^2(z) dz = 1 \tag{33}$$

can be established automatically. Equations (32) and (33) can be validated by inspecting the diagonal entries of $\mathbf{U}\mathbf{W}\mathbf{U}^{\mathrm{T}}$ and taking Equation (30) into account. Consequently, the orthonormality of (18b)–(18d) can be established.

The requirement of the accurate and efficient algorithm leads to the choice of high order Lagrange polynomials for the FEM basis. Here, we choose the cubic Lagrange polynomials

$$\begin{cases} N_0(\xi) = -\frac{1}{16}(\xi - 1)(3\xi - 1)(3\xi + 1) \\ N_1(\xi) = \frac{9}{16}(\xi - 1)(\xi + 1)(3\xi - 1) \\ N_2(\xi) = -\frac{9}{16}(\xi - 1)(\xi + 1)(3\xi + 1) \\ N_3(\xi) = \frac{1}{16}(\xi + 1)(3\xi - 1)(3\xi + 1) \end{cases} \tag{34}$$

The cubic interpolation of the eigenfunction is

$$f_i(z) = \sum_{e=0}^{3} u'_{l+e} N_e(z) \tag{35}$$

where u'_{l+e} is the successive four entries of U'_i, and $N_e(z)$ is obtained by (34) with the change in the variable

$$\xi = \frac{2z - z_a - z_b}{z_b - z_a} \tag{36}$$

where z_a and z_b are the mesh nodes corresponding to the reference interval. The numerical overflow of $f_i(z)$ is eliminated by this procedure. They are consequently well adapted for the subsequent integral computation. Furthermore, it appears to be very effective to evaluate directly the integrals (14)–(17) with the Clenshaw–Curtis quadrature, which is quoted here for completeness [28–30]

$$\int_{-1}^{1} f(x)\mathrm{d}x = \sum_{k=0}^{n} w_k f(x_k) \tag{37}$$

where the weights w_k are given by

$$w_k = \frac{g_k}{n}\left(1 - \sum_{j=1}^{\lfloor n/2 \rfloor} \frac{b_j}{4j^2-1}\cos(2jk\pi/n)\right) \tag{38}$$

and the quadrature nodes are

$$x_k = \cos\left(\frac{k\pi}{n}\right), k = 0, 1, \ldots, n \tag{39}$$

with

$$g_k = \begin{cases} 1\,, & k = 0, n \\ 2\,, & \text{otherwise} \end{cases} \tag{40}$$

$$b_j = \begin{cases} 1\,, & j = \frac{1}{2}n \\ 2\,, & \text{otherwise} \end{cases} \tag{41}$$

It follows from Equations (37)–(41) that the matrix elements of $\mathbf{T}_1$ can be computed by

$$\begin{aligned} \mathbf{T}_{1,ij} &= \int_0^b \sin(\alpha_i z) f_j(z) dz \\ &= \tfrac{b}{2}\int_{-1}^{1} \sin\left[\tfrac{b}{2}\alpha_i(1+x)\right] f_j\left[\tfrac{b}{2}(1+x)\right] dx \\ &= \tfrac{b}{2}\sum_{k=0}^{n} w_k \sin(\alpha_i z_k) f_j(z_k) \end{aligned} \tag{42}$$

where

$$z_k = \frac{b}{2}(1 + x_k) \tag{43}$$

The matrix elements of $\mathbf{T}_2$ are likewise given by

$$\begin{aligned} \mathbf{T}_{2,ij} &= \int_0^b \tfrac{1}{\mu_r^{(1)}} f_i(z) g_j(z) dz \\ &= \int_0^{b_1} f_i(z) g_j(z) dz + \tfrac{1}{\mu_r}\int_{b_1}^{b_3} f_i(z) g_j(z) dz + \int_{b_3}^{b} f_i(z) g_j(z) dz \\ &= \tfrac{b_1}{2}\sum_{k=0}^{n} w_k f_i\left(z_k^{(1)}\right) g_j\left(z_k^{(1)}\right) + \tfrac{b_3-b_1}{2}\sum_{k=0}^{n} w_k f_i\left(z_k^{(2)}\right) g_j\left(z_k^{(2)}\right) + \tfrac{b-b_3}{2}\sum_{k=0}^{n} w_k f_i\left(z_k^{(3)}\right) g_j\left(z_k^{(3)}\right) \end{aligned} \tag{44}$$

where

$$z_k^{(1)} = \frac{b_1}{2}(1 + x_k), z_k^{(2)} = \frac{b_3 + b_1}{2} + \frac{b_3 - b_1}{2}x_k, z_k^{(3)} = \frac{b + b_3}{2} + \frac{b - b_3}{2}x_k \tag{45}$$

The same analysis is also applicable to the matrix elements of $\mathbf{T}_3$ and $\mathbf{T}_4$. A flowchart is provided in Figure 4 to present the process of the novel approach.

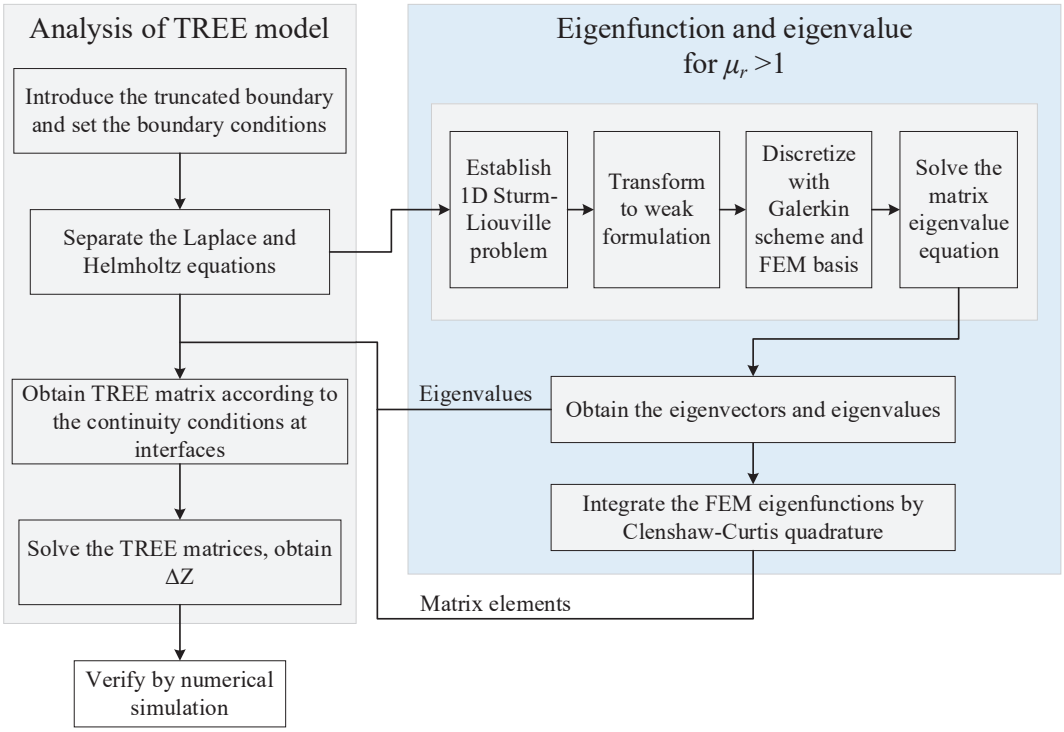

Figure 4. Flowchart of the TREE method enhanced by 1D FEM.

4. Numerical Validation

The proposed method will be verified with the parameters of the metal tube adapter and the induction coil given in Tables 1–3. The nonmagnetic alloy UNS (Unified Numbering System) C96400 (70-30 Copper-Nickel) and the magnetic stainless steels S31600 (austenitic) and S32760 (super duplex) [31] are used for the numerical validation. The coil impedance variations are calculated and plotted for these metal materials with different coil positions. The TREE results are compared with those from the FEM simulation of Comsol Multiphysics®(COMSOL Inc., Stockholm, Sweden), shown in Figure 5, where the theoretical and FEM data are denoted by solid lines and circles, respectively. The reactance of the isolated induction coil is $X_0 = \omega L_0$, with L_0 = 4.104132 mH, which can be found by the method such as in [32].

Table 1. Metals used for the tube adapter.

Metal (UNS)	Conductivity σ (MS/m)	Relative Permeability μ_r
C96400	2.9	1
S31600	1.33	1.02
S32760	1.25	29

Table 2. Geometry of the metal tube adapter.

Parameter		Parameter	
a_1 (mm)	5	b_1 (mm)	40
a_2 (mm)	8	b_2 (mm)	48
a_3 (mm)	11	b_3 (mm)	51
a_4 (mm)	14	b_4 (mm)	59
b (mm)	100		

Table 3. Parameters of the induction coil.

Parameter	
Inner radius r_1 (mm)	15
Outer radius r_2 (mm)	18
Axial length $z_2 - z_1$ (mm)	6
Number of turns	300

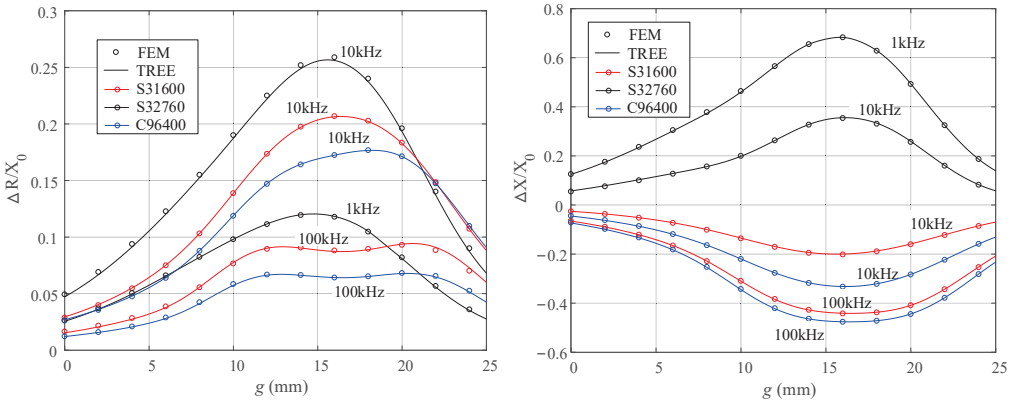

Figure 5. Normalized impedance variations with the abscissa representing the parameter g. (**a**) The resistance variation. (**b**) The reactance variation.

Further calculations are carried out for the coil impedance variation with respect to the frequencies. For the alloys of lower μ_r (C96400 and S31600), the calculation frequency ranges from 1 kHz to 100 kHz, for higher μ_r (S32760), the frequency interval [100 Hz, 10 kHz] is chosen. The results are shown in Figures 6 and 7, where the TREE data are plotted by solid lines in connection with the circles representing the data of the FEM simulation. Other parameters are referred to in Tables 2 and 3.

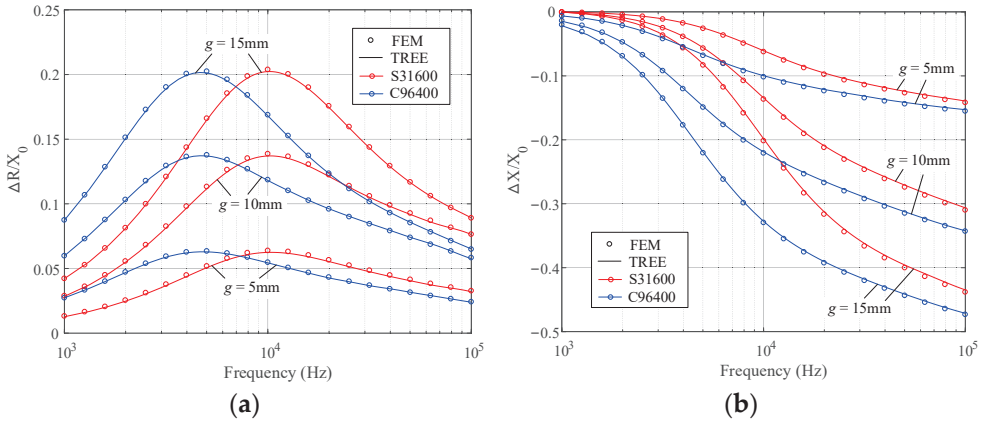

Figure 6. Normalized impedance variations with the abscissa representing the frequency. The alloys are C96400 and S31600. (**a**) The resistance variation. (**b**) The reactance variation.

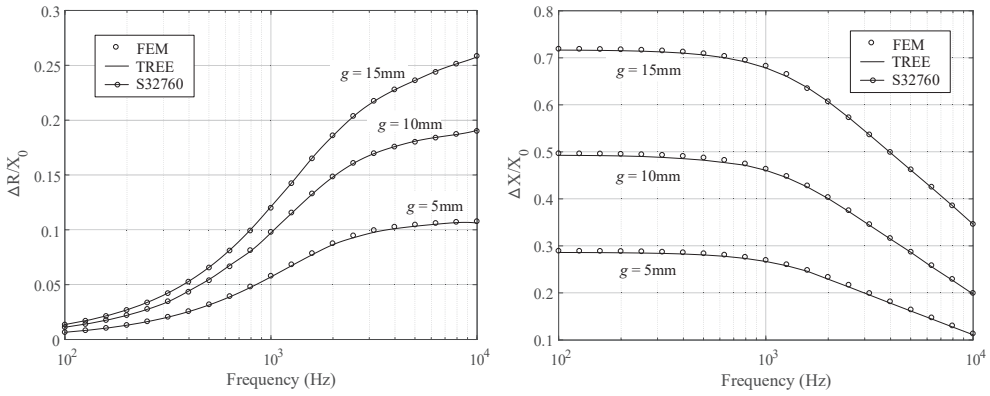

(**a**) (**b**)

Figure 7. Normalized impedance variations with the abscissa representing the frequency. The alloy is S32760. (**a**) The resistance variation. (**b**) The reactance variation.

Very good agreement is obtained between the TREE and FEM results in the numerical comparisons. The calculations were implemented on a personal computer of a 4.2 GHz processor (Intel® Core i7-7700K) and 16 GB RAM. Additional algorithm details are shown in Table 4, where the frequencies, summation terms (matrix size), mesh elements, and quadrature nodes used in the computation are listed. The execution time of the eigenvalue and eigenfunction computation and the total execution time of the TREE evaluation are also provided. No more than 1.5 s (including the time consumed by the calculation of eigenvalues and eigenfunctions) are needed for a TREE evaluation. The satisfactory algorithm efficiency provides evidence for this.

Table 4. Computation configuration and execution time of TREE method.

Metal (UNS)	Frequency	Summation Terms	Quadrature Nodes	Mesh Elements	Execution Time of Eigenvalue and Eigenfunction Computation	Total Execution Time
S31600	10 kHz	30	80	510	0.19 s	0.55 s
	100 kHz	40	80	510	0.26 s	0.73 s
S32760	1 kHz	55	80	510	0.36 s	1.00 s
	10 kHz	70	90	510	0.54 s	1.30 s
C96400	10 kHz	30	80	510	0.19 s	0.56 s
	100 kHz	50	80	510	0.34 s	0.90 s

5. Conclusions

The interaction of an eddy current coil with a metal tube adapter has been investigated using the TREE method. The numerical overflow for symbolic eigenfunctions of air–metal multi-subdomain regions has been removed via the normalization of the eigenvectors, and a satisfactory computational speed was achieved using the Clenshaw–Curtis quadrature rule applied to the integrals associated with the numerical eigenfunctions. The calculation accuracy has been verified by the numerical comparisons, and the efficiency of our approach has also been confirmed. Considerable potential has been shown for the development of new analytical models with the aid of the proposed approach.

Author Contributions: Conceptualization, Y.L. and X.Y.; methodology, Y.L.; software, Y.L. and X.Y.; data curation, X.Y.; writing—original draft preparation, Y.L.; writing—review and editing, Y.L. and X.Y. All authors have read and agreed to the published version of the manuscript.

Funding: This research received no external funding.

Institutional Review Board Statement: Not applicable.

Informed Consent Statement: Not applicable.

Data Availability Statement: Data sharing not applicable.

Conflicts of Interest: The authors declare no conflict of interest.

References

1. Dodd, C.V.; Deeds, W.E. Analytical solutions to eddy current probe-coil problems. *J. Appl. Phys.* **1968**, *39*, 2829–2838. [CrossRef]
2. Hannakam, L.; Tepe, R. Feldschwächung durch leitende Rechteckzylinder im Luftspalt. *Arch. Elektrotechnik* **1979**, *61*, 137–144. [CrossRef]
3. Theodoulidis, T.; Kriezis, E. *Eddy Current Canonical Problems (with Applications to Nondestructive Evaluation)*; Tech Science Press: Forsyth, GA, USA, 2006.
4. Theodoulidis, T. Model of ferrite-cored probes for eddy current nondestructive evaluation. *J. Appl. Phys.* **2003**, *93*, 3071–3078. [CrossRef]
5. Theodoulidis, T.; Bowler, J. Eddy current coil interaction with a right-angled conductive wedge. *Proc. R. Soc. A* **2005**, *461*, 3123–3139. [CrossRef]
6. Bowler, J.; Theodoulidis, T. Eddy currents induced in a conducting rod of finite length by a coaxial encircling coil. *J. Phys. D Appl. Phys.* **2005**, *38*, 2861–2868. [CrossRef]
7. Theodoulidis, T.; Kriezis, E. Series expansions in eddy current nondestructive evaluation models. *J. Mater. Process. Technol.* **2005**, *161*, 343–347. [CrossRef]
8. Theodoulidis, T.; Bowler, J. Eddy-current interaction of a long coil with a slot in a conductive plate. *IEEE Trans. Magn.* **2005**, *41*, 1238–1247. [CrossRef]
9. Bowler, J.; Theodoulidis, T. Coil impedance variation due to induced current at the edge of a conductive plate. *J. Phys. D Appl. Phys.* **2006**, *39*, 2862–2868. [CrossRef]
10. Hannakam, L.; Kost, A. Leitender Rechteckkeil im Felde einer Doppelleitung. *Arch. Elektrotechnik* **1982**, *65*, 363–368. [CrossRef]
11. Hannakam, L.; Orglmeister, R. Induzierte Wirbelstrombelag an ausgeprägten Massivpolen hoher Permeabilität bei Wanderfelderregung. *Arch. Elektrotechnik* **1984**, *67*, 49–55. [CrossRef]
12. Filtz, M.; Nethe, A. Bemerkung zur Lösung des dreidimensionalen Wirbelstromproblems in Kreiszylindern endlicher Länge. *Arch. Elektrotechnik* **1993**, *76*, 195–200. [CrossRef]
13. Filtz, M.; Nethe, A. Anregung dreidimensionaler Wirbelströme in massiven Kreizylindern endlicher Länge durch ein homogenes magnetisches Wechselfeld beliebiger Ausrichtung. *Arch. Elektrotechnik* **1990**, *73*, 227–237. [CrossRef]
14. Theodoulidis, T.; Bowler, J. Interaction of an eddy-current coil with a right-angled conductive wedge. *IEEE Trans. Magn.* **2010**, *46*, 1034–1042. [CrossRef]
15. Delves, L.; Lyness, J. A numerical method for locating the zeros of an analytic function. *Math. Comput.* **1967**, *21*, 543–560. [CrossRef]
16. Tytko, G.; Dawidowski, L. Locating complex eigenvalues for analytical eddy-current models used to detect flaws. *Compel* **2019**, *36*, 1800–1809. [CrossRef]
17. Vasic, D.; Ambrus, D.; Bilas, V. Computation of the eigenvalues for bounded domain. *IEEE Trans. Magn.* **2016**, *52*, 7004310. [CrossRef]
18. Yang, X.; Luo, Y.; Kyrgiazoglou, A.; Zhou, X.; Theodoulidis, T.; Tytko, G. Impedance variation of a reflection probe near the edge of a magnetic metal plate. *IEEE Sens. J.* **2023**, *23*, 15479–15488. [CrossRef]
19. Yang, X.; Luo, Y.; Kyrgiazoglou, A.; Tytko, G.; Theodoulidis, T. An analytical model of an eddy-current coil near the edge of a conductive plate. *IET Electr. Power Appl.* **2022**, *16*, 1017–1029. [CrossRef]
20. Theodoulidis, T.; Skarlatos, A.; Tytko, G. Computation of eigenvalues and eigenfunctions in the solution of eddy current problems. *Sensors* **2023**, *23*, 3055. [CrossRef]
21. Stahlmann, H.D. Der Differentialtransformator als induktiver Stellungsmelder. *Arch. Elektrotechnik* **1983**, *66*, 277–281. [CrossRef]
22. Sun, H.; Bowler, J.; Theodoulidis, T. Eddy currents induced in a finite length layered rod by a coaxial coil. *IEEE Trans. Magn.* **2005**, *41*, 2455–2461.
23. Skarlatos, A.; Theodoulidis, T. Calculation of the eddy-current flow around a cylindrical through-hole in a finite-thickness plate. *IEEE Trans. Magn.* **2015**, *15*, 6201507. [CrossRef]
24. Luo, Y. Field and inductance calculations for coaxial circular coils with magnetic cores of finite length and constant permeability. *IET Electr. Power Appl.* **2017**, *11*, 1254–1264. [CrossRef]
25. Courant, R.; Hilbert, D. *Methoden der Mathematischen Physik I*; Springer: New York, NY, USA, 1968.
26. Abramowitz, M.; Stegun, A. *Handbook of Mathematical Functions*; US Government Printing Office: Washington, DC, USA, 1972.
27. Arnoldi, W.E. The principle of minimized iterations in the solution of the matrix eigenvalue problem. *Q. Appl. Math.* **1951**, *9*, 17–29. [CrossRef]
28. Olver, F.; Lozier, D.; Boisvert, R.; Clark, C. *NIST Handbook of Mathematical Functions*; Cambridge University Press: New York, NY, USA, 2010.
29. Clenshaw, C.; Curtis, A. A method for numerical integration on an automatic computer. *Numer. Math.* **1960**, *2*, 197–205. [CrossRef]
30. Hildebrand, F.B. *Introduction to Numerical Analysis*; Dover Publications: Mineola, NY, USA, 1987.

31. Boniardi, M.; Casaroli, A. Rostfreie Edelstähle. Available online: http://www.fa-fe.com/files/pdf/libri_articoli/de/1-Rostfreie_Edelstahle.pdf (accessed on 15 August 2023).
32. Conway, T. Inductance calculations for circular coils of rectangular cross section and parallel axes using Bessel and Struve functions. *IEEE Trans. Magn.* **2010**, *46*, 75–81. [CrossRef]

applied sciences

MDPI

Article

A Through-Transmission Ultrasonic Method for the Detection of Ferrite Tile Defects

Kaiheng Huang [1], Qiaolin Li [1,*], Kaixiong Zhu [1], Baihan Chen [1], Xiang Qian [1], Xiaohao Wang [1] and Xinghui Li [1,2]

[1] Shenzhen International Graduate School, Tsinghua University, Shenzhen 518055, China; hkh21@mails.tsinghua.edu.cn (K.H.); zkx18@mails.tsinghua.edu.cn (K.Z.); chen_baihan@163.com (B.C.); qian.xiang@sz.tsinghua.edu.cn (X.Q.); wang.xiaohao@sz.tsinghua.edu.cn (X.W.); li.xinghui@sz.tsinghua.edu.cn (X.L.)

[2] Tsinghua-Berkeley Shenzhen Institute, Tsinghua University, Shenzhen 518055, China

* Correspondence: li.qiaolin@sz.tsinghua.edu.cn

Abstract: A through-transmission ultrasonic method is proposed to address limitations in conventional ultrasonic reflection methods for non-destructive testing of ferrite tiles. The method utilizes a dual-probe configuration on both sides of the test piece to measure ultrasonic transmission signals, overcoming issues related to blind zones and orientation limitations in pulse-echo reflection methods. This method demonstrates excellent capabilities for full inspection of internal and external defects in ferrite tiles. Physical field finite element simulations were conducted to analyze detection capabilities and a transmissive testing system is developed based on the simulation results. Experimental validation was performed on artificially manufactured quantified defect samples in aluminum alloy, and the same testing system was applied to evaluate ferrite tile samples. The results confirmed the effectiveness of the system in distinguishing defective (NG) signals from normal defect-free (OK) signals, with a recall rate of at least 95% on samples of various sizes up to 0.1 mm. This research provides insights for quality control and defect detection technology in ferrite tiles.

Keywords: through-transmission; ultrasonic testing; defect detection; ferrite tile

1. Introduction

Ferrite tiles are critical components in permanent magnet motors [1–3]. However, due to their high hardness and brittleness, they are prone to defects during the manufacturing process, which can adversely affect the performance and lifespan of permanent magnet motors. These defects include external flaws such as fractures and burrs, as well as internal flaws like cracks and voids [4,5]. To reduce production costs and improve efficiency, non-destructive testing of internal and external defects in ferrite tiles is required before they are magnetized to become magnetic tile products. In recent years, acoustic vibration methods have been proposed for detecting internal defects in ferrite tiles. For instance, Lu [3] applied acoustic methods to detect internal defects in ferrite tiles by analyzing the sound signals generated when the tiles were impacted by an iron block. Xie et al. [6] investigated the effectiveness of the PCA-SVM (Principal Component Analysis-Support Vector Machines) method based on acoustic resonance for detecting internal defects in ferrite tiles. On the other hand, machine vision methods have been utilized to inspect external defects in ferrite tiles. Xie et al. [1] introduced a feature fusion CNN (Convolutional Neural Networks) to address continuous image defect recognition, while Hu et al. [7] proposed a two-stage detection model called UPM-Dense Net (Upscaled PatchMatch Dense Network) to meet the precision and speed requirements for detecting small defects. Compared to other non-destructive testing methods, ultrasonic inspection offers a simple testing system and strong robustness, making it applicable to a wide range of materials. Consequently, in industrial applications, the ultrasonic test has found extensive use in areas such as detecting internal defects, measuring material properties, and health monitoring [8–10]. M. Liu et al. [11]

conducted time-domain analysis of the weld defect echo signal of stainless steel pipes according to the weld defect echo signal of stainless steel pipes, compared and analyzed the amplitude changes of different types of weld defect signals, and realized the detection of weld defects. Typically, ultrasonic pulse-echo methods detect sample defects by analyzing the time and frequency domain characteristics of echo signals. For defect detection in ferrite tiles, Cheng et al. [12] developed a pulse-echo-based approach that improved the B-scan (Brightness Scan) imaging and accurate localization of internal defects in the tiles. However, when defects are located near or at the surface of the sample, the impedance mismatch between the probe, sample, and coupling agent leads to strong surface echoes, making defect detection challenging [13,14]. As a result, ultrasonic pulse-echo methods have limitations in terms of detection accuracy and sample structures [15]. In the realm of ultrasonic testing (UT), ultrasonic transmission emerges as a defect detection technique that overcomes the limitations of traditional methods, allowing for the inspection of near-surface and surface defects and the measurement of various material properties. Several studies both domestically and internationally have utilized ultrasonic transmission methods for defect detection and measurement [16–21]. For instance, Wang [22] employed ultrasonic transmission for defect detection in complex curved resin-based composite materials, demonstrating the capability of the ultrasonic transmission method to detect bending composite parts with the aid of an automatic robot inspection system. These research outcomes suggest that ultrasonic transmission method has the potential for comprehensive defect inspection of both internal and external defects in ferrite tiles.

The ultrasonic echo test of ferrite tiles posed several challenges during the experiments. These challenges included the high damping attenuation in ferrite tiles, leading to weak echo signals and a low signal-to-noise ratio in the pulse-echo method. Moreover, the pulse-echo method exhibited more pronounced blind zones in small-sized ferrite tile samples, making defect detection difficult. Additionally, the detection of common longitudinal cracks in ferrite tiles was hindered by the influence of defect orientation. To address these difficulties, a water-immersion ultrasonic transmission method for ferrite tiles is proposed. The effectiveness of this method is validated through finite element simulation, test system design, and experimental verification. By utilizing the ultrasonic transmission method, the paper overcomes the limitations of the conventional pulse-echo method and provides a promising solution for comprehensive defect detection in both the internal and external regions of ferrite tiles.

2. Principle of Defect Detection by Liquid-Immersed Ultrasonic Transmission Method

The ultrasonic transmission method is a detection method developed based on the loss of ultrasonic waves in the medium, including the phenomena of absorption of sound waves, dissipation, scattering at interfaces, and attenuation of the diffusion of the sound beam. During the measurement, a pair of transmitting probes and receiving transducers are placed on both sides of the sample to be measured. When a piezoelectric crystal inside the transmitting probe is excited by a pulsed voltage, pulsed ultrasonic waves propagate through the sample. A focusing transducer was employed in the transmitting probe for the focus of the ultrasonic beam. This is achieved by applying an acoustic lens, which increases the sound intensity inside the sample and therefore the signal-to-noise ratio. When ultrasound is applied to the non-destructive testing of internal defects, the main consideration is the scattering and attenuation of the defects encountered by the ultrasound waves during propagation. As shown in Figure 1, ultrasonic waves are emitted from the transmitting probe at an angle perpendicular to the sample surface and propagate into the sample through the coupling agent water. When the ultrasonic wave encounters a defect during the propagation of the sample under test, a portion of the ultrasonic wave will be lost at the junction of the sample and the defect, i.e., between different media, and a certain range of masking will be formed behind the defect. According to the loss of ultrasonic energy, it is then possible to determine the presence and size of defects, including internal and external defects.

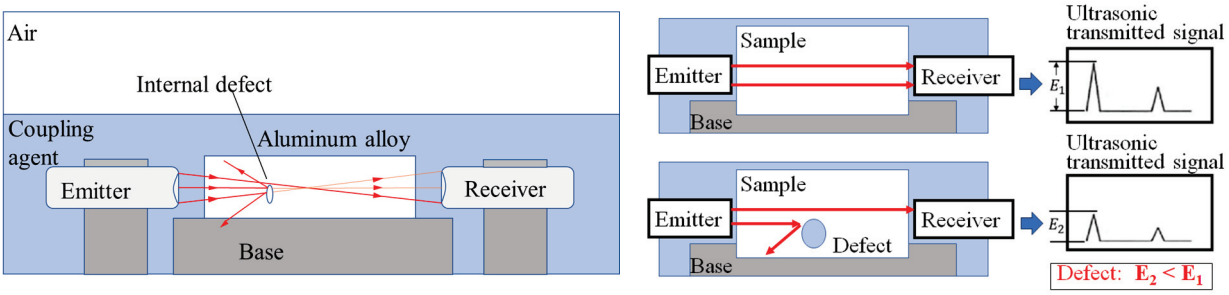

Figure 1. Focusing liquid immersion ultrasonic transmission detection method; (**a**) system diagram (**b**) the basis for judging defects.

The ultrasonic signal propagated through the coupling agent can be distinguished from the ultrasonic signal propagated through the solid sample. Because the speed of sound in a solid, such as a ferrite tile, is about 6700 m/s at room temperature of 25 °C, which is significantly higher than the speed of sound in a liquid, such as water, which is about 1500 m/s, the time of flight (TOF) for propagating the same distance of sound waves in a ferrite tile is only 1/4 of that in a water medium, resulting in the received signals showing a significant difference in the time domain. Based on the cleaning requirements after sample testing and the principle of acoustic impedance matching, the coupling agent was selected as water.

Ultrasonic waves can be regarded as linear propagation in an isotropic ideal medium, following the geometric acoustic law. Let the initial sound pressure p_0, the received sound pressure is P_i, the ultrasonic angular frequency is ω, the imaginary number unit is j and the wave number be $k = 2\pi/\lambda$, respectively. The ultrasonic sound pressure p at the sound range r is

$$\mathrm{p}_i(r,t) = \frac{p_0}{\mathrm{r}} e^{j(\omega t - kr)} \tag{1}$$

The transmittance T of ultrasonic waves between a medium with acoustic impedances z_1 and z_2 is

$$T = \left(\frac{4z_1 z_2}{z_1 + z_2}\right)^2 \tag{2}$$

The acoustic transmittance decreases with the increase of the acoustic impedance difference between the two sides of the dielectric interface. To ensure the sufficient intensity of acoustic transmission into the sample, it is necessary to match the acoustic impedance of the medium on both sides of the interface, so it is necessary to insert the liquid coupler with large acoustic impedance between the probe and the sample.

As the thickness of the thin-walled sample is less than the diameter of the probe, the perforated circular hole defect is regarded as a rigid sphere with radius a. The direction of the incident sound wave is the positive direction of θ. The wave equation of sound wave propagation is $\nabla^2 p + (\frac{\omega}{c})^2 p = 0$, then the far-field scattered sound pressure at a distance of r from the defect can be calculated by Equation (3) where j is the imaginary number unit, and $R(\theta)$ is the directionality function of the scattered sound field [23,24]:

$$p_i(r,\theta,t) = -p_0 a \frac{e^{j(\omega t - kr)}}{r} R(\theta) \tag{3}$$

The size of the $R(\theta)$ function is determined by the defect size parameter ka, which is a dimensionless parameter characterizing the defect size relative to the wavelength, expressed as shown in Equation (4) where $P_l(x)$ is the Legendre polynomial:

$$R(\theta) = \frac{1}{ka} \sum_{l=0}^{\infty} b_l e^{j\frac{l+1}{2}\pi} P_l(\cos\theta) \tag{4}$$

$$b_l = -\frac{B_l}{p_0} = (-j)^l(2l+1)\frac{\frac{d[j_l(ka)]}{d(ka)}}{\frac{d\left[h_l^{(2)}(ka)\right]}{d(ka)}} \tag{5}$$

Therefore, in an ideal isotropic medium, the sound pressure p_s received by the probe is approximately:

$$p_s(r,\theta,t) \approx \pi\left(R_r^2 - aR(\theta)\right)\frac{e^{j(\omega t - kr)}}{r} \tag{6}$$

From the formula: with the increase of the defect size, the scattered acoustic field acoustic wave sound pressure increases. Therefore, defects can be identified from the signal energy when the transmitted signal energy appears to be significantly weakened. The signal energy is defined as:

$$\mathrm{E} = \int P_s^2 dt = \sum A_i^2 \tag{7}$$

The signal energy is the integral of the square of the sound pressure received by the probe, and the sampling in practice is the amplitude A_i of the sampling point of the transmitted signal. When an ultrasonic wave encounters the interface between the medium transition in defects and samples, interactions such as attenuation and diffraction occur, which will further reduce the signal energy of the transmitted acoustic wave propagation. Therefore, it can be concluded that when the cross-sectional area of the defect is larger, the sound pressure of the ultrasonic transmitted signal is smaller. By comparing the energy of the acoustic signal, the defects and their sizes in the sample can be detected.

Based on the above conclusions, a device for detecting internal and external defects of magnetic tile samples by immersion focused transmission method is developed in this paper. Its characteristics include: the ultrasonic transmission method using one end to emit a specific frequency of ultrasonic waves, the other end to receive the corresponding sound waves, according to the waveform diagram to judge the presence and size of defects; the transmitting probe, the sample under test, and the receiving probe are immersed in the coupler to reduce the loss of ultrasonic waves between the air and the interface of the workpiece under test. This will be beneficial to the acquisition signal processing of transmitted sound waves, including filtering of transmitted wave signals in the time-frequency domain, peak extraction and so on.

3. Numerical Modeling

3.1. Establishment of Simulation Model

To assess the feasibility of ultrasonic detection for internal defects, this study employed COMSOL Multiphysics v.6 software for modeling the water-immersion ultrasonic inspection method [25–29]. In the physical field modeling, the pressure acoustics time-domain explicit physics interface was chosen for simulation modeling. The schematic representation of the overall simulation model is shown in Figure 2. Due to the symmetry of the entire model, the geometric model was set as an axisymmetric model to reduce computational time and memory requirements. The model was divided into three parts, namely, A, B, and C. Part A comprised the ultrasonic emission source and the coupling water layer. Part B represented the 3033 aluminum alloy test material with internal defects, with dimensions of 10 mm × 42 mm. Part C consisted of the coupling agent layer and the ultrasonic wave receiving transducer. The coupling material was set as water, and the thickness of the coupling layer was set at 3.5 mm. The outer side of the transmission model is completely enclosed by the ideal absorbing layer to prevent the reflection phenomenon in the boundary of the local model, and the simulated sample domain and the coupling domain extend indefinitely in this direction.

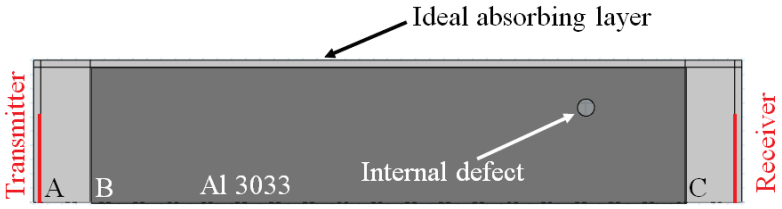

Figure 2. Internal defect detection model by liquid immersion ultrasonic transmission.

The excitation signal equation V_0 was defined as follows:

$$V_0 = e^{\left(\frac{t-2t_0}{t_0/2}\right)^2} sin(2\pi f_0 t) \quad (8)$$

where t_0 is the period of the ultrasonic wave, and f_0 is the frequency of the ultrasonic wave.

The ultrasonic frequency was set at 10 MHz, and the defect diameter ranged from 0.1 mm to 1.2 mm. The simulation time step was set at 1/10 of the ultrasonic signal period, i.e., 0.2 μs, to ensure sufficient sampling of the ultrasonic transmission signal.

3.2. Analysis of Simulation Results

3.2.1. Ultrasonic Wave Propagation in the Medium

Figure 3 shows the propagation of ultrasonic waves in different periods in the medium when detecting a circular cavity. It can be seen from the figure that the longitudinal wave and Rayleigh wave are generated and propagated together when ultrasonic wave occurs, and the longitudinal wave propagates along the normal direction with the fastest velocity. At the interface between water and the part to be tested, the ultrasonic wave is partially reflected. Because the pressure acoustic physical field interface is used to deal with the ultrasonic wave propagation in the solid, the shear wave generated by waveform conversion cannot be seen. While the longitudinal wave continues to propagate forward, the echo on the upper surface of the aluminum alloy block also oscillates back and forth in the coupled water layer and partially enters the aluminum alloy block. These waveforms will lead to the detection of different strong and weak waveforms at different times when the transmitted wave is detected. The wavelength of ultrasonic waves in aluminum alloy medium is 2.5 mm. Figure 3d shows that when it meets the circular hole defect with a diameter of 0.8 mm during its propagation, part of the reflection occurs, which leads to the reduction of the transmitted wave energy compared with that without the defect.

3.2.2. Detection Results of Different Defects at Different Locations

The simulation calculation was carried out by changing the defect diameter from 0.4 mm, 0.6 mm, 0.8 mm, 1.0 mm, 1.2 mm and the defect depth from 7 mm, 14 mm, 21 mm, 28 mm, and 35 mm. The simulation results are shown in Figure 4. The range of the first signal peak of the transmitted energy is integrated by the square of the sound pressure. It can be seen that when the defect position is unchanged, the transmission detection results of each depth independently indicated that the larger the defect diameter, the smaller the detected transmission amplitude and energy. There is a significant linear relationship between the ultrasonic energy attenuation and the size of the defect, which is consistent with the theoretical calculation results in Section 2. The principle of flooding ultrasonic transmission method for defect detection is based on this law, and the size of the defect is determined by the attenuation of energy.

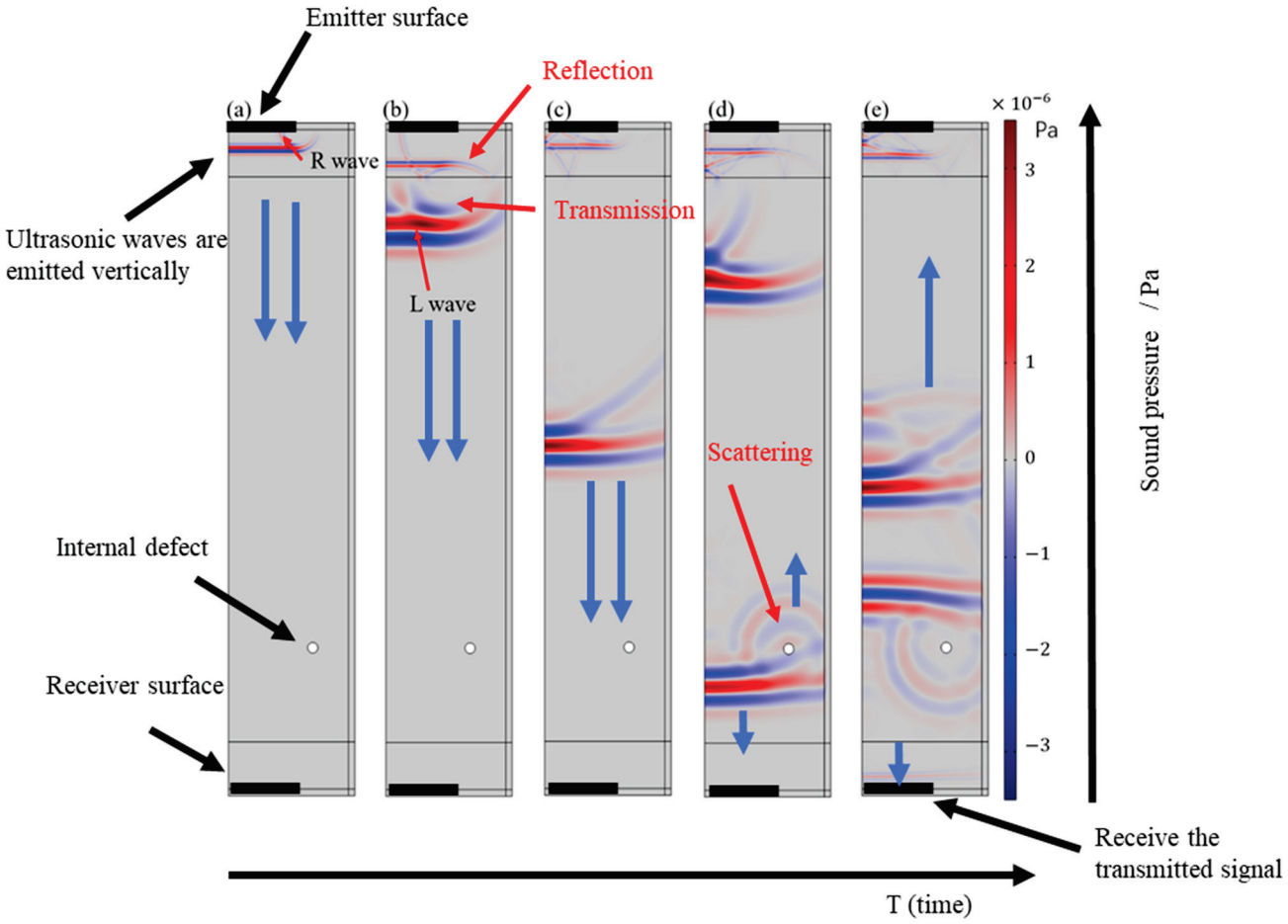

Figure 3. Sound pressure distribution of ultrasonic wave in the medium at different times: (**a**) 1.4 μs; (**b**) 4 μs; (**c**) 6.4 μs; (**d**) 9.0 μs; (**e**) 11.8 μs. Rayleigh waves (R wave), longitudinal waves (L wave).

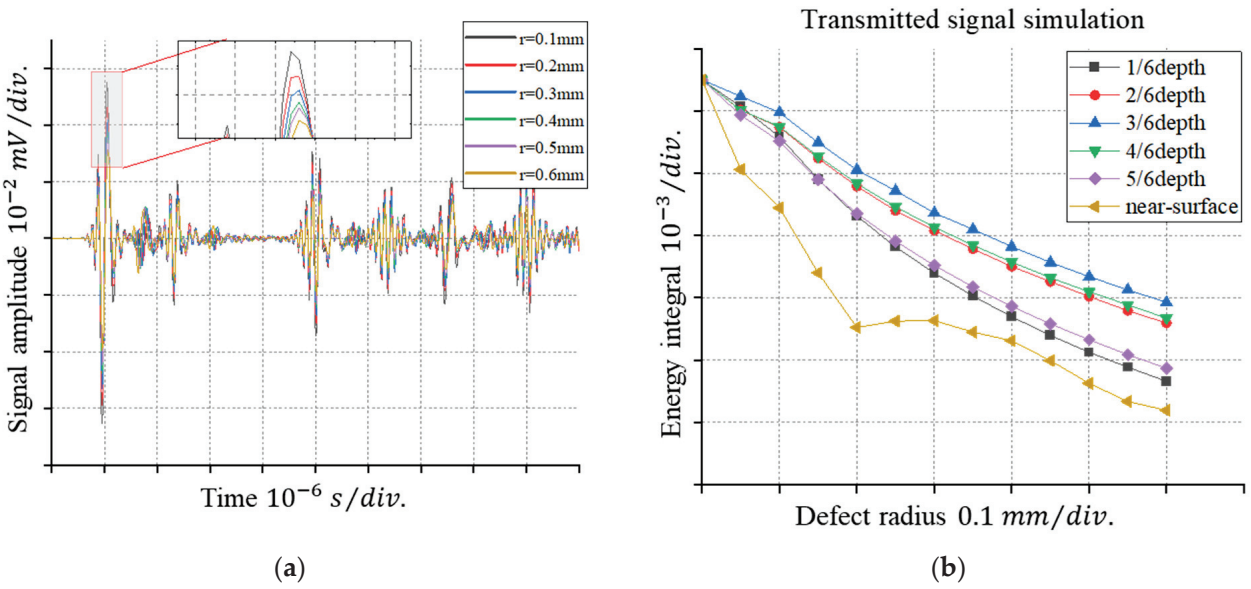

Figure 4. Ultrasonic transmission simulation results: (**a**) simulation signal in time domain (**b**) Energy map of the simulation.

4. Design and Experimentation of the Ultrasonic Transmission System

4.1. Design of Defect Detection System

The functional requirements of the detection system include aligning the probe to the fixed sample position, transmitting and acquiring ultrasonic signals, and processing the ultrasonic signals for defect assessment. As shown in Figure 5, to meet these system functions, the ultrasonic transmission inspection system consists of three parts: an automated ultrasonic wave emission and reception system, a fixture assembly, and a data post-processing system.

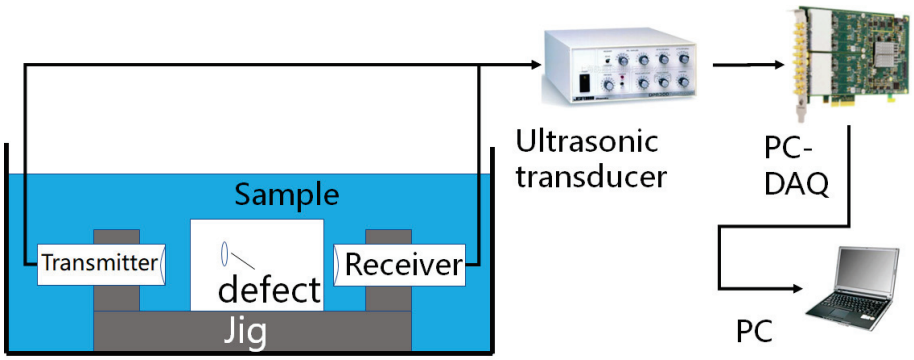

Figure 5. System composition.

The ultrasonic wave emission and reception system consist of a 100 MHz data acquisition card, a DPR300 ultrasonic pulse generator and receiver, and two 10 MHz focused probes. The two probes operate in a send-receive mode, where one probe is used to transmit ultrasonic signals through the tested sample and the other to receive and convert the transmitted ultrasonic signals into electrical signals. The ultrasonic receiver sends the data to the acquisition card and converts it into digital signals. The probes and fixture assembly are immersed in coupling agent to reduce the acoustic impedance between the probes and the sample.

As shown in Figure 6, the fixture assembly includes three parts: the base, the probe holder, and the sample holder. The base provides support and has two through-slides in different directions, restricting the movement of the holders to specific directions. The probe holder consists of rails of different heights and a probe fixture, which elevates the probes to a certain height and aligns them with each other, with the ability to adjust the distance between the probes. The sample holder also consists of rails of different heights and a probe fixture, with the rails oriented perpendicular to those of the probe holder, allowing the adjustment of the sample height to align the test area with the centerline of the probes. Each fixture can slide horizontally to adjust the horizontal position of the test sample.

The system achieves precise alignment of the transmitting probe, defect, and receiving probe, as well as the ability to quickly adjust the scanning position in the ultrasonic transmission defect detection system, by organically connecting the components of the fixture system through the slides.

The data post-processing system consists of a personal computer that utilizes a differential peak-seeking algorithm to determine the positions of the wave peaks, locate the ultrasonic transmission signal peaks, and calculate the energy of the sample signals.

4.2. Experimental Operation and Data Processing

The experimental procedure is as follows: firstly, the sample is securely fixed with the probe using a fixture, ensuring precise alignment between the probe and the sample. Next, the PC data acquisition program and motion platform are activated to scan the sample surface and collect data to obtain ultrasonic transmission signals. By analyzing the signals, the sample intervals are determined, and their energy characteristics are computed.

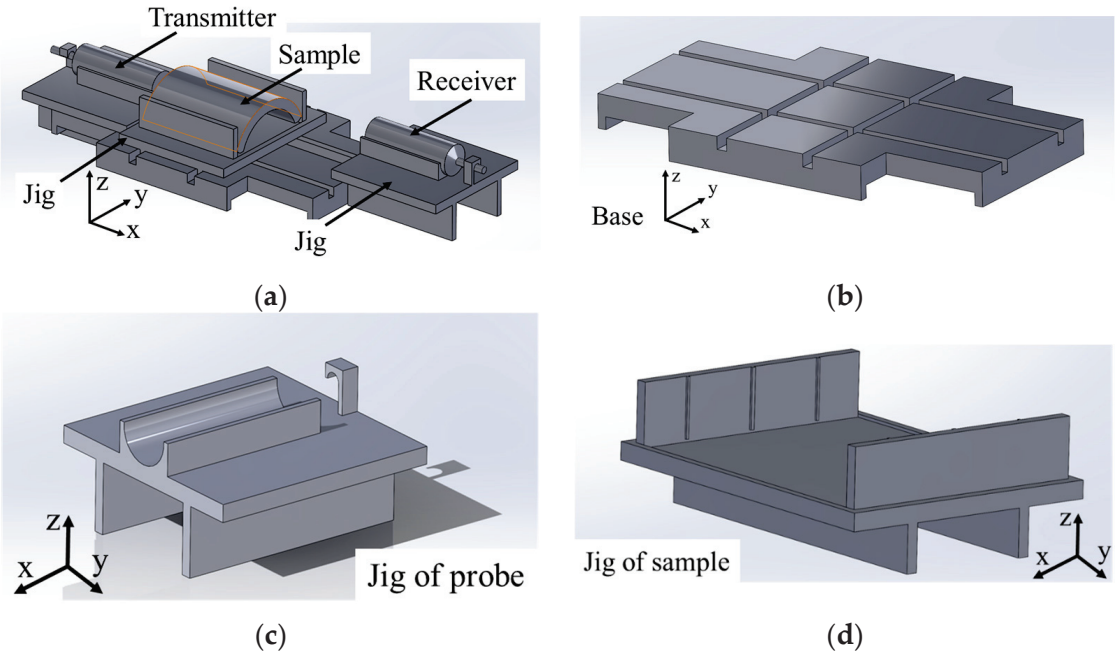

Figure 6. Fixture set assembly: (**a**) Assembly; (**b**) base; (**c**) probe clamp; (**d**) sample clamp.

As shown in Figure 7, the analysis of ultrasonic transmission signals reveals their components and sources: part 1 corresponds to the emission signature generated by circuit coupling, indicating the initiation of ultrasonic wave transmission. Part 2 represents the sample transmission signal, which is the ultrasonic wave signal passing through the sample and coupling agent via the shortest path during transmission. Its energy reflects the presence of obstacles in the transmission path. Therefore, calculating the total energy of the transmission signal provides the ultrasonic transmission energy of the sample. The signals that appear between the second and the third part are generated by ultrasonic waves repeatedly reflecting between the sidewall and surface of the measured sample, forming a series of gradually decreasing signal peaks. This part of the signal is categorized into delayed waves and triangular echoes based on their generation causes [30]. Due to the prolonged transmission path, they appear later than the second part. Part 3 corresponds to the water transmission signal. This signal is formed when ultrasonic waves only pass through the coupling medium without entering the sample for propagation, as water has a slower sound velocity compared to the solid sample, resulting in a delayed appearance.

The energy of the ultrasonic transmission signal from each emission is defined as the square of the integral of the amplitude of the signal peak in the transmission signal. Comparing the energy of the sample's transmission signal peaks with that of intact samples from the same batch can reveal the presence of defects. Since ultrasonic waves undergo multiple reflections and superimpose at the probe-water interface and sample-water interface, only the first received transmission signal peak in the time domain is considered for energy calculation, as it is less affected by interference compared to other multiply-reflected ultrasonic signals. This signal is generated by ultrasonic waves propagating along the shortest path between the probes, experiencing less interference compared to other multiply-reflected ultrasonic signals.

4.3. Experimental Results

4.3.1. Transmission Test of Aluminum Alloy Sample

The purpose of the ultrasonic transmissive experiments is to validate the detection sensitivity and capability of the proposed ultrasonic transmissive method for external defect detection. Precise cavities of varying sizes and depths were fabricated to simulate internal defects, and the defect detection system's ability to detect defects of different sizes

was tested. The ferrite tiles have a sound impedance of 28.3. Among commonly used CNC machining materials, as shown in Table 1, the aluminum alloy exhibits similar acoustic properties, with sound impedance and velocity relatively close to those of ferrite tiles. Therefore, the aluminum alloy was used to quantitatively validate the defect detection pattern using the ultrasonic transmissive method.

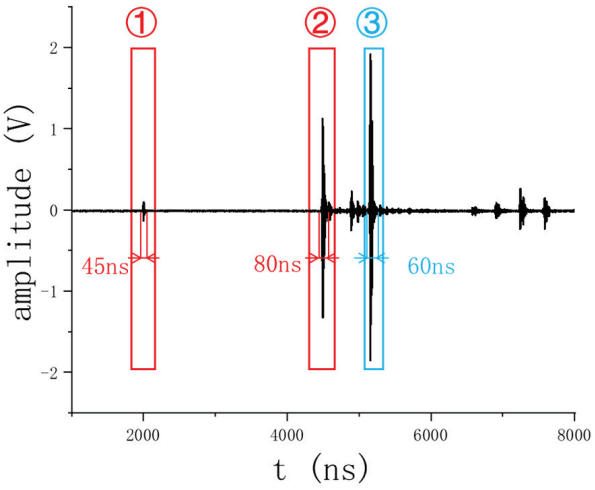

Figure 7. Example of ultrasonic transmission signal.

Table 1. Acoustic indicators of common materials.

Material	Acoustic Impedance gm/(cm^2·s)	Sound Velocity (25 °C) km/s
Ferrite	28.3	6.7
Aluminum	17.0	6.3
Copper	41.6	4.7
Steel and Stainless	45.4	5.8
Iron	45.4	5.9
Magnesium	10.1	5.77

The first set of experiments focused on artificially created aluminum alloy samples with defects. Circular hole defects of different depths (7 mm, 14 mm, 21 mm, 28 mm, and 35 mm) were CNC-machined at five equidistant points along the depth. The distribution of defects by depth and an example can be seen in Figure 8 below. The defect sizes were 0.4 mm, 0.6 mm, 0.8 mm, 1.0 mm, and 1.2 mm. Transmissive experiments were conducted on aluminum alloy samples with different defect sizes at the same depth to test the detection capability under various depth conditions and verify the simulation conclusions. Additionally, based on the machining conditions, a set of extremely small defect samples with a minimum defect diameter of 0.1 mm was prepared. These samples contain near-surface defects, with defect depths of 3 mm or shallower, resulting in the overlap of ultrasonic pulse echo signals with surface echoes, creating a near-surface detection blind zone. These samples were used to evaluate the ultrasonic transmissive method's capability to detect near-surface defects.

By performing ultrasonic A-scans (Amplitude Scan) on the defect-containing regions of the samples, the transmission energy of ultrasonic waves was measured. Figure 9 shows the experimental results of signal energy variation with defect radius for each depth, including near surface depth. As shown in the figure, the regularity is observed that as the defect size increases, the transmission signal energy decreases at all depths. The correlation coefficients between the defect diameter and transmission signal energy are both above 0.97, indicating a significant correlation between the two parameters. The attenuation functions of transmission signal energy at all depths have a correlation greater than 0.975 with the

simulation results. The maximum residual difference between the measured normalized transmission energy and the predicted value from the simulated fitted curve is 0.12, and this maximum is from samples with a radius of 0.5 mm in the depth = 21 mm group. This discrepancy might be attributed to the metal block's rust formation due to prolonged immersion in water and the potential errors in the CNC machining of the defects.

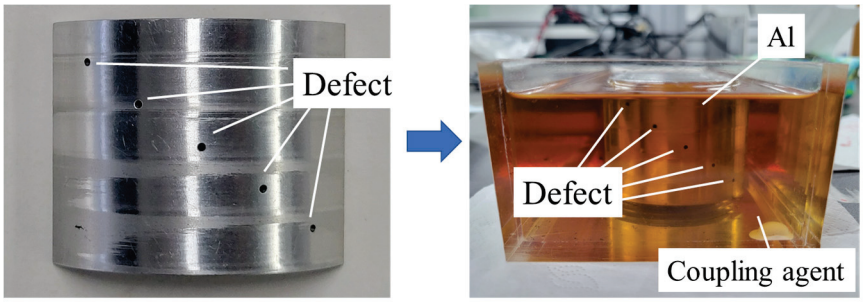

Figure 8. Examples of defects in aluminum alloys: (**a**) Aluminum alloy; (**b**) alloy immersed in coupler.

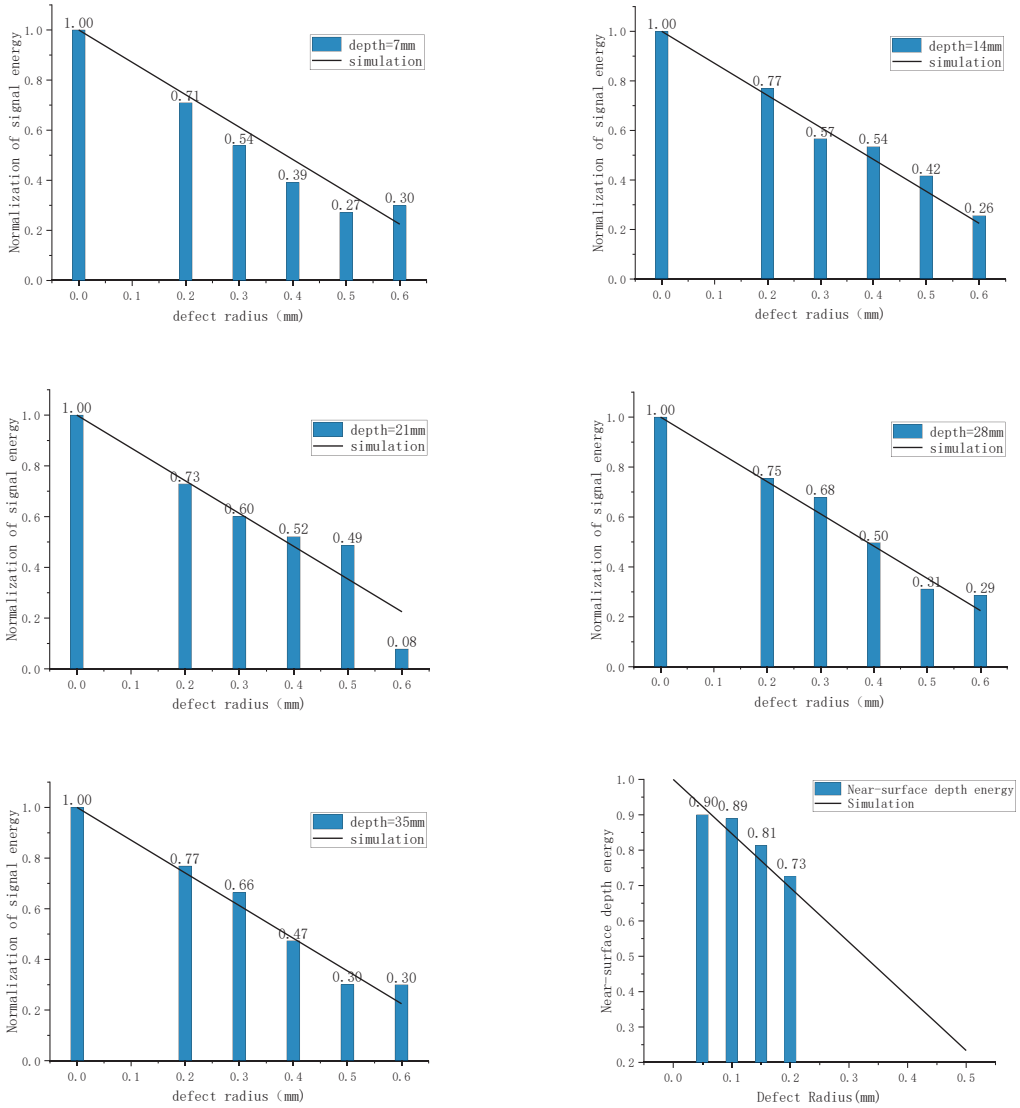

Figure 9. Transmission Experiments of Aluminum Alloys with Different Depth Defects.

The experimental results demonstrate a significant difference in transmission signal energy between defect-free and defective samples, allowing for defect detection and identification of defect sizes. Comparing the transmission signal energy of extremely small defect samples with the simulation results, a strong linear relationship between the energy and defect size is observed. The transmitted signal energy measured from the aluminum alloy sample is linearly fitted, and the residual difference between the measured attenuation slope and the simulated attenuation line is obtained by comparing the measured and simulated fitting lines. The calculated results show that the experimental data align well with the theoretical simulation model, with the maximum difference between the measured attenuation slope and the residual of the simulated attenuation line being 0.05. These findings validate the capability of ultrasonic transmissive method in detecting and determining defect sizes within the blind zone of the reflection method.

4.3.2. Transmission Experiment of Ferrite Tiles

The second set of experiments involved testing ferrite tile samples provided by the factory. Examples of ferrite tiles with internal defects and external defects are shown in Figure 10a,b respectively. The test group comprised a batch of ferrite tiles with both external and internal defects, alongside a batch of defect-free ferrite tiles. The defect types observed in the ferrite tiles were external cracks, external fractures, and internal cracks. Initially, transmission experiments were conducted on 54 defect-free ferrite tiles, and their ultrasonic transmission signals were collected. The threshold for defect-free ferrite tiles was calculated using the 3σ significance principle. The transmission energy of the tiles under inspection was measured and compared to the transmission energy of the defect-free ferrite tiles. Any ferrite tile with transmission energy below three times the standard deviation of the defect-free tiles was classified as defective.

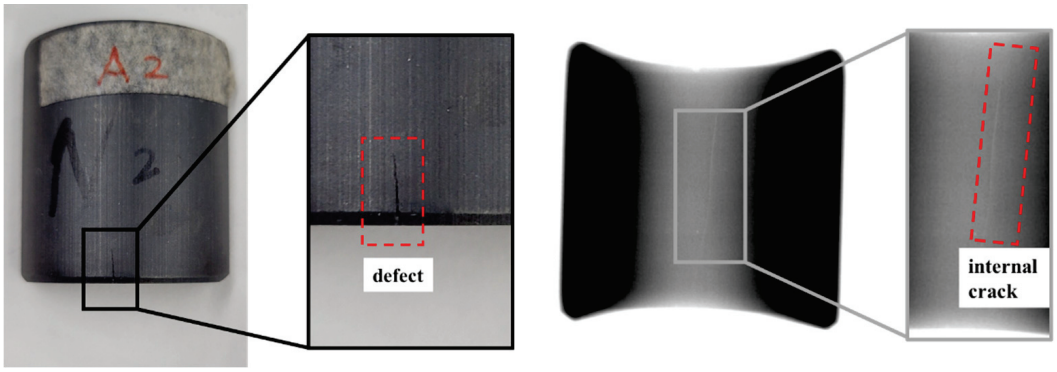

Figure 10. Ferrite tile defect example: (**a**) External crack; (**b**) Internal defects captured by X-ray imaging.

The transmission energy of 54 defect-free ferrite tiles was measured for calibration. During the experiment, the probe was aligned to the same position on the ferrite tiles to measure the ultrasonic transmission energy. The mean transmission energy of the defect-free ferrite tiles was determined as 148.7866, with a variance of 6.1653. Based on the 3σ significance principle in mathematics, the lower limit of the 99.73% confidence interval for the transmission energy of defect-free tiles was calculated as 130.2907. Any measurement result below this threshold was considered significantly deviated from the batch of samples, thus allowing for the calculation of whether the transmission energy of the tested samples was significantly lower than that of the defect-free ferrite tiles. Samples with energy below the threshold were classified as defective.

The inspection group measured the transmission energy of 92 internal defective samples and 41 external defective samples using the ultrasonic transmission method. By comparing these measurements with the threshold determined from OK ferrite tiles, as

shown in Figure 11. The threshold values well separate the OK sample from the NG sample. The detection rate for internal defects reached 96.74%, while for external defects, it reached 95.12%.

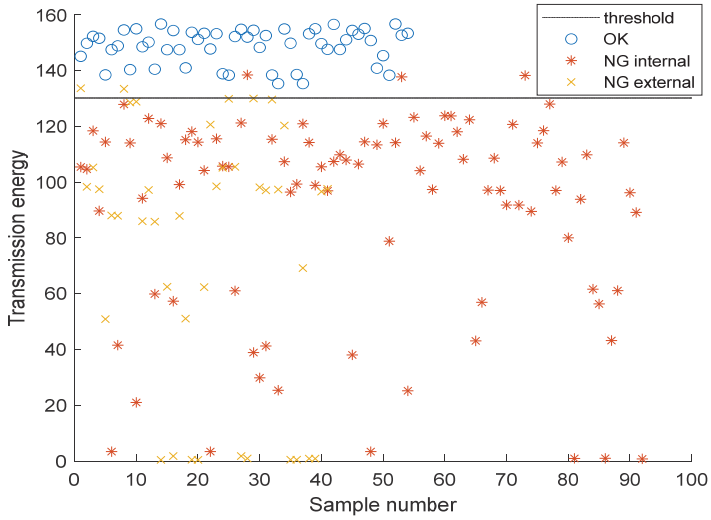

Figure 11. Results of calibration and measurement.

Both experiments conducted on aluminum alloy and ferrite tiles verified the feasibility of using ultrasonic transmission for full defect detection of both internal and external defects. The method exhibited high sensitivity in detecting defects in artificially controlled samples and showed good fitting with simulation results. Moreover, in real samples, it achieved high recall rates for samples containing both internal and external defects.

5. Conclusions

A water-immersion through-transmission ultrasonic testing method is proposed for the simultaneous detection of internal and external defects in metals and ferrite tiles. The principle of ultrasonic wave transmission is analyzed, and numerical approximations are used to calculate the energy variation of ultrasonic waves propagating through samples containing internal defects, providing a theoretical basis for defect analysis and probe positioning in subsequent simulations and analyses. The simulation results show that the variation of transmitted wave sound pressure can be used to determine the presence of defects and analyze their equivalent size. A measurement system is constructed, and experiments are conducted to further validate the capability of the water-immersion focused ultrasonic transmission method in detecting micro-cracks on ferrite tile surfaces and circular hole defects in processed aluminum alloy samples. Compared with the commonly used pulse-echo method, this approach exhibits a smaller blind zone and higher sensitivity, enabling effective detection of surface and internal defects, and significant potential is demonstrated for various applications.

However, this method also has some certain limitations, such as the inability to measure the depth of the defect. Further improvement will be carried out as follows: a combined ultrasonic transmission method and traditional pulse echo method to realize full detection of internal and external defects as well as the depth of internal defects.

Author Contributions: Conceptualization, K.H. and Q.L.; Methodology, Q.L. and K.Z.; Software, K.Z.; Formal analysis, Q.L.; Investigation, K.H.; Resources, X.W.; Data curation, B.C.; Writing original draft, K.H.; Writing; Review & Editing, Q.L. and X.L.; Visualization, X.Q.; Supervision, Q.L. and X.W.; Project administration, X.L.; Funding acquisition, X.L. All authors have read and agreed to the published version of the manuscript.

Funding: This research was funded by Tsinghua University Shenzhen International Graduate School Research Start-up Fund, grant number QD2020001N; Tsinghua University Shenzhen International Graduate School Interdisciplinary Research and Innovation Fund, grant number JC2021003.

Institutional Review Board Statement: Not applicable.

Informed Consent Statement: Not applicable.

Data Availability Statement: Data are available upon request from the corresponding author.

Acknowledgments: The author would like to thank Zhihan Intelligent Manufacturing Co., Ltd. for providing samples for the experiment, and thank Li Liang for taking X-ray pictures of the magnetic tile samples.

Conflicts of Interest: The authors declare no conflict of interest.

References

1. Xie, L.; Xiang, X.; Xu, H.; Wang, L.; Lin, L.; Yin, G. FFCNN: A Deep Neural Network for Surface Defect Detection of Magnetic Tile. *IEEE Trans. Ind. Electron.* **2020**, *68*, 3506–3516. [CrossRef]
2. Huang, Q.; Yin, Y.; Yin, G. Automatic classification of magnetic tiles internal defects based on acoustic resonance analysis. *Mech. Syst. Signal Process.* **2015**, *60–61*, 45–58. [CrossRef]
3. Lu, H.; Zhu, Y.; Yin, M.; Yin, G.; Xie, L. Multimodal Fusion Convolutional Neural Network With Cross-Attention Mechanism for Internal Defect Detection of Magnetic Tile. *IEEE Access* **2022**, *10*, 60876–60886. [CrossRef]
4. Wei, J.; Zhu, P.; Qian, X.; Zhu, S. One-stage object detection networks for inspecting the surface defects of magnetic tiles. In Proceedings of the 2019 IEEE International Conference on Imaging Systems and Techniques (IST), Abu Dhabi, United Arab Emirates, 9–10 December 2019; pp. 1–6. [CrossRef]
5. Cao, X.; Yao, B.; Chen, B.; Wang, Y. Multi-defect detection for magnetic tile based on SE-U-Net. In Proceedings of the 2020 IEEE International Symposium on Product Compliance Engineering-Asia (ISPCE-CN), Chongqing, China, 6–8 November 2020; pp. 1–6. [CrossRef]
6. Xie, L.; Yin, M.; Huang, Q.; Zhao, Y.; Deng, Z.; Xiang, Z.; Yin, G. Internal defect inspection in magnetic tile by using acoustic resonance technology. *J. Sound Vib.* **2016**, *383*, 108–123. [CrossRef]
7. Hu, C.; Liao, H.; Zhou, T.; Zhu, A.; Xu, C. Online recognition of magnetic tile defects based on UPM-DenseNet. *Mater. Today Commun.* **2022**, *30*, 103105. [CrossRef]
8. Yin, J.; Chen, S.; Wong, V.-K.; Yao, K. Thermal Sprayed Lead-Free Piezoelectric Ceramic Coatings for Ultrasonic Structural Health Monitoring. *IEEE Trans. Ultrason. Ferroelectr. Freq. Control* **2022**, *69*, 3070–3080. [CrossRef] [PubMed]
9. Ozsoy, U.; Koyunlu, G.; Ugweje, O.C.; Dayyabu, A. Nondestructive testing of concrete using ultrasonic wave propagation. In Proceedings of the 2017 13th International Conference on Electronics, Computer and Computation (ICECCO), Abuja, Nigeria, 28–29 November 2017; pp. 1–5. [CrossRef]
10. Mondal, S.; Datta, D. Ultrasonic Monitoring of Hardness of Industrial Rubbers. In Proceedings of the 2019 8th International Conference on Modeling Simulation and Applied Optimization (ICMSAO), Manama, Bahrain, 15–17 April 2019; pp. 1–6. [CrossRef]
11. Liu, M. Ultrasonic Inspection And Defect Identification of Thin—Walled Stainless Steel Welded Pipe Weld. In Proceedings of the 2022 9th International Forum on Electrical Engineering and Automation (IFEEA), Zhuhai, China, 4–6 November 2022; pp. 995–998. [CrossRef]
12. Cheng, Z.; Zhu, K.; Li, X.; Qian, X. Detection of Internal Defects Based on Empirical Mode Decomposition and Wavelets Denoising. In Proceedings of the 2021 IEEE Industrial Electronics and Applications Conference (IEACon), Penang, Malaysia, 22–23 November 2021; pp. 302–307. [CrossRef]
13. Case, T.; Waag, R. Flaw identification from time and frequency features of ultrasonic waveforms. *IEEE Trans. Ultrason. Ferroelectr. Freq. Control* **1996**, *43*, 592–600. [CrossRef]
14. Medak, D.; Posilovic, L.; Subasic, M.; Budimir, M.; Loncaric, S. Automated Defect Detection From Ultrasonic Images Using Deep Learning. *IEEE Trans. Ultrason. Ferroelectr. Freq. Control* **2021**, *68*, 3126–3134. [CrossRef]
15. Li, K.; Wu, Y.; Guo, D.; Que, K.; Chen, B. A new method of ultrasonic featured-scan for composite materials. In Proceedings of the 2011 International Symposium on Applications of Ferroelectrics (ISAF/PFM) and 2011 International Symposium on Piezoresponse Force Microscopy and Nanoscale Phenomena in Polar Materials, Vancouver, BC, Canada, 24–27 July 2011; pp. 1–3. [CrossRef]
16. Suryawanshi, V.J.; Pawar, A.C.; Palekar, S.P.; Rade, K.A. Defect detection of composite honeycomb structure by vibration analysis technique. *Mater. Today Proc.* **2020**, *27*, 2731–2735. [CrossRef]
17. Benavente, D.; Galiana-Merino, J.; Pla, C.; Martinez-Martinez, J.; Crespo-Jimenez, D. Automatic detection and characterisation of the first P- and S-wave pulse in rocks using ultrasonic transmission method. *Eng. Geol.* **2020**, *266*, 105474. [CrossRef]
18. Bang, S.J.; Song, D.G.; Jhang, K.Y. Comparisons of second- and third-order ultrasonic nonlinearity param-eters measured using through-transmission and pulse-echo methods. *NDT E Int.* **2023**, *133*, 102757. [CrossRef]

19. Miyamoto, R.; Mizutani, K.; Ebihara, T.; Wakatsuki, N. Defect detection and size estimation in billet from profile of time-of-flight using ultrasonic transmission method with linear scanning. *Jpn. J. Appl. Phys.* **2015**, *54*, 07HC11. [CrossRef]
20. Zhu, J.; Lin, Y.; Wang, B.; Wen, J.; Tian, R. Study on ultrasonic attenuation characteristics in air-droplet two-phase flow. *Ann. Nucl. Energy* **2023**, *185*, 109742. [CrossRef]
21. Liu, H.; Tan, C.; Dong, F. Improved Amplitude Extraction Method for Attenuation Reconstruction of Transmissive Ultrasonic Tomography. In Proceedings of the 2022 IEEE International Instrumentation and Measurement Technology Conference (I2MTC), Ottawa, ON, Canada, 16–19 May 2022; pp. 1–6. [CrossRef]
22. Wang, H.B. Study on Key Techniques of Ultrasonic Nondestructive Testing Composite Parts. Ph.D. Thesis, Beijing Institute of Technology, Beijing, China, 2014.
23. Song, Y.Y.; Su, M.X.; Cai, X.S.; Shen, J.Q.; Xue, M.H. Computation of Acoustic Scattering by Rigid Particles by the Boundary Element Method. *Chin. J. Process Eng.* **2009**, *9*, 107–111.
24. Huang, D.-H.; Liao, C.-K.; Wei, C.-W.; Li, P.-C. Simulations of optoacoustic wave propagation in light-absorbing media using the finite difference time-domain method. In Proceedings of the IEEE Ultrasonics Symposium, 2004, Montreal, QC, Canada, 23–27 August 2004. [CrossRef]
25. Schwartz, H.; Pineau, J.-P.; Feuillard, G.; Prax, C.; Valiere, J.-C. Development of flow characterization system using ultrasonic methods. In Proceedings of the 2012 IEEE International Ultrasonics Symposium, Dresden, Germany, 7–10 October 2012; pp. 1–4. [CrossRef]
26. Fang, L.; Yu, X.; Zeng, Q.; Zhao, N.; Li, X. Excitation Characteristics of Ultrasonic Probe. In Proceedings of the 2019 IEEE International Instru-mentation and Measurement Technology Conference (I2MTC), Auckland, New Zealand, 20–23 May 2019; pp. 1–6.
27. Pereira, D.; Le Duff, A.; Painchaud-April, G.; Belanger, P. Simulation-Based Inversion for the Characterization of Adhe-sively Bonded Joints Using Ultrasonic Guided Waves. *IEEE Trans. Ultrason. Ferroelectr. Freq. Control* **2022**, *69*, 2400–2407. [CrossRef] [PubMed]
28. Wang, M.; Zheng, D. Simulation Research on Liquid Film Thickness of Horizontal Gas-liquid Two-phase Flow Based on Ultrasonic Method. In Proceedings of the 2021 40th Chinese Control Conference (CCC), Shanghai, China, 26–28 July 2021. [CrossRef]
29. Cheng, J.; He, C.; Lyu, Y.; Zheng, Y.; Xie, L.; Wu, L. Ultrasonic inspection of the surface crack for the main shaft of a wind turbine from the end face. *NDT E Int.* **2020**, *114*, 102283. [CrossRef]
30. Dong, J.B.; Gao, H.B.; Zhang, S.J. Simulation Research and Experimental Verification of Non-defect Echoes by Ultra-sonic Testing. *Res. Explor. Lab.* **2022**, *41*, 110–116.

materials

MDPI

Article

Lock-In Thermography with Cooling for the Inspection of Composite Materials

Ryszard Dymitr Łukaszuk [1], Rafael Monteiro Marques [2] and Tomasz Chady [3,*]

[1] Doctoral School, West Pomeranian University of Technology, 70-313 Szczecin, Poland; ryszard.lukaszuk@zut.edu.pl
[2] Independent Researcher, Faculty of Electrical Engineering, West Pomeranian University of Technology, 70-313 Szczecin, Poland; rafael.monteiro2ms@gmail.com
[3] Faculty of Electrical Engineering, West Pomeranian University of Technology, 70-313 Szczecin, Poland
* Correspondence: tomasz.chady@zut.edu.pl

Abstract: This paper presents the development of the lock-in thermography system with an additional cooling system. System feasibility is tested by investigating a square-shaped glass fiber-reinforced polymer (GFRP) with artificially made outer flaws. The influence of heating mode and sinusoidal excitation period on the defect detectability is considered. Thus, the experiment is split into two modes: the sample is solely heated in the first mode or simultaneously heated and cooled in the second. In each mode, the temperature measurement is performed first with a shorter excitation signal period and second with a longer one. The signal-to-noise ratio (SNR) is used to assess defect detection quantitatively. The comparative analysis shows that employing a mixed heating–cooling mode improves the SNR compared to the conventional heating mode. The further enhancement of the SNR is obtained by extending the excitation period. The combination of simultaneous heating and cooling with longer periods of the excitation signal allows for the best SNR values for the most detected defects.

Keywords: nondestructive testing (NDT); nondestructive evaluation (NDE); lock-in thermography (LIT); glass fiber-reinforced composites

1. Introduction

A composite is a hybrid material assembled from two or more materials with different physical and chemical properties. Composites are gaining prominence over other traditional materials due to their excellent high strength-to-thickness ratio, cost-efficient manufacturing, wear resistance, low thermal expansion, and ease of customization and assembly [1,2]. However, composites exhibit high anisotropy and inhomogeneity. The continuous improvement and development of composite manufacturing methods and unique material properties has led to the widespread application of composites in modern industry branches, such as the automotive (body material, bumpers, fuel tanks) [3–5], marine (decks, hulls, propellers) [6–8], aviation (fuselages, stabilizers) [9–11], offshore (pipelines, structure reinforcements) [12–14], power engineering (wind turbine poles and blades) [15,16], and civil engineering (hydraulic structures, building claddings, maintenance holes, reinforcements) industries [2,17]. Moreover, composites are successfully used in biomedicine (dental and surgical implants, blood vessels, bone fillers) [17] and sports (cycling and sailing equipment).

During their lifetime, composites are subject to various impacts that may compromise their structural integrity [18]. Particularly hazardous are subsurface changes invisible to the human eye [19]. Independent from the composite type, manufacturing-induced inhomogeneities may occur between layers (delamination, un-infiltration), in the resin matrix (resin-rich area, void, impurity, porosity), and the fiber reinforcement (fiber misalignments such as waviness or wrinkling, breakage). Delamination is considered one of

the most dangerous composite defects because it develops without any externally visible factor. Besides the improper conditions of curing during the manufacturing process of the composite, pressure or stress load acting on the component during its service use may also instigate delamination. Another type of defect is a void. This may appear due to air intrusion during the molding process. The exact process may also contribute to the formation of resin-rich zones, which result from poor fiber integration and act as the residual stress source. Misalignment encapsulates defects such as waviness, wrinkling, brokenness, undulation, and folding. Fiber misalignments appear as a result of vulnerable impacts during various manufacturing processes. All these flaws threaten a composite's properties and performance [20–22].

Therefore, it is vital to examine the condition of composite materials by detecting and identifying inhomogeneities at the earliest stages of their formation to minimize the risk of component catastrophic failures, massive economic loss, and personnel injuries. Nondestructive testing (NDT) methods respond to the demand for safety and quality assurance and the long-term exploitation of composite structures. Several modalities are successfully used to inspect composite materials, such as terahertz spectroscopy, ultrasonic method, shearography, X-ray, and thermography, to name a few.

The terahertz method (THz) is suitable for localizing surface and internal inhomogeneities, such as intrusions, moisture, voids, or delamination. The inspection procedure does not require a coupling medium and is safe for personnel because of nonionizing radiation [23]. However, this method is restricted to nonconductive materials because of high terahertz wave attenuation in conductors [24].

The ultrasonic method emits acoustic waves into the examined structure using a transmitter. This technique detects delamination, matrix breakages, and wrinkles [25,26]. The traditional methodology presents issues, such as the need to apply a coupling agent [27]. For this reason, air-coupled and laser ultrasonic methods are under development. The undeniable merits of these approaches include a noncontact procedure and no need to use coupling [28].

Shearography is a digital optical interferometric method that detects abnormalities like impact damage, fiber cracks, and delamination [29,30]. Shearography is profitable due to the time-efficient, full-field, and noncontact procedure. One drawback is that the stress level to be induced in the examined object has to be chosen accurately and carefully to avoid structural damage [31].

In X-ray testing, ionizing radiation is used to transmit X-rays through the examined structure. This technique allows the detection of abnormalities such as porosities, inclusions, or voids. The advantages of X-rays comprise a noncontact measuring procedure, high measurement resolution, and sensitivity. A significant disadvantage is the hazardous ionizing radiation [32].

Active infrared thermography (IRT) is an advantageous and promising approach for evaluating the condition of composite materials [33]. It offers a full-field, safe-to-perform, reliable, noncontact, accurate, cost-effective, and portable inspection procedure [34,35]. During the inspection, an excitation source emits heat absorbed by the surface of the structure under inspection. Heat waves propagate inside the material, partially dissipate, and reflect from encountered inhomogeneities. The resultant reflected waves interfere with the waves originating from the excitation source [19,36]. Consequently, an infrared camera can observe and register surface temperature variations correlating with internal abnormalities. Various external excitation sources, such as light, mechanics, and microwaves, can be used for heat induction in the tested material.

Optical thermography utilizes flash lamps or lasers as an external heat excitation source. Regarding excitation mode, optical thermography is classified as lock-in (LIT) and pulse (PT). In lock-in thermography, the heating signal emitted to the structure is periodic and amplitude-modulated, usually a square or sine wave. It is advantageous because the gradual heating process reduces the hazard of thermal-induced damage, and the signal-to-noise ratio is relatively high [37]. One drawback is that the resultant

thermograms are vulnerable to numerous distortions that must be diminished during signal postprocessing [38]. On the contrary, pulse thermography employs a signal composed of short rectangular pulses. This excitation mode excessively depends on non-uniform heating and surface emissivity [39].

Vibrothermography (VT) uses ultrasonic waves to induce heating in the area of interest. When an ultrasonic wave approaches an inhomogeneity, mechanical energy is transferred into a heat wave, then captured by an infrared camera [40]. This technique has several advantages, such as ease of measuring procedure or adaptability to various component shapes [41].

Induction thermography (IT) can be applied to metallic materials and carbon fiber-reinforced polymers. In this technique, an induction coil produces a magnetic field penetrating the examined structure and induces eddy currents. Abnormalities in the inspected component disturb the eddy current paths. As a result, heat is generated and observed by an infrared camera [42].

In microwave thermography, microwaves act as a heating excitation source. If a structure to be tested is dielectric, the amount of dissipated heat depends on the permittivity of the material, microwave frequency, and the electric field magnitude. This approach is beneficial because the energy delivered to the examined component is of medium power and thus does not cause sudden temperature rises, which are potentially harmful to the structure [43].

After thermography inspection, it is imperative to handle image postprocessing to reduce the impact of the background noise and infrared camera influence on the results and thus improve the detectability of the material inhomogeneities and extract amplitude and phase images [1,44]. To achieve this, numerous algorithms are employed. Conventionally, noise reduction may be performed using spatial or frequency-domain filtering. Spatial filtering involves, e.g., arithmetic mean or median filters [45]. Frequency-domain filtering relies on applying low-pass, high-pass, or band-pass filters.

There has been intensive research in lock-in thermography for modern material evaluation. Vesala et al. proposed a lock-in thermography system with a deep anomaly detection model and successfully tested it on CFRP and GFRP structures with artificial defects. The authors used a CFRP sample with 25 flat-bottom hole defects of different diameters, namely 16 mm, 14 mm, 10 mm, 8 mm, and 4 mm, and depths, namely 0.2 mm, 0.5 mm, 0.8 mm, 1.1 mm, and 1.5 mm. A 0.01 Hz–0.1 Hz frequency sweep modulated the heat excitation flux [46]. Dong et al. performed a nondestructive inspection of samples made from CFRP, steel, and aluminum alloy using a reflective lock-in thermography system. The training sample contained 24 flat bottom hole defects with 2 mm, 5 mm, 10 mm, and 15 mm diameters. The defect depths were 0.5 mm, 0.8 mm, 1 mm, 1.2 mm, and 1.5 mm. As an excitation source, two 1000 W halogen lamps were utilized. The excitation flux was modulated with the frequencies 0.025, 0.05, 0.075, and 0.1 Hz [44]. Sapieta et al. focused on detecting flat-bottom holes in additive-manufactured samples made of PET-G. The defects' depths were 0.5 mm and 1 mm. The circular defects had a diameter of 20 mm, while the square-shaped had an edge length of 20 mm. The researchers used two types of excitation, flash lamps and halogen lamps, with heat excitation periods of 60 s and 120 s, respectively [19]. Cheng et al. developed a system for automatically detecting rectangular flat-bottom holes in CFRP. They examined a sample with 16 defects of different depths, namely 1.6 mm, 1.9 mm, 2.3 mm, and 2.6 mm, and edge lengths, namely 7 mm, 10 mm, 13 mm, and 16 mm. The authors employed a system composed of two 1000 W lamps with the excitation flux modulated with a frequency of 0.05 Hz [1].

This study focuses on the influence of different heating/cooling modes and excitation periods on the detectability of relatively small-diameter flat-bottom holes embedded in a GFRP sample.

2. Materials and Methods

Of the various techniques originating from thermography, lock-in thermography (LIT) has garnered considerable attention because of the possibility of detecting structural abnormalities quantitatively [47]. During the inspection, an external sinusoidally or square-wave-modulated light source, such as halogen lamps, emits heat absorbed by the structure's surface under examination. Heat waves propagate inside the material, partially dissipate, and reflect off encountered inhomogeneities. The resulting reflected waves interfere with those originating from the excitation source [19,36]. Consequently, an infrared camera can observe and register surface temperature variations. Several signal processing techniques for extracting thermal wave parameters are suitable: the four-point correlation method (FPCM), digital lock-in correlation method (DLCM), and fast Fourier transform (FFT). In the FPCM, four data points of the surface temperature, with the same time intervals between each other, have to be selected. The outcome comprises amplitude and phase images. The DLCM employs the correlation between a measured sinusoidal thermal wave and two reference sine/cosine functions to retrieve the amplitude and phase of the measured signal [48]. Fast Fourier transform extracts signal parameters by discretizing a thermogram, analyzing amplitude/phase in the frequency domain, and utilizing inverse Fourier transform [49].

LIT requires considering several parameters to obtain an acceptable signal-to-noise ratio value (SNR), such as excitation frequency; the number of heating periods; and the distances between the camera, the heating source, and the object to be tested [50].

This study uses a square-shaped GFRP (glass fiber-reinforced plastic) sample (150 mm × 150 mm × 4 mm) with flat-bottomed holes (Figure 1a). The flat-bottom holes have 10, 8, 6, and 4 mm diameters and depths of 1, 1.5, 2, and 3 mm (Figure 1b).

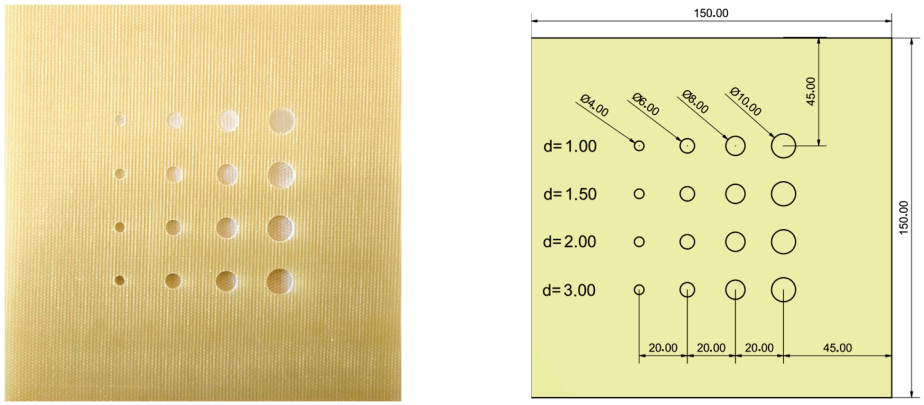

(**a**) (**b**)

Figure 1. A square-shaped GFRP sample with flat-bottomed holes: (**a**) photo of the sample; (**b**) scheme of the sample.

This study employs a self-made reflective LIT system consisting of a computer, a microcontroller (uC) Arduino Micro, a PWM unit, a cooling unit, two halogen lamps, an infrared camera, and a photoresistor with an electronic circuit. The computer programs the uC to drive the PWM unit. The PWM unit is supplied with two 300 W halogen lamps. The lamps produce sinusoidally modulated thermal waves for the heat excitation of the material to be tested. The TE-EQ1 uncooled infrared camera was placed in the front of the sample and used to register a thermal response from the sample's surface. The camera faces the unflawed side of the samples so that the visible defects are hidden from the camera. An infrared sensor composed of an IR photodiode BP104 and an operational amplifier TDA2822M was used to establish an optimal heating source location. The irradiation from two halogens measured in front of the sample was over 60 W/m^2. A schematic view of the measuring system is depicted in Figure 2, while the light (IR) sensor's circuit is shown in Figure 3. The camera parameters are presented in Table 1.

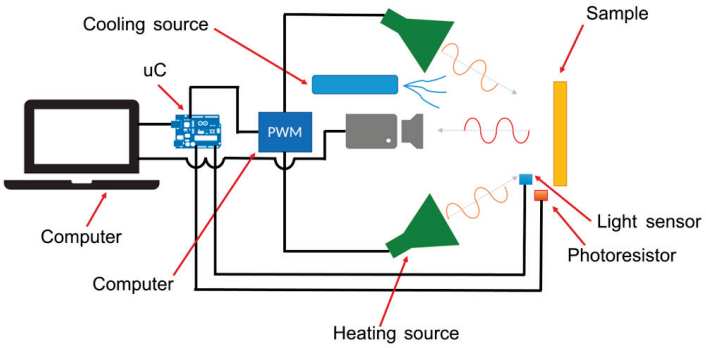

Figure 2. A schematic view of the measuring system.

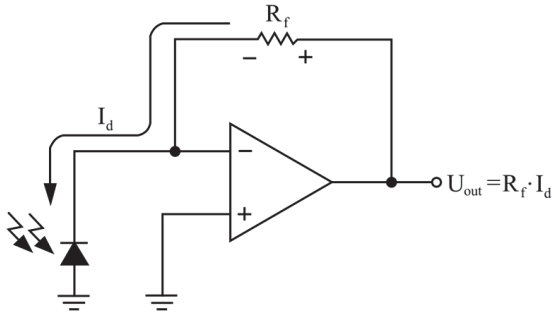

Figure 3. Circuit of the light (IR) sensor.

Table 1. Selected parameters of the infrared camera.

Parameter	Value
Camera resolution	384 × 288
Frame rate	30 fps
Thermal sensitivity	≤50 mK at F/1
Spectral range	8–14 μm
Operating temperature	−10 °C~+65 °C
Scene range temperature	−10 °C~+150 °C

3. Measurement

The study used two modes: heating mode with halogen lamps and mixed mode: parallel heating with halogens and chilling with a cooling unit. During the selected experiments, the custom-made cooling unit was utilized to lower the temperature of the sample by continuously blowing air cooled by four Peltier elements. The Peltier elements are cooled by running water to enhance cooling efficiency. The average temperature of the cooled air was around −1 °C. On the one side, the Peltier element has a lower temperature than the environment; on the other, the heat is dissipated. The component allows a reduction in temperature of about 20 °C, and regarding the temperature of the water cooler, the reduction is about 15 °C. A photo of the measuring system is presented in Figure 4. An example of a signal controlling the PWM circuit and a signal corresponding to the radiation of thermal intensity measured by the photoresistor is depicted in Figure 5.

During the heating procedure, the average temperature increases on the entire surface. Figure 6 presents two exemplary thermal response signals: one for the unflawed region of the sample under test and one for the flawed. It can be concluded that the temperature rise in the case of flaws is slower than for the healthy parts of the sample.

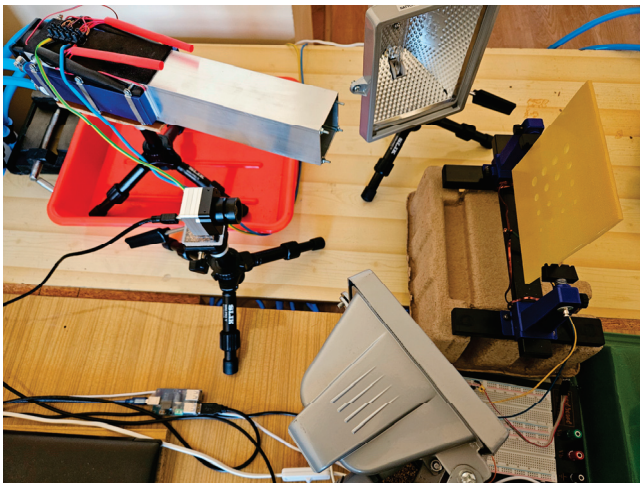

Figure 4. A photo of the measuring system.

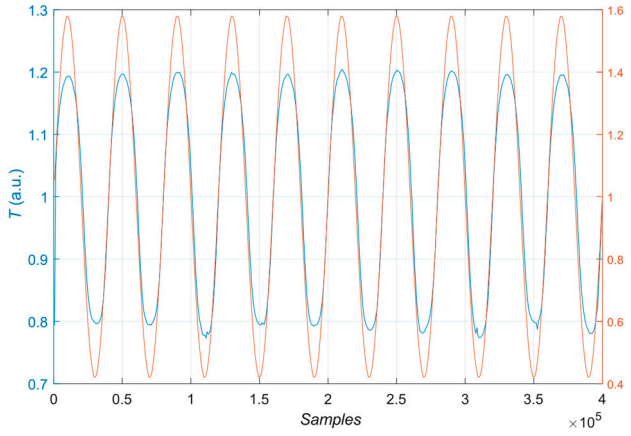

Figure 5. Normalized signals: controlling the PWM unit (orange curve) and measured using the photoresistor (blue curve).

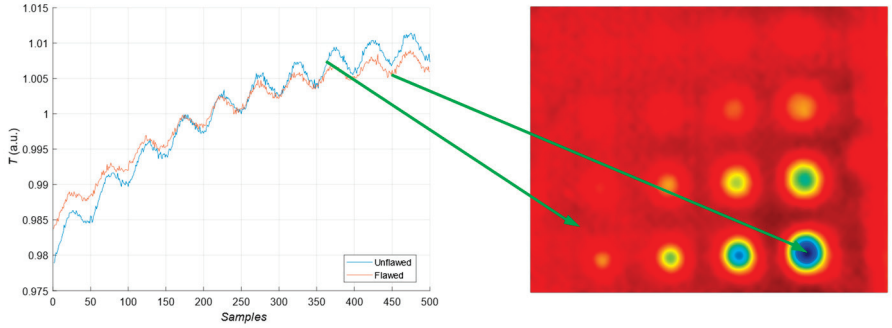

Figure 6. Exemplary normalized thermal response for the flawed (orange curve) and unflawed (blue curve) region of the sample and a thermogram.

4. Results

The results of the measurements are presented as follows: Section 4.1 contains the results obtained for an excitation period of T = 40 s, and Section 4.2 contains those for an excitation period of T = 100 s. For each period, the two versions were presented: the left column contains the results for the sample tested in the heating mode and the right column contains the results for the sample tested using the parallel heating–cooling mode. For both test modes, the following graphs are presented: heating curves of the damaged and undamaged areas of the specimen, the real and imaginary parts of the thermal response,

the average amplitude and phase of the thermal response, and the peak-to-peak amplitude of the sinusoidal waveforms acquired for each pixel.

4.1. Experiment with an Excitation Period of T = 40 s

The first experiment chose an excitation period of T = 40 s. Figure 6 depicts exemplary thermal responses for the flawed and unflawed regions of the sample under testing conditions. In the case of an uncooled sample, the average temperature rises very quickly in both the damaged and undamaged parts (Figure 7a). In contrast, the temperature rise for the simultaneously heated and cooled sample is slower, and the temperature values are much smaller, which is particularly evident for the curve corresponding to the damaged part of the sample (Figure 7b). Figure 8 contains graphs of the real part of the lock-in signal. As shown in Figure 8a, only defects with the largest diameter are detectable. The simultaneous heating and cooling process improves the detectability, as evident in Figure 8b. The following Figure 9 illustrates the imaginary part of the lock-in signal. The image for the sample without cooling (Figure 9a) highlights only 9 of the total 16 flaws. Cooling improves the defects' detectability (Figure 9b); thirteen flaws are evident. Figure 9 comprises the average amplitude of the lock-in signal. It does not show significant differences in defect detection between the mode without cooling (Figure 10a) and the mode with cooling (Figure 10b). Figure 11 includes the phase shift of the lock-in signal. The image for the uncooled sample (Figure 11a) is partially indistinct and does not allow for the identification of all defects. Applying the cooling enhances the comprehensibility of the phase image (Figure 11b). Figure 12 illustrates the peak-to-peak amplitude. Improvements in defect detection in cooling mode (Figure 12b) are also evident in this parameter, in contrast to the mode without cooling (Figure 12a).

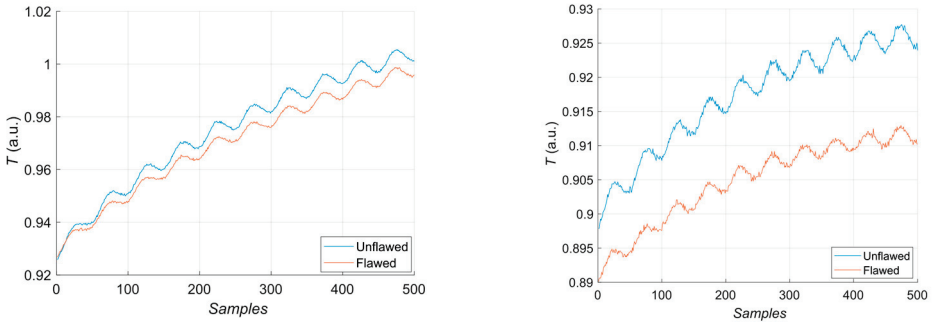

(**a**) (**b**)

Figure 7. Thermal response for the flawed: (**a**) uncooled sample; (**b**) cooled sample. Excitation Period of T = 40 s.

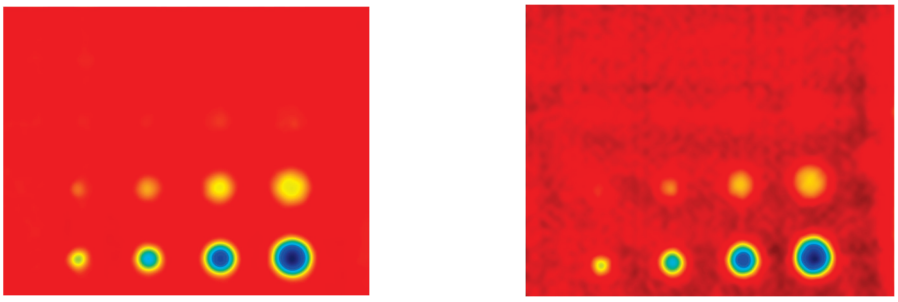

(**a**) (**b**)

Figure 8. The real part of the signal: (**a**) uncooled sample; (**b**) cooled sample. Excitation Period of T = 40 s.

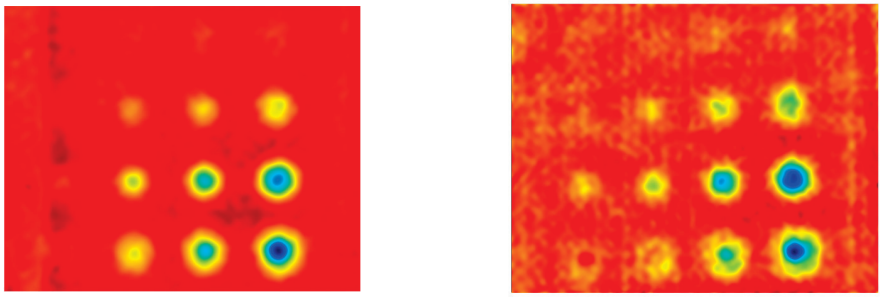

(**a**) (**b**)

Figure 9. The imaginary part of the signal: (**a**) uncooled sample; (**b**) cooled sample. Excitation Period of T = 40 s.

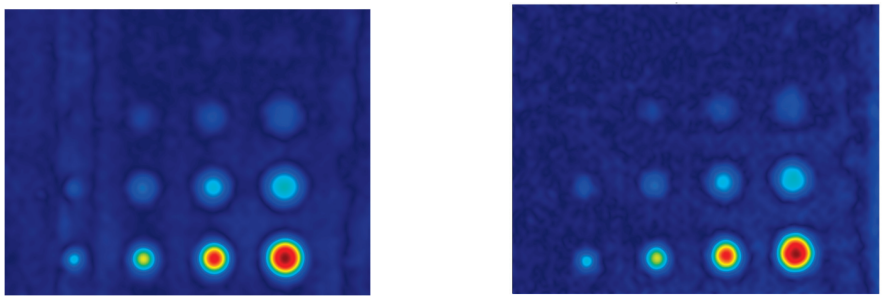

(**a**) (**b**)

Figure 10. The mean amplitude of the signal: (**a**) uncooled sample; (**b**) cooled sample. Excitation Period of T = 40 s.

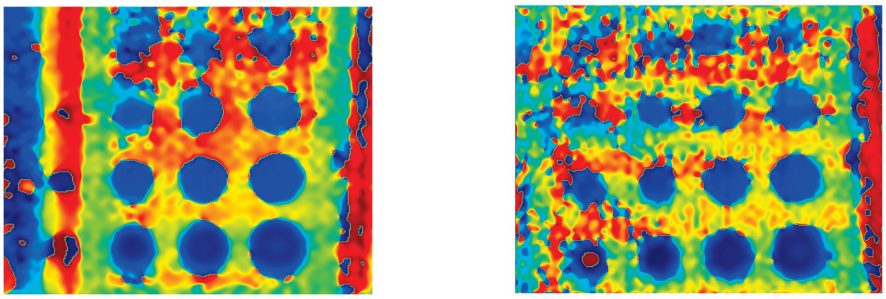

(**a**) (**b**)

Figure 11. The mean phase of the signal: (**a**) uncooled sample; (**b**) cooled sample. Excitation Period of T = 40 s.

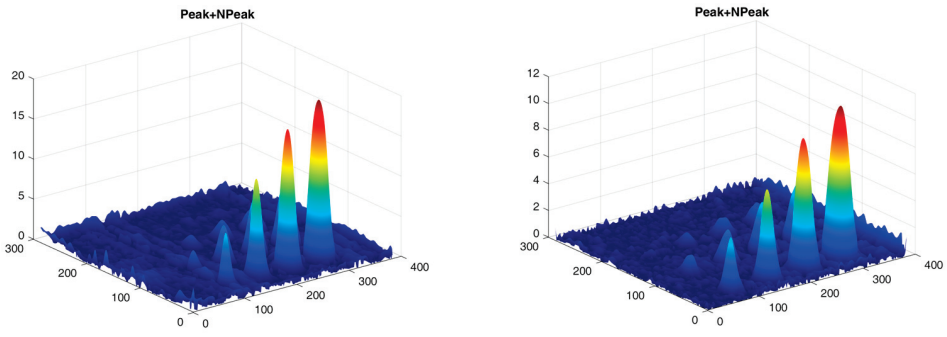

(**a**) (**b**)

Figure 12. The peak-to-peak amplitude: (**a**) uncooled sample; (**b**) cooled sample. Excitation Period of T = 40 s. The colors correspond to the signal's amplitude value.

4.2. Experiment with an Excitation Period of T = 100 s

The second experiment used an excitation period of T = 100 s. Figure 13 illustrates exemplary thermal responses for the flawed and unflawed areas of the examined sample. Similarly to the first experiment with an excitation period of 40 s, the average temperatures of the simultaneously heated and cooled sample (Figure 13b) increase at a slower rate than those of the uncooled sample (Figure 13a). Figure 14 shows the real part of the lock-in signal. As can be seen from the images, extending the period of the lock-in excitation signal from 40 to 100 s improves the detection of defects in both uncooled (Figure 14a) and parallel heating and cooling modes (Figure 14b). A similar conclusion can be drawn from Figure 15a,b, which illustrate the imaginary part of the lock-in signal. Figure 16 comprises the amplitude of the lock-in signal. Compared to the images for a period equal to 40 s, only a slight improvement in readability is apparent here. Analogously, introducing cooling parallel to the heating process (Figure 16b) instead of solely heating the sample (Figure 16a) allows for the better detectability of the flaws. Figure 17 shows the phase changes for the sample in heating mode (Figure 17a) and in heating mode with simultaneous cooling (Figure 17b). Compared with the results obtained for a period equal to 40 s, the readability of the images via the simultaneous heating–cooling improved significantly. However, the result for the heating mode remained partially blurry, so 4 of the 16 flaws are still undetectable. Figure 18a,b illustrate the peak-to-peak amplitude for both measuring modes. For this parameter, as the period of the excitation signal increased, the detection of defects improved.

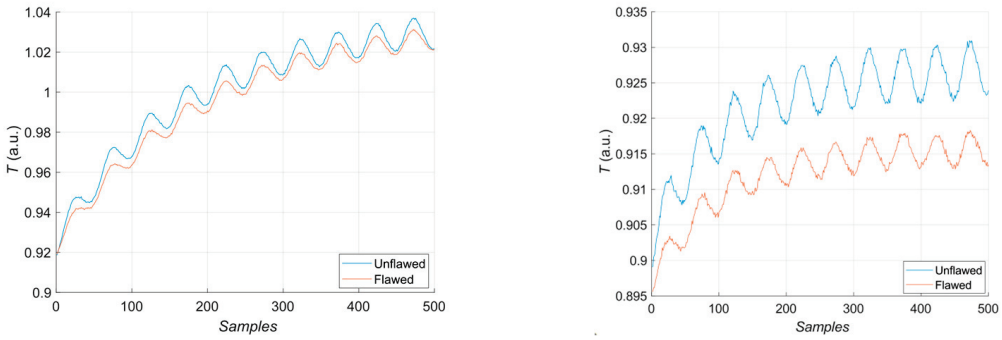

(**a**) (**b**)

Figure 13. Thermal response for the flawed: (**a**) uncooled sample; (**b**) cooled sample. Excitation Period of T = 100 s.

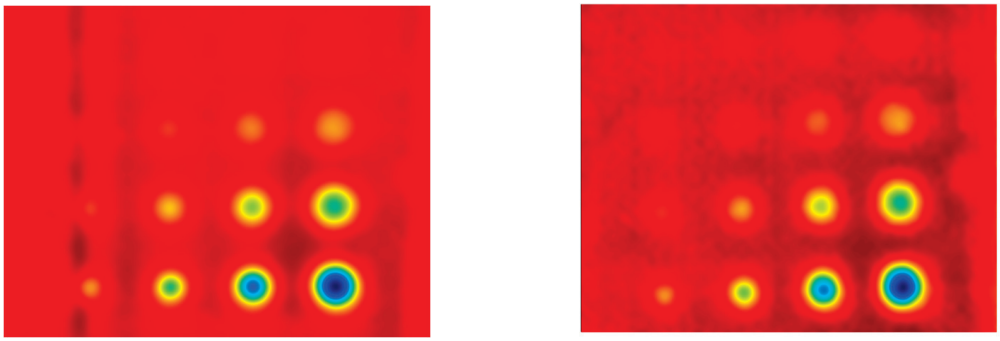

(**a**) (**b**)

Figure 14. The real part of the signal: (**a**) uncooled sample; (**b**) cooled sample. Excitation Period of T = 100 s.

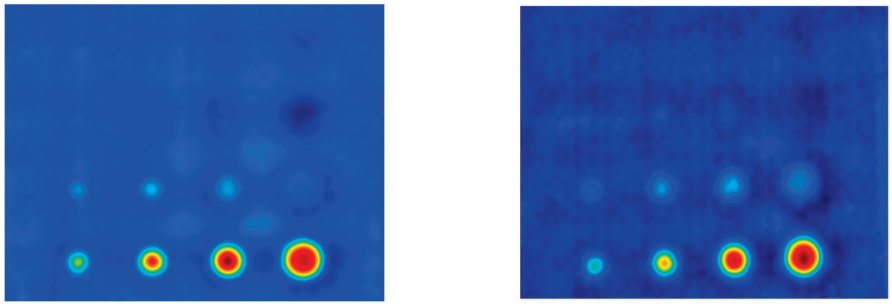

(**a**) (**b**)

Figure 15. The imaginary part of the signal: (**a**) uncooled sample; (**b**) cooled sample. Excitation Period of T = 100 s.

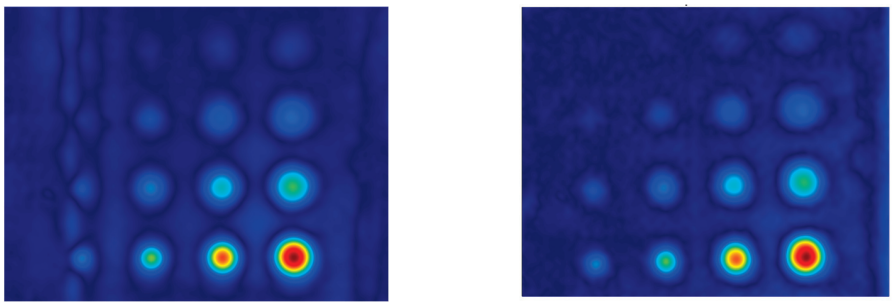

(**a**) (**b**)

Figure 16. The mean amplitude of the signal: (**a**) uncooled sample; (**b**) cooled sample. Excitation Period of T = 100 s.

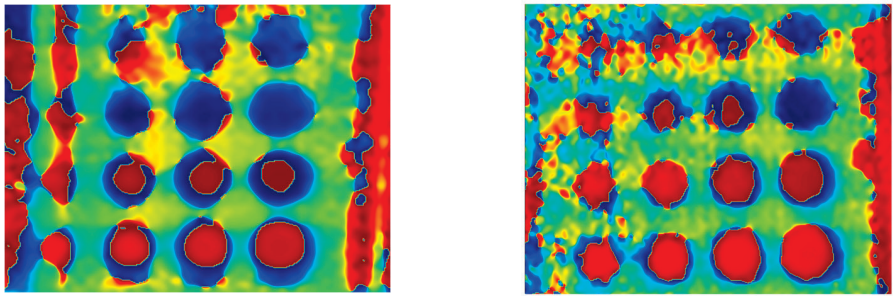

(**a**) (**b**)

Figure 17. The mean phase of the signal: (**a**) uncooled sample; (**b**) cooled sample. Excitation Period of T = 100 s.

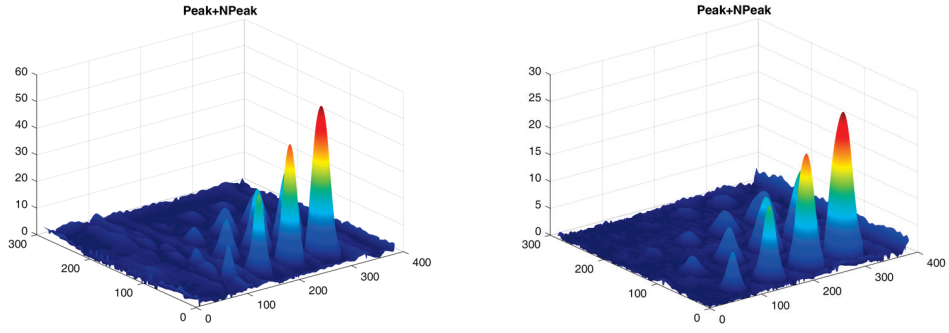

(**a**) (**b**)

Figure 18. The peak-to-peak amplitude of the signal: (**a**) uncooled sample; (**b**) cooled sample. Excitation Period of T = 100 s. The colors correspond to the signal's amplitude value.

5. Discussion

Quantitative Analysis of Heat Excitation Modes and Excitation Periods

This study used lock-in thermography to compare two different heat excitation modes of composite materials: heating and heating with simultaneous cooling. The impact of the heatwave's excitation period on the flaw detectability was also examined. In order to provide a quantitative comparison of excitation modes and periods, the signal-to-noise ratios for the individual flaws of the sample were calculated using the Formula (1)

$$SNR = \frac{|\mu_S - \mu_B|}{\sigma_B} \quad (1)$$

where μ_S is the average temperature value over the defect region; μ_B is the mean temperature value over the sound region; and σ_B is the standard deviation temperature value over the defect region.

Figures 19–22 contain bar graphs of the SNR values for the heating and heating with simultaneous cooling modes. Each figure for a defined defect depth consists of two bar graphs, one for the heat excitation period of T = 40 s and one for T = 100 s.

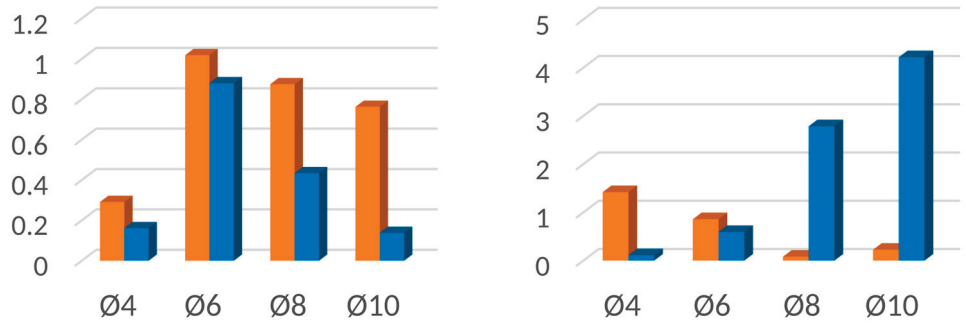

(**a**) (**b**)

Figure 19. SNR for the uncooled (orange bars) and cooled (blue bars) modes for the flaw depth d = 1 mm and the excitation period: (**a**) T = 40 s; (**b**) T = 100 s.

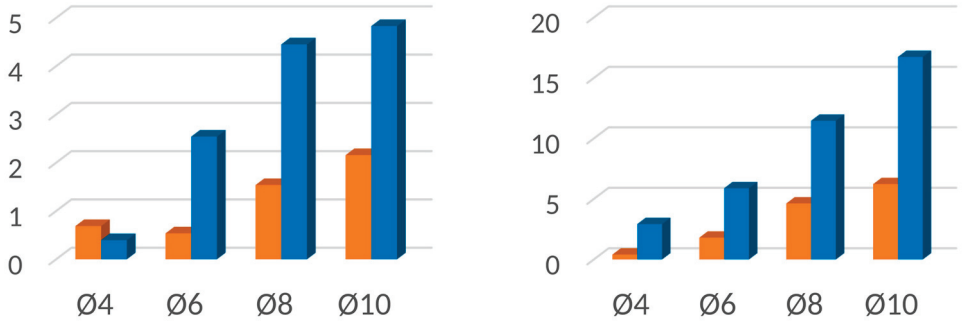

(**a**) (**b**)

Figure 20. SNR for the uncooled (orange bars) and cooled (blue bars) modes for the flaw depth d = 1.5 mm and the excitation period: (**a**) T = 40 s; (**b**) T = 100 s.

Figure 19 illustrates the SNR for the defect depth d = 1 mm. For T = 40 s, the heating–cooling mode caused a deterioration in SNR values (Figure 19a). Extending the excitation period T to 100 s improved the SNR for the defect with Ø4 mm. In the heating–cooling mode, for the defects Ø4 mm and Ø6 mm, the SNR dropped, but for Ø8 mm and Ø10 mm, it improved significantly (Figure 19b). Figure 19 contains bar graphs of the SNR for the defect depth d = 1,5. The comparison of SNR values for the heating and heating–cooling modes for T = 40 s suggests that, apart from in the case of the defect Ø4, the signal over the

defective area was enhanced markedly (Figure 20a). Further signal enhancement occurs for all defect radii in the case of the heating–cooling mode for T = 100 s (Figure 20b). As seen in Figure 21a,b, the SNR values in the case of the defect depth d = 2 mm can be slightly increased by extending the excitation period to 100 s. However, a considerable improvement in signal strength is obtained when applying the heating–cooling mode. Similar conclusions can be formulated for d = 3 mm (Figure 22a,b).

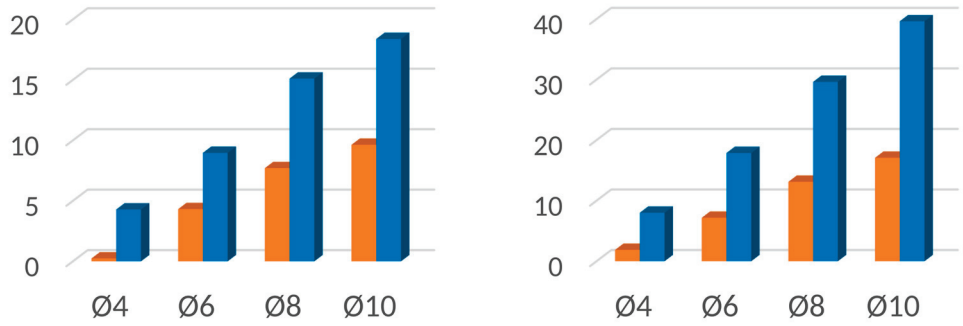

(**a**) (**b**)

Figure 21. SNR for the uncooled (orange bars) and cooled (blue bars) modes for the flaw depth d = 2 mm and the excitation period: (**a**) T = 40 s; (**b**) T = 100 s.

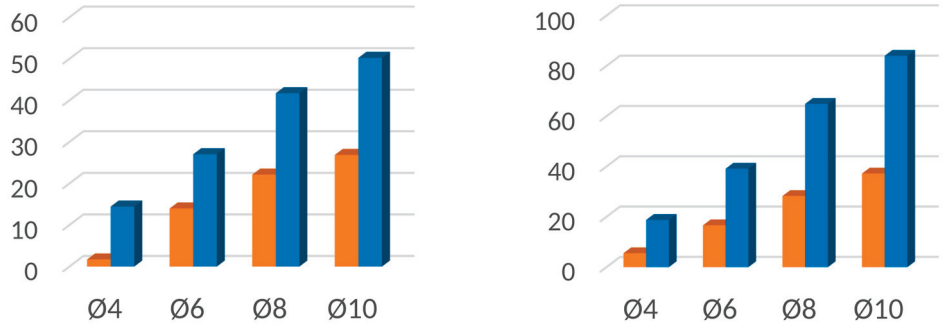

(**a**) (**b**)

Figure 22. SNR for the uncooled (orange bars) and cooled (blue bars) modes for the flaw depth d = 3 mm and the excitation period: (**a**) T = 40 s; (**b**) T = 100 s.

6. Conclusions

Lock-in thermography is a widely utilized technique for the nondestructive testing of composite structures. In the abovementioned studies, a system of lock-in thermography was built, and two modes of sample inspection were considered: heating and simultaneous heating–cooling. Particular attention was paid to studying the effect of the period of the excitation signal on detecting defects. Based on the research performed, the following conclusions can be made:

- The experimental results show that the combination of heating–cooling mode and an extended excitation period improves the SNR for most defects. However, the SNR drops for the deeper defects while introducing the heating–cooling mode. For this reason, the parameters of the proposed lock-in thermography system must be optimized to maintain high SNR for deeper defects.
- On the one hand, extending the excitation period increases the measurement time and causes the sample's average temperature to heat up more. On the other hand, the SNR of minor defects is significantly enhanced. However, the risk of overheating the sample can be overcome by attaching a cooling unit.

- Simultaneous heating and cooling improve the detection of defects even if the excitation period is small. The cooling process reduces the sample heating rate with a more extended excitation period and makes a more significant number of defects detectable and identifiable.
- The experiment was limited to examining hidden defects in the material. In future research, it would be necessary to test the method on natural defects of shapes other than circular. Different defects, such as delamination, porosity, or void, should also be considered in future studies.
- The proposed measurement system yielded satisfactory results in diagnosing defects in glass fiber-reinforced composites. In the future research, other composite materials, such as carbon fiber-reinforced polymers, should be considered.

Author Contributions: Conceptualization, T.C.; Methodology, R.D.Ł., R.M.M. and T.C.; Software, R.D.Ł., R.M.M. and T.C.; Formal analysis, R.D.Ł. and T.C.; Investigation, R.D.Ł., R.M.M. and T.C.; Resources, R.D.Ł.; Data curation, R.D.Ł., R.M.M. and T.C.; Writing—original draft, R.D.Ł.; Writing—review & editing, R.D.Ł. and T.C.; Visualization, R.D.Ł. and T.C.; Supervision, T.C.; Project administration, R.D.Ł.; Funding acquisition, R.D.Ł. All authors have read and agreed to the published version of the manuscript.

Funding: This research was partly funded by the West Pomeranian University of Technology in Szczecin, grant number ZUT/7/2023.

Institutional Review Board Statement: Not applicable.

Informed Consent Statement: Not applicable.

Data Availability Statement: Available on request.

Conflicts of Interest: The authors declare no conflict of interest.

References

1. Cheng, X.; Chen, P.; Wu, Z.; Cech, M.; Ying, Z.; Hu, X. Automatic Detection of CFRP Subsurface Defects via Thermal Signals in Long Pulse and Lock-In Thermography. *IEEE Trans. Instrum. Meas.* **2023**, *72*, 1–10. [CrossRef]
2. Frhaan, W.K.M.; Abu Bakar, B.H.; Hilal, N.; Al-Hadithi, A.I. CFRP for Strengthening and Repairing Reinforced Concrete: A Review. *Innov. Infrastruct. Solut.* **2021**, *6*, 49. [CrossRef]
3. Ahmad, H.; Markina, A.A.; Porotnikov, M.V.; Ahmad, F. A Review of Carbon Fiber Materials in Automotive Industry. *IOP Conf. Ser. Mater. Sci. Eng.* **2020**, *971*, 032011. [CrossRef]
4. Salifu, S.; Desai, D.; Ogunbiyi, O.; Mwale, K. Recent Development in the Additive Manufacturing of Polymer-Based Composites for Automotive Structures—A Review. *Int. J. Adv. Manuf. Technol.* **2022**, *119*, 6877–6891. [CrossRef]
5. Natural Fibre Composites—An Alternative to Plastics in the Automotive Industry: A Review—T. Narendiranath Babu, Suraj Shyam, Shivam Kaul, D. Rama Prabha, 2022. Available online: https://journals.sagepub.com/doi/abs/10.1177/14644207211041622 (accessed on 20 October 2023).
6. Rubino, F.; Nisticò, A.; Tucci, F.; Carlone, P. Marine Application of Fiber Reinforced Composites: A Review. *J. Mar. Sci. Eng.* **2020**, *8*, 26. [CrossRef]
7. Shreepannaga; Vijaya Kini, M.; Pai, D. The Ageing Effect on Static and Dynamic Mechanical Properties of Fibre Reinforced Polymer Composites under Marine Environment—A Review. *Mater. Today Proc.* **2022**, *52*, 689–696. [CrossRef]
8. Vizentin, G.; Vukelic, G. Marine Environment Induced Failure of FRP Composites Used in Maritime Transport. *Eng. Fail. Anal.* **2022**, *137*, 106258. [CrossRef]
9. Chung, Y.; Shrestha, R.; Lee, S.; Kim, W. Binarization Mechanism Evaluation for Water Ingress Detectability in Honeycomb Sandwich Structure Using Lock-In Thermography. *Materials* **2022**, *15*, 2333. [CrossRef]
10. Gao, Y.; Gao, M.; Wang, F.; Liu, J.; Yang, F.; Sheng, J.; Chen, M.; Wang, Y.; Yue, H. Convolution Neural Network Fusion High Power Halogen Lamp Induced Thermal-Wave Diffusion Multidimensional Features: An Intelligent Defect Identification Approach for Aviation Honeycomb Sandwich Composites. *Infrared Phys. Technol.* **2023**, *133*, 104772. [CrossRef]
11. Rijo, B.; Dias, A.P.S.; Carvalho, J.P.S. Recovery of Carbon Fibers from Aviation Epoxy Composites by Acid Solvolysis. *Sustain. Mater. Technol.* **2023**, *35*, e00545. [CrossRef]
12. Kazemi, H.; Yekrangnia, M.; Shakiba, M.; Bazli, M.; Vatani Oskouei, A. Bond Durability between Anchored GFRP Bar and Seawater Concrete under Offshore Environmental Conditions. *Mater. Struct.* **2023**, *56*, 64. [CrossRef]
13. Wei, D.; An, C.; Wu, C.; Duan, M.; Estefen, S.F. Torsional Structural Behavior of Composite Rubber Hose for Offshore Applications. *Appl. Ocean Res.* **2022**, *128*, 103333. [CrossRef]

14. Celik, E.; Sacmaozu, G.; Irez, A.B. Development of Carbon-Glass Fiber Reinforced Hybrid Composites: Applications in Offshore Wind Turbine Blades. In *Proceedings of the Mechanics of Composite, Hybrid and Multifunctional Materials, Fracture, Fatigue, Failure and Damage Evolution*; Chalivendra, V., Beese, A.M., Berke, R.B., Eds.; Springer International Publishing: Cham, Switzerland, 2022; Volume 3, pp. 17–22.
15. Zhou, H.; Li, H.; Li, L.; Liu, T.; Chen, G.; Zhu, Y.; Zhou, L.; Huang, H. Structural Composite Energy Storage Devices—A Review. *Mater. Today Energy* **2022**, *24*, 100924. [CrossRef]
16. Verma, A.S.; Yan, J.; Hu, W.; Jiang, Z.; Shi, W.; Teuwen, J.J.E. A Review of Impact Loads on Composite Wind Turbine Blades: Impact Threats and Classification. *Renew. Sustain. Energy Rev.* **2023**, *178*, 113261. [CrossRef]
17. Oladele, I.O.; Omotosho, T.F.; Adediran, A.A. Polymer-Based Composites: An Indispensable Material for Present and Future Applications. *Int. J. Polym. Sci.* **2020**, *2020*, e8834518. [CrossRef]
18. Wang, X.; Gao, M.; Wang, F.; Yang, F.; Yue, H.; Liu, J. Convolution Neural Network Fusion Lock-In Thermography: A Debonding Defect Intelligent Determination Approach for Aviation Honeycomb Sandwich Composites (HSCs). *Metals* **2023**, *13*, 881. [CrossRef]
19. Sapieta, M.; Dekýš, V.; Kopas, P.; Jakubovičová, L.; Šavrnoch, Z. The Impact of Excitation Periods on the Outcome of Lock-In Thermography. *Materials* **2023**, *16*, 2763. [CrossRef]
20. Wang, B.; Zhong, S.; Lee, T.-L.; Fancey, K.S.; Mi, J. Nondestructive Testing and Evaluation of Composite Materials/Structures: A State-of-the-Art Review. *Adv. Mech. Eng.* **2020**, *12*, 168781402091376. [CrossRef]
21. Fu, Y.; Yao, X. A Review on Manufacturing Defects and Their Detection of Fiber Reinforced Resin Matrix Composites. *Compos. Part C Open Access* **2022**, *8*, 100276. [CrossRef]
22. Suriani, M.J.; Rapi, H.Z.; Ilyas, R.A.; Petrů, M.; Sapuan, S.M. Delamination and Manufacturing Defects in Natural Fiber-Reinforced Hybrid Composite: A Review. *Polymers* **2021**, *13*, 1323. [CrossRef]
23. Nsengiyumva, W.; Zhong, S.; Luo, M.; Wang, B. Terahertz Spectroscopic Characterization and Thickness Evaluation of Internal Delamination Defects in GFRP Composites. *Chin. J. Mech. Eng.* **2023**, *36*, 6. [CrossRef]
24. Dong, J.; Pomarède, P.; Chehami, L.; Locquet, A.; Meraghni, F.; Declercq, N.F.; Citrin, D.S. Visualization of Subsurface Damage in Woven Carbon Fiber-Reinforced Composites Using Polarization-Sensitive Terahertz Imaging. *NDT E Int.* **2018**, *99*, 72–79. [CrossRef]
25. Hauffe, A.; Hähnel, F.; Wolf, K. Comparison of Algorithms to Quantify the Damaged Area in CFRP Ultrasonic Scans. *Compos. Struct.* **2020**, *235*, 111791. [CrossRef]
26. Taheri, H.; Hassen, A.A. Nondestructive Ultrasonic Inspection of Composite Materials: A Comparative Advantage of Phased Array Ultrasonic. *Appl. Sci.* **2019**, *9*, 1628. [CrossRef]
27. Wang, B.; He, P.; Kang, Y.; Jia, J.; Liu, X.; Li, N. Ultrasonic Testing of Carbon Fiber-Reinforced Polymer Composites. *J. Sens.* **2022**, *2022*, e5462237. [CrossRef]
28. Davis, G.; Nagarajah, R.; Palanisamy, S.; Rashid, R.A.R.; Rajagopal, P.; Balasubramaniam, K. Laser Ultrasonic Inspection of Additive Manufactured Components. *Int. J. Adv. Manuf. Technol.* **2019**, *102*, 2571–2579. [CrossRef]
29. Tao, N.; Anisimov, A.G.; Groves, R.M. Towards Safe Shearography Inspection of Thick Composites with Controlled Surface Temperature Heating. *NDT E Int.* **2023**, *139*, 102907. [CrossRef]
30. Tao, N.; Anisimov, A.G.; Groves, R.M. Shearography Nondestructive Testing of Thick GFRP Laminates: Numerical and Experimental Study on Defect Detection with Thermal Loading. *Compos. Struct.* **2022**, *282*, 115008. [CrossRef]
31. Spagnolo, G.S.; Leccisi, M.; Leccese, F. Simple and Economical Shearography System for Testing of Aeronautical Composite Material. In Proceedings of the 2022 IEEE 9th International Workshop on Metrology for AeroSpace (MetroAeroSpace), Pisa, Italy, 27–29 June 2022; pp. 571–576.
32. Menaria, T.; Kumar, M. Review on Radiographic Imaging Modalities for Nondestructive Testing and Evaluation (NDT & E). In Proceedings of the International Conference on Sustainable Computing in Science, Technology and Management (SUSCOM), Jaipur, India, 26–28 February 2019.
33. Matarrese, T.; Palumbo, D.; Galietti, U. Comparison in the Transient Regime of Four Lock-in Thermography Algorithms by Means of Synthetic and Experimental Data on CFRP. *NDT E Int.* **2023**, *139*, 102925. [CrossRef]
34. Ciampa, F.; Mahmoodi, P.; Pinto, F.; Meo, M. Recent Advances in Active Infrared Thermography for Nondestructive Testing of Aerospace Components. *Sensors* **2018**, *18*, 609. [CrossRef]
35. Rippa, M.; Russo, P.; Pagliarulo, V.; Bianco, V.; Ferraro, P.; Mormile, P. Lock-in Thermography as a Tool for the Detection of Damages in "Eco" Composite Materials. In Proceedings of the 2020 IEEE 7th International Workshop on Metrology for AeroSpace (MetroAeroSpace), Pisa, Italy, 22–24 June 2020; pp. 341–345.
36. Ólafsson, G.; Tighe, R.C.; Boyd, S.W.; Dulieu-Barton, J.M. Lock-in Thermography Using Miniature Infra-Red Cameras and Integrated Actuators for Defect Identification in Composite Materials. *Opt. Laser Technol.* **2022**, *147*, 107629. [CrossRef]
37. Applied Sciences | Free Full-Text | Qualitative Comparison of Lock-in Thermography (LIT) and Pulse Phase Thermography (PPT) in Mid-Wave and Long-Wave Infrared for the Inspection of Paintings. Available online: https://www.mdpi.com/2076-3417/13/7/4094 (accessed on 25 July 2023).
38. Salazar, A.; Sagarduy-Marcos, D.; Rodríguez-Aseguinolaza, J.; Mendioroz, A.; Celorrio, R. Characterization of Semi-Infinite Delaminations Using Lock-in Thermography: Theory and Numerical Experiments. *NDT E Int.* **2023**, *138*, 102883. [CrossRef]

39. Wang, F.; Liu, J.; Song, P.; Gong, J.; Peng, W.; Liu, G.; Chen, M.; Wang, Y. Multimodal Optical Excitation Pulsed Thermography: Enhanced Recognize Debonding Defects of the Solid Propellant Rocket Motor Cladding Layer. *Mech. Syst. Signal Process.* **2022**, *163*, 108164. [CrossRef]
40. Segers, J.; Hedayatrasa, S.; Verboven, E.; Poelman, G.; Van Paepegem, W.; Kersemans, M. In-Plane Local Defect Resonances for Efficient Vibrothermography of Impacted Carbon Fiber-Reinforced Polymers (CFRP). *NDT E Int.* **2019**, *102*, 218–225. [CrossRef]
41. Li, Y.; Ming, A.; Zhang, R.; Zhang, W. Investigation into Vibration Characteristic in Vibrothermography. *Photonic Sens.* **2019**, *9*, 108–114. [CrossRef]
42. Kidangan, R.T.; Krishnamurthy, C.V.; Balasubramaniam, K. Identification of the Fiber Breakage Orientation in Carbon Fiber Reinforced Polymer Composites Using Induction Thermography. *NDT E Int.* **2021**, *122*, 102498. [CrossRef]
43. Zou, X.; Mirala, A.; Sneed, L.H.; Al Qaseer, M.T.; Donnell, K. Detection of CFRP-Concrete Interfacial Debonding Using Active Microwave Thermography. *Compos. Struct.* **2021**, *260*, 113261. [CrossRef]
44. Dong, Y.; Zhao, B.; Yang, J.; Cao, Y.; Cao, Y. Two-Stage Convolutional Neural Network for Joint Removal of Sensor Noise and Background Interference in Lock-in Thermography. *NDT E Int.* **2023**, *137*, 102816. [CrossRef]
45. Sharma, A.; Singh, J. Image Denoising Using Spatial Domain Filters: A Quantitative Study. In Proceedings of the 2013 6th International Congress on Image and Signal Processing (CISP), Hangzhou, China, 16–18 December 2013; Volume 1, pp. 293–298.
46. Vesala, G.T.; Ghali, V.S.; Sastry, D.V.A.R.; Naik, R.B. Deep Anomaly Detection Model for Composite Inspection in Quadratic Frequency Modulated Thermal Wave Imaging. *NDT E Int.* **2022**, *132*, 102710. [CrossRef]
47. Image Definition and Defect Sizing in Lock-in Thermography: An Experimental Investigation | SpringerLink. Available online: https://link.springer.com/article/10.1007/s40799-021-00506-9 (accessed on 20 July 2023).
48. Liu, J.; Yang, W.; Dai, J. Research on Thermal Wave Processing of Lock-in Thermography Based on Analyzing Image Sequences for NDT. *Infrared Phys. Technol.* **2010**, *53*, 348–357. [CrossRef]
49. Ahmadi, S.; Burgholzer, P.; Mayr, G.; Jung, P.; Caire, G.; Ziegler, M. Photothermal Super Resolution Imaging: A Comparison of Different Thermographic Reconstruction Techniques. *NDT E Int.* **2020**, *111*, 102228. [CrossRef]
50. Oswald-Tranta, B. Lock-in Inductive Thermography for Surface Crack Detection in Different Metals. *Quant. InfraRed Thermogr. J.* **2019**, *16*, 276–300. [CrossRef]

materials

MDPI

Article

Exploring the Detection of Cl^- Penetration in Portland Cement Mortars via Surface Electrical Resistivity

Miguel Alberto Pablo-Calderón, Prisciliano Felipe de Jesús Cano-Barrita * and Frank Manuel León-Martínez

CIIDIR Unidad Oaxaca, Instituto Politécnico Nacional, Calle Hornos No. 1003, Colonia Noche Buena, Sta. Cruz Xoxocotlán, Oaxaca 71230, Mexico; mpabloc1600@alumno.ipn.mx (M.A.P.-C.); fmleonm@ipn.mx (F.M.L.-M.)
* Correspondence: pcano@ipn.mx

Abstract: Surface electrical resistivity is a non-destructive technique that is sensitive to the microstructure of hydrated cement paste and the chemical composition of the pore solution in cement-based materials. In this study, a Wenner array was used to measure changes in mortar resistivity due to chloride ion diffusion as a function of electrode separation. Specimens were made from four mortar mixtures: 100% Ordinary Portland cement and 60% cement + 40% fly ash at two water/binder ratios of 0.55 and 0.40. The specimens were subjected to unidirectional chloride ion diffusion in a 2.8 M NaCl solution for 175 days. To determine the chloride penetration depth, three methods were used: silver nitrate spraying, chloride concentration profiles via potentiometric titration, and chloride concentration profiles via inversion of the resistivity data using the RES1D software (version 1.00.09 Beta). The results showed a linear relationship between the chloride ion penetration depth obtained via inversion of the surface electrical resistivity data versus the penetration depth from colorimetry and from chloride concentration profiling (both with $R^2 = 0.8612$). Chloride penetration changed the conductivity of the pore solution; therefore, the resistivity decreased when increasing both the chloride concentration and the penetration depth. Inversion of surface resistivity data obtained with a Wenner array permitted non-destructive determination of chloride penetration. However, these results were obtained under laboratory environmental conditions and other scenarios must be addressed for wider applications.

Keywords: pozzolanic reaction; hydration; chloride diffusion; Friedel's salt; pore solution

1. Introduction

The durability of concrete structures is affected by chloride ion ingress, which can corrode the reinforcing steel bars. Chloride ions may enter cement-based materials through mixing with water or by external sources from environmental exposure [1]. Chlorides from external sources are mainly transported into the concrete through diffusion, which is influenced by factors like porosity, pore size distribution, ion exchange, and the chemical/physical binding of chlorides into the C-S-H and AFm phases. The capacity of chloride binding in hardened cement paste is affected by the C_3A and C_4AF content in cement, pore solution composition, addition of supplementary cementitious materials (SCMs), and leaching that alters the hydrate composition [2,3]. Chemical binding leads to the formation of Friedel's salt, which removes chlorides from the pore solution [4]. The mechanisms of ingress and the binding of chlorides in cement systems are complex, as several processes are acting simultaneously. Porosity in cement-based materials is directly related to their mechanical properties and permeability. High porosity and a well-connected pore network facilitate the ingress of harmful species that cause the deterioration of reinforced concrete structures. Porosity and pore size distribution may be estimated using mercury intrusion porosimetry [5] or nuclear magnetic resonance relaxometry [6].

There are different standard techniques used to determine the ability of concrete to resist chloride ion ingress. One technique is the rapid chloride permeability test (RCPT) [7],

which measures the amount of electrical charge passing through a saturated cylindrical concrete sample (100 mm in diameter and 50 mm in thickness) when a potential difference of 60 V of direct current is applied for six hours. This test has been subject to criticism, although it has been adopted as a standard and is widely used. The main drawbacks are that the current passed through the specimen is related to all ions in the pore solution; the measurements are made before steady-state migration is achieved; and the high voltage applied leads to an increase in temperature, which further increases the charge passed through. Another similar test is the non-steady-state migration test NT BUILD 492 [8]. This test applies an electrical potential to force chloride migration through the specimen, and the penetration depth is measured by spraying a silver nitrate solution on the fractured surface. A non-steady-state migration coefficient is then calculated. The AASHTO T 259 [9] is another type of test that measures the resistance of hardened concrete to chloride penetration by ponding the surface of concrete slabs with a three percent NaCl solution for 90 days. There is difficulty in interpreting the results because the specimens are subject to diffusion and wicking effects. Two additional tests, NT BUILD 443 [10] and ASTM C1556 [11], measure the accelerated penetration of chlorides in hardened concrete for the determination of the apparent diffusion coefficient and surface concentration based on chloride concentration profiles. These tests are expensive and time-consuming.

The techniques mentioned previously are destructive, which limits them to one measurement per test, and their results may show high variability [12]. On the other hand, there are non-destructive tests, such as ASTM C1876 [13] and AASHTO TP119 [14], that determine the bulk electrical resistivity or bulk conductivity of concrete. While these tests require molded specimens or specimens cored from actual structures, the surface electrical resistivity test on saturated concrete samples can indirectly assess the permeability of the material and provide an indication of its resistance to chloride ion penetration [15]. The Wenner array method is one test used for concrete electrical resistivity measurements that utilize four equally spaced surface electrodes. It is non-destructive [16], easy to use, rapid, and can be conducted on the same sample without special preparation [17]. According to Oleiwi et al. [18] and Cosoli et al. [16], the Wenner technique is one of the most widely used techniques for in situ tests on the surface of concrete. However, currently, there are still no widely accepted standards, other than AASHTO T358 [19], for measuring the surface electrical resistivity using the Wenner four-electrode method. Factors affecting resistivity measurements include porosity; pore size and connectivity; the tortuosity of the pore network and the composition of the pore solution, which are determined by the type of cementitious material; and the water/binder ratio (w/b). The curing method and sample conditioning also affect resistivity because they influence the properties of the pore solution, the degree of saturation, and temperature. Ambient temperature and relative humidity can be the most difficult conditions to control in real-life applications [20]. The accuracy of resistivity measurements is also dependent on the quality of the contact between the electrodes and the concrete surface. To create an electrolytic contact between the electrodes and the concrete surface, different solutions can be used. These include saturated sponges, soaked wooden plugs, a conductive gel, or localized wetting. However, these methods do not improve the contact between the electrodes and the concrete surface to a significant extent [20]. Studies indicate that the best resistivity measurements are obtained using the Wenner configuration with the largest electrode spacing [21]. An increase in separation will result in a greater penetration of the current field, covering more volume that results in lower relative values. In addition, resistivity measurements are substantially wrong if the semi-infinite geometry assumption is not met in small concrete specimens.

Regarding concrete resistivity and chloride penetration, there is an inverse correlation between resistivity and the chloride diffusion rate [22]. In addition, resistivity may be used to classify the risk of corrosion of a specific concrete structure, with low resistivities corresponding to a high risk of corrosion and vice versa. Qiao et al. [23] related the electrical resistivity of air-entrained concrete to the formation factor of the material. They found that increasing the air content decreased the formation factor of saturated concrete due to a

higher volume of fluid-filled air voids. As w/c increased, the formation factor decreased due to a higher porosity and connectivity. Other uses of resistivity include the estimation of the chloride diffusion coefficient that may be required for the service life estimation of reinforced concrete structures [24]. Higher resistivities correspond to lower chloride diffusion coefficients. The only study identified in the literature related to the present study was that of Fares et al. [25], who inverted electrical resistivity tomography (ERT) data to obtain resistivity profiles as a function of depth. They used a Wenner configuration with 14 electrodes, two concrete mixtures, and a mortar exposed to chloride diffusion. The chloride profiles obtained via ERT were compared with those obtained using the chloride content of powder samples. They observed a good agreement between ERT and destructive testing.

The purpose of this study was to investigate the feasibility of determining the chloride ion penetration depth in mortar specimens under laboratory conditions by inverting surface resistivity data obtained with a commercial Wenner array instrument with variable electrode spacing. The resistivity measurements were performed as a function of time. The estimated chloride depth was compared with the penetration depth obtained from the colorimetric test using a 0.1 N $AgNO_3$ solution sprayed on a freshly broken surface, as well as from chloride content profiles at a depth where the concentration was approximately zero. The relationship between the depths obtained non-destructively and those obtained using standard destructive tests will be explored.

2. Materials and Method

2.1. Materials

Ordinary Portland cement (OPC), class F fly ash (FA), and river sand were used. The relative density of the sand was 2.66 g/cm^3, with an absorption of 2.81% [26] and a fineness modulus of 3.28. The chemical composition of the cementitious materials used is shown in Table 1. The river sand grading is provided in Figure 1.

Table 1. Chemical composition (% by mass) of the cementitious materials used [27].

Main Oxides	SiO_2	Al_2O_3	Fe_2O_3	CaO	TiO_2	P_2O_5	MgO	Na_2O	K_2O	SO_3	LOI
OPC	21.07	3.69	4.50	61.93	0.97	0.10	1.83	0.09	0.30	2.54	4.38
FA	62.28	20.38	4.09	4.68	0.94	0.38	0.98	0.31	0.99	-	3.43

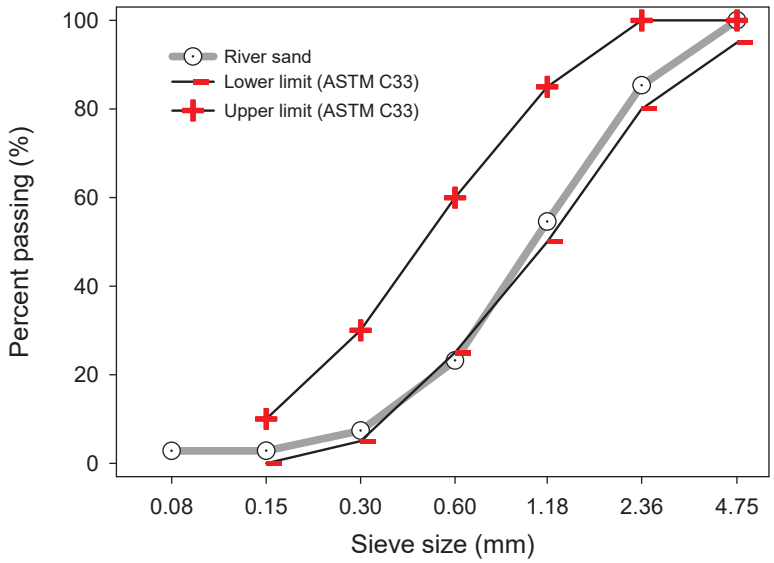

Figure 1. River sand grading used to prepare the mortar mixes.

2.2. Method

2.2.1. Preparation and Conditioning of Mortar Specimens

Mortar mixes with water/binder (w/b) ratios of 0.55 and 0.40 and a sand/binder (s/b) ratio of 2.75 were prepared according to the procedure described in the ASTM C192 standard [28]. Table 2 provides the mortar mixture proportions. The sand/binder ratio (s/b) of 2.75 was used as proposed in ASTM C109 [29] for preparing the Portland cement mortars. The w/b ratios were selected as 0.55 and 0.40 in order to produce relatively high and low chloride ion diffusion coefficients and low and high electrical resistivities. Two mortars used 100% OPC and the other two used 60% OPC + 40% FA, by mass, which were labeled as OPC0.55, FA0.55, OPC0.40, and FA0.40, respectively. FA was included in the mixes because it significantly reduces the porosity and pore size distribution in hardened cement paste, which, in turn, reduces the electrical resistivity of concrete. In addition, cement pastes containing FA chemically bind a higher amount of chlorides compared with plain OPC cement pastes. A total of 18 mortar specimens were cast from each mortar mix. Table 3 provides details on the shape and dimensions of the different specimens. As is shown in Figure 2, the size of the prismatic mortar specimens was determined to minimize edge effects and to consider the space as semi-infinite, taking the value of a as less than 1/3 of the thickness of the specimens (approximately a = h/3) [21,30,31]. Parameters α and β are dependent on the electrode spacing. The former represents the distance from the center of the electrode to the edge of the prism and it is perpendicular to the electrode array; β is the distance from the external electrode to the edge of the prism and it is parallel to the electrode array. Therefore, the dimensions were 25 cm in width, 40 cm in length, and 15 cm in height. A geometric correction factor of approximately 1.0 was obtained from the specimen size to minimize edge effects in the surface electrical resistivity measurements [21,31].

Table 2. Mortar mixture proportions.

Material	**Mix**			
(kg)	**OPC0.55**	**FA0.55**	**OPC0.40**	**FA0.40**
Cement	518	301	562	326
Fly ash	-	200	-	217
Sand	1425	1381	1544	1493
Water	285	276	225	217

Table 3. Characteristics of mortar specimens prepared from each mix.

Test	**Type**	**Dimensions**				**Quantity**
		w (cm)	**l (cm)**	**h (cm)**	**Ø (cm)**	
Surface electrical resistivity	Control prisms	25	40	15		2
	* Prisms	25	40	15		2
	Control cylinders		20		10	4
Colorimetry/chloride content profiles	Control cubes	15	15	15		2
	* Cubes	15	15	15		8

* Specimens for measurements at 7, 28, 112, and 175 days of exposure to chloride ion diffusion.

The specimens were cured via immersion in a calcium-hydroxide-saturated solution for 28 and 220 days. The longest curing time was chosen to reduce the effect of hydration reactions on the resistivity measurements. Control specimens remained in the curing conditions throughout the experiment. After the curing period, a marine epoxy coating was applied to the surface of the prismatic and cubic specimens, leaving one face of the prisms (25 cm $\times$ 40 cm) and one face of the cubes without any epoxy coating. By leaving the epoxy-coating-free faces in a 2.8 M sodium chloride solution, according to the NT BUILD 443 standard [10], the specimens were exposed to unidirectional chloride ion diffusion for 7,

28, 112, and 175 days before testing. The control specimens were kept in a saturated calcium hydroxide solution. As an accelerated test, NT BUILD 443, requires a NaCl concentration that is approximately 5 times the concentration found in seawater.

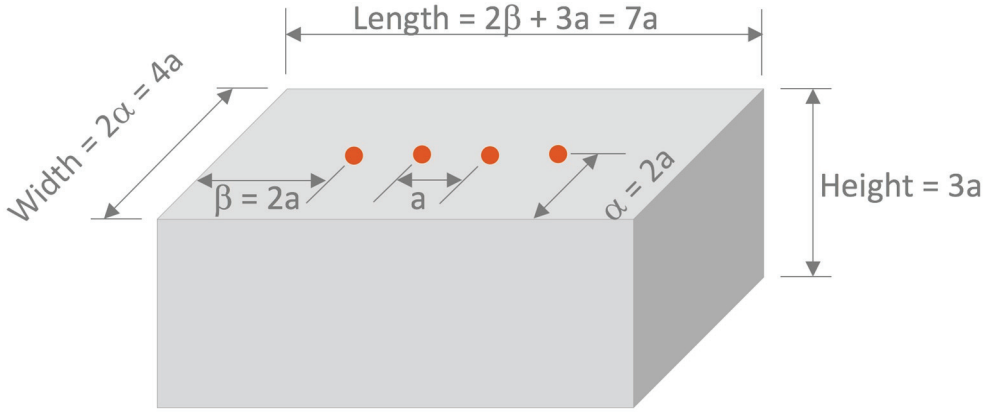

Figure 2. Criteria for estimating minimum specimen dimensions to minimize edge effects in surface electrical resistivity (r) measurements (geometric correction factor of approximately 1, and *a* represents the electrode spacing) [21,31].

2.2.2. Surface Electrical Resistivity Measurements

The surface electrical resistivity was measured using a Resipod resistivity meter (Proceq, Schwerzenbach, Zurich, Switzerland) with a Wenner array and a geometric fixture with variable electrode separation (Figure 3). There are four electrodes in the Wenner array: two external and two internal. External electrodes (A and B) apply an alternating current, while the internal electrodes (M and N) measure the potential difference. To avoid edge effects and, consequently, an overestimation of the resistivity values, the prism size was calculated according to the recommendations provided by Gowers and Millard [31] and Chun-Tao Chen et al. [32]. The resistivity readings were taken at the center along the longitudinal direction of the sample. Two axes perpendicular to each other, one longitudinal and the other transverse, were sketched on the surface of the specimens (Figure 4). The separations between the electrodes *a* were 3.8, 4.0, 4.2, 4.4, and 4.6 cm. The resistivity tests were performed on the saturated, surface-dry specimens under laboratory conditions at approximately 23 ± 1 °C. Four test groups were studied, two of which were prismatic specimens with 28 and 220 days of curing and were exposed to different chloride diffusion times. The third group had chloride-free prismatic and cylindrical specimens with 28 days of curing and a = 38 mm. Finally, the fourth had prismatic and cylindrical specimens with 220 days of moist curing and were exposed to different chloride diffusion times and using a value of a = 38 mm.

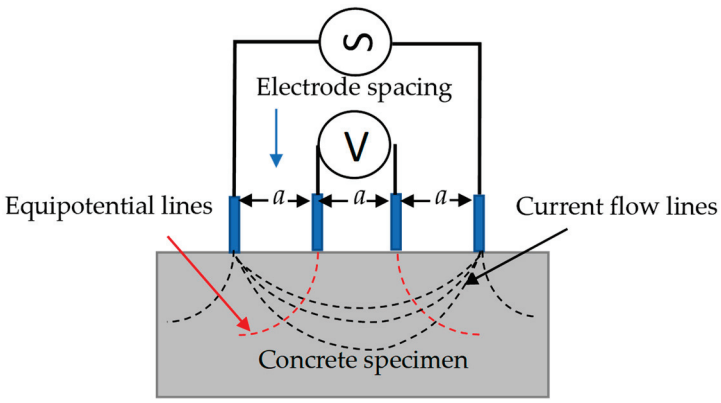

Figure 3. Illustration of the four-point Wenner array to measure surface electrical resistivity.

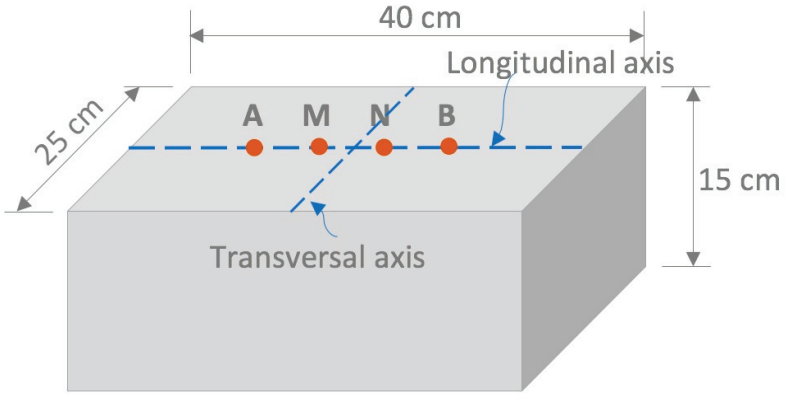

Figure 4. Diagram of the location of the reference axes used in electrical resistivity measurements as a function of electrode separation *a*. A, M, N, and B are the electrode positions in the specimen.

Three readings were taken for each electrode separation, and the mean and standard deviation were obtained. The electrical resistivity was calculated according to Equation (1), assuming a semi-infinite, homogeneous, and isotropic volume [13,14]:

$$\rho = 2\pi aR \quad (1)$$

where R is the electrical resistance, ρ is the apparent electrical resistivity, and a is the electrode separation of the Wenner array.

AASHTO T358 [19] requires correction of the resistance values based on curing in a saturated calcium hydroxide solution, which was carried out using Equation (2):

$$\rho_{corrected} = \rho\, k_{LW} \quad (2)$$

where $\rho_{corrected}$ is the true resistivity and k_{LW} is a correction factor for curing the sample in a saturated calcium hydroxide solution (k_{LW} = 1.1).

2.2.3. Data Inversion Using the RES1D Free Software

Using the RES1D free software [33], the thickness of two layers with different electrical properties (with and without chlorides) was determined. The program read a data file that contained information such as the estimate of the thickness of the surface layer, at least five data pairs of the electrode separation and their corresponding apparent resistivities (a, ρ), the number of layers sought, their resistivity (ρ), and their thickness (z). To reduce the difference between the observed and calculated values, the model and optimization subroutine modified layer thickness and resistivity were compared. The result of the data inversion represented the depth of the two layers described above.

The initial first layer thickness (penetration depth) values required for the inversion process were estimated with the solution according to Fick's second law of diffusion. The penetration depths were calculated at approximately a 0.0% chloride concentration, assuming a surface concentration of C_s = 1%. The diffusion coefficients were obtained using Equations (3)–(6) [34–36] based on a reference diffusion coefficient that considers the type of binder and w/b ratio:

$$D(t) = D_{ref}\,(t_{ref}/t)^m \quad (3)$$

where $D(t)$ is the diffusion coefficient (m^2/s) at time t; D_{ref} is the diffusion coefficient (m^2/s) at reference time t_{ref}; and m is a constant that depends on the type and amount of binder [37].

$$D_{28} = 10^{(-12.06+2.4w/b)} \quad (4)$$

$$m = 2.5\,(w/b)^{-0.6} \quad (5)$$

$$m = 0.2 + 0.4\,(\%\ FA/50) \quad (6)$$

where D_{28} is the reference diffusion coefficient (m^2/s); w/b is the water/binder ratio; and % FA is the percentage substitution of Portland cement with fly ash in the mix [35,38].

According to Polder et al. [39] and Cosoli et al. [16], the thickness of the second layer was $z \approx a$ because the resistivity measured with the Wenner configuration is considered as the average of a hemisphere of radius equal to the electrode spacing a, as long as the hypothesis that the medium is homogeneous and semi-infinite is valid.

2.2.4. Chloride Penetration Depth Using the Colorimetric Technique

The specimens were fractured along their longitudinal axis, which coincided with the axis of the electrical resistivity measurements. To conduct the colorimetric test, a freshly fractured sample was sprayed with a 0.1 N silver nitrate ($AgNO_3$) solution [40]. Silver chloride precipitated, creating a whitish region due to the rapid chemical reaction between the free chlorides and silver nitrate. This color change shows the depth of chloride penetration. The color change prevailed with time, and it was observed that the depth increased if it was measured several hours later. For this reason, measurements were taken every 10 mm with a Vernier caliper, first after spraying $AgNO_3$ and then 24 h later.

2.2.5. Chloride Content Profiles

Once the specimens used for the colorimetric tests were fractured at 7, 28, 112, and 175 days, a PF-1100 profile grinder (Germann Instruments, Evanston, IL, USA) was used to extract powder samples in 2 mm thick layers (5–7 g per layer). Finally, the powder was processed to determine the acid-soluble chloride ion content via potentiometric titration.

3. Results and Discussion

3.1. Electrical Resistivity Measurements

Figure 5 presents the electrical resistivity data versus electrode spacing in radar-type graphs for specimens that underwent (a) 28 and (b) 220 days of moist curing. The graphs show variations in the electrical resistivity of the specimens as Cl^- diffused, which resulted from the exposure time, electrode separation, w/b ratio, and the type of cementitious materials. In all cases, the percentage variations in resistivity with respect to the zero day of chloride exposure (considered as the control) were calculated.

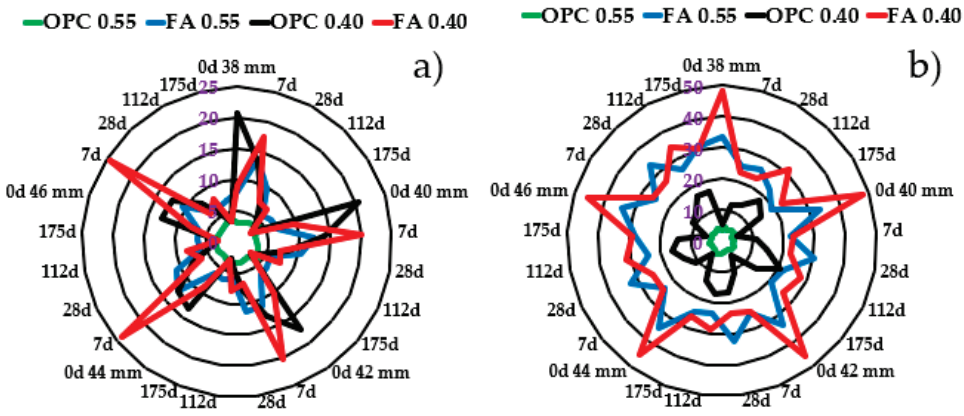

Figure 5. Electrical resistivity in mortar specimens with (**a**) 28 and (**b**) 220 days of moist curing at different Cl^- exposure times as a function of electrode spacing: 38, 40, 42, 44, and 46 mm.

When the separation of electrodes was 38 mm, it was observed that the resistivity of OPC0.55 at zero days was the lowest (3.1 kΩ·cm) compared with the other three mortars; although, by test day 175, it increased by approximately 39% of its initial value. A different behavior was exhibited by the OPC0.40, which showed the highest initial resistivity of 20.8 kΩ·cm and decreased by 35.4% at seven days. At 175 days, the resistivity decreased by 85.9%. For the FA0.55 mortar, the resistivity started at 8 kΩ·cm, increased by 73% at seven days, and then gradually decreased until it reached 18% below its initial value at 175 days.

A similar behavior was exhibited by the FA0.40, which started at 9.1 kΩ·cm and increased by 91% at seven days, and then gradually decreased until it reached 72% below its initial value. Increasing the electrode separation to 40 mm caused the resistivity to decrease by approximately 5%.

A similar behavior between zero and seven days has been described by Wang et al. [41], who observed that the resistivity does not decrease instantaneously with the ingress of Cl^- because there is no contribution to the electric current flow at the moment of chloride ion binding to the hydration products. Similarly, Loche et al. [42] reported that Cl^- ions modified the electrical response of cement-based materials. As the Cl^- ions penetrated, the electrical resistance initially increased and then decreased, which is in agreement with the behavior of specimens FA0.55 and FA0.40, which were moist-cured for 28 days. As electrical resistivity depends on the chemical composition of the pore solution, the presence of other ions, such as K^+, Na^+, OH^-, and, to a lesser extent, Ca^{2+} and SO^{2-}, could affect the resistivity measurements [43]. On the other hand, Minagawa et al. [30] found that electric current flow increases in the region of lower electrical resistivity, and Oleiwi et al. [18] observed that as the Cl^- content in the pore solution increases, the resistivity decreases. The latter is in agreement with the findings of Polder et al. [22] and Cosoli et al. [16], who consider the decrease in resistivity to be related to the presence of chloride ions.

Increased electrode spacing allowed deeper probing into the sample [21,31]; for example, by changing a from 38 mm to 46 mm, the fraction of the analyzed volume that had electrical properties of the "layer" containing chloride ions decreased and the measurements better reflected the properties of the zone that was free from these ions. Using this strategy, the current flow in the mortar is more homogeneous and the variability in the measurements is lower [22]. The resistivity also decreased as the w/b ratio increased, as expected, because of a larger porosity and connectivity.

In contrast to the mortar specimens that were moist-cured for 28 days, where the benefits of using fly ash were marginal, the resistivity of mortars with long moist curing showed a completely different behavior. Figure 5b shows that sample OPC0.55 had the lowest resistivity, with similar values and behavior to the sample that was moist-cured for 28 days. The resistivity started at 3.4 kΩ·cm and remained nearly constant during the chloride exposure time (175 days). Sample OPC0.40 showed the effects of a lower w/b ratio. Its resistivity started at 5.6 kΩ·cm and increased 2.16 times at seven days, then gradually increased until reaching 2.64 times its initial value at 175 days. For sample FA0.55, the initial resistivity value was much higher (33.8 kΩ·cm) than samples containing only cement. Its resistivity decreased by 26% in seven days and continued decreasing by up to 44% of its initial value. A similar behavior was observed for sample FA0.40, which started at a resistivity of 48.3 kΩ·cm and decreased by 53% at seven days; then, it increased at 112 days and decreased again at a resistivity value similar to the one measured at seven days. Increasing the electrode separation (40–46 mm) caused a decrease in the resistivity (by approximately 9%). There was also a decrease in resistivity as the w/b ratio increased, as expected.

Specimens that were moist-cured for 28 days had a lower surface resistivity than those cured for 220 days due to the significant cement hydration effects at the early stages, with resistivities ranging from 3 to 20 kΩ·cm. In contrast, at the longest curing time, the resistivity ranged from 3 to approximately 50 kΩ·cm (ρ OPC0.55 < ρ OPC0.40 < ρ FA0.55 < ρ FA0.40) due to the denser microstructure and higher degree of hydration. Specimens with a higher w/b ratio showed lower resistivity than those with a lower w/b ratio. Moreover, specimens with FA had higher resistivity than those constructed only with OPC. This is because of the pozzolanic reaction of FA that produced more C-S-H, thus decreasing the porosity and refining the pore structure. The formation of solid phases such as Friedel's salt may affect the resistivity.

3.1.1. Electrical Resistivity of Chloride-Free Specimens

Figure 6 shows the resistivity evolution as a function of age, w/b ratio, type of cementitious materials, and specimen geometry. Measurements were performed at 0, 28, 112, and 175 days. The age of the specimens was obtained from the sum of the 28 days of moist curing plus the testing day. As expected, due to hydration reactions, resistivity increased with age in most of the specimens, especially in those containing FA. According to Grazia et al. [44], FA and other SCMs impact concrete's microstructure and pore solution chemistry (alkalinity reduction). They found that the resistivity may increase by up to ten times when adding SCM due to the formation of additional C-S-H, which acts as an electrical barrier. The pozzolanic reaction leads to the partial consumption of portlandite from the system and a decrease in pH. According to Medeiros and Lima [45] and Kang et al. [46], blended cements have higher resistivity than OPC. Although class F FA slows down the C-S-H formation, in the present study, the resistivity was still improved compared with OPC mortars. Reducing the w/b ratio from 0.55 to 0.40 also causes an increase in resistivity due to a reduced porosity and connectivity of lower w/b ratio mortars. Hou [47] observed that the microstructure of the C(A)SH gel conducts water molecules and ions less easily due to the addition of Al^{3+}.

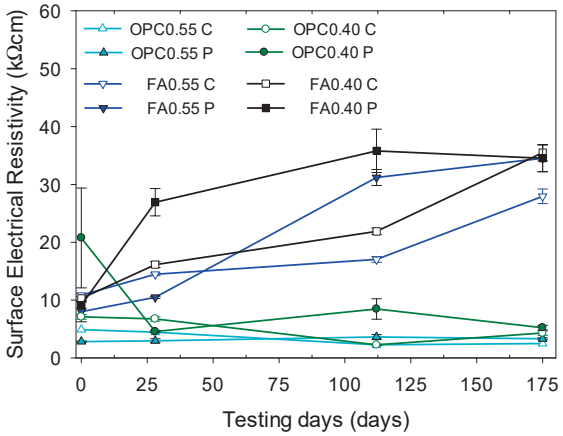

Figure 6. Evolution of electrical resistivity (using a = 38 mm) in control prismatic and cylindrical specimens after 28 days of moist curing. Error bars represent ± one standard deviation.

The shape and size of the specimens had a significant influence on the resistivity, and in all cases, cylindrical specimens showed lower values than prismatic ones. The dispersion of the measured resistivity, expressed by the standard deviation bars, was smaller for cylinders than for prisms due to the propagation geometry of electric waves [48,49]. This is in agreement with the investigations of Hornáková and Lehner [50], who determined that the variance in measured resistivity values in concrete specimens, shown through standard deviation, was two to three times lower for cylindrical geometry than for prismatic geometry.

3.1.2. Electrical Resistivity of Mortars without Hydration Effects Exposed to Chlorides

Figure 7 compares the resistivity of cylindrical and prismatic specimens after 220 days of moist curing that were then subjected to chloride ion diffusion. The effect of hydration on the resistivity of these specimens was expected to be negligible because of the long moist-curing time. As chloride ions diffused into the samples, the resistivities exhibited a distinct behavior depending on the mix composition (mortars containing FA or only OPC), type of specimen, and w/b ratio. Mortars containing only OPC exhibited the lowest resistivities, as mentioned in Section 3.1. The resistivity of the OPC0.55 specimens remained nearly constant during the 175 days. Specimens of OPC0.40 mortar with prismatic geometry demonstrated a twofold increase at seven days; then, the resistivities remained nearly constant. Contrary to this behavior, the cylinders showed a constant resistivity up to 28 days, and then it slightly increased at 112 and 175 days.

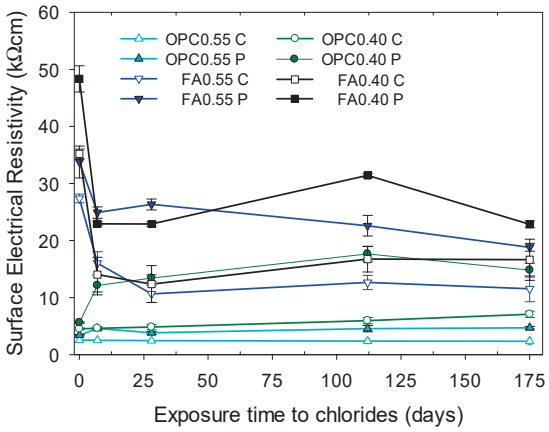

Figure 7. Electrical resistivity of cylindrical (C) and prismatic (P) specimens as a function of exposure time to a 2.8 M NaCl solution, using a = 38 mm. The specimens were previously moist-cured in a saturated calcium hydroxide solution for 220 days. Error bars represent ± one standard deviation.

Mortars containing FA exhibited a different behavior. After seven days, the resistivity of the FA0.55 specimens decreased by around 50% and then continued to decrease gradually. The resistivity of the FA0.40 specimens also significantly decreased at seven days (by approximately 53%), but then it remained nearly constant or slightly increased at 112 and 175 days. As was shown in the previous section (Section 3.1.1), cylindrical specimens had a lower resistivity than prismatic specimens.

3.2. Chloride Penetration Depth Using Three Different Techniques

Figure 8 illustrates the chloride penetration depth measured in the mortar specimens immediately after spraying silver chloride on the fractured surface. As expected, the penetration depth increased with chloride exposure time. At the end of the exposure to chlorides (175 days), the highest penetration was observed for the OPC0.55 mortar, followed by OPC0.40. The lowest penetration depth was seen for FA0.55, and FA0.40 had the highest resistivity. The chloride concentration for color change depends on the amount of OH^- ions in the pore solution. This ranges from 0.28 to 1.69% by mass of cement or between 0.072 and 0.714 mol/L for the $AgNO_3$ technique [51]. In addition, there is no consensus on the chloride concentration corresponding to the color change boundary. The average level of soluble Cl^- detected at the color change boundary was 0.9 wt.% cementitious materials or 0.12 wt.% concrete, with high coefficients of variation of 33% and 40%, respectively [40]. The amount of AgCl and Ag_2O formed at the color change boundary depends on the Cl^-/OH^- ratio in the pore solution and can be seen as an estimation of the chloride ion penetration depth, rather than the actual boundary between chloride-containing and chloride-free areas.

When performing the colorimetric test, the presence of a diffuse zone was detected between the zone with and without chlorides, which was difficult to measure immediately after spraying with $AgNO_3$. Therefore, the decision was made to keep the samples under the laboratory conditions, and a second measurement was performed 24 h later. The second measurement showed a higher chloride penetration depth than that observed immediately after spraying. Figure 9 shows photographs from two specimens at 0 and 24 h after spraying. The white region depth increased by an average of 27% at 24 h after spraying the $AgNO_3$ solution. To the best of our knowledge, this observation has not been reported in the existing literature.

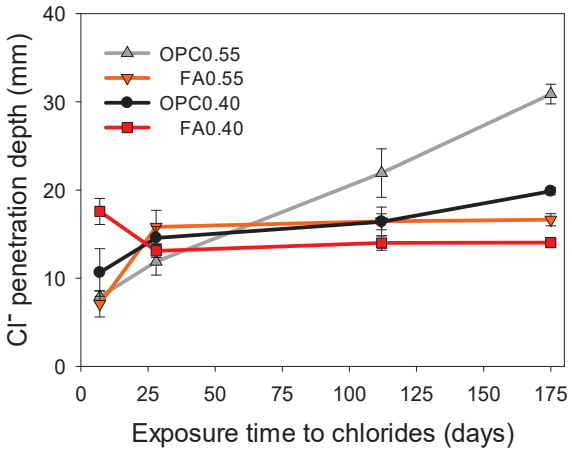

Figure 8. Chloride penetration depth versus the exposure time from $AgNO_3$ solution spraying.

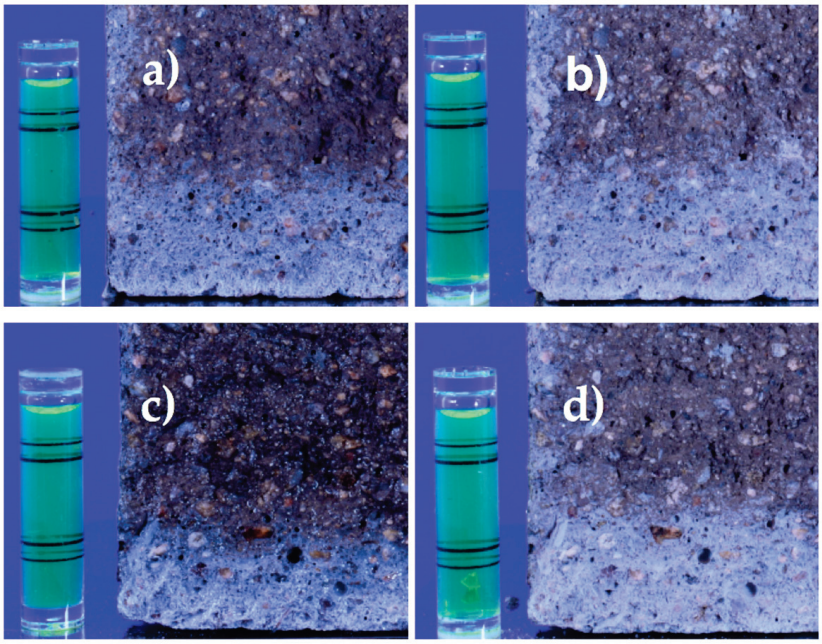

Figure 9. Change in penetration depth with time in the colorimetric test: (**a**) OPC0.55 at 0 h, (**b**) OPC0.55 at 24 h, (**c**) FA0.55 at 0 h, and (**d**) FA0.55 at 24 h after spraying the $AgNO_3$ on the broken surface. The bubble level was 40 mm in height.

SCMs change how the hydrated cement paste phases are formed, and thus, their Cl^- binding properties [52]. For example, FA is a material rich in reactive aluminates and exhibits increased AFm formation and, therefore, increased Cl^- binding in the C(A)SH. A decrease in the amount of Ca^{2+} causes a decrease in the amount of Cl^- bound to AFm and an increase in the amount bound to C(A)SH since it is a portlandite-deficient system. The ingress of Cl^- reduces the adsorption of Al^{3+} from C(A)SH and increases the amount of Al^{3+} available to form chloride-bound AFm.

In the present study, a 2.8 M NaCl concentration was used; therefore, the Cl^- ions entering the system must compete to displace the SO_4^{2-}, OH^-, and/or CO_3^{2-} anions of the different monosulfoaluminates and, finally, Friedel salt is formed [4]. According to Balonis et al. [4], at high chloride concentrations the Kuzel salt or monocarboaluminate phases are destabilized by increasing the chemically bound chloride so that a high chloride concentration would make the formation of the AFm phases, such as the Kuzel salt, impossible. When the systems destabilize, ions such as sulfate ions can be released, and

they react with calcium and aluminum, forming ettringite and causing expansion due to the increase in the molar volume of the solid and refining of the porosity [4].

Figure 10 shows the chloride content profiles for the mortar specimens obtained via potentiometric titration, as well as the chloride penetration depth obtained by spraying the $AgNO_3$ solution. Figure 10a shows that OPC0.55 had the highest Cl^- penetration, reaching a depth of approximately 38 mm at 175 days of chloride diffusion, whereas for FA0.55, the depth reached 22 mm (Figure 10b). The latter was expected because of the presence of FA. In the same manner, OPC0.40 (Figure 10c) had a 26 mm penetration, and FA0.40 (Figure 10d) exhibited the lowest penetration (18 mm). The measurements were taken at the color change boundary immediately after spraying the freshly fractured surfaces with the $AgNO^3$ solution. This test underestimates the chloride penetration depth.

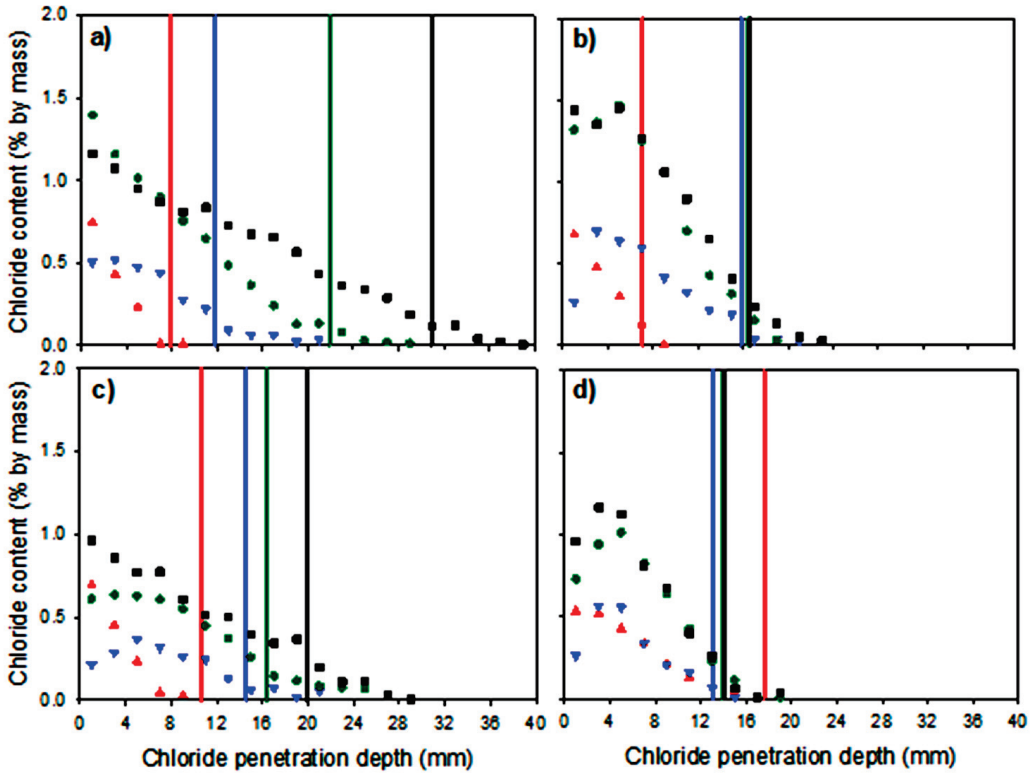

Figure 10. Total chloride content profiles and chloride penetration depth determined using colorimetry after spraying and at 7 (red), 28 (blue), 112 (green), and 175 (black) days of exposure to chlorides: (**a**) OPC0.55, (**b**) FA0.55, (**c**) OPC0.40, and (**d**) FA0.40.

Table 4 presents the apparent diffusion coefficients calculated by fitting the data of the chloride content profiles shown in Figure 10 to the solution of Fick's second law of diffusion [34]. The trends observed in the diffusion coefficient from 28 days up to 175 days of exposure to chlorides show higher values for the high w/b ratios and lower values for the low w/b ratios, as expected. Moreover, the mortars containing fly ash exhibited lower diffusion coefficients than the mortars containing only OPC because of the pozzolanic reaction that produces additional C-S-H and reduces porosity and permeability.

A linear relationship between the penetration depths from spraying the $AgNO_3$ solution and the concentration profiles is shown in Figure 11. There is a linear correlation (R^2 = 0.96) between them with a slope < 1, indicating an underestimation with the colorimetric method.

Table 4. The apparent diffusion coefficient and surface chloride concentration of mortar specimens moist-cured for 28 days determined by fitting chloride content profiles to the solution of Fick's second law of diffusion [34].

Exposure Time	OPC0.55		FA0.55		OPC0.40		FA0.40	
	D	C_s	D	C_s	D	C_s	D	C_s
(Days)	(m^2/s)	(%)	(m^2/s)	(%)	(m^2/s)	(%)	(m^2/s)	(%)
7	2.6×10^{-11}	1.09	4.1×10^{-11}	0.98	3.3×10^{-11}	1.00	1.2×10^{-10}	1.85
28	6.8×10^{-11}	0.79	5.0×10^{-11}	1.08	7.0×10^{-11}	0.70	2.9×10^{-11}	0.96
112	1.4×10^{-11}	1.62	5.6×10^{-12}	3.00	1.8×10^{-11}	1.04	5.0×10^{-12}	2.12
175	2.6×10^{-11}	1.41	5.6×10^{-12}	2.46	1.4×10^{-11}	1.00	4.0×10^{-12}	1.85

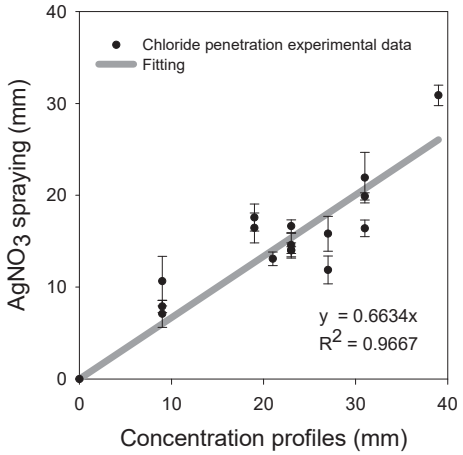

Figure 11. Relationship between the penetration depth of Cl^- in mortar specimens at different days of chloride exposure obtained using colorimetry after spraying a 0.1 N $AgNO_3$ solution, and the distance from concentration profiles. Error bars represent ± one standard deviation.

Another alternative way of obtaining the depth of chloride penetration proposed in this study is by inverting the surface electrical resistivity data obtained at different exposure times to 2.8 M NaCl. Figure 12 shows that, as expected, for mortars with high w/b ratios or the case of fly-ash-free mixtures, the chloride penetration was higher.

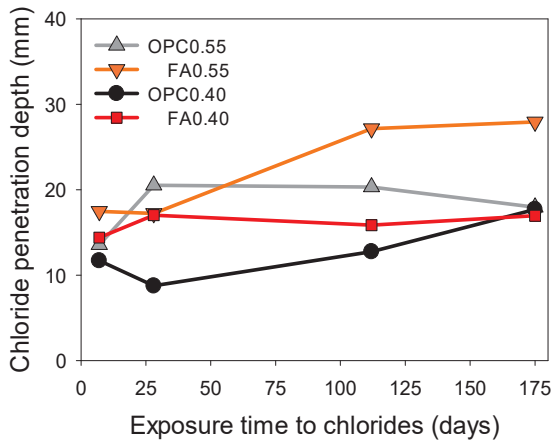

Figure 12. Chloride penetration depth in mortar specimens OPC0.55, FA0.55, OPC0.40, and FA0.40 obtained via inversion of resistivity data at different exposure times to 2.8 M NaCl solution.

Figure 13 shows two linear correlations of the chloride penetration depth determined through inversion of the resistivity data at different Cl^- exposure times. The first of these is R^2 = 0.86, determined by comparing it with the depth of chloride ion penetration obtained

via the colorimetric method, while the second is $R^2 = 0.86$, determined by comparing it with the depth of chloride ion penetration determined via the chloride content profiles. The first correlation indicates that the resistivity measurements are underestimates and the second one overestimates the chloride penetration. Fares et al. [25] obtained chloride profiles using electrical resistivity tomography (ERT) and compared them with those obtained using the chloride content of powder samples. They observed a good agreement between ERT and the destructive test because they used a smaller electrode separation than in our study, which was restricted to a minimum of 38 mm. In addition, their electrodes maintained a fixed relative position to perform the measurement with all electrode separations, which resulted in a lower variability of measurements.

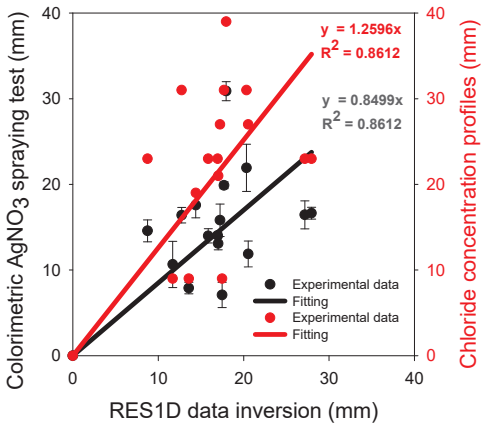

Figure 13. Correlation between Cl^- penetration depth obtained via resistivity data inversion and that obtained using the colorimetric test and chloride content profiles on mortar specimens on different days of chloride exposure. Error bars represent ± one standard deviation.

4. Conclusions

This study explored the use of a simple Wenner array to measure changes in the surface electrical resistivity of mortars subject to chloride diffusion under laboratory conditions as a function of electrode separation. The following conclusion is given: Diffusion of chlorides in mortar specimens affects the resistivity measured with a simple Wenner array with variable electrode separation after inversion with the RES1D software, which permits indirect calculation of the chloride penetration depth. This was validated through a linear correlation with $AgNO_3$ spraying and chloride concentration profiling, both resulting in an R^2 of approximately 0.86.

Author Contributions: Conceptualization, M.A.P.-C. and P.F.d.J.C.-B.; formal analysis, M.A.P.-C., P.F.d.J.C.-B. and F.M.L.-M.; funding acquisition, P.F.d.J.C.-B.; investigation, M.A.P.-C. and F.M.L.-M.; methodology, M.A.P.-C. and P.F.d.J.C.-B.; project administration, P.F.d.J.C.-B.; supervision, P.F.d.J.C.-B.; writing—original draft, M.A.P.-C.; writing—review and editing, P.F.d.J.C.-B. and F.M.L.-M. All authors have read and agreed to the published version of the manuscript.

Funding: This research was funded by SIP of Instituto Politécnico Nacional under grant numbers SIP 20210481, SIP 20221260, and SIP 20231520. The APC was funded by project SIP 20231520.

Institutional Review Board Statement: Not applicable.

Informed Consent Statement: Not applicable.

Data Availability Statement: The data presented in this study are available on request from the corresponding author.

Acknowledgments: M. Pablo-Calderón acknowledges CONACYT (now CONAHCYT) from Mexico for the Graduate Studies scholarship, COFAA-IPN for an Institutional Scholarship for Researcher Training (BEIFI), and the IPN program "Technological Development and Innovation Projects" for IPN Students 2022 for funding this project. P. Cano acknowledges SIP from IPN for funding the research projects with ID codes SIP 20210481, SIP 20221260, and SIP 20231520. The authors acknowledge Erick León Pérez for providing the photos shown in Figure 8.

Conflicts of Interest: The authors declare no conflict of interest.

References

1. Neville, A. Chloride Attack of Reinforced Concrete: An Overview. *Mater. Struct.* **1995**, *28*, 63–70. [CrossRef]
2. Spragg, R.; Bu, Y.; Snyder, K.; Bentz, D.; Weiss, J. *Electrical Testing of Cement-Based Materials: Role of Testing Techniques, Sample Conditioning, and Accelerated Curing*; Indiana Department of Transportation and Purdue University: West Lafayette, IN, USA, 2013.
3. Spragg, R.; Villani, C.; Snyder, K.; Bentz, D.; Bullard, J.; Weiss, J. Factors That Influence Electrical Resistivity Measurements in Cementitious Systems. *Transp. Res. Rec. J. Transp. Res. Board* **2013**, *2342*, 90–98. [CrossRef]
4. Balonis, M.; Lothenbach, B.; Le Saout, G.; Glasser, F.P. Impact of Chloride on the Mineralogy of Hydrated Portland Cement Systems. *Cem. Concr. Res.* **2010**, *40*, 1009–1022. [CrossRef]
5. Marvila, M.T.; de Azevedo, A.R.G.; Ferreira, R.L.S.; Vieira, C.M.F.; de Brito, J.; Adesina, A. Validation of Alternative Methodologies by Using Capillarity in the Determination of Porosity Parameters of Cement-Lime Mortars. *Mater. Struct. Constr.* **2022**, *55*, 19. [CrossRef]
6. Coates, G.R.; Xiao, L.; Prammer, M.G. *NMR Logging Principles and Applications*; Halliburton Energy Services: Houston, TX, USA, 1999; ISBN 9780080438801.
7. *ASTM C1202*; Standard Test Method for Electrical Indication of Concrete's Ability to Resist Chloride Ion Penetration. ASTM International: West Conshohocken, PA, USA, 2012.
8. *NT BUILD 492*; Concrete, Mortar and Cement-Based Repair Materials: Chloride Migration Coefficient from Non-Steady-State Migration Experiments. NORDTEST: Espoo, Finland, 1999.
9. *AASHTO T259*; Standard Method of Test for Resistance of Concrete to Chloride Ion Penetration. American Association of State Highway and Transportation Officials: Washington, DC, USA, 2009.
10. *NT BUILD 443*; Concrete, Hardened: Accelerated Chloride Penetration. NORDTEST: Espoo, Finland, 2010.
11. *ASTM C1556*; Standard Test Method for Determining the Apparent Chloride Diffusion Coefficient of Cementitious Mixtures by Bulk Diffusion. ASTM International: West Conshohocken, PA, USA, 2003.
12. Jenkins, A. *Surface Resistivity as an Alternative for Rapid Chloride Permeability Test of Hardened Concrete (FHWA-KS-14-15)*; Kansas Department of Transportation Bureau of Research: Kansas City, MO, USA, 2015.
13. *ASTM C1876-19*; Standard Test Method for Electrical Resistivity or Conductivity of Concrete. ASTM International: West Conshohocken, PA, USA, 2019.
14. *AASHTO TP 119*; Standard Method of Test for Electrical Resistivity of a Concrete Cylinder Tested in a Uniaxial Resistance Test. American Association of State Highway and Transportation Officials: Washington, DC, USA, 2017.
15. Morris, W.; Moreno, E.I.; Sagués, A.A. Practical Evaluation of Resistivity of Concrete in Test Cylinders Using a Wenner Array Probe. *Cem. Concr. Res.* **1996**, 551–556. [CrossRef]
16. Cosoli, G.; Mobili, A.; Tittarelli, F.; Revel, G.; Chiariotti, P. Electrical Resistivity and Electrical Impedance Measurement in Mortar and Concrete Elements: A Systematic Review. *Appl. Sci.* **2020**, *10*, 9152. [CrossRef]
17. Millard, S.G. Reinforced Concrete Resistivity Measurement Techniques. *Proc.-Inst. Civ. Eng. Part 2 Res. Theory* **1991**, *91*, 71–88. [CrossRef]
18. Oleiwi, H.; Wang, Y.; Xiang, N.; Chen, X.; Shabalin, I. An Experimental Study of Concrete Resistivity and the Effects of Electrode Configuration and Current Frequency on Measurement. In Proceedings of the Sixth International Conference on Durability of Concrete Structures, Leeds, UK, 18–20 July 2018; pp. 592–599.
19. *AASHTO T358-15*; Standard Method of Test for Surface Resistivity Indication of Concrete's Ability to Resist Chloride Ion Penetration. American Association of State Highway and Transportation Officials: Washington, DC, USA, 2015.
20. Cheytani, M.; Chan, S.L.I. The Applicability of the Wenner Method for Resistivity Measurement of Concrete in Atmospheric Conditions. *Case Stud. Constr. Mater.* **2021**, *15*, e00663. [CrossRef]
21. Robles, K.P.V.; Yee, J.J.; Kee, S.H. Effect of the Geometrical Constraints to the Wenner Four-Point Electrical Resistivity Test of Reinforced Concrete Slabs. *Sensors* **2021**, *21*, 4622. [CrossRef]
22. Polder, R.B. Test Methods for on Site Measurement of Resistivity of Concrete—A RILEM TC-154 Technical Recommendation. *Constr. Build. Mater.* **2001**, *15*, 125–131. [CrossRef]
23. Qiao, C.; Moradllo, M.K.; Hall, H.; Tyler Ley, M.; Weiss, W.J. Electrical Resistivity and Formation Factor of Air-Entrained Concrete. *ACI Mater. J.* **2019**, *116*, 85–93. [CrossRef]
24. Layssi, H.; Ghods, P.; Alizadeh, A.; Salehi, M. Electrical Resistivity of Concrete. *Concr. Int.* **2015**, *37*, 41–46.

25. Fares, M.; Villain, G.; Bonnet, S.; Palma Lopes, S.; Thauvin, B.; Thiery, M. Determining Chloride Content Profiles in Concrete Using an Electrical Resistivity Tomography Device. *Cem. Concr. Compos.* **2018**, *94*, 315–326. [CrossRef]
26. *ASTM C128-01*; Standard Test Method for Density, Relative Density (Specific Gravity), and Absorption. ASTM International: West Conshohocken, PA, USA, 2001.
27. Ramírez Ortiz, A.E. Respuesta Ultrasónica de Pastas de Cemento Sujetas a Difusión y Ligado de Iones Cloruro. Ph.D. Thesis, Instituto Politécnico Nacional, Ciudad de México, Mexico, 2018.
28. *ASTM C192/C192M*; Standard Practice for Making and Curing Concrete Test Specimens in the Laboratory. ASTM International: West Conshohocken, PA, USA, 2002.
29. *ASTM C109/C109M-02*; Standard Test Method for Compressive Strength of Hydraulic Cement Mortars. ASTM International: West Conshohocken, PA, USA, 2002.
30. Minagawa, H.; Miyamoio, S.; Hisada, M. Relationship of Apparent Electrical Resistivity Measured by Four Probe Method with Water Content Distribution in Concrete. *J. Adv. Concr. Technol.* **2017**, *15*, 278–289. [CrossRef]
31. Gowers, K.R.; Millard, S.G. Measurement of Concrete Resistivity for Assessment of Corrosion Severity of Steel Using Wenner Technique. *ACI Mater. J.* **1999**, *96*, 536–541. [CrossRef]
32. Chen, C.T.; Chang, J.J.; Yeih, W.C. The Effects of Specimen Parameters on the Resistivity of Concrete. *Constr. Build. Mater.* **2014**, *71*, 35–43. [CrossRef]
33. Loke, M. 1-D Resistivity, IP & SIP Inversion and Forward Modeling Wenner and Schlumberger Arrays. Available online: https://www.geotomosoft.com/downloads.php (accessed on 20 June 2019).
34. Nokken, M.; Boddy, A.; Hooton, R.D.; Thomas, M.D.A. Time Dependent Diffusion in Concrete-Three Laboratory Studies. *Cem. Concr. Res.* **2006**, *36*, 200–207. [CrossRef]
35. Bentz, E.C.; Thomas, M. Life-365 Service Life Prediction Model and Computer Program for Predicting the Service Life and Life-Cycle Cost of Reinforced Concrete Exposed to Chlorides. Available online: http://www.life-365.org/download.html (accessed on 15 January 2019).
36. Villagrán-Zaccardi, Y.A. Ingreso de Cloruro En Hormigones Con Cemento Pórtland Compuesto. Influencias Del Tiempo y de La Capacidad de Fijación. Ph.D. Thesis, Universidad Nacional del Centro de la Provincia de Buenos Aires, Tandil, Argentina, 2009.
37. Mangat, P.S.; Molloy, B.T. Prediction of Long Term Chloride Concentration in Concrete. *Mater. Struct.* **1994**, *27M*, 338–346. [CrossRef]
38. Park, K.B.; Lee, H.S.; Wang, X.Y. Prediction of Time-Dependent Chloride Diffusion Coefficients for Slag-Blended Concrete. *Adv. Mater. Sci. Eng.* **2017**, *2017*, 1901459. [CrossRef]
39. Polder, R.; Andrade, C.; Elsener, B.; Vennesland, Ø.; Gulikers, J.; Weidert, R.; Raupach, M. RILEM TC 154-EMC: Electrochemical Techniques for Measuring Metallic Corrosion. Test Methods for on Site Measurement of Resistivity of Concrete. *Mater. Struct.* **2000**, *33*, 603–611.
40. Meck, E.; Sirivivatnanon, V. Field Indicator of Chloride Penetration Depth. *Cem. Concr. Res.* **2003**, *33*, 1113–1117. [CrossRef]
41. Wang, Y.; Nanukuttan, S.; Bai, Y.; Yang, K.; Basheer, M. Electrical Resistance to Monitor Carbonation and Chloride Ingress. *ACI Mater. J.* **2019**, *116*, 129–138. [CrossRef]
42. Loche, J.M.; Ammar, A.; Dumargue, P. Influence of the Migration of Chloride Ions on the Electrochemical Impedance Spectroscopy of Mortar Paste. *Cem. Concr. Res.* **2005**, *35*, 1797–1803. [CrossRef]
43. Tibbetts, C.M.; Paris, J.M.; Ferraro, C.C.; Riding, K.A.; Towsend, T.G. Relating Water Permeability to Electrical Resistivity and Chloride Penetrability of Concrete Containing Different Supplementary Cementitious Different Supplementary Cementitious Materials. *Cem. Concr. Compos.* **2020**, *107*, 103491. [CrossRef]
44. de Grazia, M.T.; Deda, H.; Sanchez, L.F.M. The Influence of the Binder Type & Aggregate Nature on the Electrical Resistivity of Conventional Concrete. *J. Build. Eng.* **2021**, *43*, 102540. [CrossRef]
45. Medeiros, R.A.; Lima, M.G. Electrical Resistivity of Unsaturated Concrete Using Different Types of Cement. *Constr. Build. Mater.* **2016**, *107*, 11–16. [CrossRef]
46. Kang, S.; Tyler Ley, M.; Lloyd, Z.; Kim, T. Using the Particle Model to Predict Electrical Resistivity Performance of Fly Ash in Concrete. *Constr. Build. Mater.* **2020**, *261*, 119975. [CrossRef]
47. Hou, D.; Li, T.; Wang, P. Molecular Dynamics Study on the Structure and Dynamics of NaCl Solution Transport in the Nanometer Channel of CASH Gel. *ACS Sustain. Chem. Eng.* **2018**, *6*, 9498–9509. [CrossRef]
48. du Plooy, R.; Villain, G.; Palma Lopes, S.; Ihamouten, A.; Dérobert, X.; Thauvin, B. Electromagnetic Non-Destructive Evaluation Techniques for the Monitoring of Water and Chloride Ingress into Concrete: A Comparative Study. *Mater. Struct. Constr.* **2015**, *48*, 369–386. [CrossRef]
49. Samouëlian, A.; Cousin, I.; Tabbagh, A.; Bruand, A.; Richard, G. Electrical Resistivity Survey in Soil Science: A Review. *Soil Tillage Res.* **2005**, *83*, 173–193. [CrossRef]
50. Horňáková, M.; Lehner, P. Relationship of Surface and Bulk Resistivity in the Case of Mechanically Damaged Fibre Reinforced Red Ceramic Waste Aggregate Concrete. *Materials* **2020**, *23*, 5501. [CrossRef]

51. He, F.; Shi, C.; Yuan, Q.; Chen, C.; Zheng, K. $AgNO_3$ Based Colorimetric Methods for Measurement of Chloride Penetration in Concrete. *Constr. Build. Mater.* **2012**, *26*, 1–8. [CrossRef]
52. De Weerdt, K. Chloride Binding in Concrete: Recent Investigations and Recognised Knowledge Gaps: RILEM Robert L'Hermite Medal Paper 2021. *Mater. Struct.* **2021**, *54*, 1–16. [CrossRef]

applied sciences

MDPI

Article

Asphalt Pavement Transverse Cracking Detection Based on Vehicle Dynamic Response

Wenya Ye [1], Wenzhi Yuan [2] and Qun Yang [2,*]

[1] School of Civil and Transportation Engineering, Ningbo University of Technology, Ningbo 315211, China; nature000000@163.com
[2] The Key Laboratory of Road and Traffic Engineering, Ministry of Education, Tongji University, Shanghai 201804, China; 2011380@tongji.edu.cn
* Correspondence: yang667tj@163.com

Featured Application: This paper proposes a novel method for transverse cracking detection based on vehicle vibration response.

Abstract: Transverse cracking is thought of as the typical distress of asphalt pavements. A faster detection technique can provide pavement performance information for maintenance administrations. This paper proposes a novel vehicle-vibration-based method for transverse cracking detection. A theoretical model of a vehicle-cracked pavement vibration system was constructed using the d'Alembert principle. A testing system installed with a vibration sensor was put in and applied to a testing road. Then, parameter optimization of the Short-time Fourier transform (STFT) was conducted. Transverse cracking and normal sections were processed by the optimized STFT algorithm, generating two ideal indicators. The maximum power spectral density and the relative power spectral density, which were extracted from 3D time–frequency maps, performed well. It was found that the power spectral density caused by transverse cracks was above 100 dB/Hz. The power spectral density at normal sections was below 80 dB/Hz. The distribution of the power spectral density for the cracked sections is more discrete than for normal sections. The classification model based on the above two indicators had an accuracy, true positive rate, and false positive rate of 94.96%, 92.86%, and 4.80%, respectively. The proposed vehicle-vibration-based method is capable of accurately detecting pavement transverse cracking.

Keywords: asphalt pavement; transverse cracking detection; vehicle vibration; STFT; PSD

1. Introduction

Pavement distress detection is significant for road maintenance [1]. Transverse cracking is a typical form of distress that indicates asphalt pavement surface or base damage [2]. If transverse cracking cannot be repaired in time, it will deteriorate pavement strength, stiffness, and durability [3]. Furthermore, the whole transportation system cannot operate smoothly and safely. Therefore, it is vital for highway maintenance departments to detect transverse cracking efficiently and effectively.

Traditional detection methods for pavement distress include manual-based and image-based techniques. The manual-based method plays an important role in low-grade highway distress detection. This method can detect all types of distress. At the same time, its detection efficiency and accuracy remain low. However, data reprocessing of the manual-based method is highly subjective, complex, and does not fit the needs of large-scale road network detection [4]. Due to the above problems, automatic detection based on images has been proposed and applied widely [5]. Compared with the manual-based method, its detection efficiency is superior. However, its accuracy depends on features generated through a manual process or machine learning algorithm [6]. The automatic method mainly

refers to an image-based method, which needs to be trained using other methods, such as deep learning, reinforcement learning, etc. [2,5,6]. In general, if maintenance departments expect to obtain timely pavement distress information of a huge traffic network, an image-based method cannot fulfil this expectation.

In recent years, indirect damage detection of traffic infrastructure using a moving test vehicle has gradually risen [7]. Yang and co-workers first proposed extracting bridge frequencies from a moving test vehicle's dynamic response [8]. Compared with the direct method for setting vibration sensors on the traffic infrastructure, the indirect approach is generally less costly, less risky, and less laborious [9].

However, pavement distress detection based on a vehicle's dynamic response is still in developmental stages. Yu and co-workers proposed that the mechanical response of automobile vibrations can be used to detect pavement distress. The vibration response's magnitude and frequency depend on the severity of the pavement distress, including cracks and surface rutting [10]. The MIT Laboratory of Computing and Artificial Intelligence proposed a P^2 road monitoring architecture for pothole detection. During field testing, over 90% of the identified potholes needed maintenance [11]. In addition, smartphone-based vibration sensing has become a significant technique for detecting road surface conditions [12]. Nericell is a system for the monitoring of road conditions through mobile smartphones equipped with some sensors. These conditions include bumps, potholes, braking, and honking [13]. Wolverine is another typical traffic and road condition estimation system using smartphone sensors that collects acceleration in three directions. More importantly, the system adopts a machine learning method (SVM) to improve its false negative rates [14]. However, the smartphone sensing method has lower accuracy, especially in transverse cracking detection. Qun Yang and his co-workers focused on identifying transverse cracking of asphalt pavement through professional vibration sensors. Their study included the time, frequency, wavelet, and statistical analysis of the vehicle vibration signal [15]. Six main features were extracted from different domains, which generated eight classification models, and the feasibility of this method was investigated using 2292 pavement sections [6]. Bruno S's team focus on monitoring the road network through a low-cost system based on vehicle vibration, which reached the ideal effects for evaluating the pavement conditions [16–18]. Apart from that, some excellent dynamic vehicle models have been established to illustrate the basic principle between the pavement condition and the vehicle [19].

Most studies concentrate more on time or frequency domain analysis. The features extracted from the time or frequency domain are better when passing by some obvious distress, such as potholes and rutting. However, the features caused by transverse cracking are limited in the time or frequency domain, making them hard to detect. Pavement transverse cracking hardly affects the threshold of vehicle acceleration amplitude because of its limited length along the driving direction. Similarly, the Fourier transform just reflects the whole frequency distribution of the vehicle's vibration signal. It is challenging to express small signal mutations caused by transverse cracking, including its location. Apart from that, vehicle parameters are also important. Different locations can generate different dynamic responses. Different vehicle types, including fuel-driven and electric-driven, also affect the response amplitude [20]. So, it is necessary to select the right car and the ideal response location [21].

Consequently, the present work aims to accurately identify pavement transverse cracking damage using a vehicle dynamic response. To that end, this paper formulates a novel strategy to explore time–frequency features using a Short-time Fourier transform (STFT) and better characterization indicators. More importantly, this novel method can balance the key points, including detection accuracy, equipment cost, and efficiency. The detection method based on a vehicle's dynamics response solves the problems of low detection frequency and the high cost of existing detection methods. Through the optimized STFT algorithm, the method overcomes the lack of detection accuracy caused by traditional time-domain analysis or frequency-domain analysis. This is because the optimized STFT

algorithm focuses more on transverse cracking detection, which takes into account the accuracies of both time- and frequency-domain information recognition.

2. Theoretical Modeling

Suppose the vertical displacement between the wheel and the body is Z_1 and Z_2, respectively. The coordinate origin is the equilibrium position between the wheel and the body, shown in Figure 1. m_1 and m_2 denote the quality of the wheel and body, respectively. k_1 and k_2 denote the stiffness of the tire and spring, and c_2 denotes the damping coefficient of the shock absorber. In this study, we see the tire as an undamped linear spring system.

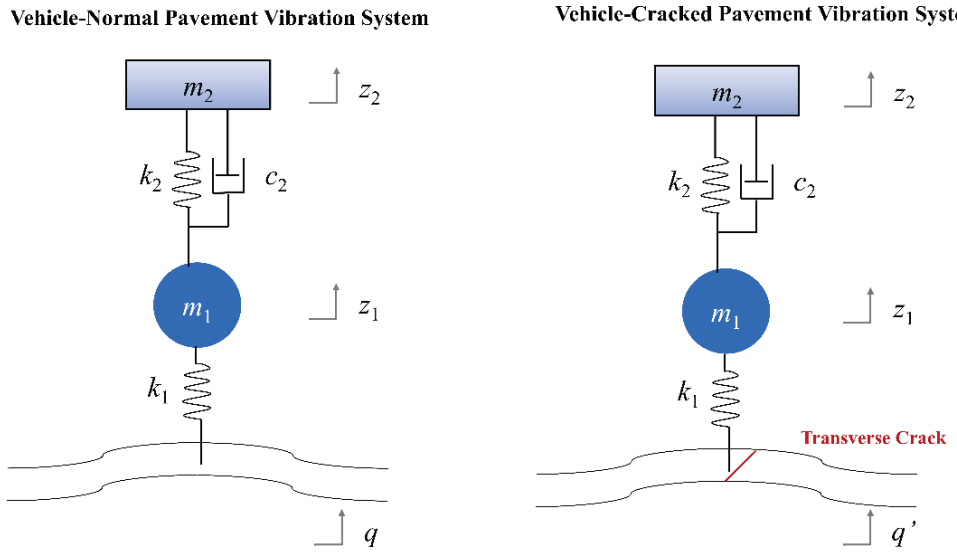

Figure 1. A quarter vehicle–pavement system.

For a quarter vehicle-normal pavement system, the equation of motion is constructed based on the d'Alembert principle [22], which is shown in Equations (1) and (2):

$$m_2\ddot{Z}_2 + c_2\left(\dot{Z}_2 - \dot{Z}_1\right) + k_2\left(Z_2 - Z_1\right) = 0 \tag{1}$$

$$m_1\ddot{Z}_1 - c_2\left(\dot{Z}_2 - \dot{Z}_1\right) - k_2\left(Z_2 - Z_1\right) + k_1 Z_1 = k_1 q \tag{2}$$

where the first-order derivation of the vertical displacement denotes the vertical speed and the second-order derivation of the vertical displacement indicates the vertical acceleration.

The equation of motion for a quarter vehicle-cracked pavement system is constructed following Equations (3) and (4).

$$m_2\ddot{Z}_2 + c_2\left(\dot{Z}_2 - \dot{Z}_1\right) + k_2\left(Z_2 - Z_1\right) = 0 \tag{3}$$

$$m_1\ddot{Z}_1 - c_2\left(\dot{Z}_2 - \dot{Z}_1\right) - k_2\left(Z_2 - Z_1\right) + k_1 Z_1 = k_1 q' \tag{4}$$

In Equations (2) and (4), the system's input is expressed as q (normal pavement) and q' (cracked pavement), which denotes the pavement's surface profile. They can be represented in the complex exponential form:

$$q = q_0^{i\omega t} \tag{5}$$

$$q' = q_0^{i\omega t} + \delta(\Delta t) \tag{6}$$

where ω denotes angular frequency, and q_0 is the initial profile. δ denotes the transient impulse caused by transverse cracking, which is affected by the crack's cracking degree. Δt is the response time that the wheel passes by the transverse crack.

The tire-cracked pavement contact process is shown in Figure 2a. During actual driving, the tire and the pavement are always in contact with a certain geometry, defined as ground contact (GC). In addition, the contact shape between transverse cracking and the tire is not a point but a certain geometric area, defined as the Areas of Crack Action (ACA).

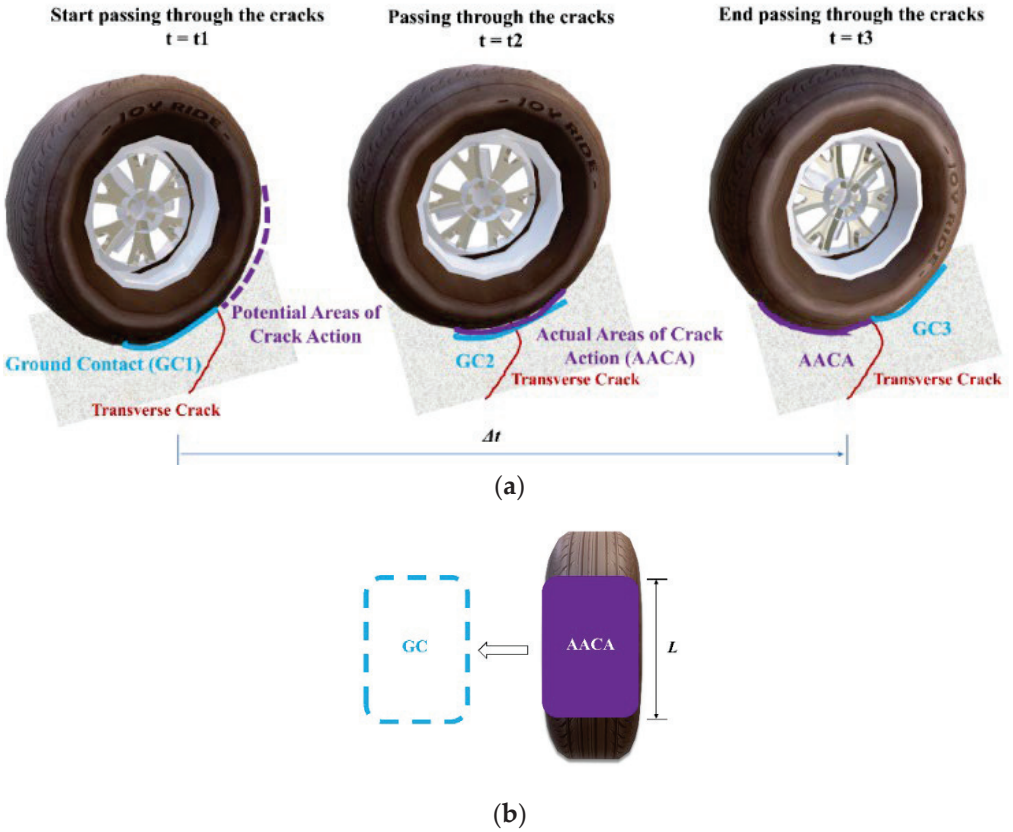

Figure 2. The tire-cracked contact model. (**a**) Tire-cracked pavement contact process; (**b**) AACA and its action length.

The cracks are located at the junction of the ground surface (GC1) and the action surface when first touching the transverse cracked pavement (t = t1). The action area is virtual, defined as the Potential Action of Crack Action (PACA), since the tire has not yet begun to adequately feel the excitation of the transverse crack.

As the wheel rolls forward (t = t2), the transverse crack and the tire act continuously, giving a sufficient transient shock. GC2 continues to iterate forward and overlaps each other, which makes up the action areas. The action areas are defined as the Actual Action of Crack Action (AACA).

By the end of the excitation of the crack (t = t3), the crack is at the AACA's end and the end of the next ground contact (GC3). It can be seen that the displacement between the crack and the tire is the length of the AACA along the direction of the vehicle (L), which is shown in Figure 2b. The geometric size of the GC is certain when the tire pressure and spring load mass are certain. As a result, the grounding area remains unchanged. While passing by different pavement conditions (transverse cracks, potholes, bumps), the AACA differs due to the significant differences in interaction characteristics caused by the changed space shape.

Therefore, the tire-cracked pavement action time can be calculated by the length (L) and the speed (v) of the grounded rectangle, which is shown in Equation (7).

$$\Delta t = \frac{L}{v} \tag{7}$$

The wheel and body frequency expression are analyzed if q and q' are substituted into the motion equation.

For the vehicle-normal pavement model:

$$Z_1(\omega) = \frac{k_1(k_2 + i\omega c_2 - m_2\omega^2)}{(k_1 + k_2 + i\omega c_2 - m_1\omega^2)(k_2 + i\omega c_2 - m_2\omega^2) - (k_2 + i\omega c_2)} \cdot {q_0}^{i\omega t} \tag{8}$$

$$Z_2(\omega) = \frac{k_1(k_2 + i\omega c_2)}{(k_1 + k_2 + i\omega c_2 - m_1\omega^2)(k_2 + i\omega c_2 - m_2\omega^2) - (k_2 + i\omega c_2)} \cdot {q_0}^{i\omega t} \tag{9}$$

For the vehicle-cracked pavement model:

$$Z_1(\omega) = \frac{k1(k_2 + i\omega c_2 - m_2\omega^2)}{(k_1 + k_2 + i\omega c_2 - m_1\omega^2)(k_2 + i\omega c_2 - m_2\omega^2) - (k_2 + i\omega c_2)} \cdot ({q_0}^{i\omega(t+\frac{L}{v})} + \delta(\frac{L}{v})) \tag{10}$$

$$Z_2(\omega) = \frac{k_1(k_2 + i\omega c_2)}{(k_1 + k_2 + i\omega c_2 - m_1\omega^2)(k_2 + i\omega c_2 - m_2\omega^2) - (k_2 + i\omega c_2)} \cdot ({q_0}^{i\omega(t+\frac{L}{v})} + \delta(\frac{L}{v})) \tag{11}$$

Since the vibration system's frequency response function is independent of external input, the frequency response function $P(\omega)$ of the above two systems is the same.

$$P(\omega)_{x1-q} = \frac{k_1(k_2 + i\omega c_2 - m_2\omega^2)}{(k1 + k_2 + i\omega c_2 - m_1\omega^2)(k_2 + i\omega c_2 - m_2\omega^2) - (k_2 + i\omega c_2)} \tag{12}$$

$$P(\omega)_{x2-q} = \frac{k_1(k_2 + i\omega c_2)}{(k_1 + k_2 + i\omega c_2 - m_1\omega^2)(k_2 + i\omega c_2 - m_2\omega^2) - (k_2 + i\omega c_2)} \tag{13}$$

The Fourier transform of the two system's input $T(\omega)$ is:

$$T(\omega) = \int_{-\infty}^{\infty} q_0^{i\omega t} e^{-i\omega t} dt \tag{14}$$

$$T'(\omega) = \int_{-\infty}^{\infty} \left[{q_0}^{i\omega(t+\frac{L}{v})} + \delta(\frac{L}{v}) \right] e^{-i\omega t} dt \tag{15}$$

According to the Fourier transform, the time-domain expression for the response of the body (x_2) and wheel (x_1) on normal pavement/transverse cracking is:

$$x_1 = \frac{1}{2\pi} \int_{-\infty}^{\infty} \frac{T(\omega)}{T'(\omega)} e^{-i\omega t} |P(\omega)|_{x1-q} \, e^{-\varphi_1 i} d\omega \tag{16}$$

$$x_2 = \frac{1}{2\pi} \int_{-\infty}^{\infty} \frac{T(\omega)}{T'(\omega)} e^{-i\omega t} |P(\omega)|_{x2-q} \, e^{-\varphi_2 i} d\omega \tag{17}$$

where φ indicates the amplitude angle.

As can be seen from the above equation, the vertical vibration response is affected by the characteristics of the vehicle system (position, structure), driving speed, transverse cracking degree, and the contact geometry.

3. Field Testing

3.1. Testing System

A testing vehicle, vibration sensor, action camera, location equipment, and vibration data processing system constitute the testing system, which can be seen in Figure 3. The test car was an eighth generation Honda Accord. The vehicle's length and height are: 4945/1845/1480 mm, displacement is 2.03, and maximum power is 115 kw, with a top speed of 197 km/h.

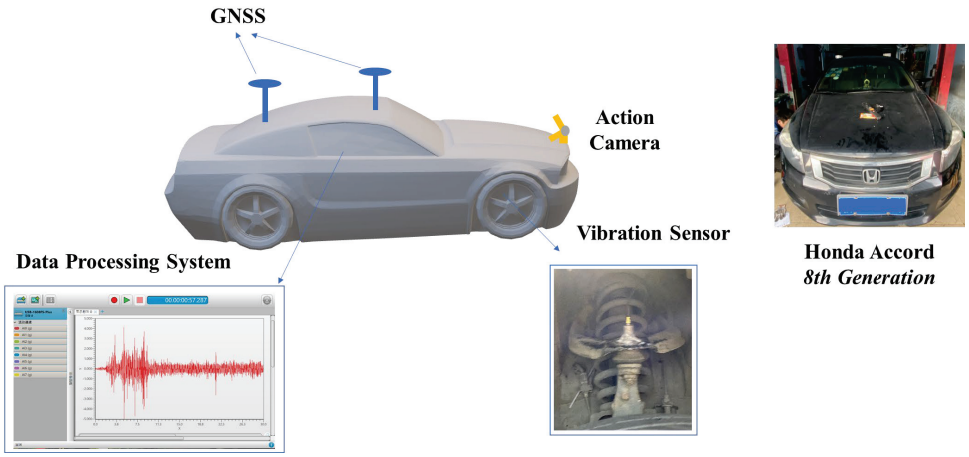

Figure 3. Testing system.

The vibration acceleration sensor is mounted below the suspension. The goal is to strengthen the stimulation caused by the transverse cracks without a shock absorber. The vibration sensor is Piezoelectric, with physical and technical parameters listed in Table 1. One host, two GNSS antennae and their cables, one 4G all-network antenna, and one power supply data cable constitute the positioning equipment. The antenna is mounted outside of the car to avoid a weak signal in a small area. When operating, the GNSS positioning module collects the vehicle's location in real-time and transmits it to the computer. The action camera collects the pavement surface's video to verify the identification accuracy. The action camera is a Go-Pro, which allowed for the acquisition of a pavement surface video with a high speeds. It has 12 million pixels and is secured to the front cover by a magnetic suction bracket to capture surface conditions more clearly. The data processing system showed the time-domain features of pavement conditions on a Lenovo computer that was used in this study that had an available storage space of 480G-SSD.

Table 1. Vibration sensor physical and technical parameters.

Parameter	Type
Technical principle	Piezo
Size (cm)	$\varphi 15 \times 25$
Weight (g)	42
Range (g)	−10~10 g
Frequency range (Hz)	0.5–3000
Sensitivity	500 mv/g
Bandwidth resolution (mg)	0.1
Resonant frequency (kHz)	5
Overload impact (g)	100

3.2. Testing Plan

A typical asphalt pavement with a semi-rigid base was chosen in Shanghai. Its service life was over ten years. The pavement structure is shown in Figure 4. The main pavement distress was transverse cracking. The driving velocity was 40 km/h and the sampling frequency was 1280 Hz. Selection of the sampling frequency requires balancing identification requirements with data storage. When the sampling frequency is increased, the mutation signal caused by the crack can be better recognized and presented, but the excessive sampling frequency will also cause the data volume to be too large, resulting in longer processing times. On the other hand, when the sampling frequency is decreased so that the processing system can be read at high speeds, this may lead to a lower accuracy of identification, resulting in increased leakage in the detection of cracks. Considering that the parameters of the subsequent short-time Fourier transform algorithm vary in the 2 integer times, the sampling frequency is set to the 2 integer times as much as possible. In general,

road surface lateral cracking is not entirely perpendicular to the traffic direction but has a certain width of expansion. To divide the road sections reasonably, this study investigated the expansion width of many asphalt pavement transverse cracks with a maximum width of less than 4 m. Therefore, 4.0 m is determined to be the length of divided sections (D), which is also the window length for signal analysis (Figure 4).

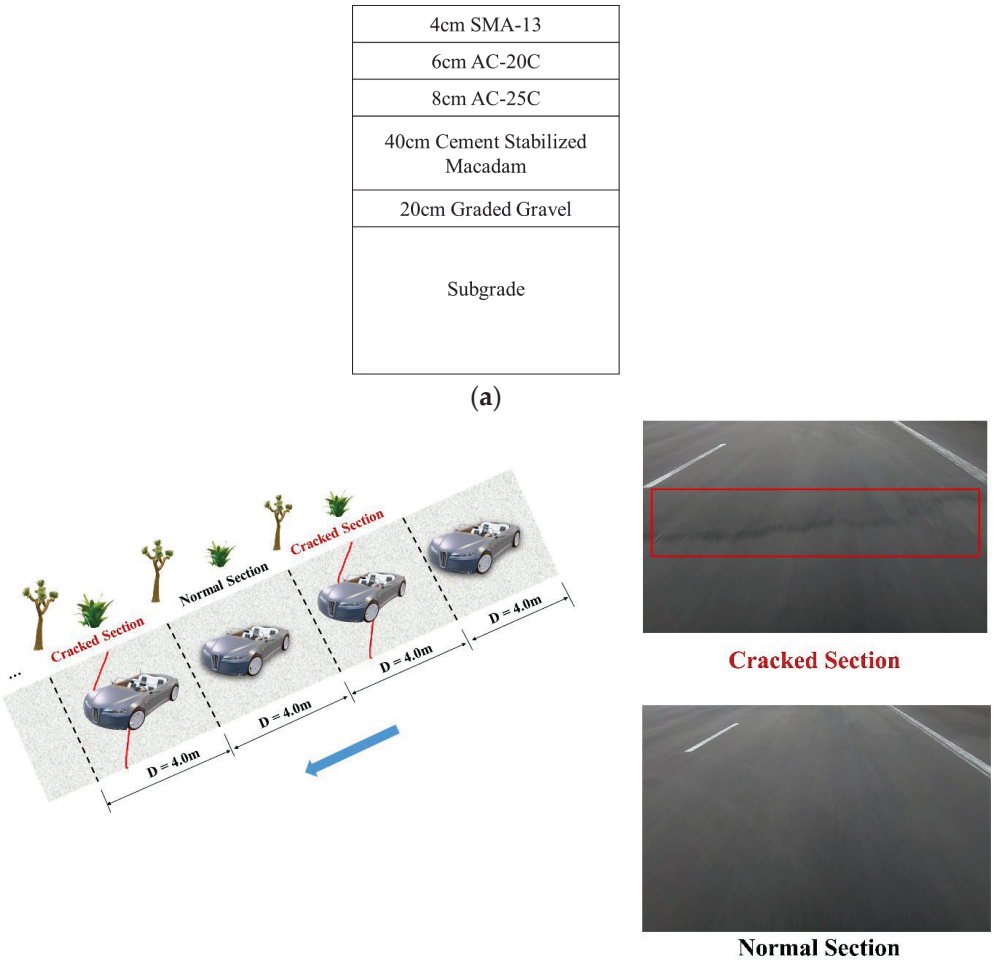

Figure 4. Testing road. (**a**) Pavement structure; (**b**) divided sections.

4. Optimized Short-Time Fourier Transform (STFT) Algorithm

4.1. Basic Principle

Traditional Fourier transforms can only reveal a signal's overall frequency component, and cannot indicate the time of each component. Therefore, two signals with significant temporal domain differences might have the same spectrum map. It is challenging to record the Fourier transform for signals that change, such as vehicle vibration signal mutations caused by minute transverse cracks. Such mutations are frequently crucial in highway pavement damage investigation.

The short-time Fourier transform (STFT) is a joint time–frequency analysis technique for time-varying and non-stationary signals. It intercepts the time domain signal using a fixed-length window function. Then, the STFT uses the intercepted signal to conduct a Fourier transform. This results in the local spectrum across a brief time window. The final transformation generates a two-dimensional function about time and frequency domains [23].

$$STFT(\omega,\ t) = \int_{-\infty}^{+\infty} F(t)\ G(t-\tau)e^{-i\omega t}dt \tag{18}$$

As is shown in Equation (18), STFT is a Fourier transform made by multiplying the signal F(t) by a τ-centered window function $G(t - \tau)$.

4.2. Parameter Optimization

The key parameters of the STFT include window type, window length, and overlap. These affect the time–frequency features, including time resolution and frequency resolution. The study takes a transverse sample and a normal pavement sample to analyze their different features in the time–frequency domain. Window type is an important part of spectrum analysis. The window function corrects the measurement inaccuracy due to the aperiodic nature of the signal and reduces leakage in the spectrum. The added window represents point multiplication in the time domain and convolution in the frequency domain. Therefore, the energy in the original signal at a certain frequency point is expressed in conjunction with the properties of the window function, thereby reducing leakage.

4.2.1. Window Type

Five window types were adopted, which are shown in Table 2:

Table 2. Different window types.

No.	Title 2
a	Rectangle window
b	Triangular window
c	Hanning window
d	Hamming window
e	Blackman window

There is no obvious difference between the time resolution and frequency resolution of the five window functions for normal pavement samples (Figure 5). The rectangular window has insufficient detail in the frequency resolution for cracked pavement samples. There is a large highlight entry in the map, which indicates a higher frequency intensity caused by transverse cracks. The time–frequency features of the other four window functions are similar. Therefore, it can be concluded that the triangular window, Hanning window, Heming window, and Brackman window are not very different in their time–frequency characteristics of a vibration signal for transverse cracking and normal pavement. Since the Hamming window is more common, we adopt the Hamming window as the standard window type.

4.2.2. Window Length (wl)

We select wl = 8, 16, 32, 64, and 128 for the analyzed values. Compared with normal pavement, transverse cracks show a significant high-frequency intensity area at the central position. The yellow part indicates the high-frequency intensity and the power spectral density of signal frequency (Figure 6). Normal pavement is relatively uniform, and no concentrated frequency intensity appears. STFT can overcome the problem that noise in the time domain greatly affects the crack feature. By increasing the window movement, the mutation of the signal at the crack can be reflected as the mutation of the intensity of each frequency component in a very short time.

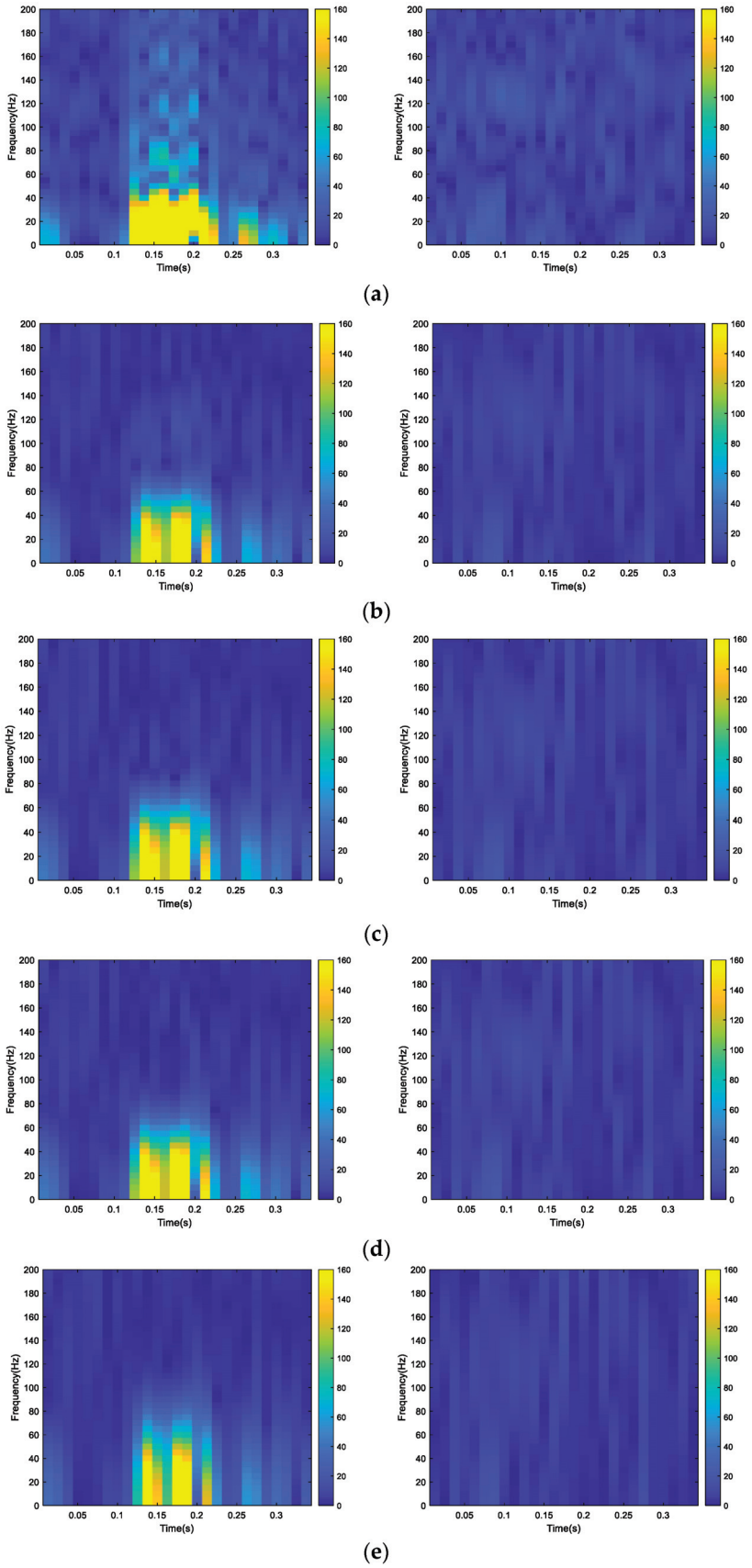

Figure 5. Different features in the time–frequency domain based on five window types between a transverse crack sample (left) and a normal section sample (right). (**a**) Rectangle window; (**b**) triangular window; (**c**) Hanning window; (**d**) Hamming window; (**e**) Blackman window.

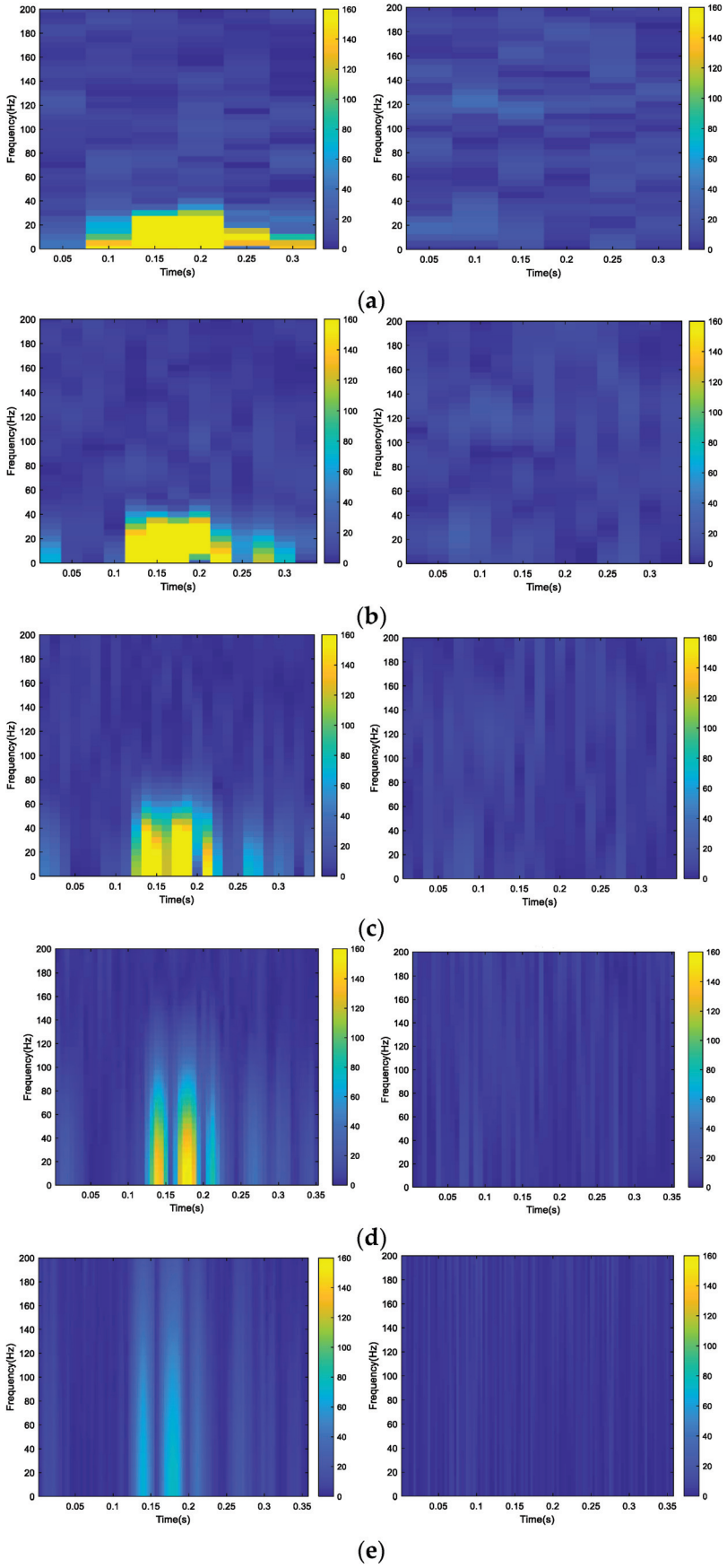

Figure 6. Time–frequency diagrams based on different *wl* between a transverse crack sample (left) and a normal section sample (right). (**a**) *wl* = 128; (**b**) *wl* = 64; (**c**) *wl* = 32; (**d**) *wl* = 16; (**e**) *wl* = 8.

Regarding spatial resolution, the window function length is equal to 128, which allows for the maximum frequency resolution. The frequency intensity in the fracture area presents a normal mountain distribution.

As the *wl* increases, the frequency resolution increases. The bar becomes column-like when using the minimum window function length included in this study, 8. The difference in frequency strength between cracks and the intact pavement is no longer obvious. But as the window function length decreases, the time resolution of cracks gradually increases.

The perception of change on the time scale is more detailed. When *wl* is equal to 128, the crack position is located at 0.2–0.3 s, which is quite different from the time domain.

When *wl* is equal to 64, it shows that the crack position is at 0.12–0.23 s, which is still different from the time domain. When *wl* is equal to 32, 16, or 8, the crack position is at 0.12–0.18 s, which is the same as the time domain.

Therefore, we select 32 as the optimal window function length considering both the frequency and time resolutions.

4.2.3. Overlap (op)

Overlap (*op*) indicates the size of the area where the window function overlaps the position of the previous window during movement. When op is 0, the signal is spaced by the window function without overlap, and each wl is performed. Corresponding to FFT, the image appears as a significant stretch in the time domain, with op increasing. Every interval length (*wl-op*) is updated once the frequency axis is updated. As op is close to *wl*, the image appears to be more delicate (Figure 7). However, the resulting increase also increases the number of calculations.

At $op \leq 8$, the entire image is not apparent in the time resolution, and it is difficult to reflect where the crack signal feature begins in the time domain.

At *op* = 16, three sets of signal power spectral density peaks begin to appear.

At *op* = 30, three more perfect bright columnar features reflect the crack's feature.

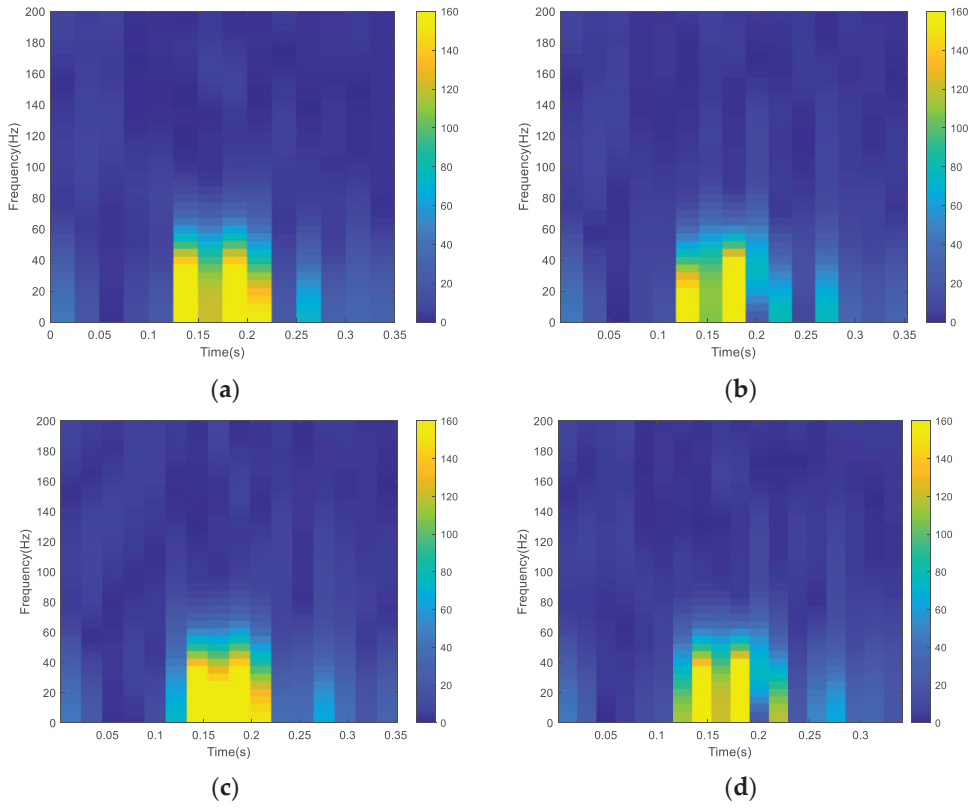

Figure 7. *Cont.*

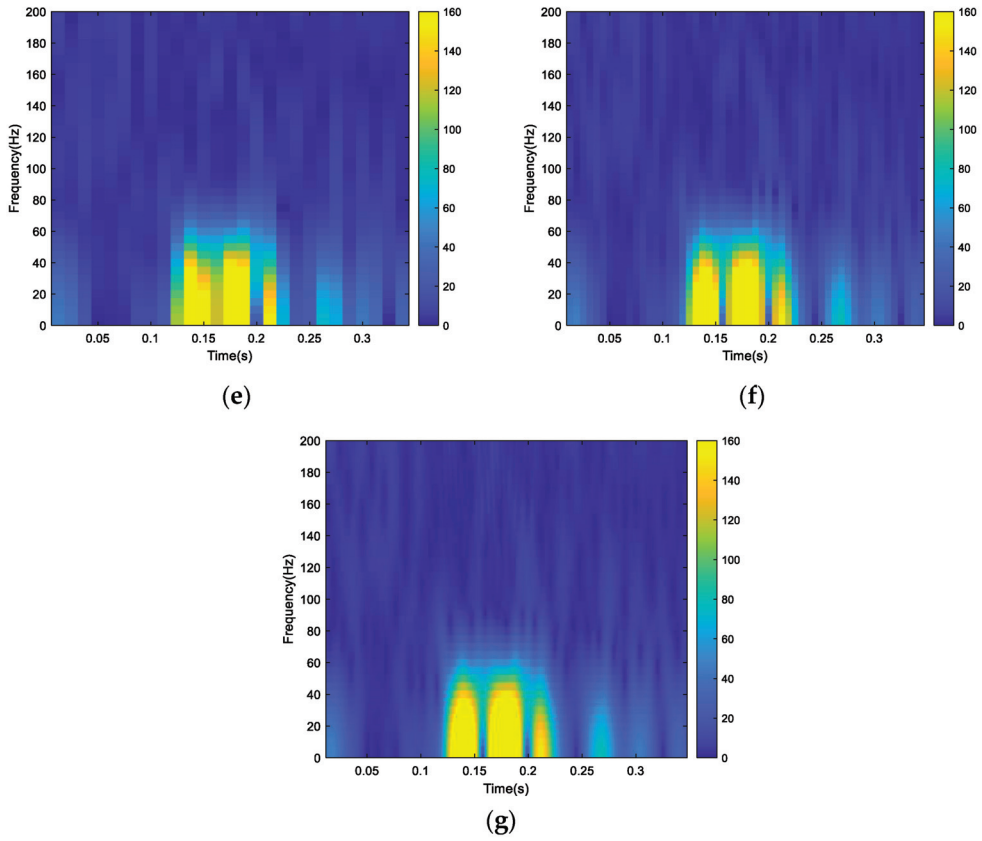

Figure 7. Time–frequency diagrams based on different *op* of a transverse crack sample. (**a**) *op* = 0; (**b**) *op* = 2; (**c**) *op* = 4; (**d**) *op* = 8; (**e**) *op* = 16; (**f**) *op* = 24; (**g**) *op* = 30.

But blindly increasing the op value is not economical for computing efficiency. Because the vehicle vibration test is expected to be used in road network asphalt surface crack detection, the greater the *op* value, the slower the timeliness of the vibration recognition for a crack. Therefore, *op* = 16 is recommended as the optimal parameter for the *op* value.

4.3. Parameter Optimization Results

The optimized STFT parameters for transverse cracking damage detection includes three key parameters: using a Hanning window type, with a window length of 32 and overlap equal to 16.

5. Data Analysis and Discussion

Based on the optimized STFT algorithm, the study chooses 30 manually labeled samples (transverse crack: 15, normal: 15) to explore their time–frequency features.

It was found that the power spectral density of the mutation feature caused by transverse cracks was above 100 dB/Hz (yellow highlight entry). While the normal pavement samples are below 80 dB/Hz (Figure 8). However, it was noted that the highlights of the three crack samples are not obvious. This results in an unreliable judge when only a feature has been mutated. The STFT algorithm demonstrates time-varying characteristics of the frequency domain brought about by signal mutations. A mutation at the cracked section causes a change in a certain frequency range. To verify this idea, we convert a two-dimensional time–frequency picture (the *x*-axis is time, the y-axis is frequency, and color depth denotes the power spectrum density) into a three-dimensional time–frequency map (the *x*-axis is time, the y-axis is frequency, and the *z*-axis is the power spectrum density).

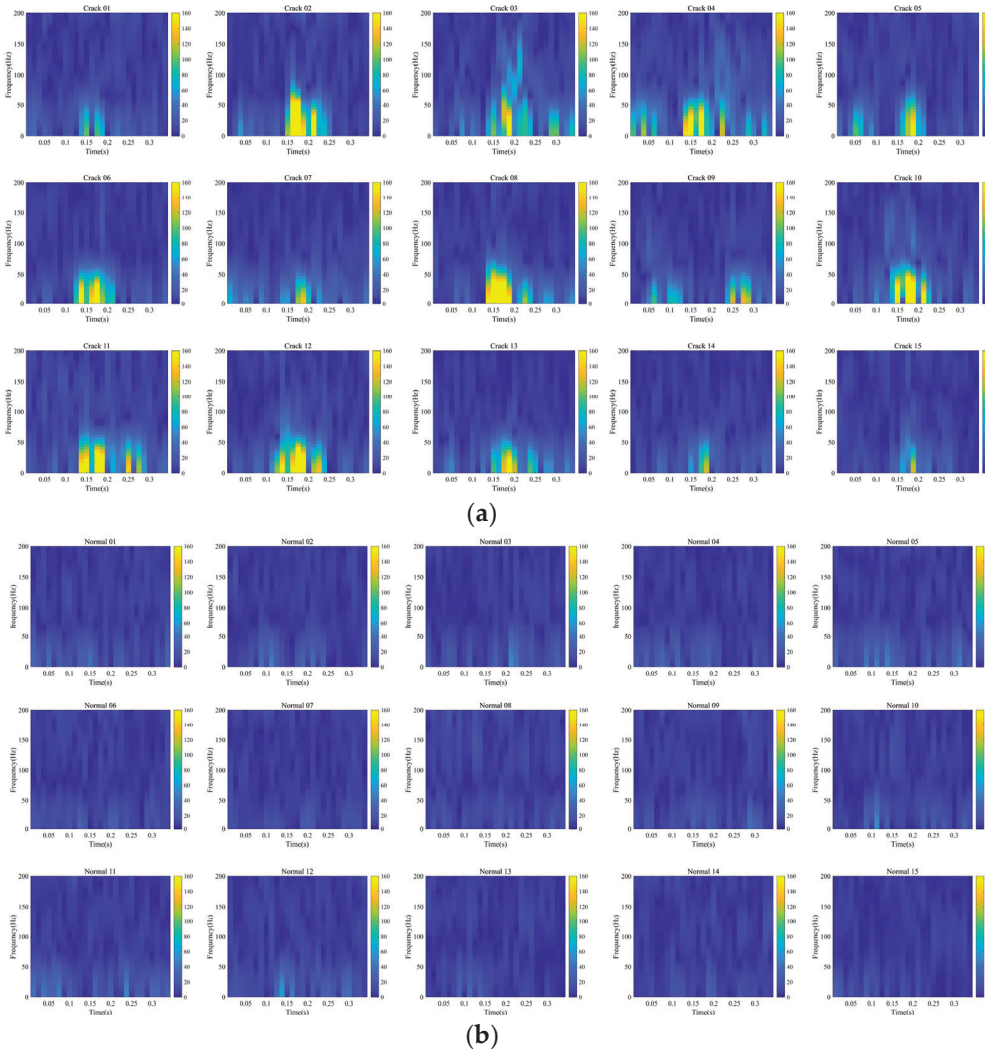

Figure 8. The 2D STFT spectrogram at cracked section or normal section. (**a**) Transverse crack; (**b**) normal pavement.

It was found that there are obvious differences between the cracked section and the normal section in the three-dimensional time–frequency diagram (Figure 9). All of the signals have a characteristic frequency range in the 0–50 Hz range. The PSD in the 0–0.1 s range is less than 30 dB/Hz for a transverse crack sample. When a signal is mutated (0.1–0.2 s), the power spectral density in the 0–50 Hz range increases rapidly, up to 102.2 Hz. As the mutation disappears (0.2–0.36 s), the PSD returns below 30 dB/Hz. The maximum power spectral density for the entire signal segment range (0–0.36 s) for the intact pavement samples is 42.5 dB/Hz. The maximum power spectral density (PSD_{max}) of the STFT is expected to be a good classification indicator.

To validate the above idea, the PSDmax of 15 transverse cracks and 15 normal pavements were calculated as shown in Figure 10. As can be seen in Figure 10a, the transverse crack's PSDmax distribution range is from 100 dB/Hz to 340 dB/Hz, with a maximum of 338.7 dB/Hz and a minimum of 102.2 dB/Hz. As shown in Figure 10b, the normal pavement's PSDmax distribution range is from 29 dB/Hz to 63 dB/Hz, with a maximum of 62.0 dB/Hz and a minimum of 29.8 dB/Hz. The mean, standard deviation, and variation coefficients are shown in Table 3. Based on comparison of the standard deviation and coefficient of variation, the transverse crack's PSDmax distribution is more discrete than the normal pavement.

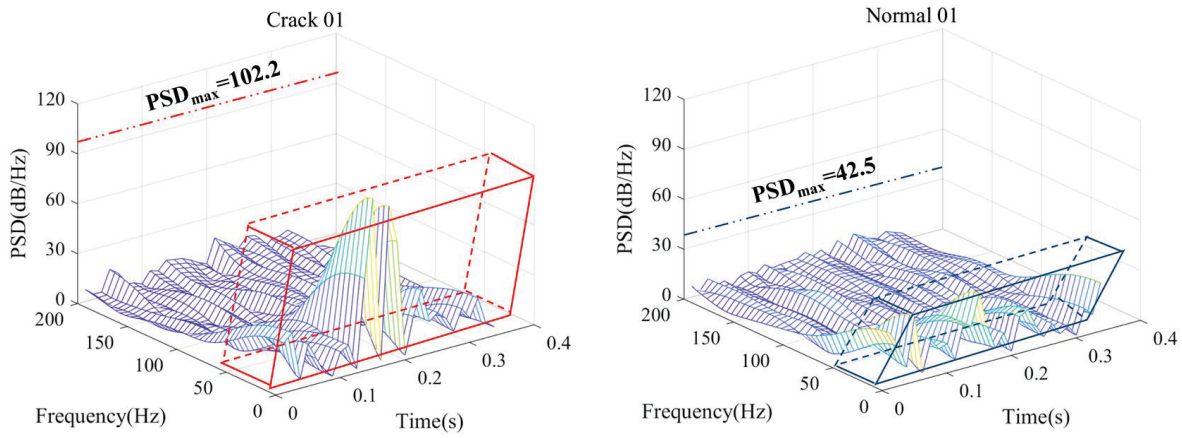

Figure 9. The 3D STFT spectrogram at the cracked section or normal section.

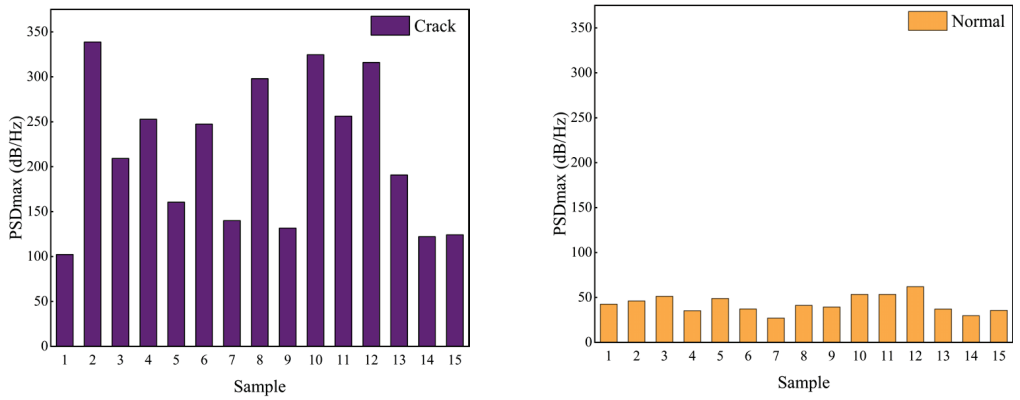

Figure 10. PSDmax at cracked sections and normal sections. (**a**) Transverse crack; (**b**) normal pavement.

Table 3. Statistical parameters of PSDmax.

Statistic Parameter	Transverse Crack	Normal
Maximum	338.7	62.0
Minimum	102.2	29.8
Mean	214.3	42.7
Standard deviation	79.3	9.4
Coefficient of variation	37.0%	22.0%

In addition, it can be seen that the minimum value of the transverse crack's PSDmax is greater than the maximum value of the intact pavement sample, PSDmax. So, it is reasonable to select the PSDmax as a classification indicator.

It should be noted that the standard deviation of the crack's PSDmax is much higher than that of the normal pavement. This can be explained by the field measurement affecting the crack's vibration response more. This is due to the varying degrees of pavement cracking (length, width, and depth), which leads to different transient shocks when the vehicle passes. This also results in a different degree of signal mutation at the cracked sections. This variability is strengthened by pavement roughness and the influence of sand and gravel. A sample of normal pavement's signal features is likely to be similar to transverse cracks, especially in the time–frequency domain. A cracked section is more easily mistaken for a normal section because it is difficult to cause a significant signal mutation due to its poor level. This ignores the structural damage of the pavement at the site and will make it difficult to carry out conservation activities in time.

Considering the above variability, the PSDmax may have a poor classification effect during field testing. The difference between a transverse crack and normal pavement is very small. However, the vibration signal at the cracked sections has three phases: stationary—non-stationary—stationary. In the time–frequency domain, these three stages are reflected in the power spectral density of the characteristic band (0–50 Hz). Therefore, the difference among the three PSD values (initial location t1, peak position t_{PSDmax}, and terminal position t2) can be considered as additional features, as defined below.

$$\Delta PSD_1 = PSD_{\max} - PSD_1 \tag{19}$$

$$\Delta PSD_2 = PSD_{\max} - PSD_2 \tag{20}$$

PSDmax is the peak of maximum power spectral density (Figure 11). PSD1 is the initial PSD of the characteristic spectral band (0–50 Hz), where PSDmax is located. PSD2 is the final PSD of the characteristic spectral band (0–50 Hz).

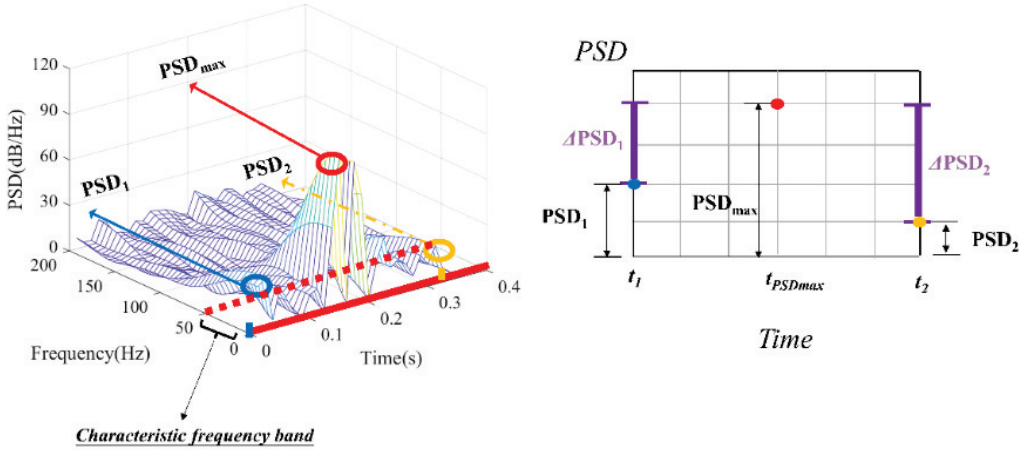

Figure 11. PSD at different time points.

Considering that PSDmax may occur at the initial or end position, we adopt the larger one (ΔPSD) in this study, comparing ΔPSD1 and ΔPSD2 as an additional feature, defined as the relative power spectral density. This is shown in Equation (21).

$$\Delta PSD = \max(\Delta PSD_1, \Delta PSD_2) \tag{21}$$

The two key classification features generated, PSDmax and ΔPSD, are mathematically linearly related. This is because the equation of the ΔPSD shows that the difference between the two variables is a linear function. For the same highway, the frequency changes due to the relative equilibrium of the roughness are small compared to cracks. Therefore, the difference is relatively stable. This fitting process is shown in Figure 12. The stability of features at normal sections is similarly verified in Figure 13. The ΔPSD at normal sections presents an agglomeration phenomenon. The data mean of this group was defined as the coordinate origin, and the radius was defined as the distance from the farthest point that makes up the circle function. All samples are strictly confined within this circle function.

Figures 14 and 15 show the above two index's classification effects. There is a divided zone between cracks and normal pavements, which can provide a flexible classification threshold.

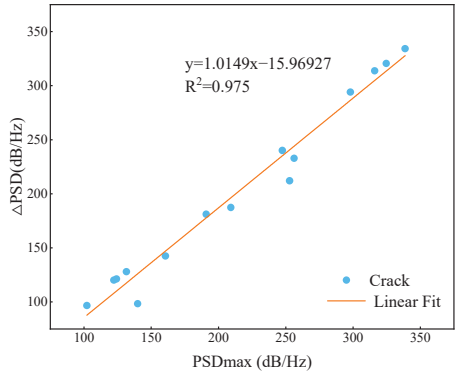

Figure 12. The fitting function between PSDmax and ΔPSD at cracked sections.

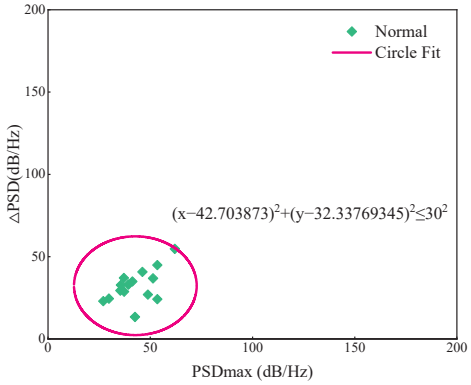

Figure 13. The fitting function between PSDmax and ΔPSD at normal sections.

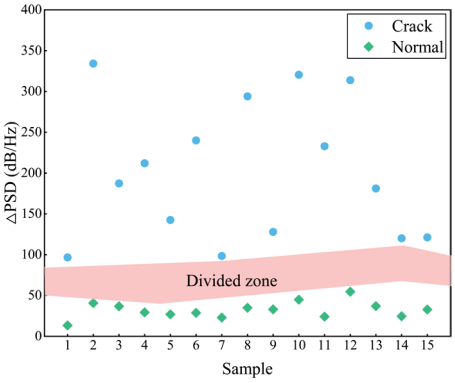

Figure 14. Classification effect of ΔPSD.

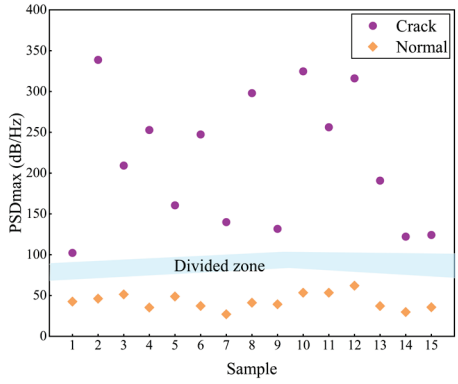

Figure 15. Classification effect of PSDmax.

6. Application Effect

The classification thresholds were set for 100 dB/Hz (PSDmax) and 95 dB/Hz (ΔPSD). If the PSDmax > 100 dB/Hz and ΔPSD > 95 dB/Hz, it is judged to be a transverse crack, and otherwise is classed as normal pavement. We applied this criterion to a large verification set of 139 sections (crack: normal = 14:125). The confusion matrix is shown in Figure 16.

$$Ac = \frac{TP + TN}{TP + FN + FP + TN} \tag{22}$$

$$TPR = \frac{TP}{TP + FN} \tag{23}$$

$$FPR = \frac{FP}{FP + TN} \tag{24}$$

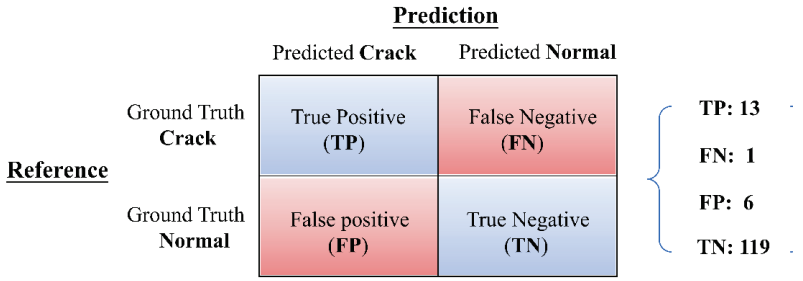

Figure 16. Confusion matrix.

This study adopts accuracy (Ac), TPR, and FPR as evaluation indicators (Table 4). The overall accuracy is high, reaching 94.96%, which is satisfactory because there is no machine learning training. It was also noted that the likelihood of detection in all crack samples is 92.86% (TPR). The probability of being misjudged as transverse cracks in all normal pavement samples is 4.80% (FPR). As most pavement sections are normal, a lower FPR means that the classification model can help to reduce the maintenance personnel's on-site error correction workload. At the same time, transverse cracks require repair to be effectively detected. Therefore, using the PSDmax and ΔPSD as classification indices is reasonable.

Table 4. Comprehensive evaluation indices of the classification model (%).

Index	Ac	TPR	FPR
value	94.62	92.86	4.80

7. Conclusions

In this paper, a vehicle-cracked pavement dynamic model illustrated the pavement transverse cracking detection principle based on vehicle dynamic response. As the typical features of pavement transverse cracking cannot be revealed better in the time or frequency domain, the raw vibration signal was transformed into a time–frequency-PSD map using optimized STFT. Two key classification indices distinguished transverse cracking sections from normal sections. The detailed conclusions of this paper are as follows:

Based on the d'Alembert principle, a vehicle-cracked pavement dynamic model was established. The model's time domain solution indicates that the vertical vibration response is affected by the characteristics of the vehicle system's driving speed, transverse cracking degree, and the vehicle–crack contact geometry feature.

The optimized STFT algorithm parameters for detecting transverse cracking were set through a parameter optimization process. The window type was a Hanning window with a length of 32, and an overlap of 16.

It was found that the power spectral density (PSD) caused by transverse cracks was above 100 dB/Hz. The PSD at normal sections was below 80 dB/Hz. The distribution of the PSD at cracked sections is more discrete than at normal sections.

The classification model based on the maximum power spectral density (PSDmax) and the relative power spectral density (ΔPSD) performed well. The accuracy reached 94.96%. TPR and FPR reached 92.86% and 4.80%, respectively.

In terms of recognition accuracy, this novel method is close to the current mainstream methods based on deep learning. In addition, this method can overcome the disadvantages of traditional signal time domain and frequency domain analysis's low accuracy. Moreover, this novel method could express small signal mutations caused by transverse cracking, including its moment.

However, the training set used in this novel method was smaller, data processing was faster, and real-time feedback was met. It was also verified that the novel model had a better effect on pavement transverse cracking detection.

Author Contributions: Conceptualization, Q.Y. and W.Y. (Wenzhi Yuan); methodology, W.Y. (Wenya Ye); validation, Q.Y. and W.Y. (Wenzhi Yuan); formal analysis, W.Y. (Wenzhi Yuan); investigation, W.Y. (Wenya Ye); resources, W.Y. (Wenya Ye); data curation, W.Y. (Wenzhi Yuan); writing—original draft preparation, W.Y. (Wenzhi Yuan); writing—review and editing, Q.Y.; visualization, W.Y. (Wenzhi Yuan); supervision, Q.Y.; project administration, W.Y. (Wenya Ye); funding acquisition, W.Y. (Wenya Ye). All authors have read and agreed to the published version of the manuscript.

Funding: This research was funded by the 2022 Ningbo Transportation Science and Technology Plan Project, grant number 202216.

Institutional Review Board Statement: Not applicable.

Informed Consent Statement: Not applicable.

Data Availability Statement: Data are contained within the article.

Acknowledgments: Thanks for Qian Xudong's contributions and help on data investigations and project administration. (Qian Xudong, who is from the Ningbo Road and Bridge Engineering Construction Co., Ltd. Ningbo, 315000, China).

Conflicts of Interest: The authors declare no conflict of interest.

References

1. Soga, K.; Kwan, V.; Pelecanos, L.; Rui, Y.; Wilcock, M. The role of distributed sensing in understanding the engineering performance of geotechnical structures. In Proceedings of the 15th European Conference on Soil Mechanics and Geotechnical Engineering, Edinburgh, UK, 1 September 2015.
2. Deng, Y.; Yang, Q. Rapid Evaluation of a Transverse Crack on a Semi-Rigid Pavement Utilising Deflection Basin Data. *Road Mater. Pavement Des.* **2019**, *20*, 929–942. [CrossRef]
3. Zhang, H.; Qian, Z.; Tan, Y.; Xie, Y.; Li, M. Investigation of Pavement Crack Detection Based on Deep Learning Method Using Weakly Supervised Instance Segmentation Framework. *Constr. Build. Mater.* **2022**, *358*, 129117. [CrossRef]
4. Bogus, S.M.; Migliaccio, G.C.; Cordova, A.A. Assessment of Data Quality for Evaluations of Manual Pavement Distress. *Transp. Res. Rec.* **2010**, *2170*, 1–8. [CrossRef]
5. Seo, H. Monitoring of CFA Pile Test Using Three Dimensional Laser Scanning and Distributed Fiber Optic Sensors. *Opt. Lasers Eng.* **2020**, *130*, 106089. [CrossRef]
6. Yang, Q.; Zhou, S.; Wang, P.; Zhang, J. Application of Signal Processing and Support Vector Machine to Transverse Cracking Detection in Asphalt Pavement. *J. Cent. South Univ.* **2021**, *28*, 2451–2462. [CrossRef]
7. Liu, J.; Xu, S.; Bergés, M.; Noh, H.Y. HierMUD: Hierarchical Multi-Task Unsupervised Domain Adaptation between Bridges for Drive-by Damage Diagnosis. *Struct. Health Monit.* **2023**, *22*, 1941–1968. [CrossRef]
8. Yang, Y.-B.; Lin, C.W.; Yau, J.D. Extracting Bridge Frequencies from the Dynamic Response of a Passing Vehicle. *J. Sound Vib.* **2004**, *272*, 471–493. [CrossRef]
9. Yang, Y.B.; Yang, J.P. State-of-the-Art Review on Modal Identification and Damage Detection of Bridges by Moving Test Vehicles. *Int. J. Str. Stab. Dyn.* **2018**, *18*, 1850025. [CrossRef]
10. Yu, B.X.; Yu, X. Vibration-Based System for Pavement Condition Evaluation. In Proceedings of the Applications of Advanced Technology in Transportation, Chicago, IL, USA, 13–16 August 2006; American Society of Civil Engineers: Chicago, IL, USA, 2006; pp. 183–189.

11. Eriksson, J.; Girod, L.; Hull, B.; Newton, R.; Madden, S.; Balakrishnan, H. The Pothole Patrol: Using a Mobile Sensor Network for Road Surface Monitoring. In Proceedings of the 6th International Conference on MOBILE Systems, Applications, and Services, Breckenridge, CO, USA, 5–7 November 2008; ACM: New York, NY, USA, 2008; pp. 29–39.
12. Zang, K.; Shen, J.; Huang, H.; Wan, M.; Shi, J. Assessing and Mapping of Road Surface Roughness Based on GPS and Accelerometer Sensors on Bicycle-Mounted Smartphones. *Sensors* **2018**, *18*, 914. [CrossRef] [PubMed]
13. Mohan, P.; Padmanabhan, V.N.; Ramjee, R. Nericell: Rich Monitoring of Road and Traffic Conditions Using Mobile Smartphones. In Proceedings of the 6th ACM Conference on Embedded Network Sensor Systems, Raleigh, NC, USA, 5–7 November 2018; ACM: New York, NY, USA, 2008; pp. 323–336.
14. Bhoraskar, R.; Vankadhara, N.; Raman, B.; Kulkarni, P. Wolverine: Traffic and Road Condition Estimation Using Smartphone Sensors. In Proceedings of the 2012 Fourth International Conference on Communication Systems and Networks (COMSNETS 2012), Bangalore, India, 3–7 January 2012; pp. 1–6.
15. Yang, Q.; Zhou, S. Identification of Asphalt Pavement Transverse Cracking Based on Vehicle Vibration Signal Analysis. *Road Mater. Pavement Des.* **2021**, *22*, 1780–1798. [CrossRef]
16. Bruno, S. Proposal for a Low-Cost Monitoring System to Assess the Pavement Deterioration in Urban Roads. *Eur. Transp./Trasp. Eur.* **2023**, 1–10. [CrossRef]
17. Múčka, P. Vibration Dose Value in Passenger Car and Road Roughness. *J. Transp. Eng. Part B Pavements* **2020**, *146*, 04020064. [CrossRef]
18. Loprencipe, G.; De Almeida Filho, F.G.V.; De Oliveira, R.H.; Bruno, S. Validation of a Low-Cost Pavement Monitoring Inertial-Based System for Urban Road Networks. *Sensors* **2021**, *21*, 3127. [CrossRef] [PubMed]
19. Loprencipe, G.; Bruno, S.; Cantisani, G.; D'Andrea, A.; Di Mascio, P.; Moretti, L. Methods for Measuring and Assessing Irregularities of Stone Pavements—Part I. *Sustainability* **2023**, *15*, 1528. [CrossRef]
20. Bingül, Ö.; Yıldız, A. Fuzzy Logic and Proportional Integral Derivative Based Multi-Objective Optimization of Active Suspension System of a 4 × 4 in-Wheel Motor Driven Electrical Vehicle. *J. Vib. Control* **2023**, *29*, 1366–1386. [CrossRef]
21. Yildiz, A. A Comparative Study on the Optimal Non-Linear Seat and Suspension Design for an Electric Vehicle Using Different Population-Based Optimisation Algorithms. *Int. J. Veh. Des.* **2019**, *80*, 241. [CrossRef]
22. Pan, G.Y. *Automotive Vibration Foundation and Its Application*; Peking University Press: Beijing, China, 2013. (In Chinese)
23. Chen, C.; Seo, H.; Zhao, Y. A Novel Pavement Transverse Cracks Detection Model Using WT-CNN and STFT-CNN for Smartphone Data Analysis. *Int. J. Pavement Eng.* **2022**, *23*, 4372–4384. [CrossRef]

sensors

MDPI

Article

An Aquaphotomics Approach for Investigation of Water-Stress-Induced Changes in Maize Plants

Daniela Moyankova [1], Petya Stoykova [1], Petya Veleva [2], Nikolai K. Christov [1], Antoniya Petrova [2] and Stefka Atanassova [2,*]

[1] AgroBioInstitute, Agricultural Academy, 1164 Sofia, Bulgaria; dmoyankova@abi.bg (D.M.); pstoykova@abi.bg (P.S.); nikolai_christov@abi.bg (N.K.C.)
[2] Faculty of Agriculture, Trakia University, 6000 Stara Zagora, Bulgaria; petya.veleva@trakia-uni.bg (P.V.); antoniya.petrova@trakia-uni.bg (A.P.)
* Correspondence: stefka.atanassova@trakia-uni.bg

Abstract: The productivity of plants is considerably affected by various environmental stresses. Exploring the specific pattern of the near-infrared spectral data acquired non-destructively from plants subjected to stress can contribute to a better understanding of biophysical and biochemical processes in plants. Experiments for investigating NIR spectra of maize plants subjected to water stress were conducted. Two maize lines were used: US corn-belt inbred line B37 and mutant inbred XM 87-136, characterized by very high drought tolerance. After reaching the 4-leaf stage, 10 plants from each line were subjected to water stress, and 10 plants were used as control, kept under a regular water regime. The drought lasted until day 17 and then the plants were recovered by watering for 4 days. A MicroNIR OnSite-W Spectrometer (VIAVI Solutions Inc., Chandler, AZ, USA) was used for in vivo measurement of each maize leaf spectra. PLS models for determining drought days were created and aquagrams were calculated separately for the plants' second, third, and fourth leaves. Differences in absorption spectra were observed between control, stressed, and recovered maize plants, as well as between different measurement days of stressed plants. Aquagrams were used to visualize the water spectral pattern in maize leaves and how it changes along the drought process.

Keywords: maize plant; water stress; NIR spectra; aquagrams

1. Introduction

The influence of environmental stress factors on plant physiology has been the subject of rigorous research over the years and a significant number of studies have been reported [1,2]. Some of the mechanisms used by plants to respond and try to adapt and recover their homeostasis have also been described [3,4]. In general, plants have developed smart and sophisticated mechanisms to overcome stress [5], although these properties are more or less pronounced depending on the plant species [6]. Plants respond by changes in metabolism, gene expression, and adjustment of developmental processes. The common theme among different types of stress conditions is the generation of reactive oxygen species in cells. These particles act as aggressive disruptors on the most important cellular structures (e.g., membrane systems) and nucleic acids [7–10]. To alleviate the negative effect of the radicals' plants, they trigger enzymatic antioxidative systems (e.g., superoxide dismutases, peroxidases, catalases, and phenol oxidase). Another route to withstand the severe destructive influence of the generated radicals and alleviate the overall negative impact is the involvement of compounds with strong reductive potential (phenols, polyamines, flavonoids, glutathione, etc.).

Maize (*Zea mays* L.) is among the most exploited cereal crops with great importance all around the world. Despite that, its production is limited by drought [11,12], which can bring a decrease of 25–30% in yield in some arid zones [13]; it is widely cultivated for

direct use as food and feed, as well as for processed production of industrial compounds. When drought stress is in place, the maize yield losses vary from 30 to 90% depending on (1) the stage of the plant as well as (2) the intensity and prolongation of the drought period. As a result, the flowering and grain-filling stages are also severely affected [14]. Maize is frequently cultivated without irrigation in dry areas, with 300–500 mm of annual rainfall despite the fact that this level is below the critical limit necessary to reach a good crop yield [14]. Maize plants are sensitive to drought stress during all developmental stages from seed germination and seedling emergence through vegetative growth and reproductive phases. Therefore, improvement in drought tolerance is a major focus of research for maize breeding [15]. It was shown that applying a solution with 0.99 MPa of osmotic potential to maize seeds significantly affects the progress of germination and post-germination phases of the treated plants [16]. The most drought-sensitive period in maize development is between emergence (VE) and the 5-leaf (V5) stage seedling [17]. Environmental stress occurring during the seedling stage can result in crop failure [18,19]. Although significant improvement of drought tolerance during the reproductive stage of maize plants was achieved recently by application of various omics approaches [20], little attention is paid to the improvement of drought tolerance at the seedling stage due to its very complex nature. Therefore, a profound understanding of the physiological mechanisms behind vegetative drought tolerance at the seedling stage will be of high value.

Plant stress detection is very important to increase crop yield. Some of the methods for quantitative estimation of stress effects, such as metabolomics methods, provide very accurate data, but they are sampling destructive and very slow, which prevents dynamical studies.

Near-infrared (NIR) spectroscopy is a non-destructive rapid method for qualitative and quantitative analyses in different scientific fields—in the industry, medicine, agriculture, etc. NIR spectroscopy is less expensive than conventional methods because it does not use special consumables and chemicals after instrument calibration, requires little or no sample preparation, and can be used for online measurements. Data on the concentration of several components can be obtained with only one measurement. Another advantage of the method is that the analyzed samples can contain high water contents, and therefore this method has the possibility for in vivo application in living systems.

Recently, spectroscopy in the visible and near-infrared region was used to investigate the effect of abiotic stress on the base of spectral reflectance [21–24]. One of the used approaches is the development of vegetation indices, typically used in remote sensing. Another approach is to use chemometric methods to extract information from the near-infrared spectra of plants and food for the determination of quantitative parameters and for classification [25–28].

Aquaphotomics is a novel scientific approach based on near-infrared spectra of water in different kinds of materials, mainly biological samples with high water content, and analysis of changes in water spectra caused by the influence of different factors [29–31]. Aquaphotomics analysis of water–light interactions is a new source of information for a better understanding of the biological world. The combination of NIRS and aquaphotomics has already been used for the non-destructive investigation of aqueous and biological systems, for the evaluation of fresh and processed fruits and vegetables quality [32–38], plant abiotic stress and diseases [39–42].

In this paper, we use a non-destructive, portable NIR spectrometer to analyze the response to drought stress of two maize inbred lines—a US corn-belt B37 and a mutant XM 87-136 with very high drought tolerance by an aquaphotomics approach.

2. Materials and Methods

2.1. Plant Materials and Experimental Conditions

Two maize (*Zea mays* L.) inbred lines were included in the present study, the well-known US corn-belt inbred line B37 and a mutant inbred, developed at Maize Research Institute, Kneja, Bulgaria. We focused on inbred lines since they are genetically uniform and

should give lower plant-to-plant variation in the experiments. The mutant line XM 87-136 was developed by chemical mutagen treatment of B37 dry seeds followed by recurrent reciprocal mutation breeding to fix the desired mutant traits [43,44]. In addition to its high yield and combining the ability to produce high-yielding hybrids, the mutant line XM 87-136 is characterized by very high drought tolerance. XM 87-136 is a parental line of one of the most drought-tolerant maize hybrids bred in Bulgaria that has now been on the market for more than 20 years. The inbred line B37Ht (Co-op ID: 3406-007) was obtained from the Maize Genetics Cooperation Stock Center (http://maizecoop.cropsci.illinois.edu, accessed on 20 October 2023). Both lines used in the present study were maintained in a homozygous state by more than 10 generations of self-fertilization (selfing) at MRI-Kneja.

Seeds were surface sterilized with 5% commercial bleach (Domestos) for 10 min, washed three times with distilled water, and placed on wet filter paper. After germination, seedlings were transferred to a pot (d 10 cm) with soil. Plants were grown well watered at 28/25 °C day/night temperature, 50 ± 5% relative air humidity, and at 150 µmol m^{-2} s^{-1}—photon flux density of light intensity for 16 h in a controlled growth chamber (MLR-351, SANYO, Osaka, Japan).

Drought stress was induced on pot plants at the 4-leaf stage by withholding water for 17 days followed by rewatering for 4 days. Measurements were made on days 3, 7, 10, 12, 14, and 17 during drought stress and on days 3 and 4 after rewatering. Control plants were well watered during the treatment. A total of 10 plants from each line were subjected to water stress, and 10 plants were used as controls and kept under a regular water regime.

The scheme of the experimental design is presented in Figure 1.

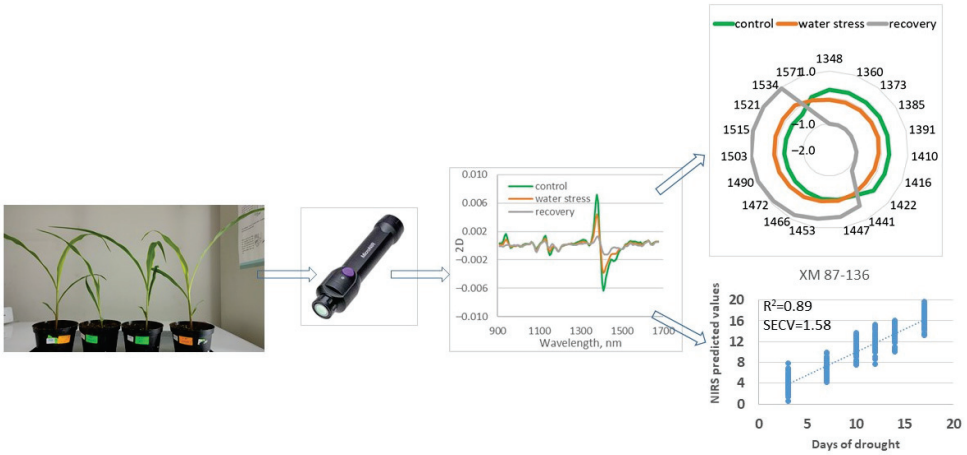

Figure 1. Scheme of experimental design.

2.2. Relative Water Content (RWC)

RWC of the 4th leaf at various time points of stress and recovery was calculated using the following formula [45]:

$$RWC\% = [(FW - DW)/(FTW - DW)] \times 100, \quad (1)$$

where *FW* is the fresh weight of the leaf, *FTW* is the fresh turgor weight measured after immersion of the leaf in distilled water for 24 h at room temperature and DW is the dry weight measured gravimetrically after drying at 80 °C in an oven for 48 h. Data are shown as the mean± standard deviation (SD) of four biological replicates.

2.3. Plant Height

The plant height (cm/plant) was measured as a distance from the soil surface to the upper end of the longest leaf at every time point during drought stress and recovery. Data are shown as the mean ± standard deviation (SD) of ten biological replicates.

2.4. NIRS Measurements

A portable, handheld MicroNIR OnSite-W spectrometer (VIAVI Solutions Inc., Chandler, AZ, USA) in the diffuse reflectance mode was used for spectral acquisition in the 908–1670 nm spectral range, with an approximately 7 nm resolution step. The second, third, and fourth leaves from each plant were measured. Each leaf was measured at three different positions. A dark 5 mm thick plate under the measuring maize leaves was used to ensure uniform measurement conditions and to avoid external interference.

2.5. Aquaphotomics and Multivariate Data Analysis

Pirouette 4.5 software (Infometrix, Inc., Bothell, WA, USA) was used for spectral data processing. Second derivative preprocessing of spectral data was applied, based on a Savitzky–Golay polynomial filter. The equations for the determination of days of water stress were created by partial least square (PLS) regression and the second derivative transformation of spectral data. Cross-validation was used for the determination of an optimum number of PLS factors in the models—the number of factors that corresponded to the lowest standard error of cross-validation SECV. Three leave-out samples were used in the cross-validation procedure because three replicates of the same leaf were measured .

Aquagram is a radar chart with coordinates, connected with specific water absorption bands of free water, dimers, trimers, solvation shells, etc., named water matrix coordinates (WAMACs) [29]. To calculate the aquagrams coefficients, first spectral data were transformed by multiplicative scatter correction (MSC) to reduce scattering effects due to the different thickness and surface properties of leaves. After that, normalized absorbance values at several wavelengths, Aq were calculated using the equation:

$$Aq_\lambda = \frac{A_\lambda - \mu_\lambda}{\sigma_\lambda} \quad (2)$$

where A_λ is the absorbance at wavelength λ, μ_λ is the mean value, and σ_λ is the standard deviation of all spectra at wavelength λ, respectively.

Aquagrams were calculated using the new 19 WAMACs, proposed by Vitalis et al. [46].

2.6. Statistical Data Analysis

Statistical data analysis included multivariate ANOVA to calculate significant differences among aquagram values at various WAMACS. Significance was determined using post hoc multiple comparisons with either Dunnett's T3 or Tukey tests, depending on the results of Levene's test for equality of error variances, at p-values of $\leq$0.05, 0.01, and 0.001. IBM SPSS Statistics 26.0 was used to process the data.

3. Results and Discussion

3.1. Physiological Changes during Drought

Two inbred maize lines—B37 (non-tolerant) and XM 87-136 (tolerant)—were subjected to water stress. Control plants from both lines have approximately 92% relative water content (RWC) (Figure 2a). When plants were exposed to drought, RWC for both lines decreased after the 7th day and reached 16% on the 17th day (Figure 3) and the leaves were not able to recover on the 4th day after rewatering. Slightly better was the recovery for the line XM 87-136.

Maize growth during drought showed the same pattern for both analyzed genotypes—plants stopped growing after the 7th day of stress treatment compared to controls (Figure 2b).

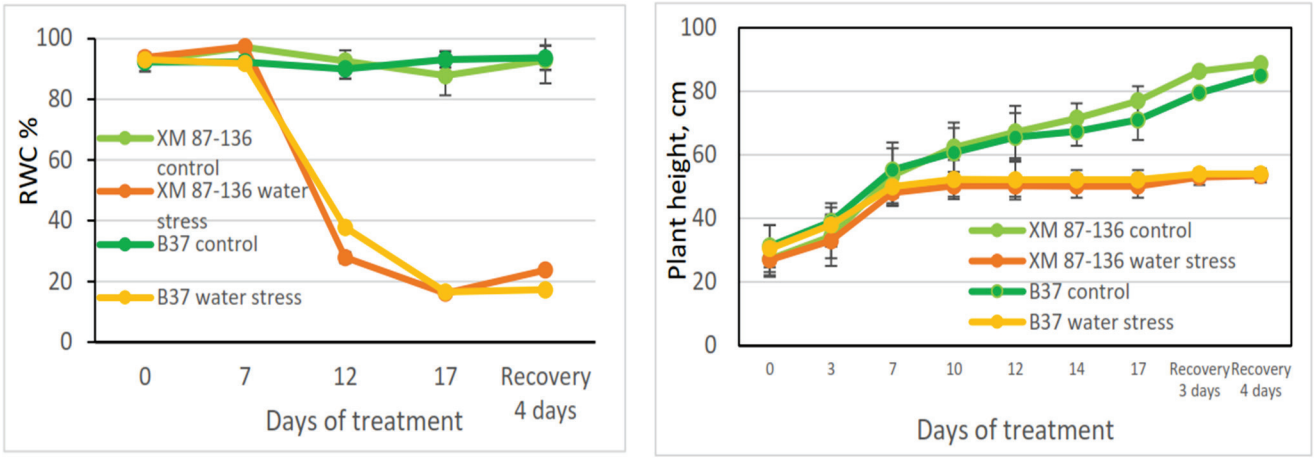

(**a**) (**b**)

Figure 2. Changes in leaf RWC (**a**) and plant growth (**b**) of inbred maize B37 and XM 87-136 during drought stress and recovery. Data are presented as the mean values ± standard deviation. (**a**) Relative water content (RWC) of tested maize lines; (**b**) plant growth of tested maize lines.

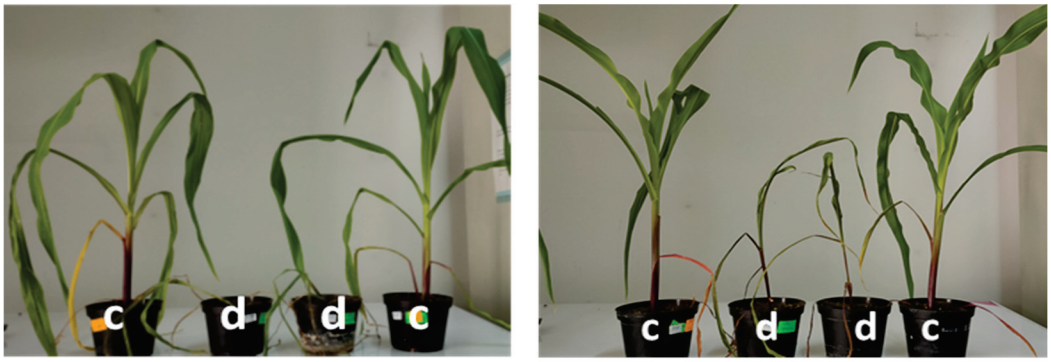

(**a**) (**b**)

Figure 3. Phenotype response of inbred maize line B37 and XM 87-136 on the 17th day of drought stress treatment. c—control plants; d—maize plants on the 17th day of drought stress. (**a**) B37—day 17; (**b**) XM 87-136—day 17.

3.2. NIR Spectra of Maize Leaves in the Process of Water Stress

Average second derivative of maize leaf spectra, measured from 3 to 17 days of drought, are shown in Figure 4 for both investigated maize lines. Absorption patterns of the two maize inbred lines were very similar. The spectra were dominated by the absorption band of water in the first overtone region between 1400 and 1500 nm. The biggest differences in the spectra for both tested maize lines could be observed at 1409 nm, connected with the absorbance of free water molecules. The absorption decreases with increasing the period of water stress. Absorption at approximately 1155 nm is connected with water absorption—a combination of the first overtone of O-H stretching and O-H bending vibration [37]. Absorption of maize leaves at 1087 nm also shows a dependence on drought days.

El-Hendawy et al. [47] also found a high positive correlation in the region 1392–1550 nm between the spectral reflectance of spring wheat, subjected to different irrigation rates and leaf water potential, and a high negative correlation with relative water content, and equivalent water thickness. In the experiment for non-destructive detection of water stress and estimation of relative water content in maize [48], it was found that the coefficient of variation in the reflectance spectra of water-stressed plants had a pronounced peak at approximately 1450

nm. The reflectance of control plant leaves was virtually invariant. Das et al. [49], in an experiment with 10 different rice genotypes, investigated water absorption bands, indices, and multivariate models for the development of non-destructive water-deficit stress phenotyping protocols using VNIR spectroscopy. Among the water absorption features at 970, 1200, 1400, and 1900 nm, 1400 nm was found to be the best for the estimation of leaf water content.

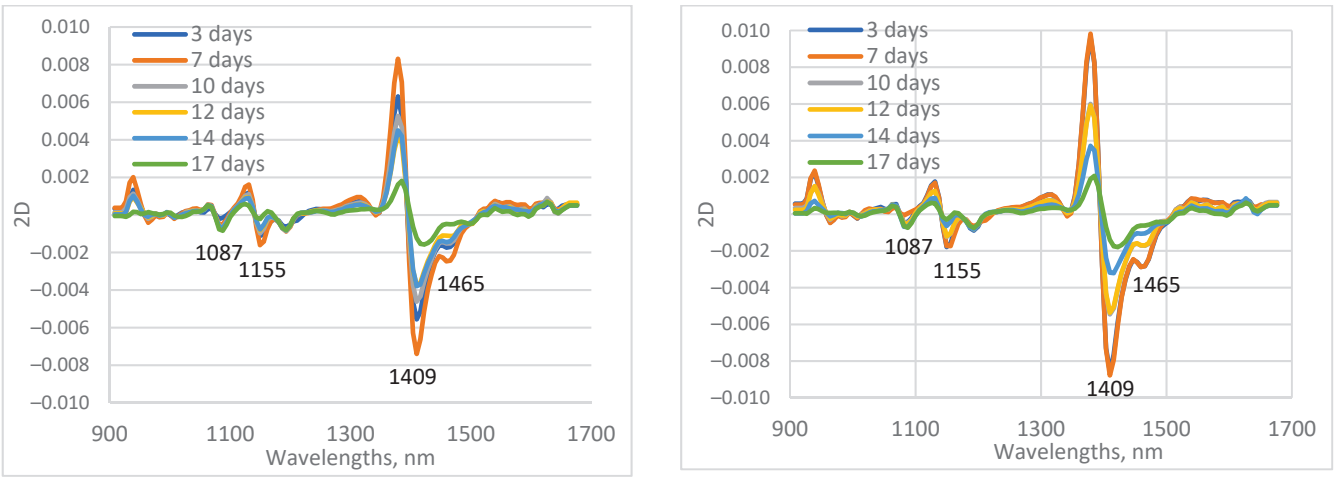

Figure 4. Average second derivative spectra (2D) of leaves of B37 and XM 87-136 maize lines in process of water stress. (**a**) B37; (**b**) XM 87-136.

The main visible difference between the two maize lines was the magnitude of absorption at 1409 nm. For all days, the absorbance values for the drought-tolerant mutant line were higher than those for B37.

The differences between spectra of maize lines, measured at 3 days of water stress and other days were calculated and presented in Figure 5. The stress responses of the two investigated maize lines now varied. For the drought-tolerant line, there are almost no differences in the spectrum until day 7 of drought. In the case of the B37, there are differences between the 7th and the 3rd day of water stress, especially at 930 nm, and the region 1350–1400 nm. The absorption at approximately 930 nm suggesting bond with either the C-H or O-H group. According to Rajkumar et al. [50], absorption at 930–935 nm is connected with O-H stretch (water solvation shell). The changes in the absorption in the area 1350–1400 nm are connected with weakly hydrogen-bonded water and trapped water or water vapor. This may indicate a loss of moisture through transpiration or a different content of trapped water, which is more significant for B37 plants [38,46]. Therefore, B37 plants undergo some physiological changes at the beginning of water stress that are different from those of XM 87–135 plants. These changes have not yet affected the physiological data at day 7 of drought, but have altered the spectral characteristics measured for B37 plants. Additionally, differences were observed in the area from 1062 to 1143 nm, mainly due to O-H and C-H vibrations [51]. This showed some differences in the processes of water stress between the two maize inbreds.

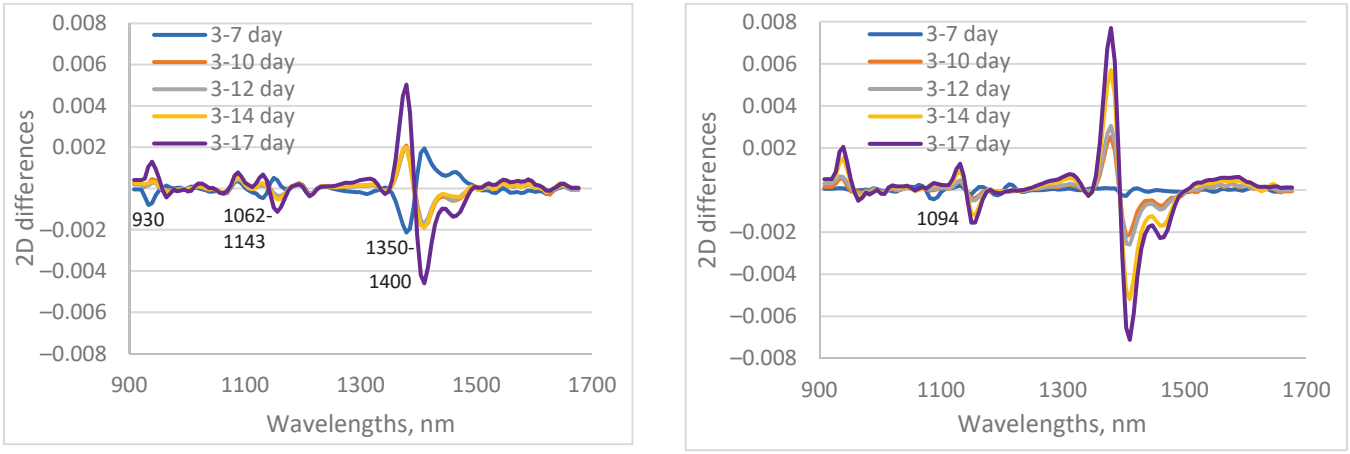

(**a**) (**b**)

Figure 5. Differences between second derivative spectra of water-stressed leaves, measured at day 3, and measured at 7, 10, 12, 14, and 17 days. (**a**) B37, 3rd leaf; (**b**) XM 87-136, 3rd leaf.

3.3. NIR Spectra of Control, Water-Stressed, and Recovery Maize Leaves

The second derivatives of average maize leaf spectra of control, water-stressed, and recovery plants are presented in Figure 6. There were clear differences among spectra of control, water-stressed, and recovered maize leaves for both investigated inbred lines.

The most intensive absorption was found in the first overtone region of water between 1400 and 1500 nm. Again, the absorbance intensity at 1409 nm and 1155 nm was greater in the control plants from drought-tolerant inbred XM 87-136, compared to the B37 line. The same finding was observed for the magnitude of absorption at 1409 nm of water-stressed plants. The spectra of plants recovered by watering for 4 days are very similar to those of water-stressed plants on the 17th day. This indicates that plants do not fully recover after 17 days of drought.

There were differences in the spectra of the second, third, and fourth leaves, mainly related to the magnitude of absorption.

Early detection of water stress is essential for efficient crop management. The obtained results confirm the possibility of using crop spectral reflectance in the visible and near-infrared regions to assess water stress [52–55]. The results of the analysis of spectral characteristics of control and water-stressed maize plants showed detectable differences after 3 days of drought for conventional and 7 days for drought-tolerant lines. In addition to monitoring, these results could also be used in breeding programs for fast and non-destructive selection of drought-tolerant maize varieties.

3.4. Aquaphotomics Analysis

Aquagrams were calculated to further investigate the changes in maize leaves caused by water stress. We used new 19 WAMACs, proposed by Vitalis et al. [44]. There is consistency in the shape and features of the aquagrams for the two maize cultivars and leaves studied. The comparison of water spectral patterns of control, water-stressed, and recovery plants provided clear differences for both maize line leaves (Figure 7).

In all cases, the values for the control plants in the range 1360–1422 nm were greater than those for the water-stressed plants. WAMACS in this range—1360 nm (C2), 1373 nm (C3), and 1385 nm (C4), are related to proton hydration, ion hydration, and trapped water. Absorption at 1409 nm is connected with free water. This indicated the loss of water in water-stressed leaves. Between 1441 and 1533 nm, we observed an inverse relationship—the values for the water-stressed plants are greater than those of the control plants. The water absorbance in this region is indicative of strongly molecularly bound water (molecules with two hydrogen bonds at 1466 nm, molecules with three hydrogen bonds at 1478 nm, and molecules with four hydrogen bonds at 1490 nm). Other WAMACs in this region were

connected with the interaction of protein and water at 1466 nm, and water and cellulose at 1503, 1521, and 1534 nm [46,56]. Aquagrams of recovery leaves were very different from those of control or water-stressed plants and indicated the loss of liquid water and strongly bound crystalline water at wavelengths above 1500 nm. The remaining water in these leaves is bound mainly to the cellulose components in the leaves.

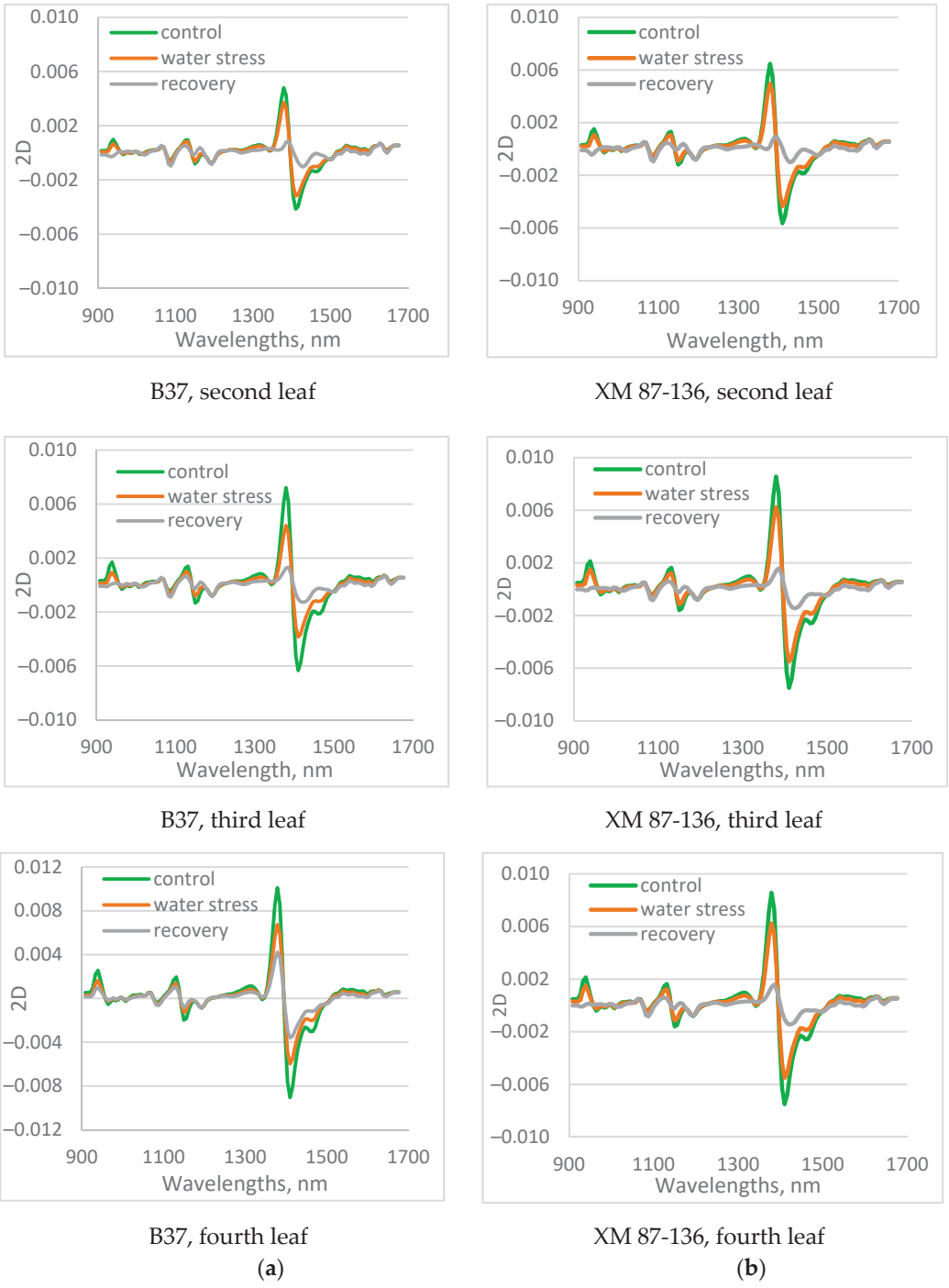

Figure 6. Average second derivative spectra of control, water-stressed, and recovery second, and fourth leaves of B37 (**a**) and XM 87-136 (**b**) maize lines.

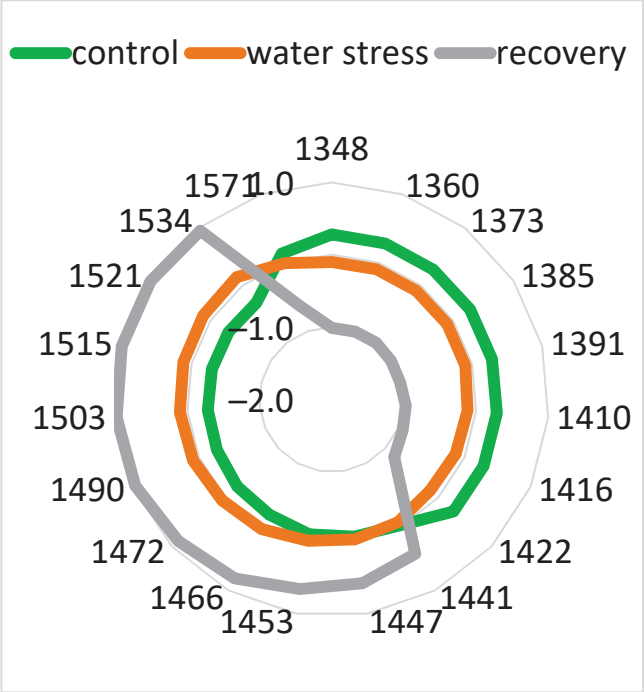

Line B37, 2 leaf

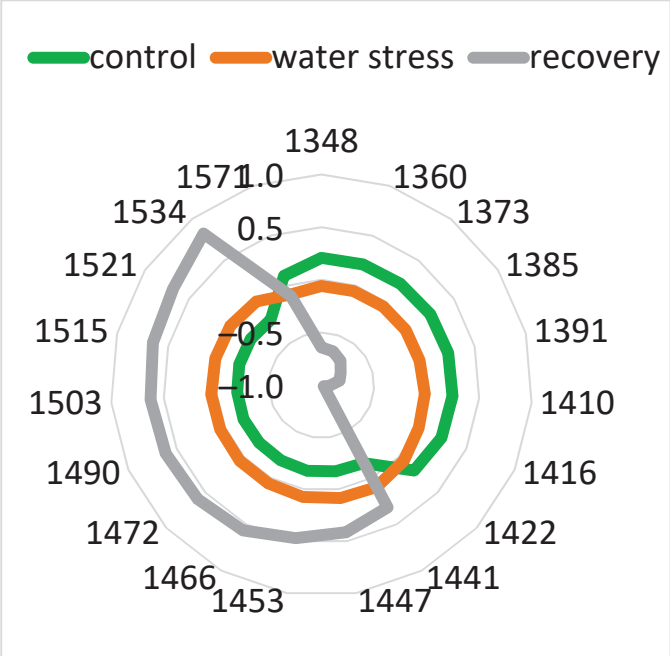

Line XM 87-136, 2 leaf

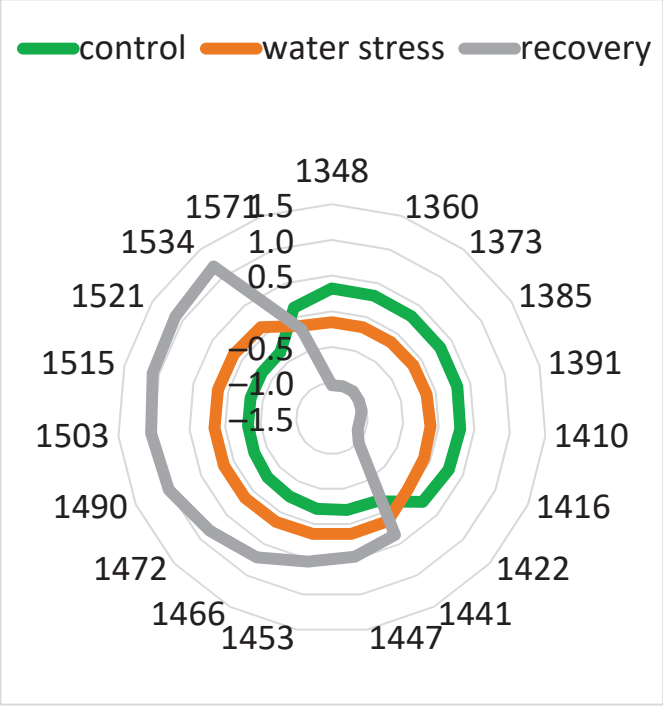

Line B37, 3 leaf

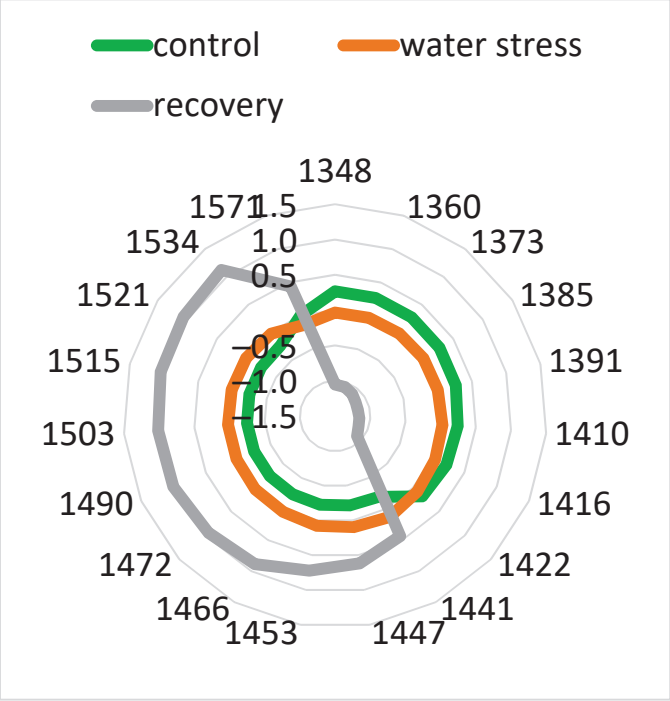

Line XM 87-136, 3 leaf

Figure 7. *Cont.*

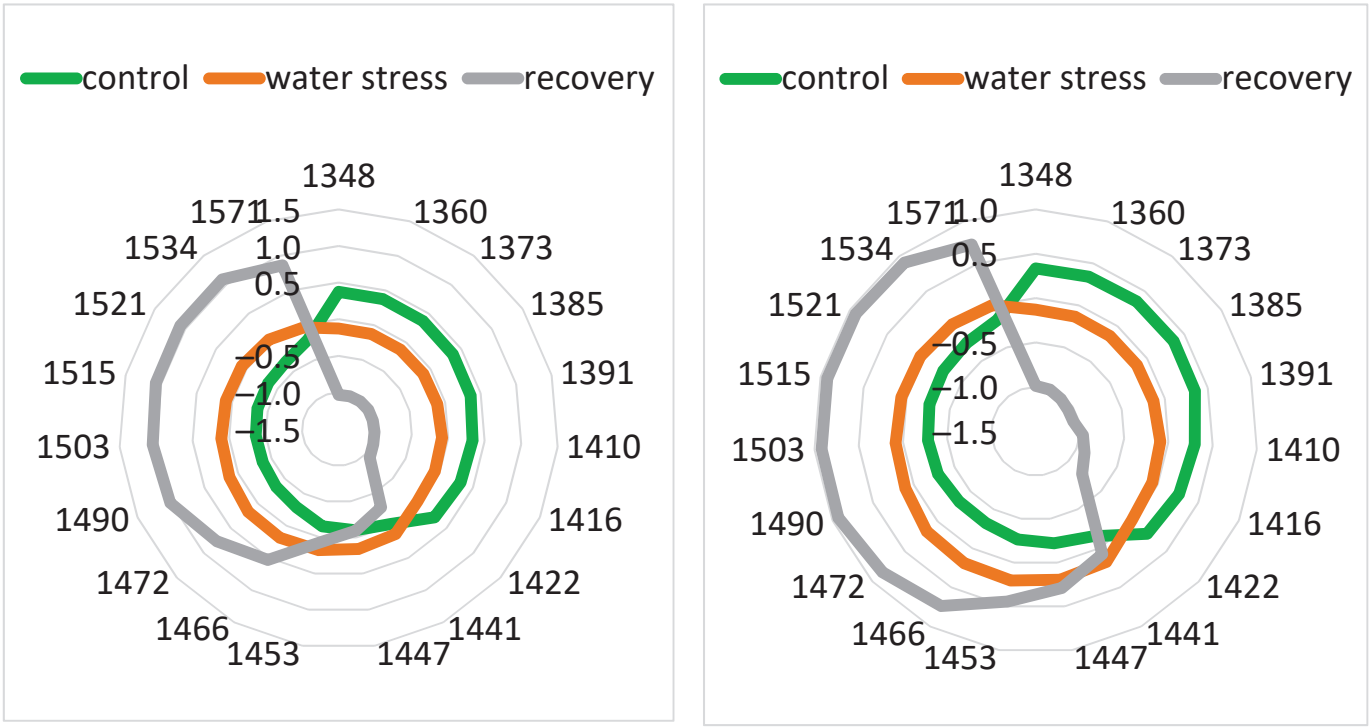

Line B37, 4 leaf **Line XM 87-136, 4 leaf**

Figure 7. Aquagrams of the different leaves of inbred maize lines—B37 and XM 87-136—during water stress, recovery, and control conditions.

Significant differences among aquagram values at various WAMACs for the third maize leaf in both cultivars can be observed in Table 1. Significant differences between control and water-stressed plants of the line XM 87-136 with different statistical strengths were found for most of the WAMACs except at 1416, 1422, and 1571 nm. Statistical significance was at level p in the range 0.001 ÷ 0.01 at 1348, 1360, 1373, 1441, 1447, and 1443 nm, and for the rest of WAMACs at level p in the range 0.01 ÷ 0.05. Statistical significant differences of greatest strength between control and recovery plants were found for most of the WAMACs. Regarding the B37 line, significant differences between control and water-stressed plants were obtained for all the WAMACs. The strongest statistical significance for the WAMACs was in the range 1348–1410 nm and 1466–1534 nm. Significant differences of greatest strength between control and recovery plants were found for all wavelengths except 1571 nm, and between water-stressed and recovery plants except 1441, 1447, and 1571 nm. Similar results were obtained for the second and fourth leaves.

The results of the statistical significance analysis between the values of the aquagram coefficients again confirm the existence of differences in the water stress processes between the two studied maize inbred lines. The statistical significance between the coefficients of the aquagrams for the drought-resistant line XM 87-136 is lower than that for the B37.

For further investigation of changes in leaves during water stress, aquagrams were calculated for different drought days (Figure 8). There is a smooth decrease in the values of the aquagram coefficients in the range of 1347–1442 nm for XM 87-136 water-stressed plants. The values for days 3 and 7 are very close, as are those for days 10 and 12. The values for days 3 to 10 in the 1440–1533 nm range are quite close. Very different from the others is the aquagram obtained for the leaves of the plants on day 17 of the water stress.

Table 1. Multivariate ANOVA results for aquagrams for the third leaf of the XM 87-136 and B37 lines.

XM 87-136				B37			
Wavelength	**Control**	**Water Stress**	**Recovery**	**Wavelength**	**Control**	**Water Stress**	**Recovery**
1347.899	a	a		1347.899	a	a	
	b		b		b		b
		c	c			c	c
1360.288	a	a		1360.288	a	a	
	b		b		b		b
		c	c			c	c
1372.677	a	a		1372.677	a	a	
	b		b		b		b
		c	c			c	c
1385.065	a	a		1385.065	a	a	
	b		b		b		b
		c	c			c	c
1391.26	a	a		1391.26	a	a	
	b		b		b		b
		c	c			c	c
1409.843	a	a		1409.843	a	a	
	b		b		b		b
		c	c			c	c
1416.037	ns	ns		1416.037	a	a	
	b		b		b		b
		c	c			c	c
1422.231	ns	ns		1422.231	a	a	
	b		b		b		b
		c	c			c	c
1440.814	a	a		1440.814	a	a	
	b		b		b		b
		ns	ns			ns	ns
1447.009	a	a		1447.009	a	a	
	b		b		b		b
		c	c			ns	ns
1453.203	a	a		1453.203	a	a	
	b		b		b		b
		c	c			c	c
1465.592	a	a		1465.592	a	a	
	b		b		b		b
		c	c			c	c
1471.786	a	a		1471.786	a	a	
	b		b		b		b
		c	c			c	c
1490.369	a	a		1490.369	a	a	
	b		b		b		b
		c	c			c	c
1502.758	a	a		1502.758	a	a	
	b		b		b		b
		c	c			c	c
1515.147	a	a		1515.147	a	a	
	b		b		b		b
		c	c			c	c
1521.341	a	a		1521.341	a	a	
	b		b		b		b
		c	c			c	c

Table 1. *Cont.*

XM 87-136				B37			
Wavelength	Control	Water Stress	Recovery	Wavelength	Control	Water Stress	Recovery
1533.73	a	a		1533.73	a	a	
	b		b		b		b
		c	c			c	c
1570.896	ns	ns		1570.896	a	a	
	b		b		ns		ns
		c	c			ns	ns

Same letters in the same row represent significant differences at $p < 0.05$; ns—insignificant differences. Different colours represent the strength of significant differences as follows: <0.001 in green; 0.001 ÷ 0.01 in blue; 0.01 ÷ 0.05 in yellow; non-significant in grey.

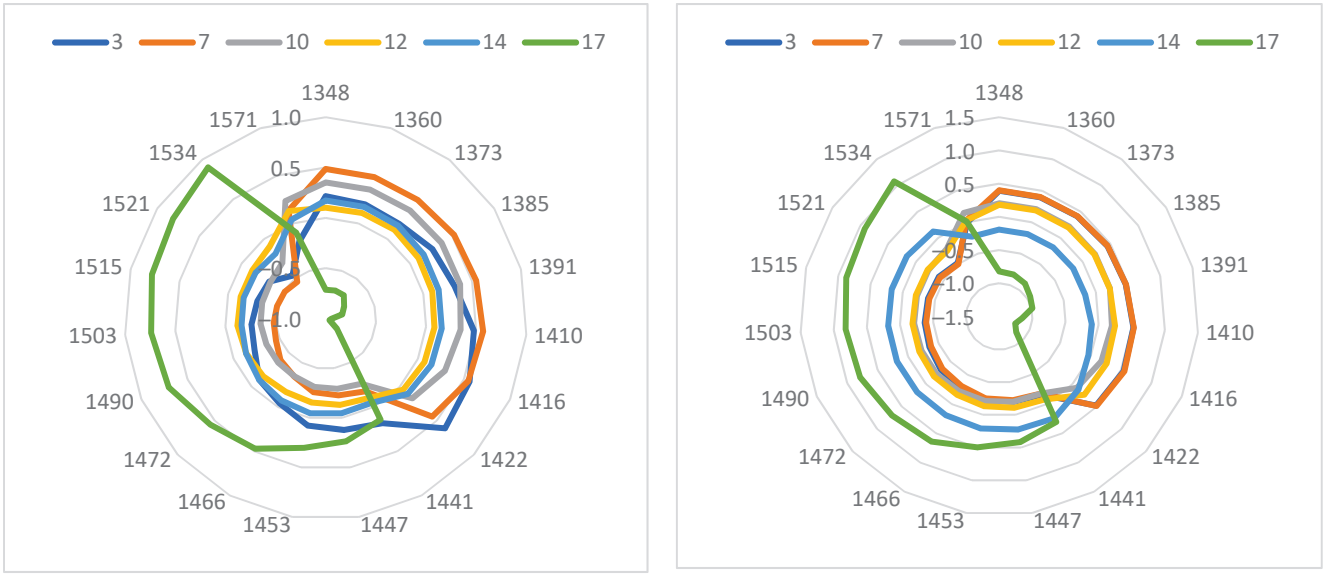

Figure 8. Aquagrams for water-stressed inbred maize lines—B37 and XM 87-137—at different days of water deprivation. (**a**) B37; (**b**) XM 87-136.

The character of the aquagrams for days 3 and 7 for B37 plants was different compared to those for the line XM 87-136. This confirms the observed differences in early drought processes between the two maize lines. They are especially significant in the range 1409–1453 nm. The water absorption at 1441 and 1447 nm is important in desiccation processes and abiotic stress [35,42].

3.5. PLS models for Determination of Days of Drought

The PLS models for the determination of days of drought were calculated separately for the data acquired for lines B37 and XM 87-136, using spectral regions from 1300 to 1600 nm, and their performances were presented in Table 2 and Figure 9. The predictions of the days of drought were successful with slightly less accuracy for the B37 inbred—SECV = 1.77 compared to SECV = 1.58 for the XM 87-136 line.

Table 2. Statistical parameters of PLS models for determination of days of drought.

Line	PLS Factors	SECV	R^2cv	SEC	R^2cal
B37	2	1.77	0.922	1.74	0.923
XM 87-136	2	1.58	0.887	1.58	0.889

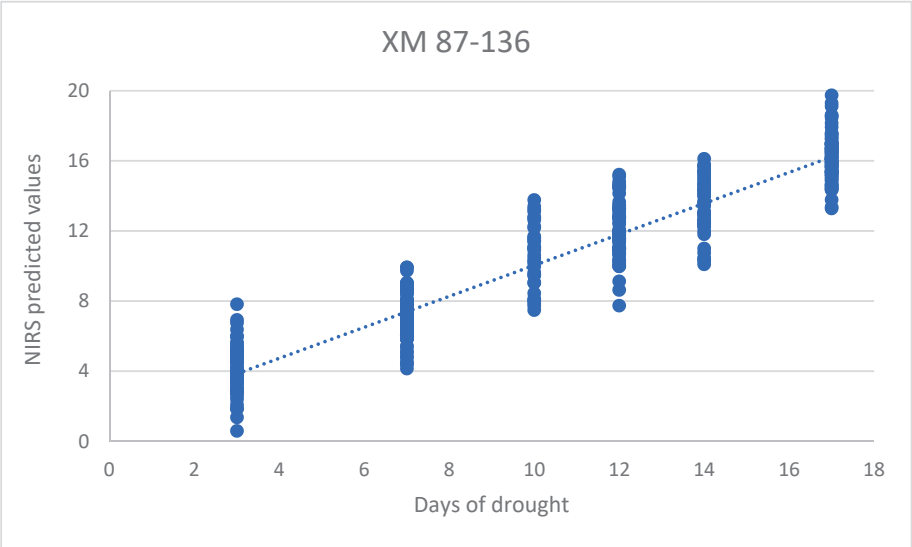

Figure 9. PLSR model for determination of days of drought of XM 87-136 plants.

Regression vectors and correlation spectra from PLS procedures were investigated to find important wavelengths for the determination of days of drought. A regression vector plot is a line plot of coefficients in the model versus wavelengths. The correlation spectrum shows a correlation between the determined parameter and spectral information. Both models for B37 and XM 87-136 provided similar regression vectors and correlation spectra (Figure 10). The most influential variables were at 1342, 1379, 1409 and approximately 930 1459 nm, which are close to WAMAC coordinates C1, C4, C5, and C9, respectively. In the area 1350–1500 nm, there was only a difference in the magnitude of regression vector coefficients. They were bigger for B37 compared to those for the XM 87-136 line. This is related to the difference in absorption values for the two types of maize plants. Small differences existed at 1521, 1527, and 1546 nm. The differences in correlation spectra were most significant in the region 1500–1600 nm, similar to the result of regression vectors. They appear at 1503 and 1527 nm in the correlation spectra of the model for the B37 line. Absorption at 1503 nm can be associated with strongly bound water. In previous investigations absorption at 1527 nm is connected with structural–water and water–cellulose interactions [57].

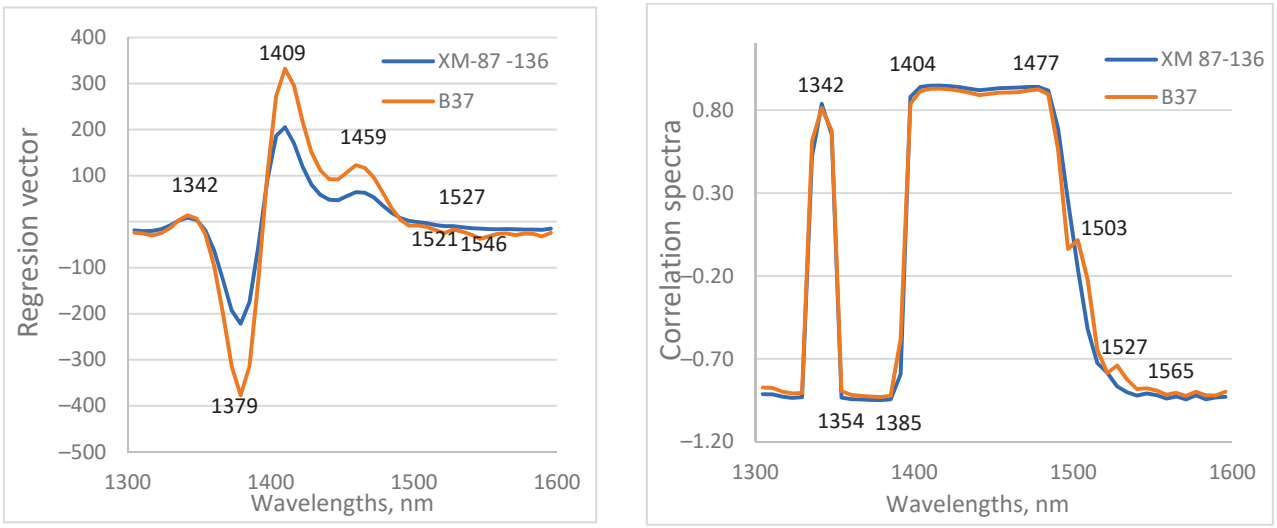

(**a**) Regression vector (**b**) Correlation spectra

Figure 10. Regression vector (**a**) and correlation spectra (**b**) of PLS models for determination of days of drought.

The results of the analysis of the regression vectors and the correlation spectra confirm the existence of differences in the spectral characteristics of the leaves of the two studied maize inbred lines. The differences are related to changes in water content and water structure during drying.

4. Conclusions

This study was conducted to investigate the changes during water stress of maize plants using an aquaphotomic approach. Spectra of plants from two inbred lines, one of them drought resistant, were analyzed.

Differences in absorption spectra in the first overtone water region from 1300 and 1600 nm were observed between control, water-stressed, and recovered maize plants, as well as between different days of stressed plants. Aquagrams clearly visualize the spectral difference. The spectral differences showed a loss of free and weakly bound water in the process of water stress. The remaining water is in the bound state with a high number of hydrogen bonds or bonded to the structural elements of plants. This statement is also confirmed by the analysis of the results of the PLS models for determining the days of drought. Aquagrams and spectra of two investigated maize lines also show the differences between the two inbred lines connected with drought tolerance.

The results of this pilot study demonstrated the potential of the aquaphotomics approach to better understand the process of water stress in plants. This can also be used as an additional approach in breeding programs for the selection of drought-tolerant maize varieties.

Author Contributions: Conceptualization, S.A., P.S. and D.M.; methodology, S.A., P.S. and D.M.; software, S.A. and P.V.; validation, S.A. and P.V.; formal analysis, P.V.; investigation, D.M., S.A., P.S., P.V., A.P. and N.K.C.; resources, D.M. and N.K.C.; data curation, S.A.; writing—original draft preparation, S.A., P.S., D.M., N.K.C. and P.V.; writing—review and editing, S.A.; visualization, S.A. and P.V.; supervision, S.A.; project administration, S.A.; funding acquisition, S.A. and P.S. All authors have read and agreed to the published version of the manuscript.

Funding: This research was funded by the National Science Fund of Bulgaria (Contract No. KP-06-N51/3). The topic of the scientific research national project is: "Aquaphotomics approach for investigation of stress-induced changes of water molecular structure in green species".

Institutional Review Board Statement: Not applicable.

Informed Consent Statement: Not applicable.

Data Availability Statement: Data are contained within the article.

Conflicts of Interest: The authors declare no conflict of interest.

References

1. Yadav, S.K. Cold stress tolerance mechanisms in plants. A review. *Agron. Sustain. Dev.* **2010**, *30*, 515–527. [CrossRef]
2. Redondo-Gómez, S. Abiotic and Biotic Stress Tolerance in Plants. In *Molecular Stress Physiology of Plants*; Rout, G.R., Das, A.B., Eds.; Springer: New Delhi, India, 2013; pp. 1–20.
3. Suzuki, N.; Rivero, R.M.; Shulaev, V.; Blumwald, E.; Mittler, R. Abiotic and biotic stress combinations. *New Phytol.* **2014**, *203*, 32–43. [CrossRef] [PubMed]
4. Mantri, N.; Patade, V.; Penna, S.; Ford, R.; Pang, E. Abiotic stress responses in plants: Present and future. In *Abiotic Stress Responses in Plants: Metabolism, Productivity and Sustainability*; Ahmad, P., Prasad, M.N.V., Eds.; Springer: New York, NY, USA, 2012.
5. Madhava Rao, K.V. Introduction. In *Physiology and Molecular Biology of Stress Tolerance in Plants*; Madhava Rao, K.V., Raghavendra, A.S., Janardhan Reddy, K., Eds.; Springer: Dordrecht, The Netherlands, 2006; pp. 1–14.
6. Smith, B.N.; Harris, L.C.; McCarlie, V.W.; Stradling, D.L.; Thygerson, T.; Walker, J.; Criddle, R.S.; Hansen, L.D. Time, plant growth, respiration, and temperature. In *Handbook of Plant and Crop Physiology*; Pessarakli, M., Ed.; Marcel Dekker: New York, NY, USA, 2001; pp. 1–12.
7. Murphy, T.M.; Huerta, A.J. Hydrogen peroxide formation in cultured rose cells in response to UV-C radiation. *Physiol. Plant.* **1990**, *78*, 247–253. [CrossRef]
8. Legendre, L.; Yueh, Y.G.; Crain, R.; Haddock, N.; Heinstein, P.F.; Low, P.S. Phospholipase C activation during elicitation of the oxidative burst in cultured plant cells. *J. Biol. Chem.* **1993**, *268*, 24559–24563. [CrossRef] [PubMed]

9. Rao, M.V.; Dubey, P.S. Response of hydrogen peroxide scavenging system in 2 soybean cultivars exposed to SO_2—Experimental evidence for the detoxification of SO_2 by enhanced H_2O_2 scavenging components. *Environ. Poll.* **1993**, *82*, 99–105. [CrossRef] [PubMed]
10. Smirnoff, N. The role of active oxygen in the response of plants to water deficit and desiccation. *New Phytol.* **1993**, *125*, 27–58. [CrossRef] [PubMed]
11. Lobell, D.B.; Roberts, M.J.; Schlenker, W.; Braun, N.; Little, B.B.; Rejesus, R.M.; Hammer, G.L. Greater sensitivity to drought accompanies maize yield increase in the U.S. Midwest. *Science* **2014**, *344*, 516–519. [CrossRef] [PubMed]
12. Zhou, B.; Sun, X.; Ding, Z.; Ma, W.; Zhao, M. Multisplit Nitrogen Application via Drip Irrigation Improves Maize Grain Yield and Nitrogen Use Efficiency. *Crop Sci.* **2017**, *57*, 1687–1703. [CrossRef]
13. Ben-Ari, T.; Adrian, J.; Klein, T.; Calanca, P.; Van der Velde, M.; Makowski, D. Identifying indicators for extreme wheat and maize yield losses. *Agric. For. Meteorol.* **2016**, *220*, 130–140. [CrossRef]
14. Liu, S.; Qin, F. Genetic dissection of maize drought tolerance for trait improvement. *Mol. Breed.* **2021**, *41*, 8. [CrossRef]
15. Sah, R.P.; Chakraborty, M.; Prasad, K.; Pandit, M.; Tudu, V.K.; Chakravarty, M.K.; Narayan, S.C.; Rana, M.; Moharana, D. Impact of water deficit stress in maize: Phenology and yield components. *Sci. Rep.* **2020**, *10*, 2944. [CrossRef] [PubMed]
16. Liu, M.; Li, M.; Liu, K.; Sui, N. Effects of drought stress on seed germination and seedling growth of different maize varieties. *J. Agric. Sci.* **2015**, *7*, 231–240. [CrossRef]
17. Bell, J. Corn Growth Stages and Development. 2017. Available online: https://amarillo.tamu.edu/files/2017/07/corn-growth-stages-and-development.pdf (accessed on 9 October 2023).
18. Fakorede, M.; Opeke, B. Weather Factors Affecting the Response of Maize to Planting Dates in a Tropical Rainforest Location. *Exp. Agric.* **1985**, *21*, 31–40. [CrossRef]
19. Bashir, N.; Mahmood, S.; Zafar, Z.U.; Rasul, S. Is drought tolerance in maize (*Zea mays* L.) cultivars atthe juvenile stage maintainedat the reproductive stage. *Pak. J. Bot.* **2016**, *48*, 1385–1392.
20. Sheoran, S.; Kaur, Y.; Kumar, S.; Shukla, S.; Rakshit, S.; Kumar, R. Recent advances for drought stress tolerance in maize (*Zea mays* L.): Present status and future prospects. *Front. Plant Sci.* **2022**, *13*, 872566. [CrossRef]
21. Safdar, M.; Shahid, M.A.; Sarwar, A.; Rasul, F.; Majeed, M.D.; Sabir, R.M. Crop Water Stress Detection Using Remote Sensing Techniques. *Environ. Sci. Proc.* **2023**, *25*, 20.
22. Crusiol, L.G.T.; Sun, L.; Sun, Z.; Chen, R.; Wu, Y.; Ma, J.; Song, C. In-Season Monitoring of Maize Leaf Water Content Using Ground-Based and UAV-Based Hyperspectral Data. *Sustainability* **2022**, *14*, 9039. [CrossRef]
23. Lowe, A.; Harrison, N.; French, A.P. Hyperspectral image analysis techniques for the detection and classification of the early onset of plant disease and stress. *Plant Methods* **2017**, *13*, 80. [CrossRef]
24. Das, B.; Mahajan, G.R.; Singh, R. *Hyperspectral Remote Sensing: Use in Detecting Abiotic Stresses in Agriculture, In Advances in Crop Environment Interaction*; Bal, S., Mukherjee, J., Choudhury, B., Dhawan, A., Eds.; Springer: Singapore, 2018; pp. 317–335.
25. Teixeira dos Santos, C.A.; Lopo, M.; Pascoa, R.; Lopes, J.A. A review on the applications of portable near-infrared spectrometers in the agro-food industry. *Appl. Spectrosc.* **2013**, *67*, 1215–1233. [CrossRef]
26. Lu, W.; Sun, D.W.; Pu, H.; Cheng, J.H. Quality analysis and classification and authentication of liquid foods by near-infrared spectroscopy: A review of recent research developments. *Crit. Rev. Food Sci. Nutr.* **2016**, *57*, 1524–1538.
27. Yakubu, H.G.; Kovacs, Z.; Toth, T.; Bazar, G. The recent advances of near-infrared spectroscopy in dairy production—A review. *Crit. Rev. Food Sci. Nutr.* **2022**, *62*, 810–831. [CrossRef] [PubMed]
28. Pandiselvam, R.; Prithviraj, V.; Manikantan, M.R.; Kothakota, A.; Rusu, A.V.; Trif, M.; Mousavi Khaneghah, A. Recent advancements in NIR spectroscopy for assessing the quality and safety of horticultural products: A comprehensive review. *Front. Nutr.* **2022**, *9*, 973457. [CrossRef]
29. Tsenkova, R. Introduction aquaphotomics: Dynamic spectroscopy of aqueous and biological systems describes peculiarities of water. *J. Near Infrared Spectrosc.* **2009**, *17*, 303–314. [CrossRef]
30. Tsenkova, R.; Muncan, J.; Pollner, B.; Kovacs, Z. Essentials of Aquaphotomics and Its Chemometrics Approaches. *Front. Chem.* **2018**, *6*, 363. [CrossRef]
31. Muncan, J.; Tsenkova, R. Aquaphotomics-From Innovative Knowledge to Integrative Platform in Science and Technology. *Molecules* **2019**, *24*, 2742. [CrossRef] [PubMed]
32. Cattaneo, T.; Vanoli, M.; Grassi, M.; Rizzolo, A.; Barzaghi, S. The aquaphotomics approach as a tool for studying the influence of food coating materials on cheese and winter melon samples. *J. Near Infrared Spectrosc.* **2016**, *24*, 381–390. [CrossRef]
33. Vanoli, M.; Lovati, F.; Grassi, M.; Buccheri, M.; Zanella, A.; Cattaneo, M.P.; Rizzolo, A. Water spectral pattern as a marker for studying apple sensory texture. *Adv. Hortic. Sci.* **2018**, *32*, 343–351.
34. Kaur, H.; Künnemeyer, R.; McGlone, A. Investigating aquaphotomics for temperature-independent prediction of soluble solids content of pure apple juice. *J. Near Infrared Spectrosc.* **2020**, *28*, 103–112. [CrossRef]
35. Cattaneo, T.; Cutini, M.; Cammerata, A.; Stellari, A.; Marinoni, L.; Bisaglia, C.; Mrambilla, M. Near infrared spectroscopic and aquaphotomic evaluation of the efficiency of solar dehydration processes in pineapple slices. *J. Near Infrared Spectrosc.* **2021**, *29*, 352–358. [CrossRef]
36. Nugraha, D.; Zaukuu, J.; Bósquez, J.; Bodor, Z.; Vitalis, F.; Kovacs, Z. Near-infrared spectroscopy and aquaphotomics for monitoring mung bean (*Vigna radiata*) sprout growth and validation of ascorbic acid content. *Sensors* **2021**, *21*, 611. [CrossRef]

37. Marinoni, L.; Buccheri, M.; Bianchi, G.; Cattaneo, T. Aquaphotomic, E-nose and electrolyte leakage to monitor quality changes during the storage of ready-to-eat rocket. *Molecules* **2022**, *27*, 2252. [CrossRef] [PubMed]
38. Malegori, C.; Muncan, J.; Mustorgi, E.; Tsenkova, R.; Oliveri, P. Analysing the water spectral pattern by near-infrared spectroscopy and chemometrics as a dynamic multidimensional biomarker in preservation: Rice germ storage monitoring. *Spectrochim. Acta A Mol. Biomol. Spectrosc.* **2022**, *265*, 120396. [CrossRef] [PubMed]
39. Jinendra, B.; Tamaki, K.; Kuroki, S.; Vassileva, M.; Yoshida, S.; Tsenkova, R. Near infrared spectroscopy and aquaphotomics: Novel approach for rapid in vivo diagnosis of virus infected soybean. *Biochem. Biophys. Res. Commun.* **2010**, *397*, 685–690. [CrossRef] [PubMed]
40. Muncan, J.; Jinendra, B.M.S.; Kuroki, S.; Tsenkova, R. Aquaphotomics Research of Cold Stress in Soybean Cultivars with Different Stress Tolerance Ability: Early Detection of Cold Stress Response. *Molecules* **2022**, *27*, 744. [CrossRef]
41. Zahir, S.A.D.M.; Omar, A.F.; Jamlos, M.F.; Mohd, A.M.A.; Muncan, J. A review of visible and near-infrared (Vis-NIR) spectroscopy application in plant stress detection. *Sens. Actuators A Phys.* **2022**, *338*, 113468. [CrossRef]
42. Kuroki, S.; Tsenkova, R.; Moyankova, D.; Muncan, J.; Morita, H.; Atanassova, S.; Djilianov, D. Water molecular structure underpins extreme desiccation tolerance of the resurrection plant Haberlea rhodopensis. *Sci. Rep.* **2019**, *9*, 3049. [CrossRef]
43. Tomlekova, N.B. Induced Mutagenesis for Crop Improvement in Bulgaria. *Plant Mutat. Rep.* **2010**, *2*, 4–27.
44. Christov, N.K.; Ilchovska, D.; Hristov, K.N. Chapter 8—Chemical mutagenesis, mutation breeding and quantitative genetic analyses of maize mutants: From theory to practice. In *Mutagenesis: Exploring Genetic Diversity of Crops*; Tomlekova, N.B., Kozgar., M.I., Wani, M.R., Eds.; Wageningen Academic Publishers: Wageningen, The Netherlands, 2014; pp. 167–194. [CrossRef]
45. Barrs, H.; Weatherley, P. A Re-Examination of the Relative Turgidity Technique for Estimating Water Defcits in Leaves. *Aust. J. Biol. Sci.* **1962**, *15*, 413. [CrossRef]
46. Vitalis, F.; Muncan, J.; Anantawittayanon, S.; Kovacs, Z.; Tsenkova, R. Aquaphotomics Monitoring of Lettuce Freshness during Cold Storage. *Foods* **2023**, *12*, 258. [CrossRef]
47. El-Hendawy, S.E.; Al-Suhaibani, N.A.; Elsayed, S.; Hassand, W.M.; Dewir, Y.H.; Refay, Y.; Abdella, K.A. Potential of the existing and novel spectral reflectance indices for estimating the leaf water status and grain yield of spring wheat exposed to different irrigation rates. *Agric. Water Manag.* **2019**, *217*, 356–373. [CrossRef]
48. Zygielbaum, A.I.; Gitelson, A.A.; Arkebauer, T.J.; Rundquist, D.C. Non-destructive detection of water stress and estimation of relative water content in maize. *Geophys. Res. Lett.* **2009**, *36*, L12403. [CrossRef]
49. Das, B.; Sahoo, R.N.; Pargal, S.; Krishna, G.; Verma, R.; Viswanathan, C.; Sehgal, V.K.; Gupta, V.K. Evaluation of different water absorption bands, indices and multivariate models for water-deficit stress monitoring in rice using visible-near infrared spectroscopy. *Spectrochim. Acta Part A Mol. Biomol. Spectrosc.* **2021**, *247*, 119104. [CrossRef]
50. Rajkumar, D.; Künnemeyer, R.; Kaur, H.; Longdell, J.; McGlone, A. Interactions of Linearly Polarized and Unpolarized Light on Kiwifruit Using Aquaphotomics. *Molecules* **2022**, *27*, 494. [CrossRef]
51. Workman, J.; Weyer, L. *Practical Guide of Interpretative Near-Infrared Spectroscopy*; Taylor and Francis Group: Abingdon, UK; CRC Press: Boca Raton, FL, USA, 2008.
52. Elvanidi, A.; Katsoulas, N.; Bartzanas, T.; Ferentinos, K.P.; Kittas, C. Crop water status assessment in controlled environment using crop reflectance and temperature measurements. *Precis. Agric.* **2017**, *18*, 332–349. [CrossRef]
53. Ihuoma, S.O.; Madramootoo, C.A. Recent advances in crop water stress detection. *Comput. Electron. Agric.* **2017**, *141*, 267–275. [CrossRef]
54. Zhang, F.; Zhou, G. Estimation of vegetation water content using hyperspectral vegetation indices: A comparison of crop water indicators in response to water stress treatments for summer maize. *BMC Ecol.* **2019**, *19*, 18. [CrossRef]
55. Naik, B.B.; Naveen, H.R.; Sreenivas, G.; Choudary, K.K.; Devkumar, D.; Adinarayana., J. Identification of Water and Nitrogen Stress Indicative Spectral Bands Using Hyperspectral Remote Sensing in Maize During Post-Monsoon Season. *J. Indian. Soc. Remote Sens.* **2020**, *48*, 1787–1795. [CrossRef]
56. Muncan, J.; Anantawittayanon, S.; Furuta, T.; Kaneko, T.; Tsenkova, R. Aquaphotomics monitoring of strawberry fruit during cold storage—A comparison of two cooling systems. *Front. Nutr.* **2022**, *9*, 058173. [CrossRef]
57. Schwanninger, M.; Rodrigues, J.; Fackler, K.A. Review of band assignments in near infrared spectra of wood and wood components. *J. Near Infrared Spectrosc.* **2011**, *19*, 287–308. [CrossRef]

energies

MDPI

Article

Effect of Combined Non-Wood and Wood Spectra of Biomass Chips on Rapid Prediction of Ultimate Analysis Parameters Using near Infrared Spectroscopy

Bijendra Shrestha [1], Jetsada Posom [2], Panmanas Sirisomboon [1,*], Bim Prasad Shrestha [3,4,*] and Axel Funke [5]

[1] Department of Agricultural Engineering, School of Engineering, King Mongkut's Institute of Technology Ladkrabang, Bangkok 10520, Thailand; 63601254@kmitl.ac.th
[2] Department of Agricultural Engineering, Faculty of Engineering, Khon Kaen University, Khon Kaen 40002, Thailand; jetspo@kku.ac.th
[3] Department of Mechanical Engineering, School of Engineering, Kathmandu University, Dhulikhel P.O. Box 6250, Nepal
[4] Department of BioEngineering, University of Washington, William H. Foege Building 3720, 15th Ave NE, Seattle, WA 98195-5061, USA
[5] Karlsruhe Institute of Technology, Institute of Catalysis Research and Technology, Hermann-von-Helmholtz-Platz 1, 76344 Eggenstein-Leopoldshafen, Germany; axel.funke@kit.edu
* Correspondence: panmanas.si@kmitl.ac.th (P.S.); shrestha@ku.edu.np (B.P.S.)

Abstract: The ultimate analysis parameters, including carbon (C), hydrogen (H), nitrogen (N), and oxygen (O) content in biomass, were rarely found to be predicted by non-destructive tests to date. In this research, we developed partial least squares regression (PLSR) models to predict the ultimate analysis parameters of chip biomass using near-infrared (NIR) raw spectra of non-wood and wood samples from fast-growing tree and agricultural residue and nine different traditional spectral preprocessing techniques. These techniques include first derivative (sd1), second derivative (sd2), constant offset, standard normal variate (SNV), multiplicative scatter correction (MSC), vector normalization, min-max normalization, mean centering, sd1 + vector normalization, and sd1 + MSC. Additionally, we employed a genetic algorithm (GA), successive projection algorithm (SPA), multi-preprocessing (MP) 5-range, and MP 3-range to develop a PLSR model for rapid prediction. A dataset consisting of 120 chip biomass samples was utilized for model development in which the samples were non-wood samples of 65–67% and wood samples of 33–35%, and the model performance was evaluated and compared. The selection of the optimum performing model was mainly based on criteria such as the coefficient of determination in the prediction set (R^2_P), root mean square error of the prediction set (RMSEP), and the ratio of prediction to deviation (RPD). The optimal model for weight percentage (wt.%) of C was obtained using GA–PLSR, yielding R^2_P, RMSEP, and RPD values of 0.6954, 1.1252 wt.%, and 1.8, respectively. Similarly, for wt.% of O, the most effective model was obtained using the multi-preprocessing PLSR–5 range method with R^2_P of 0.7150, RMSEP of 1.3088 wt.%, and RPD of 1.9. For wt.% of N, the optimal model was obtained using the MP PLSR-3 range method, resulting in R^2_P, RMSEP, and RPD values of 0.6073, 0.1008 wt.%, and 1.6, respectively. However, wt.% of the H model provided R^2_P, RMSEP, and RPD values of 0.5162, 0.2322 wt.%, and 1.5, respectively. Notably, the limit of quantification (LOQ) values for C, H, and O were lower than the minimum reference values used during model development, indicating a high level of sensitivity. However, the LOQ for N exceeded the minimum reference value, implying the samples to be predicted by the model must be in the range of reference range in the calibration set. By scatter plot analysis, the effect of combined non-wood and wood spectra of biomass chips on rapid prediction of ultimate analysis parameters using NIR spectroscopy was investigated. To include different species in a model, the species have to be not only in the different values of the constituents to make a wider range for a robust model, but also must provide their trend line characteristics in the scatter plot, i.e., correlation coefficient (R), slope, and intercept (same slope and slope approached to 1, and intercept is same (no gap) and approached zero, high R approached to 1). The effect of the R, slope, and intercept to obtain the better-optimized model was studied. The results show that the different species affected the model performance of each parameter prediction in a different manner, and by

scatter plot analysis, which of these species were affecting the model negatively and how the model could be improved was indicated. This is the first time the effect has been studied by the principle of a scatter plot.

Keywords: biomass; ultimate analysis; near-infrared spectroscopy; partial least squares regression

1. Introduction

The world is undergoing a significant transition away from fossil fuels, embracing modern renewable energy technologies to meet its escalating energy needs and demands. Bioenergy, derived from sources such as woody biomass, agricultural residues, and organic materials and waste, is pivotal in this paradigm shift, constituting the largest share (two–thirds) of global renewable energy utilization [1]. It is anticipated that bioenergy will continue to have a decisive share in future net zero emission scenarios and that its contribution to energy supply will further increase. This transition underscores the growing significance of biomass energy within the global energy landscape. However, it is worth noting that billions of people still rely on the inefficient use of traditional biomass for cooking and heating [1]. The combustion of biomass produces air pollutants similar to those emitted by fossil fuels, with the exception of sulfur oxides [2]. Furthermore, research has shown that the health impacts attributed to emissions from biomass and wood combustion can be more harmful than those from fossil fuels [3]. These emissions primarily result from incomplete biomass combustion and the release of solid particulate matter.

The adoption of woody biomass and non-wood biomass, such as agricultural residues, coupled with efficient combustion energy technologies, holds the potential to substantially reduce harmful emissions into the atmosphere while increasing its contribution to energy supply, making it a viable alternative to fossil fuels. Due to efficiency increase as compared to traditional biomass use, it is an important cornerstone of future scenarios. Despite significant investments in the research and development of biomass energy technologies, a knowledge gap persists, particularly concerning efficient, low-cost determination of biomass properties, including its elemental compositions (carbon (C), hydrogen (H), nitrogen (N), oxygen (O), sulfur (S), and others). During inefficient and incomplete combustion, harmful pollutants such as carbon monoxide, sulfur oxides (SOx), nitrogen oxides (NOx), along with particulate matter ($PM_{2.5}$ and PM_{10}) are continuously released into the environment as smoke, posing significant health risks through indoor and outdoor exposure, with women and children being the most vulnerable [4–6].

The elemental composition of biomass has a profound impact on combustion efficiency and the emission levels released into the environment. These emissions, in turn, carry significant consequences for both the energy industry and the natural surroundings. Energy release during biomass combustion correlates positively with carbon and hydrogen contents, as they are the primary contributors to its energy value [7]. High carbon content is desirable for energy production [8], and hydrogen's high energy content makes it valuable [9]. During combustion, oxygen reacts with carbon and hydrogen, reducing the available energy in biomass. Elevated oxygen and nitrogen contents decrease the calorific value, thereby reducing energy potential [10]. Nitrogen and sulfur are undesirable elements in biomass due to their contribution to the formation of harmful NOx and sulfur dioxide [11,12]. To minimize environmental impact and ensure sustainable operation and maintenance of combustion systems, low sulfur content in biomass is preferred [12]. Hence, it is crucial to rapidly, accurately, and non-invasively assess the elemental composition of biomass, including C, N, O, H, and S. This assessment is essential for understanding biomass elemental composition and the potential emissions risks during energy production.

In our previous research [13], an investigation was conducted into the application of NIR spectroscopy (NIRS) for the comprehensive analysis of the ultimate analysis parameters of ground biomass intended for energy utilization. The study concludes that NIRS

offers a reliable and non-destructive alternative method for rapidly assessing the elemental composition of ground biomass for energy-related purposes. Despite the valuable findings from previous research, these findings primarily served academic and research institutions. However, biomass normally is made into pellet form for export and to increase energy density where grinding is necessary before making pellets. Woodchips are especially useful, as they are easy to use, and sometimes, ground wood is not suitable for power operations due to the high cost and length of time necessary for sample preparation; therefore, it is a popular source of energy for power plants because of low preparation costs. Meanwhile, woodchip quality could be more effectively examined to achieve higher levels of plant efficiency [14]. Hence, this study aims to improve the applicability of NIR spectroscopy to assess the ultimate analysis parameters of chipped biomass, i.e., biomass with particle sizes commonly found in industrial applications. In consequence, this research outcome may directly benefit traders and energy companies, facilitating the utilization of research outcomes without the need for extensive biomass preparation such as grinding.

The data structure of samples used for model development in this present work was in two forms, i.e., non-wood and wood samples. As reported, the non-wood and wood species were different in their lignocellulosic constituents. Non-wood material of agricultural waste compost of lignin, holocellulose, α-cellulose, pentosan, and ash [15]. For example, agricultural residues, such as hemp and sugarcane bagasse, contained higher concentrations of cellulose and lower levels of recalcitrant lignin when compared to the average woody biomass [16,17]. However, Hawanis et al. [18] reported that non-wood contained lower cellulose and lignin while wood contained higher [19–21]. Therefore, incorporating a wider range of ultimate analysis parameters (C, H, N, O, and S) as reference values will enhance the model robustness for prediction. Previous studies have strongly correlated ultimate analysis parameters to higher heating values in biomass [22]. Hence, by predicting the ultimate analysis parameters and leveraging these correlations, the fuel heating value can be characterized. This study specifically investigated the effect of combined non-wood and wood spectra from biomass chips on rapidly predicting ultimate analysis parameters using NIR spectroscopy (NIRS).

The volume of available published studies is limited in which wood and non-wood biomasses are characterized concurrently. Generally, only one specific species of biomass was used for prediction modeling, and the determination of ultimate analysis constituents by NIRS was rarely reported. Only two reports were found, including Posom and Sirisomboon [23], who optimized the PLS models using NIR spectra of 80 bamboo chip samples for evaluation of C, H, N, S, and O content. The models showed the coefficient of determination of prediction set (R^2_P) and the ratio of prediction to deviation (RPD) of 0.803 and 2.31 for C; 0.856 and 2.65 for H; 0.973 and 6.6 for N; 0.785 and 2.19 for S; and 0.522 and 1.46 for O, respectively. Similarly, the models developed by Zhang et al. [24] used 100 accessions of sorghum biomass with R^2_P of 0.96 for wt.% of C, 0.87 for wt.% of H, 0.86 for wt.% of N, and 0.83 for wt.% of O.

There were two reports found in the available database that developed a model for two similar species to evaluate ultimate analysis parameters, C, H, N, O, and S. A total of 222 rice straw and wheat straw, collected from 24 provinces of China, were used for NIRS calibration and validation in this study where R^2_P and standard error of predictions (SEP) of independent validation were, respectively, 0.97 and 0.37% for C, 0.77 and 0.17% for H, and 0.87 and 0.10% for N [25]. Saha et al. [26] developed models by using 276 wood chip ground samples of pine trees of two species (Loblolly (*Pinus taeda*) and slash (*Pinus elliottii*)), where the biomass spectra ranged from 400 to 2498 nm at 2 nm intervals. The samples were a mix of bark, branch, needle, wood, or whole tree biomass. The prediction results show for C (sample number (n) = 43; coefficient of R^2_P = 0.90; RPD = 3.14; ratio of prediction to interquartile (RPIQ) = 3.23); for N (n = 44; R^2_P = 0.95; RPD = 4.33; RPIQ = 5.96); and for S (n = 42; R^2_P = 0.93; RPD = 3.67; RPIQ = 3.24).

There were two reports of our group contributed to the research results of NIR prediction models for ultimate analysis parameters of the non-wood and wood samples,

including Pitak et al. [27] who developed the PLS regression using the spectra obtained by line-scan NIR hyperspectral imager in which the most effective model for the prediction of C, H, and N content of 160 non-wood and wood biomass pellets including filter cake (15 pellets), *Leucaena leucocepphala* (10 pellets), bamboo (15 pellets), cassava rhizome (15 pellets), bagasse (15 pellets), sugarcane leaves (15 pellets), straw (15 pellets), rice husk (15 pellets), eucalyptus bark (15 pellets), napier grass (15 pellets), and corn cob (15 pellets) developed using iGA wavelength selection and standard normal variate (SNV) spectral pretreatment and provided the highest accuracy with R^2_{Pp} and SEP of 0.83 and 1.33% for C; 0.84 and 0.17% for H and 0.90 and 0.098% for N; respectively. The second report was contributed by Shrestha et al. [13], where the ground non-wood and wood samples spectra, which were 110 samples of agricultural residues and 90 samples of fast-growing trees, were used to develop the PLSR models combined with multi-preprocessing methods for ultimate analysis showed R^2_P and RPD for C of 0.7217 and 1.9, for N of 0.8410 and 2.7, for H of 0.7678 and 2.1, and for O of 0.6289 and 1.7, respectively.

The main objectives of this research include:

(1) Develop PLSR models using NIR raw spectra, traditional preprocessing, MP 5-range, MP 3-range, GA, and SPA for assessing chip biomass properties for energy usage by employing NIRS while the spectra of the biomass were from non-wood (agricultural residue and bamboo) and wood (fast growing trees) samples.
(2) Compare the performance of the PLSR models based on R^2_C, RMSEP, R^2_P, RMSEP, RPD, and bias.
(3) Study the effect of combined non-wood and wood species in model development on model performance by scatter plot analysis.
(4) Select the better performing PLSR-based model for each ultimate analysis parameter, compared with the performance of the ground biomass for rapidly assessing biomass properties for energy usage.
(5) Determine the limit of quantification (LOQ) value of the proposed model calibration set for each ultimate analysis parameter in chip biomass.

2. Materials and Methods

Figure 1 shows the overall research methodology for rapid prediction of ultimate analysis parameters of chip biomass by NIRS using PLSR.

2.1. Sample Preparation

A total of 120 samples were collected from ten different biomass varieties, which included wood samples and non-wood samples from various geographical locations in Nepal. Wood samples included four fast-growing species: (1) *Alnus nepalensis*, (2) *Pinux roxiburghii*, (3) *Bombax ceiba*, and (4) *Eucalyptus camaldulensis*. Non-wood samples were five agricultural residues: (1) *Zea mays* (cob), (2) *Zea mays* (shell), (3) *Zea mays* (stover), (4) *Oryza sativa*, and (5) *Saccharum officinarun,* and one fast-growing tree (6) *Bombusa vulagris*. The biomass samples, except *oryza sativa*, were manually chipped into smaller pieces, approximately sized 30 mm × 15 mm, for NIR scanning and for the reference measurement of ultimate analysis parameters [13].

2.2. Spectral Data Collection

All chip biomass samples were scanned using an FT-NIR spectrometer (MPA, Bruker, Ettlingen, Germany) in diffuse reflectance with sphere macro sample rotating mode, covering the wavelength range from 3594.87 to 12,489.48 cm^{-1}, with a resolution of 16 cm^{-1}. The scanning process consisted of 32 scans (on average) for both sample and background scans to collect the raw spectra. These raw spectra were acquired in a controlled laboratory environment with air conditioning maintaining a room temperature of 25 ± 2 °C.

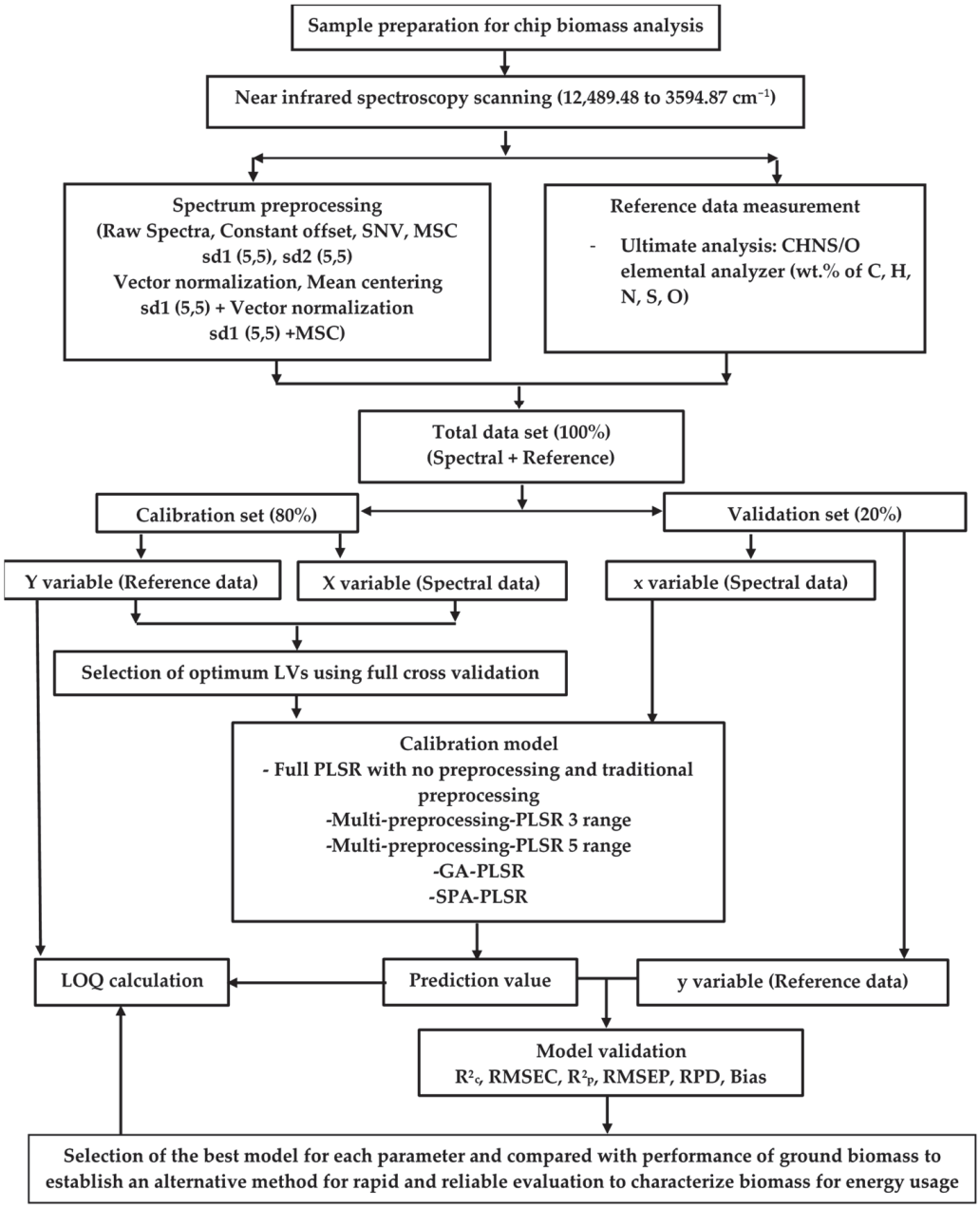

Figure 1. Flowchart of the overall research methodology for the rapid prediction of the ultimate analysis parameters of chip biomass for energy usage by NIRS using PLSR.

To compensate for the ambient influence and instrument drift on the measurement setup, background scanning was regularly performed on a gold plate as a reference for every new sample. Each biomass sample was scanned twice without changing its position, and the average of its absorbance values was calculated. All the spectra were logged as log (1/R) versus wavenumber (cm^{-1}), where R is the diffuse reflectance from the biomass sample.

Each sample was then subjected to a reference measurement of C, H, N, and S by a CHNS/O analyzer. This analyzer employs the flash dynamic combustion method, inducing complete combustion of the biomass sample within a high-temperature reactor (about 1800 °C), allowing for an accurate and precise determination of the ultimate analysis parameters.

2.3. Reference Analysis

The wt.% of C, H, N, and S on a dry basis in the chip biomass were determined at the Scientific and Technological Research Equipment Center (STREC) at Chulalongkorn University, Bangkok, Thailand, using CHNS/O analyzer (Thermo Scientific TM FLASH 2000, Waltham, MA, USA) [13]. The wt.% of O on a dry basis is calculated as:

$$\text{wt.\% O} = 100 - \text{wt.\% C} - \text{wt.\% H} - \text{wt.\% N} - \text{wt.\% S} - \text{wt.\% ash} \quad (1)$$

Here, wt.% ash is determined using a thermogravimetric analyzer (TG 209 F3 Tarsus, Netzsch, Bavaria, Germany) by combusting biomass within the temperature range between 35 to 700 °C.

2.4. Outlier and Standard Error of Laboratory

Outliers on the reference data were identified and removed using the following equation:

$$\frac{(X_i - \overline{X})}{SD} \geq |\pm 3| \quad (2)$$

where, X_i is the measured value of sample i, $\overline{X}$ is the average, and SD is the standard deviation of the measured values of all samples [13,28].

2.5. Spectral Preprocessing and Model Development

As shown in Figure 1, this study incorporates nine different types of spectral preprocessing applied to the raw spectra. These methods include constant offset, SNV, MSC, sd1, sd2, vector normalization, mean centering, sd1 + vector normalization, and sd1 + MSC.

Five different types of PLSR-based regression models, namely Full-PLSR, MP PLSR–5 range, MP PLSR-3 range, GA–PLSR, and SPA–PLSR, were developed to compare and select the best-performing model for each ultimate analysis parameter to establish a reliable and non-destructive alternative method for rapidly assessing biomass properties for energy usage [13].

The primary objective of the MP method is to optimize model performance by applying various preprocessing techniques to different divided sections within the entire wavenumber range. A built-in code in MATLAB R2020b was utilized to obtain a combination set of different preprocessing techniques based on the desired number of random pairs. The optimal combination set for each selected number of random pairs is determined through a cross-validation procedure using PLSR on reference and spectroscopic data. Using the selected combination set of preprocessing techniques, the PLSR model was developed. Here, we generate a combination set of preprocessing techniques using seven different options: 0 = empty (all absorbance values = 0), 1 = raw spectra, 2 = SNV, 3 = MSC, 4 = sd1, 5 = sd2, and 6 = constant offset. In the MP approach, two methods were adopted: in the MP PLSR-5 range method, the spectral range is divided into five equal sections, while in the MP PLSR-3 range method, it is divided into three sections. The best MP combination set for model development is then determined [13].

Both GA and SPA were employed to select concise and influential wavenumbers, aiming to prevent overfitting and result in an improved prediction model [27]. GA, inspired by Charles Darwin's theory of natural selection, utilizes an optimization technique that generates a population of potential solutions and evolves them over multiple generations through selection, crossover, and mutation. Starting with one wavenumber, each iteration adds a new one to the selection, ultimately reducing redundant information in the chosen wavenumbers [29]. Similarly, SPA is a forward feature selection method that begins with an empty set and iteratively adds one wavelength at a time to the subset. In each iteration, the wavelength contributing the most to the model, based on correlation, is selected and added to the subset. This process effectively reduces dimensionality by eliminating multicollinear and redundant variables using SPA [30–32].

2.6. Limit of Quantification (LOQ)

Based on the SD of the response to slope method from the calibration model, LOQ, which represents the lowest concentration of the analyte that can be detected and quantified with an acceptable level of accuracy and precision [28,33], is calculated as follows:

$$\mathrm{LOQ} = 10\,\frac{\sigma_c}{S_c} \tag{3}$$

where, σ_C is the residual standard deviation, i.e., the precision obtained from measured and predicted values of the calibration set, and S_C is the slope of the model regression line.

3. Results and Discussion

Table 1 shows the number of non-wood samples and wood samples in the calibration set and validation set. The wood sample number is about 33–35% of the total sample number; hence, the non-wood sample number is 65–67%. Out of 120 samples, the number of outlier samples can be evaluated by the data in Table 1.

Table 1. The number of non-wood samples and wood samples in calibration set and validation set.

Parameter	Total Sample	Calibration Set			Validation Set		
		Wood	Non-Wood	Total	Wood	Non-Wood	Total
wt.% C	111	31	58	89	8	14	22
wt.% H	119	32	63	95	8	16	24
wt.% N	116	31	62	93	9	14	23
wt.% O	102	28	54	82	8	12	20

Table 2 presents statistical data for the ultimate analysis parameters of chip biomass obtained using CHNS/O elemental analyzer (Thermo Scientific^{TM} FLASH 2000). This data was used in both the calibration and prediction sets for model development. S content in the chip biomass was not detected, possibly due to its very low content falling below the detection threshold. Therefore, a PLSR-based model for S content in the chip biomass was not developed in this study. The wt.% of O is calculated using Equation (1).

Table 2. The statistical data of the ultimate analysis parameters of the chip biomass obtained using CHNS/O elemental analyzer used in PLSR model development.

Parameter	N_T	Calibration Set					Validation Set				
		N_C	Max	Min	Mean	SD	N_P	Max	Min	Mean	SD
C (wt.%)	111	89	48.7500	38.9300	44.6330	2.1380	22	47.2800	49.7550	44.4439	2.0878
H (wt.%)	119	95	6.6200	4.9100	5.7620	0.3485	24	6.5700	4.9500	5.6490	0.3411
O (wt.%)	102	82	51.1200	37.3600	44.6322	2.8521	20	48.8000	38.8500	45.1159	2.5149
N (wt.%)	116	93	0.9100	0.0000	0.2987	0.2250	23	0.6200	0.0000	0.2714	0.1645

Table 3 shows the results of the PLSR-based model for ultimate analysis (wt.%) of chip biomass, where the bolded model shows the best performance. However, it is essential to consider the recommendation provided by Williams et al. [34], where with an R^2_P value between 0.66–0.81, the model can be used for rough screening and other suitable calibration purposes. Therefore, C, O, and N models were. For the H model, according to Williams guideline [34], a model with an R^2_P value between 0.50–0.64 is only suitable for very rough screening. Likewise, every model of biomass chips for ultimate analysis parameters was in alignment with the recommendation from Zornoza et al. [35], in which any model with an RPD value below 2 was deemed insufficient for any application.

Table 3. Results of the PLSR-based model for ultimate analysis (wt.%) of chip biomass, bolded model showing the best performance.

Parameter	Algorithm	Preprocessing	LVs	Calibration Set		Prediction Set			
				R^2_C	RMSEC	R^2_P	RMSEP	RPD	Bias
wt.% C	Full–PLSR	sd2 (g = 5, s = 5)	10	0.8215	0.8982	0.6489	1.2081	1.7	0.0854
	GA–PLSR	**sd2 (SW: 306)**	**9**	**0.8078**	**0.9320**	**0.6954**	**1.1252**	**1.8**	**0.0053**
	SPA–PLSR	sd2 (SW: 634)	10	0.8030	0.9435	0.6520	1.2028	1.7	0.1036
	MP–PLSR: 3 range	Combination set: 4,2,4	9	0.7132	1.1386	0.5514	1.3655	1.5	−0.1433
	MP–PLSR: 5 range	Combination set: 4,1,4,3,1	13	0.8628	0.7875	0.5467	1.3727	1.5	−0.1226
wt.% H	Full–PLSR	sd1 (g = 5, s = 5)	6	0.5086	0.2429	0.4996	0.2361	1.5	−0.0660
	GA–PLSR	**Vector normalization (SW: 67)**	**11**	**0.5456**	**0.2336**	**0.5162**	**0.2322**	**1.5**	**−0.0781**
	SPA–PLSR	sd2 (SW: 22)	15	0.5172	0.2408	0.4478	0.2481	1.4	−0.0586
	MP–PLSR: 3 range	Combination set: 5,5,0	7	0.5179	0.2406	0.4711	0.2428	1.4	−0.0644
	MP–PLSR: 5 range	Combination set: 5,4,4,0,4	8	0.5964	0.2201	0.4877	0.2389	1.4	−0.0625
wt.% O	Full–PLSR	sd2 (g = 5, s = 5)	8	0.6243	1.7376	0.6362	1.4788	1.7	0.0814
	GA–PLSR	Mean Centering (SW: 1025)	11	0.6347	1.7134	0.6064	1.5381	1.6	0.2414
	SPA–PLSR	Min–max normalization (SW:354)	11	0.5800	1.8370	0.5815	1.5860	1.6	0.3466
	MP–PLSR: 3 range	Combination set: 4,5,0	11	0.6572	1.6597	0.6153	1.5207	1.6	0.1064
	MP–PLSR: 5 range	**Combination set: 2,5,2,1,5**	**15**	**0.8097**	**1.2366**	**0.7150**	**1.3088**	**1.9**	**0.0733**
wt.% N	Full–PLSR	MSC	10	0.7232	0.1177	0.5865	0.1035	1.6	−0.0065
	GA–PLSR	SNV (SW: 39)	10	0.5916	0.1429	0.5625	0.1064	1.5	−0.0132
	SPA–PLSR	Min–max normalization (SW:413)	7	0.6396	0.1343	0.5869	0.1034	1.6	−0.0190
	MP–PLSR: 3 range	**Combination set: 4,0,0**	**15**	**0.8656**	**0.0820**	**0.6073**	**0.1008**	**1.6**	**0.0191**
	MP–PLSR: 5 range	Combination set:1,4,4,1,0	7	0.6436	0.1335	0.5700	0.1055	1.5	0.0143

3.1. wt.% of C

Table 3 presents the results of the PLSR-based model within the full wavenumber range of 3594.87–12,489.48 cm^{-1} for the wt.% C of chip biomass, with the best–performing model highlighted in bold.

The model, developed using GA–PLSR with spectrum preprocessing involving the sd2, a gap, and segments of five each, along with nine LVs, provided better results. It achieved R^2_C, RMSEC, R^2_P, RMSEP, RPD, and bias values of 0.8078, 0.9320 wt.%, 0.6954, 1.1252 wt.%, 1.8, and 0.0053 wt.%, respectively. By determining RMSEP, these results represent a 6.8566% improvement in the model performance compared to Full-PLSR. Utilizing Equation (3), the LOQ value was calculated as 9.3724 wt.% for C. Notably, the LOQ value is lower than the minimum wt.% C value used during model development, indicating that the model exhibits high sensitivity and can quantify wt.% C starting from 9.3724 wt.%.

Figure 2a shows a scatter plot comparing the predicted and measured wt.% of C, which was obtained using GA–PLSR. The trend line for the prediction set and calibration set overlap, indicating the same slope. The slope shows the rate of change of Y (measured value) as a function of the rate of change of X (predicted values) [34] or vice versa, hence indicating that predicted values of both sets of data have changed with the same rate and this characteristic is same for the models for O and N shown in Figure 2c,d.

Figure 3 displays the average sd2 absorbance values obtained after preprocessing, highlighting 306 selected wavenumbers (marked in red) identified through GA. These wavenumbers fall within the full spectral range of 3594.87–12,489.48 cm^{-1}. Peaks were observed at 3722, 4091, 5181, and 5285 cm^{-1}, all of which might have the potential to enhance the model performance. The wavenumbers 3722 cm^{-1} and 4091 cm^{-1} are associated with the C–H aromatic functional group, specifically the C–H aryl material type [36]. The peak at 5181 cm^{-1} corresponds to a combination of O–H stretching and HOH bending, indicative of polysaccharides [36]. Similarly, the peak at 5285 cm^{-1} is associated with the functional group of O–H hydrogen bonding between water and exposed polyvinyl alcohol OH groups [36].

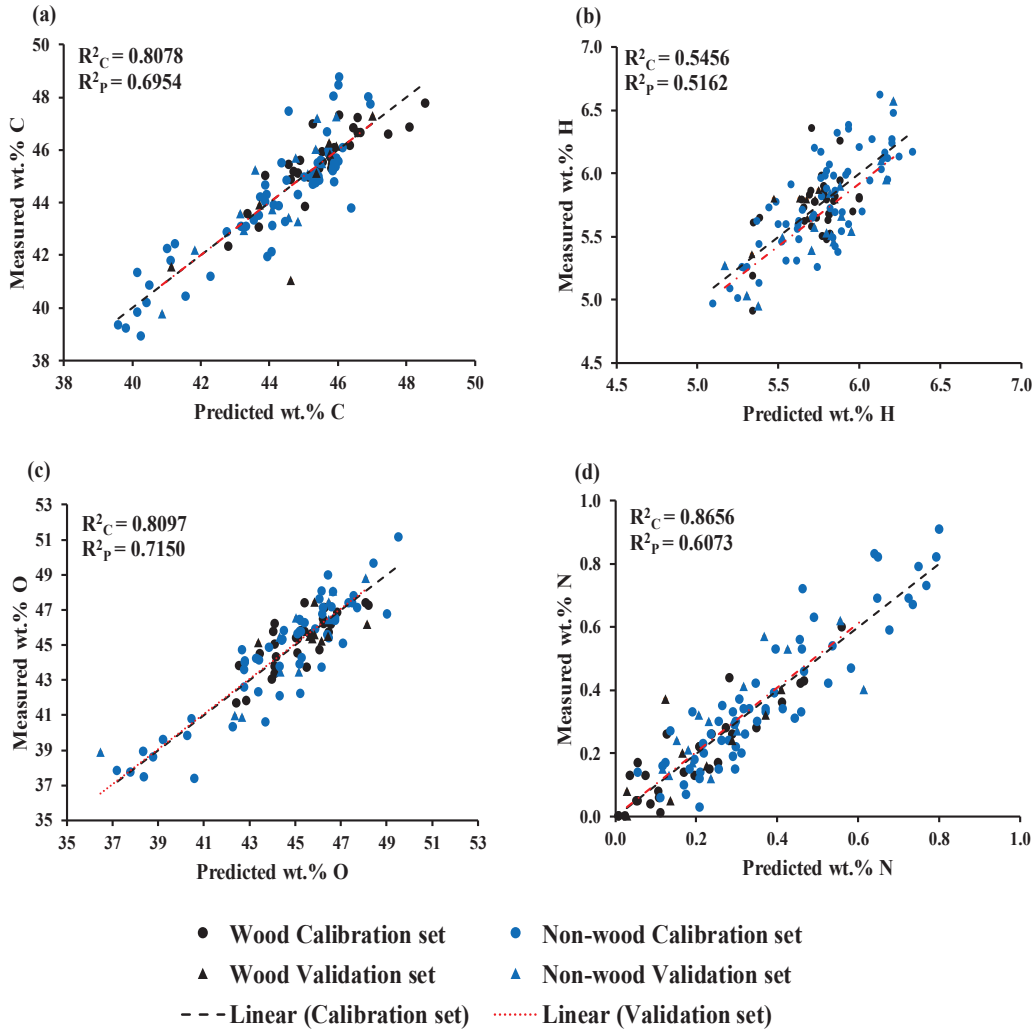

Figure 2. Measured versus predicted value in calibration and prediction sets for (**a**) wt.% of C, (**b**) wt.% of H, (**c**) wt.% of O, and (**d**) wt.% of N.

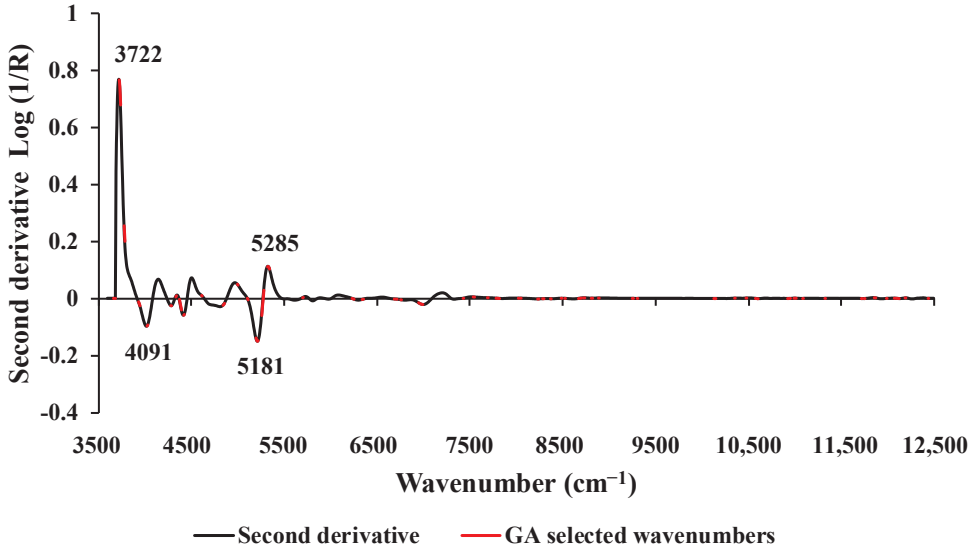

Figure 3. The second derivative absorbance value of studied biomass obtained using the sd2 preprocessing with a selection of important wavenumber obtained from GA for prediction of wt.% of C, within the full wavenumber range of 3594.87–12,489.48 cm^{-1}.

Previous studies by Zhang et al. [24] and Posom and Sirisomboon [23] have demonstrated that vibrational bands related to C–H aromatic, C–H stretching, N–H stretching, N–H deformation, O–H stretching, HOH bending, O–H hydrogen bonding, and similar factors play a crucial role in predicting the wt.% of C in various biomass varieties. These findings align with the vibration bands observed in our study, providing support for our results and suggesting that these selected peaks likely have a significant influence on the model performance.

3.2. wt.% of H

The model developed using GA–PLSR with vector normalization as preprocessing showed the best performance with 11 LVs (Table 3). It selected 67 important wavenumbers using GA. The model performance, in terms of R^2_C, RMSEC, R^2_P, RMSEP, RPD, and bias values, was 0.5456, 0.02336 wt.%, 0.5162, 0.2322 wt.%, 1.5, and −0.0781 wt.%, respectively. Compared with Full-PLSR, the GA improved the PLSR model accuracy by 1.6743%. The LOQ value was calculated as 2.3484 wt.%, which is lower than the minimum reference value used for the model development. This suggests that the selected model is sensitive and can sensitively quantify H from 2.3484 wt.%.

Figure 2b displays a scatter plot comparing the predicted and measured wt.% of H, which was obtained using GA–PLSR. It is clear that the trend line for the prediction set exhibits an offset in relation to the trend line of the calibration set and the 45-degree line. This offset raises concerns about the model constant bias along the range of the data, indicating the overestimating model.

Figure 4 displays the average absorbance values within the range of 3594.87–12,489.48 cm^{-1}. These values were obtained after preprocessing using vector normalization and highlight 67 selected wavenumbers, marked in red, which were identified using GA. Significant peaks were observed at the wavenumbers 4019, 4850, 5155, and 9852 cm^{-1}, respectively, and these may have an influence on the model performance. The peak at 4019 cm^{-1} is associated with the spectra–structure combination of C–H stretching and C–C stretching, with the material type being cellulose [36]. The peak at 4850 cm^{-1} corresponds to the functional group of N–H combination bands found in secondary amides within proteins [36]. The peak at 5155 cm^{-1} is related to the combination of O–H stretching and HOH bending, with the material type being water [36]. Finally, the peak at 9852 cm^{-1} is associated with the second overtone of the fundamental stretching band of N–H asymmetric stretching, and the material type is aromatic amine [36].

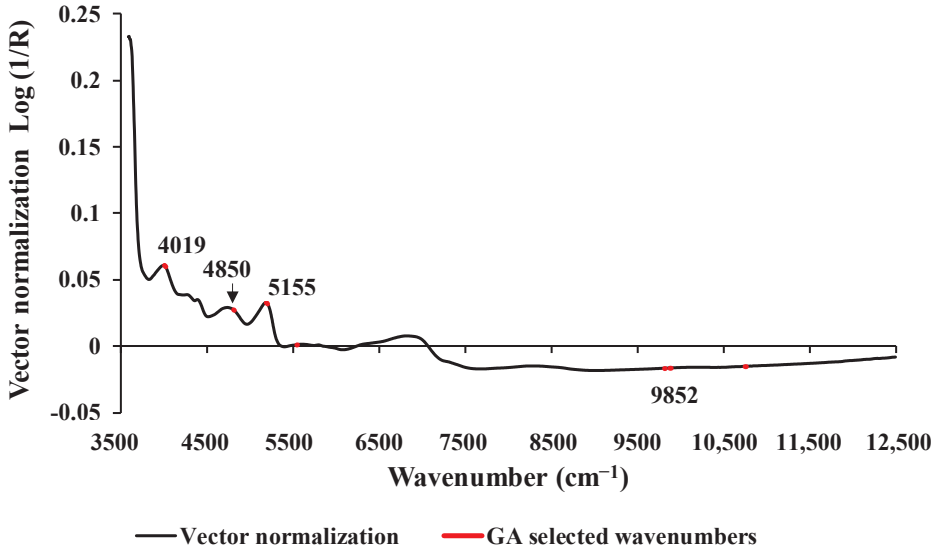

Figure 4. The vector normalization absorbance value of studied biomass obtained using the vector normalization preprocessing with a selection of important wavenumber obtained from GA for prediction of wt.% of H, within the full wavenumber range of 3594.87–12,489.48 cm^{-1}.

In comparison to previous studies conducted by Shrestha et al. [13], Zhang et al. [24], and Posom and Sirisomboon [23] that focused on measuring the wt.% of H in biomass using NIRS, our study discovered similar peaks within the range of 4000–9900 cm^{-1} and vibration bands such as O–H stretching, HOH bending, C–H stretching, and C–C stretching. Therefore, our study findings align with these earlier studies on this specific aspect. However, when evaluating the overall performance of various PLSR-based models, this study suggests that the wt.% of H was not sufficiently explained by the vibration of those mentioned bonds.

3.3. wt.% of O

Assuming that the S content in chip biomass is negligible, as its wt.% is too low to be detected by the instrument, we calculated the wt.% of O in the chip biomass for 120 samples using Equation (1). The wt.% of ash content for each biomass was determined using a TGA. Table 3 presents the optimal results from five different types of PLSR-based models. The most effective model was developed using the MP PLSR 5-range method, incorporating a spectral preprocessing combination set of 2, 5, 2, 1, and 5, which corresponded to the following ranges: 3625.72–5392.30 cm^{-1} with SNV, 5400.02–7166.59 cm^{-1} with the sd2, 7174.31–8940.89 cm^{-1} with SNV, 8948.60–10,715 cm^{-1} with raw spectra, and 10,722.9–12,489.48 cm^{-1} with the sd2. This model employed 15 LVs. Figure 2c illustrates the scatter plot comparing measured versus predicted wt.% of O obtained from the MP PLSR 5-range method. This method yielded R^2_C of 0.8097, RMSEC of 1.2366 wt.%, R^2_P of 0.7150, RMSEP of 1.3088 wt.%, RPD of 1.9, and a bias of 0.0733 wt.%. Compared with Full-PLSR method performance, the MP PLSR 5-range method significantly improved the model accuracy by 11.4913%. The LOQ value for wt.% of O was calculated as 12.4424 wt.%, which is lower than the minimum wt.% of O used during model development. This indicates that the model is highly sensitive and can quantify O content in chip biomass from 12.4424 wt.%.

Figure 5 displays the regression coefficient plot for wt.% of O content in chip biomass obtained from the MP PLSR 5-range method. Several notable peaks were observed at 3650, 4405, 8163, and 8621 cm^{-1}, each potentially exerting a significant influence on the model performance. Specifically, the peak at 3650 cm^{-1} corresponds to the O–H functional group found in the primary alcohols, characterized by the fundamental stretching vibrational absorption band of O–H [36]. The peak at 4405 cm^{-1} represents the combination of O–H stretching and C–O stretching, with cellulose as the material type [36]. The peaks at 8163 cm^{-1} and 8621 cm^{-1} are associated with the second overtone of the fundamental stretching band of C–H and the fourth overtone of the fundamental stretching band of C=O, respectively, which are typically found in hydrocarbons and aliphatic compounds [36].

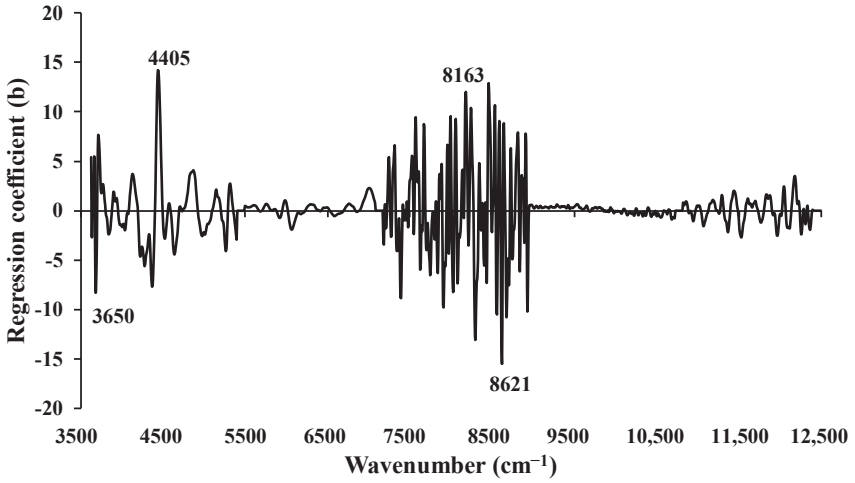

Figure 5. The regression coefficient for the wt.% O of chip biomass using the MP PLSR 5-range method.

When compared with previous studies on wt.% of O in biomass, such as those by Shrestha et al. [13], Zhang et al. [24], and Posom and Sirisomboon [23], this study reveals some contradictory peaks. However, the vibrational bands, such as O–H from primary alcohol, C=O stretching, and C–H stretching, among others, were similar. These findings supports the research result of this study, suggesting that the significant peaks observed in this study have an impact on the development of the model for assessing wt.% of O in chip biomass.

3.4. wt.% of N

The best model for rapid prediction of wt.% of N was obtained using the MP PLSR 3-range method with a spectral preprocessing combination set of 4, 0, and 0 (Table 3). This set corresponds to the sd1 from 3594.87 to 5492.59 cm^{-1} and zero absorbance from 7498.314 to 12,489.48 cm^{-1}. Figure 2d illustrates the scatter plot of measured versus predicted wt.% of N content in the chip biomass, obtained from the MP PLSR 3-range method with 15 LVs. The best–performing model achieved an R^2_C of 0.8656, RMSEC of 0.0820 wt.%, R^2_P of 0.6073, RMSEP of 0.1008 wt.%, RPD of 1.6, and a bias of 0.0191 wt.%. These results indicate that within the range 3594.87–5492.59 cm^{-1} (refer Figure 6), by effectively correcting baseline shifts and assigning zero absorbance value within the remaining wavenumber range, the model performance is enhanced. Compared with Full-PLSR using RMSEP value, the MP PLSR 3-range method improved the model performance by 2.5473%. However, based on R^2_C and R^2_P values, the selected model indicates overfitting. This suggests that our model fits the training data too closely, and too much less accurate in prediction the validation set. This was discussing in Section 5 Comparison of Model Performance between Using Chipped and Ground Biomass Spectra by refer to Cawley and Talbot [37].

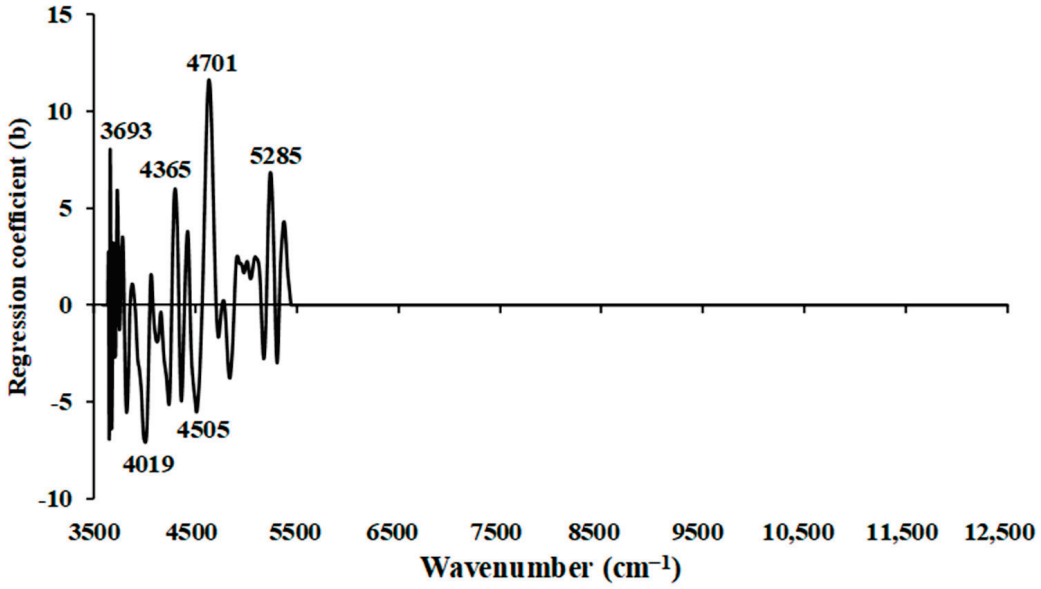

Figure 6. The regression coefficient for the wt.% N of chip biomass using the MP PLSR 3-range method.

Figure 6 illustrates the regression coefficient plot for the wt.% of N in chip biomass, obtained using the multi-preprocessing PLSR 3-range method. Significant peaks that could potentially influence the model performance were observed within the wavenumber range of 3594.87–5492.59 cm^{-1} only. These significant peaks were noticed at wavenumbers 3693, 4019, 4365, 4505, 4701, and 5285 cm^{-1}. Specifically, the peak at 3693 cm^{-1} is associated with the function group of C–H aromatic C–H bands, characterized by the material type C–H aryl. At 4019 cm^{-1}, the peak represents functional groups with a combination of C–H stretching and C–C stretching from cellulose [36]. The peak at 4365 cm^{-1} corresponds to $CONH_2$, specifically due to C=O bonded to the N–H of the peptide link termed the

α–helix structure [36]. The peak at 4505 cm^{-1} is associated with the N–H combination band [36]. Similarly, the peak at 4701 cm^{-1} corresponds to the function group of N–H/C=O combination from polyamide II [36]. Lastly, the peaks at 5285 cm^{-1} are associated with O–H hydrogen bonding between water and exposed polyvinyl alcohol OH [36]. These peaks are crucial in understanding the composition of the chip biomass and are important for model development and analysis. Furthermore, in the range of 7498.314–12,489.48 cm^{-1}, the regression coefficient value equals zero. This indicates an insufficient linear relationship between the dependent (spectral information) and independent (reference value) variables in this range, and it does not significantly contribute to the predictive model for the prediction of wt.% of N.

The previous study conducted by Posom and Sirisomboon [23], which aimed to evaluate the wt.% of N in bamboo, also revealed significant peaks within the range of 4424 to 6920 cm^{-1}. Similarly, Shrestha et al. [13] conducted a study on wt.% of N in ground biomass from the same source and exhibited important peaks within a similar range, specifically within 4019 to 6711 cm^{-1}. This finding aligns with the results of our study, providing additional support for our research. It is noteworthy that in both studies, common vibrational bands, such as N–H stretching, C=O stretching, C–H stretching, C–C stretching, aromatic C–H, and O–H bonds between water and alcohol, among others, were identified. This consistency in vibration bonds reinforces our study findings and suggests that these specific peaks likely play a crucial role in influencing the model performance.

4. Effect of Non-Wood and Wood Samples on Model Performance

Table 4 shows the reference values of wt.% of C, H, N, and O of non-wood and wood samples in calibration and validation sets. From Figure 2 and Table 4, it is obvious that the range of every element content is wider after the two sets were combined for modeling. Therefore, the models can now be regarded as more robust models than only one set was used. From Figure 2a,c, the range of wt.% of C and O of wood samples was narrower than those of the non-wood samples which were extended more to the lower wt%. Figure 2d illustrates the opposite way, where the value range of N of wood samples was lower and narrower than those of the non-wood samples. Therefore, models for wt% of C, O, and N had better performance than that of the H model. The wood sample reference values of H were grouped together and more or less had the same range as the range of non-wood samples. (Figure 2b).

Table 4. The range of wt.% of C, H, N, and O of non-wood and wood samples in calibration and validation sets.

Parameter	Calibration Set		Validation Set	
	Wood	**Non-Wood**	**Wood**	**Non-Wood**
wt.% C	47.77–42.33	48.75–39.93	47.28–41.02	47.24–39.76
wt.% H	6.36–4.91	6.62–4.97	6.57–4.95	5.87–5.36
wt.% N	0.60–0.00	0.91–0.00	0.40–0.00	0.62–0.12
wt.% O	47.40–41.68	51.12–37.36	47.43–45.14	48.80–38.85

The literature shows that the one species model of non-wood, which were bamboo wood chips [23] and sorghum [24] for evaluation of ultimate analysis parameters, C, H, N, O, and S had better performance than our combined non-wood and wood models as the results described in the introduction of this manuscript. Similarly, the two similar species of rice straw and wheat straw model [25] and the pine tree of two species (Loblolly (*Pinus taeda*) and slash (*Pinus elliottii*)) model [26] indicated better prediction performance, though they were homogeneous ground samples which might make their model performance better than the chip ones due to less scattering problem. Shrestha et al. [13] worked with ground samples of the same batch of non-wood and wood samples. Spectra from this experiment showed better R^2_P and RPD for C, N, H, and O, which is claimed to be due to the same merit of homogeneous samples.

Using larger biomass particle sizes, Pitak et al. [27] combined the non-wood and wood biomass pellet NIR spectra obtained by averaging every pixel spectrum of the pellets from a hyperspectral image (HSI). This approach provided better performance in predicting elements from the ultimate analysis than our model, i.e., in-detail data collection by the HSI leads to significant improvements.

Figure 7 shows the scatter plots of the highest performance models in this study in predicting the C, H, O, and N content of the wood and non-wood samples, which is the same as Figure 2, but the difference is Figure 7 shows the simple regression lines of each group of non-wood and wood samples both for calibration set and prediction set. For better vision, Table 5 shows the numeric data of R^2, slope, and intercept calculated from the scatter plots of wood and non-wood calibration and prediction sets. Williams et al. explained that the slope of the trend line plotted between Y (measured value) and X (NIR predicted value) indicated the rate of change of Y as a function of the rate of change of X [34]. The intercept of different species illustrated the same trend as slope interpretation, especially when the slope is more than 1, the intercept was with a minus sign, and if less than 1, the intercept was with a plus sign. While the slope was 1, the intercept was low, close to zero, and when the slope was more or less than 1, the intercept was high, far from zero.

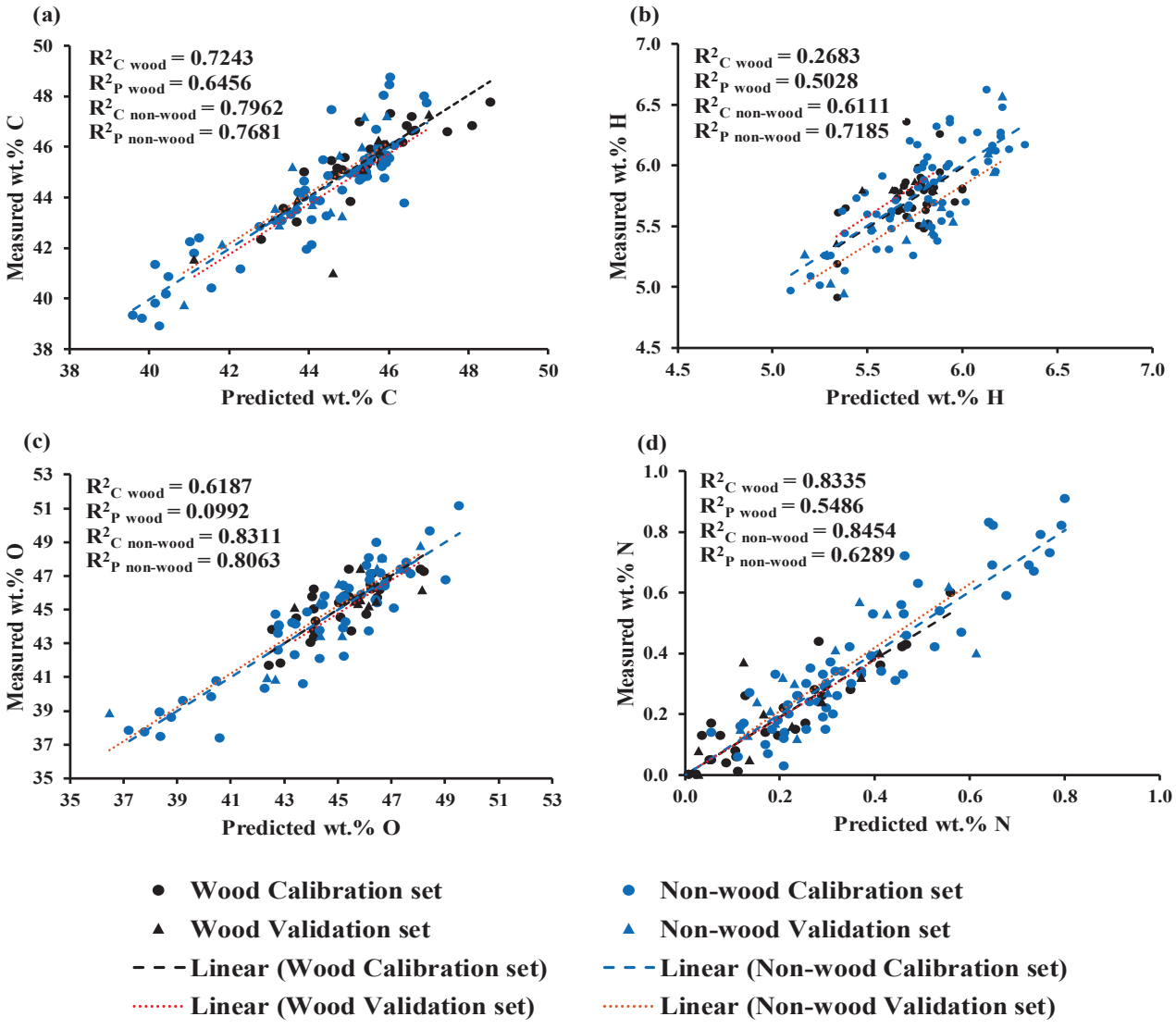

Figure 7. The scatter plots of optimized model for wt.% of (**a**) C, (**b**) H, (**c**) O, and (**d**) N where the simple regression lines of non-wood group and wood group illustrated both in calibration set and validation set.

Table 5. The trend line characteristics of the wood and non-wood species in scatter plots of the best models for C, H, N, and O.

Element	Wood						Non-Wood					
	R^2_C	R^2_P	$Slope_C$	$Slope_P$	$Intercept_C$	$Intercept_P$	R^2_C	R^2_P	$Slope_C$	$Slope_P$	$Intercept_C$	$Intercept_P$
C	0.7243	0.6456	0.8353	1.0139	7.5532	−0.8994	0.7962	0.7681	1.0243	1.2109	−1.0960	−9.1465
H	0.2683	0.5028	0.7876	0.7066	1.2085	1.7444	0.6111	0.7185	1.0342	1.1318	−0.1925	−0.9224
N	0.8335	0.5486	0.8915	0.7670	0.0197	0.0502	0.8454	0.6289	1.0368	0.8541	−0.0139	0.0708
O	0.6187	0.0992	0.8272	0.1840	7.8316	37.2740	0.8311	0.8063	1.0209	0.9519	−0.9462	2.3866

R^2_C: Coefficient of determination in the calibration set, R^2_P: Coefficient of determination in the validation set, $Slope_C$: Slope of trendline in the calibration set, $Slope_P$: Slope of trendline in the validation set, $Intercept_C$: Intercept in the calibration set, $Intercept_P$: Intercept in the validation set.

The perfect relationship between the reference values and the predicted values is when the correlation coefficient (R) and slope are equal to 1 and the intercept is equal to zero [34].

From Table 5, for the C model, the non-wood samples contributed slightly more merit on calibration model performance than wood samples for more R the slope was closer to 1, and the intercept was closer to zero. But the prediction set of non-wood provided a steeper slope and intercepted far more from zero.

By the same way of interpretation, the model for H obtained more merit from non-wood samples, while for the wood samples, the R of the trend line was very low, the slope was far from 1, and the intercept was slightly far from zero. The incongruous trend lines of both sets makes the overall performance of the model worse as shown in Table 3.

For the N model, the wood and non-wood calibration set samples more or less had the same trend line characteristics, which supplement the good calibration model performance, though the prediction sample set of both biomass species trend line characteristics shows less R and slope far from 1 led to overfit calibration models of both biomass groups (Table 5).

For the O model, the non-wood group had better trend line characteristics and contributed good merit to the model, while the poorer trend line characteristics of the wood group made the overall model inferior but by a small portion because the number of samples in the non-wood group was much more (Table 5). By the strong merit of the non-wood group, the overall model performance for O prediction was fairly acceptable (Table 3).

Tables 6–9 show the trend line characteristics, including R^2, slope, and intercept of each specific plant of wood and non-wood samples used in the optimized models for evaluation of C, N, H, and O, respectively. It was observed that most of the R^2_P of every plant was equaled to 1 for the samples of those plants in the optimized model, with only two samples connected to a straight line. Therefore, we ignored interpreting of the trend line characteristics of the prediction set, and only the R^2_C, slope, and intercept of the calibration set will be interpreted. As indicated by Williams et al. [34], when the R approached 1 and the slope approached 1 and the intercept approached zero, the model approached excellence. Therefore, to include different species in a model, the species have to be not only in the different values of the constituents to make a wider range for a robust model, but also they must provide the characteristic of the same rate of change of NIR predicted values with the measured values (same slope and slope should approach 1, and intercept is same (no gap) and approached zero). As expected, the trend of R^2, slope, and intercept of different species were not the same for their different characteristics. However, in some species whose characteristics were similar, the trends were common supported the each other but might positively or negatively to the prediction performace of the model.

Table 6. The trend line characteristics of specific biomass species for Carbon evaluation optimized model.

Carbon (wt.%)							
Particular	**Biomass Species**	$\mathbf{R^2_C}$	$\mathbf{R^2_P}$	$\mathbf{Slope_C}$	$\mathbf{Slope_P}$	$\mathbf{Intercept_C}$	$\mathbf{Intercept_P}$
Wood	Euca	0.6779	1.0000	0.9808	5.4617	0.8006	−202.6600
	Pine	0.2502	1.0000	0.2264	1.0848	36.2520	−3.7219
	Alnu	0.7491	1.0000	0.7254	−16.8990	12.7000	819.4200
	Bombax	0.8110	1.0000	1.1270	0.9097	−5.3606	4.1430
Non-Wood	*Zea mays*-Cob	0.2480	0.9542	0.6228	1.8112	16.7390	−35.8510
	Zea mays-Stover	0.6332	1.0000	1.7168	0.2151	−32.1370	33.6140
	Zea mays-Shell	0.3300	0.4618	0.8945	0.2524	5.0232	34.2500
	Ricehusk	0.3770	1.0000	0.9257	2.5087	2.9918	−62.7580
	Bagass	1.0000	1.0000	2.6090	−0.1076	−70.2900	48.2050
	Bamboo	0.9313	1.0000	1.3789	7.6002	−17.0530	−297.8600

Table 7. The trend line characteristics of specific biomass species for Nitrogen evaluation optimized model.

Nitrogen (wt.%)							
Particular	**Biomass Species**	$\mathbf{R^2_C}$	$\mathbf{R^2_P}$	$\mathbf{Slope_C}$	$\mathbf{Slope_P}$	$\mathbf{Intercept_C}$	$\mathbf{Intercept_P}$
Wood	Euca	0.5701	1.0000	0.7531	0.4663	0.0233	−0.0135
	Pine	0.2317	1.0000	0.2828	0.8790	0.0283	0.0543
	Alnu	0.5878	0.9633	0.5742	1.2687	0.1426	−0.1337
	Bombax	0.9410	1.0000	1.1614	−2.0520	−0.0748	0.6245
Non-Wood	*Zea mays*-Cob	0.6807	0.5554	0.8615	1.1809	0.0443	−0.0372
	Zea mays-Stover	0.6200	1.0000	0.9025	0.2654	0.0472	0.4721
	Zea mays-Shell	0.8641	0.6536	1.1203	1.0135	−0.0629	0.0569
	Ricehusk	0.8848	1.0000	1.1485	0.2615	−0.0518	0.2394
	Bagass	0.4801	1.0000	0.2992	−1.7907	0.0333	0.5128
	Bamboo	0.8200	1.0000	1.4186	1.6937	−0.1260	−0.0966

Table 8. The trend line characteristics of specific biomass species for Hydrogen evaluation optimized model.

Hydrogen (wt.%)							
Particular	**Biomass Species**	$\mathbf{R^2_C}$	$\mathbf{R^2_P}$	$\mathbf{Slope_C}$	$\mathbf{Slope_P}$	$\mathbf{Intercept_C}$	$\mathbf{Intercept_P}$
Wood	Euca	0.7289	1.0000	1.5193	0.8197	2.9877	0.9851
	Pine	0.0462	N/A	0.4235	-	3.3450	5.7900
	Alnu	0.0701	1.0000	−0.9476	−0.0456	11.1870	6.0566
	Bombax	0.1629	1.0000	0.5887	0.2547	2.5182	4.4059
Non-Wood	*Zea mays*-Cob	0.2752	1.0000	1.4447	−0.7296	−2.6372	9.7617
	Zea mays-Stover	0.1173	0.7335	1.2590	1.2413	−1.5538	−1.7143
	Zea mays-Shell	0.0404	0.6033	0.3791	6.5956	3.8515	−34.5000
	Ricehusk	0.7273	0.9896	1.5136	−1.5656	−2.7759	13.3580
	Bagass	0.0067	1.0000	−0.1394	−4.9031	6.4990	34.7330
	Bamboo	0.4456	0.7685	0.9438	1.0741	0.4841	−0.4794

Table 9. The trend line characteristics of specific biomass species for Oxygen evaluation optimized model.

Oxygen (wt.%)							
Particular	**Biomass Species**	**R^2_C**	**R^2_P**	**$Slope_C$**	**$Slope_P$**	**$Intercept_C$**	**$Intercept_P$**
Wood	Euca	0.3842	1.0000	0.5993	0.3416	18.5080	29.7010
	Pine	0.2854	1.0000	0.3913	−0.0362	27.5290	47.1430
	Alnu	0.4993	1.0000	0.5014	0.9362	23.0630	4.5052
	Bombax	0.7459	1.0000	1.3490	−1.1972	−15.4990	100.4800
Non-Wood	*Zea mays*-Cob	0.6501	1.0000	1.3700	8.9169	−17.1250	−368.0300
	Zea mays-Stover	0.8611	1.0000	1.5098	−0.3972	−22.8340	64.3960
	Zea mays-Shell	0.3063	0.7989	0.8399	2.0886	6.9934	−48.2230
	Ricehusk	0.9499	1.0000	1.0623	0.3529	−2.3570	25.9720
	Bagass	1.0000	NA	0.0784	NA	42.8950	NA
	Bamboo	0.9301	1.0000	1.1793	3.0761	−8.5173	−95.5720

From Tables 6–9, as expected, the intercept of different species illustrated the same trend as slope interpretation, especially when, by the fact, the slope is more than 1 the intercept was with minus sign, and if less than 1 the intercept was with plus sign. While the slope was 1, the intercept was low, closer to zero, and when the slope was more or less than 1, the intercept was high, far from zero.

Therefore, the following were the effects of specific species on the performance of the optimized models interpreted by scatter plot analysis using the R^2 and slope of the trend line of the specific plant in the model developed.

For C (Table 6), by R^2_C interpretation, most non-wood species (agricultural waste) except bagasse and bamboo show unacceptable trend lines compared to wood species samples except pines. Therefore, including the mentioned non-wood species caused a poor effect on the C model. By interpretation of slope, there were three groups of slope (by value round up), i.e., 1 including Eucalyptus, Alnus and Bombax in wood species and corn cob, corn shell, rice husk, and bamboo in non-wood species, less than 1 including pine in wood specie, and more than 1 including corn stover and bagasse indicating unequal slope of different species in the same optimized model show the effect of specific species on model performance. These can be summarized that for the model to be better, pine and corn stover should not be included in modeling for C prediction.

By the same way of interpretation, from Table 7, the optimized model for N, pine, and bagasse should not be included; from Table 8, for H, pine, Alnus, corn shell, and bagasse should not be included; and from Table 9, for O, pine should not be included for better performance of the models. These were due to the poor R and slope of the eliminated species, which were not in accordance with the other species.

These results show that the different species affected the model performance of each parameter prediction in a different manner, and by scatter plot analysis, which of these species were affecting the model negatively and how to improve the model performance were indicated.

5. Comparison of Model Performance between Using Chipped and Ground Biomass Spectra

In this section, the model performance of chipped biomass for ultimate analysis parameters to the model of ground biomass [13] derived from the same sample varieties is compared. The comparison is based on the metrics R^2_C, RMSEC, R^2_P, RMSEP, and RPD. The results demonstrate that chipped biomass generally performs less effectively in these models compared to ground biomass, except for wt.% of O.

For wt.% of C and wt.% of H, both chipped and ground biomass models demonstrated better performance when employing the GA–PLSR model. This outcome aligns with expectations, as GA optimizes feature selection to maximize fitness, while PLSR maximizes covariance between absorbance values and areas of interest.

For wt.% of C, the GA–PLSR model applied to ground biomass yielded an R^2_C of 0.7851, RMSEC of 0.9753 wt.%, R^2_P of 0.7217, RMSEP of 0.9740 wt.%, and RPD of 1.93 [13]. In contrast, the model applied to chipped biomass performed less effectively (Table 2). Therefore, it is recommended to adopt the GA–PLSR model with sd2 preprocessing on ground biomass when evaluating wt.% of C.

Similarly, the GA–PLSR model applied to ground biomass outperforms that of chipped biomass for wt.% of H. Ground biomass yielded an R^2_C of 0.8814, RMSEC of 0.1041 wt.%, R^2_P of 0.7678, RMSEP of 0.1434 wt.%, and RPD of 2.14 [13], whereas chipped biomass lagged behind (Table 2). Hence, for wt.% of H, the GA–PLSR model with spectral preprocessing from SNV on ground biomass is recommended.

Regarding wt.% of N, the MP PLSR 5-range method exhibited superior model performance on ground biomass, as evidenced by R^2_C, RMSEC, R^2_P, RMSEP, and RPD values of 0.8682, 0.0675 wt.%, 0.8410, 0.0973 wt.%, and 2.65, respectively [13], when compared to chipped biomass performance obtained from the MP PLSR 3-range method (Table 2). This underscores the suitability of ground biomass for evaluating wt.% of N.

Surprisingly, in contrast, for wt.% of O, the model derived from chipped biomass excelled, despite both models utilizing the MP PLSR 5-range method. In the ground biomass, R^2_C, RMSEC, R^2_P, RMSEP, and RPD values were 0.6674, 1.4461wt.%, 0.6289, 1.5275 wt.%, and 1.71, respectively [13], which fell short of chipped biomass results. Hence, it is recommended to adopt the MP PLSR-5 range method with the preprocessing combination set of 2, 5, 2, 1, and 5 for assessing wt.% of O in chipped biomass. This could be due to ash determination, where ash directly influences %O determination based on Equation (1). Also, ash is typically accumulating in small particles, i.e., the time of grinding in conjunction with subsampling can have an influence on ash determination.

All the above comparisons and findings underscore the importance of selecting the appropriate PLSR-based model for precise analysis of ultimate analysis parameters, depending on the specific parameter of interest. There could be several factors that contribute to the lower performance of the chipped biomass model, which can be addressed to improve the model performance. The key contributing factor to this performance difference is obviously the particle size of the biomass samples. Chipped biomass typically consists of larger and different sizes of particles, leading to increased scattering of NIR light during sample scanning. Consequently, the spectra generated from chipped biomass can be of lower quality, resulting in weaker correlations between spectral data and reference data [38]. Additionally, ground biomass exhibits a more compact and uniform sample structure, reducing the likelihood of NIR light leakage during scanning. Another significant factor affecting the lower model performance is the moisture content in biomass samples. Chipped biomass often contains higher moisture levels, and water has the property of absorbing NIR light in the near-infrared region [39]. This NIR absorption interferes with the measurements and can introduce inaccuracies, particularly for elements like C, H, O, and N.

In the chipped biomass models, it is evident that the performance of the prediction set consistently lags behind that of the calibration set. This suggests that the model closely overfits the calibration data, capturing both valuable information and noise or random variations [40]. In the machine learning context, Cawley and Talbot [37] emphasized that overfitting in model selection is likely to be most severe when the sample size is small and the number of hyperparameters to be tuned is relatively large [41]. In our case, the number of latent variables of the best models was high.

Consequently, when new samples are introduced into the prediction set, the model may struggle to generalize and provide accurate predictions. Furthermore, the presence of outliers in the prediction set, which were not accounted for in the calibration set, can further negatively impact the model performance [42].

The performance of ground biomass is better compared to chipped biomass due to several factors. Ground biomass allows for better sample homogenization, ensuring uniformity and consistent composition. Additionally, it offers more control over sample

thickness, as chips may vary in thickness, affecting accuracy. Moreover, ground samples reduce light-scattering effects and enable improved penetration of the NIRS signal, allowing for precise and accurate logging of spectral information.

6. Conclusions

In this study, PLSR-based models were developed and compared using FT–NIRS to analyze the ultimate analysis parameters of combined non-wood and wood chip biomass, specifically focusing on wt.% of C, H, O, and N content. All chipped biomass samples were scanned within 3594.87–12,489.48 cm^{-1} on the diffuse reflectance with sphere macro sample rotating mode, with a particular emphasis on their suitability for energy application. The model with the optimum performance was selected based on trade-off parameters of R^2_C, RMSEC, R^2_P, RMSEP, RPD, and bias.

The optimum model performance analysis reveals that the model selected for predicting the wt.% of C, H, N, and O in chipped biomass is suitable primarily for initial rough screening. It is recommended to adopt the multi–preprocessing PLSR 5-range method chipped biomass model for wt.% of O content analysis as an alternative method for rapid assessment. However, for the evaluation of wt.% of C, H, and N content, the chipped biomass model performance falls short of the model developed for ground biomass by Shrestha et al. [13]. Thus, it is advisable to use the chipped biomass model solely for initial screening before biomass trading. For a more comprehensive and accurate analysis, it is recommended to grind the chip biomass samples within the range of 0.01 to 3080 μm and employ the GA–PLSR model with sd1 for wt.% of C, GA–PLSR with SNV for wt.% of H, and the MP PLSR 5-range method with combination set of 4, 4, 5, 3, and 4 for wt.% of N, as developed by Shrestha et al. [13]. The LOQ values for C, H, and O were below the model minimum reference value, demonstrating high model sensitivity. However, the LOQ value for N exceeds the minimum reference value, indicating the model detection limit to the minimum value in the calibration sample set range.

By analysis of scatter plots of measured constituent and NIR predicted constituent, the effect of including different biomass species (non-wood and wood species) in the modeling samples was studied. It was concluded that to include different species in a model, the species had to be not only in the different values of the constituents to be predicted to make a wider range for a robust model, but also the different sample species must provide the same rate of change of NIR predicted values with the measured values in the scatter plot (same slope and slope approached to 1, and intercept is same (no gap) and approached zero) for the high-performance model if R is approached to one. The results show that the different species affected the model performance of each parameter prediction in a different manner, and by scatter plot analysis, which of the species affecting the model negatively were identified and dictated how to improve the model performance.

To ensure the model robustness and reliability, it is crucial to expand it by incorporating a wider array of representative non-wood and wood species biomass samples, but the different species must provide the same rate of change of NIR predicted values with the measured values in the scatter plot. Validation and updation using additional unknown samples of the same species are essential for the model effective applicability. Furthermore, exploring alternative machine learning algorithms alongside the recommended model could enhance its practicability. These steps will contribute to not just a more comprehensive and versatile model but also increase its ability for real-world application and improve its overall reliability.

Author Contributions: B.S.; conceptualization, methodology, software, formal analysis, investigation, resources, data curation, visualization, writing the original draft, writing–review and editing. J.P.; conceptualization, methodology, software, formal analysis, data curation, writing–review and editing, supervision. P.S.; conceptualization, methodology, data curation, writing the original draft, writing–review and editing, validation, supervision, project administration, funding acquisition. B.P.S.; conceptualization, methodology, writing–review and editing, and supervision. A.F.; writing the original draft, writing–review and editing, supervision. All authors have read and agreed to the published version of the manuscript.

Funding: This research received funding from KMITL doctoral scholarship (KDS 2020/052) and the APC was funded partly by School of Engineering, KMITL, BANGKOK, Thailand.

Data Availability Statement: Data are contained within the article.

Acknowledgments: The authors would like to express their sincere gratitude to the Near-Infrared Spectroscopy Research Center for Agricultural Product and Food, Department of Agricultural Engineering, School of Engineering at King Mongkut's Institute of Technology Ladkrabang, Bangkok, Thailand, for their generous research funding support provided through the KMITL doctoral scholarship (KDS 2020/052).

Conflicts of Interest: The authors declare no conflicts of interest.

Abbreviations

%	percentage	R	Correlation coefficient
C	carbon	R^2	coefficient of determination
CHNS	CHNS Elemental analyzer	R^2_C	coefficient of determination of calibration set
GA	genetic algorithm	R^2_P	coefficient of determination of validation set
H	hydrogen	RMSEC	root mean square error of calibration set
LVs	latent variable number	RMSEP	root mean square error of prediction set
LOQ	Limit of quantification	RPD	ratio of prediction to deviation
Max	maximum	S	sulfur
Min	minimum	SD	standard deviation
MP	multi-preprocessing	sd1	first derivative
MSC	multiplicative scatter correction	sd2	second derivative
N	nitrogen	SEC	standard error of calibration set
NT	total number of samples	SEP	standard error of validation set
Nc	number of samples in calibration set	SNV	standard normal variate
NIRS	near infrared spectroscopy	SPA	successive projection algorithm
Np	number of samples in validation set	SW	selected wavenumber
O	oxygen	TGA	thermogravimetric analysis
PLSR	partial least squares regression	wt.%	weight percentage

References

1. IRENA. *Bioenergy for the Energy Transition: Ensuring Sustainability and Overcoming Barriers*; International Renewable Energy Agency: Abu Dhabi, United Arab Emirates, 2022.
2. Ness, J.E.; Ravi, V.; Heath, G. *An Overview of Policies Influencing Air Pollution from the Electricity Sector in South Asia*; National Renewable Energy Laboratory: Golden, CO, USA, 2021.
3. Buonocore, J.J.; Salimifard, P.; Michanowicz, D.R.; Allen, J.G. A decade of the US energy mix transitioning away from coal: Historical reconstruction of the reductions in the public health burden of energy. *Environ. Res. Lett.* **2021**, *16*, 054030. [CrossRef]
4. Fullerton, D.G.; Bruce, N.; Gordon, S.B. Indoor air pollution from biomass fuel smoke is a major health concern in the developing world. *R. Soc. Trop. Med. Hyg.* **2008**, *102*, 843–851. [CrossRef] [PubMed]
5. Liu, T.; Chen, R.; Zheng, R.; Li, L.; Wang, S. Household air pollution from solid cooking fuel combustion and female breast cancer. *Front. Public Health* **2021**, *9*, 677851. [CrossRef] [PubMed]
6. Jin, R.; Zheng, M.; Yang, L.; Zhang, Q.; Fu, J.; Yang, R.; Liu, Q.; Shi, J.; Liu, G.; Jiang, G. Indoor exposure to products of incomplete combustion of household fuels in rural Tibetan Plateau. *Environ. Sci. Technol.* **2021**, *56*, 4711–4714. [CrossRef] [PubMed]

7. Adamovics, A.; Platace, R.; Gulbe, I.; Ivanovs, S. The content of carbon and hydrogen in grass biomass and its influence on heating value. *Eng. Rural. Dev.* **2018**, *17*, 1277–1281.
8. Jia, Y.; Li, Z.; Wang, Y.; Wang, X.; Lou, C.; Xiao, B.; Lim, M. Visualization of combustion phases of biomass particles: Effects of fuel properties. *ACS Omega.* **2021**, *6*, 27702–27710. [CrossRef] [PubMed]
9. Kalinci, Y.; Hepbasli, A.; Dincer, I. Biomass-based hydrogen production: A review and analysis. *Int. J. Hydrog. Energy* **2009**, *34*, 8799–8817. [CrossRef]
10. Silva, D.A.d.; Eloy, E.; Caron, B.O.; Trugilho, P.F. Elemental chemical composition of forest biomass at different ages for energy purposes. *Floresta Ambient.* **2019**, *26*. [CrossRef]
11. Ren, X.; Sun, R.; Meng, X.; Vorobiev, N.; Schiemann, M.; Levendis, Y.A. Carbon, sulfur and nitrogen oxide emissions from combustion of pulverized raw and torrefied biomass. *Fuel* **2017**, *188*, 310–323. [CrossRef]
12. Vainio, E. Fate of Fuel-Bound Nitrogen and Sulfur in Biomass-Fired Industrial Boilers. Ph.D. Thesis, Åbo Akademi University, Turku, Finland, 2014.
13. Shrestha, B.; Posom, J.; Sirisomboon, P.; Shrestha, B.P. Comprehensive Assessment of Biomass Properties for Energy Usage Using Near-Infrared Spectroscopy and Spectral Multi-Preprocessing Techniques. *Energies* **2023**, *16*, 5351. [CrossRef]
14. Sirisomboon, P.; Funke, A.; Posom, J. Improvement of proximate data and calorific value assessment of bamboo through near infrared wood chips acquisition. *Renew. Energy* **2020**, *147*, 1921–1931. [CrossRef]
15. Uddin, M.N.; Ferdous, T.; Islam, Z.; Jahan, M.S.; Quaiyyum, M.A. Development of chemometric model for characterization of non-wood by FT-NIR data. *J. Bioresour. Bioprod.* **2020**, *5*, 196–203. [CrossRef]
16. Kumar, P.; Barrett, D.M.; Delwiche, M.J.; Stroeve, P. Methods for Pretreatment of Lignocellulosic Biomass for Efficient Hydrolysis and Biofuel Production. *Ind. Eng. Chem. Res.* **2009**, *48*, 3713–3729. [CrossRef]
17. Worku, L.A.; Bachheti, A.; Bachheti, R.K.; Rodrigues Reis, C.E.; Chandel, A.K. Agricultural residues as raw materials for pulp and paper production: Overview and applications on membrane fabrication. *Membr. J.* **2023**, *13*, 228. [CrossRef]
18. Hawanis, H.S.N.; Ilyas, R.A.; Jalil, D.R.; Ibrahim, D.R.; Abdul Majid, D.R.; Ab Hamid, D.N.H. Insights into Lignocellulosic Fiber Feedstock and Its Impact on Pulp and Paper Manufacturing: A Comprehensive Review. 2023. Available online: https://ssrn.com/abstract=4583258 (accessed on 11 November 2023).
19. Aripin, A.M. Potential of Non-Wood Fibres for Pulp and Paper-Based Industries. Ph.D. Thesis, Universiti Tun Hussein Onn Malaysia, Batu Pahat, Malaysia, 2014.
20. Rousu, P.; Rousu, P.; Anttila, J. Sustainable pulp production from agricultural waste. *Resour. Conserv. Recycl.* **2002**, *35*, 85–103. [CrossRef]
21. Kissinger, M.; Fix, J.; Rees, W.E. Wood and non-wood pulp production: Comparative ecological footprinting on the Canadian prairies. *Ecol. Econ.* **2007**, *62*, 552–558. [CrossRef]
22. Channiwala, S.; Parikh, P. A unified correlation for estimating HHV of solid, liquid and gaseous fuels. *Fuel* **2002**, *81*, 1051–1063. [CrossRef]
23. Posom, J.; Sirisomboon, P. Evaluation of lower heating value and elemental composition of bamboo using near infrared spectroscopy. *Energy* **2017**, *121*, 147–158. [CrossRef]
24. Zhang, K.; Zhou, L.; Brady, M.; Xu, F.; Yu, J.; Wang, D. Fast analysis of high heating value and elemental compositions of sorghum biomass using near-infrared spectroscopy. *Energy* **2017**, *118*, 1353–1360. [CrossRef]
25. Huang, C.; Han, L.; Yang, Z.; Liu, X. Ultimate analysis and heating value prediction of straw by near infrared spectroscopy. *J. Waste Manag.* **2009**, *29*, 1793–1797. [CrossRef]
26. Saha, U.K.; Sonon, L.; Kane, M. Prediction of calorific values, moisture, ash, carbon, nitrogen, and sulfur content of pine tree biomass using near infrared spectroscopy. *J. Near Infrared Spectrosc.* **2017**, *25*, 242–255. [CrossRef]
27. Pitak, L.; Sirisomboon, P.; Saengprachatanarug, K.; Wongpichet, S.; Posom, J. Rapid elemental composition measurement of commercial pellets using line-scan hyperspectral imaging analysis. *Energy* **2021**, *220*, 119698. [CrossRef]
28. Shrestha, B.; Shrestha, Z.; Posom, J.; Sirisomboon, P.; Shrestha, B.P. Evaluating limit of detection and quantification for higher heating value and ultimate analysis of fast-growing trees and agricultural residues biomass using NIRS. *Eng. Appl. Sci. Res.* **2023**, *50*, 612–618.
29. Maraphum, K.; Ounkaew, A.; Kasemsiri, P.; Hiziroglu, S.; Posom, J. Wavelengths Selection Based on Genetic Algorithm (GA) and Successive Projections Algorithms (SPA) Combine With PLS Regression for Determination the Soluble Solids Content in Nam-DokMai Mangoes Based on Near Infrared Spectroscopy. *Eng. Appl. Sci. Res.* **2021**, *49*, 119–126.
30. Chen, Y.M.; Lin, P.; He, Y.; He, J.Q.; Zhang, J.; Li, X.L. Fast quantifying collision strength index of ethylene-vinyl acetate copolymer coverings on the fields based on near infrared hyperspectral imaging techniques. *Sci. Rep.* **2016**, *6*, 20843. [CrossRef] [PubMed]
31. Li, C.; He, M.; Cai, Z.; Qi, H.; Zhang, J.; Zhang, C. Hyperspectral Imaging with Machine Learning Approaches for Assessing Soluble Solids Content of Tribute Citru. *Foods* **2023**, *12*, 247. [CrossRef]
32. Araújo, M.C.U.; Saldanha, T.C.B.; Galvão, R.K.H.; Yoneyama, T.; Chame, H.C.; Visani, V. The successive projections algorithm for variable selection in spectroscopic multicomponent analysis. *Chemometr. Intell. Lab. Syst.* **2001**, *57*, 65–73. [CrossRef]
33. Armbruster, D.A.; Pry, T. Limit of blank, limit of detection and limit of quantitation. *Clin. Biochem. Rev.* **2008**, *29*, S49.
34. Williams, P.; Manley, M.; Antoniszyn, J. *Near Infrared Technology: Getting the Best out of Light*; African Sun Media: Stellenbosch, South Africa, 2019.

35. Zornoza, R.; Guerrero, C.; Mataix-Solera, J.; Scow, K.M.; Arcenegui, V.; Mataix-Beneyto, J. Near infrared spectroscopy for determination of various physical, chemical and biochemical properties in Mediterranean soils. *Soil Biol. Biochem.* **2008**, *40*, 1923–1930. [CrossRef]
36. Workman, J., Jr.; Weyer, L. *Practical Guide to Interpretive Near-Infrared Spectroscopy*; CRC Press: Boca Raton, FL, USA, 2007.
37. Cawley, G.C.; Talbot, N.L.C. On over-fitting in model selection and subsequent selection bias in performance evaluation. *J. Mach. Learn. Res.* **2010**, *11*, 2079–2107.
38. Hans, G.; Allison, B. On-line characterization of wood chip brightness and chemical composition by means of visible and near-infrared spectroscopy. *Holzforschung* **2021**, *75*, 989–1000. [CrossRef]
39. Liang, L.; Fang, G.; Deng, Y.; Xiong, Z.; Wu, T. Determination of moisture content and basic density of poplar wood chips under various moisture conditions by near-infrared spectroscopy. *For. Sci.* **2019**, *65*, 548–555. [CrossRef]
40. Gillespie, G.D.; Everard, C.D.; McDonnell, K.P. Prediction of biomass pellet quality indices using near infrared spectroscopy. *Energy* **2015**, *80*, 582–588. [CrossRef]
41. Ludwig, B.; Murugan, R.; Parama, V.R.; Vohland, M. Accuracy of estimating soil properties with mid-infrared spectroscopy: Implications of different chemometric approaches and software packages related to calibration sample size. *Soil Sci. Soc. Am. J.* **2019**, *83*, 1542–1552. [CrossRef]
42. Toscano, G.; Leoni, E.; Gasperini, T.; Picchi, G. Performance of a portable NIR spectrometer for the determination of moisture content of industrial wood chips fuel. *Fuel* **2022**, *320*, 123948. [CrossRef]

applied sciences

MDPI

Article

Adhesion Testing Device for 3D Printed Objects on Diverse Printing Bed Materials: Design and Evaluation

Jakub Kaščak [1,*], Marek Kočiško [1,*], Adrián Vodilka [1], Jozef Török [1] and Tomáš Coranič [2]

[1] Department of Computer Aided Manufacturing Technologies, Faculty of Manufacturing Technologies with a Seat in Presov, Technical University of Kosice, Bayerova 1, 08001 Presov, Slovakia; adrian.vodilka@tuke.sk (A.V.); jozef.torok@tuke.sk (J.T.)

[2] Department of Design and Monitoring of Technical Systems, Faculty of Manufacturing Technologies with a Seat in Presov, Technical University of Kosice, Bayerova 1, 08001 Presov, Slovakia; tomas.coranic@tuke.sk

* Correspondence: jakub.kascak@tuke.sk (J.K.); marek.kocisko@tuke.sk (M.K.)

Abstract: The persistent challenge of adhesion in Fused Filament Fabrication (FFF) technology is deeply rooted in the mechanical and chemical properties of utilized materials, necessitating the exploration of potential resolutions. This involves adjustments targeting the interplay of printing parameters, the mechanical fortification of print beds, and the integration of more adhesive materials, resonating across user levels, from enthusiasts to complex industrial configurations. An in-depth investigation is outlined in this paper, detailing the plan for a systematically designed device. Engineered for FFF device installation, the device facilitates the detachment of printed models, while precisely recording the detachment process, capturing the maximum force, and its progression over time. The primary objective is fabricating a comprehensive measurement apparatus, created for adhesion assessment. The device is adaptable across diverse FFF machines and print bed typologies, conforming to pre-defined conditions, with key features including compactness, facile manipulability, and capacity for recurrent measurements. This pursuit involves evaluating adhesion levels in prints made from diverse materials on varying print bed compositions, aiming to establish a comprehensive database. This repository facilitates judicious material and bed type selection, emphasizing maximal compatibility. Emphasis is placed on operating within a thermally stable context, a pivotal prerequisite for consistent and reproducible results.

Keywords: print quality; device design; adhesion testing; 3D printing; FFF

1. Introduction

According to current statistics, FFF technology is continuously expanding. New design solutions for devices are emerging, making them faster, more precise, and capable of producing models of various sizes. Considering all these innovations, there is an evident demand for new, alternative, or composite types of materials for these devices. However, there is a considerable research gap in this area. Several companies, or filament producers for FFF devices, follow established procedures for filament creation but offer limited information on its use in collaboration with FFF devices. Users often encounter basic information regarding process parameters, filament diameter deviation, and type designation correlated with the material predominantly represented in the filament. However, this information often proves insufficient for experienced users or industrial production. A relatively common occurrence is model wrapping from print beds due to unsuitable materials or other types of deformations. As an example, the currently known Polypropylene (PP)-based filament is challenging to process using FFF technology in its pure form. Internal stress within layers or susceptibility to deformation during uneven cooling complicates filament production. The result is the utilization of additives to improve the filament extrusion process, which naturally alters adhesive and mechanical properties and consequently affects the visual appearance of the filament or the resulting model.

The publication is thus focused precisely on addressing this shortfall and deals with the design and gradual verification of a device intended for testing the adhesive properties of materials to various types of print beds or their coating materials. Concerning this design, several problematic areas can be identified, including:

- The necessity to create a universal device that is adaptable or usable across a wide range of FFF device constructions. As depicted in Figure 1 [1], various FFF device constructions, in this case, Cartesian types, exhibit diversity. Therefore, the device should be usable across as many of these variations as possible.
- The design of the measurement apparatus must be small and compact, while also being sufficiently robust to handle materials with superior adhesive properties [2].
- The execution of the adhesion test must be smooth and repeatable. Manual execution of the measurement is not feasible in this case. Due to the test's location and nature, it requires Computer Numerical Control (CNC).
- The selection of suitable types of printing materials and print bed materials appropriate for verifying the functionality of the device.

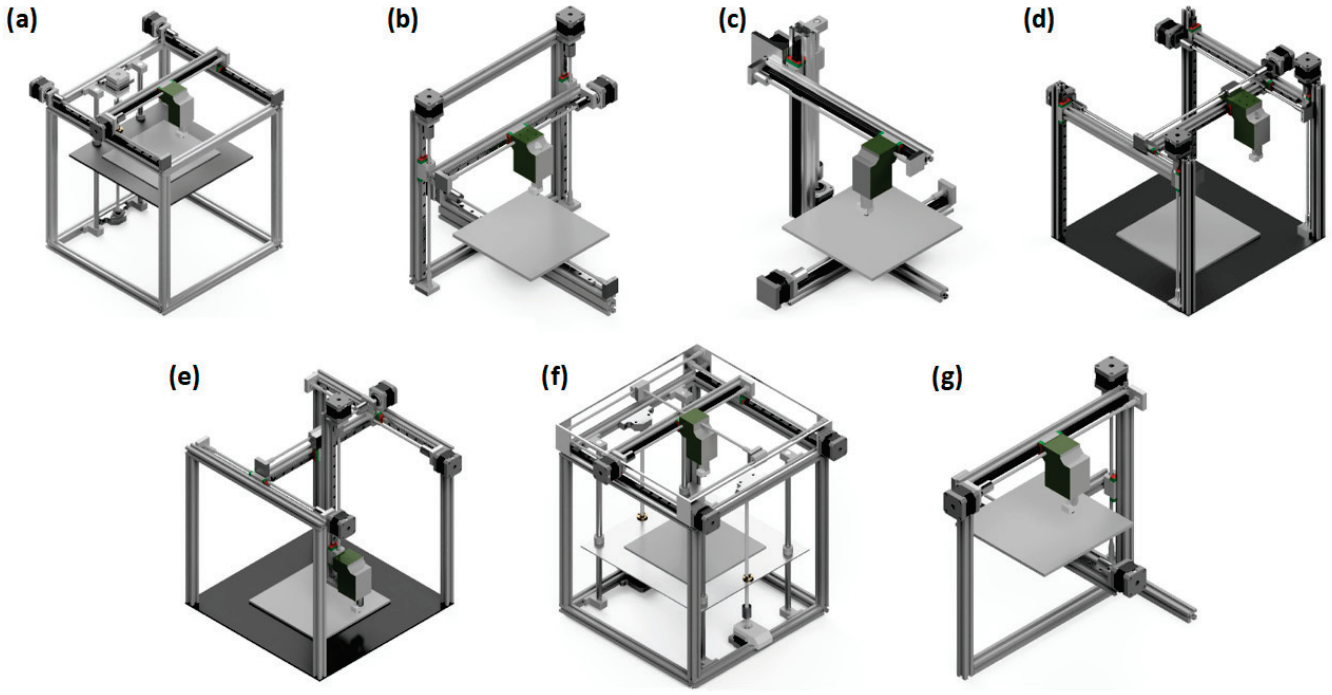

Figure 1. An illustration of existing Cartesian-type FFF device constructions.

Figure 1 informatively describes different types of Cartesian FFF devices, outlining their fundamental differences, which include:

- Figure 1a shows an FFF device with the movement of the toolhead along the *X* and *Y* axes and the print bed along the *Z* axis. The benefit of this design is the reduction of the influence of acceleration forces on the printed model placed on the print bed.
- Figure 1b shows an FFF device with the movement of the toolhead along the *X* and *Z* axes and the print bed along the *Y* axis. Due to its rigid and simple construction, it has become widely used as one of the most common types of FFF printers at present.
- Figure 1c shows an FFF device with the movement of the toolhead along the *X* and *Z* axes and the print bed along the *Y* axis. This construction requires rigid components, whereby a weight is applied to the *X* axis mountings.
- Figure 1d,e shows an FFF device with the movement of the toolhead along with movement of the toolhead along the *X*, Y, and *Z* axes. Within these devices, the position of the print bed remains fixed throughout the printing process.

- Figure 1f shows an FFF device with the movement of the toolhead along the *X* and *Y* axes and the print bed along the *Z* axis. As opposed to the device shown in Figure 1a, the printing bed is driven by two stepper motors which increase the stability of the printing bed.
- Figure 1g shows an FFF device with the movement of the toolhead along the *X* axis and the print bed along the *Y* and *Z* axis. These devices use a simple design resulting in relatively lower production costs.

All these types of 3D printer solutions are the subject of extensive research conducted by the authoring team, aiming to create a database known as Correlating Print Materials and Print Bed Materials. Such a database, once established, would significantly streamline the utilization of various material types, effectively reduce failure rates, and comprehensively enhance FFF manufacturing as a whole. To this end, the publication presents a methodical procedure for the design and subsequent implementation of a device intended for measuring adhesion on various types of print beds [3]. The device's design is planned to be adaptable for use across a wide array of FFF constructions.

2. Literature Review

Given the topicality of the addressed issue, the following chapter describes ongoing or already conducted research. This research delineates various approaches concerning the adhesive properties of print beds and materials for FFF manufacturing. It is imperative to highlight the relevance of the research topic in the introduction. Malengier et al. studied the adhesion of the initial layers of printed models produced using FFF technology on a textile substrate [4]. To assess this adhesion, they introduced three testing methods: perpendicular tensile testing, shear testing, and peel testing, applied to six different textile substrates. For printing, Polylactic Acid (PLA) filament was selected, and the objects were fabricated on a textile base affixed to the printer bed. The study's contribution lies in identifying that the most suitable method for testing the adhesion of the initial model layer is the perpendicular tensile test, presenting a lower risk of tearing the textile substrate. Nazan et al. presented research on warping deformations of printed models using FFF technology [5]. Laser scanning was utilized for deformation measurements and comparison against the nominal model. Epoxy adhesive was applied to the print bed to enhance the adhesion of the initial layer. It was observed that, when using PLA material, deformations have a reduced impact on the manufactured model. They underscored the necessity of using a heated bed, particularly when printing ABS material, emphasizing the importance of proper printing conditions for the initial layer's adhesion and its influence on overall deformations and detachment of the resulting print. However, despite measuring model deformations with a laser scanner, the study did not directly investigate the adhesion of the initial layer.

Spoerk et al. focused on improving the adhesion of the initial layer in 3D-printed models produced by FFF technology [6]. They investigated the influence of different print bed temperatures when printing PLA and Acrylonitrile Butadiene Styrene (ABS) materials using multiple print bed types. It was discovered that print bed temperature significantly affects the initial layer's adhesion, with higher temperatures enhancing adhesion. They recommend utilizing a print bed heated slightly above the glass temperature of the filament. Additionally, they proposed a custom-designed shear-off force testing device for assessing the initial layer's adhesion. This device tested the shear-off force acting on the printed model in a parallel direction to the printed layers but did not study the adhesive properties of the initial layer perpendicular to the print bed. Płaczek examined the adhesive properties of 3D-printed models using FFF technology on a print bed with the application of tapes [7]. For measuring the adhesive forces of the initial layer on the bed, an experimental device was proposed, focusing on force measurements perpendicular to the print bed. The contribution of the study lies in the design proposal of an experimental testing device and the validation of its functionality.

Snapp et al. studied the adhesive forces of printed models and the influence of print bed temperature with borosilicate glass and polyamide surface materials [8]. They designed a testing device to measure these adhesive forces. Within this device, measurements were conducted parallel to the printed layers, highlighting the potential use of applying and measuring force magnitude on the manufactured part, unlike pulling the part from the print bed. Brancewicz-Steinmetz et al. conducted research on the adhesive properties during printing between PLA and Thermoplastic Polyurethane (TPU) materials [9]. The focus of this research was on testing the influence of process parameters on the mutual adhesion of these materials, utilizing shear tests for measuring these forces. It was found that inadequately chosen process parameters affect layer adhesion, potentially causing unsuccessful printing. Thumsorn et al. investigated the impact of process parameters and additives when using composite materials on layer adhesion in FFF printed models [10]. They analyzed layer adhesion morphologically, thermal properties, and dynamic mechanical properties. The research highlighted the possibility of reducing layer adhesion due to larger void areas between raster and printed layers when utilizing composite PLA compared to pure PLA material.

Laumann et al. examined the initial layer adhesion in Fused Filament Fabrication (FFF) printed models and aimed to reduce warping effects due to thermal shrinkage [11]. They proposed an experimental testing device combining FFF technology and a tensile testing machine, designed to test the adhesion of the initial print layer immediately after completing printing. The device applied force perpendicular to the print bed for model detachment. The contribution lies in the expanded documentation of the device's design and measurement method. However, while the device operates as an independent FFF technology, offering advantages and disadvantages, it cannot be used for testing the adhesion of the initial layer on existing FFF and FDM technologies. Kujawa studied the adhesion of initial layer parts printed using FFF technology, highlighting insufficient research in this domain, the absence of a standardized method for measuring part adhesion to the print bed, and its crucial role in employing FFF technology [12]. For the device design to measure adhesion forces, the existing RapCraft 1.4 FFF technology was utilized, integrating the measuring device onto it. This approach combined a tensile testing machine with FFF technology, enabling the measurement of adhesive forces upon detachment under real conditions. However, proper installation of the tensile testing machine onto FFF technology is necessary, and its use with other FFF, particularly FDM technologies, depends on the design of these technologies, making its installation often challenging.

This overview of the current state of research in the field of adhesion of initial material layers to print beds confirms the research gap in this area. The efforts of authorial collectives to compensate for insufficient information in this domain underscores the timeliness of the subject matter.

3. Materials and Methods

Considering the ongoing research and the requirements for the measuring device outlined in the previous chapters, it becomes apparent that, in the case of the apparatus intended for adhesion tests, a certain form of compatibility with FFF devices is necessary. The materials used in the construction of the adhesion testing device and the specifications of the model tested for adhesion are pivotal components in evaluating the adhesion properties of 3D-printed objects on various substrate materials [13]. This section provides a detailed description of the materials used in the construction of the testing device and emphasizes the specifications of the polyethylene terephthalate glycol (PETG) material model used for adhesion testing. It constitutes a relatively straightforward concept consisting of few fundamental parts. The first part comprises a compact frame made of aluminum profiles of 20×20 and 20×40 mm dimensions. This frame serves as the supporting section of the entire device, directly placed onto the print bed of the FFF device. The construction of this frame includes:

- Aluminum profiles of specific lengths, 20 × 20 and 20 × 40 mm: an aluminum frame measuring 20 × 40 mm served as the foundational frame for the testing device, ensuring structural stability.
- 3D printed parts: specially designed components essential for ensuring the functionality and stability of the testing device, as well as the placement of other components, were manufactured using ABS material in the 3D printing process.
- Fastening materials: a range of screws and nuts were employed for securely fastening and assembling various parts of the testing device, ensuring strength and stability during evaluation.

Given the compactness of the entire measuring system and the endeavor to position it on the print beds of FFF devices, it is evident that there is no room in the design for dimensionally large measuring devices. For this reason, the EMS20-5kN sensor (EMSYST spol. s r.o., Trenčín, Slovak) was selected [14]. This sensor, in collaboration with the DAQ device and EMS Center v1.0 software, enables the measurement, transformation, and recording of the tensile force over time. The measurement section of the proposed device thus consists of:

- Force sensor (Emsyst EMS20-5kN): the experiment utilized the Emsyst EMS20-5kN force sensor, visible in Figure 2, along with its parameters, which were pivotal for quantifying adhesive forces between the 3D printed model and various substrate materials.
- Data Acquisition System (DAQ) (Emsyst EMS650, EMSYST spol. s r.o., Trenčín, Slovak): the data acquisition system, Emsyst EMS650 (Figure 2), was integrated with the force sensor to ensure the collection and recording of adhesion-related data during evaluation using the corresponding EMS Center v1.0 software.

Capacity	5 kN
F.S Output mV/V	1.492
Zero balance % F.S.	0.5498
Non- linearity %F.S.	0.173
Hysteresis %F.S	0.064
TC on Zero % F.S./10K	0
Imput resist. Ohm	377
Output resist. Ohm	353
Insulat resist. Mohm	>5000

Figure 2. The Emsyst EMS20-5KN sensor with the converter EMS650.

The Prusa Mk3s+ was selected as the testing FFF device, and four types of materials were placed on its print beds. This device is equipped with a direct extrusion head, enabling more precise material dosing, and features a wide range of 3D print beds with recommended manufacturer settings. The only adjusted parameter was the temperature of the printing bed. It had to be corrected for better adhesion of the model to its surface. Models designed for the optimization of the printing process were not subjected to measurements due to their frequent deformations. The result of the optimization of the printing process for the chosen material-produced parameters is presented in Table 1. Subsequently, these parameters were employed in the production of all samples designated for testing purposes.

Among other components, such as threaded rods and guiding nuts, an indispensable part of the device, or the diagnostic system, is the test model [15]. PETG was chosen as the material for this model, which is one of the most commonly used materials in the realm of FFF technology, whose adhesion to print beds has been a perennial subject of discussion. The model utilized for adhesion testing was specifically designed to evaluate adhesive properties across various substrate materials.

- Characteristics of the PETG model: the PETG model was designed with a specific geometric form that allowed for easy fixation within the jaws of the measuring instrument.

Its form was selected to evaluate adhesion properties under controlled conditions, ensuring consistent and replicable testing scenarios.

- Geometric design for adhesion testing: the PETG model's design encompassed specific features intended to evaluate adhesion properties under various conditions, enabling controlled and systematic investigation of the bonding force between the model and diverse print bed materials.

Table 1. Description of the chosen parameters for the production of samples.

Printing temperature	255 °C
Print bed temperature	N/A
Printing material	PETG; 1.75 mm
Nozzle diameter	0.40 mm
Layer cooling	Off-for all layers
Print speed	50 mm/s
Number of outline perimeters	3
Number of top and bottom layers	2
Infill	100%
Infill pattern	Grid
Layer height	0.23 mm

As depicted in Figure 3 [16], two materials were considered for the execution of the test model, which could be deemed the most commonly used or widely recognized. However, the material PLA was excluded from this process, characterized as the "most straightforward" in terms of its utilization within FFF technology and the printing process itself. As highlighted in Table 2, discrepancies in bed temperatures, melting temperatures, and other properties essentially disqualified PLA from this process. PLA is a material widely acknowledged for often not requiring the heating of the print bed in many instances. With appropriate initialization layer settings, its adhesive properties are deemed sufficient for nearly any commonly used uncontaminated surface.

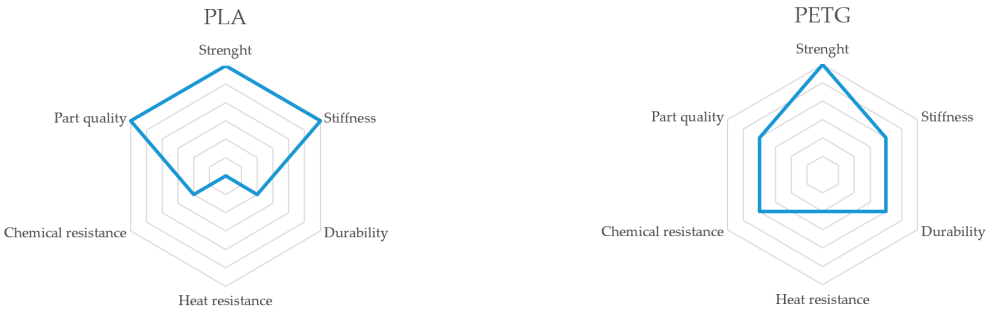

Figure 3. Graphical representation of generally known properties of PLA and PETG materials.

Table 2. Comparison of properties between PLA and PETG materials from a user perspective.

PLA Characteristics	PETG Characteristics
Extruder temperature: 190–220 °C	Extruder temperature 230–250 °C
No particular resistance	Water/fatigue/chemically resistant
Made from renewable resources	Oil-based polymer
Bed temperature: 45–60 °C	Bed temperature: 75–90 °C

Based on the preceding selection of materials and components for the measuring apparatus, its utility, and integration within FFF setups allow for the following observations:

- The device's frame will be compact and adaptable to build plates of various types of equipment.
- The construction of the frame must possess adequate stability and rigidity while enabling the placement of all necessary components of the measuring system.
- The motion or detachment of the model from the print bed must be uniform and monitored throughout the entire process. The apparatus must include a drive mechanism and means for transforming its movement.
- The model for testing adhesive properties must be compatible with the designed apparatus.
- The same sample and the same FFF equipment must be used for each experimental measurement.
- The test model must be consistently positioned at the center of the print bed to ensure the correct alignment of the measuring device and the model.
- Measurements are conducted by the same individual under stable laboratory conditions.
- Models used for optimizing the printing process for a new type of print bed are not included in the measurements.

Several designs of the measuring device were created based on these requirements. The following chapter introduces one of the suitable prototypes, thoroughly describing its operational principles, and highlighting the obtained results and issues.

4. Results

As depicted in Figure 4, the prototype of the measuring apparatus appears relatively straightforward in design. The basic dimensions of the proposed and testing device are 200 × 300 × 160 mm, with a maximum vertical (*z*-axis) travel of 50 mm. As previously mentioned, it comprises a compact frame housing all requisite components [17]. The device features a supporting section (1), wherein all the necessary measuring elements are positioned. At its uppermost part resides the stepper motor, specifically a Nema 23 (2) delivering a torque of 1.23 Nm, as discernible from the illustration. The rotational motion of the motor is transmitted via gears (3) onto trapezoidal threaded rods (4), whose rotational movement induces the displacement of guide nuts and consequently propels the EMS 20-5kN sensor (6) along the *Z*-axis. This motion facilitates the detachment of the test model perpendicular to the pressure plate [18]. All specified components are situated on the device frame of the apparatus (5).

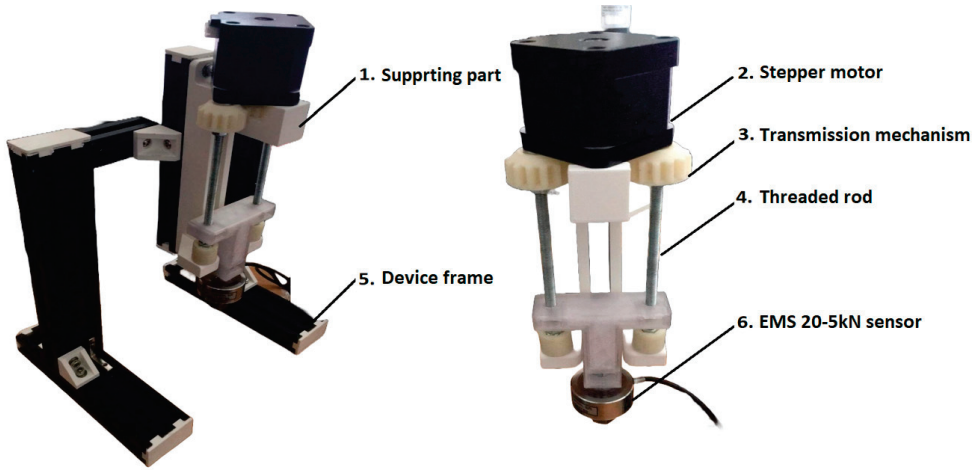

Figure 4. The construction of the prototype designed for adhesive testing.

The entire process is methodically recorded in time and visualized through EMS Center v1.0 software, which subsequently generates data from individual measurements showcased in Tables 3 and 4.

Table 3. Comparison of maximum shear forces between surfaces with PI and borosilicate coatings.

	Max. Tear-Off Force from the Build Plate [N]	
	Tempered Glass with PI Layer	**Borosilicate Glass Plate**
Trial No. 1	51.24	51.69
Trial No. 2	54.06	63.69
Trial No. 3	57.89	55.52
Trial No. 4	63.31	44.76
Trial No. 5	63.13	42.33
Trial No. 6	51.12	67.55
Trial No. 7	54.31	41.27
Trial No. 8	60.07	52.03
Trial No. 9	51.41	62.77
Trial No. 10	67.19	75.25
Trial No. 11	64.85	63.12
Trial No. 12	56.86	35.83
Mean deviation	57.95	54.65
Standard deviation	5.70	12.10

Table 4. Comparison of maximum shear forces between uncoated aluminum bed and bed with PEI coating.

	Max. Tear-Off Force from the Build Plate [N]	
	Pure Aluminium Sheet	**Spring Steel with PEI Coating**
Trial No. 1	30.97	47.30
Trial No. 2	34.51	46.98
Trial No. 3	32.52	41.36
Trial No. 4	28.32	43.69
Trial No. 5	27.67	51.72
Trial No. 6	29.13	55.79
Trial No. 7	31.15	61.07
Trial No. 8	29.45	66.56
Trial No. 9	48.09	62.61
Trial No. 10	34.51	56.15
Trial No. 11	37.09	49.70
Trial No. 12	33.63	58.88
Mean deviation	33.09	53.48
Standard deviation	5.52	7.95

This section delves into the empirical outcomes derived from conducted adhesion test measurements, encompassing an extensive array of tables and graphs. These analyses are instrumental in elucidating the adhesion properties of 3D-printed objects on a spectrum of materials, namely pure aluminum plate, spring steel coated with Polyetherimide (PEI), a magnetic plate coated with Polyimide (PI), and borosilicate tempered glass. Through systematic experimentation and data collection, this chapter offers profound insights into the complex interplay between material composition, surface texture, and 3D printing adherence [19].

To better interpret the results of measurements of the maximum force upon detachment of the model from the print bed, the measured values were supplemented with the average and standard deviation values in the measurement context.

$$\overline{x} = \frac{\sum_{i-1}^{n} x_i}{n} \tag{1}$$

where:

$\overline{x}$—is the mean (average).
n—is the number of values in the dataset.
x_i—represents each individual value in the dataset.

$$\sigma = \sqrt{\frac{\sum_{i-1}^{n} (x_i - \overline{x})^2}{n}} \tag{2}$$

where:

σ—is the standard deviation.
n—is the number of values in the dataset.
x_i—represents each individual value in the dataset.
$\overline{x}$—is the mean of the values.

As depicted in Table 3, the initial comparison involved tempered borosilicate glass and tempered glass with a PI layer as the first set of print beds analyzed. Each measurement, as evident, underwent twelve repetitions, focusing on determining the maximum force required to detach the PETG model from the print bed. Notably, each print bed surface required distinct print settings for the initial layer and subsequent layers. This process presented challenges, particularly with certain materials, resulting in a considerable number of defective models.

As evident from twelve separate measurements comparing the borosilicate layer with the PI layer, their parameters exhibit a high degree of similarity. The measurements show no significantly disparate values that would substantially distort the outcome. The chart visible in Figure 5 highlights the similar adhesive properties of these two surfaces concerning the PETG material.

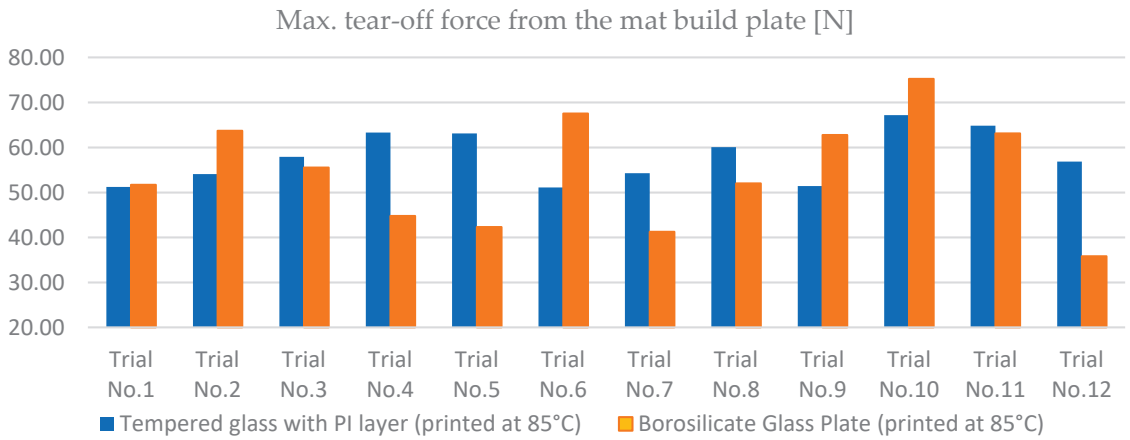

Figure 5. Comparison of maximum forces when detaching the bed with PI and borosilicate coatings.

The second series of measurements proceeded under the same conditions as in the first instance. The sole alteration was, of course, the change in the used print beds, assuming an alteration in adhesive properties. Given the highly similar results observed in the initial case, an extreme change in one of the print beds was chosen for device functionality verification. As depicted in Table 4, the comparison involves an evaluation of the adhesive properties between the currently most widely used print bed surface, PEI, and a

substantially decreased aluminum plate. The latter was selected due to the anticipation of a pronounced difference in the measured outcomes.

The significance of the monitored data is demonstrated through the outcomes visualized in Figure 6. The primary objective was to showcase the applicability and effectiveness of the device in evaluating a print bed characterized by notably adverse adhesive properties for the PETG material. This endeavor aimed to provide a clear depiction of how the prototype device functioned when assessing challenging print surfaces.

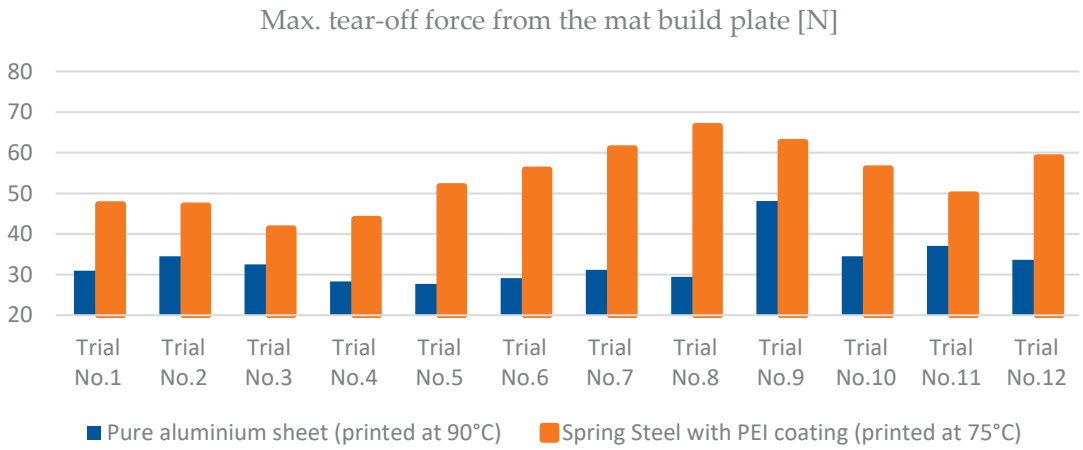

Figure 6. Comparison of maximum forces when detaching the bed with and without a PEI coating.

The chart in Figure 6 serves as a compelling visual representation, delineating a tangible contrast between the adhesive behavior of the PEI surface and the clean aluminum plate. This stark difference between these two distinct surfaces accentuates the device's capability to discern and measure the dissimilar adhesion attributes across varying print bed materials.

By employing the prototype device for such evaluations, the outcomes unequivocally delineate the divergence in adhesion performance between these surfaces. The evident disparity validates the effectiveness of the measurements conducted using the prototype device, underscoring its potential to discern minute differences in adhesive properties even in situations where the print surface exhibits particularly challenging or adverse adhesion characteristics for PETG material. This successful demonstration underscores the pivotal role of the prototype device in comprehensively evaluating adhesion dynamics across a spectrum of print bed materials, from which, in this case, the maximum force upon detachment of the model from the print bed is depicted. This insight provides valuable information for optimizing 3D printing processes and considering material compatibility.

It is important to emphasize that the measurements excluded what could be termed as significant errors resulting from incorrect settings of the initial printing layer. If there were visible signs of warping, insufficient adhesion to the print bed, or within the layers either during or after printing the models, the measurement would have been deemed irrelevant. The optimization process focused on determining the ideal extrusion temperature, printing speed, and correlating the software-declared and actually extruded volume of material, nearly eliminating these shortcomings.

These findings underscore the significance of these measurements in understanding the dynamics of adhesion in 3D printing technology. The visual representations, comprehensive analyses, and systematic comparisons presented in this chapter shed light on the intricate relationships between materials, surface textures, and printing adherence. As can be seen in Figure 7, the expected correlation between PI and PEI coatings in adhesion further confirms the accuracy of the measurements conducted by the prototype for adhesion tests. These insights hold substantial promise for refining printing processes and advancing material compatibility in the realm of 3D printing. It is imperative to emphasize that the measurements excluded gross errors resulting from incorrect initial printing layer

settings or visible signs of warping, insufficient adhesion, or defects within the printed models. These exclusions ensure the reliability and relevance of the obtained data, offering a foundational understanding of adhesion in this evolving technological landscape.

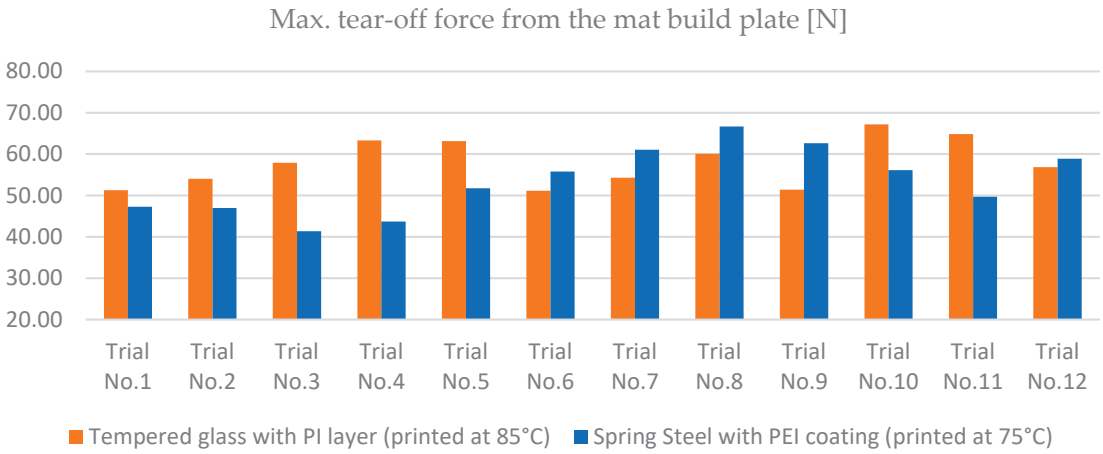

Figure 7. Comparison of maximum forces when detaching the bed with PEI and PI coatings.

5. Discussion

Given that it is a prototype device for measuring adhesion to print beds and the values of standard deviations of the measurements, it is evident that its operation is not flawless. Therefore, the concluding discussion revolves around evaluating the prototype's functionality, advantages, disadvantages, and potential enhancements aimed at improving the efficiency, precision, and user-friendliness of the proposed device. Based on the presented results, it is clear that the device performed adequately in all 48 measurements conducted. The complete force-displacement curves were recorded, focusing on the maximum force at detachment. In terms of the subjective opinion of the authoring team regarding the prototype device's use, several specific advantages can be highlighted:

- The requirements for compactness, i.e., the small dimensions of the measuring device, were met. The prototype's placement was tested on various types of FFF devices, including Creality CR-max, Neo V2, Ender v1 and Pro, Prusa MK2S, and MK3S+, among many others.
- The device's positioning and the sensor's location at the center of gravity ensure detachment of the model perpendicular to the print bed, ensuring a relevant and repeatable result. The construction of the device is designed in a way that its attachment to the model other than at its center of gravity is not possible.
- The frame of the device is stable and significantly overdesigned despite its dimensions. This ensures its sufficient stability and prevents any negative influences from affecting the test results.
- As previously mentioned, the device is designed to be as intuitive as possible in its placement and utilization. Its design prohibits its use in any alternative manner.

This discussion serves as a critical evaluation of the prototype's performance, highlighting its strengths and areas for potential improvement to further refine its functionality and usability in adhesion testing to print beds.

During the prototype usage, several drawbacks related to its structural design emerged. The measurement process used for verification proceeded smoothly. However, the only observable drawback was the optimization of the printing process for PETG material models. PETG models tended to detach relatively frequently from various types of print beds, necessitating constant adjustments to the FFF device's process parameters. An illustrative example of a detached printed model can be seen in Figure 8. Among other drawbacks of the prototype, the following can be highlighted:

- Inadequate stepper motor performance or improper gearing under extreme surface adhesion. When treating the print bed with adhesive agents like acetone and ABS solutions or silicone-based preparations, which significantly enhance adhesive properties, instances occurred where the adhesion became so extreme that the stepper motor lacked sufficient power to separate the model from the bed without damaging it.
- Substitution of materials in certain key components. As it is a prototype, some of its components were manufactured using FFF technology with ABS material. Minor flaws arising from the plastic construction can be rectified by replacing them with metal alternatives.
- Modification of the device's transformation mechanisms. Swapping the trapezoidal lead screws and nuts for larger diameter alternatives would enhance the device's operation, improving its stability and reducing the risk of slippage in cases of insufficient stepper motor power.

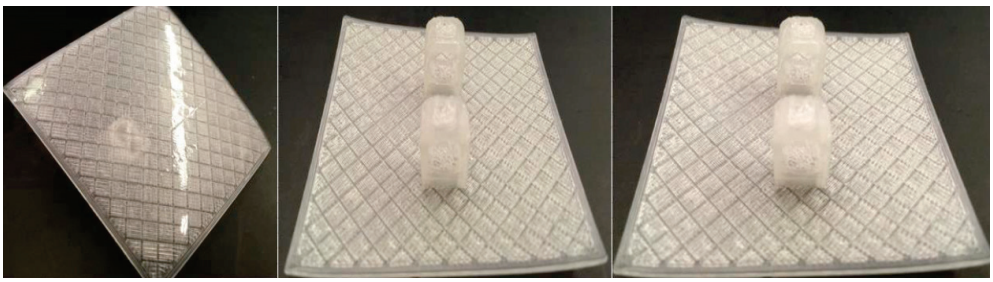

Figure 8. Example of the most common deficiencies of the test model.

In conclusion, despite the functional operation of the prototype in conducting measurements for verification purposes, several shortcomings related to its structural design surfaced during its practical usage. The measurement procedures proceeded smoothly, yet the challenges in optimizing the printing process for PETG material models remained apparent due to frequent detachment issues. These challenges necessitated continual adjustments to the FFF device's process parameters to ensure consistent results.

Among the identified drawbacks of the prototype, issues such as insufficient stepper motor performance under extreme adhesion, material substitutions in critical components, and the need for modification in transformation mechanisms were observed. Addressing these shortcomings through potential enhancements in motor power, material selection, and mechanical modifications can significantly improve the device's overall efficacy, stability, and reliability.

The acknowledgment and rectification of these limitations stand as crucial steps toward refining the prototype, ensuring its suitability for reliable and consistent adhesion testing to diverse print bed substrates. These enhancements are pivotal for establishing a more robust and efficient adhesion testing device, thereby contributing to the advancement of research in material adherence in additive manufacturing technologies.

The suggested prototype device designed for assessing adhesion to print beds offers potential advantages in the realm of FFF manufacturing. Its utility extends to establishing a comprehensive database that could significantly streamline the deployment of diverse material types, leading to a marked reduction in failure rates and an overarching enhancement of FFF manufacturing practices. The substantial reduction in failure rates not only optimizes manufacturing time and material usage but also contributes to a more environmentally sustainable FFF manufacturing process, particularly when employing non-biodegradable materials subjected to intricate recycling procedures.

A notable attribute of this compact, portable, adaptable, and robust device lies in its applicability across various FFF constructions and technologies. Despite the proposed design's relative cost-effectiveness, a substantial portion of the manufacturing cost pertains to acquiring the force sensor and data acquisition system. However, the device's flexibility allows for the integration of equivalent force sensors and data acquisition systems, while

preserving their requisite characteristics. The device facilitates comprehensive monitoring throughout the adhesion measurement process. The obtained measurement results can be instrumental in refining printing processes and advancing material compatibility, especially given the extensive array of adjustable FFF production process parameters corresponding to a specific filament material, printing material, and chosen FFF technology.

6. Conclusions

The exploration of adhesion properties in FFF technology remains an ongoing challenge that demands thorough scrutiny and continual investigation. This is driven by the need for improved material compatibility, the reinforcement of print bed mechanics, and the adoption of more cohesive materials. This article outlines a strategic approach to address these complexities, catering to a broad spectrum of users from enthusiasts to industrial stakeholders. The foundation of this research revolves around the design and iterative validation of a sophisticated device crafted specifically for testing material adhesion to various print bed types or their coating materials. This initiative is marked by the identification of key problematic areas, necessitating the development of a versatile device adaptable to diverse FFF device constructions. The compactness and robustness of the measurement apparatus are crucial considerations, enabling its usability across materials with superior adhesive properties.

Furthermore, attention to testing execution is emphasized, necessitating CNC control due to the test's location and inherent nature. The selection of suitable printing materials and bed typologies for verifying device functionality remains a critical facet of this pursuit. The comprehensively detailed materials and methods section elucidates the careful selection of components and testing specifications integral to evaluating adhesion properties in 3D-printed models across diverse substrate materials. Notably, the focus on PETG as the testing material illuminates its significance and relevance within FFF technology, offering insights into its adhesion behavior compared to other materials such as PLA.

The results section showcases extensive empirical data derived from adhesion tests conducted on various surface coatings and materials. These analyses provide crucial insights into the detachments' force dynamics, shedding light on the interplay between different coating materials and their adhesive behaviors. The presented tables and graphs offer a comprehensive visual depiction of these relationships, laying the groundwork for a nuanced understanding of adhesion between printed models and the print bed in 3D printing technology. It is important to emphasize that these measurements were conducted in a way that excluded significant errors stemming from incorrect initial layer settings or visible signs of wrapping or inadequate adhesion to the print bed.

In summary, this exhaustive exploration underscores the criticality of addressing adhesion challenges in FFF technology. The findings pave the way for a deeper comprehension of material adhesion, offering significant implications for optimizing printing processes and fostering material compatibility across diverse print bed typologies.

Author Contributions: Conceptualization, J.K.; methodology, J.K. and T.C.; software and measurements J.K. and T.C.; validation, M.K. and J.T.; formal analysis, J.K.; investigation, J.K. and A.V.; resources, A.V. and J.T.; writing—original draft preparation, M.K.; review and editing, J.K.; visualization, T.C.; supervision, M.K.; funding acquisition, M.K. All authors have read and agreed to the published version of the manuscript.

Funding: This research was funded by projects VEGA 1/0026/22 and KEGA 002TUKE-4/2023 granted by the Ministry of Education, Science, Research and Sport of the Slovak Republic.

Institutional Review Board Statement: Not applicable.

Informed Consent Statement: Not applicable.

Data Availability Statement: Dataset available on request from the authors. The raw data supporting the conclusions of this article will be made available by the authors on request.

Conflicts of Interest: The authors declare no conflicts of interest.

References

1. Kopets, E.; Karimov, A.; Scalera, L.; Butusov, D. Estimating Natural Frequencies of Cartesian 3D Printer Based on Kinematic Scheme. *Appl. Sci.* **2022**, *12*, 4514. [CrossRef]
2. Husar, J.; Knapcikova, L.; Balog, M. Implementation of Material Flow Simulation as a Learning Tool. In *Design, Simulation, Manufacturing: The Innovation Exchange*; Springer: Cham, Switzerland, 2019; pp. 33–41. [CrossRef]
3. Kaščak, J.; Gašpár, Š.; Paško, J.; Knapčíková, L.; Husár, J.; Baron, P.; Török, J. Design of an Atypical Construction of Equipment for Additive Manufacturing with a Conceptual Solution of a Printhead Intended for the Use of Recycled Plastic Materials. *Appl. Sci.* **2021**, *11*, 2928. [CrossRef]
4. Malengier, B.; Hertleer, C.; Cardon, L.; Van Langenhove, L.; Reynders, D. 3D Printing on Textiles: Testing of Adhesion. *J. Fash. Technol. Text. Eng.* **2018**, *S4*, 013. [CrossRef]
5. Nazan, M.A.; Ramli, F.R.; Alkahari, M.R.; Abdullah, M.A.; Sudin, M.N. An Exploration of Polymer Adhesion on 3D Printer Bed. *IOP Conf. Ser. Mater. Sci. Eng.* **2017**, *210*, 012062. [CrossRef]
6. Spoerk, M.; Gonzalez-Gutierrez, J.; Sapkota, J.; Schuschnigg, S.; Holzer, C. Effect of the Printing Bed Temperature on the Adhesion of Parts Produced by Fused Filament Fabrication. *Plast. Rubber Compos.* **2018**, *47*, 17–24. [CrossRef]
7. Płaczek, D. Adhesion between the Bed and Component Manufactured in FDM Technology Using Selected Types of Intermediary Materials. *MATEC Web Conf.* **2019**, *290*, 01012. [CrossRef]
8. Snapp, K.L.; Gongora, A.E.; Brown, K.A. Increasing Throughput in Fused Deposition Modeling by Modulating Bed Temperature. *J. Manuf. Sci. Eng.* **2021**, *143*, 094502. [CrossRef]
9. Brancewicz-Steinmetz, E.; Sawicki, J.; Byczkowska, P. The Influence of 3D Printing Parameters on Adhesion between Polylactic Acid (PLA) and Thermoplastic Polyurethane (TPU). *Materials* **2021**, *14*, 6464. [CrossRef]
10. Thumsorn, S.; Prasong, W.; Kurose, T.; Ishigami, A.; Kobayashi, Y.; Ito, H. Rheological Behavior and Dynamic Mechanical Properties for Interpretation of Layer Adhesion in FDM 3D Printing. *Polymers* **2022**, *14*, 2721. [CrossRef]
11. Laumann, D.; Spiehl, D.; Dörsam, E. Device for Measuring Part Adhesion in FFF Process. *HardwareX* **2022**, *11*, e00258. [CrossRef] [PubMed]
12. Kujawa, M. The Influence of First Layer Parameters on Adhesion between the 3D Printer's Glass Bed and ABS. In *Interdyscyplinarność badań Naukowych 2017*; Oficyna Wydawnicza Politechniki Wrocławskiej: Wrocław, Poland, 2017; pp. 76–81. ISBN 9788374939935.
13. Adamczak, M.; Kolinski, A.; Trojanowska, J.; Husár, J. Digitalization Trend and Its Influence on the Development of the Operational Process in Production Companies. *Appl. Sci.* **2023**, *13*, 1393. [CrossRef]
14. Kaščak, J.; Gašpár, Š.; Paško, J.; Husár, J.; Knapčíková, L. Polylactic Acid and Its Cellulose Based Composite as a Significant Tool for the Production of Optimized Models Modified for Additive Manufacturing. *Sustainability* **2021**, *13*, 1256. [CrossRef]
15. Maščenik, J.; Pavlenko, S. Determination of stress and deformation during laser welding of aluminium alloys with the PC support. *MM Sci. J.* **2020**, *2020*, 4104–4107. [CrossRef]
16. Hal'ko, J.; Maščenik, J. Differential with an integrated, newly-developed two-stage transfer. In Proceedings of the Applied Mechanics and Materials: ICMEAT 2013: 3rd International Conference on Materials Engineering for Advanced Technologies, Brisbane, Australia, 31 December–2 January 2014; Volume 510, pp. 215–219, ISBN 978-303835018-7.
17. Hrehova, S.; Knapčíková, L. Design of Mathematical Model and Selected Coefficient Specifications for Composite Materials Reinforced with Fabric from Waste Tyres. *Materials* **2023**, *16*, 5046. [CrossRef] [PubMed]
18. Acierno, D.; Patti, A. Fused Deposition Modelling (FDM) of Thermoplastic-Based Filaments: Process and Rheological Properties—An Overview. *Materials* **2023**, *16*, 7664. [CrossRef]
19. Zhang, X.; Li, B.; Wang, K.; Zhang, Q.; Fu, Q. The effect of interfacial adhesion on the impact strength of immiscible PP/PETG blends compatibilized with triblock copolymers. *Polymer* **2009**, *50*, 4737–4744. [CrossRef]

applied sciences

MDPI

Review

Corrosion Monitoring Techniques in Subcritical and Supercritical Water Environments

Yanhui Li [1,2,*], Zhouyang Bai [1], Limei Xing [1], Qian Zhang [1], Shaoming Ding [1], Yinan Zhang [1], Pengfei Gao [1], Zhihong Yu [1] and Donghai Xu [1]

[1] Key Laboratory of Thermo-Fluid Science & Engineering, School of Energy and Power Engineering, Xi'an Jiaotong University, Ministry of Education, Xi'an 710049, China; b15735171052@stu.xjtu.edu.cn (Z.B.); xinglm2022@163.com (L.X.); qianzhang2024@163.com (Q.Z.); smding21@stu.xjtu.edu.cn (S.D.); zhangyn_xianjtdx@163.com (Y.Z.); g731215@163.com (P.G.); y18833253765@stu.xjtu.edu.cn (Z.Y.); xudonghai@mail.xjtu.edu.cn (D.X.)

[2] Departments of Nuclear Engineering & Materials Science and Engineering, University of California, Berkeley, CA 94720, USA

* Correspondence: yhli19@mail.xjtu.edu.cn

Abstract: A series of advanced equipment exposed to sub-/supercritical water environments at high temperatures, high pressures, and extreme water chemistry with high salt and dissolved oxygen content faces serious corrosion problems. Obtaining on-site corrosion data for typical materials in harsh environments is crucial for operating and maintaining related equipment and optimizing various corrosion prediction models. First, this article introduces the advantages and disadvantages, usage scenarios, and future development potential of several in situ monitoring technologies, including ultrasonic thickness measurement, the infrared thermography method, microwave imaging, eddy current detection, and acoustic emission. Considering the importance of electrochemical corrosion data in revealing microscale and nanoscale corrosion mechanisms, in situ testing techniques such as electrical resistance probes, electrochemical corrosion potential, electrochemical impedance spectroscopy, and electrochemical noise that can be applied to sub-/supercritical water systems were systematically discussed. The testing platform and typical data obtained were discussed with thick and heavy colors to establish a mechanical prediction model for corrosion behavior. It is of great significance to promote the development of corrosion monitoring techniques, such as breaking through testing temperature limitations and broadening the industrial application scenarios and maturity.

Keywords: corrosion; supercritical water; monitoring techniques; research platform

1. Introduction

Supercritical water (SCW) has both temperature and pressure above the critical point of water (374.15 °C and 22.12 MPa) [1], while subcritical water refers to water that is heated above the boiling point and below the critical point, and the system pressure is controlled to keep the water in a liquid state [2]. Due to its unique physical and chemical properties, subcritical or supercritical water has been widely used in energy and environmental protection. In nuclear power generation, the current technologically mature pressurized water reactor and boiling water reactor nuclear power plants have subcritical water as their heat transfer medium (coolant) [3]. Although the Chernobyl and Fukushima nuclear power plant accidents cast a shadow over the development of nuclear power plants, nuclear power remains an efficient and pollution-free source of electricity. The fourth-generation reactor is expected to be put into use after 2030. Promoting commercial small reactors has brought new opportunities for developing nuclear energy [4]. The temperature of the core of modern nuclear power reactors is usually between 260 °C and 320 °C. In this high-temperature and strong irradiation environment, water is prone to ionizing strong oxidants (such as O_2 and H_2O_2). Most of these species are electroactive (i.e., they may

participate in charge transfer reactions) [5]. In addition, metal pipelines are subjected to long-term high pressure, and nuclear power plants have been threatened with severe local corrosion damage, such as pitting corrosion and stress corrosion cracking, since their inception [5]. Statistics show that the atomic power events that have occurred globally so far are generally caused by localized corrosion. Additionally, ultra-supercritical plants have gradually replaced low-parameter units and become the primary thermal power plants. Due to the complexity of combustion conditions and gas-solid flow, high-temperature corrosion of water-cooled wall pipes is caused and influenced by various factors [6]. With the improvement of unit parameters and the modification of low NOx burners, the problem of high-temperature corrosion of water-cooled wall pipes has become more serious, which leads to a higher possibility of boiler pipe explosion [7].

On the other hand, corrosion is also a crucial factor affecting the safety of equipment and facilities in the exploration, extraction, transportation, and refining processes of oil and gas [8–11]. The environment of oil and gas fields is complex and harsh, often characterized by high temperature, high pressure, high salinity, and high mineralization. In harsh subcritical water environments, oil pipes are prone to corrosion and even perforation, seriously affecting oil and gas wells' average production and operation. As an essential transportation system for underwater oil and gas development, the proportion of accidents caused by corrosion can reach 37%. Once oil and gas field pipelines in long-term service rupture or fail due to corrosion, it will cause substantial economic losses and safety hazards [12].

In addition to the energy field, supercritical water oxidation (SCWO) technology can efficiently and thoroughly degrade various high-concentration organic wastes, such as waste fluid, sludge, and hazardous solid waste, with broad application prospects. However, in SCWO treatment systems, the preheating and reaction initiation stages of the initial liquid or slurry materials and the cooling phase of the corresponding reaction products inevitably undergo transcritical water environments due to the predominant electrochemical corrosion [1,13]. The actual operation of some SCWO demonstration/industrialization plants indicates that the current equipment exposed to the transcritical water environment, such as preheaters, reactor fronts, and coolers for reaction effluents, has the highest risk of corrosion failure [13,14], which is a common bottleneck problem that restricts the industrial promotion of various supercritical water treatment techniques, including supercritical water gasification for hydrogen production from organics, supercritical hydrothermal combustion, etc., as well as the SCWO [13,15–17]. The SCWO treatment units constructed by HydroProcessing in Harlingen, TX, USA and Shinko Pante in Kobelco, Japan were forced to shut down due to severe corrosion in the preheater and reactor front [16]. Pitting corrosion is an essential cause of material failure in chlorine-containing subcritical/supercritical water systems [18].

A summary of the above discussion can be obtained: Advanced nuclear water-cooled reactors, (ultra) supercritical thermal power plants, as well as a series of supercritical water treatment techniques all involve highly harsh sub-/supercritical aqueous systems, which can lead to severe corrosion problems of materials [19,20]. In sub-/supercritical water environments, changes in temperature and pressure can cause changes in water density, dielectric constant, viscosity, and other characteristics. Taking water density as an example, an increase in temperature leads to a continuous decrease in water density, a reduction in charge transfer rate, and a shift in the corrosion process within the system from electrochemical reaction influence to chemical reaction influence, and this has been discussed in detail in other papers [1,13]. Materials used in sub-/supercritical water environments mainly include stainless steel, nickel-based alloys, and ceramics. However, nickel-based alloys with stronger corrosion resistance are the most commonly used for more complex supercritical water environments containing salt and oxygen. At the same time, ceramic materials have a risk of fragmentation and are, therefore, less commonly used [14]. Meanwhile, the application of some chromium-containing coatings, zirconia coatings, and titanium oxide coatings in subcritical/supercritical water environments has also been widely studied [21–23]. Studying and solving the corrosion problem of typical alloys in

sub-/supercritical water environments is significant for promoting the development of the techniques mentioned earlier. However, the current investigation on alloy corrosion in sub-/supercritical water mainly focuses on the use of offline testing methods, which often require cutting and sampling of equipment walls, pipelines, etc., causing irreversible damage and the inability to obtain real-time corrosion data during long-term operation, resulting in significant limitations [6,24–27]. On the other hand, there is an error between the data measured under the laboratory simulation system and the actual corrosion data during equipment operation [28], so the method of in situ online monitoring of corrosion data is essential.

To date, various in situ online corrosion monitoring technologies have been developed to compensate for the shortcomings of offline characterization testing techniques. Non-invasive testing techniques, such as ultrasonic monitoring, infrared thermography, etc., do not directly contact the system, avoiding damage to monitoring equipment and testing systems. However, considering that the corrosion of alloys is predominantly caused by the electrochemical processes that occur in subcritical and high-density supercritical water systems, several electrochemical in situ online monitoring technologies as invasive methods are equally significant. Therefore, this article systematically summarizes and compares the principles, advantages and disadvantages, applicable scenarios, and development progress of representative monitoring technologies from the perspectives of non-invasive and invasive methods. This work has essential academic and engineering significance for deepening corrosion scientific research, promoting the development of corrosion monitoring techniques, and ensuring the mature landing and safe operation of a series of advanced sub- and supercritical water equipment in new energy, power generation, and environmental protection.

2. Non-Invasive Monitoring Techniques

Non-intrusive monitoring techniques, which means that the monitoring device does not have any contact with the tested system, mainly include (laser) ultrasonic monitoring, optical fiber sensing, Eddy current monitoring, magnetic flux leakage monitoring, microwave monitoring, terahertz (THz) monitoring, thermography method, radiograph monitoring, acoustic emission, etc. Due to space limitations, this article will only focus on the representative non-invasive monitoring technologies, of which the summaries are given in Table 1. The detailed introduction is as follows.

Table 1. Summary of various non-invasive monitoring methods and their characteristics.

Monitoring Techniques	Principle	Data Presentation	Advantages	Disadvantages	Application	Error or Accuracy
Ultrasonic measurement [29,30]	Highly sensitive to structural damage; high permeability to materials	Depth of corrosion pits and thickness of corrosion layer	Real-time, suitable for both internal and external corrosion	Not appropriate for small, thin materials	Large-scale testing of oil pipelines and other facilities	Error less than 15%
Infrared thermography [31,32]	Recording electromagnetic waves emitted by objects and establishing a clear relationship between temperature and material corrosion defects	Defect size, depth, and thermal characteristics	Reliable, fast, direct, and wide testing range	Required heating and cooling processes; not suitable for thick materials; costly	Extreme temperatures and environments	Affected by changes in the thermal characteristics of objects and environmental conditions

Table 1. *Cont.*

Monitoring Techniques	Principle	Data Presentation	Advantages	Disadvantages	Application	Error or Accuracy
Microwave imaging [33,34]	Based on the interaction between microwaves and dielectric materials	The dielectric performance changes caused by defects or structural abnormalities are converted into readable voltage values and then processed and output as images.	Easily accessible to the coated materials.	Have difficulties penetrating conductive materials; it is limited to surface corrosion detection, whereas the deeper corrosion is undetectable.	Determine concrete properties, etc.	Accuracy better than 1/100 of the period length
Eddy current detection [35,36]	Detect discontinuities such as corrosion and material loss by monitoring changes in coil impedance or measuring induced magnetic fields.	Depth of corrosion layer, corrosion rate, conductivity and permeability, etc.	It is fast and most commonly used in conductive materials; it is portable and cheap	It is sensitive to skin effects and is surface-oriented.	Suitable for materials of various shapes	Error less than 5% for the thickness of various corrosion [36]
Acoustic emission [37,38]	Materials emit transient sound waves locally due to the rapid release of energy.	Deposition of corrosion products, the rupture of passivation films, and the initiation and propagation of cracks	Passive, non-intrusive, low-cost real-time and remote monitoring	Sensitive to background noise	wavelet analysis, modern spectral analysis, and neural network analysis	The accuracy of signal classification is about 65%

Note: The above accuracy or error data are reference values, and actual monitoring errors are influenced by various factors such as testing methods, properties of the tested item, and environmental factors.

2.1. Ultrasonic Thickness Measurement

The fundamental principle of the ultrasonic monitoring method is to generate mechanical waves or vibrations in tested samples in experimental laboratories or actual environments [8,39], as shown in Figure 1a. Ultrasound is generated and received in different ways. The most common method of generating and receiving ultrasonic waves is piezoelectric transducers, which are transmitted to the tested material through an acoustic coupler, while electromagnetic acoustic transducers generate waves directly in the tested material [29]. Ultrasound is highly sensitive to structural damage and has high permeability to materials. The second harmonic provides valuable information about material damage conditions by measuring the amplitude ratio of the fundamental and second harmonics [40,41]. In some countries, ultrasonic monitoring has been used as a standardized evaluation method for compressive strength and material crack depth [30]. When conducting large-scale corrosion monitoring on the high-temperature pipes of thermal power plants and oil pipelines, ultrasonic monitoring can accurately and quickly determine where corrosion occurs. Using guided ultrasound in these situations has the following advantages: fast response speed, high sensitivity in detecting minor defects, and suitability for large-scale and long-distance testing [30,42]. Meanwhile, ultrasonic monitoring can be directly performed outside the

component without using probes in contact with the corrosive environment during the testing process, so it is non-invasive to closed containers [43].

The commonly used monitoring methods based on ultrasonic testing techniques include contact piezoelectric transducers [44], lasers [45], and capacitance techniques. Contact piezoelectric transducers have low operating costs but higher requirements on the polishing degree of the contact surface to ensure good contact between the detection element (the transducer) and the sample surface. Unfortunately, this technique is unsuitable for harsh environments with high temperatures, high pressure, and strong corrosivity. Another method, the ultrasonic laser wave method, can somewhat compensate for these shortcomings. The advantage of the ultrasonic laser is that it can measure without sample contact and allows for point detection. It still has high-resolution scanning ability when working under high temperatures and pressure [46,47]. However, this test requires a sufficiently high surface finish of the sample [48]. Therefore, the signal-to-noise ratio is high. The third ultrasonic method, the capacitive ultrasonic transducer, has high sensitivity and can measure the absolute displacement of first and second harmonics. However, sample preparation is cumbersome [30,49].

Liu et al. [50] introduced the use of the piezoelectric pulse-echo method in corrosion monitoring. As shown in Figure 1a, the ultrasonic signal travels through the water medium, is then reflected by the specimen, and is finally received by the transducer. The typical time-domain signals from piezoelectric pulse-echo measurements of high-temperature nickel-based alloys with different corrosion layer thicknesses are displayed in Figure 1b. The signal is offset to compare the thickness of varying corrosion layers. The green line represents the reflectivity of the pipe back, while the red line represents that of the internal interface.

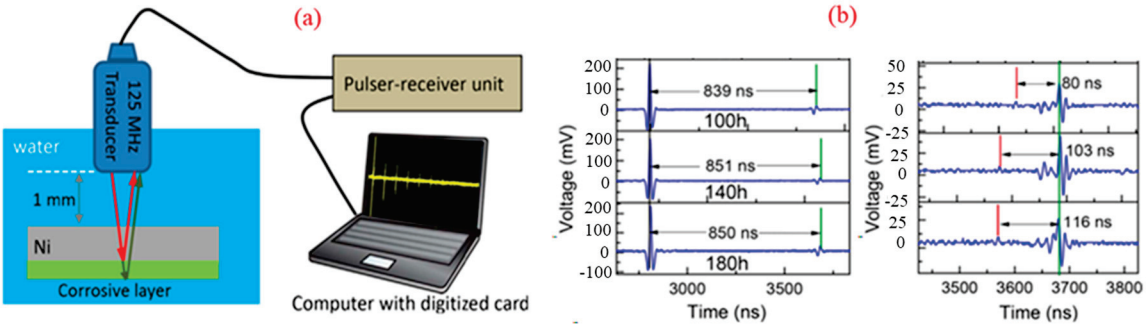

Figure 1. Schematic diagram of the device and principle for ultrasonic measurement (**a**) and typical results (**b**) Reprinted from Ref. [50]. 2018, Elsevier.

2.2. Infrared Thermography Method

Temperature is one of the most common indicators to measure the health status of equipment and components [32,51,52], and based on this, the infrared thermal (IRT) imaging technique has been developed. It provides a reliable, fast, direct evaluation method with a broad response range. It uses infrared imaging systems (such as infrared cameras) to record electromagnetic waves emitted by objects and establish a clear relationship between temperature and material corrosion defects [53]. The advantages of IRT are as follows: as a non-invasive technique, IRT does not affect the target [51,54] and can safely monitor very high temperatures or dangerous objects [54]; IRT provides two-dimensional images for comparison of different regions of the target [54]; IRT is an online (real-time) monitoring technique that can achieve large-scale real-time monitoring (with the help of advanced image processing techniques) [32,54,55].

Thermal imaging techniques can be divided into two categories: active and passive. In active thermal imaging, in addition to a thermal imager, an external excitation source is also needed to stimulate the thermal evolution inside the object during heating or cooling. On the contrary, passive thermal imaging does not require an external stimulus source because the object is at a temperature naturally different from the background

(such as the human body). Passive thermal imaging is more commonly considered a qualitative method for identifying abnormal temperature patterns. Worthy of special description, it is the particular controlled requirements of the active thermal imaging method, including the amount and form of stimulation, that enable it to allow for not only the identification of defects but also quantitative analysis of anomalies, such as the characterization of the physical and thermal characteristics of defects. The excitation mechanisms in active imaging techniques mainly include optical thermography, laser thermography [56], induction thermography [57], vibrothermography [58], and microwave thermography [59,60].

Metal defect size, defect depth recovery/reconstruction, and defect thermal characteristics, such as thermal diffusivity, are considered quantitative IRT methods for evaluating corrosion and metal loss [32]. During the analysis and processing of corrosion data measured by IRT, thermal contrast calculation is the most commonly used method to improve the visibility of subsurface defects. Among them, absolute temperature contrast is achieved by assigning color or intensity to each infrared energy level corresponding to electromagnetic flux or exact temperature (through radiometry), converting images obtained using infrared cameras into visible images (heat maps) [54]. Absolute thermal comparison requires consideration of two critical assumptions. Firstly, we need to understand the sound field's position within the field of view of an infrared camera; secondly, we need to consider that thermal stimulation is uniform on the sample. To address the testing limitations brought by these two hypotheses, Pilla et al. proposed a modified version of absolute thermal contrast, named differential absolute contrast (DAC). In addition, the analysis methods for IRT results also include temperature signal reconstruction (TSR) using temperature and contrast derivatives, statistical techniques, matrix factorization, phase-sensitive techniques, and artistic intelligence-based techniques. Please refer to [32] for detailed information.

As for the IRT mechanism exhibited in Figure 2, the total radiation received by the camera comes from three typical sources: emission from the target object (E_{obj}), emission and reflection from the surrounding environment (E_{refl}), and emission from the atmosphere (E_{atm}). However, since not all received radiation comes from the target object, to accurately measure temperature, it is necessary to compensate by removing radiation from other sources (such as surrounding objects or the atmosphere) when converting to temperature [54].

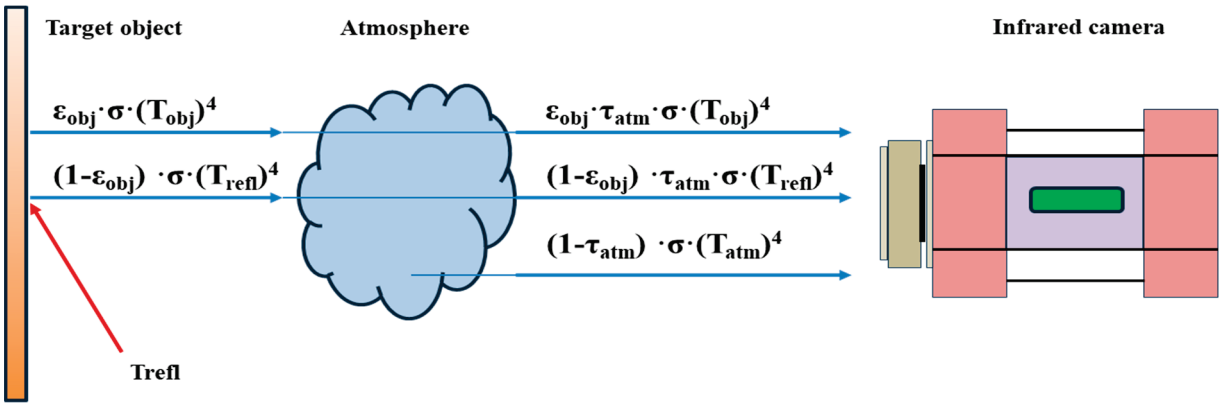

Figure 2. Radiation energy received by the infrared camera Adapted with permission from Ref. [54]. 2014, MDPI.

IRT can also detect water inclusion defects in composite sandwich structures. Figure 3 shows the effective detection of water corresponding to colder surface areas in the actual rudder of an aircraft by IRT. Thermal imaging can detect the phase change energy required for melting and infiltrating water, as it generates temperature changes.

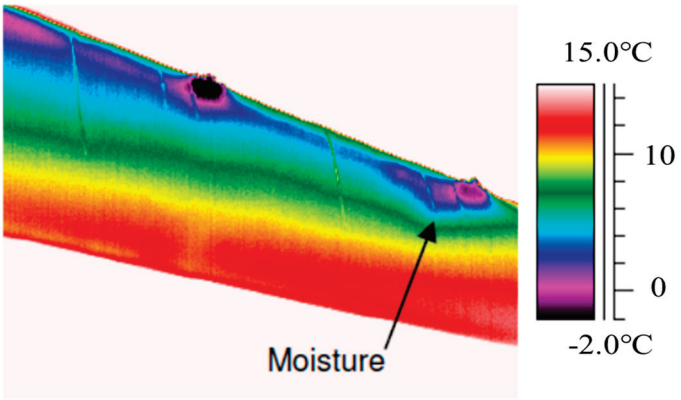

Figure 3. Moisture detected under the upper hinge of the rudder test sample Reprint with permission from Ref. [54]. 2014, MDPI.

2.3. Microwave Imaging

Microwave non-destructive testing is based on the interaction between microwaves and dielectric materials. The frequency range of employed microwaves is generally 5–50 GHz. At this frequency range, defects or structural abnormalities in the material can cause enough changes in dielectric property. With the help of corresponding analysis software, this dielectric difference can be converted into readable voltage values, which can then be restored to images of internal defects and structures through specific algorithms. The schematic diagram of the microwave detection is shown in Figure 4a, taking one steel plate covered by coating as an example. The near-field of an open waveguide illuminates the incident signal. It is transmitted into layered media (the coatings and the steel plate substrate) and reflected by conductive plates. The ratio of these two signals gives the effective reflection coefficient of the tested sample [61].

The microwave transmitter inside the energy emission device emits the selected microwave signal within a specific frequency range, ensuring the microwave propagates in the tested dielectric material. Different dielectric characteristics will reflect changes in the material structure or internal defects. These subtle differences can cause changes in the amplitude and phase of the reflected microwaves. The receiving sensor within the measurement unit can recognize and collect the performance parameters of the reflected waves and perform real-time analysis and calculation, ultimately displaying real-time images of the dielectric material's internal structure and defect morphology, as given in Figure 4b,c. Microwaves can effectively penetrate dielectric materials, and any small discontinuity in the material can cause changes in its dielectric properties. Microwaves are very sensitive to changes in dielectric properties, so they have a very high detection sensitivity for any slight defects in dielectric materials [62].

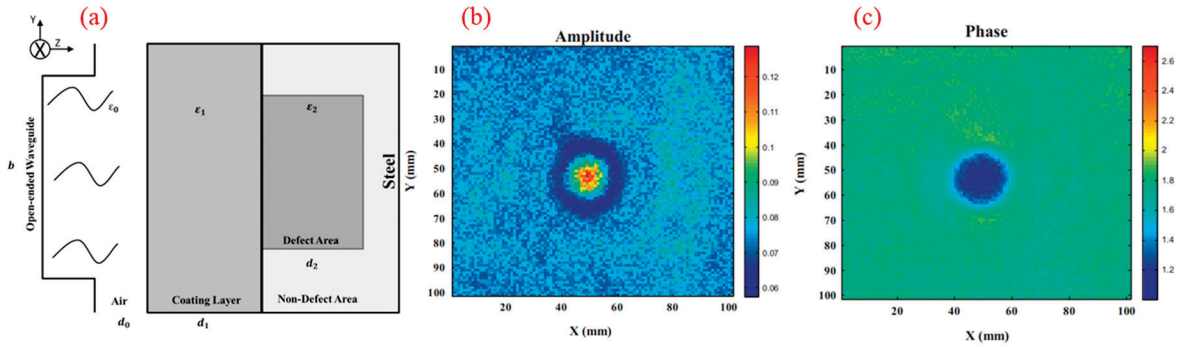

Figure 4. Microwave reflection and transmission for coated metal (**a**) and the changes in amplitude (**b**) and phase (**c**) microwave detection Reprinted from Ref. [61]. 2013, Elsevier.

The microwave non-destructive monitoring supports remote detection, estimates defects' physical size and direction, and is easy to operate [63,64]. Microwave NDT techniques may be the unique solution in some situations (such as high temperature applications) [61]. Near-field open waveguide non-destructive microwave imaging seems to be one of the most promising techniques for detecting the presence of a particular layer or internal defects in layered structures [61,65]. In recent years, microwave non-destructive testing (MNDT) has significant potential in determining the properties of concrete, as it is highly effective in detecting pores, cracks, unevenness, and defects [33].

The main application of microwave imaging techniques in metal corrosion monitoring is as follows: a waveguide probe with primary mode excitation is used to irradiate structures with electromagnetic waves in the proper frequency range. The amplitude and phase difference between the reflection coefficients of non-coated and coated samples are related to the tested layer thickness and dielectric constant. Generally, there is a significant difference in attenuation and reflection signals between the defect and non-defect areas. The differential characteristics recorded in the reflection signal are employed to detect and determine the defect size of the tested sample. The calculation of reflection coefficients for various media mainly includes deriving the forward and backward propagating electric and magnetic field components in each layer based on the known incident field and applying appropriate boundary conditions at each interface. These complex reflection coefficients refer to the complex number of spectral changes in their phase and amplitude. The measurement data will provide information about the location and size of defects [66]. This highly sensitive interaction is a function of defect size and position within the waveguide aperture [61].

2.4. Eddy Current Detection

Eddy current testing (ECT) is based on the interaction between the main magnetic field and the tested material to generate eddy currents within the specimen [67,68]. Discontinuity features such as corrosion and material loss can be detected by monitoring changes in coil impedance or measuring induced magnetic fields [36,67,69]. The significant advantage of ECT is that it can detect defects under high-temperature conditions, and its probes can be made into various shapes to adapt to different objects. However, the ECT detection of deeper defects within the material substrate still faces issues of lower penetration depth and skin effects of ferromagnetic materials [35]. Traditional ECT works at a single frequency, where a sine wave drives the excitation coil, of which the application, in the case of non-conductive composite materials, may be limited by penetration depth due to the impact of delamination on the signal-to-noise ratio [70,71]. Typical eddy current probes include impedance change probes and excitation detection probes. Several commercial probes, such as absolute and differential tube probes, electric rotary probe coils, and array probes, have been widely used for pipeline detection [72]. ECT has several advantages: (1) non-contact detection can penetrate the coating layer without coupling medium; (2) defects can be detected under the condition of high temperatures, and the probe of ECT can be made into various shapes to adapt to different objects; (3) it has a higher sensitivity to near-surface defects [35].

The general schematic of the pulse eddy current (PEC) system is depicted in Figure 5a, by which Yunze He et al. [73] investigated the corrosion problem of soft steel (S275). The PEC response caused by corrosion is a complex combination of many factors. The two time-domain features extracted from the PEC response, representing the changes in conductivity and permeability of the corrosion layer or actual corrosion area, are generally used to characterize corrosion behavior. Additionally, the relationship between PEC characteristics and exposure time, which can be used for measuring corrosion rate and early corrosion assessment and prediction, has been derived. The experimentally obtained values and fitting lines of PV (Bnorm) for uncoated and coated samples are shown in Figure 5b [73]. The measurements at different exposure times were performed under the same excitation, taking the average measured results as the experimentally obtained values.

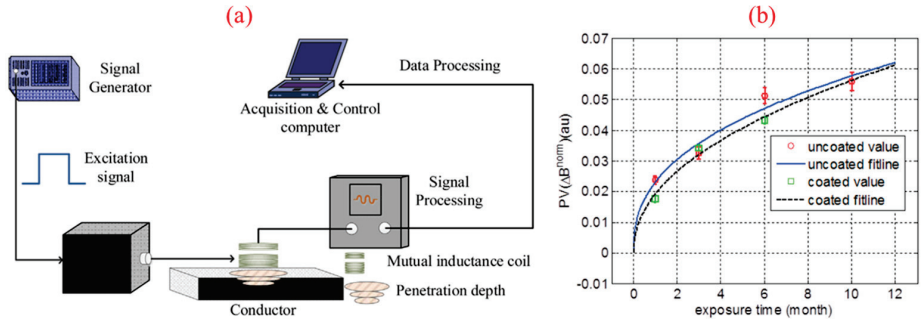

Figure 5. A typical schematic of the PEC system (**a**), as well as the measured values and fitted lines of PV(Bnorm) for uncoated and coated corrosion (**b**) Reprinted with permission from Ref. [35]. 2019, Elsevier and from Ref. [73]. 2012, IEEE.

2.5. Acoustic Emission

Acoustic emission (AE) refers to the phenomenon where a material emits transient sound waves locally due to the rapid release of energy. The deposition of corrosion products, the rupture of passivation films, and the initiation and propagation of cracks all generate AE signals with different characteristic parameters [38,74]. Therefore, based on this information, the occurrence time, starting sites, and severity of corrosion damage can be determined. The application of acoustic emission techniques in electrochemical corrosion research has a history of more than 40 years, with existing research mainly focusing on monitoring acoustic emission signals during the electrochemical corrosion processes to determine the corrosion locations and degrees.

Actually, during the electrochemical corrosion process, the generation and movement of hydrogen gas, stress changes of the metal surface, deposition of corrosion products, rupture of passivation films or salt layers, and oxygen reduction may all be sources of acoustic emission. Meanwhile, it is necessary to establish the relationship between acoustic emission signals and electrochemical corrosion rate, corrosion potential, etc. Based on this, it is possible to identify the characteristic acoustic emission signals in the electrochemical corrosion process and clarify the corresponding physical correspondence [75]. The application of AE in the on-site measurement of small-diameter drilling processing status is shown in Figure 6.

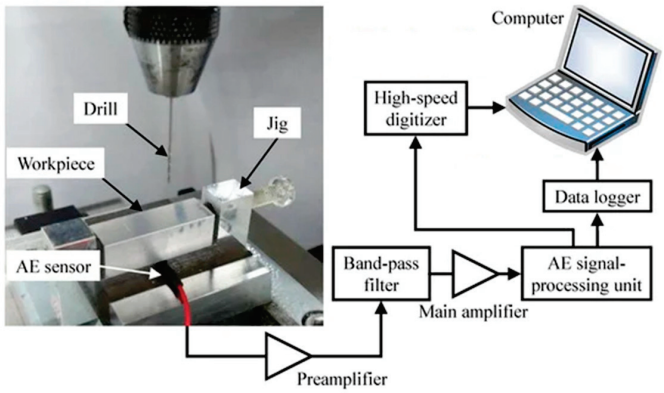

Figure 6. Experimental setup and the AE measurement system mounted on a small automatic drilling machine Reprint with permission from Ref. [76]. 2024, MDPI.

However, the difficulty in AE monitoring under normal and high-temperature conditions is how to analyze the signal. The diversity of AE sources and the suddenness and uncertainty of signals pose significant challenges to analyzing AE data and establishing corresponding relationships between AE signals and corrosion behavior. In addition, attenuation of sound signals, reflection of sound waves, mode conversion, structural correlations or discontinuities, and interference from background noise can all hinder the analysis of

AE signals [77]. Currently, the commonly used AE analysis method is parameter analysis. Various signal processing techniques, such as wavelet analysis, modern spectral analysis, and neural network analysis, have been successfully applied. The development of modal AE theory and related techniques has provided a new way to further explain AE signals' physical meaning [75].

AE has been used to monitor the coupled environmental cracking process in high-temperature and high-pressure water environments [78,79]. Yuyama et al. [80] believe that compared to room temperature, the oxide film formed on the surface of materials in high-temperature and high-pressure water environments is thicker and that the amplitude of AE signals generated by crack initiation and propagation is relatively higher, making it possible to monitor cracks. Alekseev et al. [81] investigated the sensitivity of various materials to SCC in chloride-containing environments at 300–320 °C and 70–80 MPa via AE. They indicate that the combination of the event count and amplitude of AE signals can determine cracks' initiation and instability. Cassagne et al. [82] conducted a similar study on nickel-based alloy 600 in a simulated PWR environment (290–330 °C) but used characteristic parameters such as the AE signal's amplitude, energy, and rise time. Máthis et al. [78] and Xu Jian et al. [79,83] studied the SCC process of solid solution and sensitized 304SS in high-temperature and high-pressure water. The AE signals generated during the transgranular SCC process include sudden and continuous types, with corresponding AE sources being crack propagation and plastic deformation [78,83]. However, only continuous AE signals are generated during the intergranular SCC process, corresponding to plastic deformation [79]. Although some studies suggest that AE is highly sensitive to the very early stages of crack development in high-temperature water, there are few related studies [84].

Various other non-invasive corrosion monitoring technologies are also widely used in engineering practice. Multi-frequency electromagnetic sensors, consisting of a transmitter and receiver coil, can be used for the corrosion and integrity detection of oil pipelines. Due to the skin effect, low-frequency electromagnetic scanning can calculate the thickness of pipeline metal, while high-frequency electromagnetic scanning can detect the characteristics of the inner wall [44]. Optical fiber sensors (OFS) are also small, flexible, lightweight, susceptible, and compatible with fiber optic data communication networks, which can measure corrosion in several areas within a single optical channel. Passive radio-frequency identification (RFID) sensors, especially chipless passive RFID sensors, are a comprehensive wireless sensor family for pipeline corrosion, with low cost, compact size, lightweight, and remote sensing [8]. These non-destructive monitoring techniques are primarily based on physical methods, which monitor the contour, depth, and other characteristic information of the corrosion layer online and, to some extent, provide information on alloy corrosion behavior. They have broad application prospects in the corrosion monitoring of pipes and equipment exposed to sub-/supercritical water systems. Please see the literature for more detailed information on non-destructive monitoring techniques for alloy corrosion [8,85].

3. Invasive Corrosion Monitoring Techniques

The electrochemical online corrosion monitoring technique has the characteristics of high sensitivity, fast response speed, stable long-term service, a simple process, and low cost. It can accurately determine the corrosion rate and form of materials and achieve automatic feedback control at industrial sites. More importantly, based on alloys' electrochemical corrosion data, corrosion rate prediction, stress corrosion cracking evaluation, and other related determinations can be carried out. Electrochemical corrosion monitoring methods have broad application prospects in complex extreme sub-/supercritical water environments, such as higher temperatures, pressures, and high content of salts and dissolved oxygen; occurrence in cooled-water nuclear power plants; and advanced supercritical water treatment equipment.

3.1. Electrical Resistance Probe

The electrical resistance probe technique obtains corrosion loss and corrosion rate data by measuring the resistance change of metal specimens. The corrosion products of metals, such as metal oxides, are mostly non-conductive. If current is applied to a metal sheet, as corrosion progresses, the thickness of the metal sheet will decrease, increasing electrical resistance. The corrosion rate can be obtained after extending the information on resistance variation over time to the relationship between material thickness and corrosion time. This type of resistance probe is also known as an electronic mount [86,87].

As shown in Figure 7, during the monitoring process, one side of the metal specimen is exposed to the environment t, and a current goes through the metal specimen. The electrical resistance of the metal specimen can be calculated as follows:

$$R = \rho \frac{l}{A} \tag{1}$$

In the formula, ρ represents the conductivity of the metal test piece, A is the cross-sectional area of the metal piece, and l stands for the length.

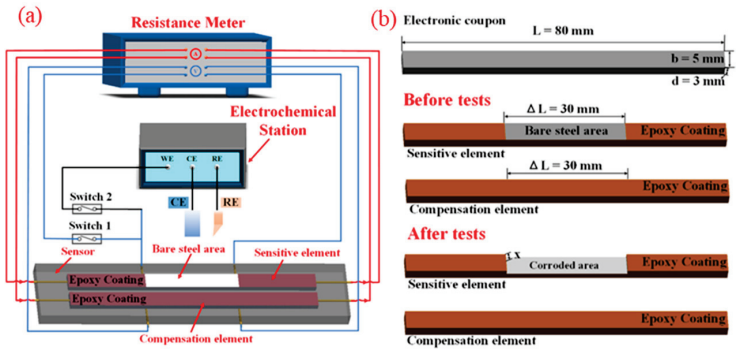

Figure 7. Schematics of the electrical resistance sensor for corrosion measurement: (**a**) the measurement circuit and (**b**) a three-dimensional diagram of the sensitive and compensation elements Reprint with permission from Ref. [88]. 2022, MDPI.

Liu et al. [88,89] used an electrical resistance probe to study the corrosion of pipeline steels, as depicted in Figure 7. As corrosion progresses, by monitoring the change in resistance value, the change in corrosion thickness can be derived based on Formula (1), thereby obtaining information on corrosion loss and corrosion rate. The electrical resistance probe technique is available for measurement in liquid solutions (electrolyte or nonelectrolyte), gas environments, and other media. It has the characteristics of relatively simple operation, easy maintenance, and easy data analysis. Moreover, it can achieve real-time corrosion data collection and transportation. Compared with other monitoring methods, it is highly reliable and has a better economy, making it widely used in industries such as oil and gas production, pipelines, the chemical industry, cultural relic preservation, and power generation.

3.2. Electrochemical Corrosion Potential

When electrochemical corrosion is carried out on an isolated metal material, the cathodic and anodic reactions occur at the same potential, which is the mixed potential of these two electrode reactions coupled with each other. In corrosion electrochemistry, it is called the electrochemical corrosion potential (ECP) [90]. Since the corrosion of materials in aqueous solutions is essentially controlled by electrochemical processes, there is a specific correspondence between the ECP of materials and their corrosion behavior. Therefore, measuring ECP can be used to determine the corresponding corrosion status of materials, which can serve as a basis for adjusting environmental parameters and achieving the goal of controlling corrosion behavior. The measurement of ECP has no interference with the tested system and can perform in situ, non-destructive, long-term continuous measurement.

Constructing an alarm system based on the changes in ECP signals is easy and suitable for on-site corrosion monitoring.

The ECP test results for two nickel-based alloys are shown in Figure 8 [91]. In fact, in most studies, the OCP test results are used to roughly represent the ECP values; the ECP described in Figure 8 is the OCP test result. Figure 8a shows that the corrosion potential of 690 and 800 alloys monotonically decreases with the increase in pressure at 25 °C. Figure 8b shows that at a constant pressure of 10.0 MPa, the self-correction potential of 690 and 800 alloys varies with temperature at different temperatures, which can be roughly divided into two temperature influence intervals. The first temperature influence interval is from 25 °C to 250 °C, and with the increase in temperature, the self-corrosion potential of 690 alloy and 800 alloy decreases almost linearly, with the second temperature range being 250 °C to 300 °C. The average self-corrosion potential of 690 alloy and 800 alloy is very similar.

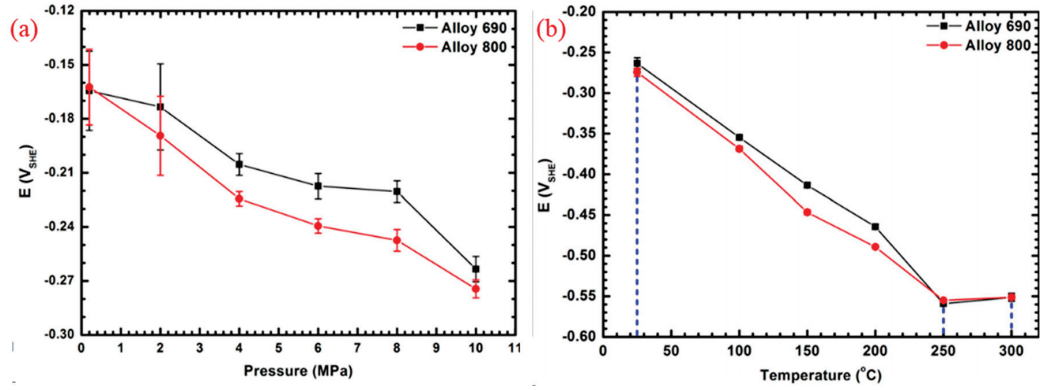

Figure 8. Typical dependence of ECP (OCP) on (**a**) pressure at 25 °C and (**b**) temperature at 10 MPa for Alloy 690 and Alloy 800 Reprinted from Ref. [91]. 2013, Elsevier.

The acquisition of ECP data requires using a potential meter with a high internal resistance (significantly greater than 10^6 Ω) to monitor the system composed of the working material to be tested and the stable reference electrode. As for the ECP of materials, it is usually necessary for guiding the polarization curve measurement, assisting the drawing of potential–pH diagrams (E–pH), as well as determining the critical or sensitive potential ranges for local corrosion behaviors, such as pitting corrosion, crevice corrosion, and stress corrosion cracking (SCC). Based on the mutual verification relationship between these electrical corrosion data, judging whether the material will undergo corrosion problems is convenient.

ECP monitoring at nuclear power plants is the most representative application. So far, ECP monitoring is the only method not requiring depressurization, current limiting, or cooling sampling to obtain in situ electrochemical information on the water chemistry and corrosion environment of advanced water-cooled nuclear reactors. Currently, ECP is mainly used as a data reference for the hydrogenation water chemistry of BWRs and PWRs and the oxygenation water chemistry of PWR secondary circuits in nuclear power corrosion monitoring [92]. Corrosion prevention and control can be achieved by adjusting the ECP below the SCC critical potential and to the stable range of the oxide film by combining the E-pH diagram [93,94].

Due to each nuclear power plant's different operating environmental parameters, the consistency of ECP monitoring results is poor. Therefore, conducting online ECP monitoring at each nuclear power plant is necessary. However, there are still the following issues in the current ECP monitoring of nuclear power plants: (1) there is no mature high-temperature reference electrode that fully meets the long-term monitoring requirements; (2) due to the complex structure of nuclear power plants, the corrosion reactions occurring at different structural sites are also complex. The cost is high once the online ECP monitoring is performed on many sites.

The theoretical calculation of ECP can somewhat solve the complex, costly online monitoring problem. Christensen et al. [95], Dixon et al. [96], and Burn et al. [97] proposed a water radiolysis model that can calculate the concentrations of oxidation–reduction substances at selected locations inside nuclear power plants. Kim et al. [98] and Macdonald et al. [99,100] combined the water radiolysis model with the mixed potential model and then proposed a semi-empirical formula based on laboratory test results to calculate the ECP value of 304SS at a selected location inside the BWR reactor. Macdonald et al. [101] also extended the ECP calculation to PWR. However, due to the lack of primary thermodynamic data, there are currently no reports on ECP calculations for other materials, and the reliability of the calculated ECP values also needs to be verified.

3.3. Electrochemical Impedance Spectroscopy

Electrochemical impedance spectroscopy (EIS) is a frequency-domain data analysis that studies the variation of electrochemical impedance with frequency by applying a small-amplitude sinusoidal AC excitation signal when the electrochemical system is under a stable DC polarization condition. EIS measurement has a lower system disturbance and a wide testing frequency range. It can obtain in situ dynamics data on electrochemical processes and electrode interface structure information related to electrochemical corrosion without damaging the system. It is suitable for online corrosion monitoring. On the other hand, there is an approximate linear relationship between disturbance and the corresponding system, which can simplify the mathematical processing of test results. As a branch of the impedance spectroscopy technique, dynamic electrochemical impedance spectroscopy can obtain richer electrochemical information and has been used in the study of material passivation films [102].

Electrochemical impedance spectroscopy contains rich information on the microscopic mechanisms and microscale process dynamics behind electrochemical corrosion behavior [103,104]. However, most studies usually use the "direct equivalent circuit method" to analyze electrochemical impedance spectroscopy data, which can only obtain macroscopic values of equivalent circuit components in the corrosion system, such as resistance, capacitance, etc., and fail to provide microscale process information such as atomic-scale dynamics of alloy corrosion. Establishing an impedance mathematical model of the alloy matrix | passivation film system based on the corrosion microscale process is a crucial foundation for obtaining information on the corrosion microscale process by analyzing electrochemical impedance spectroscopy data. The Bode plots of several typical impedance spectrum test results are shown in Figure 9.

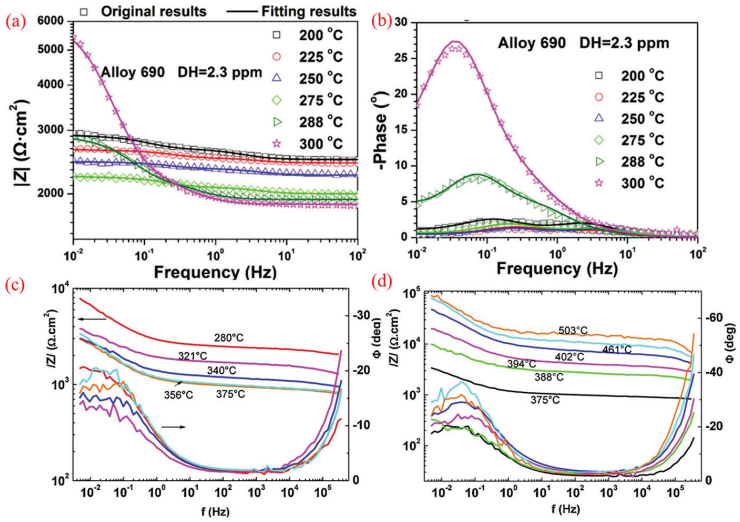

Figure 9. Typical electrochemical impedance spectroscopy data for (**a**,**b**) alloy 690 at 200–300 °C Reprinted from Ref. [105]. 2018, Elsevier and for (**c**,**d**) 316L stainless steel in subcritical and supercritical water Reprinted from Ref. [106]. 2019, Elsevier.

Ai et al. [107] and the authors of this paper [108,109] have employed the point defect models and the experimentally obtained EIS data to analyze the atomic scale corrosion anodic processes of some metals and alloys, such as zirconium alloy, stainless steel 304, and nickel-based alloy 600, under high-temperature conditions. For example, Ai et al. [107] pointed out that the rate constant of "the transformation from zirconium atom to the lattice zirconium within ZrO_2" at the interface of the polycrystalline zirconium matrix/passivation film at 250 °C is 2.42 × 10^{-15} mol·cm^{-2}·s^{-1}, with a charge transfer coefficient of approximately 0.27. The authors' previous research found that the growth of the barrier layer of the passivation film and the thickening of the film's porous outer layer are determined by two atomic-scale processes at the interface between the passivation film and the substrate of stainless steel 304 in a PWR coolant simulation solution at 300 °C. They are, respectively, the process of the chromium-predominant metal atoms converting into lattice cations in chromium-rich oxides of the barrier layer and the transformation process of the iron-dominated metal atoms, which release electrons and enter the passivation film in the form of cation interstitials. The reaction rates are all approximately 10^{-11} mol·cm^{-2}·s^{-1} and are influenced by water chemistry parameters such as pH value and dissolved oxygen content [109]. In the similar simulated solutions of the primary circuit coolant of PWRs, the rate of metal atom conversion to cations at the interface between the alloy substrate and the passivation oxide film for nickel-based alloy 600 is relatively lower, ranging from 1.5–4 × 10^{-12} mol·cm^{-2}·s^{-1}, than that of the stainless steel 304 [108]. The relevant content, such as point defect theory and electrochemical impedance spectroscopy analysis, has been detailed in our previous articles [1,110] and will not be further elaborated here.

3.4. Electrochemical Noise

Electrochemical noise (EN) refers to the random non-equilibrium fluctuation phenomenon of electrochemical state parameters (such as electrode potential, external measured current density, etc.) during the evolution of electrochemical dynamic systems [111]. This fluctuation phenomenon provides rich evolutionary information for the system. The electrochemical noise technique has been widely applied in industrial electrochemistry, including metal corrosion and protection, chemical power supply, and metal electrodeposition [111,112]. As an in situ, online, and non-interference detection method, it can monitor the uniform and local corrosion of materials online and the type and strength of corrosion remotely [113].

When applying electrochemical noise techniques to monitor electrochemical corrosion in high-temperature water, attention is usually paid to corrosion potential or current noise. Monitoring the current noise usually involves connecting two working electrodes of the same material through a zero-resistance meter to monitor the coupling current between them. However, monitoring potential noise requires using reference or pseudo-reference electrodes, which face the same hardware limitations as ECP testing. In addition, the difficulty of applying EN in high-temperature water systems lies in how to reduce the internal noise of equipment to improve the accuracy and precision of data [84]. The key to successful monitoring is to use stable and reliable reference electrodes, ensure high conductivity of the test solution [114], and reduce the distance between the test electrode and the reference electrode to reduce background noise [115].

Figure 10 shows an example of EN monitoring results for Q235B steel exposed to the atmosphere of Tianjin city for 20 days [86]. When the humidity is low, the electrochemical current noise (ECN) and electrochemical potential noise (EPN) amplitudes are very small, with only a few nanoamps and millivolts, indicating a significantly lower corrosion rate. When the relative humidity increases to 65%, the fluctuation amplitude of ECN and EPN substantially increases, and the corrosion rate of Q235B steel correspondingly increases. The evolution of noise resistance (Rn) is closely related to humidity. As humidity rises, Rn values decrease accordingly; Rn increases correspondingly with the decrease in moisture [116].

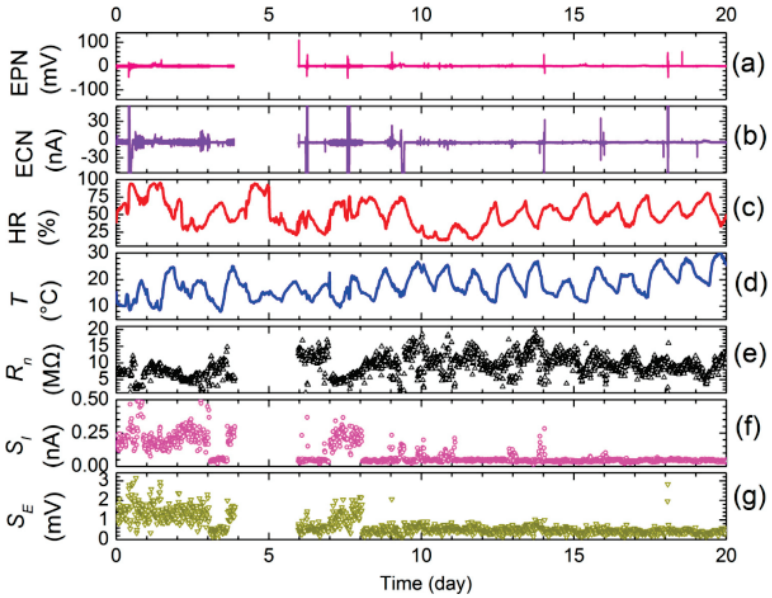

Figure 10. EN monitoring results of Q235B steel exposed to Tianjin urban atmosphere over 20 days. (**a**) electrochemical potential noise; (**b**) electrochemical current noise; (**c**) relative humidity; (**d**) temperature; (**e**) noise resistance; (**f**) ECN standard deviation; (**g**) EPN standard deviation Reprinted from Ref. [116]. 2017, SAGE journals.

On this basis, analyzing EN data and extracting feature information containing electrochemical processes is crucial. The analysis of EN data can usually be divided into two types: time-domain and frequency-domain. Time domain analysis is a visual inspection, image fitting process (transient analysis), or statistical analysis of the original EN data. The temporary shape contains basic information about electrochemical processes. Some characteristic parameters obtained from statistical analysis, such as standard deviation, root mean square value, skewness, local index, etc., can be used for qualitative evaluation of pitting, SCC, and crevice corrosion processes [117], and the obtained noise resistance can quantitatively evaluate corrosion rate [118]. Some studies use the Fast Fourier Transform (FFT) or Maximum Entropy method, converting the EN signal from a time domain to a frequency domain and obtaining the Fourier spectrum or power spectral density [119].

In 1968, Iverson observed, for the first time, the random fluctuation of corrosion electrode potential over time in a corrosion electrochemical system (i.e., electrochemical noise) [120]. In the last decade, the application of electrochemical noise techniques in corrosion science and related scientific fields has increasingly attracted widespread attention. In the study of the local corrosion of metals, electrochemical noise can be used to determine corrosion types and study pitting corrosion and stress corrosion cracking characteristics. At the same time, the electrochemical noise technique can also be applied to coating performance evaluation and corrosion inhibitor screening, providing a powerful technique for studying material corrosion problems, protection, and surgical support.

Some scholars at home and abroad have adopted electrochemical noise techniques to investigate corrosion issues in high-temperature and high-pressure water systems. Zhou et al. [121] found a linear relationship between the weight loss rate of 304SS in high-temperature water and the reciprocal of noise resistance, consistent with the research results in room-temperature systems. Macák et al. studied the corrosion behavior of 304SS [122] and 08CH18N10T steel [123] in high-temperature water. They found that during the initial soaking stage, the noise resistance increased first and finally became stable. The average corrosion rate calculated using the experimentally obtained noise resistance is consistent with the EIS results. Song Shizhe et al. [124] performed the EN monitoring for stainless steel and carbon steel pipelines in the laboratory and industrial sites. They found that as the temperature increased, the measured noise resistance showed

a decreasing trend, and the value of the noise resistance corresponded to the rust on the surface of the pipeline. Another critical piece of research in the exploratory stage focuses on the online monitoring of EN signals for environmentally assisted cracking. Preliminary research has indicated that electrochemical noise signals are more sensitive to crack propagations, during which both the current signal's increase and the voltage signal's decrease can be monitored simultaneously [125,126]. If the crack propagation is discontinuous, a potential reduction with a long time interval will occur, accompanied by a significant increase in current. Suppose the crack rapidly expands and the surface oxide film does not have time to undergo re-passivation. In that case, it will decrease the potential signal and cause a continuous increase in the current signal [126]. However, due to the weak noise signals generated during the initiation and early propagation stages of cracks and the high interference of background noise, it is challenging to study the initial stage of environmentally assisted cracking using the EN technique.

3.5. Research Platform of In Situ Electrochemical Corrosion Testing

To investigate the electrochemical corrosion of alloys in high-temperature and high-pressure water systems, it is necessary to establish a research platform for simulating experimental environments. MacDonald and his group have extensively researched high-temperature electrochemical corrosion [127–130]. They have designed the circulating flow loop with a hydrodynamic autoclave vessel, as shown in Figure 11, which contains the storage tank, a high-pressure positive displacement pump (2 L/h capacity pulsating diaphragm pump), a hydraulic accumulator, a regenerative heat exchanger (cooled by freshwater), and so on. The circulating flow loop with a hydrodynamic autoclave can continuously update the solution in the reactor, keep the simulated solution in the testing area fresh, and avoid the interference of impurities and salt deposition during long-term experimental processes. Due to the existence of circulating loops, the reactor's design requirements and production costs are reduced. In addition, the circulating flow loop with a hydrodynamic autoclave designed in the research platform is consistent with most engineering practical application scenarios. The reference electrode is the core component of the electrochemical research platform, which mainly includes various reference electrodes such as hydrogen electrodes, YSZ electrodes, metal/metal oxide electrodes, external pressure balance reference electrodes, etc., especially the YSZ electrode, which has been successfully applied in high-temperature conditions exceeding 500 °C [1,106]. These contents are extensive and complex and will be further explored in another review article.

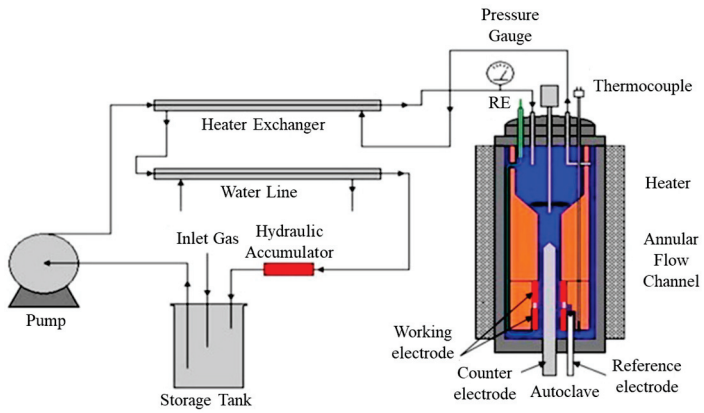

Figure 11. Once-through recirculating flow loop with hydrodynamic autoclave vessel Reprinted from Ref. [129]. 2010, Elsevier.

Based on the research platform established by Macdonald's group, researchers from the Institute of Metals (IMR) in the Chinese Academy of Sciences have developed a high-temperature electrochemical research platform that can monitor and control water quality, as shown in Figure 12. Two refreshed autoclaves were connected in series in the loop, with autoclave 1 arranged in the upstream section. Both autoclaves are made of stainless steel and have a 2 L volume. Autoclave 1 is lined with pure Ni, while autoclave 2 is not. These two autoclaves could be used collectively or solely during the exposure experiments. The inlet and outlet water chemistry parameters, namely dissolved oxygen concentration (DO) and conductivity, were monitored with METTLER TOLEDO Thornton Model 3X7-210 (METTLER TOLEDO, Zurich, Switzerland) dissolved oxygen sensors and Model 240-201 conductivity sensors, respectively. A computer with Labview 8.5 software was used to control temperature and DO. Temperature fluctuations in both autoclaves were controlled well within ± 0.5 °C, and DO fluctuation in inlet water was within ± 10 ppb (by weight) [131–133].

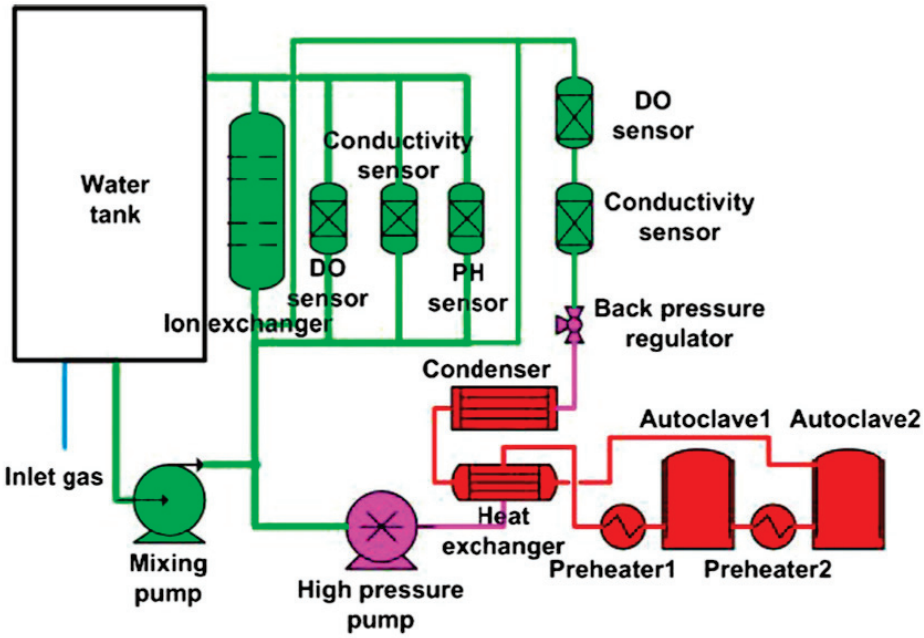

Figure 12. Schematic diagram of the high-temperature and high-pressure water loop in IMR Reprinted with permission from Ref. [131]. 2017, Elsevier.

Huang et al. investigated the corrosion electrochemical characteristics of nickel-based alloy 690 using the research platform, as shown in Figure 13 [134]. Figure 13a shows potentiodynamic polarization curves for Alloy 690 at 300 °C in 1500 ppm B and different concentrations of Li solutions without Zn injection. As the pH value increases, the electrochemical corrosion potential sharply decreases, and the passivation current density slightly decreases. This indicates that the 690 alloy forms an oxide film in all pH solutions studied and exhibits good corrosion resistance in alkaline solutions. Figure 13b shows the polarization curves of 690 alloy in solutions with different zinc concentrations at 300 °C, indicating an increase in zinc concentration enhances corrosion resistance. The passivation current density is 10^{-4} A·cm^{-2}.

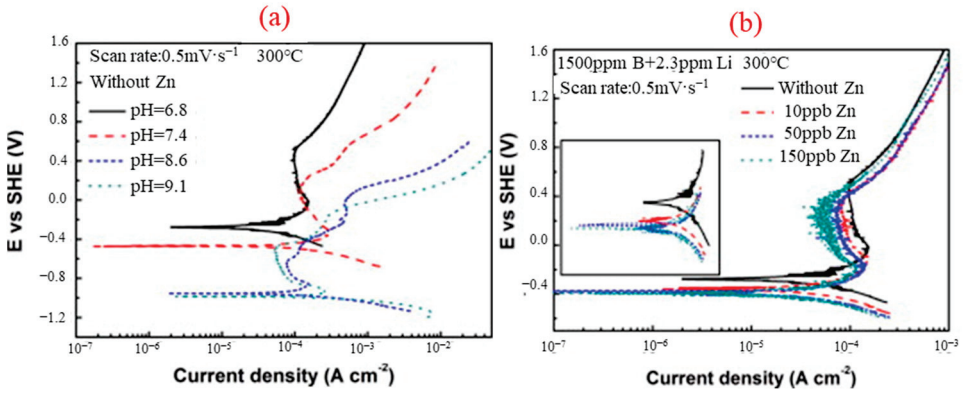

Figure 13. High-temperature potentiodynamic curves for Alloy 690 at 300 °C (**a**) in different pH solutions without Zn, (**b**) in solutions with 1500 ppm B, 2.3 ppm Li, and several Zn concentrations Reprinted with permission from Ref. [134]. 2011, Elsevier.

Li et al. from Xi'an Jiaotong University (XJTU) developed a new generation of multi-functional electrochemical research platforms, as shown in Figure 14 [135]. It comprises a high-pressure gas injection circuit, a low-pressure gas dissolution control circuit, a sub-/supercritical hydrochemical research device, and a sub-/supercritical water primary circuit. By comparison, this system directly introduces the target gas into the reactor through a liquid gas tank, which can effectively increase the upper limit of the dissolved gas concentration in the solution and is suitable for studying the effect of high-concentration liquefied gas on the electrochemical corrosion behavior of materials. Meanwhile, high concentrations of dissolved gases are beneficial for electrochemical catalytic synthesis. On the other hand, the combination of wire-through-type high-temperature sealing components, high-temperature insulation sealing materials, threaded connections, and welding can achieve sealing and insulation between the electrode and the reactor under high-temperature and high-pressure conditions. The hanging connection method improves the flexibility of the electrode and makes it less susceptible to mechanical impact damage.

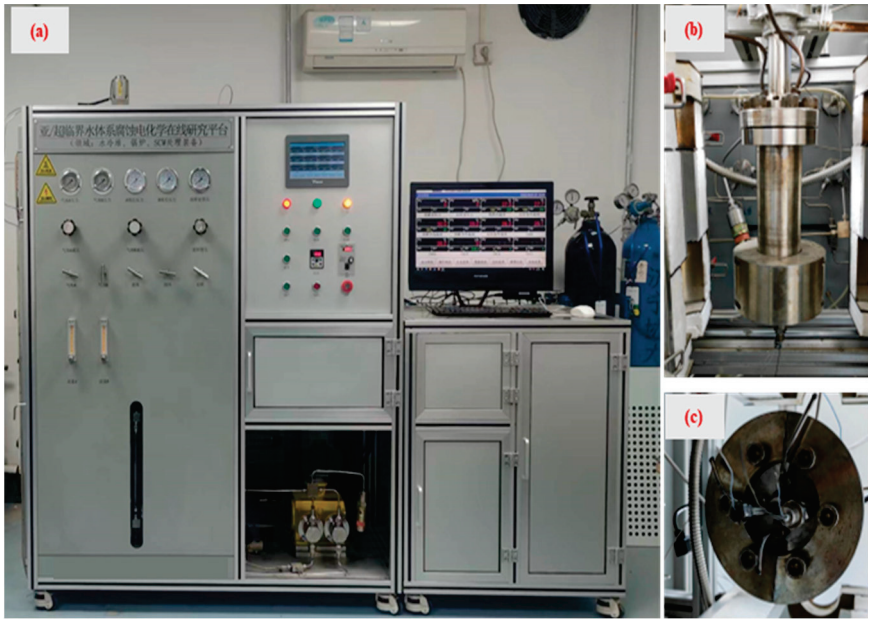

Figure 14. Photo show of a multi-functional sub-/supercritical water electrochemical research platform built in XJTU. (**a**) the main view of the research platform, (**b**) autoclave, (**c**) Reactor base and electrode arrangement.

Yang and Li et al. [136] obtained the electrochemical corrosion data of nickel-based alloy 690 samples in simulated primary coolants of PWRs at temperatures of 200–300 °C. The simulated primary coolant is a lithium borate solution with a dissolved oxygen concentration of 400 ppb, 2000 ppm B, and 2 ppm Li. As shown in Figure 15, as the experimental temperature increases, the open circuit potentials of alloy 690 decrease from −0.553 V_{SHE} to −0.783 V_{SHE}. On the other hand, the current density is independent of the formation potential of the passivation film at the same temperature. In addition, the study also tested the electrochemical impedance spectrum at open circuit potentials, and the results showed that the absolute value of impedance decreased with increasing temperature, indicating a decrease in overall corrosion resistance. This is consistent with the current behavior of passivation.

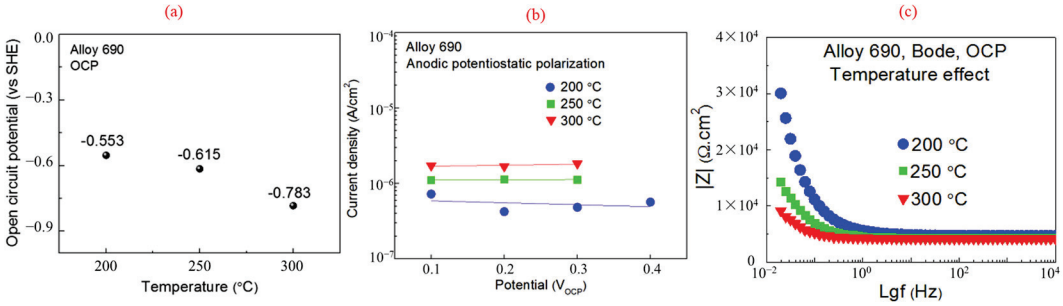

Figure 15. Change of open circuit potential with temperature (**a**), variation of the passive current densities with typical anodic potentials and temperatures (**b**), and Bode diagrams (**c**) for alloy 690 in lithium borate solutions Reprinted with permission from Ref. [136]. 2019, Elsevier.

In summary, the current research apparatus used for electrochemical testing in high-temperature and high-pressure water systems are mainly the continuous flow platforms established by scholars represented by McDonald. New platforms are upgraded and rebuilt based on them. These continuous platforms solve the problems of solution contamination and salt deposition in sequential batch platforms. They are often used to simulate the corrosion problem of the primary circuit of PWRs. However, due to the issue of electrode sealing insulation, it is challenging to apply it to tests above 300 °C. The newly established platform developed by Li's team at Xi'an Jiaotong University based on McDonald's design concept can meet the higher temperature requirements of 550 °C and achieve a wide adjustable content range of interested dissolved gases in the system [137]. In addition, the research platform based on tube furnaces designed by Sen Lin et al. introduces a new electrode installation and sealing method, which can further increase the operating temperature to 700 °C [138].

4. Conclusions

Subcritical/supercritical water is widely employed in energy and environmental fields. The extremely high temperature and high-pressure hydrochemical conditions, coupled with the possible existence of corrosive species such as dissolved oxygen and various inorganic salts, pose significant challenges to developing, designing, and safely operating various subcritical/supercritical water-related equipment due to corrosion. Studying and controlling the corrosion behavior of typical materials in sub-/supercritical water systems is the key to solving the corrosion problem, especially when performing in situ corrosion monitoring. It helps capture real-time corrosion information and promptly adjust relevant equipment parameters for corrosion control. It also provides accurate data references for optimizing and improving various corrosion prediction models.

This paper first comprehensively introduces the fundamentals, advantages and disadvantages, and applications of several non-invasive in situ monitoring technologies, such as ultrasonic measurement, infrared thermal imaging, microwave monitoring, eddy current detection, and acoustic emission, which can be used in a wide temperature range and can be employed as portable corrosion monitoring instruments in practical engineering

applications. Additionally, considering the importance of electrochemical corrosion in the study of corrosion mechanisms and prediction of corrosion behavior in sub-/supercritical water systems, invasive in situ electrochemical testing methods, including electrochemical corrosion potential, electrochemical impedance spectroscopy, and electrochemical noise, are also discussed in detail. The typical existing electrochemical research platform for sub- and supercritical aqueous systems can achieve in situ online water chemistry monitoring and regulation. Some new electrode installation methods, such as using pyrophyllite for sealing and the hanging connection, may elevate the operating temperature up to 700 °C, providing fresh ideas for upgrading and renovating existing mainstream research platforms.

Author Contributions: Z.B. and Y.L. contribute equally. Conceptualization, Y.L. and Z.B.; Investigation, Z.B., L.X., Q.Z. and S.D.; writing—original draft preparation, Y.L., Z.B. and Y.Z.; writing—review and editing, Y.L., P.G. and Z.Y.; visualization, Z.B. and L.X.; supervision, Y.L.; funding acquisition, Y.L. and D.X. All authors have read and agreed to the published version of the manuscript.

Funding: This work is supported by the National Natural Science Foundation of China (22378322, 22008190), the Key Research and Development Program of Shaanxi (2024GX-YBXM-425), the China Postdoctoral Science Foundation (2022M722526), the Fundamental Research Funds for the Central Universities (xtr052022009), and the National Key Research and Development Program of China (2021YFE0104900).

Conflicts of Interest: The authors declare no conflicts of interest.

References

1. Li, Y.; Bai, Z.; Ding, S.; Macdonald, D.D.; Qiu, J.; Wang, K.; Jiang, Z.; Wang, S. Electrochemical techniques and mechanisms for the corrosion of metals and alloys in sub- and supercritical aqueous systems. *J. Supercrit. Fluids* **2023**, *194*, 105835. [CrossRef]
2. Wang, Y.; Oshima, Y.; Akizuki, M. Catalytic Performance of Solid Base Na-ZrO_2 in Subcritical Water. *J. Chem. Eng. Jpn.* **2024**, *57*, 2293044. [CrossRef]
3. Ehrlich, K.; Konys, J.; Heikinheimo, L. Materials for high performance light water reactors. *J. Nucl. Mater.* **2004**, *327*, 140–147. [CrossRef]
4. Han, J.; Kim, S.; Kim, S.J.; Lee, Y.K.; Hur, D.H. Fouling behavior of a printed circuit steam generator under simulated operating conditions of a small modular reactor. *Ann. Nucl. Energy* **2022**, *173*, 109127. [CrossRef]
5. Macdonald, D.D.; Urquidi-Macdonald, M. The Electrochemistry of Nuclear Reactor Coolant Circuits. In *Encyclopedia of Electrochemistry*; Wiley-VCH Verlag GmbH & Co. KGaA: Weinheim, Germany, 2007.
6. Xiong, X.; Liu, X.; Tan, H.; Deng, S. Investigation on high temperature corrosion of water-cooled wall tubes at a 300 MW boiler. *J. Energy Inst.* **2020**, *93*, 377–386. [CrossRef]
7. Sun, X.; Ning, Y.H.; Yang, J.; Zhao, Y.; Yang, Z.J.; Zhou, X.Z. Study on high temperature corrosion mechanism of water wall tubes of 350 MW supercritical unit. *Eng. Fail. Anal.* **2021**, *121*, 105131. [CrossRef]
8. May, Z.; Alam, M.K.; Nayan, N.A. Recent Advances in Non-destructive Method and Assessment of Corrosion Undercoating in Carbon-Steel Pipelines. *Sensors* **2022**, *22*, 6654. [CrossRef]
9. Solovyeva, V.A.; Almuhammadi, K.H.; Badeghaish, W.O. Current Downhole Corrosion Control Solutions and Trends in the Oil and Gas Industry: A Review. *Materials* **2023**, *16*, 1795. [CrossRef]
10. Jack, T.A.; Szpunar, J. Effect of Nb-induced microstructure on pipeline steel corrosion and stress corrosion cracking performance in acidic environment. *Corros. Sci.* **2023**, *218*, 111196. [CrossRef]
11. Finsgar, M.; Jackson, J. Application of corrosion inhibitors for steels in acidic media for the oil and gas industry: A review. *Corros. Sci.* **2014**, *86*, 17–41. [CrossRef]
12. Li, X.; Zhang, D.; Liu, Z.; Li, Z.; Du, C.; Dong, C. Share corrosion data. *Nature* **2015**, *527*, 441–442. [CrossRef] [PubMed]
13. Li, Y.H.; Wang, S.Z.; Xu, T.T.; Li, J.N.; Zhang, Y.S.; Xu, T.T.; Yang, J.Q. Novel designs for the reliability and safety of supercritical water oxidation process for sludge treatment. *Process Saf. Environ. Prot.* **2021**, *149*, 385–398. [CrossRef]
14. Kritzer, P. Corrosion in high-temperature and supercritical water and aqueous solutions: A review. *J. Supercrit. Fluids* **2004**, *29*, 1–29. [CrossRef]
15. De Souza, G.B.M.; Pereira, M.B.; Mourao, L.C.; dos Santos, M.P.; de Oliveira, J.A.; Garde, I.A.A.; Alonso, C.G.; Jegatheesan, V.; Cardozo-Filho, L. Supercritical water technology: An emerging treatment process for contaminated wastewaters and sludge. *Rev. Environ. Sci. Bio/Technol.* **2022**, *21*, 75–104. [CrossRef]
16. Marrone, P.A. Supercritical water oxidation-Current status of full-scale commercial activity for waste destruction. *J. Supercrit. Fluids* **2013**, *79*, 283–288. [CrossRef]
17. Li, Y.; Ding, S.; Bai, Z.; Wang, S.; Zhang, F.; Zhang, J.; Xu, D.; Yang, J. Corrosion characteristics and mechanisms of typical iron/nickel-based alloys in reductive supercritical water environments containing sulfides. *J. Supercrit. Fluids* **2022**, *187*, 105599. [CrossRef]

18. Wang, L.; Li, H.; Liu, Q.; Xu, L.; Lin, S. Effect of sodium chloride on the electrochemical corrosion of Inconel 625 at high temperature and pressure. *J. Alloys Compd.* **2017**, *703*, 523–529. [CrossRef]
19. Tang, X.; Wang, S.; Qian, L.; Ren, M.; Sun, P.; Li, Y.; Yang, J. Corrosion Properties of Candidate Materials in Supercritical Water Oxidation Process. *J. Adv. Oxid. Technol.* **2016**, *19*, 141–157. [CrossRef]
20. Guo, S.; Xu, D.; Li, Y.; Guo, Y.; Wang, S.; Macdonald, D.D. Corrosion characteristics and mechanisms of typical Ni-based corrosion-resistant alloys in sub- and supercritical water. *J. Supercrit. Fluids* **2021**, *170*, 105138. [CrossRef]
21. Guo, S.; Xu, D.; Liang, Y.; Gong, Y.; Li, Y.; Yang, J. Corrosion characterization of ZrO_2 and TiO_2 ceramic coatings via air plasma spraying on 316 stainless steel in oxygenated sub- and supercritical water. *J. Supercrit. Fluids* **2020**, *157*, 104716. [CrossRef]
22. Shome, A.; Das, A.; Borbora, A.; Dhar, M.; Manna, U. Role of chemistry in bio-inspired liquid wettability. *Chem. Soc. Rev.* **2022**, *51*, 5452–5497. [CrossRef]
23. Qian, H.; Xu, D.; Du, C.; Zhang, D.; Li, X.; Huang, L.; Deng, L.; Tu, Y.; Mol, J.M.C.; Terryn, H.A. Dual-action smart coatings with a self-healing superhydrophobic surface and anti-corrosion properties. *J. Mater. Chem. A* **2017**, *5*, 2355–2364. [CrossRef]
24. Wu, B.; Zhang, Y.; Meng, F.; Zhang, Z.; Li, Y.; Wang, J.; Han, E.-H.; Ming, H. Insights into stress corrosion cracking in scratched area of alloy 690TT steam generator tubes. *Acta Mater.* **2023**, *255*, 119083. [CrossRef]
25. Gholamzadeh, H.; Shaik, A.; Daub, K.; Topping, M.; Daymond, M.R.; Persaud, S.Y. A mechanistic study on dealloying-induced stress corrosion cracking of Alloy 800 in boiling caustic solutions. *Corros. Sci.* **2023**, *220*, 111284. [CrossRef]
26. Wang, X.; Shang, C.; Li, Z.; Bai, Y.; Liu, T.; Lu, Y.; Shoji, T. Study on the SCC behavior induced by creep cavities on scratched surface of Alloy 690TT in high temperature water. *Corros. Sci.* **2022**, *196*, 110017. [CrossRef]
27. Li, J.; Cao, T.; Zhang, C.; Cheng, C.; Zhao, J. Failure analysis of reheater tubes in a 350 MW supercritical circulating fluidized bed boiler. *Eng. Failure Anal.* **2022**, *137*, 106285. [CrossRef]
28. Xiong, X.; Chen, F.; Li, L.; Tan, H. Water Wall Tubes' High Temperature Corrosion Root Cause Investigation: A 300 MW Level Boiler Case. *Energies* **2023**, *16*, 1767. [CrossRef]
29. Honarvar, F.; Varvani-Farahani, A. A review of ultrasonic testing applications in additive manufacturing: Defect evaluation, material characterization, and process control. *Ultrasonics* **2020**, *108*, 106227. [CrossRef]
30. Marcantonio, V.; Monarca, D.; Colantoni, A.; Cecchini, M. Ultrasonic waves for materials evaluation in fatigue, thermal and corrosion damage: A review. *Mech. Syst. Signal Process.* **2019**, *120*, 32–42. [CrossRef]
31. Liu, W.; Hou, B.P.; Wang, Y.X.; Yao, Y.; Zhou, L. Sparse Structural Principal Component Thermography for Defect Signal Enhancement in Subsurface Defects Detection of Composite Materials. *J. Non-Destr. Eval.* **2022**, *41*, 8. [CrossRef]
32. Doshvarpassand, S.; Wu, C.Z.; Wang, X.Y. An overview of corrosion defect characterization using active infrared thermography. *Infrared Phys. Technol.* **2019**, *96*, 366–389. [CrossRef]
33. Wahab, A.; Aziz, M.M.A.; Sam, A.R.M.; You, K.Y.; Bhatti, A.Q.; Kassim, K.A. Review on microwave non-destructive testing techniques and its applications in concrete technology. *Constr. Build. Mater.* **2019**, *209*, 135–146. [CrossRef]
34. Mazzinghi, A.; Freni, A.; Capineri, L. A microwave non-destructive testing method for controlling polymeric coating of metal layers in industrial products. *NDT&E Int.* **2019**, *102*, 207–217. [CrossRef]
35. Xie, L.; Gao, B.; Tian, G.Y.; Tan, J.D.; Feng, B.; Yin, Y. Coupling pulse eddy current sensor for deeper defects NDT. *Sens. Actuator A* **2019**, *293*, 189–199. [CrossRef]
36. Grosso, M.; Pacheco, C.J.; Arenas, M.P.; Lima, A.H.M.; Margarit-Mattos, I.C.P.; Soares, S.D.; Pereira, G.R. Eddy current and inspection of coatings for storage tanks. *J. Mater. Res. Technol.* **2018**, *7*, 356–360. [CrossRef]
37. Erlinger, T.; Kralovec, C.; Schagerl, M. Monitoring of Atmospheric Corrosion of Aircraft Aluminum Alloy AA2024 by Acoustic Emission Measurements. *Appl. Sci.* **2023**, *13*, 370. [CrossRef]
38. May, Z.; Alam, K.; A'In, N.; Rahman, A.; Nayan, N.A. Denoising of Hydrogen Evolution Acoustic Emission Signal Based on Non-Decimated Stationary Wavelet Transform. *Processes* **2020**, *8*, 1460. [CrossRef]
39. Kowalczyk, J.; Josko, M.; Wieczorek, D.; Sedlak, K.; Nowak, M. The Influence of the Hardness of the Tested Material and the Surface Preparation Method on the Results of Ultrasonic Testing. *Appl. Sci.* **2023**, *13*, 9904. [CrossRef]
40. Ruiz, A.; Ortiz, N.; Medina, A.; Kim, J.Y.; Jacobs, L.J. Application of ultrasonic methods for early detection of thermal damage in 2205 duplex stainless steel. *NDT&E Int.* **2013**, *54*, 19–26. [CrossRef]
41. Li, W.; Cho, Y. Thermal Fatigue Damage Assessment in an Isotropic Pipe Using Nonlinear Ultrasonic Guided Waves. *Exp. Mech.* **2014**, *54*, 1309–1318. [CrossRef]
42. Chillara, V.K.; Lissenden, C.J. Review of nonlinear ultrasonic guided wave non-destructive evaluation: Theory, numerics, and experiments. *Opt. Eng.* **2016**, *55*, 9904. [CrossRef]
43. Fangxin, Z. Data-Enabled Quantitative Corrosion Monitoring using Ultrasound. *Data-Enabled Discov. Appl.* **2018**, *2*, 8.
44. Dace, G.E.; Thompson, R.B.; Brasche, L.J.H.; Rehbein, D.K.; Buck, O. *Nonlinear Acoustics, a Technique to Determine Microstructural Changes in Materials*; Springer: Boston, MA, USA, 1991.
45. Hurley, D.C.; Yost, W.T.; Boltz, E.S.; Fortunko, C.M. Experimental Comparison of Ultrasonic Techniques to Determine the Nonlinearity Parameter. In Proceedings of the Ultrasonics Symposium, Lake Buena Vista, FL, USA, 8–11 December 1991.
46. Tanaka, T.; Izawa, Y. Non-destructive Detection of Small Internal Defects in Carbon Steel by Laser Ultrasonics. *Jpn. J. Appl. Phys.* **2001**, *40*, 1477. [CrossRef]
47. Clorennec, D.; Royer, D.; Walaszek, H. Non-destructive evaluation of cylindrical parts using laser ultrasonics. *Ultrasonics* **2002**, *40*, 783–789. [CrossRef] [PubMed]

48. Kishore Chakrapani, S.; Howard, A.; Barnard, D. Influence of surface roughness on the measurement of acoustic nonlinearity parameter of solids using contact piezoelectric transducers. *Ultrasonics* **2018**, *84*, 112–118. [CrossRef] [PubMed]
49. Ergun, A.S.; Temelkuran, B.; Ozbay, E.; Atalar, A. A new detection method for capacitive micromachined ultrasonic transducers. In Proceedings of the Ultrasonics Symposium, Atlanta, GA, USA, 8–11 October 2002; pp. 1007–1010.
50. Liu, H.; Zhang, L.; Liu, H.; Chen, S.T.; Wang, S.H.; Wong, Z.Z.; Yao, K. High-frequency ultrasonic methods for determining corrosion layer thickness of hollow metallic components. *Ultrasonics* **2018**, *89*, 166–172. [CrossRef] [PubMed]
51. Bagavathiappan, S.; Lahiri, B.B.; Saravanan, T.; Philip, J.; Jayakumar, T. Infrared thermography for condition monitoring—A review. *Infrared Phys. Technol.* **2013**, *60*, 35–55. [CrossRef]
52. Behravan, A.; Tran, T.Q.Q.; Li, Y.; Davis, M.; Shaikh, M.S.; DeJong, M.M.M.; Hernandez, A.; Brand, A.S.S. Field Inspection of High-Density Polyethylene (HDPE) Storage Tanks Using Infrared Thermography and Ultrasonic Methods. *Appl. Sci.* **2023**, *13*, 1396. [CrossRef]
53. Cadelano, G.; Bortolin, A.; Ferrarini, G.; Molinas, B.; Giantin, D.; Zonta, P.; Bison, P. Corrosion Detection in Pipelines Using Infrared Thermography: Experiments and Data Processing Methods. *J. Non-Destr. Eval.* **2016**, *35*, 49. [CrossRef]
54. Usamentiaga, R.; Venegas, P.; Guerediaga, J.; Vega, L.; Molleda, J.; Bulnes, F. Infrared Thermography for Temperature Measurement and Non-Destructive Testing. *Sensors* **2014**, *14*, 12305–12348. [CrossRef]
55. Ibarra-Castanedo, C.; Tarpani, J.R.; Maldague, X.P.V. Nondestructive testing with thermography. *Eur. J. Phys.* **2013**, *34*, S91. [CrossRef]
56. Cernuschi, F.; Russo, A.; Lorenzoni, L.; Figari, A. In plane thermal diffusivity evaluation by infrared thermography. *Rev. Sci. Instrum.* **2001**, *72*, 3988–3995. [CrossRef]
57. Riegert, G.; Zweschper, T.; Busse, G. Lockin thermography with eddy current excitation. *Quant. InfraRed Thermogr. J.* **2004**, *1*, 21–32. [CrossRef]
58. Favro, L.D.; Han, X.; Ouyang, Z.; Sun, G.; Sui, H.; Thomas, R.L. Infrared imaging of defects heated by a sonic pulse. *Rev. Sci. Instrum.* **2000**, *71*, 2418–2421. [CrossRef]
59. Cuccurullo, G.; Berardi, P.G.; Carfagna, R.; Pierro, V. IR temperature measurements in microwave heating. *Infrared Phys. Technol.* **2002**, *43*, 145–150. [CrossRef]
60. Osiander, R.; Spicer, J.W.M. Time-resolved infrared radiometry with step heating. A review. *Rev. Générale Therm.* **1998**, *37*, 680–692. [CrossRef]
61. Zhang, H.; Gao, B.; Tian, G.Y.; Woo, W.L.; Bai, L.B. Metal defects sizing and detection under thick coating using microwave NDT. *NDT&E Int.* **2013**, *60*, 52–61. [CrossRef]
62. Wang, D.; Che, F.; Wang, Y.; Zhu, L.; Shen, K.; Wang, Y. Application of Microwave Non-destructive Testing of External Anti-Corrosion Coating. *Total Corros. Control* **2022**, *36*, 5.
63. Mazlumi, F.; Sadeghi, S.H.H.; Moini, R. Analysis technique for interaction of rectangular open-ended waveguides with surface cracks of arbitrary shape in metals. *NDT&E Int.* **2003**, *36*, 331–338. [CrossRef]
64. Sayar, M.; Seo, D.; Ogawa, K. Non-destructive microwave detection of layer thickness in degraded thermal barrier coatings using K- and W-band frequency range. *NDT&E Int.* **2009**, *42*, 398–403. [CrossRef]
65. Qaddoumi, N.N.; Saleh, W.M.; Abou-Khousa, M. Innovative near-field microwave nondestructive testing of corroded metallic structures utilizing open-ended rectangular waveguide probes. *IEEE Trans. Instrum. Meas.* **2007**, *56*, 1961–1966. [CrossRef]
66. Zoughi, R.; Kharkovsky, S. Microwave and millimetre wave sensors for crack detection. *Fatigue Fract. Eng. Mater. Struct.* **2008**, *31*, 695–713. [CrossRef]
67. García-Martín, J.; Gómez-Gil, J.; Vázquez-Sánchez, E. Non-Destructive Techniques Based on Eddy Current Testing. *Sensors* **2011**, *11*, 2525–2565. [CrossRef]
68. Newton, M.; Chowdhury, T.; Gravagne, I.; Jack, D. Non-Destructive Evaluation of In-Plane Waviness in Carbon Fiber Laminates Using Eddy Current Testing. *Appl. Sci.* **2023**, *13*, 6009. [CrossRef]
69. Ramos, H.G.; Ribeiro, A.L. Present and Future Impact of Magnetic Sensors in NDE. In Proceedings of the 1st International Conference on Structural Integrity (ICONS), Kalpakkam, India, 4–7 February 2014; pp. 406–419.
70. Mook, G.; Hesse, O.; Uchanin, V. Deep penetrating eddy currents and probes. *Materialprufung* **2007**, *49*, 258–264. [CrossRef]
71. Papaelias, M.; Cheng, L.; Kogia, M.; Mohimi, A.; Kappatos, V.; Selcuk, C.; Constantinou, L.; Muñoz, C.Q.G.; Marquez, F.P.G.; Gan, T.H. Inspection and Structural Health Monitoring techniques for Concentrated Solar Power plants. *Renew. Energy* **2016**, *85*, 1178–1191. [CrossRef]
72. Rifai, D.; Abdalla, A.N.; Ali, K.; Razali, R. Giant Magnetoresistance Sensors: A Review on Structures and Non-Destructive Eddy Current Testing Applications. *Sensors* **2016**, *16*, 298. [CrossRef]
73. He, Y.Z.; Tian, G.Y.; Zhang, H.; Alamin, M.; Simm, A.; Jackson, P. Steel Corrosion Characterization Using Pulsed Eddy Current Systems. *IEEE Sens. J.* **2012**, *12*, 2113–2120. [CrossRef]
74. Xu, Y.; Hu, J.; He, P.; Wang, G.; Pan, H. Research on Acoustic Emission Characteristics and Crack Evolution during Rock Failure under Tensile and Tensile- and Compressive-Shear Stress States. *Appl. Sci.* **2024**, *14*, 545. [CrossRef]
75. Xu, J.; Wu, X.; Han, E.; Ke, W. Application of acoustic emission technique in study of electrochemical corrosion and stress corrosion cracking progresses of metals. *Corros. Sci. Prot. Technol.* **2009**, *21*, 472–476. [CrossRef]
76. Hase, A. In Situ Measurement of the Machining State in Small-Diameter Drilling by Acoustic Emission Sensing. *Coatings* **2024**, *14*, 193. [CrossRef]

77. Ding, Y.; Reuben, R.L.; Steel, J.A. A new method for waveform analysis for estimating AE wave arrival times using wavelet decomposition. *NDT&E Int.* **2004**, *37*, 279–290.
78. Máthis, K.; Prchal, D.; Novotný, R.; Hähner, P. Acoustic emission monitoring of slow strain rate tensile tests of 304L stainless steel in supercritical water environment. *Corros. Sci.* **2011**, *53*, 59–63. [CrossRef]
79. Xu, J.; Wu, X.; Han, E.H. Acoustic emission response of sensitized 304 stainless steel during intergranular corrosion and stress corrosion cracking. *Corros. Sci.* **2013**, *73*, 262–273. [CrossRef]
80. Yuyama, S.; Kishi, T.; Hisamatsu, Y. Effect of environment, mechanical conditions, and materials characteristics on AE behavior during corrosion fatigue processes of an austenitic stainless steel. *Nucl. Eng. Des.* **1984**, *81*, 345–355. [CrossRef]
81. Alekseev, A.B.; Averin, S.A.; Geferova, M.N.; Kondrat'Ev, V.P.; Shikhalev, V.S. Corrosion resistance of austenitic steels and alloys in high temperature water. *J. Nucl. Mater.* **1996**, *233*, 1367–1371. [CrossRef]
82. Cassagne, T.; Caron, D.; Daret, J.; Proust, A.; Boulanger, D. Initial Results on the Stress Corrosion Cracking Monitoring of Alloy 600 in High Temperature Water Using Acoustic Emission. In Proceedings of the Ninth International Symposium on Environmental Degradation of Materials in Nuclear Power Systems—Water Reactors, Asheville, NC, USA, 11–15 August 2013.
83. Xu, J.; Han, E.H.; Wu, X. Acoustic emission response of 304 stainless steel during constant load test in high temperature aqueous environment. *Corros. Sci.* **2012**, *63*, 91–99. [CrossRef]
84. Ritter, S.; Horner, D.A.; Bosch, R.W. corrosion monitoring techniques for detection of crack initiation under simulated light water reactor conditions. *Br. Corros. J.* **2013**, *47*, 251–264. [CrossRef]
85. Wang, B.; Zhong, S.; Lee, T.L.; Fancey, K.S.; Mi, J. Non-destructive testing and evaluation of composite materials/structures: A state-of-the-art review. *Adv. Mech. Eng.* **2020**, *12*, 1687814020913761. [CrossRef]
86. Thompson, N.G.; Yunovich, M.; Dunmire, D. Cost of corrosion and corrosion maintenance strategies. *Corros. Rev.* **2007**, *25*, 247–261. [CrossRef]
87. Kim, M.K.; Chung, D.D.L. Electrical-Connection-Related Stray Inductance Causing Overassessment of the Electrical Resistance Measured by Using the Two-Probe Method. *J. Electron. Mater.* **2023**, *53*, 1026–1034. [CrossRef]
88. Liu, K.; Jiang, W.; Chen, W.; Liu, L.; Xu, Y.; Huang, Y. Probing the Dynamic Progression of Erosion-Corrosion of X65 Pipeline Steel Using the Electrical Resistance Method in Conjunction with Galvanostatic Polarization. *Lubricants* **2022**, *10*, 345. [CrossRef]
89. Liu, L.; Xu, Y.; Wang, Z.; Li, G.; Wang, X.; Huang, Y. Probing and separating corrosion and erosion of pipeline steel using electrical resistance method in conjunction with electrochemical measurements. *Measurement* **2021**, *183*, 109797. [CrossRef]
90. Cao, C. *Principles of Electrochemistry of Corrosion*; Chemical Industry Press: Beijing, China, 2008; pp. 37–38.
91. Li, X.; Wang, J.; Han, E.H.; Ke, W. Corrosion behavior for Alloy 690 and Alloy 800 tubes in simulated primary water. *Corros. Sci.* **2013**, *67*, 169–178. [CrossRef]
92. Molander, A.; Ullberg, M. New technique for in-plant high mass transfer rate electrochemical potential monitoring. *Energy Mat.* **2008**, *3*, 99–103. [CrossRef]
93. Ramar, A.; Grundler, P.V.; Karastoyanov, V.; Günther-Leopold, I.; Abolhassani-Dadras, S.; Kivel, N.; Ritter, S. Effect of Pt injection rate on corrosion potential and Pt distribution on stainless steel under simulated boiling water reactor conditions. *Corros. Eng. Sci. Technol.* **2012**, *47*, 489–497. [CrossRef]
94. Uchida, S.; Naitoh, M.; Okada, H.; Uehara, Y.; Koshizuka, S.; Lister, D.H. Effects of Water Chemistry on Flow Accelerated Corrosion and Liquid Droplet Impingement. In Proceedings of the Symposium on Water Chemistry and Corrosion in Nuclear Power Plants in Asia, Nagoya, Japan, 28–30 October 2009.
95. Christensen, H. Remodeling of the oxidant species during radiolysis of high-temperature water in a pressurized water reactor. *Nucl. Technol.* **1995**, *109*, 373–382. [CrossRef]
96. Rosinger, E.L.J.; Dixon, R.S. *Mathematical Modelling of Water Radiolysis; A Discussion of Various Methods*; Whiteshell Nuclear Research Establishment: Pinawa, MB, Canada, 1977; p. 76.
97. Burns, W.G.; Moore, P.B. Water radiolysis and its effect upon in-reactor zircaloy corrosion. *Radiat. Eff.* **1976**, *30*, 233–242. [CrossRef]
98. Kim, Y.J.; Niedrach, L.W.; Lin, C.C.K.S. *Development of ECP Models for BWR Applications*; NACE International: Houston, TX, USA, 1995.
99. Macdonald, D.D.; Urquidi-Macdonald, M.D. Interpretation of Corrosion Potential Data from Boiling-Water Reactors Under Hydrogen Water Chemistry Conditions. *Corrosion* **1996**, *52*, 659–670. [CrossRef]
100. Macdonald, D.D. Viability of Hydrogen Water Chemistry for Protecting In-Vessel Components of Boiling Water Reactors. *Corrosion* **1992**, *48*, 194–205. [CrossRef]
101. Urquidi-Macdonald, M.; Pitt, J.; Macdonald, D.D. The impact of radiolytic yield on the calculated ECP in PWR primary coolant circuits. *J. Nucl. Mater.* **2007**, *362*, 1–13. [CrossRef]
102. Cheng, X.; Li, C.; Dong, C.; Li, X. Constituent phases of the passive film formed on 2205 stainless steel by dynamic electrochemical impedance spectroscopy. *Int. J. Miner. Metall. Mater.* **2011**, *18*, 42–47. [CrossRef]
103. Lei, X.; Wang, H.; Mao, F.; Zhang, J.; Zhao, M.; Fu, A.; Feng, Y.; Macdonald, D.D. Electrochemical behaviour of martensitic stainless steel after immersion in a H2S-saturated solution. *Corros. Sci.* **2018**, *131*, 164–173. [CrossRef]
104. Euch, S.E.L.; Bricault, D.; Cachet, H.; Sutter, E.M.M.; Tran, M.T.T.; Vivier, V.; Engler, N.; Marion, A.; Skocic, M.; Huerta-Ortega, B. Temperature dependence of the electrochemical behavior of the 690 Ni-base alloy between 25 and 325 °C. *Electrochim. Acta* **2019**, *317*, 509–520. [CrossRef]

105. Wang, J.; Wang, J.; Ming, H.; Zhang, Z.; Han, E.-H. Effect of temperature on corrosion behavior of alloy 690 in high temperature hydrogenated water. *J. Mater. Sci. Technol.* **2018**, *34*, 1419–1427. [CrossRef]
106. Macak, J.; Novotny, R.; Sajdl, P.; Bystriansky, V.; Tuma, L.; Novak, M. In-situ electrochemical impedance measurements of corroding stainless steel in high subcritical and supercritical water. *Corros. Sci.* **2019**, *150*, 9–16. [CrossRef]
107. Ai, J.; Chen, Y.; Urquidi-Macdonald, M.; Macdonald, D.D. Electrochemical Impedance Spectroscopic Study of Passive Zirconium: I. High-Temperature, Deaerated Aqueous Solutions. *J. Electrochem. Soc.* **2007**, *154*, C43–C51. [CrossRef]
108. Yang, J.; Li, Y.H.; Macdonald, D.D. Effects of temperature and pH on the electrochemical behaviour of alloy 600 in simulated pressurized water reactor primary water. *J. Nucl. Mater.* **2020**, *528*, 151850. [CrossRef]
109. Li, Y.; Yang, J.; Macdonald, D.D.; Wang, S. Study of Steady-state Electrochemical Reactions on Stainless Steels in Elevated Temperature Aqueous Systems. In Proceedings of the 21st International Conference on Water Chemistry in Nuclear Reactor Systems, San Francisco, CA, USA, 9–14 September 2018; p. 12.
110. Li, Y.; Macdonald, D.D.; Yang, J.; Qiu, J.; Wang, S. Point defect model for the corrosion of steels in supercritical water: Part I, film growth kinetics. *Corros. Sci.* **2020**, *163*, 108280. [CrossRef]
111. Zhang, J.; Zhang, Z.; Wang, J.; Cao, C. Analysis and application of electrochemical noise technology—I. Theory of electrochemical noise analysis. *J. Chin. Soc. Corros. Prot.* **2001**, *21*, 11.
112. Zhang, J.; Zhang, Z.; Wang, J.; Cheng, S.; Cao, C. Analysis and application of electrochemical noise technology II. Application of electrochemical noise. *J. Chin. Soc. Corros. Prot.* **2002**, *22*, 241–248.
113. Guo, Q.; Wu, X.; Xu, S.; Feng, B.; Hu, B.; Lu, J. Research status and development of high temperature and high pressure on-line corrosion monitoring technology. *Corros. Sci. Prot. Technol.* **2016**, *28*, 7.
114. Taylor, D.F.; Hickling, J.; Andresen, P.L. Use of electrochemical noise to detect stress corrosion crack initiation in simulated BWR environments. *Mater. Corros.* **1999**, *49*, 651–658.
115. Ritter, S.; Seifert, H.P. Influence of reference electrode distance and hydrogen content on electrochemical potential noise during SCC in high purity, high temperature water. *Br. Corros. J.* **2013**, *48*, 199–206. [CrossRef]
116. Ma, C.; Song, S.; Gao, Z.; Wang, J.; Xia, D.H. Electrochemical Noise Monitoring of the Atmospheric Corrosion of Steels: Identifying Corrosion Form Using Wavelet Analysis. *Corros. Eng. Sci. Technol.* **2017**, *52*, 432–440. [CrossRef]
117. Eckermann, F.; Suter, T.; Uggowitzer, P.J.; Afseth, A.; Davenport, A.J.; Connolly, B.J.; Larsen, M.H.; Carlo, F.D.; Schmutz, P. In situ monitoring of corrosion processes within the bulk of AlMgSi alloys using X-ray microtomography. *Corros. Sci.* **2008**, *50*, 3455–3466. [CrossRef]
118. Chen, J.F.; Bogaerts, W.F. The physical meaning of noise resistance. *Corros. Sci.* **1995**, *37*, 1839–1842. [CrossRef]
119. Xiao, H.; Mansfeld, F. Evaluation of Coating Degradation with Electrochemical Impedance Spectroscopy and Electrochemical Noise-Analysis. *J. Electrochem. Soc.* **1994**, *141*, 2332–2337. [CrossRef]
120. Iverson, W.P. Transient Voltage Changes Produced in Corroding Metals and Alloys. *J. Electrochem. Soc.* **1968**, *115*, 617. [CrossRef]
121. Zhou, X.Y.; Lvov, S.N.; Wei, X.J.; Benning, L.G.; Macdonald, D.D. Quantitative evaluation of general corrosion of Type 304 stainless steel in subcritical and supercritical aqueous solutions via electrochemical noise analysis. *Corros. Sci.* **2002**, *44*, 841–860. [CrossRef]
122. Macak, J.; Sajdl, P.; Kucera, P.; Novotny, R.; Vosta, J. In situ electrochemical impedance and noise measurements of corroding stainless steel in high temperature water. *Electrochim. Acta* **2006**, *51*, 3566–3577. [CrossRef]
123. Ku?Era, P.; Macák, J.; Sajdl, P.; Novotny, R. Evaluation of 08CH18N10T stainless steel corrosion in subcritical water by electrochemical noise analysis. *Mater. Corros.* **2008**, *59*, 719–726.
124. Song, S.; Wang, J.; Li, J.; Zhao, W.; Gao, Z. Electrochemical noise technology for detecting corrosion damage of nuclear power environmental materials. *Prog. Chin. Mater.* **2011**, *30*, 7.
125. Arganis-Juarez, C.R.; Malo, J.M.; Uruchurtu, J. Electrochemical noise measurements of stainless steel in high temperature water. *Nucl. Eng. Des.* **2007**, *237*, 2283–2291. [CrossRef]
126. Stewart, J.; Wells, D.B.; Scott, P.M.; Williams, D.E. Electrochemical noise measurements of stress corrosion cracking of sensitised austenitic stainless steel in high-purity oxygenated water at 288 °C. *Corros. Sci.* **1992**, *33*, 73–88. [CrossRef]
127. Kim, H.S. A Study for Modeling Electrochemistry in Light Water Reactors. Ph.D. Thesis, The Pennsylvania State University, State College, PA, USA, 2007.
128. Karaminezhaad-Ranjbar, M.; Mankowski, J.; Macdonald, D.D. Pitting Corrosion of Inconel 600 in High Temperature Chloride Solution under Controlled Hydrodynamic Conditions. *Corrosion* **1985**, *41*, 197–204. [CrossRef]
129. Kim, H.; Macdonald, D.D. Measurement of steady-state hydrogen electrode reactions on Alloys 600 and 690 tubes. *Corrosion Science* **2010**, *52*, 1139–1145. [CrossRef]
130. Macdonald, D.D.; Mankowski, J.; Karaminezhaadranjbar, M.; Hu, Y.H. Apparatus for Controlled Hydrodynamic Electrochemical and Corrosion Studies in High-Temperature Aqueous Systems. *Corrosion* **1988**, *44*, 186–192. [CrossRef]
131. Kuang, W.; Wu, X.; Han, E.-H.; Rao, J. Effect of alternately changing the dissolved Ni ion concentration on the oxidation of 304 stainless steel in oxygenated high temperature water. *Corros. Sci.* **2011**, *53*, 2582–2591. [CrossRef]
132. Kuang, W.; Wu, X.; Han, E.-H. The oxidation behaviour of 304 stainless steel in oxygenated high temperature water. *Corros. Sci.* **2010**, *52*, 4081–4087. [CrossRef]
133. Kuang, W.; Wu, X.; Han, E.H.; Rao, J. The mechanism of oxide film formation on Alloy 690 in oxygenated high temperature water. *Corros. Sci.* **2011**, *53*, 3853–3860. [CrossRef]

134. Huang, J.; Liu, X.; Han, E.-H.; Wu, X. Influence of Zn on oxide films on Alloy 690 in borated and lithiated high temperature water. *Corros. Sci.* **2011**, *53*, 3254–3261. [CrossRef]
135. Li, Y.; Bai, Z.; Ding, S.; Wang, S.; Zhang, F.; Liu, H. An Online Testing System for Electrochemical Corrosion Behavior in Supercritical Water Systems. CN202210499746.6, 29 July 2022.
136. Yang, J.; Li, Y.; Xu, A.; Fekete, B.; Macdonald, D.D. The electrochemical properties of alloy 690 in simulated pressurized water reactor primary water: Effect of temperature. *J. Nucl. Mater.* **2019**, *518*, 305–315. [CrossRef]
137. Li, Y.; Bai, Z.; Ding, S.; Wang, S.; Li, Z.; Sun, S. A Multifunctional Electrochemical Research Platform Suitable for Sub/Supercritical Water Environments. CN202210499044.8, 5 August 2022.
138. Lin, S.; Li, H.P.; Xu, L.P.; Zhang, Y.Q.; Cui, C. A novel experimental device for electrochemical measurements in supercritical fluids up to 700 degrees C/1000 bar and its application in the corrosion study of superalloy Inconel 740H. *RSC Adv.* **2017**, *7*, 33914–33920. [CrossRef]

sensors

MDPI

Article

Quantitative Prediction of Surface Hardness in Cr12MoV Steel and S136 Steel with Two Magnetic Barkhausen Noise Feature Extraction Methods

Xianxian Wang, Yanchao Cai, Xiucheng Liu * and Cunfu He

Department of information, Beijing University of Technology, Beijing 100124, China; wangxx0902@163.com (X.W.); 13001102233@163.com (Y.C.); hecunfu@bjut.edu.cn (C.H.)
* Correspondence: xiuchliu@bjut.edu.cn

Abstract: The correlation between magnetic Barkhausen noise (MBN) features and the surface hardness of two types of die steels (Cr12MoV steel and S136 steel in Chinese standards) was investigated in this study. Back-propagation neural network (BP-NN) models were established with MBN magnetic features extracted by different methods as the input nodes to realize the quantitative prediction of surface hardness. The accuracy of the BP-NN model largely depended on the quality of the input features. In the extraction process of magnetic features, simplifying parameter settings and reducing manual intervention could significantly improve the stability of magnetic features. In this study, we proposed a method similar to the magnetic Barkhausen noise hysteresis loop (MBNHL) and extracted features. Compared with traditional MBN feature extraction methods, this method simplifies the steps of parameter setting in the feature extraction process and improves the stability of the features. Finally, a BP-NN model of surface hardness was established and compared with the traditional MBN feature extraction methods. The proposed MBNHL method achieved the advantages of simple parameter setting, less manual intervention, and stability of the extracted parameters at the cost of small accuracy reduction.

Keywords: magnetic Barkhausen noise; surface hardness; MBNHL; BP-NN

1. Introduction

A mold is a key processing tool for manufacturing parts in machinery manufacturing, electrical machinery, electrical appliances, and other industrial fields. The quality of its raw material, die steel, determines the service life of the mold. Surface hardness is an important indicator of the resistance to external forces and can be used to evaluate the quality of die steel. With the common indentation surface hardness test method, it is difficult to measure the surface hardness of complex parts due to sampling problems and destructive measurements. Fraunhofer IZFP in Germany [1–3] developed a 3MA-II versatile micromagnetic testing instrument as an alternative tool to the indentation tester to perform nondestructive evaluation of the surface hardness of ferromagnetic materials.

The microstructures (dislocations, grain boundaries, etc.) of ferromagnetic materials have a pinning effect on the magnetization behavior of magnetic domains (walls) [4–6]. In addition, the macroscopic mechanical properties (surface hardness) of grains under externally applied loads are controlled by microstructures and residual stresses [7,8]. In the micromagnetic detection methods of surface hardness, based on the intrinsic correlation between surface hardness, microstructure, and magnetic properties of a material [9,10], a correlation model between magnetic parameters and surface hardness is established by means of the calibration experimental method [11–13]. Before determining this correlation, it is necessary to explore the extraction method of micromagnetic parameters and correlation modeling method [14,15].

The performance of the micromagnetic detection method in the nondestructive evaluation of surface hardness has been verified. Nahak et al. [16] used MBN for nondestructive characterization of the surface hardness of electro-discharged machined specimens and found that the peak value and root-mean-square (RMS) value extracted from MBN had a good inverse proportion with surface hardness. Franco et al. [17] reported the approximately linear dependence of magnetic parameters (peak position and derivative of peak height) on the surface hardness of SAE 4140. Liu et al. [18] extracted a total of 11 magnetic features from magnetic Barkhausen noise and tangential magnetic field signals, established a multiple linear regression model and a BP neural network model, which realized the average prediction errors of surface hardness for 12CrMoV (13.7% and 3.7%).

The measurement accuracy of surface hardness with micromagnetic methods depends largely on the stability of magnetic feature signals and the correlation between magnetic features and surface hardness [12,19]. Abundant magnetic features have been extracted from MBN signals using various methods for the characterization of mechanical properties such as surface hardness. In the commonly used MBN processing method, the MBN butterfly curve [20,21] is first plotted, and the peak value, peak position, and other characteristic values are then extracted from the plotted curve to establish the correlation model for the quantitative evaluation of surface hardness. VASHISTA et al. [22] introduced two eigenvalues of counts and events to describe MBN signals, but the features were greatly affected by the artificial selection of the threshold and signal interception time. In addition, many scholars also used the features of MBN signals, including root-mean-square, average amplitude, Barkhausen noise energy, number of counts of the Barkhausen effect impulses [23], and peak-to-width ratio [24] to evaluate the mechanical properties of materials. MBN signals are random noise signals, so the signals collected at different times showed the differences in the peak value and width. Conventional MBN feature extraction methods have some problems, such as complex parameter settings and many manual interventions. Therefore, it is urgent to develop a new feature parameter extraction method to improve the stability of features.

In this study, based on the consideration of the complex parameter setting and frequent manual intervention in the plotting process of MBN butterfly curves and the feature extraction process, a hysteresis loop-shaped MBNHL method was introduced to extract magnetic features. Then, the quantitative prediction of surface hardness of Cr12MoV steel and S136 steel was carried out with self-developed dual-function micro magnetic detection sensors and devices. The MBN butterfly curve and MBNHL curve were plotted with the same set of collected data, and the repeatability of the two methods in extracting magnetic features was evaluated with the coefficient of variation. The magnetic features extracted by the MBNHL method had higher repeatability. Based on the comprehensive consideration of the repeatability of two methods for extracting magnetic features and the performance of magnetic features in surface hardness evaluation, a BP-NN characterization model for surface hardness was established. Compared with the model established by the MBN method, the proposed MBNH method realized the advantages of simple parameter setting, less manual intervention, and stable parameter extraction at the small cost of a slight reduction in prediction accuracy.

2. Experimental Device and Preparation of Samples

2.1. Experimental Device

In micromagnetic detection methods, multiple magnetic signals (magnetic Barkhausen noise, tangential magnetic field (TMF), and magnetic incremental permeability (EIP)) are combined together to characterize the mechanical properties of materials [20,25]. In this paper, a sensor (Figure 1a) was developed to simultaneously detect two types of magnetic signals (TMF and MBN). The sensor consisted of a yoke of Fe–Si, an excitation coil, and a detection element (induction coil and Hall element). The low-frequency excitation field was provided by a U-shaped yoke with an excitation coil (0.35 mm in diameter and 300 coil turns) wound at the top, which was made of ferrite with a cross-sectional area of

10 mm × 10 mm. The Hall element (Honeywell SS39E, with a dynamic operating range of ±1000 Gs and a sensitivity of 1.4 mV/Gs) and the induction coil (800 turns in total) in the sensor were used to detect the TMF signal and the MBN signal at the specimen surface, respectively. A Zn–Mn ferrite core (height = 9 mm; diameter = 2 mm) was embedded inside the induction coil to enhance the strength of detected signals.

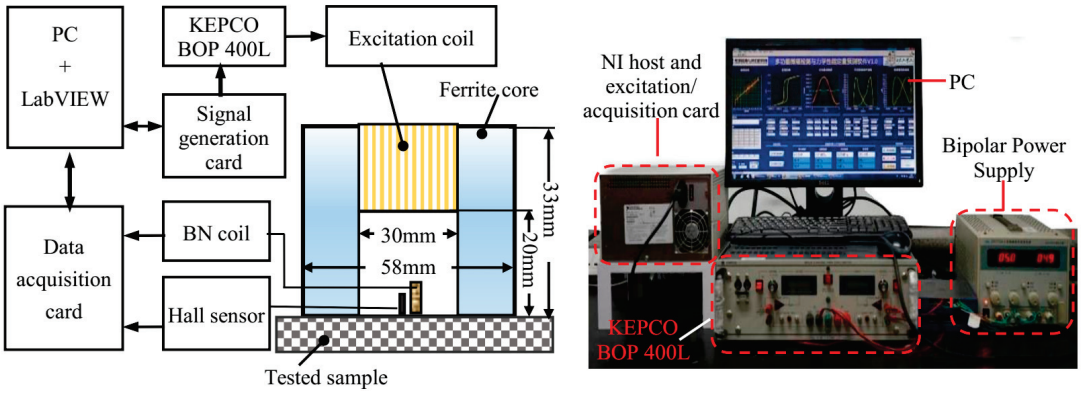

Figure 1. Schematic diagram of MBN detection device. (**a**) configuration of the sensor. (**b**) Picture of the micro-magnetic testing system.

The experimental device used in this study consisted of a PXI chassis (including a signal generation card and data acquisition card), a power amplifier BOP100-400L, a bipolar power supply, a micromagnetic sensor, and a LABVIEW-based control and analysis software (Figure 1b). The sinusoidal signal (frequency = 12 Hz, amplitude = 8 V) generated by the signal excitation card was first amplified by the BOP power supply and then fed into the excitation coil of the transducer to generate an alternating magnetic field for cyclic magnetization of the specimens. During the cyclic magnetization of the material, the induction coil received the MBN signal, and the Hall element was used to measure the TMF strength change on the material surface. The sampling frequency and the number of sampling points were kept as 1 MS/s and 1 M, respectively. MBN and TMF signals were acquired by the NI PXIe multichannel acquisition card and processed with the LabVIEW 2015 software in the host computer.

2.2. Sample Preparation

In this study, two die steels (Cr12MoV steel and S136 steel in Chinese) were selected to prepare the specimens to be tested. For each material, 60 specimens with the same size (length × width × height = 200 mm × 60 mm × 3 mm) were cut from the steel plate in the rolling direction. Both materials were subjected to the same quenching and tempering processes, and the surface hardness of specimens was adjusted by changing the tempering temperature. The main processes are introduced as follows: Firstly, in the quenching process, all specimens were gradually heated to 1030 °C. Temperature and holding time are shown in Figure 2a. Secondly, in the tempering process, the specimens of each material were divided into 12 batches (5 specimens per batch), and the specimens of Cr12MoV steel and S136 steel were tempered in batches for 210 min in the range of 180 to 720 °C to obtain steel plate specimens with different hardness. The thermally treated specimens were polished at the center (Figure 2b). The MBN and TMF signals of the two materials (a total of 120 specimens) were first tested with a micromagnetic testing system, and then the surface hardness of specimens was tested with a Vickers hardness tester (30 HV with a 30-kg load). The micromagnetic testing and Vickers hardness measurements were carried out in the same magnetized area (Figure 2b).

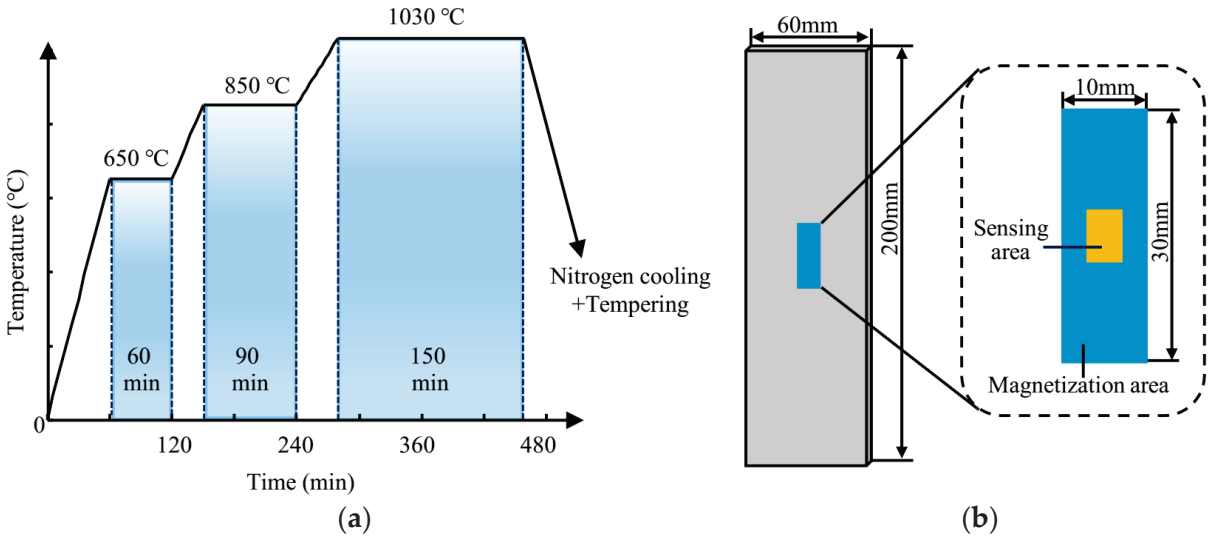

Figure 2. (**a**) Thermal treatment process and (**b**) dimensions of hardness specimens.

The entire specimen was placed in the furnace for heat treatment, so each specimen was assumed to have a uniform hardness. After testing the magnetic signals of all samples, a microhardness tester (HV30 with a load of 30 kg) is used to test the Vickers hardness value of the specimen surface. It is worth noting that the microhardness test position should be consistent with the magnetic signal test position. To ensure the accuracy and reliability of the test results, three tests were conducted at close positions on the specimen, and the average value was calculated. The average values of the three tests are shown in Figure 3. The surface hardness of Cr12MoV and S136 steels fluctuated within the ranges of 350 HV to 750 HV and 250 HV to 600 HV. The five specimens in the same batch had similar surface hardness with slight differences.

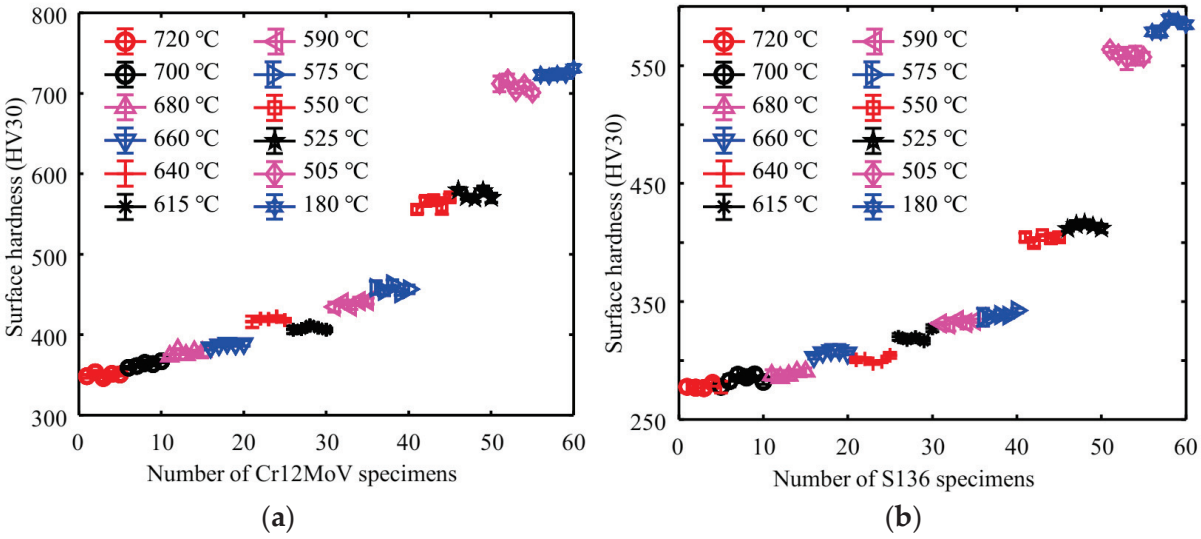

Figure 3. Test results of tempering temperature and surface hardness of (**a**) Cr12MoV and (**b**) S136.

2.3. MBN Detection Experiments

To evaluate the repeatability of the MBN and TMF signals, 60 specimens of each material were tested multiple times. For a single specimen, 15 sets of repeated tests with MBN and TMF signals were performed at the same location. A demagnetization device was used to demagnetize the specimens before each test, and a Gauss meter was used to measure the residual magnetic strength to ensure that the initial magnetic state of the

samples remained unchanged. Upon the completion of the tests, 15 × 60 = 900 sets of magnetic signals were obtained for each material.

3. Processing Methods of MBN Signals

The stability of the magnetic features used as model inputs is significant in the construction of an accurate surface hardness model. MBN signals are random, so stable MBN features are conducive to constructing a high-precision model.

3.1. MBN Butterfly Curve

The MBN butterfly curve describes the variation of the magnetic Barkhausen noise envelope with the tangential magnetic field strength waveform within one cycle. Plotting the MBN butterfly curve is a common way to extract MBN features. The plotting process of the MBN butterfly curve is shown in Figure 4 and includes signal filtering (filter type, high/low cutoff frequency, order, etc.), signal interception, and curve plotting.

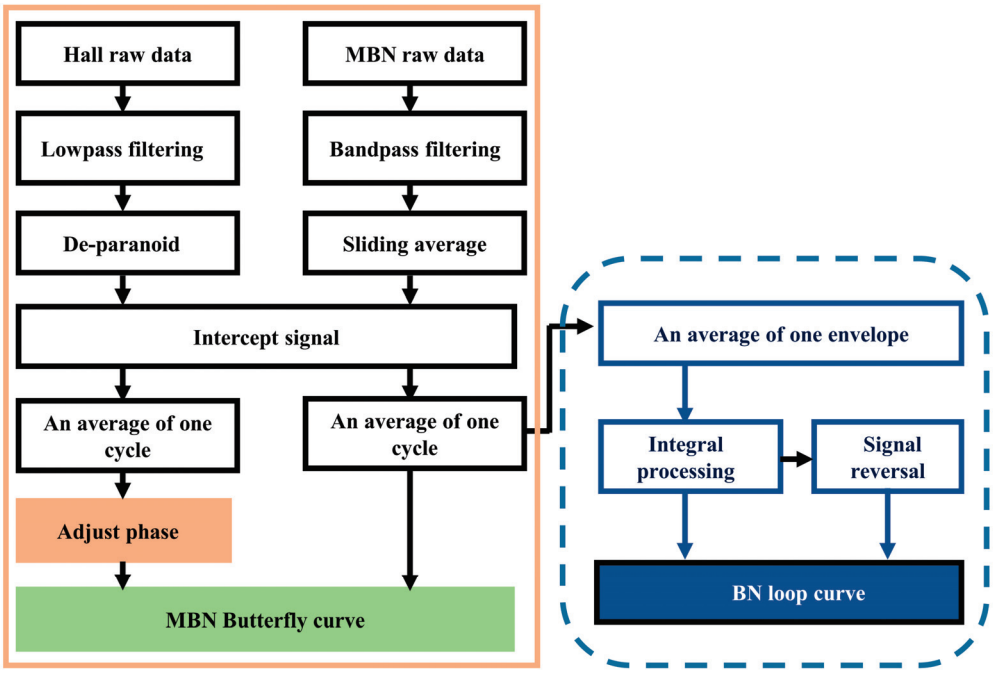

Figure 4. Flow chart of plotting the BN butterfly curve and BN loop curve.

In the first step, TMF signals were filtered. The raw signals measured by the Hall sensor were superimposed with high-frequency interference noise, which should be removed with a low-pass filter. A Butterworth low-pass filter (cutoff frequency of 200 Hz) was selected to filter the signals. After the DC bias was removed, the TMF signal was obtained through the calculation with Equation (1). Figure 5a and Figure 5b, respectively, show the TMF signals measured in different hardness specimens of Cr12MoV and S136 steel. The TMF signals are affected by the hysteresis characteristics in the tested specimens, and the TMF waveforms of different specimens are different.

$$H = \frac{V}{k \times \mu_0}, \tag{1}$$

where V is the Hall voltage after subtracting the bias; k is the conversion coefficient of the Hall sensor and equals 1.5 mV/G; and μ_0 is the permeability of vacuum and equals $4 \times \pi \times 10^{-7}$.

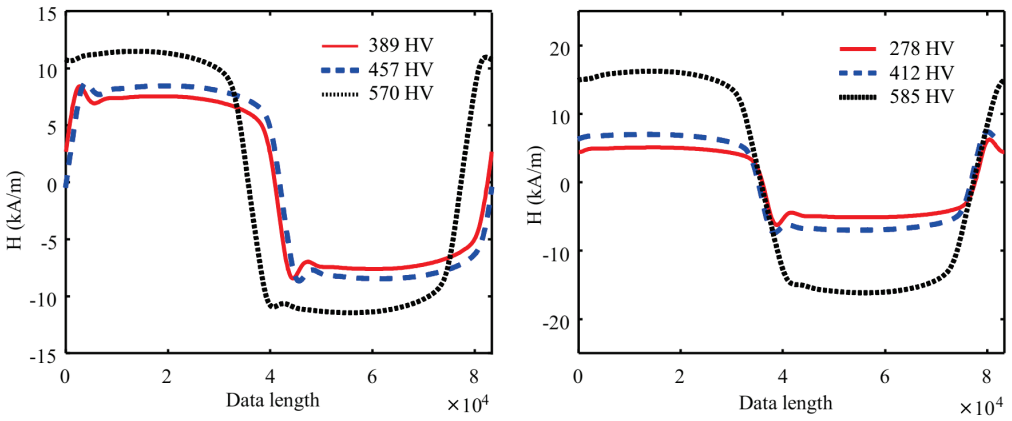

(**a**) Cr12MoV steel. (**b**) S136 steel.

Figure 5. TMF signals for different surface hardness specimens.

In the second step, MBN signals were filtered. The MBN signal is a random electromagnetic noise signal. During signal reception, the detection coil outputs a wide-band signal, so the filtering process of detection signals is required. The correct choice of filtering frequency is crucial for post-processing the noise signal. In this study, a 4-th order Butterworth band-pass filter (filter frequency band 30 kHz to 90 kHz) was used to filter the signals detected with the receiver coil. Typical MBN signals measured in the different surface hardness specimens of Cr12MoV steel and S136 steels are shown in Figure 6a,b. Both the waveforms and peaks of MBN signals are affected by surface hardness, which essentially suggests microstructural change.

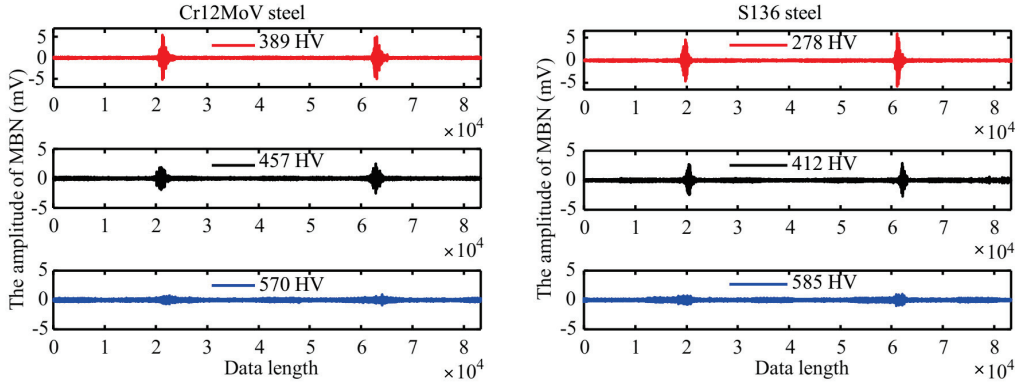

(**a**) Cr12MoV steel. (**b**) S136 steel.

Figure 6. MBN signals of different surface hardness specimens.

In order to extract the features of MBN, the filtered MBN signals were processed by sliding average. The window size n was selected for the sliding average and the root-mean-square (RMS) operation was performed with the data in the window. Starting from the first data point, the operation then slid to the next data point in sequence. The smoothness of the MBN envelope is determined by the value of n and should be determined according to the actual situation. Based on prior experience, in this paper, an n = 400 was selected to perform four repetitions of sliding RMS operation in order to obtain a smooth MBN signal envelope.

In the third step, signals were intercepted. In the process of magnetic signal testing, the initial magnetization and remnant magnetization state of the material interfered with the obtained signals, and the whole cycle interception of the filtered TMF and MBN signals could eliminate the interference. In this paper, the 4th maximum point of the TMF signal was selected as the starting point, and eight cycles of the TMF signal and MBN signal were intercepted and retained synchronously.

In the fourth step, the MBN butterfly curve was plotted. The micromagnetic signals are related to the magnetization process of magnetic domains, which is a random process. The magnetic features measured in multiple magnetization cycles had random fluctuations. The intercepted eight-cycle TMF and MBN signals are simultaneously processed with an average envelope to obtain one-cycle TMF and MBN signals (Figure 7). The magnetic Barkhausen noise butterfly curves were plotted with the signal envelopes (Figure 7a,b) as horizontal and vertical coordinates, respectively.

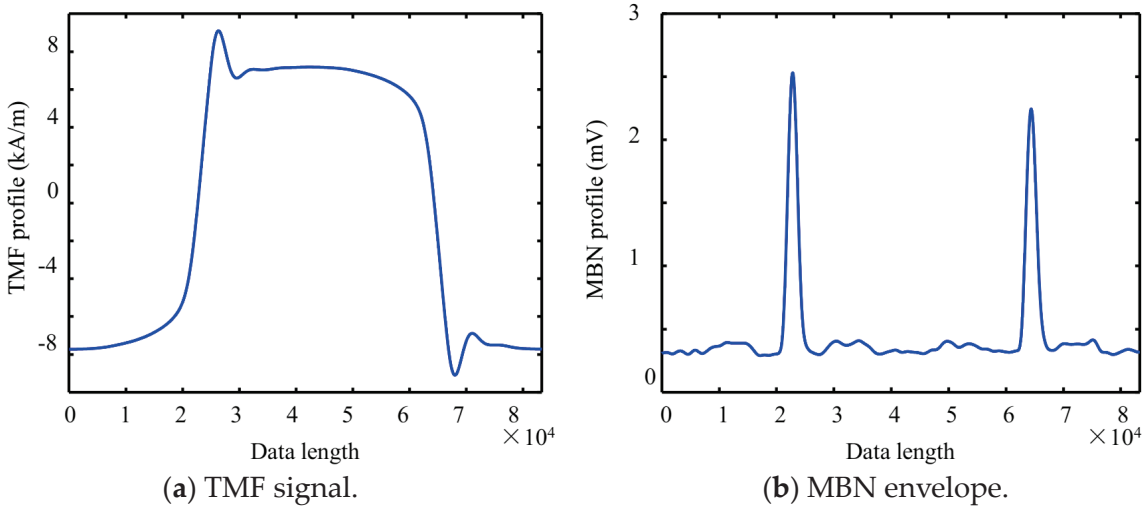

(**a**) TMF signal. (**b**) MBN envelope.

Figure 7. One cycle magnetic signal.

In the process of filtering and sliding the average of TMF and MBN signals, a phase shift of the signals was inevitable. The magnitude of the phase shift directly affected the shape of the plotted butterfly curve and magnetic features. Generally, MBN appeared at the moment of TMF reversal. During signal processing, time-shift adjustment of TMF signals was performed to improve the quality of the MBN butterfly curve. At present, phase adjustment between TMF signals and MBN envelope is mainly performed based on personal experiences and parameter adjustment is not introduced in related theories or standards.

Figure 8 illustrates the butterfly curve obtained after different time-shift adjustments from the same data set. In this paper, the time-shift adjustment was performed in such a way that the peak of the MBN envelope was close to the over-zero position of TMF. Table 1 lists the magnetic features and coefficient of variation σ (σ = standard deviation/mean value) extracted from the butterfly curves through different time-shift adjustments. A small coefficient of variation indicated good repeatability and stability of the signals in repeated experiments. A large coefficient of variation indicated that the system had poor repeatability detection performance for magnetic covariates, which was not conducive to the high-precision quantitative characterization of surface hardness. The coefficients of variation of the magnetic parameters (*Hcm*, *DH75M*, and *DH50M*) extracted from the butterfly curves respectively reached 38.8%, 23.1%, and 14.6% when the phase was not adjusted (Table 1). When the time-shift adjustment was performed within about 1/80 cycle, the coefficients of variation of the repeated detection data of the above magnetic parameters reduced to 5%. For the actual detection signals in this paper, a time-shift adjustment of the 1/80 cycle was chosen.

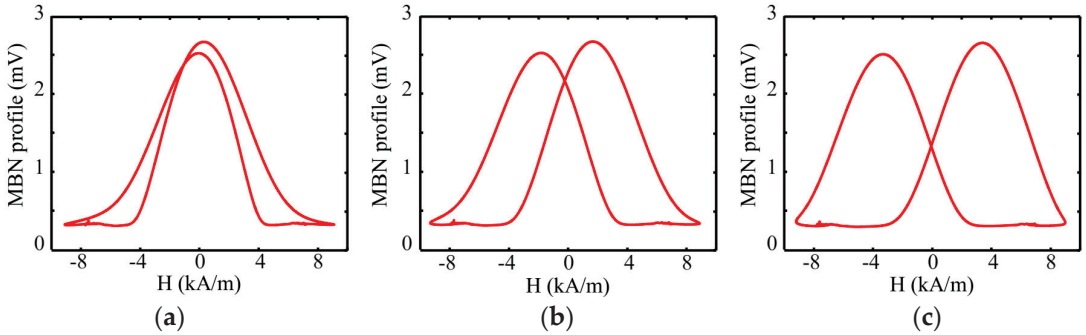

Figure 8. Butterfly-like MBN curves of different time-shift adjustments: (**a**) 0 cycle; (**b**) 1/160 cycle; and (**c**) 1/80 cycle.

Table 1. Coefficients of variation of conventional features extracted from the MBN profile.

Features	MBN Signals	0	1/160	1/80	Cr12MoV	S136
x_1	Peak height of the MBN butterfly curve, *Mmax*	3.9%	3.9%	3.9%	3.1%	3.5%
x_2	Peak position of the MBN butterfly curve, *Hcm*	38.8%	3.7%	1.5%	1.3%	2.1%
x_3	Intercept of MBN envelope at the vertical axis, *Mr*	3.9%	3.9%	4.1%	3.9%	3.4%
x_4	Mean value of MBN envelope, *Mmean*	3.9%	3.9%	3.8%	3.1%	2.9%
x_5	Full width at 75% of maxima of MBN butterfly curve, *DH75M*	23.1%	3.5%	1.9%	2.0%	2.4%
x_6	Full width at 50% of maxima of MBN butterfly curve, *DH50M*	14.6%	3.1%	1.5%	15.4%	9.1%

After the parameter setting was determined during signal processing, the magnetic features obtained from the surface hardness tests of Cr12MoV steels and S136 steels (60 specimens for each steel) were analyzed. The average values of the coefficients of variation for the two materials are listed in Table 1. The *DH50M* coefficient of variation was greater than 5%, so it was not used in subsequent surface hardness modeling. Figures 9 and 10 show the dependency of typical magnetic signatures on the surface hardness of the specimens of Cr12MoV steel and S136 steel. The same magnetic features of Cr12MoV and S136 steels showed a similar trend with surface hardness. *Mmax* shows a decreasing trend with the increase in surface hardness, whereas *Hcm* values showed the opposite trend. The difference might be interpreted as follows: The specimens with high surface hardness had a high percentage of martensitic volume content, which had a strong pinning effect on magnetic domains. Therefore, the flip of magnetic domains in the specimen required more energy from the applied magnetic field.

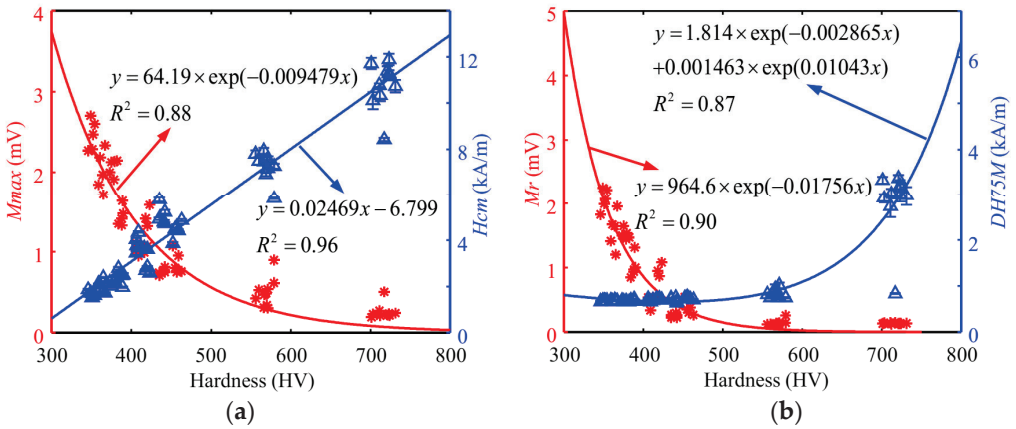

Figure 9. Dependency of the features on the surface hardness of Cr12MoV steel. (**a**) The relationship between *Mmax* (*Hcm*) and hardness. (**b**) The relationship between *Mr* (*Hcm*) and hardness.

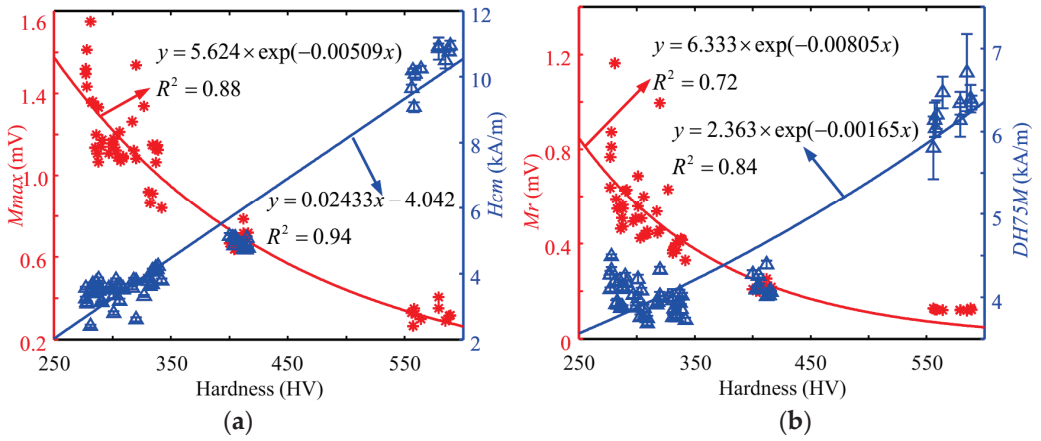

Figure 10. Dependency of the features on the surface hardness of S136 steel. (**a**) The relationship between *Mmax* (*Hcm*) and hardness. (**b**) The relationship between *Mr* (*DH75M*) and hardness.

3.2. Calculation of MBN Hysteretic Curve

In the plotting process of MBN butterfly curves, artificial time-shift adjustment is required and characterized by complicated parameter settings and many manual interventions. In this paper, we proposed a new processing method for MBN signals, in which the envelope of MBN signals was integrated to obtain the hysteresis loop-shaped MBNHL curve and then new features were extracted to determine their relationship with surface hardness.

The plotting steps of the MBNHL curve are shown in Figure 4. After the MBN signal processing steps of band-pass filtering, sliding average, and signal interception were completed according to Step 1 to Step 3 in Section 3.1, the MBN envelope was integrated and calculated. Firstly, the MBN envelope was averaged over eight magnetization cycles to obtain the envelope curve for a single magnetization cycle (Figure 11a). Then, with the first point of the single cycle as the starting point, the envelope of the first half cycle was integrated, and the envelope of the second half cycle was integrated and flipped. Finally, a closed curve was obtained through the envelope integration of the first half cycle and the envelope integration and flipping of the second half cycle. The MBNHL curve was obtained by integrating the MBN signal envelope so that the MBNHL feature corresponded to the MBN feature. For example, the maximum slope of MBNHL was the peak value of the MBN signal, *Mmax*, and the location where the maximum slope occurred was the peak location, *Hcm*. In addition to the features mapped by the MBN envelope, new features shown in Table 2 could be extracted based on the MBNHL curve.

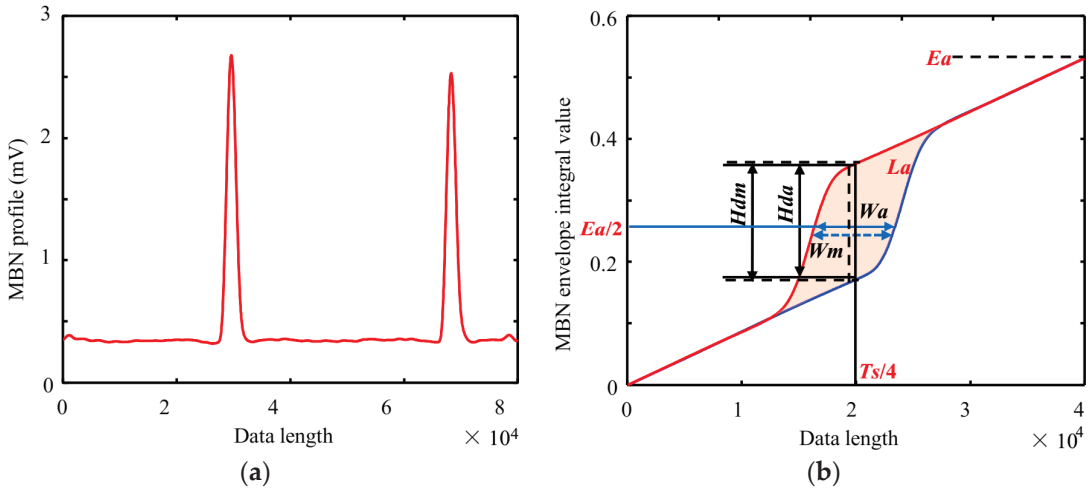

Figure 11. (**a**) MBN envelope obtained after resampling and (**b**) MBNHL curve.

Table 2. Features extracted from the MBNHL and coefficient of the variation.

Features	MBNHL Curve Explanation	Coefficient of Variation (%)	
		Cr12MoV	S136
x_7	Maximum point on the integration curve, *Ea*	1.9	1.5
x_8	Time difference between two points on the integration curve corresponding to Ea/2, *Wa*	1.1	1.1
x_9	Maximum time difference for the same integral value on the integration curve, *Wm*	1.6	1.2
x_{10}	Height difference between the two integration curve at Ts/4, *Hda*	3.5	3.5
x_{11}	Maximum difference between two integration curves at the same time, *Hdm*	3.2	3.2
x_{12}	The area of the closed curve, *La*	3.6	3.9

Typical MBNHL curves plotted for different surface hardness specimens of Cr12MoV steel and S136 steel are shown in Figure 12a,b. The MBNHL curve could be used to distinguish the hardness variation and was sensitive to surface hardness. The coefficients of variation of the six features extracted from the MBNHL were less than 2% (Table 2), indicating the highly stable magnetic features extracted by the MBNHL method.

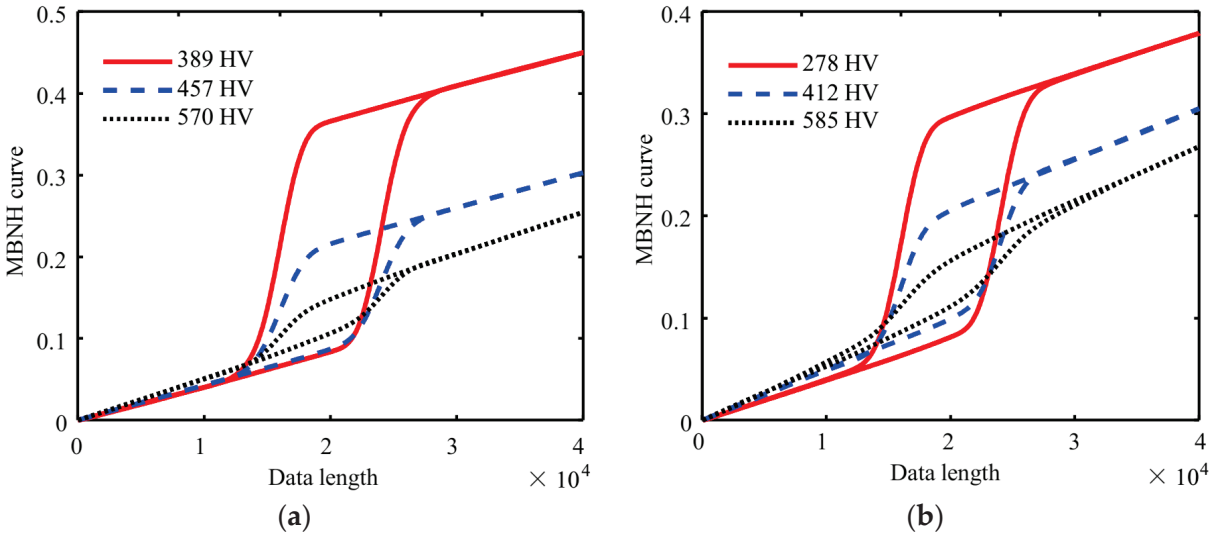

Figure 12. MBNHL curves for different surface hardness specimens of (**a**) Cr12MoV steel and (**b**) S136 steel.

Figure 13 shows the correlation between MBNHL features and surface hardness. The peak and area of MBNHL curves for both materials showed a decreasing trend with the increase in surface hardness. It is worth noting that the changing trend of one magnetic feature with surface hardness is the same for both materials and shows a nonlinear correlation.

The key to the quantitative prediction of surface hardness with the micromagnetic method is to provide stable and reliable input data. Compared with the traditional MBN butterfly curve method, the waveform processing and features extraction method of the MBNHL curve showed the advantages of simple parameter setting, less manual intervention, and stable data.

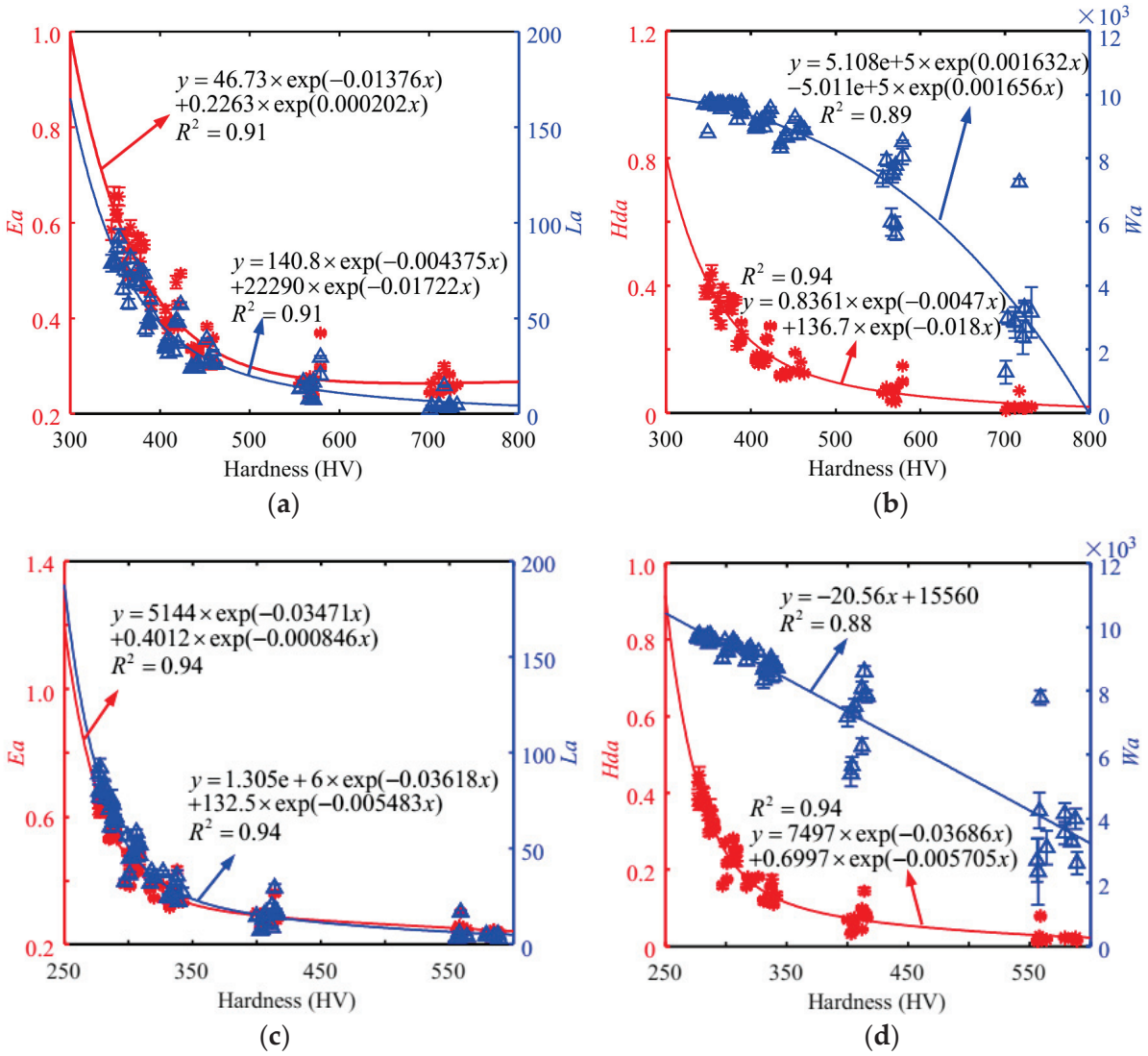

Figure 13. Dependency of the features of *Ea*, *La*, *Hda*, and *Wa* on the surface hardness of (**a**,**b**) Cr12MoV steel and (**c**,**d**) S136 steel.

4. Results and Discussion

The mechanism of microstructure influence on magnetic domain motion has not been well explained [26], so it is not possible to establish an accurate analytical model between the microstructure of the material and the surface hardness [27]. Therefore, a new method of micromagnetic nondestructive measurement of mechanical properties is developed to obtain the macroscopic magnetic feature signals and mechanical properties of materials step by step through calibration experiments and to establish quantitative prediction models of mechanical properties using artificial intelligence algorithms. With the multifunctional micromagnetic inspection instrument, abundant magnetic features that were sensitive to surface hardness were obtained in Section 3. Considering the nonlinear relationship between most of the magnetic features and surface hardness and the excellent performance of neural networks in solving nonlinear problems, a neural network prediction model of surface hardness was developed with several sensitive magnetic parameters as the input to characterize surface hardness in the study.

The selection of input parameters directly affects the performance of a BP neural network model. The mean influence value (MIV) method can be used to evaluate the weight of the influence of each parameter of the input neural network on output variables. A BP neural network with a three-layer structure (input, hidden, and output layers) was

chosen to find the MIV value for each magnetic parameter of the input model, where the number of neurons in the middle-hidden layer was fixed at 10. The absolute value of MIV represented the degree of influence of each parameter in the model. Figure 14 shows the MIV analysis results of both materials.

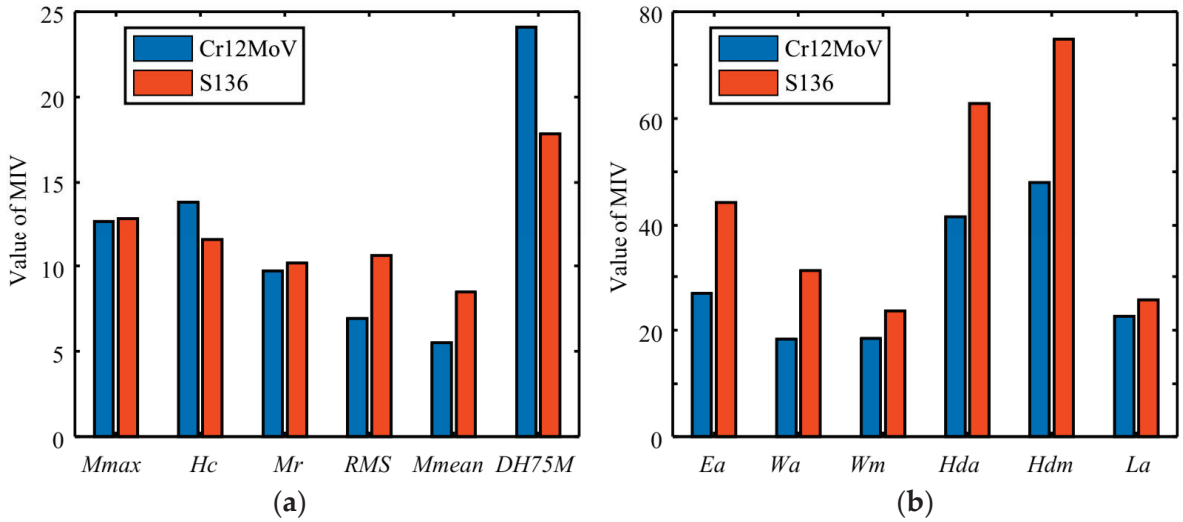

Figure 14. Analysis results of MIV weight coefficients with the data from (**a**) MBN and (**b**) MBNHL.

The features were input into the model in descending order of MIV weight coefficients, and the number of input nodes for the BP model was determined with the training data for internal validation and RMSE estimation of the BP model. Figure 15 shows the RMSE results of the BP model with different input nodes. The six magnetic features calculated with the MBN method were input into the model in descending order of weighting coefficients. The RMSE decreased significantly when the number of input nodes was increased from one to five in the models of Cr12MoV and S136 steels (Figure 15a). RMSE increased when the number of input nodes increased to six (Figure 15a). Therefore, parameters x_1, x_2, x_3, x_4, and x_6 were selected and used in the final training phase of the BP model. The same analysis was performed for the six magnetic features obtained with the MBNHL method (Figure 15b). The RMSE of the model decreased with the increase in input features, and the input nodes of the final prediction model for Cr12MoV and S136 steels were x_7 to x_{12}.

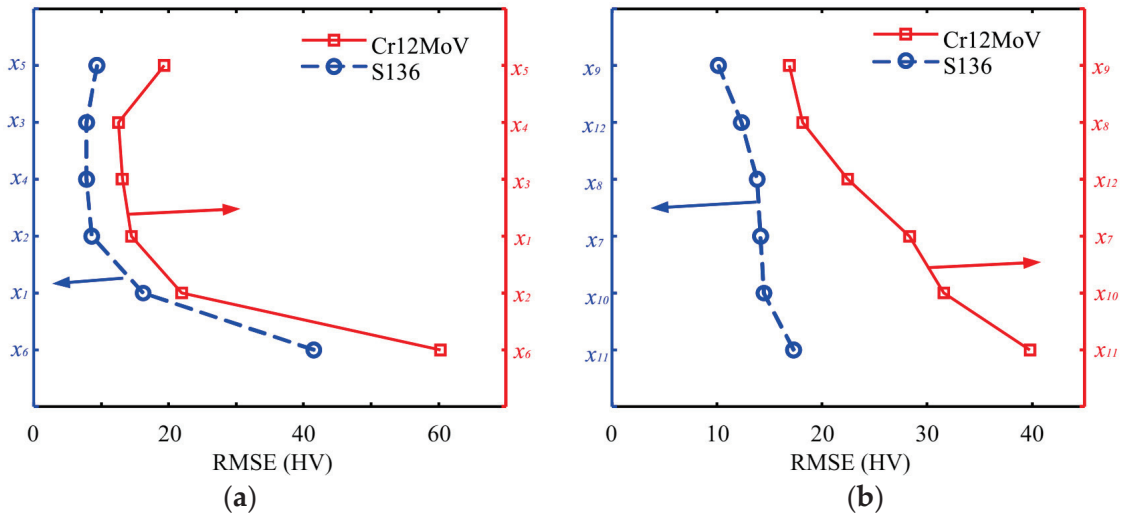

Figure 15. RSME values of the BP model with the input data from (**a**) MBN and (**b**) MBNHL.

A BP neural network was used to construct a quantitative prediction model of surface hardness after the input parameters and nodes were identified. Both the training and

validation sets were normalized before they were input into the BP neural network model. The predicted values produced by the model were then subjected to reverse normalization. Based on the neural network toolbox (nntool) in the Matlab 2020b software, the activation functions of the hidden layer and output layer were, respectively, the "tansig" function and the "purelin" function, and the "trainlm" training function. The chosen magnetic parameters were selected as input nodes, and surface hardness was the output node.

In order to train the model, two-thirds of the magnetic parameters derived from MBN for Cr12MoV steel and S136 steel were randomly chosen as the training set (600 sets of data), and the remaining one-third of the data (300 sets of data) was utilized as the validation set to assess the prediction accuracy of the model. Figure 16 displays the prediction errors of surface hardness of Cr12MoV steel and S136 steel. For the two materials, the average prediction errors of surface hardness were 1.4% and 3.25%, respectively. The largest errors were, respectively, 8.0% and 12.5%. Among the 300 cases, only nine of the S136 data points had a prediction error of more than 10%.

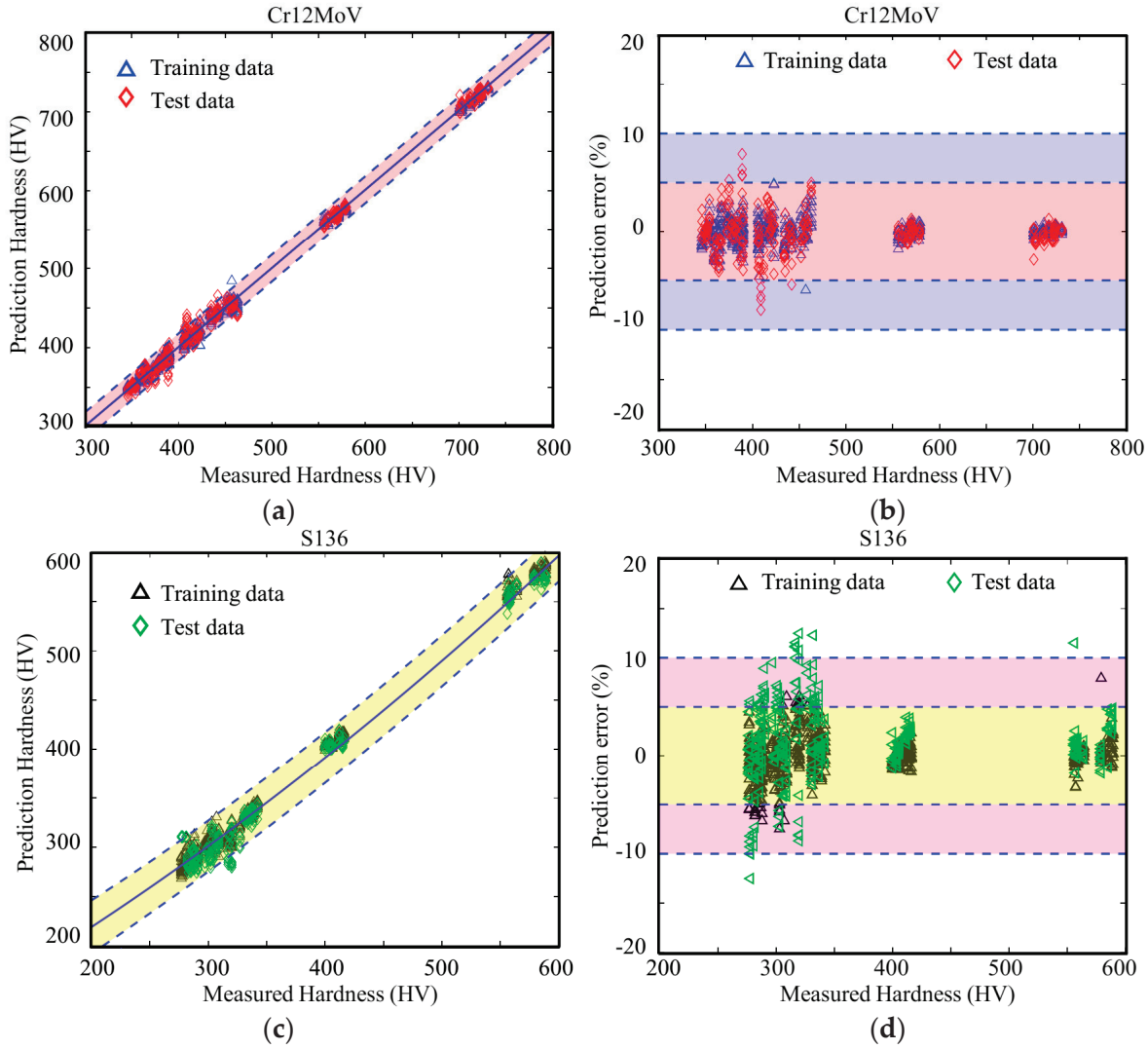

Figure 16. Prediction errors of the models based on the parameters obtained with the MBN method for (**a**,**b**) Cr12MoV steel and (**c**,**d**) 3Cr13 steel.

When the network structure and model parameters of the BP model were fixed, 2/3 (600 sets of data) of the magnetic parameters generated by MBNHL were randomly chosen as the training set, and the remaining 1/3 data set (300 sets of data) were used to assess the prediction accuracy of the model. The average errors of surface hardness of Cr12MoV

steel and S136 steel were, respectively, 2.5% and 3.8% (Figure 17). The maximum errors of Cr12MoV steel and S136 steel were, respectively, 9.9% and 13.7%. In the 300 cases of Cr12MoV steel and S136 steel, the prediction errors of 22 cases of S136 steel were larger than 10%.

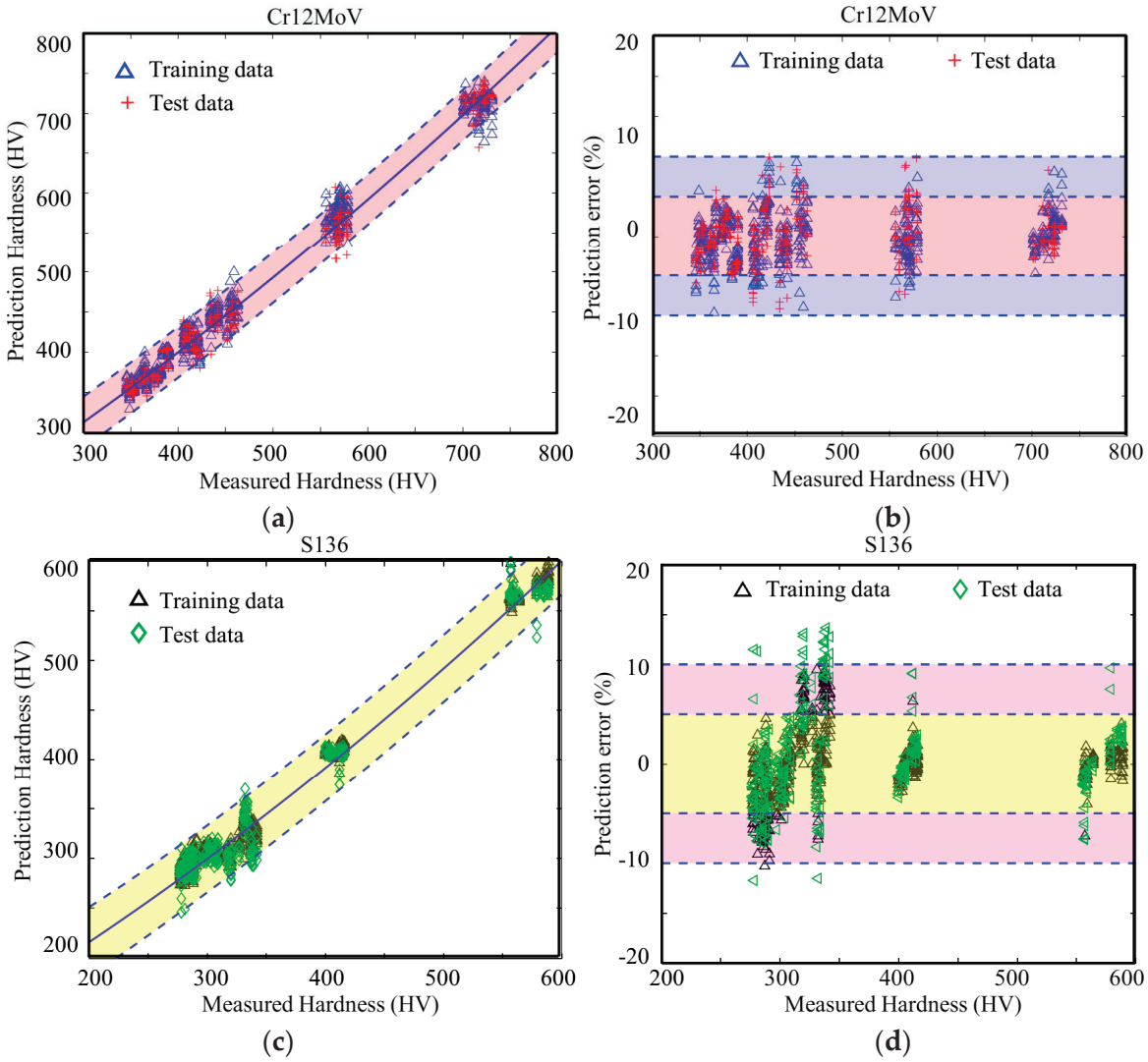

Figure 17. Prediction errors of the models based on parameters obtained with the MBNHL method for (**a**,**b**) Cr12MoV steel and (**c**,**d**) 3Cr13 steel.

5. Conclusions

In this study, BP-NN and micro-magnetic testing were combined together to achieve a quantitative prediction of the surface hardness of S136 and Cr12MoV steels. The phase adjustment in the curve plotting process had a significant impact on the shape of the plotted butterfly curve and the stability of feature extraction. The generally used MBN butterfly curve plotting method is easily influenced by personnel experiences. A plotting and parameter extraction of a hysteresis loop-shaped BN circular curve was proposed in order to address the problems of complex parameter setting and excessive user intervention in the plotting process of MBN butterfly curves. Surface hardness and the newly derived features exhibited a strong association. Compared with traditional MBN feature extraction methods, the new features exhibited high stability.

For the purpose of making a quantitative prediction of the surface hardness of Cr12MoV steel and S136 steel, a BP-NN model with the same structural parameters was established. For Cr12MoV steel and S136 steel, the average prediction errors of the fea-

tures derived by MBN were about 1.4% and 3.25%, respectively. The average prediction errors of the features extracted with the MBNHL method were 2.5% and 3.8%, respectively. Compared to the MBN method, the proposed MBNHL method is characterized by simple parameter configuration, reduced user intervention, simple parameter extraction, and comparable prediction accuracy.

Author Contributions: Writing—review and editing, X.W.; data curation, Y.C.; methodology, X.L.; funding acquisition, C.H. All authors have read and agreed to the published version of the manuscript.

Funding: This study was supported by the National Natural Science Foundation of China (Project Nos. 11527801, 12122201, and 11872081) and the Beijing Nova Program of Science and Technology under grant No. Z191100001119044.

Institutional Review Board Statement: Not applicable.

Informed Consent Statement: Not applicable.

Data Availability Statement: Data are contained within the article.

Conflicts of Interest: All authors certify that they have no affiliations with or involvement in any organization or entity with any financial interest or non-financial interest in the subject matter or materials discussed in this manuscript.

References

1. Hanke, R. Fraunhofer institute for non-destructive testing IZFP—Expanding the potential of NDT across the entire product life cycle. In Proceedings of the 55th Annual Conference of the British Institute of Non-Destructive Testing, NDT 2016, Nottingham, UK, 12–14 September 2016; pp. 305–308.
2. Dobmann, G. Physical basics and industrial applications of 3MA—Micromagnetic multiparameter microstructure and stress analysis. In Proceedings of the 10th European Conference on Nondestructive Testing, ECNDT 2010, Moscow, Russia, 7–11 June 2010; pp. 7–11.
3. Wolter, B.; Gabi, Y.; Conrad, C. Nondestructive Testing with 3MA—An Overview of Principles and Applications. *Appl. Sci.* **2019**, *9*, 1068. [CrossRef]
4. Sorsa, A.; Santa-Aho, S.; Aylott, C. Case Depth Prediction of Nitrided Samples with Barkhausen Noise Measurement. *Metals* **2019**, *9*, 325. [CrossRef]
5. Stupakov, A.; Perevertov, A.; Neslusan, M. Reading depth of the magnetic Barkhausen noise. i.one-phase semi-hard ribbons. *J. Magn. Magn. Mater.* **2020**, *513*, 167086. [CrossRef]
6. Stashkov, A.N.; Schapova, E.A.; Nichipuruk, A.P. Magnetic incremental permeability as indicator of compression stress in low-carbon steel. *NDT E Int.* **2021**, *118*, 102398. [CrossRef]
7. Golling, S.; Frómeta, D.; Casellas, D. Influence of microstructure on the fracture toughness of hot stamped boron steel. *Mater. Eng. A* **2019**, *743*, 529–539. [CrossRef]
8. Qiu, F.; Ren, W.; Tian, G.Y. Characterization of applied tensile stress using domain wall dynamic behavior of grain-oriented electrical steel. *J. Magn. Magn. Mater.* **2017**, *432*, 250–259. [CrossRef]
9. Ghanel, S.; Kashefi, M.; Mazinani, M. Comparative study of eddy current and Barkhausennoise nondestructive testing methods in microstructural examination of ferrite–martensitedual-phase steel. *J. Magn. Magn. Mater.* **2014**, *356*, 103–110. [CrossRef]
10. Liu, X.C.; Shang, W.L.; He, C.F. Simultaneous quantitative prediction of tensile stress, surface hardness and case depth in medium carbon steel rods based on multifunctional magnetic testing techniques. *Measurement* **2018**, *128*, 455–463. [CrossRef]
11. Ding, S.; Tian, G. Non-destructive hardness prediction for 18CrNiMo7-6 steel based on feature selection and fusion of Magnetic Barkhausen Noise. *NDT E Int.* **2019**, *107*, 102138. [CrossRef]
12. Jedamski, R.; Epp, J. Non-Destructive Micromagnetic Determination of Hardness and Case Hardening Depth Using Linear Regression Analysis and Artificial Neural Networks. *Metals* **2020**, *11*, 18. [CrossRef]
13. Yan, Z.X.; Sun, G.M.; Liu, X.C. FilterNet: A deep convolutional neural network for measuring plastic deformation from raw Barkhausen noise waveform. *J. Magn. Magn. Mater.* **2022**, *555*, 169330. [CrossRef]
14. Zhu, B.; Xu, Z.; Wang, K.; Zhang, Y. Nondestructive evaluation of hot stamping boron steel with martensite/bainite mixed microstructures based on magnetic Barkhausen noise detection. *J. Magn. Magn. Mater.* **2020**, *503*, 166598. [CrossRef]
15. Krause, A.K.; Underhill, P.R.; Krause, T.W.; Clapham, L. Magnetic Flux Density Superposition in Nonlinear Anisotropic Ferromagnetic Material and Resulting Magnetic Barkhausen Noise. *IEEE Trans. Magn.* **2021**, *57*, 6101007. [CrossRef]
16. Nahak, B.; Srivastava, A. Non-destructive monitoring of electro-discharge machined die steel. *Arab. J. Sci. Eng.* **2022**, *47*, 15153–15160. [CrossRef]
17. Franco, F.A.; González, M.F.R. Relation Between Magnetic Barkhausen Noise and Hardness for Jominy Quench Tests in SAE 4140 and 6150 Steels. *J. Nondestruct. Eval.* **2013**, *32*, 93–103. [CrossRef]

18. Liu, X.; Zhang, R. Quantitative Prediction of Surface Hardness in 12CrMoV Steel Plate Based on Magnetic Barkhausen Noise and Tangential Magnetic Field Measurements. *J. Nondestruct. Eval.* **2018**, *37*, 38.
19. Akhlaghi, I.A.; Kahrobaee, S.; Nezhad, K.K. An accurate non-destructive method for determining mechanical properties of plain carbon steel parts using MHL and GRNN. *Nondestruct. Test. Eval.* **2020**, *36*, 278–296. [CrossRef]
20. Wang, X.X.; He, C.F.; Li, P. Micromagnetic and quantitative prediction of surface hardness in carbon steels based on a joint classification-regression method. *J. Nondestruct. Eval.* **2022**, *41*, 62. [CrossRef]
21. Dong, H.; Liu, X.; Song, Y. Quantitative Evaluation of Residual Stress and Surface Hardness in Deep Drawn Parts Based on Magnetic Barkhausen Noise Technology. *Measurement* **2021**, *168*, 108473. [CrossRef]
22. Vashista, M.; Paul, S. Novel processing of Barkhausen noise signal for assessment of residual stress in surface ground components exhibiting poor magnetic response. *J. Magn. Magn. Mater.* **2011**, *323*, 2579–2584. [CrossRef]
23. Stefanita, C.G.; Atherton, D.L.; Clapham, L. Plastic versus elastic deformation on magnetic Barkhausen noise in steel. *Acta Mater.* **2000**, *48*, 3545–3551. [CrossRef]
24. Ding, S.; Tian, G.Y.; Moorthy, V. New feature extraction for applied stress detection on ferromagnetic material using magnetic Barkhausen noise. *Measurement* **2015**, *73*, 515–519. [CrossRef]
25. Xing, Z.X.; Wang, X.X.; Ning, N.M. Micromagnetic and robust evaluation of surface hardness in Cr12MoV steel considering repeatability of the instrument. *Sensors* **2023**, *23*, 1273. [CrossRef]
26. Qiu, F.; Jovičević-Klug, M.; Tian, G.; Wu, G.; McCord, J. Correlation of magnetic field and stress-induced magnetic domain reorientation with Barkhausen Noise. *J. Magn. Magn. Mater.* **2021**, *523*, 167588. [CrossRef]
27. Takács, J. *Mathematics of Hysteretic Phenomena: The T(x) Model for the Description of Hysteresis*; Wiley-VCH: Weinheim, Germany, 2003.

materials

MDPI

Article

A Study on the Materials Used in Ancient Wooden Architectural Paintings at DaZhong Gate in Confucius Temple, Qufu, Shandong, China

Kuiju Li [1], Kezhu Han [1], Gele Teri [1], Yuxiao Tian [1], Menglei Cui [2,*], Yunpeng Qi [1,*] and Yuhu Li [1,*]

[1] Engineering Research Center of Historical Cultural Heritage Conservation, Ministry of Education, School of Materials Science and Engineering, Shaanxi Normal University, Xi'an 710119, China; kuijuli@163.com (K.L.); hankekezhu@126.com (K.H.); tianyuxiaotyx@163.com (Y.T.)

[2] Northwest Nonferrous Survey and Engineering Company, Xi'an 710000, China

* Correspondence: mengleicui@163.com (M.C.); qiyunpeng@snnu.edu.cn (Y.Q.); liyuhu@snnu.edu.cn (Y.L.)

Abstract: This study analyzes the pigments and binders used in the painted wooden structure of DaZhong Gate in the Confucius Temple in Qufu, Shandong Province, China. Five samples were collected from the building and analyzed using techniques such as polarized light microscopy (PLM), energy-dispersive X-ray spectroscopy (EDX), micro-Raman spectroscopy (m-RS), and Fourier-transform infrared spectroscopy (FT-IR). The findings reveal that the red, yellow, green, and blue pigments are identified as lead red, lead chromate yellow, emerald green, and ultramarine, respectively. The white pigment is determined to be a combination of chalk and lead white or anglesite. Considering the production period of the yellow and green pigments, it is inferred that architectural paintings underwent restoration or repainting during the late Qing Dynasty. The analysis of the binder in the pigment using pyrolysis–gas chromatography/mass spectrometry (Py-GC/MS) reveals that the binder employed is a protein-based glue. Additionally, the detected presence of Heat-bodied tung oil suggests a potential connection to traditional Chinese painting techniques on wooden surfaces. This discovery not only contributes to the historical research of the Confucius Temple but also provides crucial data for the conservation and restoration efforts of this culturally significant heritage site.

Keywords: ancient wooden architecture; color painting; pigments; binders; technical analysis

1. Introduction

The Confucius Temple, situated in Qufu City, Shandong Province, China (Figure 1), was originally erected in the year 479 BCE. This shrine venerates Confucius, the esteemed ancient Chinese philosopher and educator. The temple's design mirrors Confucius's dwelling and adheres to the architectural standards of an imperial palace. It stands as one of the four major ancient architectural complexes in China, holding considerable significance in world architectural history. The temple is of profound historical and cultural importance, possessing artistic value as well. In 1191 CE, the Confucius Temple experienced substantial expansion through the construction of additional structures, such as the DaZhong Gate. In the second year of the Yongzheng reign of the Qing Dynasty (1724 AD), the Temple of Confucius in Qufu was destroyed by lightning fire, and it took six years to rebuild it. In 1959, the partial restoration of the painted decorations on buildings such as the Shengshi Gate, DaZhong Gate, and Shengji Hall of the Temple of Confucius in Qufu was carried out. Over the centuries, the temple has undergone numerous expansions and renovations, ensuring its preservation to the present day.

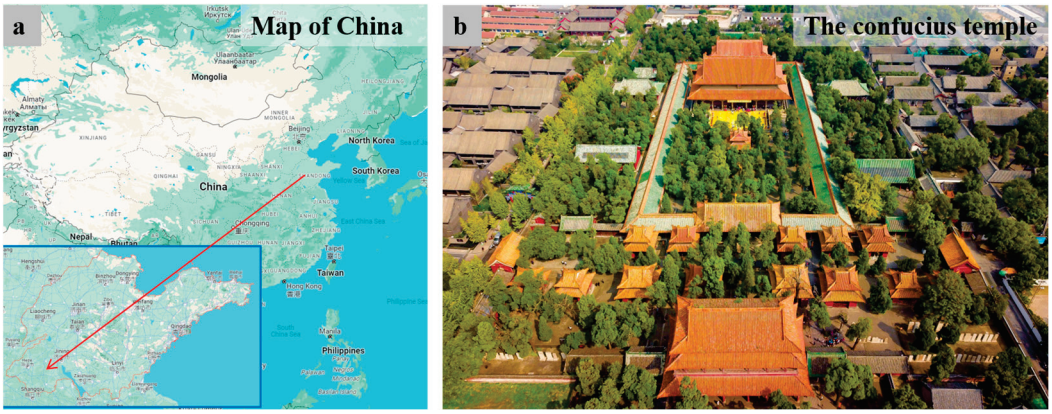

Figure 1. (**a**) The location of the Confucius Temple in Qufu City, Shandong Province; (**b**) an aerial view of the Confucius Temple (figure).

The DaZhong Gate, situated within the Confucius Temple's ancient architectural complex in Qufu, is adorned with a plethora of architectural paintings. Ancient Chinese architectural paintings encompass the artistic practice of embellishing buildings with colored paintings, reflecting a rich tradition with roots extending back to the Spring and Autumn Period. Historical records from this era mention the application of red paint to wooden structures. This artistic form evolved and matured across various dynasties, including the Qin, Han, Wei, Jin, Southern and Northern dynasties, Sui, Tang, Song, Yuan, and beyond [1]. The pinnacle of architectural paintings was reached during the Ming and Qing dynasties [1]. Commonly adorning structures such as temples, palaces, and government buildings, these paintings typically depict various themes like floral patterns, dragons and phoenixes, figures, stories, landscapes, and more. Beyond their decorative function, these artworks serve reflective purposes, offering glimpses into the cultural characteristics of the society during the respective periods.

The ancient Chinese architectural paintings extensively utilized natural and probably artificial mineral pigments [2,3]. For instance, the more widely used red pigments are cinnabar (HgS) [4], hematite (α-Fe_2O_3), red lead (Pb_3O_4), and synthetic red lead; the yellow pigments are orpiment (As_2S_3), realgar (As_4S_4) [1], and goethite (FeO·OH); the green colors are malachite [$CuCO_3 \cdot Cu(OH)_2$] [5], emerald green [$Cu(CH_3COO)_2 \cdot 3Cu(AsO_2)_2$], and atacamite [$Cu_2(OH)_3Cl$]; the blue pigments are lapis lazuli [$(Na,Ca)_8(AlSiO_4)_6(S,Cl)_2$], Chinese blue ($BaCuSi_4O_{10}$), and azurite [$2CuCO_3 \cdot Cu(OH)_2$]; the white pigments are lead white [$2PbCO_3 \cdot Pb(OH)_2$], synthetic lead white, chalk ($CaCO_3$), and dolomite [$CaMg(CO_3)_4$]; and the black pigments include carbon black (C) and magnetite (Fe_3O_4). In the Du Le Temple of the Liao Dynasty (10th century AD), materials such as carbon black, cinnabar, lapis lazuli, massicot (β-PbO), litharge (α-PbO), and atacamite were used [6]. In the Longju Temple of the Ming Dynasty (15th century AD), materials like atacamite, azurite, carbon black, and cinnabar were utilized [4]. In the Taiping Heavenly Kingdom Prince Dai's Mansion during the Qing Dynasty (19th century AD), materials such as cinnabar, ivory black (C), indigo blue ($C_{16}H_8N_2Na_2O_8S_2$) and phthalocyanine green ($CuC_{32}N_8Cl_{16}$) were employed [3]. To express it clearly, some commonly used pigments are listed in Table 1. To ensure adherence for an extended period on the plaster of wooden structures or silica-based walls, these mineral pigments were mixed with binders. Binders typically consisted of natural organic substances like animal skin glue, egg white, casein, peach gum, and linseed oil [7]. For instance, the binder of the mineral pigments used in Qin Shihuang's Terracotta Warriors (3rd century BC) included animal glue and egg whites [8,9]. Animal glue was also found in the marinade layer of the Western Han Dynasty (3rd century BC) painted pottery terracotta warriors [10]. Plaster, a traditional Chinese civil engineering technique, was applied to the surface of wooden structures to prevent decay and moisture while providing a substrate for painting [11]. The plaster for painting ancient wooden buildings typically comprised tung oil, flour, lime water, brick powder, and plant fiber. In Qing Dynasty's Buddhist Temple in

Beijing (17th century AD), the plaster layer incorporated brick powder and ramie fibers [12]. The Yi Ma Wu Hui layer of Putuo Zongcheng Temple (18th century AD) utilized tung oil, gray brick powder, and ramie fiber [11].

Table 1. The examples of usage and the enumeration of common pigments mentioned in the Introduction.

Color	Pigment Name	Chemical Formula	Location of Use
Red	Cinnabar	HgS	Du Le Temple (10th century AD), etc.
	Red lead	Pb_3O_4	Royal Residence (19th century AD)
	Litharge	α-PbO	Du Le Temple (10th century AD)
Yellow	Orpiment	As_2S_3	Assembly Hall (19th century)
	Realgar	As_4S_4	Royal Taoist Temple (16th century)
	Massicot	β-PbO	Du Le Temple (10th century AD)
green	Emerald Green	$Cu(CH_3COO)_2 \cdot 3Cu(AsO_2)_2$	Jiangxue Palace (15th century AD)
	Atacamite	$Cu_2(OH)_3Cl$	Longju Temple (15th century AD), etc.
	Phthalocyanine	$CuC_{32}N_8Cl_{16}$	Prince Dai's Mansion (19th century AD)
Blue	Lapis lazuli	$(Na,Ca)_8(AlSiO_4)_6(S,Cl)_2$	Du Le Temple (10th century AD)
	Azurite	$2CuCO_3 \cdot Cu(OH)_2$	Longju Temple (15th century AD)
	Indigo blue	$C_{16}H_8N_2Na_2O_8S_2$	Prince Dai's Mansion (19th century AD)
White	Lead white	$2PbCO_3 \cdot Pb(OH)_2$	Puren Temple (18th century AD)
Black	Carbon black	C	Longju Temple (15th century AD), etc.

The analysis of mineral pigments entails a thorough examination across three dimensions: morphology observation, elemental determination, and composition identification [3]. The utilization of polarized light microscopy (PLM) [3,13] facilitates the observation and assessment of morphological intricacies, optical properties, and crystalline features of mineral pigments. Advanced techniques, including energy-dispersive X-ray spectroscopy (EDX) [14], scanning electron microscopy with energy-dispersive spectroscopy (SEM-EDS) [15], and energy-dispersive X-ray fluorescence (XRF) [16], are employed to determine the elemental constitution of the pigments. Moreover, sophisticated methods like X-ray diffraction (XRD) [17], Fourier-transform infrared spectroscopy (FT-IR) [6], and micro-Raman spectroscopy (m-RS) [18] further delineate the compositional constituents of these pigments. Throughout this investigation, we employed a combination of analytical techniques for the identification of pigment components. PLM, EDX, m-RS, and FT-IR were utilized to discern the constituents of the pigments. Simultaneously, pyrolysis–gas chromatography/mass spectrometry (Py-GC/MS) [19] was applied to ascertain the composition of binders within the pigments. This comprehensive approach ensures a thorough understanding of both the physical and chemical characteristics of the mineral pigments and their binder components.

In the current study, small samples of pigments were collected from the ancient architectural color paintings of the DaZhong Gate in the Confucius Temple, Qufu. Our investigation involved a thorough analysis of the components present in both the pigments and binders used in these historical artworks.

2. Materials and Methods

2.1. Pigment Sample Information

On the inner side of the wooden main beam in the DaZhong Gate of the Confucius Temple, as shown in Figure 2, we collected samples displaying five distinct colors: red, yellow, green, blue, and white. There is a scale bar with a length of 5 mm in the figure, and the area of the sample is approximately 1 cm^2. All five samples had dirt that was difficult to remove. To enhance the conservation of the color paintings, each sampled segment was meticulously chosen from regions either already detached or showing signs of imminent detachment.

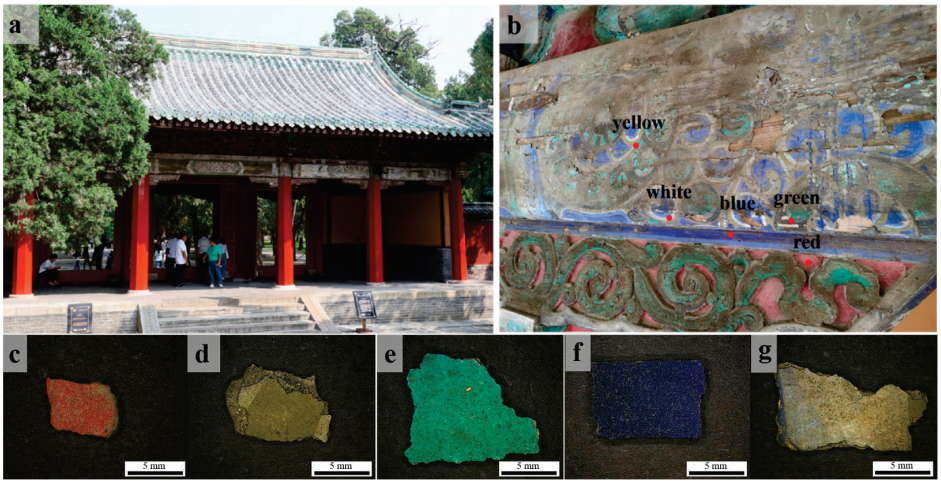

Figure 2. (**a**) The DaZhong Gate of the Confucius Temple; (**b**) marked positions of the sampling points inside the building; photographs of the sampled pigments: (**c**) DZ-1 (red), (**d**) DZ-2 (yellow), (**e**) DZ-3 (green), (**f**) DZ-4 (blue), and (**g**) DZ-5 (white). The length of the scale bar in the image is 5 mm.

2.2. Experimental Methods and Instrumentation

2.2.1. Polarized Light Microscopy (PLM)

The samples were initially subjected to pretreatment, where pigment particles were delicately scraped from the specimen using a surgical blade. These particles were then added to alcohol and dispersed for 30 min using an ultrasonic disperser. The dispersed pigment suspension was dropped onto a glass slide, and after the alcohol evaporated, a cover slip was placed over it. Subsequently, the entire slide was heated to 60–70 °C on a temperature-controlled heater, allowing the resin (Meltmount, Cargille; Cedar Grove, NJ, USA; refractive index of 1.662) to melt and permeate the entire cover slip. The cover slip was then slid along one side to secure the pigment particles.

Observations were carried out employing a polarized light microscope (Olympus BX53M, Shinjuku, Japan) with a magnification of 50 × 10.

2.2.2. Energy-Dispersive X-ray Spectroscopy (EDX)

The samples were directly placed on the sample stage for testing in ambient conditions, with each sample requiring approximately 5 min for analysis. The corresponding results are shown in Table 2.

Table 2. Overview of techniques used for pigment analysis and elemental composition obtained by EDX analysis for respective pigment samples.

Sample	Color	Experimental Methods	Elements (Wt %)
DZ-1	Red	PLM, EDX, m-RS	Pb (57.8), Ba (20.6), Ca (6.6), Si (6.0), Ce (3.7)
DZ-2	Yellow	PLM, EDX, m-RS	Ca (32.5), Ba (18.9), Zn (16.9), Pb (16.7), Si (7.2), Cr (4.3)
DZ-3	Green	PLM, EDX, m-RS	As (35.9), Cu (33.1), Ca (11.5), Si (11.3), S (6.2)
DZ-4	Blue	PLM, EDX, m-RS	Ca (33.1), S (27.2), Si (25.2), Pb (7.6), K (3.0)
DZ-5	White	PLM, EDX, m-RS, FT-IR	Ca (33.4), S (22.1), Ba (19.9), Zn (8.5), Si (7.3), Pb (3.3)

Energy-dispersive X-ray spectroscopy (EDX, EDX-7000, Shimadzu, Kyoto, Japan) was employed for the elemental characterization of the pigments. The X-ray tube within the EDX system comprised a rhodium target and a silicon drift detector, enabling the detection of various elements spanning from sodium (Na) to uranium (U).

2.2.3. Micro-Raman Spectroscopy (m-RS)

The samples were directly placed on glass slides and positioned on the sample stage. Utilizing a microscope system, crystal particles within the samples were located, and Raman spectra were acquired using the Renishaw Invia reflection system (Invia Reflex, Renishaw, UK).

Micro-Raman spectroscopy was employed for the spectral analysis of pigment samples. It utilized a grating with 400 lines/mm and a 2-micron spot size, covering a spectral range from 100 cm^{-1} to 3500 cm^{-1}. Excitation wavelengths of 532 nm and 785 nm were available. The objective had a magnification of 50×, with an exposure time of 30 s, an accumulation time of 1 s, and a laser power of 2 mW. The Renishaw Wire software version 4.3 (Wotton-under-Edge, UK) was used for spectrum processing equipped with an argon ion laser, Leica microscopes, and a charge-coupled detector (CCD).

2.2.4. Fourier-Transform Infrared Spectroscopy (FT-IR)

Potassium bromide (KBr) was placed in a drying oven at 300 °C for 3 h. Pigment particles were delicately scraped from the specimen using a surgical blade. Subsequently, the scraped pigment particles weighing 2 mg in total were mixed and ground with 150 mg of dried potassium bromide, and the resulting mixture was pressed into a thin plate using a hydraulic press.

Fourier-transform infrared spectroscopy (FT-IR, Thermo Scientific Nicolet iS10, Waltham, MA, USA) was employed to scan and detect the pretreated sample pellets in the wavelength range of 500–4000 cm^{-1}. The spectral resolution was set at 1 cm^{-1}.

2.2.5. Pyrolysis–Gas Chromatography/Mass Spectrometry (Py-GC/MS)

An amount of 0.1 mg of the sample was taken, powdered, and placed into a thermally cleaved sample cup. Then, 2 μL of a 25% mass fraction solution of tetramethylammonium hydroxide (TMAH, Aladdin, Shanghai, China) was added and allowed to precipitate for 1 h. Subsequently, the mixture was placed under an infrared lamp and left to cleave after water evaporation. During the analysis, the pyrolysis temperature was set at 600 °C, the pyrolysis interface temperature was 300 °C, and the pyrolysis inlet temperature was 250 °C. The 40 °C chromatographic column was ramped to 280 °C at a rate of 10 °C/min, and this rate was maintained for 20 min. In the GC/MS procedure, a high-purity helium carrier gas was used with an inlet pressure of 15.2 kPa and a split ratio of 1:100. A constant flow mode was maintained in the electron pressure control system. The mass spectrometer was run with electron ionization at an ionization energy of 70 eV. The scanning range was set from 50 to 750, with a cycle time of 0.5 s. Subsequently, we used NIST14 and the corresponding mass spectrometer to identify the separated substances.

The pyrolysis–gas chromatography/mass spectrometry (Py-GC/MS) technique involved the use of a pyrolysis unit (EGA/PY-3030D, Frontier Labs, Fukushima, Japan) and a gas chromatography/mass spectrometry instrument (GC/MS-QP2010Ultra, Shimadzu, Japan). The chromatographic column utilized in this method was SLB-SMS (5% diphenyl/95% dimethyl siloxane), which has a length of 30 m, an inner diameter of 0.25 mm, and a film thickness of 0.23 mm.

3. Results and Discussion

3.1. Pigments

3.1.1. Red

The morphology of the DZ-1 sample particles was observed using PLM. As illustrated in Figure 3a,b, under single polarized light (plane-polarized light), the pigment particles exhibited an indistinct crystalline edge. Under orthogonally polarized light (cross-polarized light), the pigment particles displayed strong extinction. Considering these characteristics, we preliminarily deduce that its optical properties belong to either cinnabar or red lead (Pb_3O_4) [20]. Further, EDX elemental analysis results (Table 2) revealed a significant amount of lead in the DZ-1 sample, confirming its definite content of red lead. None of the other red

pigments contain lead elements, and the sample lacks characteristic elements of cinnabar as well. Analyzing the sample with m-RS, as shown in Figure 4a, peaks were observed in the Raman spectrum at 120, 151, 222, 312, 388, 478, and 548 cm^{-1}. Comparing these peaks with standard Raman spectra of red pigments, we can see that they align precisely with the Raman spectrum of red lead [21–25]. Notably, the peak at 548 cm^{-1} is attributed to the Pb–O stretching vibration in red lead [26].

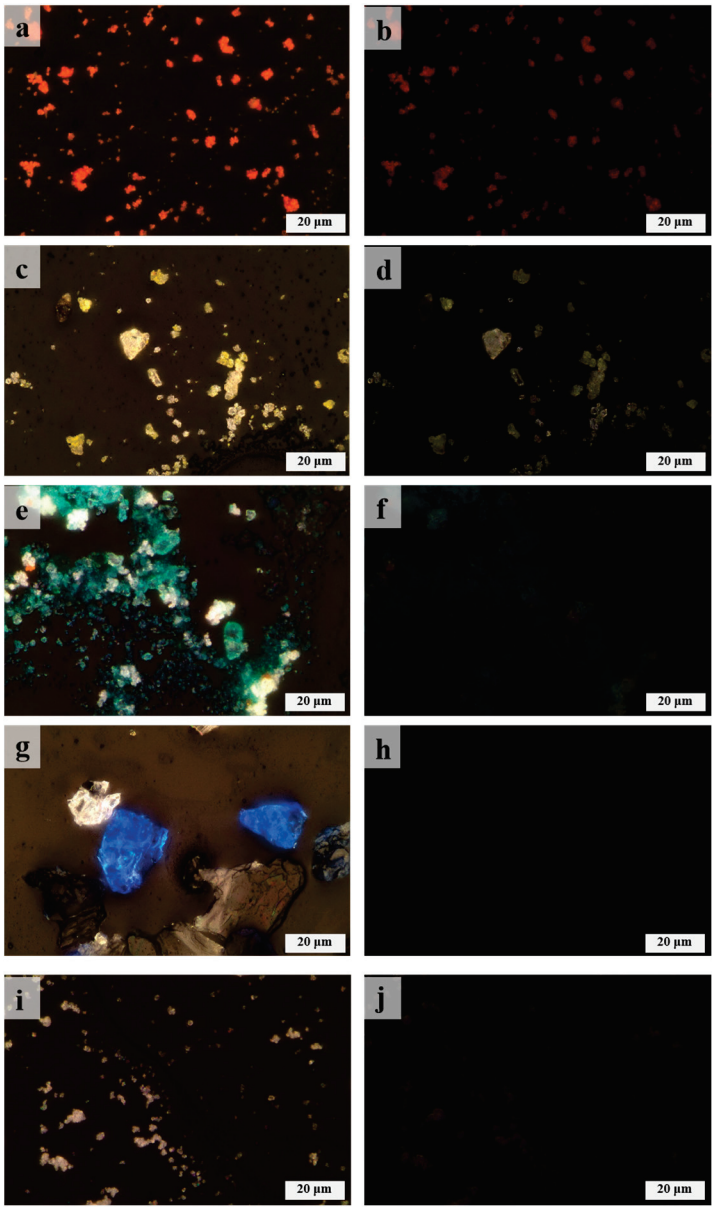

Figure 3. PLM images observed under single and orthogonally polarized light for (**a**,**b**) red, (**c**,**d**) yellow, (**e**,**f**) green, (**g**,**h**) blue, and (**i**,**j**) white pigments. All samples were observed under 100 × 5 magnifications. The sampling positions are shown in Figure 2.

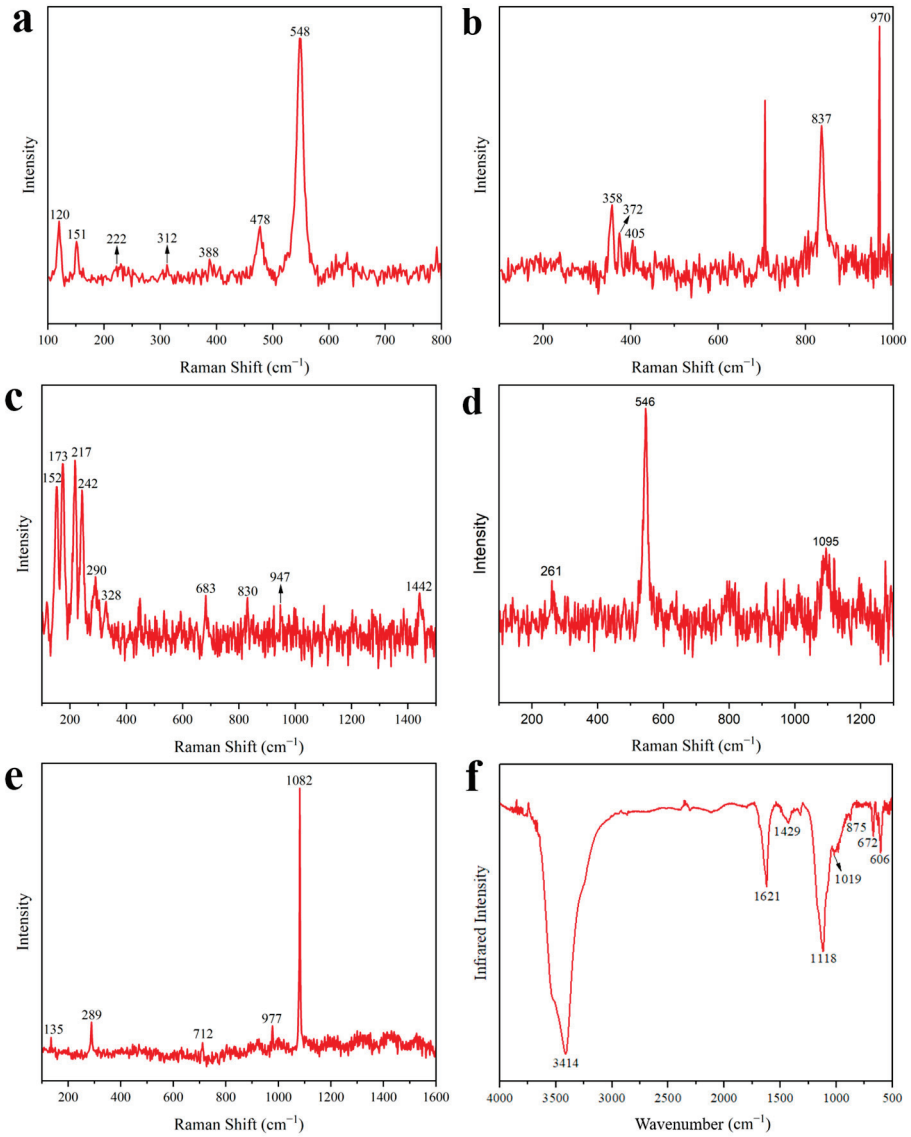

Figure 4. (**a**) Raman spectrum for red pigment (DZ-1); (**b**) Raman spectrum for yellow pigment (DZ-2); (**c**) Raman spectrum for green pigment (DZ-3); (**d**) Raman spectrum for blue pigment (DZ-4); (**e**) Raman spectrum of white pigment (DZ-5); (**f**) FT-IR spectrum for white pigment (DZ-5).

Red lead, known as lead tetroxide or minium, is one of the most commonly used red pigments in ancient China. The manufacturing process of red lead has been documented in China since the 3rd century BCE, and records about red lead can also be found in Roman literature from the 1st century AD. The DZ-1 sample exhibits localized darkening on its surface under a macro lens, as shown in Figure 2c, a characteristic feature of red lead distinct from other red pigments. Due to its lively chemical nature, ancient lead-containing pigments, such as red lead, are prone to environmental erosion and can easily discolor into plattnerite (PbO_2) during prolonged preservation. Reports of red lead aging into lead dioxide have been documented in the Dunhuang Mogao Caves in China [27] and Panselinos' Byzantine wall paintings in Greece [28]. Red lead may also contain other substances similar to massicot. The ancient Chinese production of red lead involved heating lead, and as the temperature increased, metallic lead would first react with oxygen in the air to form massicot (β-PbO). When the temperature reached 450–470 °C, it would further oxidize into the red pigment red lead [29,30]. Consequently, some red lead pigments may contain a mixture of massicot.

3.1.2. Yellow

The elements detected in the sample using EDX include Pb and Cr (Table 2), and based on the elemental composition, it corresponds to the yellow pigment lead chromate yellow [22]. However, the EDX analysis results show the presence of Ca, Ba, and Zn. Based on their chemical formulas, they may correspond to barium chromate and zinc chromate. Barium chromate typically exhibits strong peaks at 863 cm^{-1} and medium-intensity peaks at 901 cm^{-1} in Raman spectra [22]. Zinc chromate usually shows a strong peak at 872 cm^{-1} and medium-intensity peaks at 343 cm^{-1} and 941 cm^{-1} in Raman spectra [22]. As shown in Figure 4b, none of these peaks were observed in the Raman detection results of sample DZ-2. Therefore, we speculate that the existence of these two pigments is unlikely. Additionally, barium chromate and zinc chromate are not commonly found in the pigments used in ancient Chinese architectural paintings. Moreover, there are some stains on the surface of sample DZ-2 that are difficult to remove, so it is inferred that Ca, Ba, and Zn are impurities in the sample. Figure 3c,d show particle photos of the DZ-2 sample under single polarized light and orthogonally polarized light. As shown in Figure 4b, in the m-RS analysis of DZ-2, peaks appear at 358, 372, 405, and 837 cm^{-1}. Comparing with the standard Raman spectroscopy database, these peaks correspond to chrome yellow deep ($PbCrO_4 \cdot PbO$) [1,22,24]. The strong peak at 970 cm^{-1} possibly corresponds to lead white [$2PbCO_3 \cdot Pb(OH)_2$] or anglesite ($PbSO_4$), and in the DZ-2 sample, it is located near the junction of the yellow and white areas, suggesting a possible mixture of white pigment. It is also possible that the yellow and white pigments were mixed to achieve the desired color by the painter.

Chrome yellow deep is the aged form of lead chromate yellow, also known as chrome yellow. Lead chromate yellow was first synthesized by the French chemist L.N. Vauquelin in 1809, and its industrial production began in Germany in 1818. It has been discovered in Ming Dynasty polychrome sculptures at the Chongyang Temple in Shanxi Province, China [31]. As this pigment was discovered relatively late, the author suggests that the painted decorations on the DaZhong Gate of the Confucius Temple might have undergone restoration and repainting during the late Qing Dynasty.

3.1.3. Green

Using PLM to observe the DZ-3 sample, as shown in Figure 3e,f, it can be seen that under single polarized light, it presents a fan-shaped or even circular-fan surface shape, some even showing a rounded and angular shape. Under orthogonally polarized light, it exhibits strong extinction. Its color is a vibrant blue-green. Through EDX testing (Table 2), it is observed that the content of As and Cu elements is particularly high. Combined with the characteristics observed under PLM and the results of EDX analysis, it is preliminarily determined that DZ-3 contains emerald green [$Cu(CH_3COO)_2 \cdot 3Cu(AsO_2)_2$] [13,20]. Analyzing DZ-3 with m-RS, the obtained spectrum in Figure 4c shows strong peaks at 152, 173, 217, and 242 cm^{-1}, and relatively weaker peaks at 290, 328, 683, 830, 947, and 1442 cm^{-1}. Compared with the standard Raman spectrum of emerald green, it is found that these peaks correspond to the standard spectrum [22]. Therefore, we can confirm that the green pigment in DZ-3 is emerald green. Emerald green exhibits numerous peaks in the 100–400 cm^{-1} wavelength range, originating from the vibrations of Cu–O and As–O [32]. The peaks at 947 and 1442 cm^{-1} correspond to the acetate groups C–C and $–CO_2$ in emerald green [33].

Emerald green is a synthetically produced pigment that is highly toxic, and it tends to turn black upon exposure to hydrogen sulfide (HS). It was first synthesized in Germany in 1814 [34] and was introduced to China in the mid-19th century [35]. It was widely used in the ancient architectural paintings of late Qing Dynasty China. Examples of its use can be found in the Wuying Hall of the Imperial Palace in Beijing, China [35], and the Summer Palace in Beijing [36], China. According to the appearance time of this green pigment, the authors believe that the use of emerald green suggests that the architectural paintings might have undergone restoration and repainting during the late Qing Dynasty.

3.1.4. Blue

The polarization characteristics of DZ-4 were observed using PLM. As shown in Figure 3g, under single polarized light, the pigment particles exhibited mineral angular shapes and a vivid deep blue color. As shown in Figure 3h, under orthogonally polarized light, there was a strong extinction effect, even complete extinction. Leveraging the characteristic of full extinction under PLM, among common blue pigments, it can be tentatively inferred that the pigment used is ultramarine [20]. Further analysis using EDX on sample DZ-4 revealed a significant amount of Ca, S, and Si (Table 2). Comparing the chemical formulas of blue pigments, only ultramarine and Egyptian blue ($CaCuSi_4O_{10}$) roughly matched these elements; in fact, Egyptian blue was not found, since no copper was detected. Performing m-RS analysis on the sample, the Raman spectrum in Figure 4d shows a strong peak at 546 cm^{-1}, with weaker peaks at 261 and 1095 cm^{-1}. Compared with the standard Raman spectrum, it is consistent with the characteristic peaks of ultramarine [22]. It is worth noting that the sulfur-free radical, mainly S^{3-}, as the chromophore in ultramarine produces a strong Raman band at 544 cm^{-1} [35]. Combining PLM, EDX, and m-RS, it can be confirmed that the blue pigment used in DZ-4 is ultramarine.

Ultramarine blue comprises both natural ultramarine (lapis lazuli) [$(Na,Ca)_8(AlSiO_4)_6(S,Cl)_2$] and synthetic ultramarine ($Na_7Al_6Si_6O_{24}S_3$), making them challenging to distinguish through Raman spectroscopy [37]. The first synthetic ultramarine was produced in 1828. Due to its complex chemical structure, a fully quantitative analysis method was not established until the early 19th century to elucidate the chemical composition of ultramarine. Ultramarine tends to fade and decompose under acidic or alkaline conditions, even at low acid concentrations over an extended period. It has been extensively used in ancient Chinese architectural color paintings, such as found in Tanxi Hall of the Forbidden City in Beijing, China [38], and Tongcai paintings in Guangzhou, China [39].

3.1.5. White

EDX spectrum analysis was performed on the white sample DZ-5, revealing a significant presence of Ca, S, and Ba elements (Table 2). Comparing the elemental composition of white pigments, chalk ($CaCO_3$) and gypsum ($CaSO_4$) primarily contain Ca, while barite ($BaSO_4$) contains Ba. The sample may also contain white pigments with Zn and Pb. As shown in Figure 3i,j, the PLM analysis of DZ-5 displays pronounced extinction under orthogonally polarized light. The m-RS analysis of DZ-5 yielded a Raman spectrum, shown in Figure 4e, featuring a super-strong peak at 1082 cm^{-1} and relatively weaker peaks at 132, 289, 712, and 977 cm^{-1}. Compared with the standard Raman spectra of white pigments, these peaks correspond to those of chalk [22]. Specifically, 1082 cm^{-1} corresponds to the ν_1 symmetric stretching vibration of CO_3^{2-}; 289 cm^{-1} corresponds to the motion of Ca^{2+} relative to the CO_3^{2-} group; and 712 cm^{-1} is attributed to the ν_4 symmetric deformation vibration of CO_3^{2-} [40,41]. Peaks at 135 and 977 cm^{-1} correspond to the standard spectrum of lead white [$2PbCO_3 \cdot Pb(OH)_2$] or anglesite ($PbSO_4$) [22,42]. Additionally, as shown in Figure 4b, the Raman spectrum of DZ-2 shows a peak at 970 cm^{-1}, consistent with the peak of lead white or anglesite [22]. Since the yellow and white regions in DZ-2 are adjacent and considering the presence of Pb and S in the EDX analysis of the white sample, it is plausible that the white sample contains lead white or anglesite. The FT-IR analysis of the white sample DZ-5, as shown in Figure 4f, indicates the presence of OH^-, CO_3^{2-}, and SO_4^{2-} groups. Specifically, 1429 is attributed to the ν_3 and anti-symmetric stretching vibrations of carbonate ions [26,43,44]; 875 cm^{-1} corresponds to the out-of-plane deformation vibration of CO_3^{2-} [45]; 1118 cm^{-1} corresponds to the S–O anti-symmetric stretching vibration in SO_4^{2-} [46]; 606 cm^{-1} corresponds to the S–O anti-symmetric bending vibration [46]; 3414 cm^{-1} corresponds to the OH stretching vibration [26]; and 1019 cm^{-1} corresponds to the OH bending vibration [26]. Considering all these analyses, it can be inferred that the white pigment in DZ-5 is predominantly chalk, with a small amount of lead white or anglesite mixed pigment and possibly other SO_4^{2-}-containing white pigments. Unfortunately,

the complete Raman spectra of lead white or anglesite, as well as other SO_4^{2-}-containing white pigments, were not obtained during the white sample analysis.

Chalk and lead white were commonly used painting pigments in ancient China. The combination of various pigments in ancient Chinese architectural paintings was also common. Lead white is a lead-containing pigment that easily transforms into black lead dioxide (PbO_2) in the atmospheric environment, causing a darkening of color. The absence of black color in DZ-5 suggests that the low content of lead white in the mixed pigments may contribute to this phenomenon.

3.2. Binder

Using Py-GC/MS, an analysis was conducted on the yellow pigment sample DZ-2. The total ion chromatogram (TIC) of the analysis results is depicted in Figure 5, with representative and major peaks marked and listed in Table 3. The presence of amino acids such as glycine (peak 3), alanine (peak 6), valine (peak 7), L-proline, 1-methyl-, methyl ester (peak 8), hydroxyproline (peak 13), and some nitrogen-containing substances like methylamine, N,N-dimethyl- (peak 1), 1H-pyrrole, 1-methyl- (peak 2), methyl 1-methylpyrrole-2-carboxylate (peak 9), and benzene, isocyanato (peak 23) indicates the presence of proteins in DZ-2 [19], suggesting the existence of protein-based binders. The presence of naphthalene (peak 10) and 1H-indene, 1-methylene- (peak 11) also supports the presence of proteins [26]. The detected hydroxyproline in the sample is a characteristic amino acid of animal collagen [36]. Additionally, protein (peak 12) and protein blood and glue (peak 18) were directly detected in the sample. Furthermore, as shown in Figure 4f, in the infrared detection results of the white pigment sample, the absorption peak at 1621 cm^{-1} can be attributed to the amide I band, which is an important component of amino acids in proteins. Considering all the analyses, the binder used in the pigments primarily contains proteins. Due to prolonged exposure to outdoor conditions, the binder has undergone significant aging, resulting in a decrease in protein content compared to a fresh binder. The application of methylation technology is the reason why the test results contain a large number of methyl ester compounds, such as octanedioic acid, dimethyl ester (peak 15), nonanedioic acid, and dimethyl ester (peak 16). Since pigment binders on the same artwork are generally consistent [3,47], we focused our analysis on the pigment binder of the yellow sample in this study.

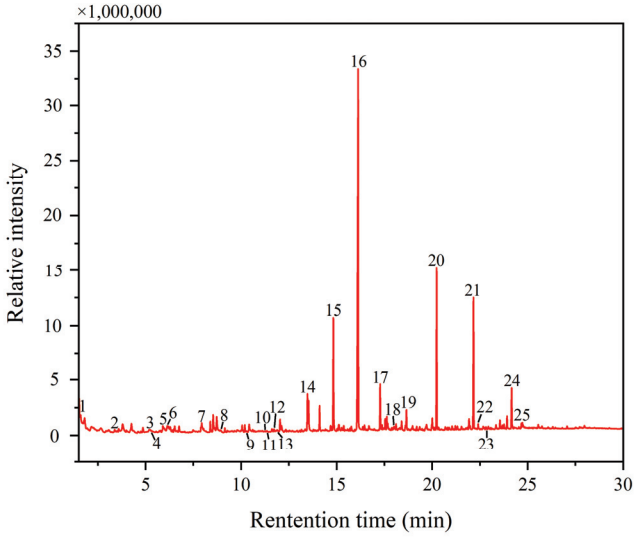

Figure 5. The total ion chromatogram (TIC) of the yellow pigment samples (DZ-2).

Table 3. Component compositions of the yellow pigment sample (DZ-2).

Peak Number	Retention Time (min)	Area (%)	Compound
1	1.6057	0.26	Methylamine, N,N-dimethyl-
2	3.381	0.27	1H-Pyrrole, 1-methyl-
3	5.2443	0.04	glycine
4	5.2507	0.02	TMAH reagent
5	5.9213	0.44	1,3,5-Triazine, hexahydro-1,3,5-trimethyl-
6	6.1153	0.08	Alanine
7	7.873	0.01	valine
8	8.9157	0.06	L-Proline, 1-methyl-, methyl ester
9	10.237	0.05	Methyl 1-methylpyrrole-2-carboxylate
10	11.2533	0.04	Naphthalene
11	11.2567	0.06	1H-Indene, 1-methylene-
12	11.7583	0.06	Protein
13	11.8607	0.03	hydroxyproline
14	13.4727	2.99	Heptanedioic acid, dimethyl ester
15	14.8307	8.81	Octanedioic acid, dimethyl ester
16	16.127	38.56	Nonanedioic acid, dimethyl ester
17	17.279	3.09	Decanedioic acid, dimethyl ester
18	17.992	0.11	Protein—blood and glue
19	18.6543	1.44	Drying oil
20	20.2363	10.70	Hexadecanoic acid, methyl ester
21	22.164	8.95	Octadecanoic acid, methyl ester
22	22.409	0.27	Heat bodied oil
23	22.844	0.01	Benzene, isocyanato
24	24.1617	3.62	Drying oil
25	24.6707	0.29	Drying oil

Simultaneously, Py-GC/MS was employed to detect the fatty acids in the DZ-2 sample, and the results are presented in Figure 6. Both monobasic carboxylic fatty acids and dibasic carboxylic fatty acids were identified in the sample. Additionally, substances classified as alkylphenyl alkanoates (APAs) were detected, suggesting the presence of heat-bodied tung oil [19,26,48]. The ratio of palmitic acid to stearic acid (P/S) is usually used to distinguish various types of dry oil [49]. The P/S value detected in the sample was 1.19, further validating the speculation. Heat-bodied tung oil was obtained by heating or refining tung oil before use. Furthermore, the test results revealed a small amount of aged glue containing proteins, confirming the presence of animal glue.

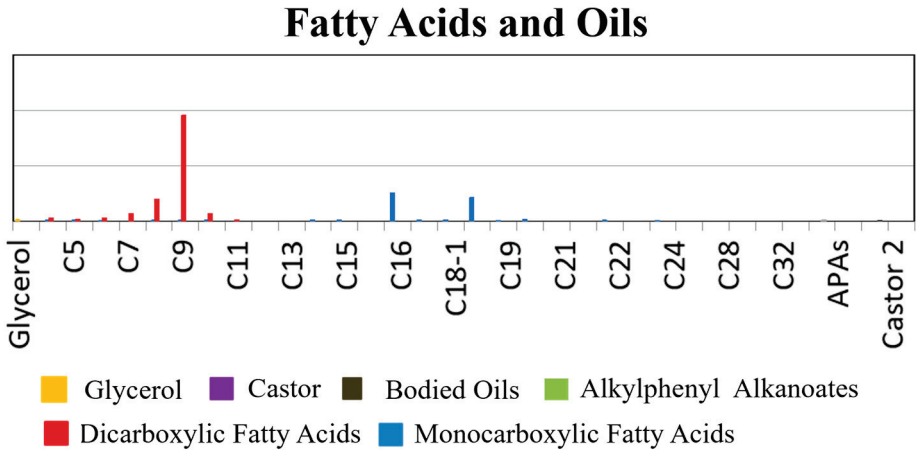

Figure 6. The relative concentrations of fatty acids for the yellow pigment sample (DZ-2) obtained by Py-GC/MS; carboxylic acid is shown with carbon numbers of n. The very small amounts of substances detected in the sample are not apparent in the figure.

4. Conclusions

This study involved a comprehensive analysis of five pigment samples collected from the peeling areas of the DaZhong Gate in the Confucius Temple in Qufu. The techniques

used included PLM, EDX, m-RS, and FT-IR. The results revealed that the red pigment is lead red, the yellow pigment is lead chromate yellow, the green pigment is emerald green, the blue pigment is ultramarine, and the white pigment is a mixture of chalk and lead white or anglesite. Lead red, ultramarine, chalk, and lead white are commonly used pigments in ancient Chinese architecture. It is noteworthy that lead chromate yellow and emerald green, which appeared in 1809 and 1814, respectively, were extensively used in architectural paintings during the late Qing Dynasty. Therefore, it is speculated that the architectural paintings of DaZhong Gate underwent restoration or repainting during the late Qing Dynasty.

The analysis of the Py-GC/MS detection results indicates that the binder used in the pigments contains protein-based glue, and based on the characteristic amino acid hydroxyproline, it is speculated that it may contain animal glue. The presence of fatty acids in the detection results suggests the inclusion of heat-bodied tung oil in the pigments. The occurrence of drying oil can be explained by the traditional Chinese painting technique on wooden surfaces. Before applying the pigment layer, a layer of heat-bodied tung oil was brushed on the plaster, and over time, it mixed with pigments and glue during the painting process.

The study of the pigments and binders used in the architectural paintings of DaZhong Gate in the Confucius Temple provides a universal method for the future identification of components in ancient architectural paintings. This research contributes data and evidence to support the conservation and better management of the architectural paintings in the DaZhong Gate of the Confucius Temple. Additionally, more research on the preservation status of other paintings is needed for more effective preventive and intervention-based conservation efforts.

Author Contributions: Conceptualization, K.L. and K.H.; methodology, G.T.; software, K.L. and Y.L.; validation, Y.T., K.L. and G.T.; formal analysis, K.H.; investigation, K.H.; resources, M.C. validation, M.C; data curation, Y.Q. and Y.L.; writing—original draft preparation, K.L.; writing—review and editing, Y.Q. All authors have read and agreed to the published version of the manuscript.

Funding: This research received no external funding.

Institutional Review Board Statement: Not applicable.

Informed Consent Statement: Not applicable.

Data Availability Statement: The datasets analyzed during the current study are available from the corresponding author upon reasonable request.

Conflicts of Interest: Author Menglei Cui was employed by the Northwest Nonferrous Survey and Engineering Company. The remaining authors declare that the research was conducted in the absence of any commercial or financial relationships that could be construed as a potential conflict of interest.

References

1. Lei, Z.; Wu, W.; Shang, G.; Wu, Y.; Wang, J. Study on colored pattern pigments of a royal Taoist temple beside the Forbidden City (Beijing, China). *Vib. Spectrosc.* **2017**, *92*, 234–244. [CrossRef]
2. Zou, W.; Zou, W.; Yeo, S.-Y. Investigation on the painting materials and profile structures used in ancient chinese folk architectural paintings by multiple analytical methods. *Coatings* **2022**, *12*, 320. [CrossRef]
3. Han, K.; Yang, H.; Teri, G.; Hu, S.; Li, J.; Li, Y.; Ma, E.; Tian, Y.; Fu, P.; Luo, Y. Spectroscopic investigation of a color painting on an ancient wooden architecture from the taiping heavenly kingdom prince dai's mansion in Jiangsu, China. *Minerals* **2023**, *13*, 224. [CrossRef]
4. Chen, E.; Zhang, B.; Zhao, F.; Wang, C. Pigments and binding media of polychrome relics from the central hall of Longju temple in Sichuan, China. *Herit. Sci.* **2019**, *7*, 45. [CrossRef]
5. Teri, G.; Han, K.; Huang, D.; Li, Y.; Tian, Y.; Chao, X.; Jia, Z.; Fu, P.; Li, Y. A study on the materials used in the ancient architectural paintings from the qing dynasty tibetan buddhist monastery of Puren, China. *Materials* **2023**, *16*, 6404. [CrossRef] [PubMed]
6. Wang, X.; Zhen, G.; Hao, X.; Zhou, P.; Wang, Z.; Jia, J.; Gao, Y.; Dong, S.; Tong, H. Micro-raman, XRD and THM-Py-GC/MS analysis to characterize the materials used in the eleven-faced guanyin of the Du Le Temple of the Liao Dynasty, China. *Microchem. J.* **2021**, *171*, 106828. [CrossRef]

7. Li, J.; Zhang, B. Study of identification results of proteinous binding agents in Chinese painted cultural relics. *J. Cult. Herit.* **2020**, *43*, 73–79. [CrossRef]
8. Bonaduce, I.; Blaensdorf, C.; Dietemann, P.; Colombini, M.P. The binding media of the polychromy of Qin Shihuang's Terracotta Army. *J. Cult. Herit.* **2008**, *9*, 103–108.
9. Yan, H.; An, J.; Zhou, T.; Xia, Y.; Rong, B. Identification of proteinaceous binding media for the polychrome terracotta army of Emperor Qin Shihuang by MALDI-TOF-MS. *Chin. Sci. Bull.* **2014**, *59*, 2574–2581. [CrossRef]
10. Wei, S.; Ma, Q.; Schreiner, M. Scientific investigation of the paint and adhesive materials used in the Western Han dynasty polychromy terracotta army, Qingzhou, China. *J. Archaeol. Sci.* **2012**, *39*, 1628–1633. [CrossRef]
11. Peifan, Q.; Deqi, Y.; Qi, M.; Aijun, S.; Jingqi, S.; Zengjun, Z.; Jianwei, H. Study and restoration of the Yi Ma Wu Hui Layer of the ancient coating on the Putuo Zongcheng Temple. *Int. J. Archit. Herit.* **2020**, *15*, 1707–1721. [CrossRef]
12. Zhu, T.; Li, T.; Liu, N.; Chen, J.; Huang, H.; Fu, Q.; Zhang, S. Hexi painting on Xitian Fanjing, a Qing imperial Buddhist temple in Beijing, China: Technology revealed by analytical approaches (an initial report). *Herit. Sci.* **2016**, *4*, 42. [CrossRef]
13. Fu, P.; Teri, G.; Li, J.; Huo, Y.; Yang, H.; Li, Y. Analysis of an ancient architectural painting from the Jiangxue Palace in the Imperial Museum, Beijing, China. *Anal. Lett.* **2021**, *54*, 684–697. [CrossRef]
14. Li, Y.; Guo, H.; Xiao, K.; Liu, P.; Chao, X.; Fu, P.; Xing, H.; Li, Y. A Study of pigment, adhesive, and firing temperature in pottery figurines excavated from the tomb of Qibi Ming, China. *Molecules* **2023**, *28*, 7739. [CrossRef]
15. Go, I.; Mun, S.; Lee, J.; Jeong, H. A case study on Hoeamsa Temple, Korea: Technical examination and identification of pigments and paper unearthed from the temple site. *Herit. Sci.* **2022**, *10*, 20. [CrossRef]
16. Klisińska-Kopacz, A. Non-destructive characterization of 17th century painted silk banner by the combined use of Raman and XRF portable systems. *J. Raman Spectrosc.* **2015**, *46*, 317–321. [CrossRef]
17. Cerrato, E.J.; Cosano, D.; Esquivel, D.; Otero, R.; Jiménez-Sanchidrián, C.; Ruiz, J.R. A multi-analytical study of a wall painting in the satyr domus in Córdoba, Spain. *Spectrochim. Acta Part A Mol. Biomol. Spectrosc.* **2020**, *232*, 118148. [CrossRef] [PubMed]
18. Dawson, P. The vibrational spectrum of α-mercuric sulphide. *Spectrochim. Acta Part A Mol. Spectrosc.* **1972**, *28*, 2305–2310. [CrossRef]
19. Hao, X.; Schilling, M.R.; Wang, X.; Khanjian, H.; Heginbotham, A.; Han, J.; Auffret, S.; Wu, X.; Fang, B.; Tong, H. Use of THM-PY-GC/MS technique to characterize complex, multilayered Chinese lacquer. *J. Anal. Appl. Pyrolysis* **2019**, *140*, 339–348. [CrossRef]
20. Xia, Y. *Chinese Historical Pigments in Polarized Light Microscope*; Science Press: Beijing, China, 2017.
21. Arjonilla, P.; Domínguez-Vidal, A.; Correa-Gómez, E.; Domene-Ruiz, M.J.; Ayora-Cañada, M.J. Raman and fourier transform infrared microspectroscopies reveal medieval Hispano–Muslim wood painting techniques and provide new insights into red lead production technology. *J. Raman Spectrosc.* **2019**, *50*, 1537–1545. [CrossRef]
22. Bell, I.M.; Clark, R.J.H.; Gibbs, P.J. Raman spectroscopic library of natural and synthetic pigments (pre- ≈ 1850 AD). *Spectrochim. Acta Part A Mol. Biomol. Spectrosc.* **1997**, *53*, 2159–2179. [CrossRef] [PubMed]
23. Doménech-Carbó, A.; Doménech-Carbó, M.T.; Mas-Barberá, X. Identification of lead pigments in nanosamples from ancient paintings and polychromed sculptures using voltammetry of nanoparticles/atomic force microscopy. *Talanta* **2007**, *71*, 1569–1579. [CrossRef] [PubMed]
24. Li, Y.; Wang, F.; Ma, J.; He, K.; Zhang, M. Study on the pigments of Chinese architectural colored drawings in the Altar of Agriculture (Beijing, China) by portable Raman spectroscopy and ED-XRF spectrometers. *Vib. Spectrosc.* **2021**, *116*, 103291. [CrossRef]
25. Mazzocchin, G.A.; Agnoli, F.; Mazzocchin, S.; Colpo, I. Analysis of pigments from Roman wall paintings found in Vicenza. *Talanta* **2003**, *61*, 565–572. [CrossRef] [PubMed]
26. Wang, X.; Zhen, G.; Hao, X.; Tong, T.; Ni, F.; Wang, Z.; Jia, J.; Li, L.; Tong, H. Spectroscopic investigation and comprehensive analysis of the polychrome clay sculpture of Hua Yan Temple of the Liao Dynasty. *Spectrochim. Acta Part A Mol. Biomol. Spectrosc.* **2020**, *240*, 118574. [CrossRef] [PubMed]
27. Zhao, Y.; Tang, Y.; Tong, T.; Sun, Z.; Yu, Z.; Zhu, Y.; Tong, H. Red lead degradation: Monitoring of color change over time. *New J. Chem.* **2016**, *40*, 3686–3692. [CrossRef]
28. Daniilia, S.; Sotiropoulou, S.; Bikiaris, D.; Salpistis, C.; Karagiannis, G.; Chryssoulakis, Y.; Price, B.A.; Carlson, J.H. Panselinos' Byzantine wall paintings in the Protaton Church, Mount Athos, Greece: A technical examination. *J. Cult. Herit.* **2000**, *1*, 91–110. [CrossRef]
29. Jinyu, W. Challenge of lithargyrum's extraterritorial introduction. *Chin. Med. Cult.* **2022**, *17*, 216–225. [CrossRef]
30. Weidon, K.; Shangxin, Z.; Qianli, F. Pigment study of the stone coffin from Yang Hui's tomb of the Tang Dynasty. *Sci. Conserv. Archaeol.* **2023**, *35*, 114–122. [CrossRef]
31. Yanying, M.; Jianhua, Z.; Hu, D. Scientific analysis of a Ming Dynasty polychrome star sculpture from Shanxi Art Museum, Taiyuan, China. *Sci. Conserv. Archaeol.* **2015**, *27*, 50–60. [CrossRef]
32. Petrova, O.; Pankin, D.; Povolotckaia, A.; Borisov, E.; Beznosova, M.; Krivul'ko, T.; Kurochkin, A. Identification of pigments in colored layers of a painting by raman spectroscopy. *Opt. Spectrosc.* **2017**, *123*, 965–969. [CrossRef]
33. Rosi, F.; Miliani, C.; Borgia, I.; Brunetti, B.; Sgamellotti, A. Identification of nineteenth century blue and green pigments by in situ X-ray fluorescence and micro-Raman spectroscopy. *J. Raman Spectrosc.* **2004**, *35*, 610–615. [CrossRef]

34. Castillejo, M.; Martín, M.; Silva, D.; Stratoudaki, T.; Anglos, D.; Burgio, L.; Clark, R.J. Laser-induced breakdown spectroscopy and Raman microscopy for analysis of pigments in polychromes. *J. Cult. Herit.* **2000**, *1*, S297–S302. [CrossRef]
35. Shen, A.G.; Wang, X.H.; Xie, W.; Shen, J.; Li, H.Y.; Liu, Z.A.; Hu, J.M. Pigment identification of colored drawings from Wuying Hall of the Imperial Palace by micro-Raman spectroscopy and energy dispersive X-ray spectroscopy. *J. Raman Spectrosc.* **2006**, *37*, 230–234. [CrossRef]
36. Ma, Z.; Wang, L.; Yan, J.; Zhou, W.; Pitthard, V.; Bayerova, T.; Krist, G. Chromatographic, microscopic, and spectroscopic characterization of a wooden architectural painting from the Summer Palace, Beijing, China. *Anal. Lett.* **2019**, *52*, 1670–1680. [CrossRef]
37. Favaro, M.; Guastoni, A.; Marini, F.; Bianchin, S.; Gambirasi, A. Characterization of lapis lazuli and corresponding purified pigments for a provenance study of ultramarine pigments used in works of art. *Anal. Bioanal. Chem.* **2012**, *402*, 2195–2208. [CrossRef]
38. Liu, L.-Y.; Zhang, B.; Yang, H.; Zhang, Q. The analysis of the colored paintings from the Yanxi Hall in the Forbidden City. *Guangpuxue Yu Guangpu Fenxi Spectrosc. Spectr. Anal.* **2018**, *38*, 2054–2063.
39. Zhang, C.; Huang, J.; Zhu, T.; Zhang, R. Guangzhou Tongcao painting in late China Qing Dynasty (1840–1912 AD): Technology revealed by analytical approaches. *Herit. Sci.* **2021**, *9*, 9. [CrossRef]
40. Gunasekaran, S.; Anbalagan, G.; Pandi, S.; Scattering, R. Raman and infrared spectra of carbonates of calcite structure. *J. Raman Spectrosc.* **2006**, *37*, 892–899. [CrossRef]
41. Petrova, O.; Pankin, D.; Povolotckaia, A.; Borisov, E.; Krivul'ko, T.; Kurganov, N.; Kurochkin, A. Pigment palette study of the XIX century plafond painting by Raman spectroscopy. *J. Cult. Herit.* **2019**, *37*, 233–237. [CrossRef]
42. Vagnini, M.; Vivani, R.; Viscuso, E.; Favazza, M.; Brunetti, B.; Sgamellotti, A.; Miliani, C. Investigation on the process of lead white blackening by Raman spectroscopy, XRD and other methods: Study of Cimabue's paintings in Assisi. *Vib. Spectrosc.* **2018**, *98*, 41–49. [CrossRef]
43. Bruni, S.; Cariati, F.; Casadio, F.; Toniolo, L. Spectrochemical characterization by micro-FTIR spectroscopy of blue pigments in different polychrome works of art. *Vib. Spectrosc.* **1999**, *20*, 15–25. [CrossRef]
44. Zaffino, C.; Guglielmi, V.; Faraone, S.; Vinaccia, A.; Bruni, S. Exploiting external reflection FTIR spectroscopy for the in-situ identification of pigments and binders in illuminated manuscripts. Brochantite and posnjakite as a case study. *Spectrochim. Acta Part A Mol. Biomol. Spectrosc.* **2015**, *136*, 1076–1085. [CrossRef] [PubMed]
45. Zhao, H.; Hou, X. Deposit in bleached pulp production system and its infrared spectrum identification. *China Pulp Pap. Ind.* **2022**, *43*, 20–24.
46. Xin, H.; Anxin, L.; Jin, Z. Simultaneous quantitative analysis of SO_4^{2-} and NO_3^- in soil by diffuse reflectance fourier transform infrared spectroscopy. *Chin. J. Anal. Lab.* **2015**, *34*, 1428–1431. [CrossRef]
47. Kurouski, D.; Zaleski, S.; Casadio, F.; Van Duyne, R.P.; Shah, N.C. Tip-enhanced Raman spectroscopy (TERS) for in situ identification of indigo and iron gall ink on paper. *J. Am. Chem. Soc.* **2014**, *136*, 8677–8684. [CrossRef] [PubMed]
48. Ling, H.; Maiqian, N.; Chiavari, G.; Mazzeo, R. Analytical characterization of binding medium used in ancient Chinese artworks by pyrolysis–gas chromatography/mass spectrometry. *Microchem. J.* **2007**, *85*, 347–353. [CrossRef]
49. Wang, N.; He, L.; Zhao, X.; Simon, S. Comparative analysis of eastern and western drying-oil binding media used in polychromic artworks by pyrolysis–gas chromatography/mass spectrometry under the influence of pigments. *Microchem. J.* **2015**, *123*, 201–210. [CrossRef]

sensors

MDPI

Article

Operational Deflection Shape Measurements on Bladed Disks with Continuous Scanning Laser Doppler Vibrometry

Cuihong Liu [1,2,*], Tengzhou Xu [1,2], Tao Chen [1,2], Shi Su [1,2], Jie Huang [1,2] and Yijin Li [1,2]

[1] School of Aeronautic Engineering, Nanjing Vocational University of Industry Technology, Nanjing 210023, China; 2018100938@niit.edu.cn (T.X.); taochen@niit.edu.cn (T.C.); shi.su@niit.edu.cn (S.S.); 2004100333@niit.edu.cn (J.H.); 2021101199@niit.edu.cn (Y.L.)

[2] Aeronautic Intelligent Manufacturing and Digital Health Management Technology Engineering Research Center of Jiangsu Province, Nanjing 210023, China

* Correspondence: 2021101192@niit.edu.cn

Abstract: The continuous scanning laser Doppler vibrometry (CSLDV) technique is usually used to evaluate the vibration operational deflection shapes (ODSs) of structures with continuous surfaces. In this paper, an extended CSLDV is demonstrated to measure the non-continuous surface of the bladed disk and to obtain the ODS efficiently. For a bladed disk, the blades are uniformly distributed on a given disk. Although the ODS of each blade can be derived from its response data along the scanning path with CSLDV, the relative vibration direction between different blades cannot be determined from those data. Therefore, it is difficult to reconstruct the complete vibration mode of the whole blade disk. In order to measure the complete ODS of the bladed disk, a method based on ODS frequency response functions (ODS FRFs) has been proposed. While the ODS of each blade is measured by designing the suitable scanning paths in CSLDV, an additional response signal is obtained at a fixed point as the reference signal to identify the relative vibration phase between the blade and the blade of the bladed disk. Finally, a measurement is performed with a simple bladed disk and the results demonstrate the feasibility and effectiveness of the proposed extended CSLDV method.

Keywords: bladed disk; laser Doppler vibrometry; ODS FRF; phase identification

1. Instruction

A bladed disk is one of the important components of rotating machinery such as aeroengines, turbines and impellers, etc. High vibratory stresses of turbomachinery components can be a major cause of vibration cracks and even breaking for blades [1–3], so the dynamic behavior of bladed disks has always interested the engineering community over the years. In recent decades, there have been several numerical methods used to predict the dynamic characteristics of bladed disks via numerical modeling [3,4] and finite element modeling (FEM) [5,6]. These studies indicate that the bladed disk is highly sensitive to mistuning, such that even small deviations in the structural properties of individual sectors of the bladed disks can result in the localization of vibration energy and a significant increase in forced responses. There are many causes that can change the properties of the nominal design. However, it is very difficult to take uncertain factors into account when establishing finite element modeling.

To more precisely explore the dynamic features of the bladed disk structure, an experimental study is indispensable. Zhao Z B et al. [7] took the bladed disk with 12 blades as an example to conduct an experimental study on the natural characteristics of the tuned and detuned bladed disks. Yao J et al. [8,9] studied the spatial distributions of the mistuned mode shapes and the mode location of a simplified bladed disk, demonstrating the deformation characteristics of all the modes within the experimental frequency band and the deformation differences among the various modes through the test data of 120 measuring

points. To experimentally acquire the modal shape of the bladed disk, a large amount of measuring points need to be arranged on the surface of the bladed disk. However, this greatly increases the time and cost of experimental testing and it is difficult to obtain accurate vibration mode shapes. Therefore, the experimental measurement of the operational deflection shapes of bladed disks is still a relatively demanding task.

In recent years, laser Doppler vibrometry (LDV), as a new non-contact measurement method, has been widely used in aerospace [10], automobile [11] and other fields due to its advantages of long-distance measurement, high measurement accuracy and no installation. Heinemann [12] et al. measured the natural frequencies and the modal shapes of a five-blade axial-flow fan with scanning laser Doppler vibrometry (SLDV). In fact, the density of measurement points has been improved to some extent, but also greatly increased the time-consuming nature and the storage requirements of test data. In order to further improve the test efficiency and the density of test points, continuous scanning laser Doppler vibrometry (CSLDV) is proposed based on SLDV, where the laser point, instead of dwelling at a fixed location, is continuously moving across a measurement surface along the designed path. The SLDV was used in vibrational measurements to extract only a few dozen measured points across the grid. However, the CSLDV is able to measure thousands of vibration points in a few seconds and reconstruct a more accurate ODS through the demodulation method, arranging each single ODS according to the position of scan paths on the measured structure. Therefore, this CSLDV is also called the full-field measurement technique. Sriram P. et al. [13] first applied the CSLDV to measure the vibration of a cantilever beam in the line scanning mode. With the application of the CSLDV, Y Hu et al. performed an experiment on a free-hanging aluminum plate in a thermal environment, and the findings revealed that the accuracy of the ODS was improved by 20 times compared to a manual-moving LDV method [14]. Additionally, there are also some studies reported on excitation methods for the CLSDV [15–18]. K Yuan et al. [19,20] obtained the modal parameters of a model turbine blade with a curved surface excited by white noise by the CSLDV, and the results demonstrated that the identified modal parameters possess significantly higher accuracy and efficiency in comparison to those from the SLDV.

Most of the studies reported on CSLDV techniques are mainly based on the simple continuous surface of structures, such as beams, plates, disks or a single blade [21], and the measurement can be completed at once along a continuous scanning path. However, there is still a great challenge for the testing of discontinuous multi surfaces of structures such as bladed disks. For the bladed disk, if the laser beam conducts a continuous scanning test within a large area covering the bladed disk, laser leakage will occur in the area without the bladed disk. And then in the output data of the LDV corresponding to the scanning trajectory, there will be some small segments of invalid data. The invalid data segments will reduce the accuracy of the reconstructed ODS. Therefore, it is best that the scanning path precisely matches the bladed disk. The continuous scanning path of the laser precisely switches from one blade to another to exactly cover the structure surface while also ensuring that the scanning frequency does not change, which is rather complicated. Because reconstruction of the ODS from the output data in CSLDV demanded that the scanning frequencies of the laser beam in the x direction and the y direction should be unchanged during the entire scanning process, this will pose great difficulties for the CSLDV applied to the bladed disk.

To address these issues of the ODS testing of the bladed disk in CSLDV, this paper has also conducted some studies. The aim of the present paper is to extend the CSLDV techniques for bladed disk structures, in that a suitable continuous scanning path for a multi-blade disk structure is designed and the ODSs of all the blades can be derived from the sideband patterns of the CSLDV output spectrum. Then, a vibration phase identification method of all blades is needed to reconstruct the ODS of the whole-bladed disk. As an example, a 16-blade disk for vibration measurement is taken. A continuous scanning path suitable for full field testing in CSLDV is designed and the ODS of the bladed disk is

reconstructed by identifying the vibration phase between each blade. The results show that the design of the continuous scanning path is feasible and the effectiveness of the identification method of the vibration phase in serving CSLDV is evaluated.

The rest of this paper is organized as follows. Section 2 describes the theoretical basis of ODS reconstruction in CSLDV. In Section 3, the design of the measurement campaigns on a 16-blade disk is discussed, including how to switch the laser beam to scan the next test blade. The ODSs of all blades were reconstructed from the measured sideband spectrums. The identification method of the vibration phase between each blade is described in Section 4. The main purpose of this section is to obtain the relative vibration phase of all the blades and to reconstruct the ODS of the whole-bladed disk.

2. Theoretical Basis of ODS Reconstruction in CSLDV

The small damping structure will resonate when the excited frequency is near the natural frequency. The vibration response of the structure measured by the laser Doppler vibrometers, which can be expressed as follows:

$$v(x,y,t) = d'(x,y,t) = V_R(x,y)\cos\omega t + V_I(x,y)\sin\omega t \tag{1}$$

where $v(x,y,t)$ is the vibrational velocity of point (x,y) at time t. $V_R(x,y)$ and $V_I(x,y)$ are the real and imaginary components of the vibration, respectively. They can be fitted by the polynomial series as follows:

$$\begin{aligned} V_R(x,y) &= \sum_{m,n=0}^{p,q} V_{Rm,n}x^m y^n \\ V_I(x,y) &= \sum_{m,n=0}^{p,q} V_{Im,n}x^m y^n \end{aligned} \tag{2}$$

where p and q are the polynomial order in the x and y direction, respectively. For a rectangular plate, the scanning path of the area sine scan moved on the surface of the structure can be expressed by two sinewaves equations when the scanning speed of the laser spot has a sine variation.

$$\begin{aligned} x &= \cos(\omega_{sx}t) \\ y &= \cos(\omega_{sy}t) \end{aligned} \tag{3}$$

where ω_{sx} and ω_{sy} are the scanning frequencies of the laser point along the X and Y directions, respectively. The scanning paths covered on the rectangular plates can be generated by dissimilar frequency sinusoids using sinusoidal trajectories, e.g., 2D Lissajou trajectories, as shown in Figure 1.

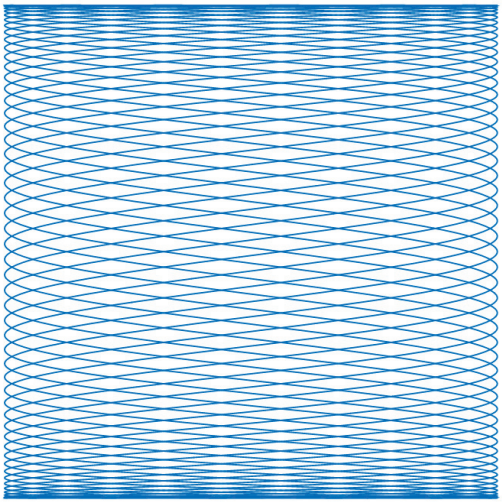

Figure 1. Continuous surface scanning path diagram.

Substituting Equations (2) and (3) into Equation (1), and expanding out trigonometrically, the following form of the vibration signal is derived:

$$v(x,y,t) = \sum_{m,n=0}^{p,q} A_{Rm,n} \cos[(\omega \pm m\omega_{sx} \pm n\omega_{sy})t] + \sum_{m,n=0}^{p,q} A_{Im,n} \sin[(\omega \pm m\omega_{sx} \pm n\omega_{sy})t] \quad (4)$$

where $A_{Rm,n}$ and $A_{Im,n}$ are the sideband spectrum amplitudes of real and imaginary components at different frequencies, respectively. According to Equation (4), the sideband spectrum of vibration velocity signal obtained by laser continuous surface scanning test consists of all components when m and n are taken as different values. It can be deduced that the transformation to recover the polynomial coefficients from the spectral amplitudes of the LDV output is:

$$\begin{aligned} [A_R]_{m\times n} &= [T]_{m\times m}[V_R]_{m\times n}[T]^T_{n\times n} \\ [A_I]_{m\times n} &= [T]_{m\times m}[V_I]_{m\times n}[T]^T_{n\times n} \end{aligned} \quad (5)$$

Each element of matrix T satisfies the following equation:

$$T(i,j) = \begin{cases} 0 & i+j \text{ is odd, } i > j \\ \frac{C_i^{i-j}}{2^i} & i+j \text{ is even} \end{cases}, \quad i \text{ and } j \text{ are natural number} \quad (6)$$

By expanding the Fourier series of the vibration signal obtained from the output of CSLDV, the amplitudes of the sideband spectrum $A_{Rm,n}$, $A_{Im,n}$ and the transformation matrix T can be deduced. Therefore, the real and imaginary components of the operational deflection shape can be obtained as follows:

$$\begin{aligned} [V_R] &= [T]^{-1}[A_R][T]^T \\ [V_I] &= [T]^{-1}[A_I][T]^T \end{aligned} \quad (7)$$

3. ODS of Bladed Disc in CSLDV

3.1. Modal Characteristics of Bladed Disk

A bladed disk, as shown in Figure 2a, is a circularly symmetric structure whose modes are described by the mode shapes of a single sector and numbers of nodal diameter. The thickness of the structure is 2 mm, and the other dimensions are shown in Figure 2b. The finite element model (FEM) of a single sector is built with hexahedral elements, as shown in Figure 2c. Material properties are given as follows: the density and the Young's modulus are 7840 Kg/m^3 and 206 GPa, respectively. Poisson's ratio is 0.3.

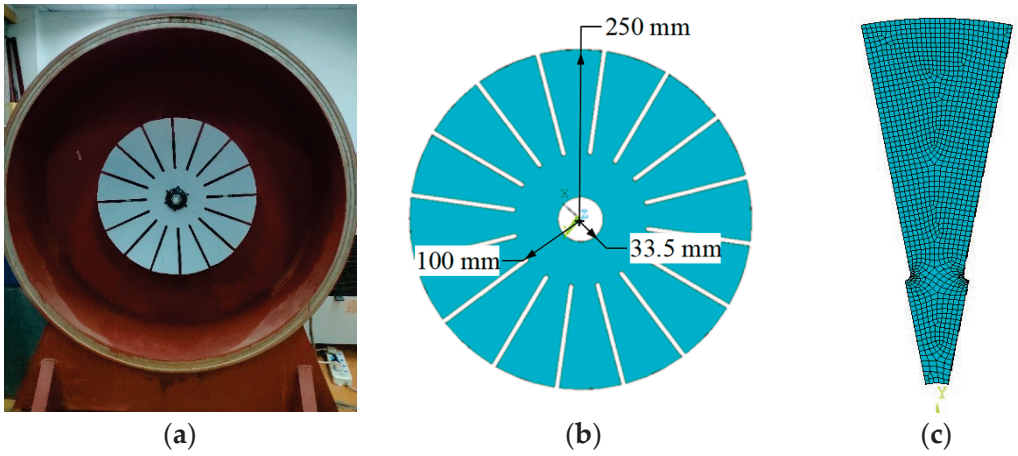

Figure 2. Bladed disk. (**a**) Bladed disk. (**b**) Model. (**c**) FEM of a single sector.

The modal frequencies of the first 16 modes derived from the FEM as listed in Table 1. The modal frequencies appear in pairs due to the characteristic of circularly symmetric structure, except for the modes which Nd = 0 and Nd = 8 for the 16-blade disk. The two modes of a modal pair have the same frequencies and orthogonal mode shapes, which are demonstrated in Figure 3 (only one of the mode shapes is shown for modal pairs). In the figure, the '*' indicates the frequency values of different nodal diameters, and the arrow points to is the modal vibration mode corresponding to this frequency.

Table 1. Frequencies of the 1st family of modes.

Order	Frequency/Hz	Nd	Order	Frequency/Hz	Nd
1	26.74	1	9	38.40	4
2	26.74	1	10	41.16	5
3	27.10	0	11	41.16	5
4	28.51	2	12	42.76	6
5	28.51	2	13	42.76	6
6	33.89	3	14	43.61	7
7	33.89	3	15	43.61	7
8	38.40	4	16	43.87	8

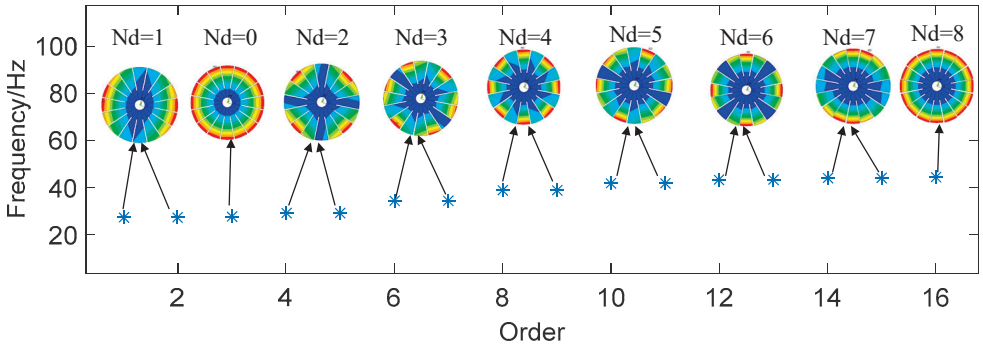

Figure 3. Modal shapes of different nodal diameters.

3.2. Measurement in CSLDV

3.2.1. Design of the Continuous Scanning Path

The bladed disk shown in Figure 2a is employed to measure operational deflection shapes in CSLDV. The fan-shaped blades cannot be completely covered by the continuous scanning path of the laser spot described in Equation (3), so it is necessary to design a suitable continuous scanning path for the specific surface.

The scan pattern of the fan-shaped blades is much more complicated than the rectangular plate, as shown by the following:

$$\begin{aligned} x(t) &= \left[\frac{R_o - R_i}{2}\cos(2\pi\omega_{sy}t) + \frac{R_o + R_i}{2}\right]\cos(\phi(t) + \tau) \\ y(t) &= \left[\frac{R_o - R_i}{2}\cos(2\pi\omega_{sy}t) + \frac{R_o + R_i}{2}\right]\sin(\phi(t) + \tau) \end{aligned} \tag{8}$$

where R_o and R_i are the initial radius and final radius of the scanning range in the radial direction, respectively. τ is the initial phase angular position, while $\phi(t)$ is the circumferential scanning control parameters which is described by the equation:

$$\phi(t) = \theta\sin(2\pi\omega_{sx}t) \tag{9}$$

where θ is the edge amplitude of the blades.

Take the scanning frequency $\omega_{sy} = 3$ Hz, $\omega_{sx} = 30$ Hz as an example, the scanning path of the laser spot on the blade surface is shown in Figure 4.

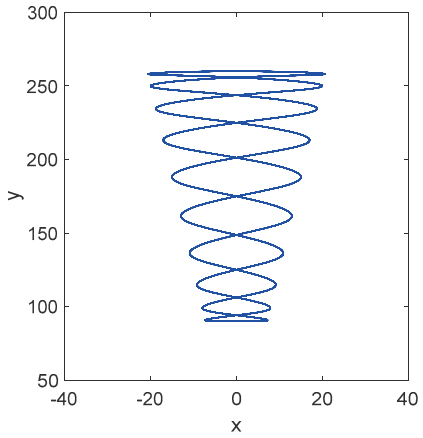

Figure 4. Scanning path on blades.

For the different blades, the scanning pattern is the same except for the initial phase angular position τ. The blades are evenly distributed on the circumference of the disk; therefore, the initial phase angular position of each blade in Equation (8) is instead given by τ_n, which can be expressed as:

$$\tau_n = \frac{\pi}{2} + \frac{n-1}{N} \cdot 2\pi \tag{10}$$

where n is the number of blades, N is the total number of blades of the bladed disk. Therefore, the continuous scanning test of all blades could be carried out by changing different blade numbers n ($n = 1, 2, 3, \cdots, N$).

3.2.2. Experimental Test

The scanning frequencies are set to $\omega_{sy} = 1.1$ Hz and $\omega_{sx} = 10$ Hz, respectively. The sampling frequency Fs is 8192 Hz, which needs to satisfy Nyquist's sampling theorem. In this experiment, the design of CSLDV is used to measure the fan-shaped blade, the vibration data is collected for 5 s, and then the next blade is switched for testing until all the blades are traversed. The experimental four-nodal diameter bending mode of the bladed disk measured by LDV is 36.88 Hz, and there is a deviation of 3.96% compared with the 38.40 Hz derived from the FEM. Thus, a sinusoidal signal with a single frequency $\omega = 36.88$ Hz was supplied to the electromagnetic exciter to excite the bladed disk in the test. It is known in advance that when the excitation frequency approaches or equals the natural frequency, the mode corresponding to that natural frequency can be well excited.

The continuous scanning path of all blades (No. 1–16) is shown in Figure 5.

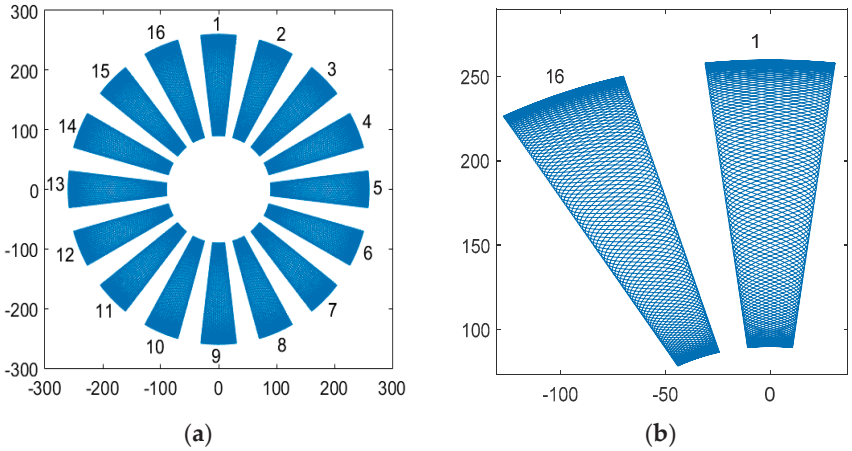

Figure 5. Continuous scanning path of all blades. (**a**) Scanning path. (**b**) Local zoom.

The CSLDV measurements are carried out on all blades and the vibration signals in the time domain are obtained from the output of a laser Doppler vibrometer. Taking the first four blades as an example, the vibration signal and the sideband spectrums are shown in Figure 6. It can be found that the vibration forms of the odd-numbered blades shown in Figure 6a,c are consistent and their vibration amplitudes are relatively small, while the vibration forms of even-numbered blades shown in Figure 6b,d have the same form and larger amplitude. This phenomenon coincides with the four-nodal diameter mode of the first family mode of the bladed disk. The values of m and n are determined by the sideband spectrums. Specifically, according to the sideband spectrums shown in Figure 6, the values of the sideband number m and n of the odd-numbered blades are both 0 and ± 1, while the values of the even blades are $m = 0$, $n = 0, \pm 1$, respectively.

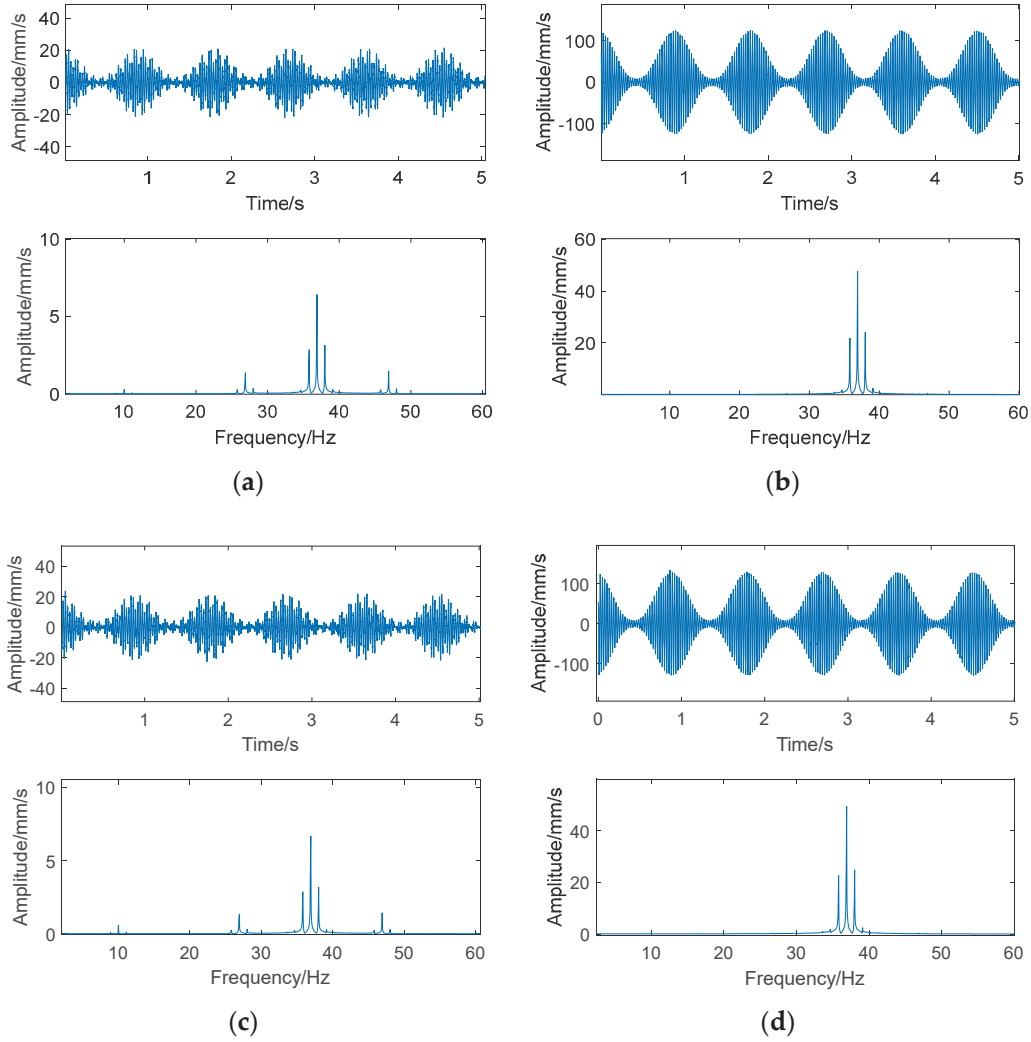

Figure 6. Vibration signals and sideband spectrums of blades. (**a**) No. 1. (**b**) No. 2. (**c**) No. 3. (**d**) No. 4.

The operational deflection shapes of all the blades have been reconstructed from the measured sideband spectrums, and are listed in Table 2. The results show that the vibration amplitude of the even-numbered blades is much larger than that of the odd-numbered blades. According to the number sequence and vibration amplitude of blades, it can be concluded that all the odd blades in the operation condition are located in the four-nodal diameter positions of the bladed disk.

Table 2. ODSs of all blades.

No.	ODS	No.	ODS
1	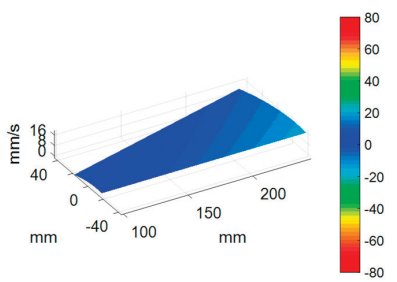	2	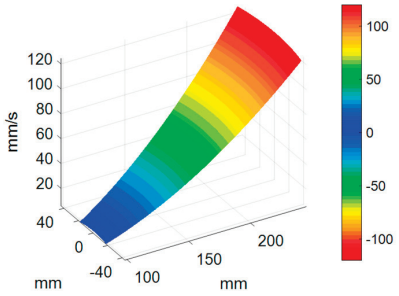
3	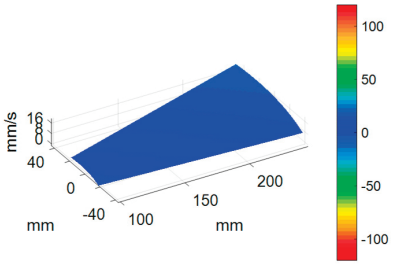	4	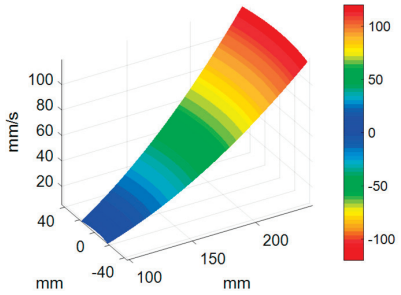
5	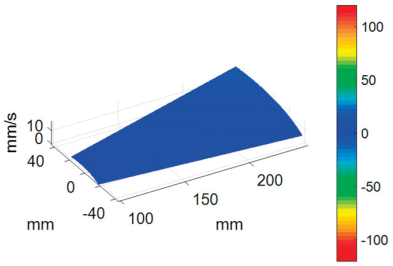	6	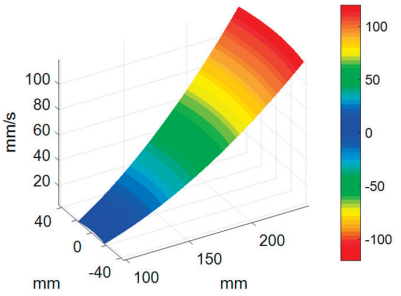
7	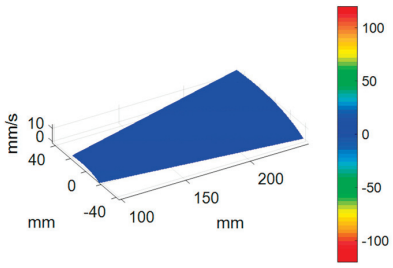	8	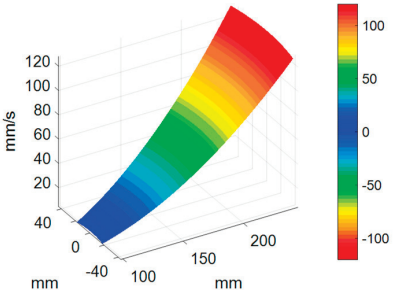
9	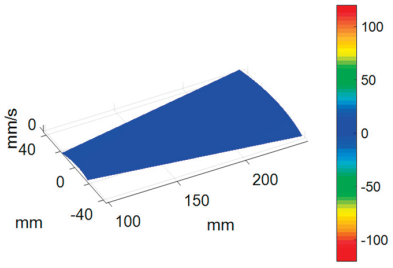	10	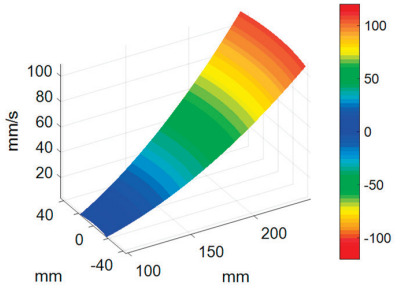

Table 2. *Cont.*

No.	ODS	No.	ODS
11	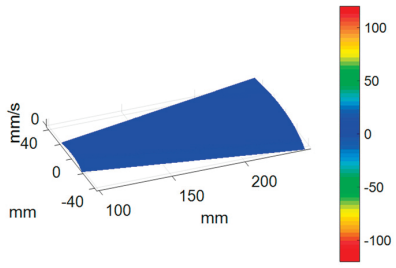	12	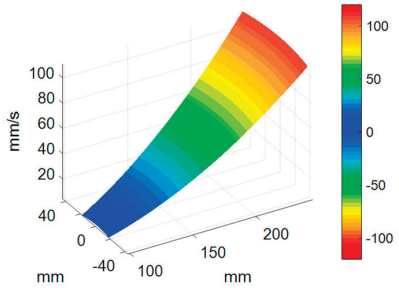
13	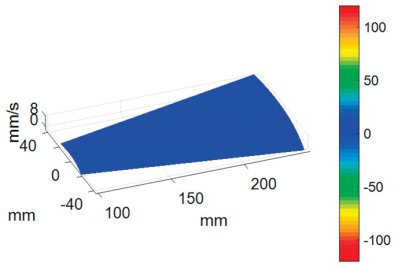	14	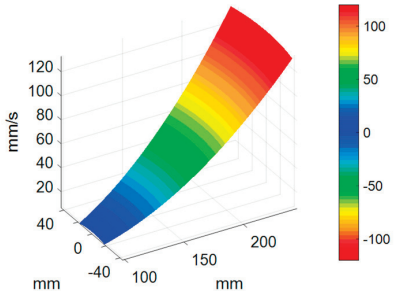
15	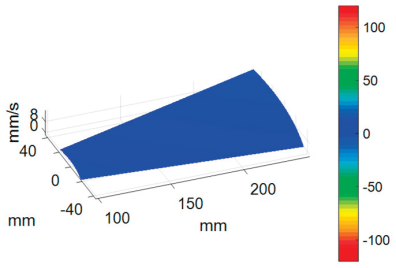	16	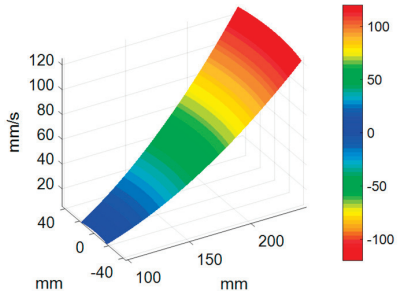

Although all ODSs of the blades are obtained by using the extended CSLDV, the ODS of the whole-bladed disk cannot be directly reconstructed because of the unknown vibration phase of different blades, which cannot be derived from the sideband spectra of CSLDV. Therefore, it is necessary to identify the vibration phase between the blades for reconstructing the ODS of the whole-bladed disk.

3.3. Identification of Vibration Phase and ODS Reconstruction of the Whole-Bladed Disk

For continuous scanning tests, the vibration phase of different blades cannot be directly identified. However, that can be derived from the frequency response function of a series of points on all blades. That is to say, to ensure the same installation and excitation conditions as the above continuous scanning test, a series of points is selected at the same position of each blade to obtain the frequency response functions (FRFs). The vibration phase angle of all blades can be determined by the phase frequency curve of FRFs. But for the conditions of unknown excitation, it is impossible to directly measure the FRF, so the reference response is necessary to obtain the ODS FRF of the series of points. The ODS FRFs of each measurement point are measured by calculating the response of the test point with the response of a fixed reference point, from which the relative vibration phase between different blades can be extracted. The selection of measuring points and the fixed reference point used for blade identification of the vibration phase are shown in Figure 7a. The measurement system employed in this experiment is composed of a Polytec-PSV-400 scanning laser vibrometer and a self-developed external scanning system, as presented in Figure 7b. The self-developed external scanning system is used to obtain the response

of the measuring points on each blade, while the Polytec-PSV-400 is used to measure the response data of the fixed reference point simultaneously.

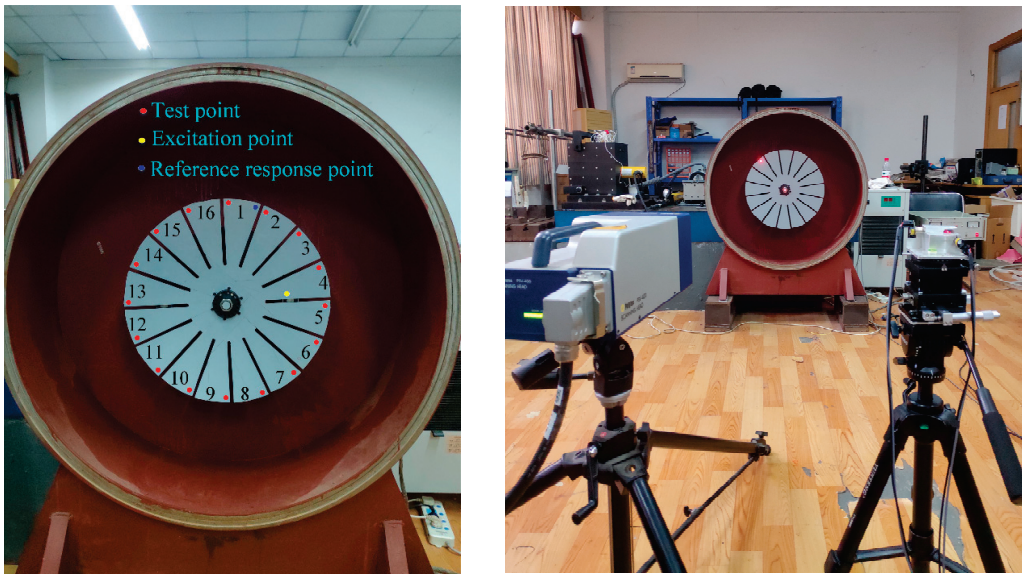

(**a**) (**b**)

Figure 7. Testing scheme. (**a**) Location of measuring points. (**b**) Measurement system.

3.3.1. Identification of Vibration Phase Based on FRF

In the test of identification of the vibration phase, the electromagnet exciter is also supplied to the sine signal with a frequency of 36.88 Hz, which is exactly the same as the continuous scanning test. A total of 16 measuring points are selected from the same position on each blade and the fixed reference point is located on the tip of the No. 1 blade. The motion equation of the excited structure is given by:

$$\boldsymbol{M}\ddot{x}(t) + \boldsymbol{C}\dot{x} + \boldsymbol{K}x(t) = \boldsymbol{F}(t) \tag{11}$$

where $\boldsymbol{M}$, $\boldsymbol{C}$ and $\boldsymbol{K}$ are the Mass matrix, damping matrix and stiffness matrix, respectively. $\boldsymbol{F}(t)$ is the vector of excitation force. The frequency response function can be directly derived from the motion equation, and is expressed as:

$$\boldsymbol{H}(\omega) = (\boldsymbol{K} - \omega\boldsymbol{M} + i\omega\boldsymbol{C})^{-1} = \frac{\{\boldsymbol{X}\}}{\{\boldsymbol{F}\}} \tag{12}$$

In this paper, the non-contact electromagnet exciter is used to excite the bladed disk and the frequency response function is obtained by dividing the vibration response of the input signal of the exciter [22]. Taking the frequency response function of the previous six measuring points as an example, the frequency response functions of measuring points are shown in Figure 8. It can be found that only one peak appears in the frequency amplitude curve near the excitation frequency of 36.88 Hz.

The vibration phase angles corresponding to the peak frequency are extracted from the phase frequency curve of the 16 measurement points, as shown in Table 3. It is obvious that the difference in phase angle between adjacent the even-numbered blades is about 180°.

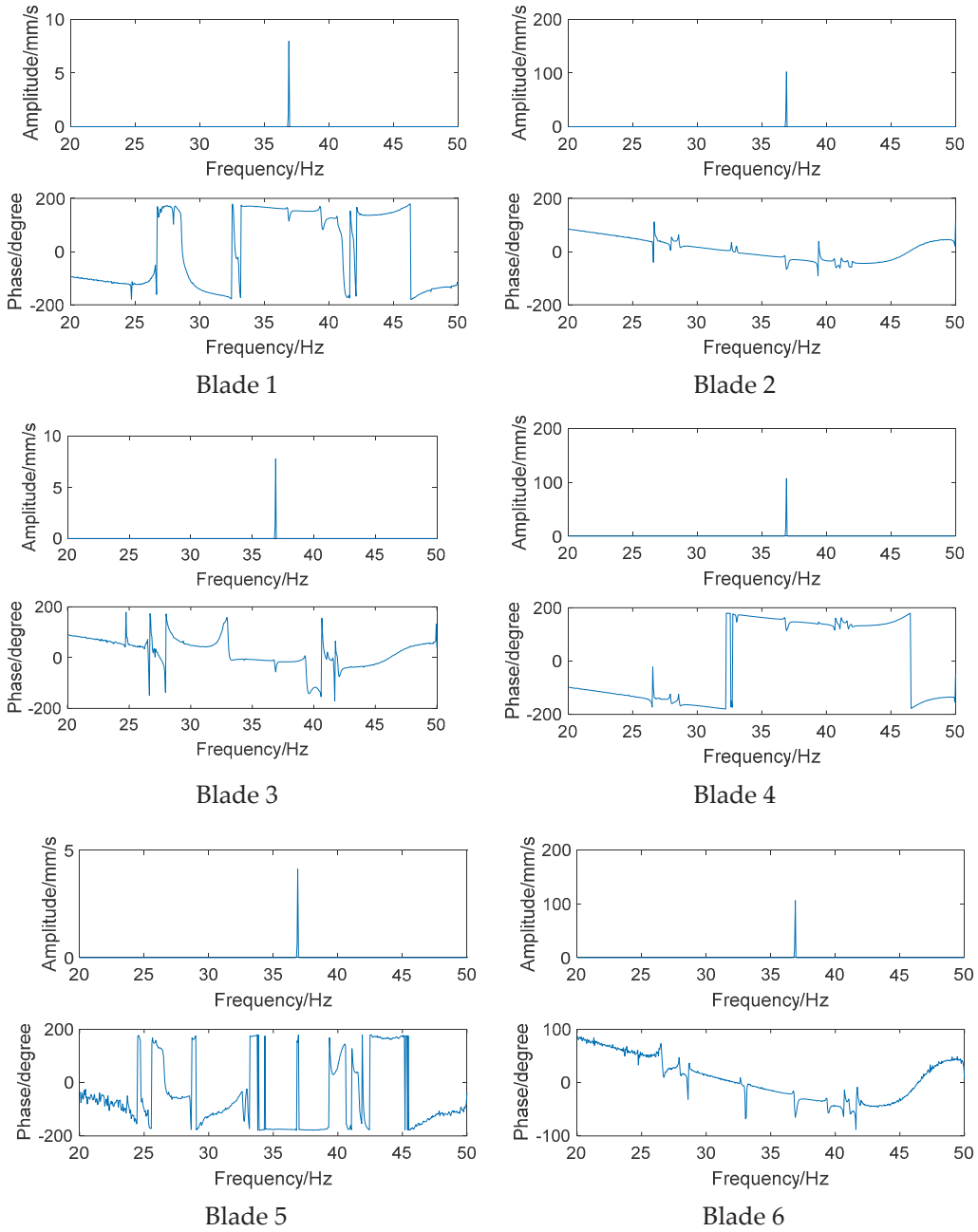

Figure 8. Frequency response functions.

Table 3. Phase angles of all blades based on FRF.

No.	Phase Angle/°	No.	Phase Angle/°
1	113.63	2	−67.65
3	−56.86	4	112.8
5	149.26	6	−65.49
7	20.83	8	115.42
9	−4.97	10	−65.03
11	152.42	12	114.58
13	−4.96	14	−64.41
15	−85.40	16	114.76

3.3.2. Identification of Vibration Phase Based on ODS FRF

When the excitation signal is unknown, the frequency response function of the measurement point cannot be obtained directly. However, the transfer function between the reference point and the measurement point can be obtained by taking the response of a fixed point as a reference signal as follows:

$$T_{xy}(\omega) = \frac{X_x(\omega)}{X_y(\omega)} \tag{13}$$

where $X_x(\omega)$, $X_y(\omega)$ are the frequency spectrums of the measuring points and the reference points, respectively. In order to improve the signal-to-noise ratio in practical engineering test, auto power spectrum and cross power spectrum are usually used to optimize the transfer function as follows:

$$\widetilde{T}_{xy}(\omega) = \frac{X_x(\omega) \cdot X_y^*(\omega)}{X_y(\omega) \cdot X_y^*(\omega)} = \frac{G_{xy}(\omega)}{G_{yy}(\omega)} \tag{14}$$

The concept of ODS FRF on the basis of transfer function is first proposed by Richardson M H [23] in 1997. Similar to the transfer function, ODS FRFs are similarly calculated by the auto spectrum and cross-spectrum between the response of fixed reference point and the responses of the measuring points:

$$\text{ODSFRF}(\omega) = \sqrt{G_{xx}(\omega)} \cdot \frac{G_{xy}(\omega)}{|G_{xy}(\omega)|} = |X_x(\omega)| \cdot \frac{G_{xy}(\omega)}{|G_{xy}(\omega)|} = \overline{X_x}(\omega) \tag{15}$$

ODS FRF not only contains the correct amplitude of the response of each measuring point but also the phase information relative to the reference point. Compared with the transfer function, ODS FRF has a higher signal-to-noise ratio [24,25]. According to the ODS FRF theory, the test for vibration phase identification is carried out and makes sure that it is consistent with the condition and environment of the continuous scanning laser test. In the phase identification experiment based on ODS FRF, two laser beams are necessary to obtain the response of the measurement point and the fixed reference point simultaneously, and the experiment flow is shown in Figure 9.

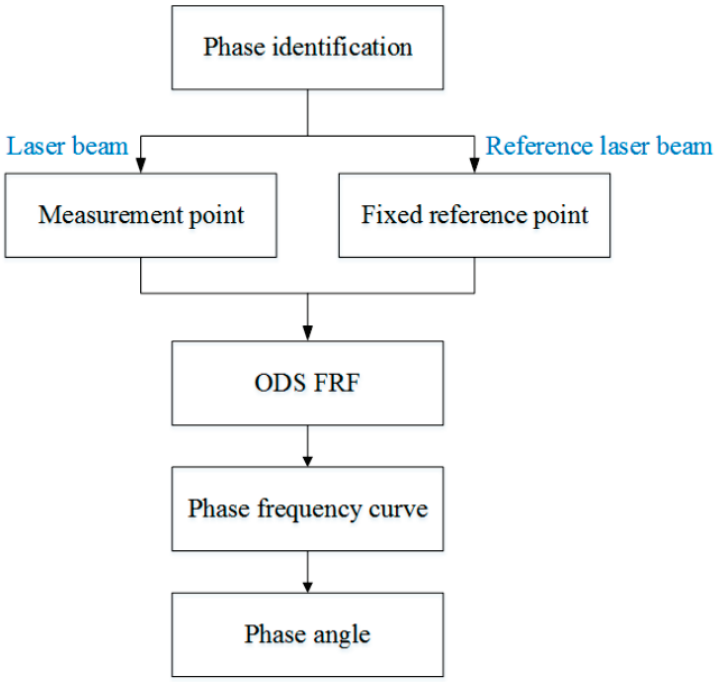

Figure 9. Experiment flow chart.

First, a fixed reference response point needs to be selected on the blade disk (see Figure 7). Then, two laser beams are used to simultaneously measure the response of the fixed reference point and the response of each blade measurement point. Take the ODS FRFs measured from blade 1 and blade 2 as an example, the frequency amplitude curves and the phase frequency curves are shown in Figure 10. The phase angles can be easily extracted from the phase frequency curves of ODS FRF. For the two blades, they are $-0.6°$ and $179.3°$, respectively.

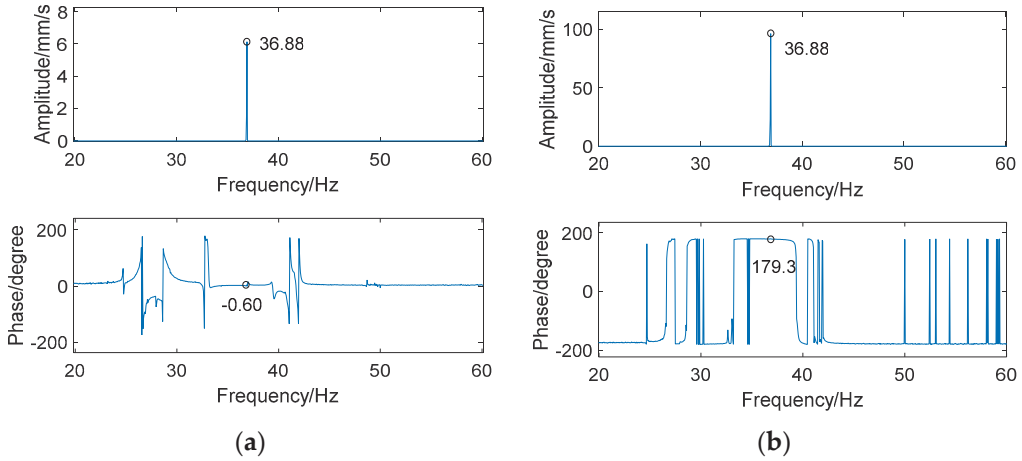

Figure 10. ODS FRF. (**a**) Blade 1. (**b**) Blade 2.

The phase angles of relative vibration between different blades are extracted from ODS FRFs of measuring points, as shown in Table 4. The results show that the difference in the vibration phase of two adjacent even-numbered blades is about $180°$, which signifies that the vibration direction of two adjacent even-numbered blades is opposite. This is consistent with the phase identification results derived from the method based on FRF.

Table 4. Vibration phase angles of all blades based on ODS FRF.

No. of Blade	Phase Angle	No. of Blade	Phase Angle
1	−0.60	2	179.28
3	−171.02	4	−0.79
5	36.01	6	179.24
7	−93.00	8	−0.08
9	−123.11	10	179.5
11	35.16	12	−0.71
13	−123.26	14	179.41
15	156.99	16	−0.66

3.3.3. ODS Reconstruction of the Whole-Bladed Disk

Combined with the vibration phase angles of all blades identified by the above methods and the ODS of all blades tested in Section 3.2.2, the ODS of the whole-bladed disk is reconstructed, as shown in Figure 11. To verify the accuracy of the measurement, a comparison with the FEM (as presented in Section 3.1) is made. The modal assurance criterion (MAC) value is typically to quantitatively describe the similarity between two modes. The closer the MAC value approaches to 1, the higher the consistency between the two modes. The results showed that the MAC value between the ODS of the bladed disk obtained through testing and the ODS calculated by the finite element method is 0.91. The errors are mainly caused by the fact that the boundary conditions in FEM are not exactly the same as the actual situation, as well as experimental errors, etc.

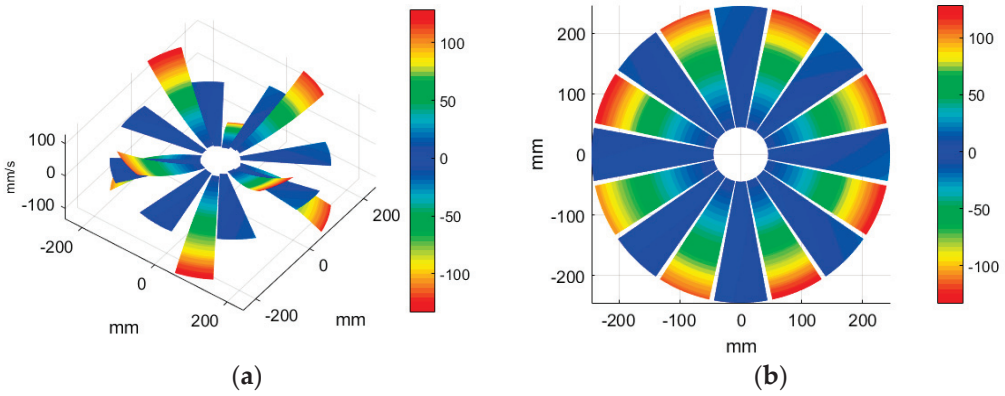

(**a**) (**b**)

Figure 11. ODS of the whole-bladed disk. (**a**) Three-dimensional perspective. (**b**) Plane perspective.

To better investigate the validity and accuracy of the ODS reconstruction method based on ODSFRF in CSLDV, the conventional SLDV method is also employed to conduct experiments in the same installation conditions and experimental environment for comparison. Regarding the test, the fewer the measuring points are, the rougher the obtained modal vibration mode will be. For the test, 5×9 measurement points were arranged on each blade, and there are a total of 1440 measurement points on the entire bladed disk as shown in Figure 12a. In order to reduce the random error in the testing process, each measuring point is tested three times, and the single testing time is 4.096 s. The frequency response function adopts the average of three times. It takes about 3 h to complete the entire test. Finally, the four-nodal diameter bending mode of the bladed disk from the test data in SLDV is shown in Figure 12b.

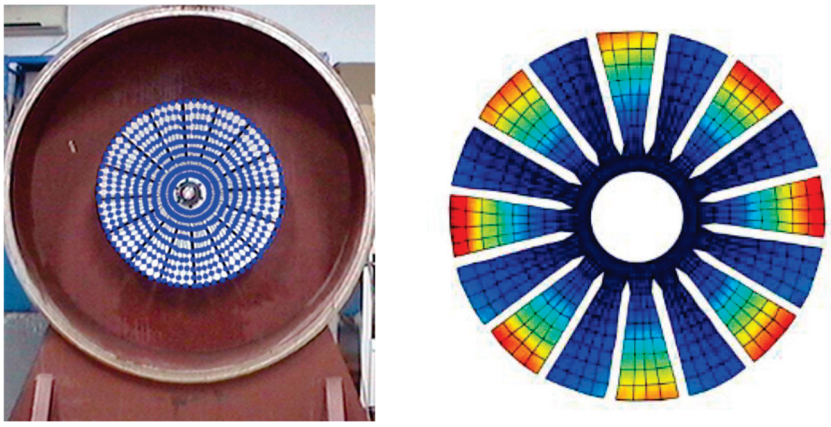

(**a**) (**b**)

Figure 12. Measurement of ODS in SLDV. (**a**) Arrangement of measuring points. (**b**) The 4-nodal diameter bending mode.

Compared to SLDV, the ODS reconstruction method based on CSLDV only takes a few minutes in terms of time consumption. However, the MAC value between the ODS obtained by the two is as high as 0.97. This demonstrates that the measurement method proposed in this paper is feasible and accurate.

4. Conclusions

In this paper, a fast measurement method of operational deflection shapes of bladed disks with CSLDV is presented, in which all blades are tested in the same condition by switching the initial phase of the laser point and a phase identification method based on ODSFRF is proposed to reconstruct the ODS of the whole-bladed disk. In order to determine the relative vibration phase between each blade, two laser beams are needed

to participate in the experiment. In this paper, the vibration phases of each blade of the bladed disk are, respectively, identified through the utilization of FRFs and ODSFRFs, and the two methods yield consistent results. However, the ODSFRF is applicable in the situation of unknown excitation. Bladed disks typically rotate at high speeds, and the excitation under operating conditions is rather difficult to measure. Hence, this ODSFRF method is anticipated to be potentially applied in the ODS measurement of rotating bladed disks. According to the ODSs and the relative vibration phase angles of all blades, the ODS of the whole-bladed disk has been reconstructed. The effects of the extended CSLDV measurement method and phase identification of the bladed disk have been investigated experimentally. To validate the accuracy of the ODS reconstructed based on CSLDV and ODSFRF, a discrete point testing experiment in SLDV was carried out supplementarily. The results show that the CSLDV and phase identification method for the bladed disks are feasible and they take less time to obtain the same high-precision ODS.

Author Contributions: Conceptualization, C.L.; methodology, C.L.; software, C.L. and T.X.; validation, T.C.; formal analysis, J.H. and S.S.; investigation T.X. and Y.L.; resources, C.L. and T.X.; writing—original draft preparation, C.L.; writing—review and editing, C.L., T.C. and J.H.; visualization, Y.L. and T.C.; supervision, J.H., S.S. and T.X.; project administration, C.L. and T.C. All authors have read and agreed to the published version of the manuscript.

Funding: This research was funded by the Start-up Fund for New Talented Researchers of Nanjing Vocational University of Industry Technology (YK21-03-05, YK21-03-02), the Natural Science Foundation of Jiangsu Higher Education Institutions of China (23KJD470004). High-level Training Project for Professional-leader Teachers of Higher Vocational Colleges in Jiangsu Province (Grant 2023TDFX007) and Grant No. HK23-51-10. Natural Science Foundation of Jiangsu Province (BK20160702) and Qing Lan Project for Excellent Young Core Teachers of Jiangsu Province.

Data Availability Statement: Data are contained within the article.

Conflicts of Interest: The authors declare no conflicts of interest.

References

1. Chatterjee, A.; Kotambkar, M.S. Modal characteristics of turbine blade packets under lacing wire damage induced mistuning. *J. Sound Vib.* **2015**, *343*, 49–70. [CrossRef]
2. Lu, Y.H.; Mei, Q.; Lei, M.Z.; Yu, J.J. Vibration stress test and dynamical evaluation for high rotational speed compressor. *J. Propuls. Technol.* **2014**, *35*, 1398–1403. (In Chinese)
3. Philippe, J.; Thouverez, F.; Blanc, L.; Gruin, M. Vibratory behavior prediction of mistuned stator vane cluster: An industrial application. *Comput. Struct.* **2018**, *196*, 12–23. [CrossRef]
4. Tang, W.; Epureanu, B.I.; Fillppi, S. Models for blisks with large blends and small mistuning. *Mech. Syst. Signal Process.* **2017**, *87*, 161–179. [CrossRef]
5. Lim, H.S.; Chung, J.; Yoo, H.H. Modal analysis of a rotating multi-packet blade system. *J. Sound Vib.* **2009**, *325*, 513–531. [CrossRef]
6. Witek, L.; Stachowicz, F. Modal analysis of the turbine blade at complex thermomechanical loads. *Strength Mater.* **2016**, *48*, 474–480. [CrossRef]
7. Zhao, Z.B.; He, E.M.; Wang, H.J. Experimental Investigation on Natural Characteristics and Forced Response of Bladed Disks. *Appl. Mech. Mater.* **2011**, *105–107*, 34–37. [CrossRef]
8. Yao, J.; Wang, J.; Li, Q. Improved Modal Localization and Excitation Factors for Understanding Mistuned Bladed Disk Response. *J. Propuls. Power* **2011**, *27*, 50–60. [CrossRef]
9. Liao, H.; Wang, J.; Wang, S.; Li, Q. Experimental investigation of the worst-case mode localization for a mistuned bladed disk assemblies. *J. Aerosp. Power* **2011**, *26*, 8.
10. Kumar, R.R.; Pandey, K.M. Static structural and modal analysis of gas Turbine blade. *IOP Conf. Ser. Mater. Sci. Eng.* **2017**, *225*, 012102. [CrossRef]
11. Hancox, J.; Staples, B.C.; Parker, R.J. The application of scanning laser Doppler vibrometry in aero-engine development. *Proc. Inst. Mech. Eng. Part G J. Aerosp. Eng.* **2016**, *209*, 35–42. [CrossRef]
12. Junge, B. Experiences with scanning laser vibrometry in automotive industries. International Conference on Vibration Measurements by Laser Techniques: Advances and Applications. *Int. Soc. Opt. Photonics* **1994**, *2358*, 377–385.
13. Heinemann, T.; Becker, S. Axial fan blade vibration assessment under inlet cross-flow conditions using laser scanning vibrometry. *Appl. Sci.* **2017**, *7*, 862. [CrossRef]

14. Hu, Y.; Kang, Y.; Yu, K.; Zhu, W.; Zhao, R. Complete operating deflection shapes and model updating for an excited structure in thermal environments via an optimized continuously scanning laser Doppler vibrometer with a two-dimension scan scheme. *J. Sound Vib.* **2023**, *544*, 117411. [CrossRef]
15. Sriram, P.; Craig, J.I.; Hanagud, S. A scanning laser Doppler vibrometer for modal testing. *Inst. Math. Its Appl.* **1990**, *5*, 155–167.
16. Halkon, B.J.; Frizzel, S.R.; Rothberg, S.J. Vibration measurements using continuous scanning laser vibrometry: Velocity sensitivity model experimental validation. *Meas. Sci. Technol.* **2003**, *14*, 382–393. [CrossRef]
17. Stanbridge, A.B.; Martarelli, M.; Ewins, D.J. Measuring area vibration mode shapes with a continuous-scan LDV. *Measurement* **2004**, *35*, 181–189. [CrossRef]
18. Stanbridge, A.B.; Ewins, D.J. Modal testing using a scanning laser Doppler vibrometer. *Mech. Syst. Signal Process.* **1999**, *13*, 255–270. [CrossRef]
19. Yuan, K.; Zhu, W.D. Identification of modal parameters of a model turbine blade with a curved surface under random excitation with a three-dimensional continuously scanning laser Doppler vibrometer system. *Measurement* **2023**, *214*, 112759. [CrossRef]
20. Yuan, K.; Zhu, W.D. A novel general-purpose three-dimensional continuously scanning laser Doppler vibrometer system for full-field vibration measurement of a structure with a curved surface. *J. Sound Vib.* **2022**, *540*, 117274. [CrossRef]
21. Boudreau, A.; Paillard, B.; Rowntree, P. Broadband vibration measurements using a continuously scanning laser vibrometer. *Meas. Sci. Technol.* **2002**, *13*, 1574.
22. Liu, C.; Zang, C.; Zhou, B. Extension of continuous scanning laser Doppler vibrometry measurement for complex structures with curved surfaces. *Chin. J. Aeronaut.* **2020**, *33*, 3220–3227. [CrossRef]
23. Liu, C.H.; Zang, C.P.; Li, F.; Petrov, E.P. High Frequency Modal Testing of the Multiblade Packets Using a Noncontact Measurement and Excitation System. *Shock Vib.* **2020**, *5*, 1–12. [CrossRef]
24. Richardson, M.H. Is it a mode shape, or an operating deflection shape? *Sound Vib.* **1997**, *31*, 54–61.
25. Zhang, Y.L.; Zhang, L.M.; Sun, W.G.; Qiu, F.L. Modal contribution analysis of intercity rails under working conditions based on ODS FRF. *Noise Vib. Control* **2014**, *34*, 65–69. (In Chinese)

sensors

MDPI

Article

Detection of Multi-Layered Bond Delamination Defects Based on Full Waveform Inversion

Jiawei Wen [1,2], Can Jiang [1,*] and Hao Chen [1,2,*]

[1] Institute of Acoustics, Chinese Academy of Sciences, Beijing 100190, China; wenjiawei@mail.ioa.ac.cn
[2] School of Electronic, Electrical and Communication Engineering, University of Chinese Academy of Sciences, Beijing 100049, China
* Correspondence: jiangcan@mail.ioa.ac.cn (C.J.); chh@mail.ioa.ac.cn (H.C.)

Abstract: This study aimed to address the challenges encountered in traditional bulk wave delamination detection methods characterized by low detection efficiency. Additionally, the limitations of guided wave delamination detection methods were addressed, particularly those utilizing reflected waves, which are susceptible to edge reflections, thus complicating effective defect extraction. Leveraging the full waveform inversion algorithm, an innovative approach was established for detecting delamination defects in multi-layered structures using ultrasonic guided wave arrays. First, finite element modeling was employed to simulate guided wave data acquisition by a circular array within an aluminum–epoxy bilayer structure with embedded delamination defects. Subsequently, the full waveform inversion algorithm was applied to reconstruct both regular and irregular delamination defects. Analysis results indicated the efficacy of the proposed approach in accurately identifying delamination defects of varying shapes. Furthermore, an experimental platform for guided wave delamination defect detection was established, and experiments were conducted on a steel–cement bilayer structure containing an irregular delamination defect. The experimental results validated the exceptional imaging precision of our proposed technique for identifying delamination defects in multi-layered boards. In summary, the proposed method can accurately determine both the positions and sizes of defects with higher detection efficiency than traditional pulse-echo delamination detection methods.

Keywords: ultrasonic guided waves; plate structures; full waveform inversion; delamination defects

1. Introduction

Adhesive structures comprise assemblies formed by bonding metals to metals, metals to non-metals, or non-metals to non-metals using adhesives. These structures are renowned for their lightweight nature, cost-effectiveness, and ease of manufacture. Additionally, owing to their exceptional fatigue resistance, high-temperature tolerance, corrosion resistance, and uniform stress distribution, adhesive structures have garnered extensive utilization across critical sectors such as aviation, aerospace, automotive, and artificial satellite industries [1]. However, throughout their service life, adhesive structures are susceptible to delamination at their bonding interfaces due to factors such as adhesive processes, environmental conditions, and aging. Consequently, advancing and employing adhesive structures necessitates a dependable assessment of their integrity during research, development, and operational phases, achievable through non-destructive testing techniques [2].

Ultrasonic testing stands out as a significant non-destructive evaluation method, providing high-resolution detection of subsurface defects such as corrosion, delamination, voids, and cracks in materials [3–5]. Conventional ultrasonic testing typically employs bulk waves, characterized by high frequency and short wavelengths relative to the component thickness. While this approach yields high detection accuracy, it exhibits lower efficiency

when dealing with large-area components. By contrast, guided wave inspection employs signals with wavelengths comparable to the thickness of the structural walls, enabling the inspection of large-area components [6]. Guided wave non-destructive testing and structural health monitoring employ guided wave array imaging technology, which facilitates rapid localization and identification of cracks, through-holes, and delamination damage in plate-like structures [7].

Various guided wave array imaging techniques are employed for delamination detection, including reverse-time migration, spatial wavenumber filter, time-reversal imaging, machine learning imaging, and tomography. Reverse-time migration and spatial wavenumber filters primarily employ reflection wave imaging, which is notably influenced by edge reflections of the specimen [8,9]. While time-reversal imaging techniques can achieve sub-wavelength super-resolution imaging, they cannot precisely evaluate sub-wavelength damage features such as location, size, and type, resulting in a lack of crucial information for effective non-destructive testing [10,11]. Machine learning imaging methods offer high accuracy; however, these methods lack interpretability of the underlying physical processes, often necessitating large amounts of training data [12]. Guided wave tomography, on the other hand, detects defects by harnessing the dispersion properties of guided waves. The technique deploys transducer arrays around the region of interest, enabling the inversion of collected ultrasonic guided wave signals and the reconstruction of areas of material debonding [13]. Existing guided wave tomography algorithms primarily include travel-time tomography [14,15], diffraction tomography [16], HARBUT tomography [17,18], and full waveform inversion tomography [19].

Compared with alternative tomography methodologies, full waveform inversion (FWI) stands out for its ability to achieve superior resolution through the comprehensive integration of waveform travel times, phases, and amplitudes, even under conditions of limited data availability. This approach facilitates multi-parameter modeling, thereby encapsulating the intricate acoustic wave dynamics inherent in predictive data simulations [20,21]. Within the domain of industrial non-destructive testing, FWI has garnered considerable attention for its efficacy in both bulk wave and guided wave detection. In the context of bulk wave detection, Nguyen et al. applied the FWI algorithm to discern the stratification within concrete bridge decks, yielding promising outcomes in both simulated and experimental settings [22]. He et al. [23] extended the application of FWI to irregularly shaped objects, showcasing its capacity to accurately reconstruct inclusions within gear assemblies based on numerical simulations. Furthermore, Rao integrated FWI with the reverse time migration (RTM) algorithm, achieving high-resolution reconstruction of void defects within multi-layered materials [24]. In guided wave detection, pioneering work by Rao et al. [25] employed FWI for the reconstruction of residual thickness in aluminum plates, leveraging both numerical simulations and experimental A0 mode wave measurements to achieve remarkable imaging resolution. The FWI method surpasses conventional tomographic techniques in terms of imaging fidelity [26]. Additionally, the utilization of FWI enabled researchers to conduct a comprehensive analysis of velocity and attenuation characteristics associated with the S0 mode, facilitating high-resolution reconstruction of corrosion defects in aluminum plates [27]. Ratassepp et al. [28] refined forward modeling techniques to elucidate wave propagation behaviors within anisotropic plates, resulting in precise reconstructions of delamination locations and extent within composite material plates.

Currently, FWI-based guided wave tomography (GWT) technology primarily targets the detection of single-layer or anisotropic materials, with relatively less research focused on detecting delamination defects in multi-layered materials. Therefore, this paper proposes a novel methodology for detecting delamination defects in double-layered boards utilizing FWI. Compared to traditional bulk wave detection methods, this significantly enhances detection efficiency. Both simulation and experimental results underscore the method's efficacy in detecting delamination defects with high accuracy. The subsequent sections of this paper are structured as follows: Section 2 provides a succinct overview of guided wave detection principles based on FWI. Section 3 presents numerical studies validating

the algorithm's efficacy in detecting delamination defects of varying geometries within aluminum–epoxy bilayer materials. Section 4 comprises experimental validation, wherein the proposed method is applied to detect irregular delamination defects within steel–cement bilayer boards. Finally, Section 5 offers concluding remarks.

2. Method

2.1. Full Waveform Inversion

The full waveform inversion method comprises two key components: (1) forward simulation based on predefined model parameters and (2) calculation of the objective function gradient and parameter updates using a suitable optimization algorithm. The flow diagram of the FWI-GWT is illustrated in Figure 1.

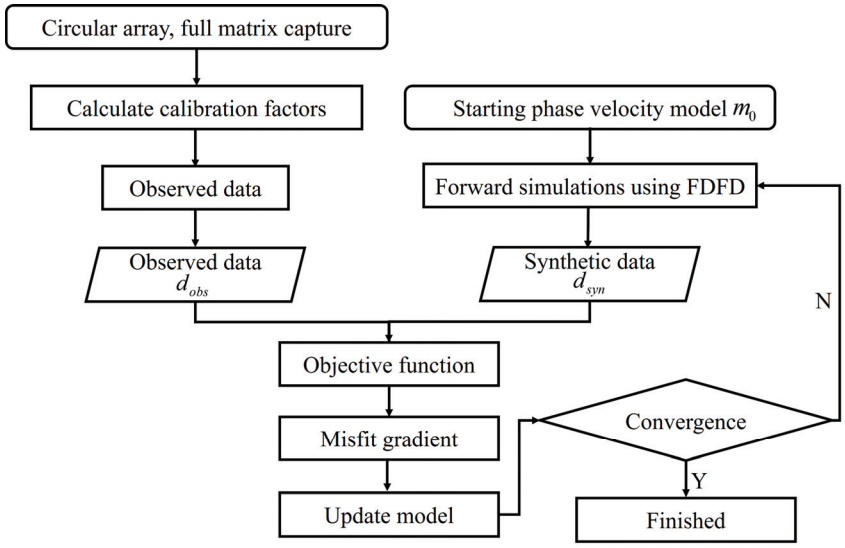

Figure 1. Flow diagram of the GWT algorithm based on FWI.

2.1.1. Forward Simulation

In the gradient computation phase of FWI, two forward wavefield simulations are necessary: (1) generating the incident wavefield based on the source and (2) computing the residual at the receiver location and utilizing it as a source to compute the back-propagated wavefield. Hence, the efficiency of gradient computation is directly linked to the efficiency of forward simulation. In guided wave detection, the propagation of guided waves in thin structures is commonly described using the constant-density acoustic wave equation. In the frequency domain, this equation can be represented by the Helmholtz equation:

$$\left(\nabla^2 + \frac{\omega^2}{v^2}\right) p(r,\omega) = -s(\omega)\delta(r - r_s) \tag{1}$$

where $\nabla^2 = \frac{\partial}{\partial x^2} + \frac{\partial}{\partial y^2} = \partial_x^2 + \partial_y^2$ represents the Laplace operator, $\omega = 2\pi f$ denotes the angular frequency, and f denotes frequency; v denotes the speed of wave propagation; $r(x, y)$ denotes the position in two-dimensional space and $p(r, \omega)$ denotes the acoustic pressure field; $s(\omega)$ represents the spectrum of the source signal; $\delta(r - r_s)$ represents the Dirac function; and r_s denotes the position of the sound source in two-dimensional space. In this study, we employed a nine-point differencing scheme to discretize Equation (1) [29]. To minimize interference from boundary reflections, perfectly matched layers were positioned around the computational domain to absorb the reflected acoustic wave energy. Equation (1) can be represented using matrices through finite-difference discretization:

$$Ap = s \tag{2}$$

where $A = \nabla^2 + \frac{\omega^2}{v^2}$ is a $N \times N$ complex impedance matrix associated with material properties, frequency, boundary conditions, and discretization format; N represents the total number of grid points in the two-dimensional grid, while p and s are $N \times 1$ vectors representing the acoustic pressure field and the source function, respectively. To enhance computational efficiency, the LU decomposition [30] can be employed to solve the wavefield p:

$$LU[p_1, p_1, \ldots, p_n] = [s_1, s_2, \ldots, s_n] \tag{3}$$

where L and U represent the upper triangular matrix and lower triangular matrix of the LU decomposition, respectively. This method employs the decomposed matrix A to simultaneously solve the forward problems for multiple sources, notably accelerating the computation speed.

In our inversion method, to enhance efficiency, the forward modeling process employs the acoustic wave equation to simulate the propagation of guided waves, which differs from actual guided wave propagation. Therefore, it is necessary to calibrate the measured data to reduce the differences between these two models [25]. The method of calibrating data involves calculating correction factors based on Equation (4) and multiplying the measured data or finite element simulation data by these correction factors to reduce discrepancies. The calibration factor Q can be represented as follows:

$$Q = \frac{fft(\psi_0)}{fft(d_{obs,0})} \tag{4}$$

where $d_{obs,0}$ represents the time-domain signal unaffected by defect scattering obtained from finite element simulations or experimental measurements, ψ_0 represents the time-domain signal in a homogeneous medium simulated using finite difference methods, and $fft()$ denotes the fast Fourier transform.

2.1.2. Inversion Theory

For a specific single-frequency component, the frequency domain L2 objective function can be expressed as follows:

$$E(v) = \frac{1}{2}\sum_{x_s}\sum_{x_r}\left[Rd_{syn}(\omega, x, x_s; v) - d_{obs}(\omega, x_r, x_s)\right]^2 \tag{5}$$

where $d_{syn}(\omega, x, x_s; v)$ denotes the synthetic data related to the model parameters v, $d_{obs}(\omega, x_r, x_s)$ are the observed data, and R denotes the operator associated with the receiver positions.

To circumvent the computation and storage challenges posed by the enormous Frechet derivative matrix, this study employed the adjoint-state method [31] to calculate the gradient of the objective function with respect to velocity. The expression for the gradient is as follows:

$$g(v) = \frac{\delta E(v)}{\delta v} = -\frac{2\omega^2}{v^3}\sum_{x_s} d_{syn} B^*[R^*(Rd_{syn} - d_{obs})] \tag{6}$$

where B denotes the forward operator and holds that $B = A^{-1}$. Assuming $u = B^*[R^*(Ru - d_{obs})]$,

$$g(v) = -\frac{2\omega^2}{v^3}\sum_{x_s} dp \tag{7}$$

The gradient is computed based on the results derived from the incident wavefield d and the back-propagated wavefield p.

Given the gradient expression, the process of updating the model parameters can be formulated as follows:

$$v^{(k+1)} = v^{(k)} - \alpha g^{(k)} \tag{8}$$

where α represents the optimization step length, $g^{(k)}$ denotes the gradient value at the k-th iteration, and $v^{(k)}$ represents the model parameters at the k-th iteration.

Considering only first-order derivatives, the corresponding technique is the steepest descent method. However, this method exhibits slow convergence speed, thereby limiting its applicability to large-scale problems. By contrast, the Newton algorithm possesses second-order convergence properties and high solution accuracy. The iterative process for updating the model parameters using the Newton algorithm can be expressed as follows:

$$v^{(k+1)} = v^{(k)} - \alpha H^{-1(k)} g^{(k)} \tag{9}$$

where $H^{-1(k)}$ represents the inverse of the Hessian matrix. Nevertheless, computing the Hessian matrix imposes significant demands on the computational power and storage space of computers. Therefore, the limited-memory Broyden–Fletcher–Goldfarb–Shanno (L-BFGS) method [32] is employed for updating the model. This method approximates the Hessian matrix by disregarding complex terms, leading to faster convergence compared to the first-order steepest descent method and a notably lighter computational burden compared to the second-order Newton method.

2.2. Regularization Methods

In the iterative imaging process, Gaussian filtering is a widely utilized technique to mitigate the effects of noise and artifacts, thereby enhancing imaging precision. For the FWI algorithm based on the elastic model, the resolution typically ranges between 1.5 and 2λ. Based on empirical knowledge, in this study, the standard deviation of the Gaussian filter is set to $\lambda/2$, where λ represents the wavelength.

In addition to the aforementioned methods, we also employ variable relaxation regularization and threshold regularization methods [33]. Threshold regularization relies on the actual phase velocity dispersion curve, where unreasonable reconstructed velocity values are adjusted to match the background velocity. Conversely, variable relaxation regularization is inspired by Tikhonov regularization. It regulates the amplification of spatial fluctuations in each iteration, stemming from noise and sensor limitations, thereby facilitating the precise reconstruction of localized defects above the noise threshold. Denoted as v_{ij} before regularization and v'_{ij} after regularization, variable relaxation regularization can be defined as follows:

$$v'_{ij} = \begin{cases} \widetilde{v} + \dfrac{v_{ij} - \widetilde{v}}{(1 + \frac{1}{z_{ij}^2})^{\frac{\alpha}{2}}} & 0 < \left| v_{ij} - \widetilde{v} \right| < \gamma\beta\widetilde{v} \\ v_{ij} & \text{otherwise} \end{cases}$$

$$z_{ij} = \begin{cases} \dfrac{\left| v_{ij} - \widetilde{v} \right|}{\beta\widetilde{d}} & \left| v_{ij} - \widetilde{v} \right| < \beta\widetilde{v} \\ \dfrac{\left| v_{ij} - \widetilde{v} \right|}{0.5\beta\left[1 - \cos(\pi \frac{\left| v_{ij} - \widetilde{v} \right| - \gamma\beta\widetilde{v}}{(1-\gamma)\beta\widetilde{v}})\right]} & \beta\widetilde{v} \le \left| v_{ij} - \widetilde{v} \right| < \gamma\beta\widetilde{v} \end{cases} \tag{10}$$

where $\widetilde{v}$ represents the reference velocity for regularization, typically aligned with the velocity of the homogeneous model. $\beta \in [0,\ 1]$ denotes a value contingent upon data noise, with larger values resulting in diminished background noise post-regularization. $\gamma \in [1, +\infty)$ stands for the relaxation constant, and the product of γ and β determines the extent of regularization on velocity; a larger product yields a broader range of regularization. $\alpha \in \mathbb{R}_+$ constitutes a constant that defines the strength of regularization; higher values translate to fewer artifacts in the reconstructed velocity map, albeit with larger reconstruction errors. This study set $\alpha = 2$, $\beta = 0.1$, and $\gamma = 3$.

2.3. Error Analysis

The root mean square error (RMSE) is used to assess the reconstruction accuracy. The expression of the RMSE is as follows:

$$RMSE = \sqrt{\frac{\|\widetilde{v} - v\|_2^2}{N}} \tag{11}$$

where $\widetilde{v}$ is the true phase velocity, v is the velocity reconstructed by the FWI, and N is the total number of pixels. A smaller RMSE corresponds to a more accurate reconstruction of the defects.

3. Numerical Test

Figure 2 depicts the finite element simulation model of a double-layered bonded structure comprising primarily aluminum and epoxy. To mitigate boundary-induced reflection waves, a 30 mm absorbing boundary is extended outward from a 400 mm × 400 mm research area. Transducers are evenly distributed along a 200 mm radius circle centered at the geometric center of the bonded plate. The irregular gray area represents the debonding defect.

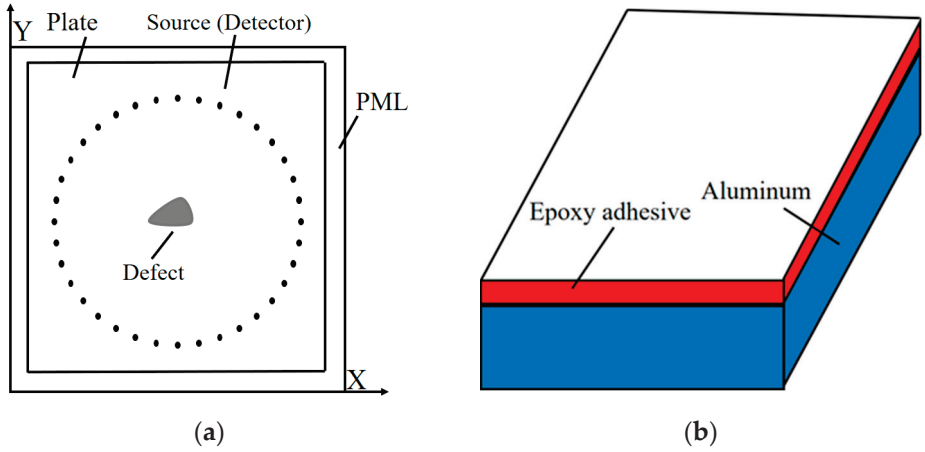

Figure 2. Finite element simulation model for debonding detection of aluminum–epoxy layered plates. (**a**) Geometrical schematic for marking the transducer position. (**b**) Aluminum–epoxy adhesive bonding model.

Table 1 provides the material parameters of the aluminum–epoxy laminate. Based on these parameters, we computed the dispersion curve. Given that the A0 mode is an asymmetric mode and is more readily excited in practical inspection processes, we have opted for the A0 mode for debonding defect detection in this study.

Table 1. Material parameters of aluminum–epoxy laminated plate [34].

Material	ρ (kg/m^3)	c_T (m/s)	c_s (m/s)
Aluminum	2700	6364	3170
Epoxy adhesive	1170	2610	1102

Assuming the total thickness of the aluminum–epoxy bilayered plates is 12 mm, the solid lines of different colors in Figure 3 show the A0 mode phase velocity dispersion curves of the aluminum–epoxy layer for different thickness ratios. In the theoretical simulation part of this study, we represent the debonding of the aluminum–epoxy bilayered plates by the complete disappearance of the epoxy layer. Therefore, we have also plotted the dispersion curves of aluminum at the corresponding thickness, as shown by the dashed lines of different colors in the figure. From these dispersion curves, it is evident that for

frequencies greater than 70 kHz (black dashed line), complete debonding (disappearance of epoxy) in aluminum–epoxy bilayered plates leads to an increase in the phase velocity of the A0 mode within the debonding region. The full waveform inversion algorithm relies on capturing these changes in phase velocity to detect the debonding region. Additionally, at higher frequencies, the phase velocity differences induced by debonding become more pronounced. However, simultaneously, more modes emerge, increasing the complexity of the signal processing. Therefore, selecting appropriate frequencies is crucial in practical inspection processes.

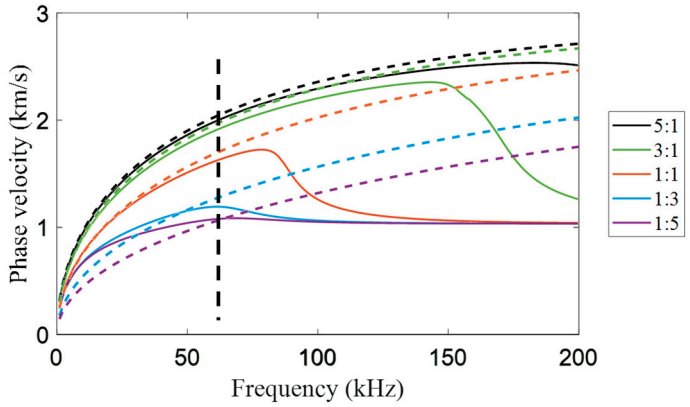

Figure 3. Dispersion curve of A0 mode phase velocity under different thickness ratios of aluminum–epoxy adhesive laminates. The position of the black dashed line indicates a frequency of 70 kHz.

For the debonding detection issue in multi-layered plates, it is essential not only to consider the impact of phase velocity changes induced by debonding on reconstruction accuracy but also to account for the influence of transducer arrangement. Below, we will separately verify the effects of these two factors.

3.1. The Effect of the Degree of Phase Velocity Variation on Detection Accuracy

Figure 4a presents a model diagram of a circular debonding defect located at the center of an aluminum–epoxy adhesive bilayer structure. The blue-filled area in the figure indicates the circular debonding region with a diameter of 50 mm, which is made of aluminum. This area exhibits a faster phase velocity compared to the aluminum–epoxy structure. According to Huthwaite [17], the maximum transducer spacing is recommended to be less than half a wavelength. However, deploying an excessive number of transducers in practical experiments is not feasible. Consequently, transducer spacing is usually set within one wavelength [26]. Fifty transducers, centered at a frequency of 80 kHz, are evenly distributed along the circumference of a circle with a radius of 200 mm on one side of the aluminum plate. At this spacing, the distance between transducers is less than one wavelength for the A0 mode. Using the phase velocity of the A0 mode under well-bonded conditions (aluminum–epoxy) as the initial model, Figure 4b,c show the debonding defect images reconstructed using the FWI algorithm for different thickness ratios of aluminum and epoxy. In comparison, Figure 4c exhibits a higher degree of artifacts, primarily because the phase velocity change between well-bonded and debonded conditions at this thickness ratio is only 3 m/s. Table 2 presents the RMSE for the two thickness ratios, showing that the reconstruction accuracy is higher when the thickness ratio is 5:1. Therefore, in practical detection processes, more significant phase velocity changes are advantageous for improving detection accuracy.

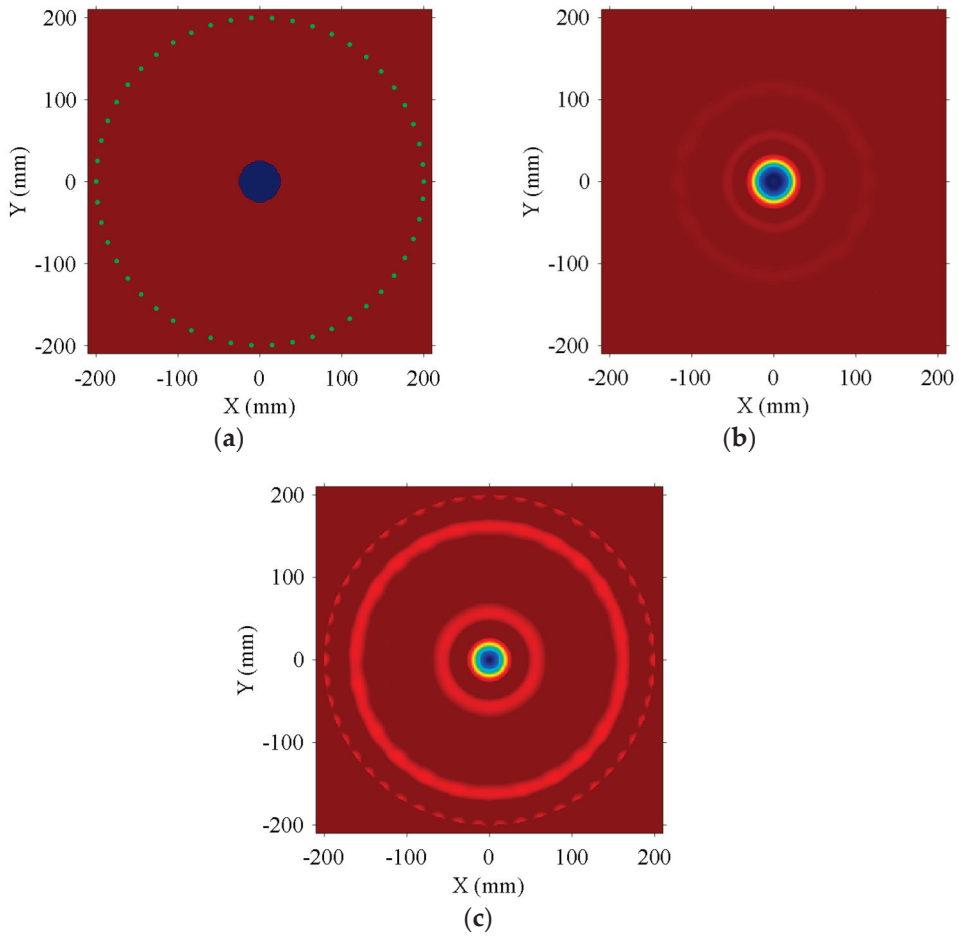

Figure 4. Reconstruction results of aluminum and epoxy adhesive at different thickness ratios. (**a**) Original model; (**b**) 5:1; (**c**) 1:3.

Table 2. RMSE of reconstruction results for aluminum and epoxy adhesive at different thickness ratios.

Thickness Ratio	RMSE (m/s)
5:1	1.80
1:3	2.97

3.2. The Effect of Transducer Installation Position on Detection Accuracy

Considering that debonding defects in practical situations may have various irregular shapes, an irregular debonding area was set up on the model of a bilayer plate with an aluminum–epoxy thickness ratio of 5:1, as shown in Figure 5a. This irregular shape consists of two circular regions with a radius of 25 mm each. Similar to Section 3.1, the blue-filled area in the figure indicates the debonding region, which is made of aluminum. This area exhibits a faster phase velocity compared to the aluminum–epoxy structure. Fifty transducers, with a center frequency of 80 kHz, are evenly spaced along a circumference with a radius of 200 mm. The acoustic source is loaded in the normal direction. The reconstruction result from the transducer array placed on the aluminum plate surface is shown in Figure 5b, and the reconstruction result from the transducer array placed on the epoxy surface is shown in Figure 5c. Table 3 shows the RMSE of the reconstruction results with transducers installed at different positions. The imaging results indicate that the debonding defect location can be accurately reconstructed regardless of which side of the plate the transducers are installed on. Additionally, applying the normal displacement source on the aluminum plate surface achieves higher imaging resolution. To analyze the

reason for this, we plotted the displacement wave structure characteristics of the A0 mode at 80 kHz, as shown in Figure 6. The solid line represents in-plane displacement, while the dashed line represents out-of-plane displacement. From the figure, it can be seen that on the aluminum plate surface, the A0 mode primarily exhibits out-of-plane displacement vibration. Therefore, installing the transducers on the aluminum plate surface is more advantageous for exciting the A0 mode, thereby achieving higher detection accuracy.

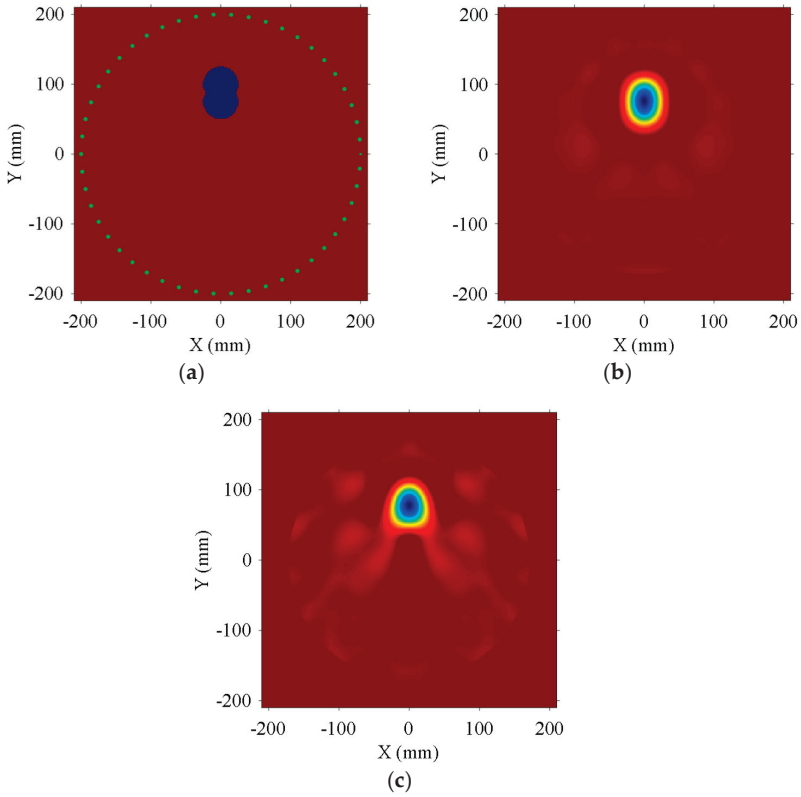

Figure 5. Reconstruction results of different transducer installation positions. (**a**) Original model. (**b**) Transducer mounted on aluminum plate surface. (**c**) Transducer mounted on epoxy adhesive surface.

Table 3. RMSE of reconstruction results for different transducer installation positions.

Transducer Installation Positions	RMSE (m/s)
Aluminum plate surface	1.92
Epoxy adhesive surface	2.21

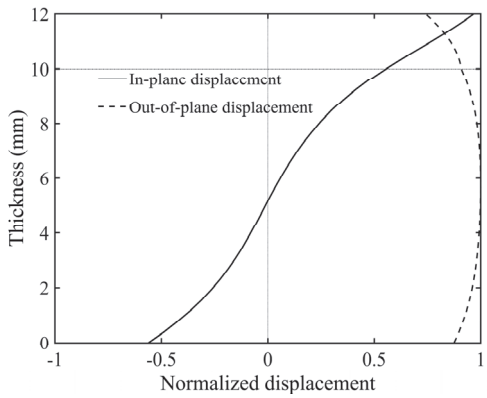

Figure 6. Displacement wave structure of the A0 mode at 80 kHz in aluminum–epoxy adhesive laminate.

4. Experimental Test

To further validate the feasibility of FWI-guided wave tomography in practical inspection processes, corresponding experiments on guided wave detection of the bilayer board were conducted. As illustrated in Figure 7a, a PTFE film was affixed to the interface of the steel–cement bilayer plate to simulate an area with poor adhesion. Subsequently, cement was poured onto the steel plate's surface and allowed to settle for 48 h, resulting in the steel–cement bilayer structure depicted in Figure 7b. This structure comprises a 2 mm thick cold-rolled steel plate and a 10 mm thick cement layer. The longitudinal and shear wave velocities, as well as the densities of steel and cement, were measured and are shown in Table 4.

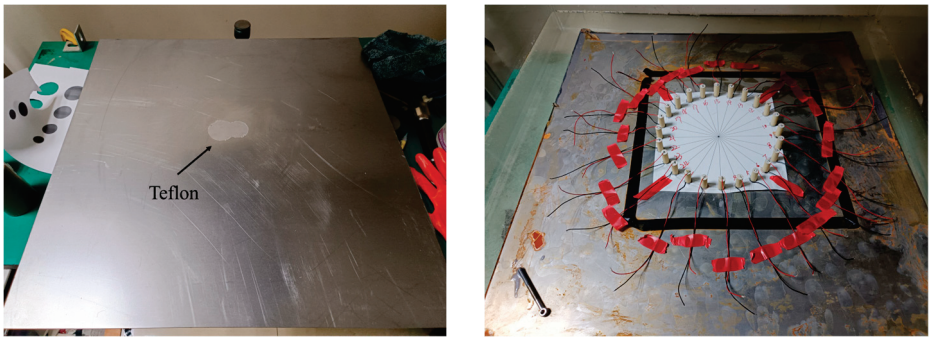

(**a**) (**b**)

Figure 7. Guided wave detection experiment photo of a steel–cement bilayer plate. (**a**) Irregularly shaped PTFE film adhered to a 2 mm thick steel plate. (**b**) Twenty-four piezoelectric transducers mounted on the steel–cement bilayer plate.

Table 4. Material parameters of the steel–cement laminated plate.

Material	ρ (kg/m^3)	c_T (m/s)	c_s (m/s)
Steel	7850	5890	3240
Cement	1865	2930	1741

4.1. Pulse-Echo Method

To assess the bonding quality, we initially employed the conventional pulse-echo method for inspecting the bonding condition of the steel–cement bilayer plate. Figure 8 illustrates the experimental setup for pulse-echo debonding detection. The bilayer plate in the lower left corner represents the test specimen, with "T" denoting the emitter and "R" indicating the receiver. During measurements, the emitter transmits ultrasonic waves vertically toward the plate. A mechanical positioning device is employed to comprehensively inspect the specimen using the "S"-shaped water immersion scanning method. The experiment utilized an 5072PR (Olympus, Tokyo, Japan) pulse signal generator as the excitation device, which stimulated the emitter. Additionally, the emitter served as the receiver to collect the signals. The collected signals passed through a preamplifier, were displayed on an oscilloscope, and were stored in real time on a computer. Figure 9 shows multiple echo measurement signals obtained at one of the positions on the plate [35]. The first and largest peak represents the echo signal from the top surface of the plate and does not contain any information about defects within the plate. The first and second echoes indicated by arrows are the signals used to assess the bonding quality. To determine the presence of debonded areas, one only needs to calculate the ratio of the maximum peak of the first echo to the maximum peak of the second echo. Figure 10 displays the imaging results obtained after multiple-wave amplitude processing of the collected array data. The yellow area in the image indicated poor bonding quality, while the green area indicated good bonding. The image clearly revealed an "8"-shaped debonding defect in the middle

caused by the PTFE film, confirming the experiment's feasibility. However, despite offering high imaging accuracy, traditional ultrasonic scanning is relatively slow. Therefore, we evaluated the bonding quality using the guided wave tomography technique based on full waveform inversion.

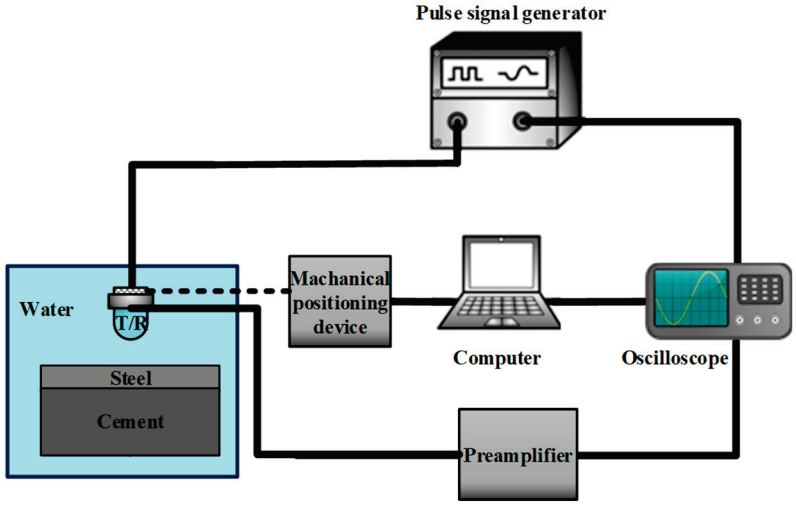

Figure 8. Experimental equipment and measurement principles for pulse-echo debonding defect detection.

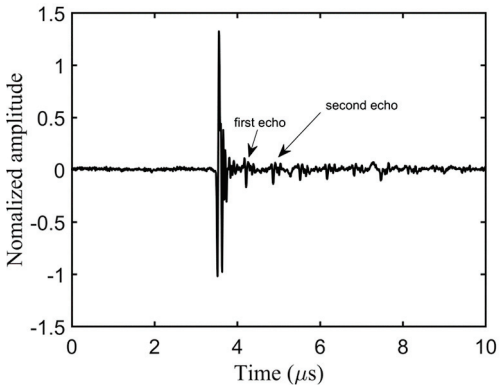

Figure 9. Steel–cement multiple wave measurement signals.

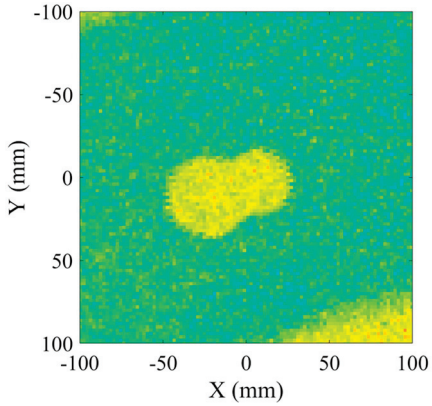

Figure 10. Reconstruction results of the pulse-echo method.

4.2. FWI Method

Based on longitudinal and transverse wave velocities from Table 4, we plotted the dispersion curves of the A0 mode wave in the bilayer board under various bonding

qualities, as illustrated in Figure 11. Given the smoother surface of the steel plate, we mounted the transducers on it. Analysis of the dispersion curves revealed that the phase velocity difference between the steel and steel–cement bilayer plates initially increased and then decreased with increasing frequency within the frequency-thickness product range of 0-100 kHz×mm. Therefore, we selected a five-cycle Hanning window-modulated cosine with a center frequency of 50 kHz as the excitation signal. Figure 12 displays the displacement wave structure curve of the A0 mode wave in the steel–cement bilayer plate at 50 kHz, demonstrating predominantly out-of-plane displacement on the steel plate side. Therefore, we arranged 24 d31-mode piezoelectric transducers (Baoding Hongsheng Ceramic Inc., Baoding, China) at the geometric center of the steel side of the steel–cement bilayer plate, as illustrated in Figure 7b. These transducers were evenly spaced along a circumference with a radius of 100 mm and were directly attached to the steel plate surface using AB glue. Each d31 piezoelectric sensor had a diameter of 10 mm and a length of 26 mm. Figure 13 illustrates the experimental setup for array data acquisition, comprising a computer, power amplifier, signal generator, oscilloscope, ultrasonic transducers, and the stee–cement bilayer board. The experiment employed a power amplifier to amplify the signal from the signal generator, serving as the input to the emitter. Subsequently, the received signal on the receiver was observed on an oscilloscope, which was connected to a computer for real-time storage of the acquired data.

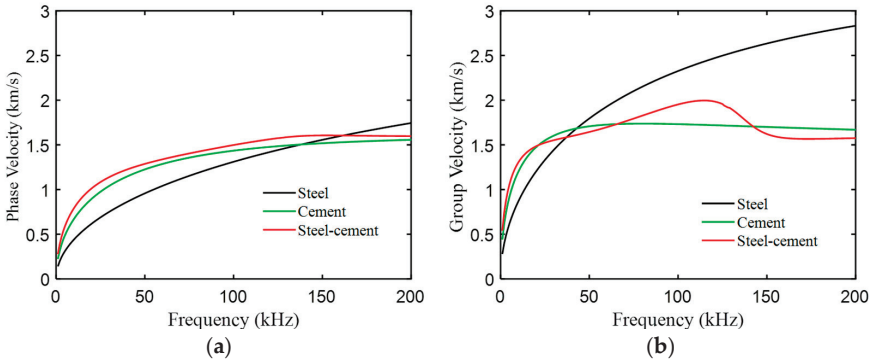

Figure 11. Dispersion curve of A0 mode waves in steel–cement laminated plate. (**a**) Phase velocity. (**b**) Group velocity.

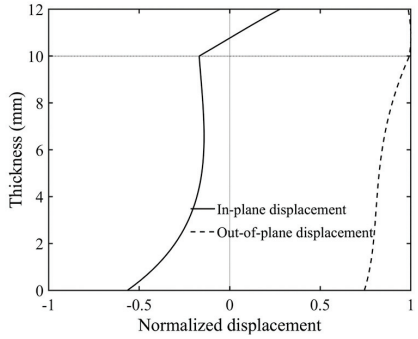

Figure 12. Displacement wave structure of the A0 mode at 50 kHz in a steel–cement laminate.

During the signal acquisition process, noise often accompanies the data. Interference signals can distort measurements and must be mitigated. To address this, a bandpass filter tailored to the transducer's bandwidth is applied. In practical settings, unlike simulated scenarios, measurements are influenced by reflected waves from the plate's edges. These reflections, devoid of defect-related information, are filtered out. In this study, the method outlined in [36] was employed to extract the A0 mode. The method involved applying a Tukey window to the original signals based on the group velocity dispersion curve, as shown in Figure 11b. Figure 14 displays the waveform captured by a single emitter–

receiver pair. The black solid line represents the normalized original waveform, the red solid line depicts the Tukey window function, and the blue solid line illustrates the extracted A0 mode. After the Fourier transformation of the A0 mode data, the frequency-domain FWI method was employed for defect imaging.

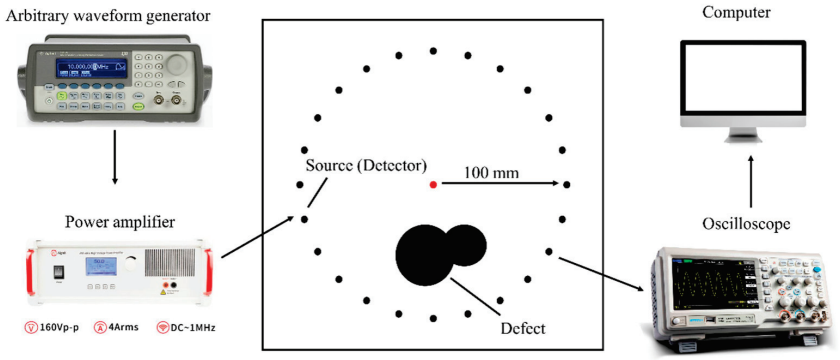

Figure 13. Experimental setup.

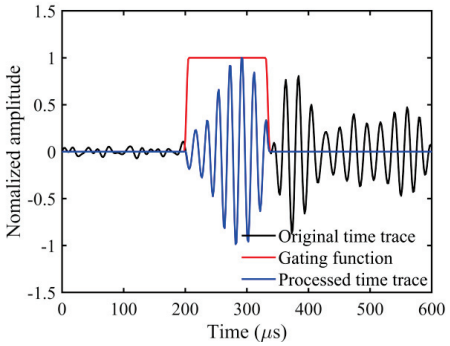

Figure 14. Waveform acquired from an emitter–receiver pair.

Figure 15 presents the reconstructed location of the delamination defect at the highest frequency obtained via the FWI algorithm. The blue area delineates the reconstructed delamination region, while the red area denotes the uniformly bonded region. The green dots mark the transducers' positions, and the green dashed lines indicate the original delamination region's extent. Despite minor shape distortions and artifacts, likely due to uneven cement thickness, the position of the delamination area is accurately reconstructed. These results confirm the effectiveness of the proposed method in reconstructing the delamination area's shape and position. Compared with traditional pulse-echo delamination detection methods, the FWI-based guided wave detection method offers expedited detection.

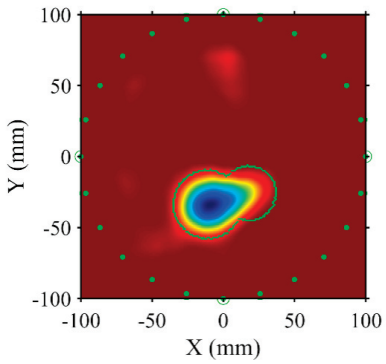

Figure 15. Reconstruction results of delamination defects in steel–cement laminated plate. Green dots mark the positions of the sensors. The Green dashed line represents the contour of the actual position of the PTFE film.

5. Conclusions

This study established a method for detecting delamination defects in bilayer structures using ultrasonic guided wave arrays based on the FWI algorithm. Numerical investigations demonstrated that FWI-based guided wave debonding defect detection effectively captures changes in phase velocity caused by defects, enabling accurate defect identification. Regardless of regular or irregular patterns in the delamination area, the proposed method reliably reconstructs the approximate defect position. Delamination detection in steel–cement bilayer plates revealed that the new detection approach, compared to traditional pulse-echo methods, enhanced detection efficiency.

The research in this study focuses on the detection of delamination defects in multi-layer plates. When the thickness of the pipe wall is much smaller than the pipe diameter, and the guided wave wavelength is smaller than or comparable to the thickness of the pipe wall, the propagation characteristics of the guided wave in the plate are similar to those in the pipe wall [37]. Currently, there is relatively little research on delamination defect detection in multi-layer pipes in aerospace, petrochemical, and other fields. Corresponding work will be conducted in the future.

Author Contributions: Conceptualization, J.W.; methodology, J.W. and H.C.; data curation, C.J.; writing—original draft preparation, J.W.; writing—review and editing, H.C. All authors have read and agreed to the published version of the manuscript.

Funding: The National Natural Science Foundation of China with grant Nos. 42304142, 52227901, and 12274432.

Institutional Review Board Statement: Not applicable.

Informed Consent Statement: Not applicable.

Data Availability Statement: The data underlying the results presented in this paper are not publicly available at this time but may be obtained from the authors upon reasonable request.

Conflicts of Interest: The authors declare no conflicts of interest.

References

1. Guyott, C.C.H.; Cawley, P.; Adams, R.D. The non-destructive testing of adhesively bonded structure: A review. *J. Adhes.* **1986**, *20*, 129–159.
2. Cawley, P. Ultrasonic measurements for the quantitative NDE of adhesive joints-potential and challenges. In Proceedings of the IEEE 1992 Ultrasonics Symposium, Tucson, AZ, USA, 20–23 October 1992; IEEE: New York, NY, USA, 1992; pp. 767–772.
3. Honarvar, F.; Varvani-Farahani, A. A review of ultrasonic testing applications in additive manufacturing: Defect evaluation, material characterization, and process control. *Ultrasonics* **2020**, *108*, 106227. [PubMed]
4. Fang, Y.; Lin, L.; Feng, H.; Lu, Z.; Emms, G.W. Review of the use of air-coupled ultrasonic technologies for nondestructive testing of wood and wood products. *Comput. Electron. Agric.* **2017**, *137*, 79–87.
5. Szilard, J. *Ultrasonic Testing: Non-Conventional Testing Techniques*; John Wiley & Sons, Inc.: New York, NY, USA, 1982; Volume 640, p. 1982.
6. Zhao, X.; Royer, R.L.; Owens, S.E.; Rose, J.L. Ultrasonic Lamb wave tomography in structural health monitoring. *Smart Mater. Struct.* **2011**, *20*, 105002.
7. Liu, Z.; Zhong, X.; Xie, M.; Liu, X.; He, C.; Wu, B. Damage imaging in composite plate by using double-turn coil omnidirectional shear-horizontal wave magnetostrictive patch transducer array. *Adv. Compos. Mater.* **2017**, *26* (Suppl. S1), 67–78.
8. He, J.; Yuan, F.G. Damage identification for composite structures using a cross-correlation reverse-time migration technique. *Struct. Health Monit.* **2015**, *14*, 558–570. [CrossRef]
9. Qiu, L.; Liu, B.; Yuan, S.; Su, Z.; Ren, Y. A scanning spatial-wavenumber filter and PZT 2-D cruciform array based on-line damage imaging method of composite structure. *Sens. Actuators A Phys.* **2016**, *248*, 62–72.
10. Zhao, G.; Zhang, D.; Zhang, L.; Wang, B. Detection of defects in reinforced concrete structures using ultrasonic nondestructive evaluation with piezoceramic transducers and the time reversal method. *Sensors* **2018**, *18*, 4176. [CrossRef]
11. Wang, J.; Shen, Y. An enhanced Lamb wave virtual time reversal technique for damage detection with transducer transfer function compensation. *Smart Mater. Struct.* **2019**, *28*, 085017.
12. Tong, J.; Lin, M.; Wang, X.; Li, J.; Ren, J.; Liang, L.; Liu, Y. Deep learning inversion with supervision: A rapid and cascaded imaging technique. *Ultrasonics* **2022**, *122*, 106686. [CrossRef]
13. Qian, Z.; Wang, B.; Zhang, Y.; Wang, S.; Li, P.; Qian, Z.; Kuznetsova, I. Guided Wave Tomography of Surface Defects Based on the Method of Moments. *Adv. Theory Simul.* **2023**, *6*, 2300121. [CrossRef]

14. McKeon, J.C.P.; Hinders, M.K. Parallel projection and crosshole Lamb wave contact scanning tomography. *J. Acoust. Soc. Am.* **1999**, *106*, 2568–2577. [CrossRef]
15. Malyarenko, E.V.; Hinders, M.K. Fan beam and double crosshole Lamb wave tomography for mapping flaws in aging aircraft structures. *J. Acoust. Soc. Am.* **2000**, *108*, 1631–1639. [CrossRef] [PubMed]
16. Belanger, P.; Cawley, P.; Simonetti, F. Guided wave diffraction tomography within the born approximation. *IEEE Trans. Ultrason. Ferroelectr. Freq. Control* **2010**, *57*, 1405–1418. [CrossRef] [PubMed]
17. Huthwaite, P. Evaluation of inversion approaches for guided wave thickness mapping. *Proc. R. Soc. A Math. Phys. Eng. Sci.* **2014**, *470*, 20140063. [CrossRef]
18. Huthwaite, P.; Simonetti, F. High-resolution imaging without iteration: A fast and robust method for breast ultrasound tomography. *J. Acoust. Soc. Am.* **2011**, *130*, 1721–1734. [CrossRef] [PubMed]
19. Virieux, J.; Operto, S. An overview of full-waveform inversion in exploration geophysics. *Geophysics* **2009**, *74*, WCC1–WCC26. [CrossRef]
20. Bernard, S.; Monteiller, V.; Komatitsch, D.; Lasaygues, P.L. Ultrasonic computed tomography based on full-waveform inversion for bone quantitative imaging. *Phys. Med. Biol.* **2017**, *62*, 7011. [CrossRef]
21. Pérez-Liva, M.; Herraiz, J.L.; Udías, J.M.; Miller, E.; Cox, B.T.; Treeby, B.E. Time domain reconstruction of sound speed and attenuation in ultrasound computed tomography using full wave inversion. *J. Acoust. Soc. Am.* **2017**, *141*, 1595–1604. [CrossRef]
22. Nguyen, T.D.; Tran, K.T.; Gucunski, N. Detection of bridge-deck delamination using full ultrasonic waveform tomography. *J. Infrastruct. Syst.* **2017**, *23*, 04016027. [CrossRef]
23. He, J.; Rao, J.; Fleming, J.D.; Gharti, H.N.; Nguyen, L.T.; Morrison, G. Numerical ultrasonic full waveform inversion (FWI) for complex structures in coupled 2D solid/fluid media. *Smart Mater. Struct.* **2021**, *30*, 085044. [CrossRef]
24. Rao, J.; Sing, S.L.; Lim, J.C.W.; Yeong, W.Y.; Yang, J.; Fan, Z.; Hazell, P. Detection and characterisation of defects in directed energy deposited multi-material components using full waveform inversion and reverse time migration. *Virtual Phys. Prototyp.* **2022**, *17*, 1047–1057. [CrossRef]
25. Rao, J.; Ratassepp, M.; Fan, Z. Guided wave tomography based on full waveform inversion. *IEEE Trans. Ultrason. Ferroelectr. Freq. Control* **2016**, *63*, 737–745. [CrossRef] [PubMed]
26. Rao, J.; Ratassepp, M.; Fan, Z. Investigation of the reconstruction accuracy of guided wave tomography using full waveform inversion. *J. Sound Vib.* **2017**, *400*, 317–328. [CrossRef]
27. Rao, J.; Ratassepp, M.; Fan, Z. Quantification of thickness loss in a liquid-loaded plate using ultrasonic guided wave tomography. *Smart Mater. Struct.* **2017**, *26*, 125017. [CrossRef]
28. Ratassepp, M.; Rao, J.; Yu, X.; Fan, Z. Modeling the Effect of Anisotropy in Ultrasonic-Guided Wave Tomography. *IEEE Trans. Ultrason. Ferroelectr. Freq. Control* **2021**, *69*, 330–339. [CrossRef] [PubMed]
29. Hustedt, B.; Operto, S.; Virieux, J. Mixed-grid and staggered-grid finite-difference methods for frequency-domain acoustic wave modelling. *Geophys. J. Int.* **2004**, *157*, 1269–1296. [CrossRef]
30. Zhang, Y.; Sun, Q. Symbol LU decomposition method of large scale sparse linear equations. *Comput. Eng. Appl.* **2007**, *43*, 29–30.
31. Plessix, R. A review of the adjoint-state method for computing the gradient of a functional with geophysical applications. *Geophys. J. Int.* **2006**, *167*, 495–503. [CrossRef]
32. Guitton, A.; Symes, W.W. Robust inversion of seismic data using the Huber norm. *Geophysics* **2003**, *68*, 1310–1319. [CrossRef]
33. Druet, T.; Tastet, J.L.; Chapuis, B.; Moulin, E. Autocalibration method for guided wave tomography with undersampled data. *Wave Motion* **2019**, *89*, 265–283. [CrossRef]
34. Zheng, J. Research on Baseline Free Lamb Wave Damage Detection Method Based on Time Reversal. Master's Thesis, Nanjing University of Aeronautics and Astronautics, Nanjing, China, 2011.
35. Zhang, Y.Y.; Zhang, P.Y.; Yang, R.R.; Wen, Y.T.; Li, Z.L. Recognition Method of Bonding Defects between Component Layers Based on Ultrasonic Testing. *Meas. Control Technol.* **2021**, *40*, 57–62.
36. Xu, W.; Yuan, M.; Xuan, W.; Ji, X.; Chen, Y. Quantitative Inspection of Complex-Shaped Parts Based on Ice-Coupled Ultrasonic Full Waveform Inversion Technology. *Appl. Sci.* **2021**, *11*, 4433. [CrossRef]
37. Li, J.; Rose, J.L. Natural beam focusing of non-axisymmetric guided waves in large-diameter pipes. *Ultrasonics* **2006**, *44*, 35–45. [CrossRef] [PubMed]

sensors

MDPI

Article

Pinpointing Moisture: The Capacitive Detection for Standing Tree Health

Jianan Yao, Zonglin Zhen, Huadong Xu *, Liming Zhao, Yuying Duan and Xuhui Guo

College of Mechanical and Electrical Engineering, Northeast Forestry University, Harbin 150040, China; yjn@nefu.edu.cn (J.Y.)
* Correspondence: huadongxu@nefu.edu.cn; Tel.: +86-138-3612-9359

Abstract: Background: the feasibility of the capacitance method for detecting the water content in standing tree trunks was investigated using capacitance-based equipment that was designed for measuring the water content of standing tree trunks. Methods: In laboratory experiments, the best insertion depth of the probe for standing wood was determined by measurement experiments conducted at various depths. The bark was to be peeled when specimens and standing wood were being measured. The actual water content of the test object was obtained by specimens being weighed and the standing wood being weighed after the wood core was extracted. Results: A forecast of the moisture content of standing wood within a range of 0 to 180% was achieved by the measuring instrument. The feasibility of the device for basswood and fir trees is preliminarily studied. When compared to the drying method, the average error of the test results was found to be less than 8%, with basswood at 7.75%, and fir at 7.35%. Conclusions: It was concluded that the measuring instrument has a wide measuring range and is suitable for measuring wood with low moisture content, as well as standing timber with high moisture content. The measuring instrument, being small in size, easy to carry, and capable of switching modes, is considered to have a good application prospect in the field of forest precision monitoring and quality improvement.

Keywords: capacitance method; standing tree; moisture content; measuring instrument

1. Introduction

Measuring the dielectric constant of standing wood is very important for measuring the water content of standing wood. At present, the dielectric constant is measured using the reflection method or resonance method. These methods usually use time domain reflectometry, network analysis, and other large measuring equipment; they usually use 220 V AC power supply, have poor portability, are expensive, and have a high retrofit cost. It is more suitable for indoor analysis and research, and cannot adapt to the timely measurement needs in the complex environment in the field. It is necessary to find a physical parameter that can include the dielectric constant. Take parallel plate capacitors as an example, as follows:

Assume that the upper and lower plates, as shown in Figure 1, carry a charge of $+q$ and $-q$, respectively; the charge is evenly distributed on the opposite side of the two plates, the electric field between plates is uniform, and its electric field intensity is as follows:

$$E = \frac{q}{\varepsilon_0 \cdot \varepsilon_r \cdot S} \quad (1)$$

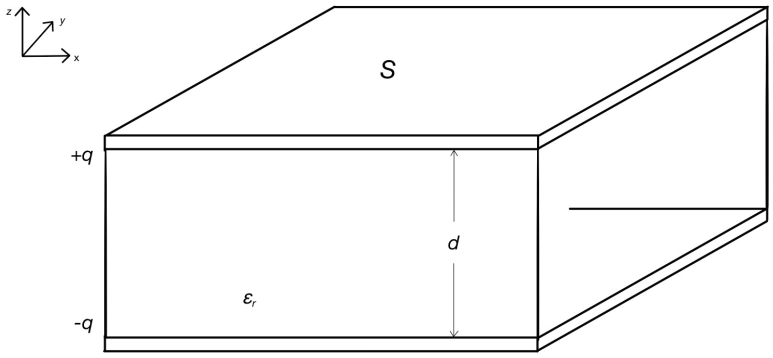

Figure 1. Plane−parallel capacitor.

$\varepsilon_0 \approx 8.85 \times 10^{-12} F/m$, $\varepsilon_0 = 1/4\pi k$ (k = 8.9880 × 10^9, unit: Nm^2/C^2).
The plate length is L, the width is D, and the plate area is

$$S = D \cdot L \tag{2}$$

The potential difference between two plates is

$$U = Ed = \frac{q \cdot d}{\varepsilon_0 \cdot \varepsilon_r \cdot S} \tag{3}$$

According to capacitance definition,

$$C = \frac{q}{U} \tag{4}$$

The dual plate capacitance is

$$C = \frac{\varepsilon_0 \cdot \varepsilon_r \cdot S}{d} \tag{5}$$

The relative permittivity of air is 1, and water is 81. Bringing these two extreme values into the equation gives a capacitance value between 0.07 and 5.67 pF, thus calculating the capacitance of the probe and the live wood sapwood medium.

The capacitance method is one of the most typical test methods for the detection of water content in standing trees, which works by detecting electrical parameters of the standing tree. Numerous moisture content (MC) measuring instruments developed over the years leverage the high correlation between the MC of the product and its electrical conductivity or dielectric constant [1]. The capacitance method for measuring water content is commonly used in other fields, such as measuring the water content of crops like wheat, corn, rice, and peanuts, as well as crude oil [2,3], and soil [4]. The current capacitance-based method of wood moisture content measurement is widely used in the wood industry. In the field of low moisture content wood, Shaogang Liu [5–7] and Guocui [8] have explored a capacitance sensor-based wood moisture content detection system, and the results showed that the capacitance method has a good mathematical model relationship for wood moisture content detection. Additionally, some scholars have ventured into predicting the water content of live standing trees' trunks using the capacitive method. For instance, Matheny [9] used a capacitive probe calibration sensor combined with the frequency domain reflection method to detect the water content of tree stems. The results show that the species-specific calibration can convert the measured dielectric constant into the volume water content of the species with different densities. The Japanese scholar Tham [10] and others combined the two methods of wood capacitance measurement and near-infrared spectroscopy to predict water content of trees, and to construct different mathematical models of capacitance and spectra, which provide a basis for analytical methods to evaluate other properties of wood and woody materials. All of these studies show that the capacitance method has

a good application, not only in the field of low water content wood detection, but it also has great potential in the detection of water content in the trunk of standing trees (high water content).

Studies have shown that the change in the capacitance signal due to the change in wood moisture content is particularly pronounced at low frequency excitation signals [11]. At present, wood moisture content testing equipment is mostly in the laboratory stage, there is still a lack of moisture content measuring instruments applied in the field for measuring live wood trunk moisture content, and it is difficult to measure live wood with high moisture content. Moreover, traditional measuring instruments have limited range and low accuracy. Therefore, it is necessary to study the capacitance-based field instrument for measuring the water content of standing tree trunks. This study takes basswood and fir as the primary research objects, and verifies their performance through laboratory and field experiments, providing technical support for the accurate measurement of water content in a standing tree, and the precise monitoring and quality improvement of forests.

2. Materials and Methods

2.1. Instrument Design

The equipment development mainly includes a detection probe, temperature acquisition circuit, live tree trunk moisture content signal detection circuit, keypad circuit, LCD display circuit, power supply, voltage regulator circuit, microcontroller minimum system, and software system; the system framework is shown in Figure 2.

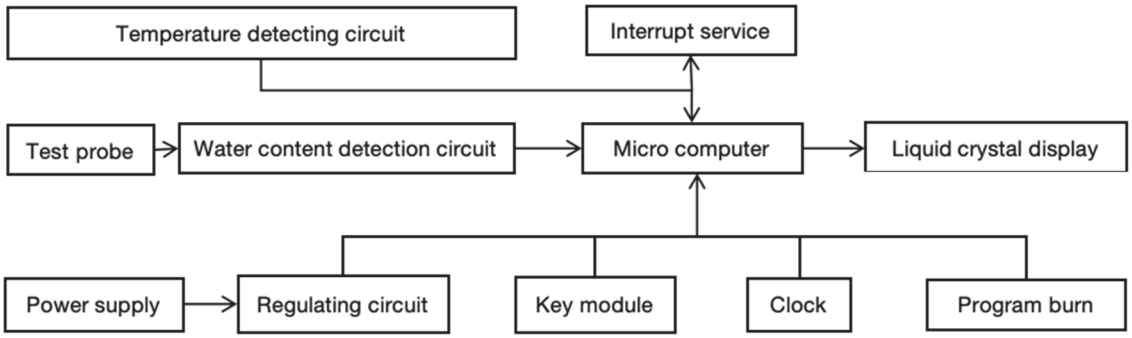

Figure 2. Block diagram of the system of standing tree trunk moisture content measurement.

The two searching units of the detection probe are equated into a parallel pole plate capacitor [12,13]. The parallel pole plate capacitor consists of a probe, a shell, and a fixed block. The distance between the two probes is 10 mm. The probe is made of a purple copper rod (Carnation Copper Industry Copper Material Manufacturers, Wenzhou, China) with a diameter of 2 mm and a length of 40 mm. There are 10 mm left in the shell for fixing, and the outer shell is made of an industrial high polymer heat shrink tube (Okes Wire and Cable Company, Dongguan, China), which is fixed on the probe after hot processing. The fixed block is machined from a mold and glued to the sensor using a hot melt adhesive. Wood between the pole plates of the capacitor is used as the dielectric. Different dielectric water rates lead to different dielectric constants, which in turn cause changes in capacitance between the parallel pole plates of the capacitor. The capacitance is calculated as

$$C = \frac{\varepsilon \cdot S}{4\pi k d}, \quad (6)$$

where

C is capacitance,
ε is relative permittivity of the medium between the plates,
S is area of the parallel plates (unit: m^2),
k is electrostatic constant ($k = 8.9880 \times 10^9$, unit: Nm^2/C^2),
d is vertical distance between the two plates (unit: m).

The detection probe constituting the capacitor serves as detection input C_i; the water content signal detection circuit uses a 555 multi-harmonic oscillation circuit (Limao Electronic Technology Company, Shenzhen, China), as shown in Figure 3. In the non-stationary mode of operation, the 555 multi-harmonic oscillation circuit outputs a continuous, frequency-specific electromagnetic wave [14]. The frequency of the output electromagnetic wave is determined by R_1, R_2, and C_i. The formula for calculating electromagnetic wave frequency is as follows:

$$T \approx 0.7(R_1 + 2R_2) * C_i, \tag{7}$$

where

T is electromagnetic wave frequency (unit: Hz),

R_1 and R_2 are resistance of the circuit (unit: Ω),

C_i is changing capacitance between the parallel poles (unit: F). Duty cycle is determined by R_1 and R_2.

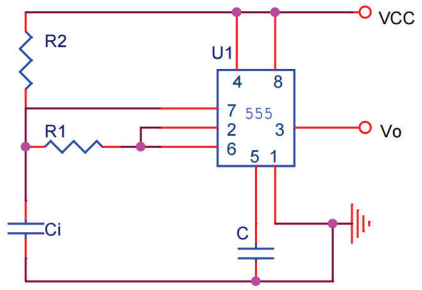

Figure 3. 555 multiple resonant swing circuit diagram.

In the testing process, direct measurement of capacitance values is more complicated [15–17]. A frequency of the output electromagnetic wave is used to indirectly characterize the change in capacitance due to the measurability of the electromagnetic wave frequency of the 555 multi-harmonic oscillation circuit. To facilitate calculation, the inverse of electromagnetic wave frequency, i.e., the electromagnetic wave period, is used to complete the entire test verification process. Changes in wood moisture content lead to variations in the dielectric constant and, consequently, alterations in the electromagnetic wave of the multi-harmonic oscillation circuit. The moisture content signal from the measured live wood trunk is collected by detection probe and converted into an electromagnetic wave periodic analog signal through a moisture content signal detection circuit. The analog signal is converted into a digital signal through the modular (A/D) converter of a minimum system of a single chip microcomputer. The STM32F103VET6 (Xintai Electronics, Shenzhen, China) is the microcomputer, and a series of functions, such as multi-resonant circuit output signal measurement, temperature signal processing, key selection measurement mode, calibration formula input and modification, zero calibration, and serial communication, are realized in the burning program using the 12-bit AD converter of STM32. A digital signal is put into the moisture content calculation formula to calculate real moisture content of the live wood trunk, and the final result is displayed on a Liquid Crystal Display (LCD) screen.

The uneven surface of the bark and different sizes of tree diameters directly influence the insertion process of two searching units' detection probes. In order to ensure that the probe can be easily inserted into the live standing wood, and to reduce the interference of the magnetic field on the detection circuit, the material used for the detection probe was selected with a certain toughness and stiffness of purple copper T2. To prevent short circuiting during insertion, an insulation layer cover was used. The temperature detection circuit sensor utilizes a DS18B20 chip, externally powered, with advantages including high system accuracy, strong resolution, and good anti-interference performance [18]. The key part uses three independent keys, RESET, Key0, and Key1, which occupy three IO ports, WK UP, KEY0, and KEY1 of the microcomputer, respectively, whereas RESET (WK UP)

controls the reset of the microcomputer, and the other two (KEY0, KEY1) are mode selection keys, which can enter a selection state by long press. Figure 4 shows key schematics of this design. For the modular design of the LCD display, a 2.4 inch TFT LCD display is integrated into the dedicated interface of the microcontroller minimum system board, with required registers configured and initialized.

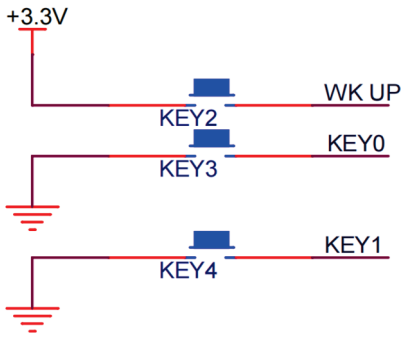

Figure 4. Key schematic diagram.

Firstly, the main program design involves initializing internal resources, such as an analog to digital converter (ADC) conversion module and clock configuration of the microcontroller and peripheral modules, such as a keypad module and LCD display, and the user selects the appropriate mode according to the detected tree species. Each tree species corresponds to a specific fitting equation, and the fitting equation is written into the subroutine corresponding to each keypad. In each processing cycle, the detected signal is substituted into the fitting equation to derive the water content value, which is then displayed on the LCD screen.

Next is the interrupt program design. The moisture content signal is collected by detection probe and processed through detection circuit, resulting in a periodic electromagnetic wave signal. Secondly, frequency is determined by measuring the number of falling edges of the electromagnetic wave within a unit time, followed by the calculation of the electromagnetic wave period. When the falling edge of electromagnetic wave signal is generated, the external interrupt service is triggered, leading to the entry into the external interrupt program. Upon the occurrence of a falling edge in the electromagnetic wave, the variable of "times" is incremented. When the time "t" reaches 1 s, the timer's interrupt service is triggered, initiating the entry into the timer interrupt program. The value of the variable "times" is then assigned to the variable of "last times", the variable of "times" is cleared to zero, and the total number of falling edges of the electromagnetic wave within a 1 s interval is recorded. Exiting the interrupt program, the system re-enters the main program to proceed with the next 1 s timer interrupt process. The value of "last times" can be used to calculate the frequency of the electromagnetic wave, and then calculate the period of the electromagnetic wave.

The experimental data obtained after A/D conversion will have certain errors, and data collected by the microcontroller need to be optimized to reduce errors brought by the experiment and outside world, and to improve detection accuracy. The data collected within 1 s are arranged from smallest to largest by comparing them one by one, and are stored in an array for easy recall, as follows:

$$a[0], a[1], a[2], a[3] \ldots\ldots a[n], \tag{8}$$

remove the first four numbers and last four numbers of experimental data and rearrange the entire array as follows:

$$a[0], a[1], a[2], a[3] \ldots\ldots a[n-8], \tag{9}$$

The error caused by the experimental interference can be eliminated by removing extreme values. In addition, noise inevitably interferes with the circuit during the testing process. In order reduce this unavoidable global error, the method of averaging data is used for filtering processing, and, finally, the data are stored in a defined variable.

2.2. Measuring Standing Tree Area

Sapwood and heartwood are two important zones in the wood. Sapwood has a higher water content, and because sapwood is outside the tree, it usually has a higher water content; this is because sapwood is the main channel for trees to transport water and nutrients, so it contains a lot of water. Heartwood is located in the center of the tree, near the inside of the tree. Heartwood usually contains less water than sapwood; this is because heartwood does not contain living cells, and the water and nutrients have been removed or converted into other substances. Due to the low moisture content in the heartwood and the dense wood structure, the moisture content of the heartwood is relatively stable and not susceptible to seasonal and climatic changes. Therefore, the sapwood of trees is chosen as the research object.

2.3. Instrument Verification

To verify reliability of the measuring instrument, the instrument was first calibrated in a laboratory, including using the distilled water medium test and the wood medium test, and the experimentally fitted relationship equation of the electromagnetic wave period and water content was imported into the microcontroller of a detector. Then the instrument was field tested in an experimental forestry field in Liangshui, Yichun. The equipment measurement procedure is as follows: 30 basswood trees and 15 fir trees were randomly selected, and the bark was peeled at a height of 1 m from the ground. A small electric hand drill is used to drill two parallel small holes with a diameter of 3 mm and a depth of 4 cm in the vertical direction (1 cm apart). A small hole of the same size is drilled with a growth cone next to the lower hole, and the sapwood sample (wood core) is taken out and weighed with an electronic balance (to record the total weight of the wood core) and bagged for use. The device is inserted into the tree, with a wait time of 30 s to 1 min, until the data no longer fluctuate; reading and recording the input square wave period is obtained by the water content detector.

Figure 5 shows the physical diagram of the standing tree moisture content meter, which is divided into the following four parts: searching units, detection circuit, lithium battery, and minimum system board. Figure 5a shows the front view of the instrument, and Figure 5b displays the field measurement of the standing tree trunk moisture content meter. The measuring instrument is located 1 m above the ground (the area selected by the red line is the measuring instrument).

(**a**) (**b**)

Figure 5. Standing tree trunk moisture meter. (**a**): front view of the instrument. (**b**) field measurement of tree moisture content.

According to the principle of the measuring instrument, the period of electromagnetic wave output of the device is affected by moisture content of the wood; a distilled water medium test can be used as a pretest to observe the sensitivity of the test device to water and the degree of influence of the insertion depth change on the period signal, as a blank control for subsequent tests. The distilled water experiment is shown in Figure 6, and test results are shown in Figure 6b. Figure 6b shows that the electromagnetic wave period becomes longer as insertion depth increases. Correlation coefficient R^2 of the fitted curve is as high as 0.99, indicating that the independent variable has a good linear relationship with the dependent variable when testing distilled water media, and the meter has good sensitivity to distilled water. The distilled water medium test can provide a good reference basis for the detection of water content of live tree trunks in the field.

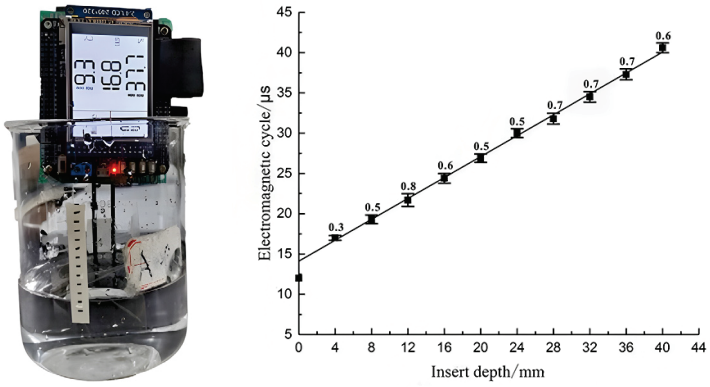

(**a**) (**b**)

Figure 6. Relation diagram of insertion depth and electromagnetic wave period in water medium test. (**a**) Distilled water medium test; (**b**) fitted curve of the average of six experiments.

2.4. Instrument Calibration

Laboratory wood media tests were conducted using water-soaked basswood and fir disc specimens instead of live timber. First, two holes were drilled in each of the specimens, which were then soaked in water for four weeks. Subsequently, the disc specimens were removed once saturated, wiped dry, and left to stand for 1 h. The searching units of the probe were then inserted into the drilled holes at depths of 30 mm and 40 mm, respectively, to monitor and record the electromagnetic wave cycle in real time. Readings were recorded every 30 s for a total of five times. After data recording, the specimens were placed into an oven for drying at 105 °C, where they were dried for half an hour each time for high moisture content (>30%), and for 1 to 3 h each time for low moisture content (≤30%) [19]. After each drying, the weight of the specimens was measured and left to dry for 1 h in the room (room temperature of 15 to 20 °C), and weighed and recorded (accuracy 0.1 g). According to the same test steps, the output electromagnetic wave period is detected, and the test data are recorded. These steps were repeated until the specimen reached a constant weight. The absolute dry mass was weighed, and the moisture content was calculated for each test.

In the same experimental site in Liangshui [20], basswood and fir standing trees were randomly selected; 30 basswood trees and 15 fir trees were sampled. Two holes were drilled in each test tree, moisture content was checked with a measuring instrument, and test data were recorded; at the same time, the wood core was removed with a growth cone, oven-dried, and the moisture content of the trunk of standing trees was calculated and compared to the data measured by the measuring instrument.

3. Results

3.1. Wood Media Test

Figure 7 shows the fitted relationship between the moisture content and electromagnetic wave period for basswood and fir, and fitted equations are shown in Table 1; R^2 of the fitted equation for the basswood disc at 40 mm insertion depth was as high as 0.99, and the model fit was good and reliable (Figure 7a). The fitted curve of the fir disc specimen showed obvious segmentation (Figure 7b), and the moisture content of the cut-off point was around 30% (near the wood fiber saturation point). The fitted equations of fir disc specimens were better fitted at an insertion depth of 30 mm, and R^2 of both fitted curves was greater than 0.95, while fir discs had low accuracy and larger errors at the insertion depth of 40 mm. Therefore, fitted equations under 40 mm and 30 mm insertion depths were selected for basswood and fir, respectively, and written into the microcontroller to facilitate field tests for verification.

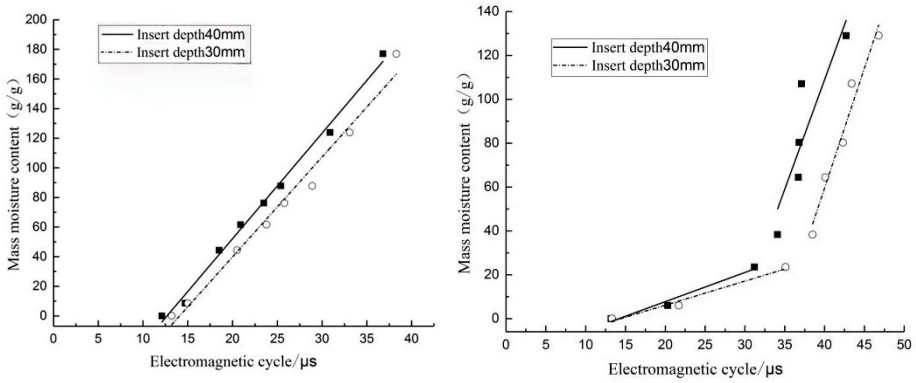

(**a**) (**b**)

Figure 7. Fitting diagram of electromagnetic wave period and water content of basswood and fir. (**a**) Basswood; (**b**) fir.

Table 1. Fitting relation between electromagnetic wave period and mass moisture content of basswood and fir.

Tree Species	Insert Depth	Fitting Equation		R^2	
Basswood	30 mm	$y = 6.75x - 95.10$		0.98	
	40 mm	$y = 7.13x - 90.39$		0.99	
		Moisture content is less than 30%	Moisture content is more than 30%	$R_1{}^2$	$R_2{}^2$
Fir	30 mm	$y = 1.10x - 15.85$	$y = 10.92x - 377.31$	0.98	0.96
	40 mm	$y = 1.33x - 18.87$	$y = 9.99x - 290.52$	0.98	0.79

Note: $R_1{}^2$ corresponds to the fitted curve with water content less than 30%, and $R_2{}^2$ corresponds to the fitted curve with water content less than 30%.

3.2. Field Test Validation

The actual water content of trees was compared to the results obtained by the measuring instrument, and comparison results are shown in Figure 8. Due to the complex measurement environment, measurement results of the meter were slightly lower than indoor measurement results. The R^2 values of fitted curves of basswood were all greater than 0.8, and measurement results were more satisfactory (Figure 8a), while R^2 of fitted curves of fir were all greater than 0.95 (Figure 8b), and the fitting effect was better than that of basswood, as shown in Table 2. The average error in water content measured by the two methods was calculated and shown to be 7.75% for basswood and 7.35% for fir, and a comparison of the data is shown in Figure 9. The fitted curves of the capacitance method were better than the drying method for both tree species in Figure 9, indicating that the fitted curves of the capacitance method had some credibility, produced less fluctuation

in the measured data, and had higher accuracy of detection with less errors. Therefore, the capacitance method holds practical value in predicting the moisture content of live standing tree trunks.

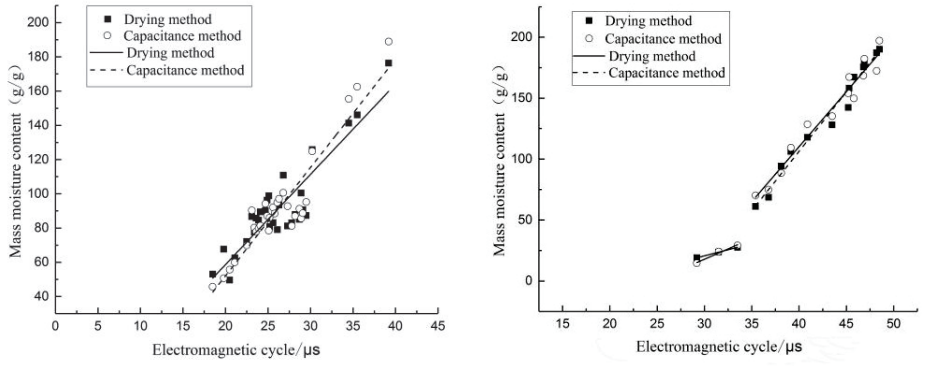

(**a**) (**b**)

Figure 8. Comparison diagram of water content fitting curve between capacitive method and drying method of basswood and fir. (**a**) Basswood; (**b**) fir.

Table 2. Fitting relation between electromagnetic wave period and water content of basswood and fir in different methods.

Tree Species	Insert Depth	Processing Method	Fitting Equation		R^2	
Bass wood	40 mm	Drying method	$y = 5.27x - 46.90$		0.81	
		Capacitance method	$y = 6.33x - 74.50$		0.87	
			Moisture content is less than 30%	Moisture content is more than 30%	$R_1{}^2$	$R_2{}^2$
Fir	30 mm	Drying method	$y = 3.40x - 84.34$	$y = 9.03x - 250.87$	0.98	0.96
		Capacitance method	$y = 2.00x - 39.29$	$y = 9.73x - 282.78$	0.99	0.98

Note: $R_1{}^2$ corresponds to the fitted curve with water content less than 30%, and $R_2{}^2$ corresponds to fitted curve with water content less than 30%.

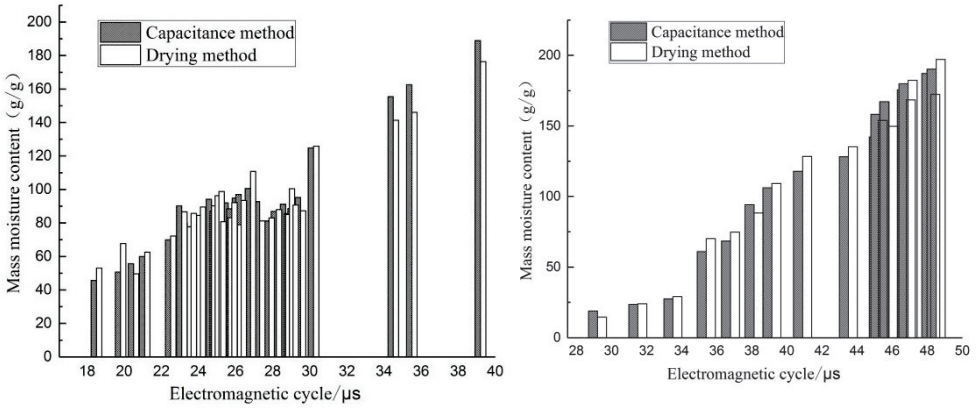

(**a**) (**b**)

Figure 9. Comparison of basswood and fir measurements with real data. (**a**) Basswood; (**b**) fir.

4. Discussion

In this study, the moisture content of two species was studied in the laboratory and field, and the function equations of the electromagnetic wave period and moisture content

were constructed for the two species of basswood and fir. This moisture content detector is small in volume, and the measurement is accurate and can display the electromagnetic wave reflection time and moisture content in real time. Compared to the relevant studies of SK Korkua (2020) [21] and P Chetpattananondh (2017) [22], we can write calibration equations of multiple tree species into the device in advance, so that different tree species can be easily measured in actual measurements.

5. Conclusions

Based on the capacitance method, we designed a live tree trunk water content meter, constructed an equation of the electromagnetic wave period as a function of water content through indoor tests, and wrote it into a microcontroller, and then used it to measure water content of live tree trunks in the field to verify the reliability of the meter. Conclusions show the following:

1. The equipment is optimized from both hardware and software aspects. Due to the good conductivity of purple copper, it is chosen as the probe material, which can better retain the integrity of an electrical signal; the microcontroller judges pulse the trailing edge to determine that the frequency is stable and reliable; and the 555 timing circuit has high sensitivity to capacitance changes. The software structure is optimized in terms of sampling, especially software filtering, which reduces the occurrence of accidental errors and improves accuracy of data.
2. Pretests on distilled water prior to laboratory testing of moisture content of live tree trunks showed that the electromagnetic wave period gradually increased with the increase in insertion depth, i.e., the increase in moisture, and the goodness of fit was 0.99, indicating that the meter has excellent sensitivity to water.
3. The field and indoor tests showed that applicability of the moisture content meter for standing tree trunks was verified by constructing mathematical models for different tree species. The instrument is capable of measuring moisture content of basswood and fir tree trunks in the range of 0 to 180%, with a wide range of measurements. The average error of measurement was 7.75% for basswood and 7.35% for fir, both within 8%. Overall, the design and measurement results of the instrument were satisfactory.

The moisture content measurement instrument designed in this study can achieve more accurate measurements of the moisture content of standing wood trunks with minimal error, applicable to both low and high moisture content live standing wood trunks. An accurate capacitance moisture content detector is designed, which is convenient to carry, small in size, and can be viewed in real time; furthermore, the preset mode can be imported into the device in advance, and different modes can be switched at any time.

We still need to conduct a lot of experiments to make the calibration equation more accurate. In the future, different tree species will be calibrated and input into the device. Secondly, we can also study the water content at different locations and heights of the same tree, which helps us to make more accurate measurements. It is also necessary to add storage capabilities to the device later on, so that the tree can be measured in the form of a record for a long time.

Author Contributions: Conceptualization, J.Y. and Z.Z.; methodology, J.Y.; software, L.Z.; validation, J.Y. and Y.D.; formal analysis, Z.Z.; investigation, X.G.; resources, H.X.; data curation, J.Y.; writing—original draft preparation, J.Y.; writing—review and editing, J.Y.; supervision, H.X.; project administration, H.X.; funding acquisition, H.X. All authors have read and agreed to the published version of the manuscript.

Funding: This research received no external funding.

Institutional Review Board Statement: Not applicable.

Informed Consent Statement: Not applicable.

Data Availability Statement: Data are contained within the article.

Conflicts of Interest: The authors declare no conflict of interest.

References

1. Nelson, S.O. Use of electrical properties of grain-moisture measurement. *J. Microw. Power* **1977**, *12*, 67–72. [CrossRef]
2. Hammer, E.A.; Tollefsen, J.; Olsvik, K. Capacitance transducers for non-intrusive measurement of water in crude oil. *Flow Meas. Instrum.* **1989**, *1*, 51–58. [CrossRef]
3. Schuller, R.B.; Gundersen, T.; Halleraker, M.; Engebretsen, B. Measurement of water concentration in oil/water dispersions with a circular single-electrode capacitance probe. *IEEE Trans. Instrum. Meas.* **2004**, *53*, 1378–1383. [CrossRef]
4. Eller, H.; Denoth, A. A capacitive soil moisture sensor. *J. Hydrol.* **1996**, *185*, 137–146. [CrossRef]
5. Liu, S.; An, J.; Luo, Y.; Ge, Y.; Wang, J.; Wang, S. Mathematical model and finite element solution of single plane capacitive sensor. *J. Harbin Eng. Univ.* **2011**, *32*, 79–84.
6. Kong, L. Research on Wood Moisture Content Detection System Based on Forked-Finger Capacitive Sensor. Master's Thesis, Harbin Engineering University, Harbin, China, 2016.
7. Liu, S.; Li, F.; Zhao, D.; Li, S.; Gu, Q.; Zhou, Z. Design of micro-capacitor detection system based on AD7746. *Appl. Sci. Technol.* **2011**, *38*, 1–5.
8. Guo, C. Mathematical Model of Capacitive Sensor and Its Algorithm for Detecting Moisture Content of Wood. Ph.D. Thesis, Harbin Engineering University, Harbin, China, 2014.
9. Matheny, A.M.; Garrity, S.R.; Bohrer, G. The Calibration and Use of Capacitance Sensors to Monitor Stem Water Content in Trees. *J. Vis. Exp. JoVE* **2017**, *130*, e57062.
10. Vu, T.H.T.; Tetsuya, I.; Satoru, T. A new approach based on a combination of capacitance and near-infrared spectroscopy for estimating the moisture content of timber. *Wood Sci. Technol.* **2019**, *53*, 579–599.
11. Lev, J.; Křepčík, V.; Šarauskis, E.; Kumhála, F. Electrical Capacitance Characteristics of Wood Chips at Low Frequency Ranges: A Cheap Tool for Quality Assessment. *Sensors* **2021**, *21*, 3494. [CrossRef]
12. Oskouei, F.J.; Masoudi, A.A.; Khorrami, M. The static and dynamic behavior of a simple parallel-plate capacitor with Casimir force. *Chaos Solitons Fractals Interdiscip. J. Nonlinear Sci. Nonequilibrium Complex Phenom.* **2021**, *150*, 111199. [CrossRef]
13. Grove, T.T.; Masters, M.F.; Miers, R.E. Determining dielectric constants using a parallel plate capacitor. *Am. J. Phys.* **2005**, *73*, 52–56. [CrossRef]
14. *AN170. NE555 and NE556 Applications*; Integrated Circuits; Philips Semiconductors: Eindhoven, The Netherlands, 1988.
15. Drevinskas, T.; Kaljurand, M.; Maruška, A. Capacitance-to-digital: A single chip detector for capillary electrophoresis. *Electrophoresis* **2014**, *35*, 2401–2407. [CrossRef] [PubMed]
16. Lee, K.; Shur, M.S.; Drummond, T.J.; Morkoc, H. Current—Voltage and capacitance—Voltage characteristics of modulation-doped field-effect transistors. *IEEE Trans. Electron. Devices* **1983**, *30*, 207–212.
17. Chen, T.S. Determination of the capacitance, inductance, and characteristic impedance of rectangular lines. *IRE Trans. Microw. Theory Tech.* **1960**, *8*, 510–519. [CrossRef]
18. Saha, R.; Biswas, S.; Sarmah, S.; Karmakar, S.; Das, P. A Working Prototype Using DS18B20 Temperature Sensor and Arduino for Health Monitoring. *SN Comput. Sci.* **2021**, *2*, 33.
19. Xu, Q.; Xu, H.; Di, Y.; Li, Q. Effect of probe insertion depth on the accuracy of inversion of water content of birch trunks by time-domain reflection method. *J. For. Eng.* **2019**, *4*, 120–126.
20. Wang, Y.; Xu, H.; Zhou, H.; Cao, Y.; Ji, L. Effect of ambient temperature on the change of internal moisture content of standing trees. *J. Nanjing For. Univ. Nat. Sci. Ed.* **2017**, *41*, 107–113.
21. Korkua, S.K.; Sakphrom, S. Low-cost capacitive sensor for detecting palm-wood moisture content in real-time. *Heliyon* **2020**, *6*, e04555. [CrossRef]
22. Chetpattananondh, P.; Thongpull, K.; Chetpattananondh, K. Interdigital capacitance sensing of moisture content in rubber wood. *Comput. Electron. Agric.* **2017**, *142*, 545–551. [CrossRef]

sensors

MDPI

Article

Localization for Dual Partial Discharge Sources in Transformer Oil Using Pressure-Balanced Fiber-Optic Ultrasonic Sensor Array

Feng Liu *, Yansheng Shi, Shuainan Zhang and Wei Wang

School of Electrical and Electronic Engineering, North China Electric Power University, Beijing 102206, China
* Correspondence: 1182101049@ncepu.edu.cn

Abstract: The power transformer is one of the most crucial pieces of high-voltage equipment in the power system, and its stable operation is crucial to the reliability of power transmission. Partial discharge (PD) is a key factor leading to the degradation and failure of the insulation performance of power transformers. Therefore, online monitoring of partial discharge can not only obtain real-time information on the operating status of the equipment but also effectively predict the remaining service life of the transformer. Meanwhile, accurate localization of partial discharge sources can assist maintenance personnel in developing more precise and efficient maintenance plans, ensuring the stable operation of the power system. Dual partial discharge sources in transformer oil represent a more complex fault type, and piezoelectric transducers installed outside the transformer oil tank often fail to accurately capture such discharge waveforms. Additionally, the sensitivity of the built-in F-P sensors can decrease when installed deep within the oil tank due to the influence of oil pressure on its sensing diaphragm, resulting in an inability to accurately detect dual partial discharge sources in transformer oil. To address the impact of oil pressure on sensor sensitivity and achieve the detection of dual partial discharge sources under high-voltage conditions in transformers, this paper proposes an optical fiber ultrasonic sensor with a pressure-balancing structure. This sensor can adapt to changes in oil pressure environments inside transformers, has strong electromagnetic interference resistance, and can be installed deep within the oil tank to detect dual partial discharge sources. In this study, a dual PD detection system based on this sensor array is developed, employing a cross-positioning algorithm to achieve detection and localization of dual partial discharge sources in transformer oil. When applied to a 35 kV single-phase transformer for dual partial discharge source detection in different regions, the sensor array exhibits good sensitivity under high oil pressure conditions, enabling the detection and localization of dual partial discharge sources in oil and winding interturn without obstruction. For fault regions with obstructions, such as within the oil channel of the transformer winding, the sensor exhibits the capability to detect the discharge waveform stemming from dual partial discharge sources. Overall, the sensor demonstrates good sensitivity and directional clarity, providing effective detection of dual PD sources generated inside transformers.

Keywords: partial discharge; pressure-balanced fiber-optic ultrasonic sensor; fault localization; dual partial discharge sources detection

1. Introduction

Transformers are common high-voltage power equipment, characterized by a large installation base and high economic value. Their safe and stable operation directly affects the reliability of the power grid. Among the various fault types, insulation failure in transformers is one of the most common, making online monitoring and fault diagnosis of transformer insulation status paramount [1]. Partial discharge (PD) occurs in the insulated portions of electrical equipment under prolonged high-voltage conditions, manifesting as localized discharges. These discharges often originate from various defects within the insulation media, such as minute cracks, hidden bubbles, or accumulations of metallic impurities. The discharge process not only generates gases and chemical substances but

also significantly elevates local temperatures, leading to adverse effects like corrosion on insulation materials. These consequences accelerate the degradation process at the insulation defects, thereby shortening the service life of the equipment [2]. Therefore, the monitoring and prevention of partial discharges are crucial steps in ensuring the safe and stable operation of power equipment.

Partial discharge testing is an effective method to evaluate the PD level in transformers, accurately reflecting the health status and insulation aging degree of high-voltage electrical equipment [3]. In large transformers with high voltage ratings, due to their compact internal structure, high and unevenly distributed electric field strengths, the discharge types are more complex, often leading to simultaneous discharges from multiple PD sources [4]. These discharges, with their superimposed waveforms, become more intricate, making it challenging for traditional external sensors to detect and distinguish such discharge types. Even if the simultaneous discharge waveforms of multiple PD sources are captured, they are difficult to differentiate from environmental interference waveforms. These issues increase the difficulty for maintenance personnel, and missed detections or repairs can result in poor maintenance outcomes for power equipment, while repeated maintenance inspections further increase transformer maintenance costs. Overall, research on multi-point detection and localization techniques for internal PD in transformers is crucial for enhancing the accuracy and efficiency of fault detection and allowing maintenance personnel to optimize maintenance plans [5]. Therefore, an in-depth study of the discharge characteristics of dual PD sources under complex internal conditions in large transformers, the accurate identification of discharge types, and the precise localization of PD areas are significant for timely detecting potential faults, predicting the remaining life of equipment, and developing maintenance plans [6]. This will contribute to ensuring the safe and stable operation of power systems.

During the occurrence of partial discharge, it is often accompanied by phenomena such as pulse current, radiation light, and sound. These characteristic signals contain information about the energy intensity and positional direction of the PD sources [7]. Through digital signal processing techniques and the application of corresponding algorithms, quantitative analysis of PD phenomena can be achieved. This holds significant academic value and practical implications for the in-depth study of PD mechanisms and the guidance of fault inspection and repair work. Currently, there are two major categories of PD localization techniques: electrical signal localization and acoustic signal localization. Depending on the different characteristic quantities, they can be further divided into the pulse current method, the ultra-high frequency method, and the ultrasonic localization method. As an effective and accurate localization method, acoustic methods have been widely used in the industry, and many scholars have conducted extensive research on this method. The general acoustic localization method employs a piezoelectric transducer array placed on the outer wall of the transformer oil tank. It utilizes the time difference of ultrasonic signals reaching different sensors to solve equations and determine the location of the partial discharge source. Depending on the adopted reference time scale, it can be further divided into "acoustic-acoustic" and "electric-acoustic" methods [8,9]. This method is cost-effective and relatively easy to install, but ultrasonic waves undergo attenuation and distortion after reflection from the transformer oil tank. Additionally, the external environment of the oil tank is prone to signal interference, resulting in a low signal-to-noise ratio [10]. Therefore, the distributed installation of sensors is required to achieve high localization accuracy. The received ultrasonic signals are scattered, and the signals received by different sensor elements vary significantly, which can easily lead to the non-convergence of the algorithm's solution. In particular, for dual PD sources occurring inside the transformer, traditional piezoelectric transducers cannot be expected to clearly distinguish and accurately locate them. The Fabry–Perot (F-P) sensor utilizes the ultrasonic signals generated by PD to deform the silica diaphragm located at the probe [11]. By analyzing the optical changes within the F-P cavity, fault detection of PD can be achieved. This fiber-optic ultrasonic sensor, with its optical signal as the signal transmission medium, boasts excellent insulation

properties and can be built into the transformer's interior [12,13]. Currently, most of these built-in detection devices are installed at the oil change valve at the bottom of the transformer oil tank. However, under the influence of oil pressure, the sensitivity of the sensing diaphragm decreases, and the sensor cannot fully respond to dual PD signals. This limits its detection range and fails to provide accurate partial discharge detection for the transformer's overall, especially the winding section located at the bottom.

To address the aforementioned issues, this paper presents a pressure-balanced optical fiber ultrasonic sensor. By introducing perforation, transformer oil can enter the F-P interference cavity, thus minimizing the impact of oil pressure on the diaphragm's sensitivity. However, the ingress of transformer oil can reduce the reflectivity of light. To counter this, we have implemented an alternating coating of SiO_2 and Ta_2O_5 on the silica diaphragm and fiber end face, enhancing reflectivity and mitigating the interference caused by transformer oil in the F-P interference cavity. Utilizing light as the signal transmission medium, this sensor boasts a high insulation level, enabling the detection of dual PD ultrasonic signals from the bottom of transformer oil tanks. The collected PD ultrasonic signals from the sensor array are processed using a direction-finding cross-localization algorithm, accurately identifying and precisely locating the dual PD sources within the tank. Experimental evaluations conducted on a 35 kV single-phase transformer at various locations have demonstrated the effectiveness and precision of this method in detecting and locating dual PD sources in transformer winding interturn. However, for PD sources within the oil channels, the method offers qualitative detection but fails to achieve precise localization.

In order to detect the discharge fault of dual partial discharge sources in transformer oil, this paper designs an optical fiber ultrasonic sensor with a pressure balance structure, which allows transformer oil to enter the sensor cavity through drilling. In order to minimize the influence of transformer oil on the sensitivity of the sensor, the reflectivity of the silica diaphragm and the fiber end face is improved by coating. The well-fabricated sensors are assembled into a sensor array, and the method of cross-direction measurement is used to locate the fault position of the dual partial discharge sources and detect the discharge phenomenon of dual partial discharge sources at different positions of the transformer.

In summary, the combination of the pressure-balanced ultrasonic sensor array and the direction-finding cross-localization algorithm exhibits excellent performance in detecting and locating dual PD sources in transformer oil tanks, particularly in scenarios without obstacles. This approach provides a novel solution and research direction for localizing complex PD faults in high-voltage power transformers. The organizational structure of this writing is illustrated in Figure 1. The first-level purple area represents the overall purpose of this paper, which is to detect and locate the discharge phenomena of dual partial discharge sources in transformer oil. The second-level gray area covers the sensor fabrication section, corresponding to Section 2 of the paper. In this section, we have developed sensors that can adapt to the oil pressure of transformers. The improvements focus on two main points: the first is drilling holes in the sensor cavity to allow transformer oil to enter, and the second is coating the sensor to enhance its reflectivity. Finally, we conducted vertical sensitivity tests using the fabricated sensors. The third-level blue section represents the localization method, which corresponds to the content of Section 3 in the article. The first step is to determine the direction of the partial discharge sources, and the second step is to use the results of the directional measurements to perform cross-localization. The fourth-level green area represents the experiments we conducted for detecting and localizing dual partial discharge sources at different locations within the transformer, specifically in three representative positions: inside the transformer oil, within the transformer oil channel, and at the interturn of the transformer winding. These locations have varying degrees of obstruction to the ultrasonic waves.

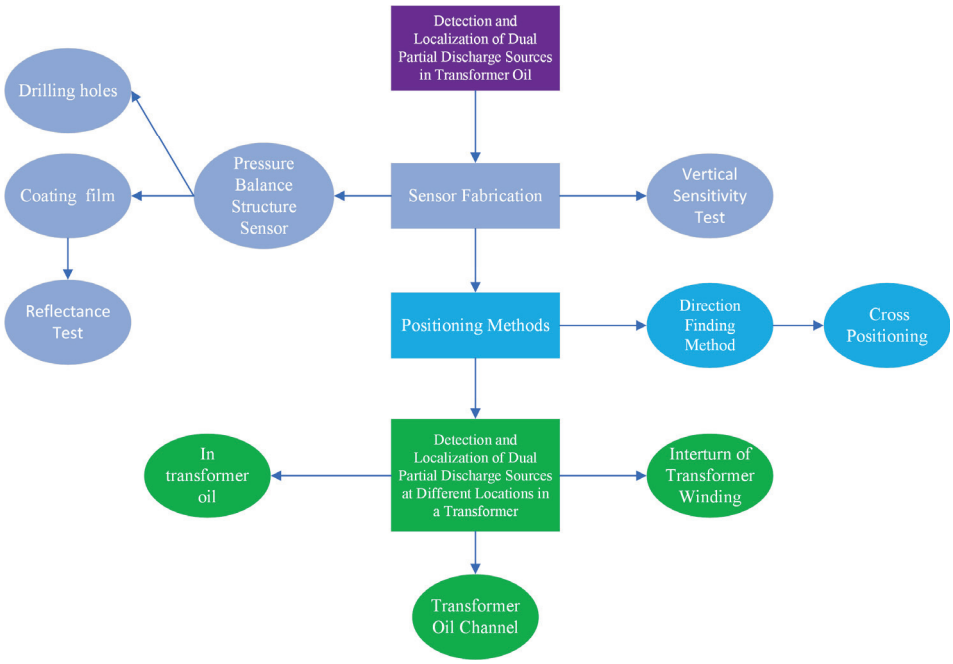

Figure 1. Writing organization structure diagram.

2. Pressure-Balanced Fiber-Optic Ultrasonic Sensor and Dual PD Localization System

The structure of the pressure-balanced fiber-optic ultrasonic sensor is illustrated in Figure 2. The dual PD source localization system comprises a sensor probe, laser source, coupler, and photodetector, and they are interconnected via a single-mode fiber (SMF). The sensor probe features a small hole at the F-P cavity, allowing transformer oil to enter the cavity, thereby minimizing the hindrance of oil pressure on diaphragm vibrations. However, the influx of transformer oil can impact the optical performance of the F-P cavity. To address this, the inner surface of the silica diaphragm is coated with a total reflection film, while the fiber end face is coated with an optical dielectric film composite of Ta_2O_5 and SiO_2. Ta_2O_5 is an insulating material with stable molecular properties, exhibiting exceptional thermal and chemical stability, high voltage resistance, a high refractive index, and a high transmission coefficient. Ta_2O_5 coatings are commonly used for high-refractive-index thin-film materials [14]. SiO_2, another insulating material with a high refractive index, boasts a melting point of up to 1723 °C, chemical inertness, and high voltage resistance [15]. By employing an alternating coating process with these two materials, the sensor achieves both high reflectivity and excellent adhesion, leading to a long service life. In contrast to the metal material coating solution, this sensor design does not create a floating potential, ensuring no impact on the internal electric field distribution of the transformer.

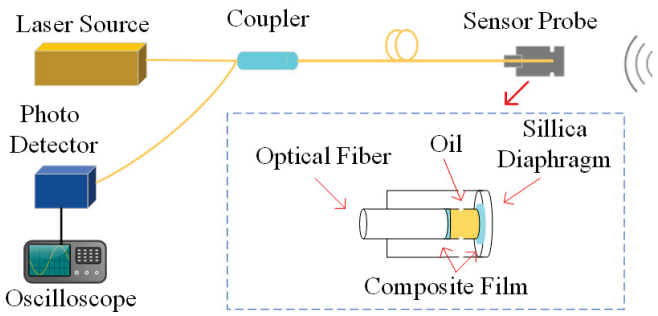

Figure 2. Structure of the dual PD detection system.

The laser source emits monochromatic light that propagates along SMF and enters the F-P cavity. According to the Huygens–Fresnel principle, the reflectivity of the incident light at the interface between the fiber end face and air is approximately 3.6%, while the remaining 96.4% of the incident light passes through the interface and enters the F-P cavity, striking the silica diaphragm. Most of this light transmits through the silica diaphragm, and the remaining 3.3% reflects back into the fiber at the inner surface of the silica diaphragm. The ultrasonic signal generated by partial discharge reaching the sensor diaphragm causes vibrational deformation of the diaphragm, resulting in a slight change in the length of the F-P cavity [16]. This change triggers an interference pattern between the two beams of light, leading to a change in light intensity. By detecting this change in light intensity through the circulator port and converting it into an electrical signal detectable by an oscilloscope using a photodetector, the interference-modulated light intensity can be expressed as follows:

$$\mathrm{I_r}(l) = \frac{r_1 + r_2 - 2\sqrt{r_1 r_2}\cos\delta}{1 + r_1 r_2 - 2\sqrt{r_1 r_2}\cos\delta}\mathrm{I_0}(l) \tag{1}$$

$$\delta = \frac{4\pi\Delta l}{\lambda} \tag{2}$$

In the expression, l represents the length from the fiber end face to the inner surface of the silica diaphragm, which is also known as the length of the F-P cavity. $\mathrm{I_0}(l)$ denotes the incident light intensity (the unit is $\mathrm{mW/m^2}$), which remains constant when there is no external signal, as the F-P cavity length remains unchanged. λ is the wavelength of the laser light source (the unit is μm). r_1 represents the reflectance at the fiber end interface, while r_2 represents the reflectance at the inner surface of the silica diaphragm. δ is the phase difference between adjacent beams (the unit is rad); Δl is the optical path difference between the two interfering light beams (the unit is μm). With fixed reflection coefficients r_1 and r_2, the intensity of the interference light after the reflection of the two beams is solely dependent on the F-P cavity length (l) of the sensor.

When external vibration signals act on the sensor, they cause the diaphragm to undergo bending deformation, altering the cavity length of the sensor and subsequently changing the intensity of the interference light between the two beams. By demodulating the received optical intensity signal, the measurement of the partial discharge ultrasonic signal can be achieved.

The cladding diameter of the single-mode fiber used in the pressure-balanced fiber-optic ultrasonic sensor is 125 μm. The coating area must cover the entire region where the incident light beam strikes the inner surface of the silica diaphragm. To minimize the impact on the vibration of the silica diaphragm, the coating radius should be as small as possible, while also considering potential deviations during the welding of the silica diaphragm and the sensor cavity during the manufacturing process. Therefore, we deposited a circular film with a diameter of 500 μm and a thickness of 260 nm at the center of the inner surface of the silica diaphragm, which has a diameter of 3.5 mm and a thickness of 30 μm. Considering economic costs, we did not opt for an expensive, fully reflective film. Instead, combining engineering practicality, this article adopts a cost-effective coating with a relatively high reflectance. After coating the inner surface of the silica diaphragm, we tested its refractive index, and the results are shown in Figure 3. The laser source used in the partial discharge detection system designed in this article has a center wavelength of approximately 1550 nm. According to the reflectance curve, it can be seen that the reflectance of the inner surface of the silica diaphragm after coating is approximately 99.7%.

Given the technical challenges of coating the fiber end face and the fact that the F-P interference cavity relies on transmitted light, a comprehensive consideration of the relationship between reflectance and transmittance is essential. In this paper, the reflectance of the fiber end face after coating is set at 20%, with a transmittance of 80%. The processed sensor was placed in transformer oil for 48 h to allow the oil to completely penetrate into the F-P cavity. Utilizing the MS9740A spectrometer (The MS9740A spectrometer is manufactured by Anritsu in Atsugi, Japan, and we purchased it from Shanghai, China), its

optical power was measured at 534.6 μW, with a reflectance of 19.8%. Compared to the 3.6% reflectance without coating, this method significantly enhances the overall performance of the sensor after transformer oil enters the F-P interference cavity. Considering the practical application of placing the sensor at different depths inside the transformer, this paper designed an experiment to investigate the vertical sensitivity of the sensor in transformer oil. The vertical sensitivity characteristic refers to the variation in the maximum voltage amplitude of the sensor's output waveform at different depths in the transformer oil.

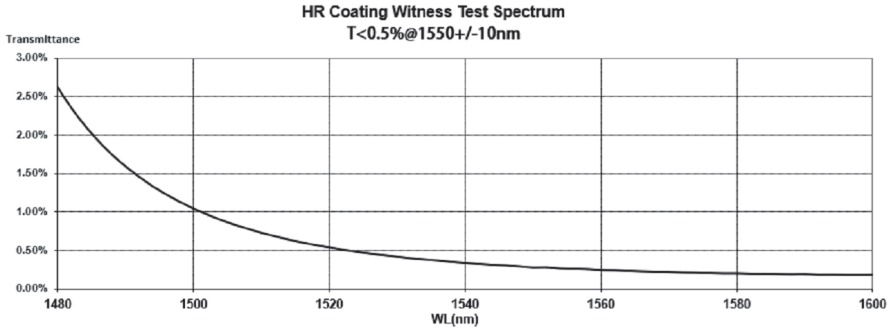

Figure 3. Reflectivity curve of the inner surface of the quartz film after coating.

The sensor was fixed on an insulating wooden strip with a needle-plate electrode, maintaining a spacing of 60 cm. The probe of the sensor was positioned directly facing the needle-plate electrode. Both the sensor and the needle-plate electrode were submerged into the transformer oil at depths ranging from 10 cm to 70 cm, as depicted in Figure 4. During each experiment, the maximum value of the waveform voltage was selected, and the experimental results are presented in Figure 5. It is worth noting that the sensors used in this study were not precisely manufactured by a factory with uniform specifications. Instead, after the components were processed, they were manually cut and welded in our laboratory, resulting in significant variations in sensor sensitivity. Furthermore, considering the inherent randomness of simulating partial discharge in insulating oil, the discharge magnitude was not a fixed value, leading to certain deviations in ultrasonic energy. Therefore, Figure 5 can only qualitatively demonstrate the influence of oil pressure on the sensitivity of a single sensor.

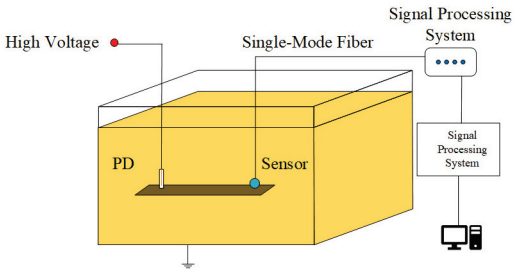

Figure 4. Layout diagram for vertical sensitivity test of sensor.

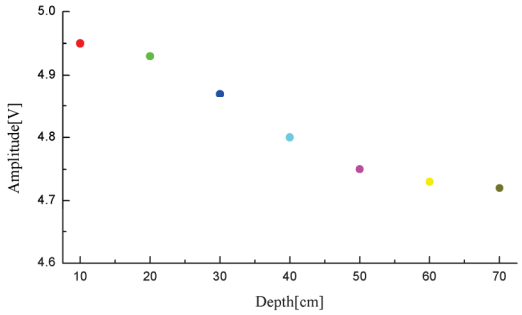

Figure 5. Vertical sensitivity decay curve of the sensor.

Overall, as the depth increases and the oil pressure rises, the viscous coefficient acting on the sensor diaphragm increases, subsequently elevating the vibrational resistance, resulting in a decrease in sensor sensitivity. Based on this pressure-balanced structure sensor, this study has further designed a sensor array for the localization of dual PD sources. According to phased array theory, to mitigate the radiation energy occupied by grating lobes and enhance the array antenna gain, the element spacing should be less than or equal to half of the wavelength of the target being measured. Additionally, to guarantee a sufficiently large effective area for signal reception and a high resolution, half of the wavelength is chosen as the element spacing. In the experiments conducted in this paper, the propagation velocity of ultrasonic waves in oil is 1420 m/s, with a central frequency of 30 kHz, resulting in a wavelength of 47.33 mm. Moreover, to ensure a sufficiently large receiving surface for the array and similar signal reception among elements, thereby avoiding positioning errors caused by inconsistent element responses, the array layout was optimized through multiple experiments. Ultimately, a regular tetrahedron structure with an element spacing of 20 mm was adopted. Under these parameters, the pressure-balanced fiber-optic ultrasonic sensor array exhibits excellent signal acquisition performance. The spatial structure diagram of the array is presented in Figure 6, where θ and ϕ represent the azimuth and elevation angles of the PD source, respectively. The method of establishing the three-dimensional Cartesian coordinate system for the sensor array is also applicable to subsequent discussions and calculations involving PD source direction measurements in this paper. The technical changes of the sensors in this section are summarized in Table 1.

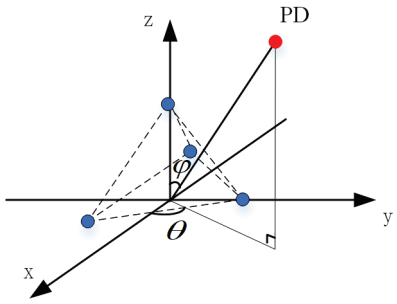

Figure 6. Spatial structure diagram of sensor array.

Table 1. The summary table of technical changes for this section.

Unresolved Issues	Solution	Significance
The transformer oil pressure impedes the sensor diaphragm's response, preventing the detection of ultrasonic signals from dual partial discharge sources.	Sensor chamber drilling	Allowing transformer oil to enter and achieve pressure balance
	Silica diaphragm coating	To improve the reflectivity of the reflective end face and reduce the impact of transformer oil entering.
	Fiber optic end face coating	

3. Method for Locating Dual PD Sources

The Multiple Signal Classification (MUSIC) algorithm is a high-resolution spectral estimation technique utilized in sensor array signal processing. It relies on the orthogonality principle between signal subspaces and noise subspaces and determines the direction of signals by searching for the peaks in the spatial spectrum [17]. As a result, MUSIC is a direction-finding method that is based on the energy of sound sources.

3.1. The Principle of Direction-Finding with the MUSIC Algorithm

Based on the principle of spatial spectrum estimation, assuming $X(t)$ represents the received signal at the array, its covariance matrix is computed as follows:

$$R = E\left\{X(t)X(t)^{\mathrm{H}}\right\} = A(\varphi,\theta)R_S A^{\mathrm{H}}(\varphi,\theta) + R_N \tag{3}$$

In the expression, R represents the covariance matrix of the array signal, while $A(\varphi, \theta)$ is the steering vector of the signal, encoding the direction of arrival (DOA) of the PD source [18]. Specifically, θ denotes the azimuth angle, and φ represents the elevation angle of the PD source, as illustrated in Figure 3. R_S and R_N are the signal covariance matrix and noise covariance matrix, respectively. By performing an eigendecomposition on the array signal covariance matrix R, a function involving the noise subspace U_N can be obtained. According to the properties of subspaces, the signal steering vector is orthogonal to the noise subspace. However, in practical scenarios, noise is always present, and thus the orthogonality is not perfect. The actual DOA estimation is achieved by evaluating all possible DOA values and identifying the minimum value. This minimum-finding process can be transformed into a maximum-seeking problem through a reciprocal relationship.

$$P_{music} = \frac{1}{A^{\mathrm{H}}(\varphi,\theta)U_N U_N^{\mathrm{H}} A(\varphi,\theta)} \tag{4}$$

P_{music} is a spatial spectrum function, serving as a calculation formula for energy. The energy value of ultrasonic signals at the location of partial discharge is significantly higher than that at non-partial discharge locations where only sound wave reflections are present. For a single PD source, after searching through the entire spatial spectrum, the MUSIC algorithm identifies the peak with the highest energy. The corresponding values of φ and θ at this peak represent the directional information of the PD source. This is the foundation of the MUSIC algorithm for DOA finding. Even in the case of continuous discharge from a single point, the location of the energy extremum in the spatial spectrum remains unchanged, with only one peak representing the direction of the partial discharge source. Therefore, it can be distinguished from the case of simultaneous discharge from dual PD sources. By constructing a spatial spectrum function, the MUSIC algorithm enables DOA estimation of PD sources, offering better resolution compared to traditional beamforming methods. This allows for direction finding of dual PD sources signals simultaneously.

3.2. Localization Algorithm

The fundamental principle of the direction-finding cross-localization algorithm relies on two direction-finding stations, each comprising sensor arrays, to determine the DOA of a common target. Subsequently, through spatial geometric calculations, the coordinate position of the target is accurately determined, as depicted in Figure 7. This approach enables precise localization based on the intersection of the DOA measurements from the two stations.

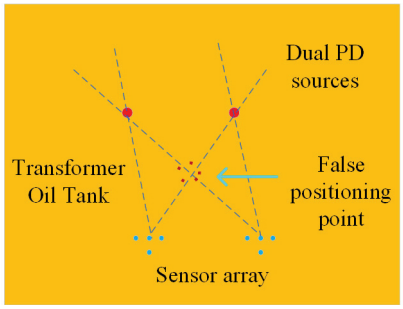

Figure 7. Schematic diagram of cross location for dual PD sources direction finding.

As depicted in the localization schematic diagram in Figure 6, when the sensor arrays and the partial discharge location are situated on the same horizontal plane, theoretically, the localization method may encounter false positioning points. However, taking into account the actual direction-finding errors, the occurrence of false positioning points is rare. Furthermore, considering the redundancy inherent in equipment maintenance plans,

maintenance personnel tend to prioritize avoiding missed fault detections during practical inspections. Therefore, in the subsequent discussions of this paper, the scenario of false positioning points will be disregarded.

4. Experimental Testing and Result Analysis

The dual PD sources localization testing platform for transformer oil comprises a transformer oil tank, a sensor array, a high-voltage pulse generator, and two needle-plate electrode discharge tubes simulating partial discharges. The transformer oil tank has dimensions of 200 cm in length, 100 cm in width, and 150 cm in height. It is filled with 25# high-voltage electrical insulation oil, and the outer shell of the tank is grounded. To simulate the fault scenario of simultaneous discharges from dual PD sources, we connect the two discharge tubes in series to the high-voltage pulse generator. By adjusting the spacing between the two needle-plate electrodes and through multiple voltage pressurization attempts, under the excitation of a 20 kV high-voltage pulse, the two series-connected needle-plate electrodes can simultaneously undergo breakdown and discharge, and the discharge waveform can be detected through an oscilloscope.

4.1. Detection Experiment of Dual PD Sources in Transformer Oil

As depicted in Figure 6, a spatial Cartesian coordinate system is established, connecting the PD sources to the origin. Through spatial geometry knowledge, the DOA estimation of the acoustic sources can be obtained, specifically the azimuth angle and the elevation angle. Furthermore, to evaluate the performance of the dual PD sources localization system, it is imperative to define the distance error between the actual PD source position and the theoretically estimated position. Therefore, the spatial distance between the actual PD source's position and the estimated position is defined as the distance error. This definition holds true for the subsequent error analysis presented in the following sections.

With the right bottom corner of the transformer oil tank serving as the origin, a comprehensive spatial Cartesian coordinate system is established. Two sensor arrays are deployed inside the tank at positions (45 cm, 10 cm, and 50 cm) and (55 cm, 10 cm, and 50 cm), respectively. To test the overall localization performance of the system for PD sources at different locations, the oil tank is divided into three zones, and localization experiments are conducted sequentially in each zone. Figure 8 provides a top-view of the layout of the dual PD sources positions, while Figure 8 illustrates the experimental setup.

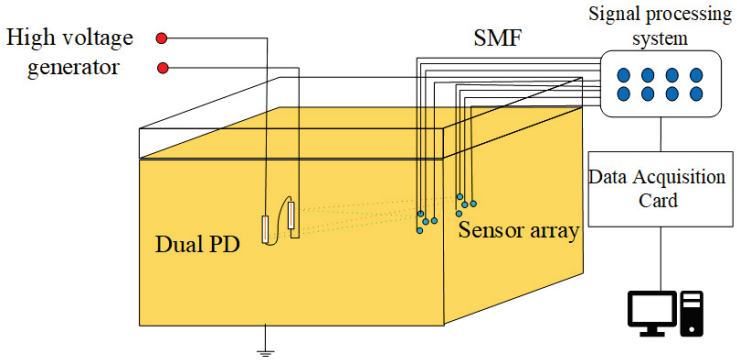

Figure 8. Layout diagram for the localization experiment of dual PD sources in transformer oil.

In the first experiment, two PD sources were placed at 47 cm, 48 cm, and 47 cm and 50 cm, 27 cm, and 53 cm, corresponding to the circular positions in Figure 9. Upon the occurrence of partial discharges, the waveforms detected by the sensors are presented in Figure 10. As observed from the waveform plots, the pressure-balanced fiber-optic ultrasonic sensors were able to accurately detect the discharge waveforms from both PD sources. Based on the signals detected by the sensor array and processed through a direction-finding and cross-localization algorithm, the estimated positions were determined

as 42.7 cm, 58.8 cm, and 41.2 cm and 48.2 cm, 21.1 cm, and 48.6 cm, with distance errors of 12.9 cm and 7.6 cm, respectively.

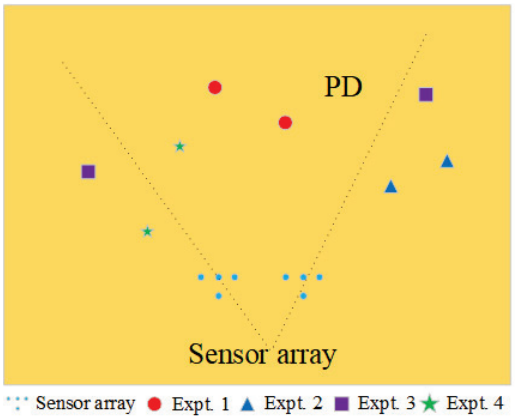

Figure 9. Aerial view of the layout of dual PD sources.

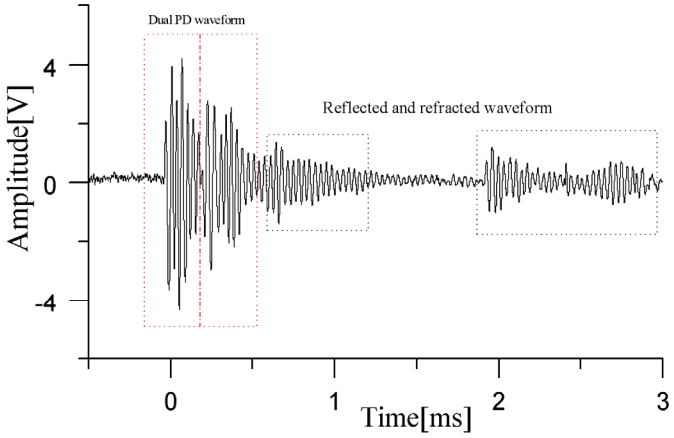

Figure 10. Ultrasonic waveform of dual PD sources in transformer oil detected by the sensor.

Subsequently, following the methodology of the first experiment, the dual PD sources were placed at different locations. In the second experiment, the two PD sources were located on the same side of the sensor array, corresponding to the triangular positions in Figure 9; in the third experiment, the PD sources were positioned on opposite sides of the two arrays, at the square positions in Figure 9; and in the fourth group of experiments, the partial discharge source is located at the position of the star in Figure 9, respectively, to verify the positioning accuracy when the deviation between the dual PD sources is significant. The experimental results are presented in Table 2, which indicates that the positioning accuracy of the sensor array with a pressure-balanced structure generally meets engineering requirements, with the maximum distance errors being 17.7 cm and 13.1 cm in the second experiment with the triangular layout. This is attributed to the fact that in this region, there are more overlapping areas between the waveforms of the two PD sources, resulting in less distinct peak amplitudes of the direct waves, thereby causing a larger error in solving the energy extremum using the localization algorithm. In contrast, the circular layout in the first experiment exhibited the smallest positioning error, with distance errors of 12.9 cm and 7.6 cm. This is because in this region, the sensor array has the best directivity, receiving signals with higher energy and better sensitivity. Considering that only four sensors were used to form the array in this study, using a larger array with more sensors to cover a broader reception area would result in the reception of richer partial discharge signals, further enhancing the positioning accuracy for dual PD sources.

Table 2. Results of localization for dual PD sources in transformer oil.

Number	PD Source Coordinates/cm	Localization Results/cm	Distance Error/cm
1	(47, 48, 47) (50, 27, 53)	(42.7, 58.8, 41.2) (48.2, 21.1, 48.6)	12.9 7.6
2	(70, 40, 49) (50, 57, 53)	(85.1, 47.1, 55.1) (41.9, 66.2, 48.3)	17.7 13.1
3	(30, 41, 50) (75, 47, 56)	(27.3, 47.2, 45.1) (68.7, 56.3, 67.2)	8.4 15.9
4	(40, 26, 40) (44, 38, 51)	(37, 34, 52) (51, 45, 47)	14.7 10.7

In practical scenarios, if the dual PD sources are located inside the transformer winding and the sensor array is arranged outside the windings within the oil tank, the ultrasonic signals will encounter obstructions from the insulating pressboard. These adverse factors can increase the difficulty of detecting partial discharge signals. To simulate this situation, a 60 cm × 100 cm, 2 mm thick insulating pressboard was inserted between the sensor array and the PD sources. To more realistically mimic the internal environment of a transformer, the insulating pressboard was fully soaked with transformer oil beforehand. Through repeated experiments, it was found that the sensors had difficulty responding in the presence of such obstacles. In rare cases, partial discharge waveforms could be detected, as shown in Figure 11, but the waveforms that penetrated the pressboard were mixed with diffracted waves bypassing the insulating pressboard, resulting in very low voltage amplitudes and making it impossible to distinguish between direct waves and diffracted waves.

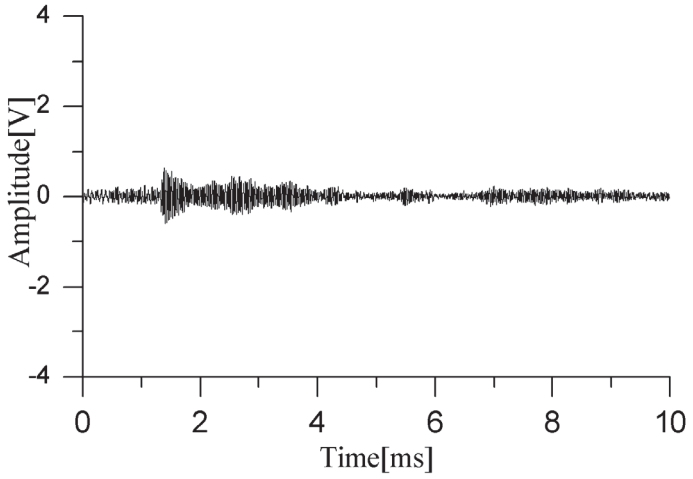

Figure 11. Ultrasonic waveform of dual PD sources after adding insulating pressboard.

Next, further experimental studies will be conducted to investigate the impact of transformer winding on the detection of dual partial discharge sources.

4.2. Detection Experiment of Dual PD Sources in the Transformer Oil Channel

To verify the accuracy of the partial discharge localization system, we further conducted experiments using a 35 kV single-phase transformer winding model. This model consists of inner and outer windings with oil ducts in-between and 2 mm thick insulating pressboards. Detailed parameters are presented in Table 3. A realistic image of the windings is shown in Figure 12. The experimental setup for the localization of dual partial discharge sources in the transformer oil channel is depicted in Figure 13.

Table 3. 35 kV single-phase transformer winding model dimensions.

Terms	Size (cm)
Outer diameter of the outer winding	50
Inner diameter of the outer winding	38
Outer diameter of the inner winding	26
Inner diameter of the inner winding	20
Winding height	60

Figure 12. Physical diagram of transformer winding model.

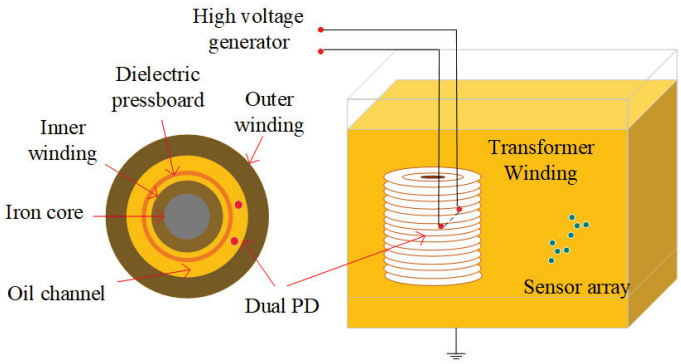

Figure 13. Layout diagram for the experiment of dual PD sources in transformer oil channel.

When dual partial discharge occurs in the transformer oil channel, the ultrasonic signal needs to pass through the gap between the outer windings to reach the sensor array inside the oil tank. The waveform of the dual partial discharge detected by the sensor is shown in Figure 14. It can be seen that the ultrasonic wave can pass through the gap between the winding to reach the sensor array, but the signal amplitude is attenuated, and due to the blocking of the winding, the waveform is distorted and does not show the normal oscillating attenuation trend. Such a waveform cannot be used for actual engineering localization.

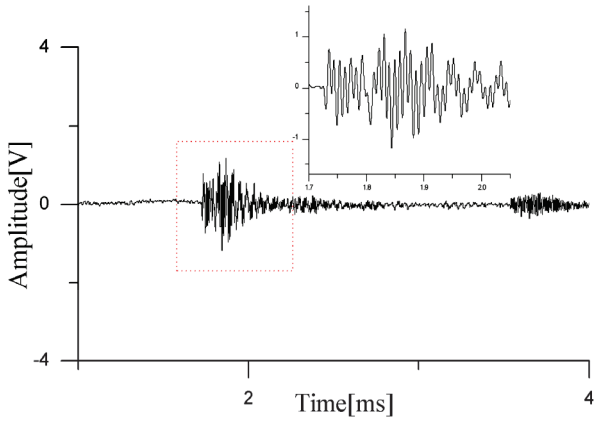

Figure 14. Ultrasonic waveform of dual PD sources in transformer oil channel.

4.3. Detection Experiment for Dual PD Sources in Transformer Winding Interturn

The interturn of transformer windings refers to the uniform gap between stacked winding cakes of different layers, which are separated by insulating paper and insulating cardboard. Due to poor manufacturing processes and the introduction of impurities during later operation of the transformer, it can lead to local electric field concentration, causing partial discharge and resulting in interturn short-circuit of the winding coil [19]. This is a common fault type in transformer windings. When a relatively minor interturn short-circuit occurs in the winding, the transformer can still operate. However, if it continues to operate with the fault for a long time, it may lead to more severe consequences or even damage the transformer [20]. Multiple partial discharges can accelerate the speed of insulation degradation and increase the risk of an interturn short circuit. The experimental layout for testing the dual partial discharge sources in transformer winding interturn is shown in Figure 15.

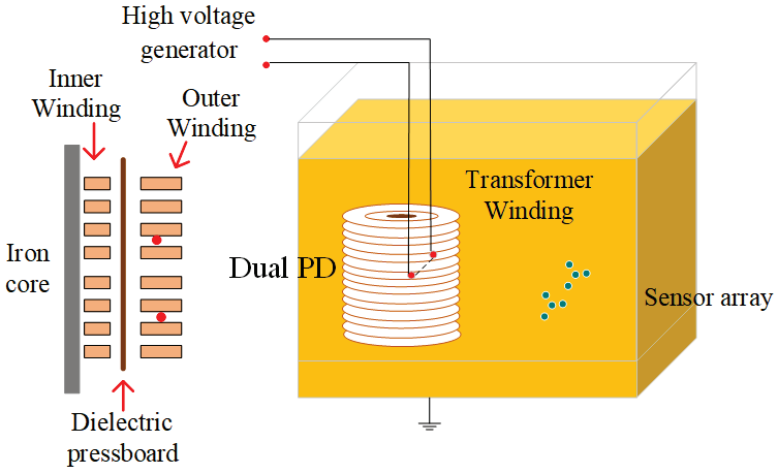

Figure 15. Experiment on locating dual PD in transformer winding interturn.

When dual partial discharge sources are arranged between the turns of the outer winding, a partial discharge waveform is detected by the sensor, as shown in Figure 16, and the localization results are presented in Table 4.

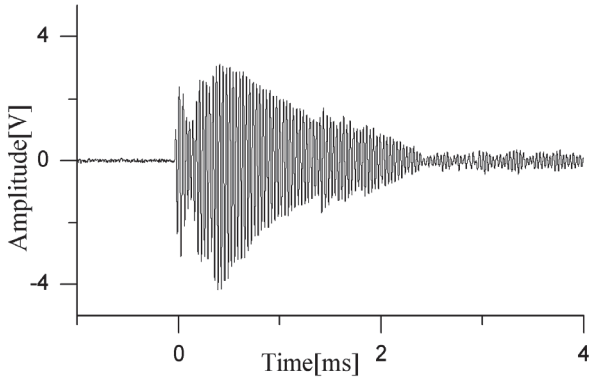

Figure 16. Ultrasonic waveform of dual PD sources in transformer winding interturn.

Table 4. Results of localization for dual PD sources in transformer winding interturn.

Number	PD Source Coordinates/cm	Localization Results/cm	Distance Error/cm
1	(43, 170, 25) (54, 168, 30)	(49.4, 185.6, 30.7) (60.7, 162.2, 38.1)	17.8 12.0
2	(52, 167, 45) (59, 174, 30)	(61.2, 171.3, 39.8) (65.2, 169.1, 48.1)	11.4 19.7
3	(39, 176, 25) (58, 172, 45)	(34.2, 170.3, 29.3) (62.3, 176.7, 40.3)	9.4 7.9
4	(42, 171, 35) (48, 166, 40)	(49.1, 164.4, 42.9) (41.6, 176.2, 31.4)	12.5 14.8
5	(52, 167, 25) (58, 172, 40)	(61.2, 175.2, 35.1) (51.2, 180.2, 31.9)	15.9 13.4

As seen from the signals received by the sensor in Figure 15, when the dual PD sources are located in the winding interturn, the ultrasonic signals emitted by the PD sources are not blocked by the windings. The first few cycles of the waveform can propagate through the gaps of the winding to the sensor array without distortion. Due to the refraction and reflection of the ultrasonic waves by the winding gaps, the latter half of the signal exhibits more reverberations. The amplitudes of these interfering waveforms are significantly lower than those of the direct wave signals. From an energy perspective, these interferences may increase the number of energy peaks, but they do not affect the selection of the first and second extreme values, which represent the positional information of the two sound sources. Therefore, by arranging four sensor arrays on both sides, it is possible to achieve the localization of dual partial discharge sources occurring in the interturn space and on the surface of the transformer windings.

Our method for detecting dual partial discharge sources involves placing sensors inside the transformer, which differs from the approach of installing sensors outside the transformer's metal tank. The latter method is unable to detect the simultaneous discharge of dual partial discharge sources due to ultrasonic attenuation and interference from external signals. The built-in detection method offers high accuracy but faces two major challenges. The first is that the sensors need to overcome the decrease in sensitivity caused by the pressure of the transformer's insulating oil, which is an objective technical issue that our improved sensors aim to address. The second challenge is a subjective concern stemming from manufacturers and users' worries about this invasive detection method. The more sensors used, the greater their concern. Currently, there are few algorithms suitable for simultaneous localization of dual sound sources. Currently, we can only use a single sensor array for direction finding and cross-check the results from two arrays to achieve localization, which is a cumbersome and complex method and a last resort as

we have not found a better solution yet. A sensor array requires four sensors, and two arrays would need eight sensors. To detect and locate partial discharges on both sides of a single-phase winding, the number of sensors required could reach up to 16. Therefore, the current localization method of the paper can only be implemented under laboratory conditions, and it will be of engineering practicability only after reducing the number of sensors used. Therefore, we did not conduct too much research on this localization method. Our future research will focus on solving the problem of dual partial discharge sources localization using a smaller number of sensors. We are currently exploring two technical routes concurrently. One team is studying ways to reduce the number of array elements in the sensor array, potentially sacrificing some precision to achieve a reduction in sensor count. The other team is searching for novel localization methods. We look forward to developing more practical and acceptable localization techniques that will be welcomed by transformer manufacturers and users.

5. Conclusions

This paper proposes a novel method for detecting and localizing dual PD sources inside transformers using a pressure-balanced fiber-optic ultrasonic sensor array with a regular tetrahedron structure and a direction-finding cross-localization algorithm. The sensor can be installed deep in the transformer oil, and its pressure-balanced structure design can reduce the obstruction of oil pressure on the diaphragm vibration, enabling it to capture the discharge signals from dual partial discharge sources. For scenarios where there are no obstacles blocking the discharge of dual PD sources, this method can achieve localization of dual PD sources inside transformer oil using only two sensor arrays.

When dual partial discharge sources occur in the oil channel of the winding, the ultrasonic signals generated by PD will undergo attenuation and distortion. In such cases, the detected waveforms can only be used for qualitative partial discharge detection and cannot accurately locate the fault point. If the periodic amplitude of the direct wave contained in the partial discharge ultrasonic signal is not attenuated, such as when it occurs in the interturn of the transformer winding, then its waveform can be used for localization. Otherwise, the position of the sensors needs to be adjusted to reduce the attenuation of the direct wave period caused by obstacles.

This detection method has a high dependence on sensor sensitivity and the direct wave of partial discharge. In the subsequent research work, different coating processes will be tried to reduce the diaphragm thickness and improve the sensor sensitivity. In addition, sensors will be installed at different positions of the transformer to allow the ultrasonic signals of partial discharges from different fault areas to directly reach the sensor array, avoiding obstruction. Furthermore, the localization method needs to be improved, using a smaller number of sensors to achieve more precise localization.

Author Contributions: Conceptualization, W.W.; methodology, W.W. and F.L.; validation, F.L., Y.S. and S.Z.; data curation, Y.S. and S.Z.; writing—original draft preparation, F.L.; writing—review and editing, W.W. and F.L.; funding acquisition, W.W. All authors have read and agreed to the published version of the manuscript.

Funding: This research was funded by the National Natural Science Foundation of China, grant number 51577063.

Institutional Review Board Statement: Not applicable.

Informed Consent Statement: Not applicable.

Data Availability Statement: The data supporting the results presented in this article are available upon request.

Conflicts of Interest: The authors declare no conflicts of interest.

References

1. El-kenawy, E.-S.M.; Albalawi, F.; Ward, S.A.; Ghoneim, S.S.M.; Eid, M.M.; Abdelhamid, A.A.; Bailek, N.; Ibrahim, A. Feature Selection and Classification of Transformer Faults Based on Novel Meta-Heuristic Algorithm. *Mathematics* **2022**, *10*, 3144. [CrossRef]
2. Zhu, Y.; Zhou, L.; Xu, H. Application of improved genetic algorithm in ultrasonic location of transformer partial discharge. *Neural Comput. Appl.* **2020**, *32*, 1755–1764. [CrossRef]
3. Zhang, X.; Guo, R.; Yang, Y.; Hu, Y.; Zhang, Z.; Li, J.; Han, X. Partial Discharge Measurement and Analysis of Transformer Under Oscillating Lightning Impulse Voltage. *IEEE Trans. Dielectr. Electr. Insul.* **2022**, *29*, 2303–2311. [CrossRef]
4. Cai, J.; Zhou, L.; Zhang, Y.; Wang, D.; Liao, W.; Zhang, C. Convenient Online Approach to Multisource Partial Discharge Localization in Transformer. *IEEE Trans. Ind. Electron.* **2022**, *69*, 9440–9450. [CrossRef]
5. Jia, J.; Hu, C.; Yang, Q.; Lu, Y.; Wang, B.; Zhao, H. Localization of Partial Discharge in Electrical Transformer Considering Multimedia Refraction and Diffraction. *IEEE Trans. Ind. Inform.* **2021**, *17*, 5260–5269. [CrossRef]
6. Baker, E.; Nese, S.V.; Dursun, E. Hybrid Condition Monitoring System for Power Transformer Fault Diagnosis. *Energies* **2023**, *16*, 1151. [CrossRef]
7. Uehara, H.; Okamoto, T. Modeling and Analysis of Partial Discharge Phenomena Using Integral Equations. *IEEE Trans. Dielectr. Electr. Insul.* **2020**, *27*, 1915–1923. [CrossRef]
8. Witos, F.; Olszewska, A. Investigation of Partial Discharges within Power Oil Transformers by Acoustic Emission. *Energies* **2023**, *16*, 3779. [CrossRef]
9. Rathod, V.B.; Kumbhar, G.B.; Bhalja, B.R. Partial Discharge Detection and Localization in Power Transformers based on Acoustic Emission: Theory, Methods, and Recent Trends. *IETE Tech. Rev.* **2022**, *39*, 540–552. [CrossRef]
10. Sikorski, W.; Wielewski, A. Low-Cost Online Partial Discharge Monitoring System for Power Transformers. *Sensors* **2023**, *23*, 3405. [CrossRef] [PubMed]
11. Qian, G.; Chen, W.; Wu, K.; Liu, H.; Wang, J.; Zhang, Z. Research on Transformer Omnidirectional Partial Discharge Ultrasound Sensing Method Combining F-P Cavity and FBG. *Sensors* **2023**, *23*, 9642. [CrossRef] [PubMed]
12. Zhang, Z.; Chen, W.; Wu, K.; Tian, H.; Song, R.; Song, Y.; Liu, H.; Wang, J. Partial Discharge Pattern Recognition Based on a Multifrequency F–P Sensing Array, AOK Time–Frequency Representation, and Deep Learning. *IEEE Trans. Dielectr. Electr. Insul.* **2022**, *29*, 1701–1710. [CrossRef]
13. Li, H.; Bu, J.; Li, W.; Lv, J.; Wang, X.; Hu, K.; Yu, Y. Fiber optic Fabry–Perot sensor that can amplify ultrasonic wave for an enhanced partial discharge detection. *Sci. Rep.* **2021**, *11*, 8661. [CrossRef] [PubMed]
14. Ding, Z.; Zhou, Q.; Wang, Y.; Ding, Z.; Tang, Y.; He, Q. Microstructure and properties of monolayer, bilayer and multilayer Ta2O5-based coatings on biomedical Ti-6Al-4V alloy by magnetron sputtering. *Ceram. Int.* **2021**, *47*, 1133–1144. [CrossRef]
15. Gao, L.; Lemarchand, F.; Lequime, M. Refractive index determination of SiO_2 layer in the UV/Vis/NIR range: Spectrophotometric reverse engineering on single and bi-layer designs. *J. Eur. Opt. Soc.-Rapid Publ.* **2013**, *8*, 13010. [CrossRef]
16. Li, Z.; Wang, S.; Jiang, J.; Sang, M.; Yu, Y.; Liu, W.; Zhang, P.; Liu, T. Real-Time Pressure Measurement Method Based on Rapid Phase Demodulation of Multi-Cavities F-P Sensor. *IEEE Sens. J.* **2021**, *21*, 26624–26630. [CrossRef]
17. Merkofer, J.P.; Revach, G.; Shlezinger, N.; Routtenberg, T.; van Sloun, R.J.G. DA-MUSIC: Data-Driven DoA Estimation via Deep Augmented MUSIC Algorithm. *IEEE Trans. Veh. Technol.* **2024**, *73*, 2771–2785. [CrossRef]
18. Zhou, C.; Gu, Y.; Fan, X.; Shi, Z.; Mao, G.; Zhang, Y.D. Direction-of-Arrival Estimation for Coprime Array via Virtual Array Interpolation. *IEEE Trans. Signal Process.* **2018**, *66*, 5956–5971. [CrossRef]
19. Venikar, P.A.; Ballal, M.S.; Umre, B.S.; Suryawanshi, H.M. Search Coil Based Online Diagnostics of Transformer Internal Faults. *IEEE Trans. Power Deliv.* **2017**, *32*, 2520–2529. [CrossRef]
20. Xian, R.; Wang, L.; Zhang, B.; Li, J.; Xian, R.; Li, J. Identification Method of Interturn Short Circuit Fault for Distribution Transformer Based on Power Loss Variation. *IEEE Trans. Ind. Inform.* **2024**, *20*, 2444–2454. [CrossRef]

sensors

MDPI

Article

Study on the Impact of Pole Spacing on Magnetic Flux Leakage Detection under Oversaturated Magnetization

Wenlong Liu, Lemei Ren * and Guansan Tian

School of Thermal Engineering, Shandong Jianzhu University, Jinan 250100, China; 19861806215@163.com (W.L.); tgs4170@sdjzu.edu.cn (G.T.)
* Correspondence: 24332@sdjzu.edu.cn

Abstract: Magnetic flux leakage (MFL) inspection employs leakage magnetic fields to effectively detect and locate pipeline defects. The spacing between magnetic poles significantly affects the leakage magnetic field strength. While most detectors typically opt for moderate pole spacing for routine detection, this study investigates the propagation characteristics of MFL signals at small pole spacings (under specimen oversaturated magnetization) and their impact on MFL detection. Through finite element simulation and experiments, it reveals a new signal phenomenon in the radial MFL signal B_y at small pole spacings, the double peak–valley (DPV) phenomenon, characterized by outer and inner peaks and valleys. Theoretical analysis based on the simulation results elucidates the mechanisms for this DPV phenomenon. Based on this, the impact of defect size, pipe wall thickness, and magnetic pole and rigid brush height on MFL signals under small magnetic pole spacings is examined. It is demonstrated that, under a smaller magnetic pole spacing, a potent background magnetic field manifests in the air above the defect. This DPV phenomenon is generated by the magnetic diffusion and compression interactions between the background and defect leakage magnetic fields. Notably, the intensity of the background magnetic field can be mitigated by reducing the height of the rigid brush. In contrast, the pipe wall thickness and magnetic pole height exhibit a negligible influence on the DPV phenomenon. The emergence of the DPV precipitates a reduction in the peak-to-valley difference within the MFL signal, constricting the depth range of detectable defects. However, the presence of DPV increases the identification of defects with smaller opening sizes. These findings reveal the characterization of the MFL signal under small pole spacing, offering a preliminary study on identifying specific defects using unconventional signals. This study provides valuable guidance for MFL detection.

Keywords: magnetic flux leakage (MFL); leakage magnetic field; double peak–valley (DPV) phenomenon; magnetic pole spacing

1. Introduction

Pipelines play a key role in oil and gas transmission. Their safe operation is crucial to energy support and economic development [1]. It is possible for these pipelines to develop cracks, corrosion, deformation, and other defects in the long-term transportation process, threatening the safety of production [2,3]. Therefore, it is necessary to test pipelines regularly. Nondestructive testing (NDT) is a widely used method for inspecting pipelines without causing damage to the tested material. The common NDT methods include ultrasonic testing (UT), eddy current testing (ECT), and magnetic flux leakage (MFL) testing [4]. Compared to other NDT methods, MFL detection technology has the advantages of a strong anti-interference ability, a fast signal acquisition speed, and no need for coupling agents; so, it has become the mainstream technology for pipeline detection worldwide [5,6].

Pipeline defects can be identified, located, and quantified by analyzing the MFL signals [7]. Many scholars have found that MFL signals are influenced by many factors, such as defect size, sensor detection angle and direction, temperature, stress, scanning

speed, lift-off value, pipe shielding effects, and specimen surface roughness. Kopp et al. [8] employed a magnetic dipole model (MDM) to investigate how the defect size impacts MFL signals, establishing a clear correlation between signal characteristics and defect geometric parameters. Tri-axial signals were utilized to approximate defect opening sizes. To address probe tilt due to detector vibration during detection, Long et al. [9] proposed a dual-sensor probe to compensate for probe tilt. This approach effectively achieves the compensation of the original MFL signal. The scanning direction of the sensor also affects the MFL signal. Wu et al. [10] using the MDM revealed that the MFL signal is most effective when the defect's extension direction is perpendicular to the scanning direction of the sensor. Wang et al. [11] developed a temperature-dependent MDM that considers the combined effects of the temperature and thermal stress, noting a parabolic signal amplitude variation within specific temperature ranges. Based on the J-A theory, Liu et al. [12] investigated the relationship between stress and the saturation magnetization strength of ferromagnets. They observed that, under high magnetic field stress, the saturation magnetization strength of ferromagnets decreases exponentially with the increase in stress. This reduction diminishes the amplitude of the MFL signal, potentially leading to an underestimation of defect depth. Wu investigated the impact of uniform and non-uniform stress on bi-axial MFL signals, observing changes in signal amplitude both perpendicular and parallel to the stress direction. Furthermore, it was noted that these signals effectively characterize the magnitude and distribution of stress inhomogeneity [13]. Eddy current effects, resulting from the relative motion between magnetization devices and pipelines, diminish MFL signal strength [14,15]. Pullen's study revealed that increasing the detection speed results in insufficient magnetization strength in the pipe wall. This causes the MFL signal strength of outer wall defects to decrease, while that of inner wall defects increases [16,17]. Usarek found that both the tangential and normal components of the magnetic field increase linearly with speed. To compensate for this effect, an empirical fitting equation was employed to adjust the MFL signal [18]. The lift-off value between the sensor probe and the detection object increases the noise in the MFL signal. Peng et al. [19] and Feng et al. [20] analyzed the influence of the lift-off value on the MFL signal based on the MDM and finite element model (FEM). They proposed compensation methods for the sensor lift-off effect on the MFL signal. Liu et al. [21] addressed pipe wall shielding effects on MFL signal propagation, integrating a wall propagation compensation factor into the MDM for accurate defect detection on outer pipe walls. Deng et al. [22] discussed the effect of ferromagnetic specimen surface roughness on the MFL signals. It was found that surface roughness generates excess MFL signals, which could obscure weaker signals and increase the risk of missed defect detections. Additionally, Yousaf analyzed magnetic pole spacing impacts on the MFL testing of steel bars, determining the optimal spacing considering leakage magnetic field intensity and magnetic pole interaction effects [23].

In conclusion, while there have been many studies on the factors that affect MFL signals, research on the impact of magnetic pole spacing is still relatively scarce. This is because the majority of detectors have been designed with the pole spacing already set according to the conventional detection scenario. Generally, reducing the magnetic pole spacing can enhance the amplitude of the MFL signal. However, further reductions may disturb it [24]. Studies on the amplitude and waveform characteristics of MFL signals with small pole spacing are notably sparse, particularly when the pipe wall is oversaturated with magnetization.

This paper thoroughly investigates the variation pattern of MFL signals under small magnetic pole spacing through theoretical analysis and experimental research. Firstly, the influence of magnetic pole spacing on the MFL signal is analyzed, and a new signal phenomenon is discovered. The cause of the phenomenon is also analyzed through FEM simulations. Subsequently, we examine the effects of defect size, wall thickness, magnetic pole, and rigid brush height on the MFL signal under wall saturation and oversaturation conditions.

2. Methods

2.1. The Model of MFL Detection

The internal detector for the pipe MFL comprises a battery section, a detection section, a data recording section, and a mileage wheel, as illustrated in Figure 1a. Among these components, the MFL detection section is responsible for magnetizing the pipe wall and collecting the MFL signals using magnetic sensors. The collected signals are then filtered, amplified, and stored in the recording section. The battery section provides power to the detector and also drives the detector's movement. The mileage wheel is capable of recording the detection mileage and movement speed of the detector. The magnetic sensors used to collect the MFL signals in the detection section are distributed as shown in Figure 1b. The sensor capsules are uniformly distributed on the whole circumference, and 12 Hall sensors are uniformly distributed in each sensor capsule.

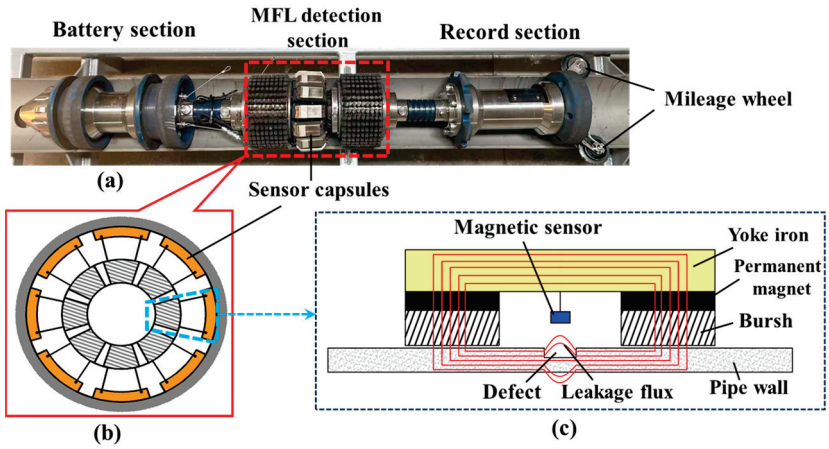

Figure 1. The principle of the MFL detection: (**a**) schematic diagram of MFL inspection detector, (**b**) cross-sectional illustration of MFL detection section, and (**c**) the principle of MFL signal collection.

Figure 1c illustrates the principle of MFL signal collection, which relies on the high magnetic permeability of ferromagnetic materials. To achieve a saturated or near-saturated state, a permanent magnet, a yoke iron, and a rigid brush are used to fully magnetize the pipe wall. In the absence of defects, the magnetic force lines run parallel to the inside of the pipe. However, if surface or near-surface defects, for example, are present, the magnetic force lines become obstructed, causing some of them to leak out of the pipe surface. This leakage magnetic field can be detected using a magnetic sensor, enabling the identification and characterization of the defect.

The magnetic field is the physical variable in the MFL detection system. Therefore, Maxwell equations are used to describe the leakage magnetic field. As this study does not consider the velocity effect, a static magnetic field model is used to describe the leakage magnetic field [25]. Thus, it can be described by

$$\nabla \times H = J \tag{1}$$

$$\nabla \cdot B = 0 \tag{2}$$

where ∇ is the Hami operator, H is the magnetic field strength, J is the equivalent current density, and B is the magnetic flux density.

The relationship between the electromagnetic materials is described as

$$B = \mu \cdot H \tag{3}$$

where μ is the medium's permeability.

Due to the source-free nature of magnetic fields, introducing the vector magnetic potential A allows for the following:

$$\nabla \times A = B \tag{4}$$

From Equations (1)–(4) and the vector identity $\nabla \times (\nabla \times A) = \nabla (\nabla A) - \nabla^2 A$, we can derive

$$\frac{1}{\mu}\nabla^2 \times A = -J \tag{5}$$

To solve Equation (5), the following boundary conditions are introduced:

$$\begin{cases} A = 0 & \text{At the boundary of the model} \\ A_1 = A_2 & \text{At the junction of two mediums} \end{cases} \tag{6}$$

By utilizing the boundary conditions to solve Equation (5), the axial and radial components of the MFL signal can be calculated as follows:

$$\begin{cases} B_x = \frac{\partial A}{\partial y} \\ B_y = -\frac{\partial A}{\partial x} \end{cases} \tag{7}$$

where B_x and B_y represent the axial and radial components of the magnetic field, B, respectively.

2.2. Finite Element Model of MFL Detection

The FEM is a numerical analysis model based on Maxwell equations for solving leakage magnetic fields and has found extensive application in the field of MFL inspection. This study utilized ANSYS 2021 R2 software to construct a complete 3D MFL detection FEM, as shown in Figure 2a. This consists of 18 magnetization device pieces, which are arranged in a circle around the pipe wall. The magnetization device comprises a yoke iron and two opposing permanent magnets. A layer of inflexible brushes is positioned on the surface of the permanent magnets, which come into direct contact with the steel pipe specimen. The inflexible brushes are magnetized to saturation by the permanent magnets, and their magnetic permeability can be considered constant. Their purpose is to prevent friction between the permanent magnets and the pipe wall during the detection process. The steel pipes used in high- and medium-pressure gas pipelines in urban areas have a diameter of 300 mm and a wall thickness T ranging from 6 mm to 10 mm. Figure 2b provides a detailed description of the composition and dimensions of the magnetization device, while Table 1 contains the material parameters. The pit-like defects on the inner surface of the steel pipe specimen have dimensions of length L × width W × depth D and are rectangular in shape. Figure 3 shows the nonlinear B-H curve of the steel pipe. The air domain encloses the entire MFL detection device.

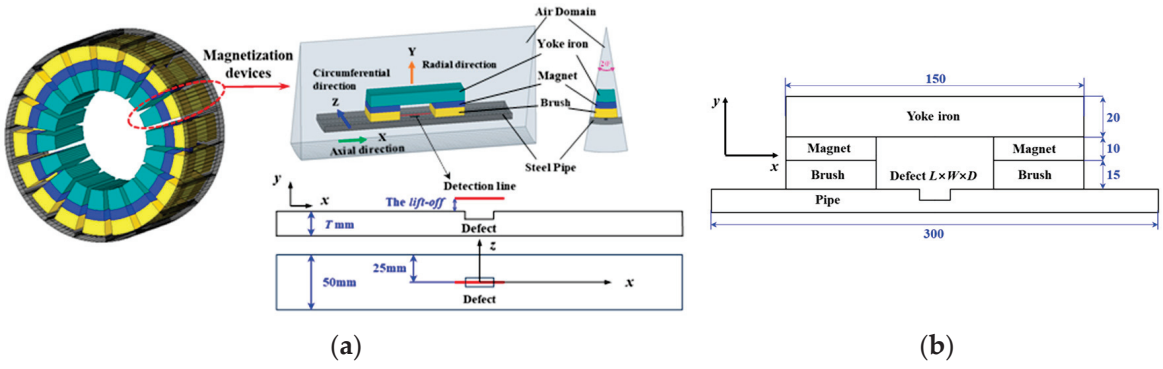

Figure 2. Three-dimensional defect leakage magnetic field FEM: (**a**) geometric model; (**b**) dimensions of the magnetizing device (mm).

Table 1. Material parameter settings.

Components	Materials	Permeability	Remanent Magnetization (T)
Magnet	Neodymium	1	1.3
Magnetizer	Iron	5000	-
Brush	Steel 1008	3000	-
Steel Pipe	Steel	*B-H* curve in Figure 3	-
Air Domain	Air	1	-

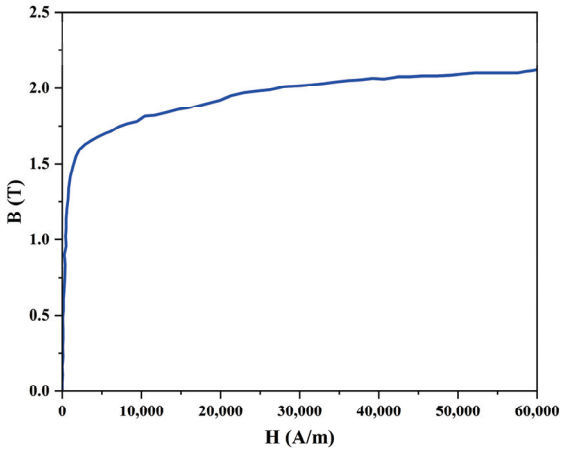

Figure 3. Nonlinear *BH* characteristic curve of the steel pipe.

For the convenience of data extraction, the detection lines were arranged axially above the defects, as indicated by the red line in Figure 2a. The lift-off value was set at 1 mm, and the sampling interval was set to 0.001 mm.

Mesh independence validation: To account for the range of cases with larger specimen volumes and small defect sizes, various grid sizes are utilized in different regions [26]. The computational domain is partitioned into an unstructured mesh, with local refinement applied to the air domain near the defect. As the mesh is progressively refined, the computed results tend to become more stable. A mesh count of 123,000 was adopted in this study as further increasing the number of meshes does not yield substantial changes in the computed results.

2.3. Physical Experiments

The manual adjustment of the pole spacing is challenging due to the strong magnetic suction in front of the magnetic poles and the yoke. Consequently, the research team devised a special mechanical structure to design an MFL detection device that employs bolts to facilitate the autonomous adjustment of the pole spacing X, as illustrated in Figure 4a. The fixing nut is fixed on the magnetic poles, and by adjusting the bolt during the experiment, the magnetic poles can be driven to move along the slide until the ideal pole spacing X is reached. The magnetizing device of the MFL detection system comprises a yoke and poles, which are connected to the rigid brushes that magnetize the tube wall. The magnetic poles have a remanent magnetic strength of 1.3 T. The MFL detection probe comprises four Hall sensors, with an axial sampling interval of 0.05 mm and a circumferential sampling interval of 5 mm, as shown in Figure 4b. The scanning speed is 0.1 m/s, and the sensor lift-off value is set to 2 mm. The flat-plate ferromagnetic specimen being tested has a wall thickness of 6 mm. A rectangular metal defect with dimensions of L = 30 mm, W = 6 mm, and D = 2.4 mm, along with a circular metal loss defect with dimensions of $\varnothing$ = 5 mm and D = 2.4 mm, were observed on the specimen, as shown in Figure 4c,d. The MFL signals collected by the sensors are initially stored in the signal storage device of the testing device. After detection, they are transmitted to the host computer for data processing and analysis using the local area network (LAN) provided by the router. The detection principle,

material properties, and probe performance of this experimental setup are identical to those of a real pipe MFL internal detector. Consequently, this detector can be employed as a highly accurate substitute in theoretical analyses of the impact of magnetic pole spacing on the MFL signal.

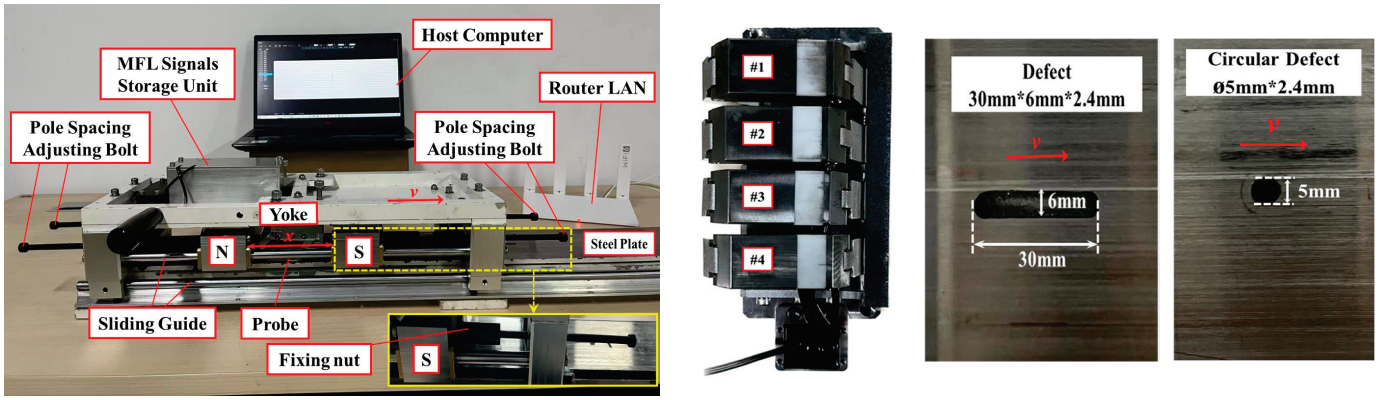

Figure 4. The experimental setup: (**a**) MFL detection device and signal transmission processing system, (**b**) schematic diagram of sensor probe, (**c**) rectangular metal loss defect, and (**d**) circular metal loss defect.

3. Results of Simulation and Experiments

3.1. FEM Simulation

3.1.1. For Rectangular Defects

Rectangular defects are frequently studied in the context of MFL detection. When analyzing the characteristics of these defects, they can generally be approximated as rectangular by using three equivalent shape parameters: equivalent length, width, and depth [27,28]. Figure 5 shows the variation in the MFL signal for a defect with dimensions of L = 6 mm, W = 3 mm, and D = 5 mm at five different magnetic pole spacings X (20 mm, 40 mm, 60 mm, 80 mm, and 100 mm), with a wall thickness of T = 10 mm. The magnetic field B_x is illustrated in Figure 5a. The graph shows that the magnetic field B_x is enhanced as the magnetic pole spacing decreases. It is suggested that decreasing the magnetic pole spacing improves the detection accuracy. Additionally, the amplitude of the magnetic field B_x increases at a greater rate when the pole spacing is reduced from 100 mm to 40 mm. The simulation results demonstrate that reducing the magnetic pole spacing increases the amplitude of B_x while maintaining its waveform. Conversely, Figure 5b illustrates significant alterations in both the waveform and amplitude of the magnetic field B_y. Hence, due to spatial limitations, this paper mainly concentrated on analyzing the magnetic field B_y rather than B_x.

When the pole spacing is 20 mm, B_y demonstrates a distinct double peak and valley pattern. The outer peak and valley exhibit positive values followed by negative ones, whereas the inner peak and valley demonstrate negative values followed by positive ones. Additionally, the MFL signal curve at both ends of the scanning range displays a steep slope, with the signal intensity rapidly increasing. This study refers to this phenomenon as a double peak–valley (DPV). Even with a magnetic pole spacing of 30 mm, a slight DPV phenomenon is observed in B_y. This phenomenon results in a decrease in the $B_{p\text{-}v}$ (the peak-to-valley value) of the B_y signal when the magnetic pole spacing is reduced from 40 mm to 20 mm. Figure 6 displays the histogram of the $B_{p\text{-}v}$ of B_y. The figure shows that the $B_{p\text{-}v}$ of the MFL signal first increases and then decreases as the magnetic pole spacing decreases. At a magnetic pole spacing of 40 mm, $B_{p\text{-}v}$ reaches a maximum value of 621 Gs. However, at a magnetic pole spacing of 20 mm, the $B_{p\text{-}v}$ of the MFL signal is only 370 Gs. At this time, the pipe wall is oversaturated with magnetization, which disrupts the distribution of the magnetic field and hampers the detection of defects in the pipe.

Therefore, this paper assumed that, in the FEM simulation, the pipe wall can be considered as having oversaturated magnetization when the magnetic pole spacing is less than or equal to 20 mm.

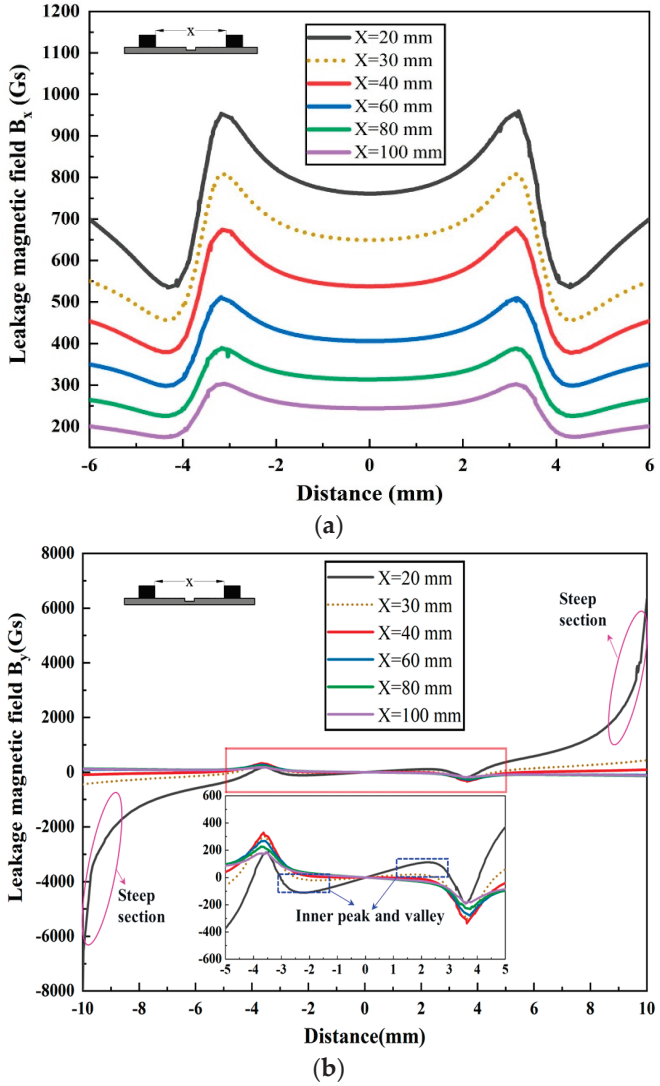

Figure 5. Propagation characteristics of the MFL signal with different magnetic pole spacings: (**a**) the leakage magnetic field axial component B_x; (**b**) the leakage magnetic field radial component B_y.

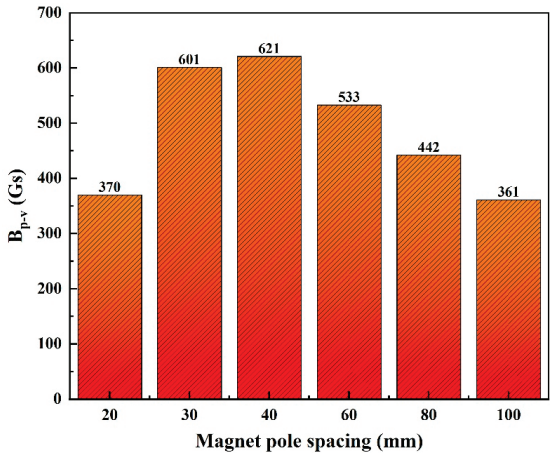

Figure 6. Column chart of the $B_{p\text{-}v}$ of the magnetic field B_y.

To investigate the effect of smaller magnetic pole spacings on the MFL signals of pipeline defects, this study conducted simulations and calculations for magnetic pole spacings ranging from 15 mm to 20 mm. The magnetic field B_y is shown in Figure 7. With the decrease in magnetic pole spacing, the DPV phenomenon becomes more pronounced. Concurrently, the inner $B_{p\text{-}v}$ steadily increases while the outer $B_{p\text{-}v}$ decreases, and the rates of their increase and decrease also accelerate progressively.

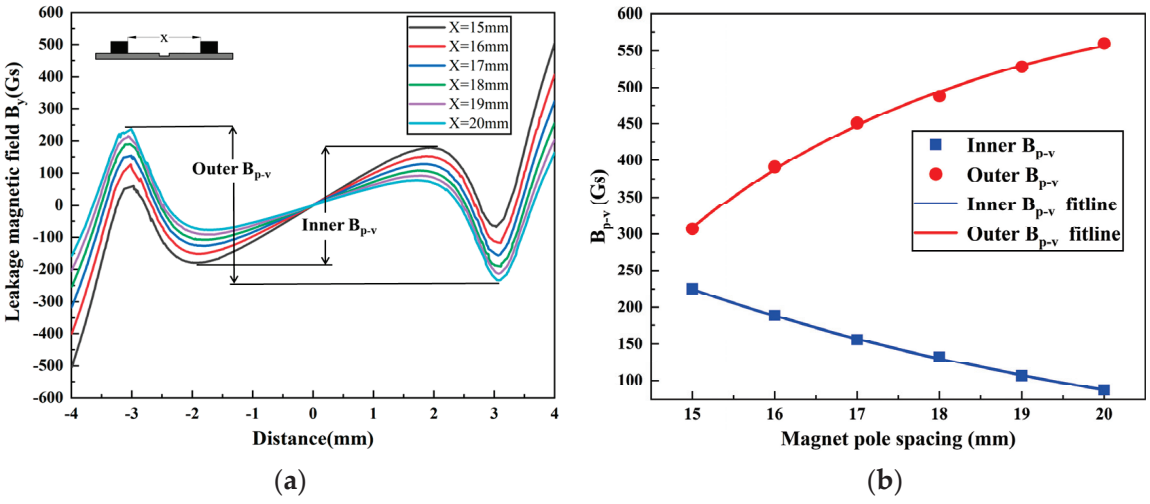

Figure 7. The MFL signals with different magnetic pole spacings: (**a**) the leakage magnetic field B_y; (**b**) variation in $B_{p\text{-}v}$.

3.1.2. For Circular Defects

Given the varied contours of actual pipe defects, this paper also investigated circular defects. The research team employed FEM to compute circular defects with an opening radius of 3 mm and a depth of 5 mm across various pole spacings, with a wall thickness of T = 10 mm. As depicted in Figure 8, the amplitude of the MFL signal reaches its maximum at a pole spacing of 40 mm. When the magnetic pole spacing is less than 20 mm, the MFL signals begin to exhibit DPV phenomena, with sharp increases in the signal amplitude at both ends of the sweep range. As the magnetic pole spacing decreases, the DPV signature of the signal becomes apparent. Compared to the rectangular defects illustrated in Figure 7a, both demonstrate similar characteristic patterns of change.

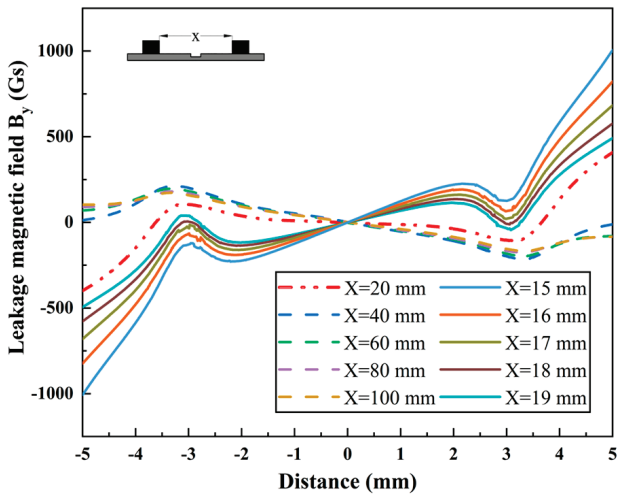

Figure 8. The variation in the leakage magnetic field B_y of circular defect with different pole spacings.

3.2. Physical Experiments

The research team conducted experiments to test the defect MFL signals at the magnetic pole spacings of 50 mm, 58 mm, and 110 mm using the experimental setup and defect samples shown in Figure 4. The magnetic field B_y is presented in Figure 9. For both rectangular and circular metal loss defects, at a pole spacing of 110 mm, a typical radial MFL signal is observed, characterized by a pair of peaks and valleys corresponding to the axial length of the defect. However, with a reduced magnetic pole spacing of 58 mm, the magnetic field B_y begins to exhibit DPV phenomena. As the magnetic pole spacing further decreases, the outer $B_{p\text{-}v}$ decreases continuously while the inner $B_{p\text{-}v}$ increases steadily. Simultaneously, the amplitude of B_y also increases sharply on both sides of the scanning range, consistent with the distribution characteristics of simulated signals in Figures 7 and 8, and the variation in $B_{p\text{-}v}$ with magnetic pole spacing. Moreover, the experimental signal amplitudes remain within the same order of magnitude as the simulated signals, further confirming the presence of DPV and the correctness of the FEM.

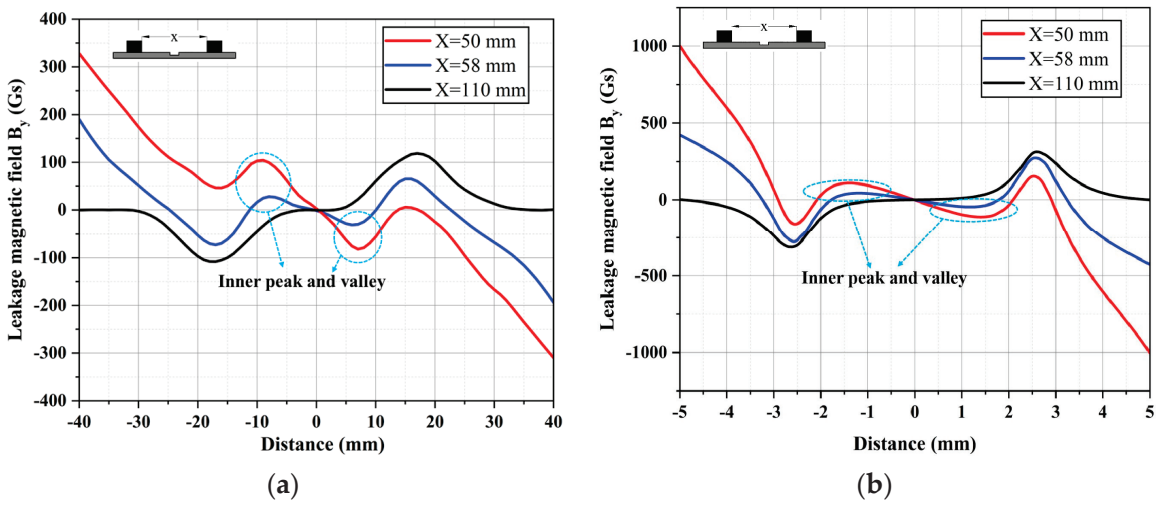

Figure 9. The leakage magnetic field B_y at the magnetic pole spacings of 50 mm, 58 mm, and 110 mm: (**a**) rectangular metal loss defect; (**b**) circular metal loss defect.

Additionally, it is noteworthy that, under the same magnetic pole spacing, the DPV phenomenon exhibited by the rectangular defect in Figure 9a is significantly more pronounced than that of the circular defect in Figure 9b. This difference arises from the shorter axial length of the circular defect compared to the rectangular one, resulting in a less pronounced DPV in their radial MFL signals. The influence of defect size on the DPV phenomenon will be further discussed in Section 4.

4. Discussion

This section compares and investigates the effects of defect size, pipe wall thickness, magnetic pole, and rigid brush height on the MFL signal in the case of saturated and oversaturated magnetization (selected pole spacings of 40 mm and 20 mm, respectively), using a rectangular defect as an example. The mechanisms for the DPV phenomenon of the MFL signal are also theoretically analyzed based on the FEM simulation results.

4.1. The Effect of Defect Depth on the Characteristics of MFL Signals

A pipe wall thickness of T = 10 mm and a defect length and width of L = 5 mm and W = 3 mm, respectively, were used for the simulation calculations. The magnetic field B_y was simulated for defect depths D = 1, 2, 3, 4, and 5 mm at magnetic pole spacings of 40 mm and 20 mm, as shown in Figure 10a,b, respectively. Figure 10c shows the variation curve of the $B_{p\text{-}v}$ of the radial MFL signal B_y concerning the defect depth for different magnetic pole spacings.

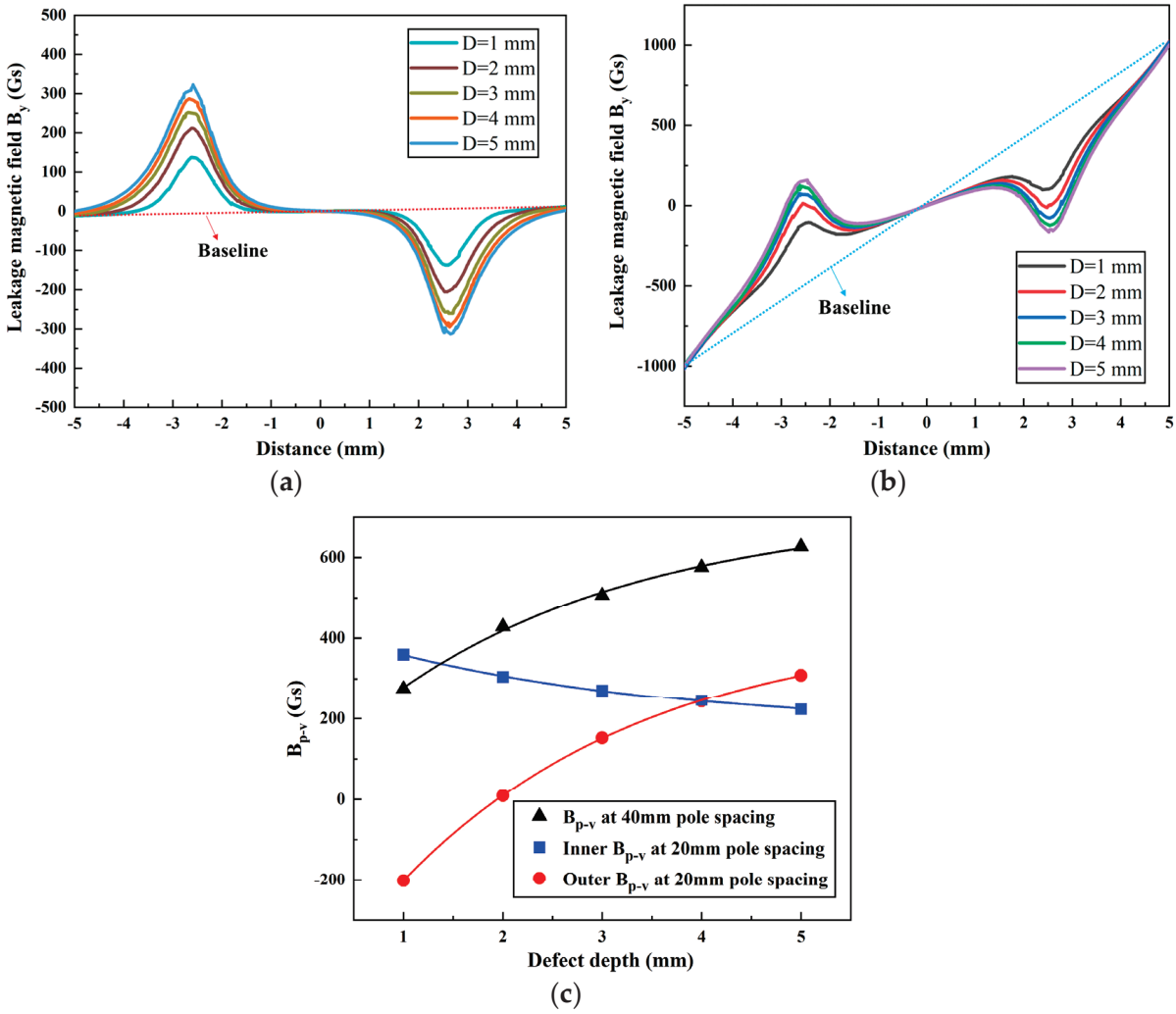

Figure 10. The leakage magnetic field B_y at different defect depths: magnetic pole spacings of (**a**) 40 mm and (**b**) 20 mm; and (**c**) the variation in $B_{p\text{-}v}$.

From the figure, it can be seen that, for a magnetic pole spacing of 40 mm, the $B_{p\text{-}v}$ shows an increasing trend as the defect depth ranges from 1 mm to 5 mm. Specifically, the $B_{p\text{-}v}$ increases from 275 Gs to 627 Gs with a gradually decreasing growth rate. At a magnetic pole spacing of 20 mm, as the defect depth increases from 1 mm to 5 mm, the outer $B_{p\text{-}v}$ gradually increases and reaches a value of 510 Gs. Conversely, the inner $B_{p\text{-}v}$ gradually decreases to a value of 136 Gs. When the defect depth is less than 4 mm, the inner $B_{p\text{-}v}$ is higher than that on the outer one. However, when the defect depth is between 4 and 5 mm, the outer $B_{p\text{-}v}$ becomes higher than that of the inner one. Furthermore, at a magnetic pole spacing of 20 mm, the MFL curve shows abrupt changes at both ends of the scan. The baseline of the MFL signal changes from a horizontal to an inclined line, as shown by the dashed line in the figure.

Comparing the MFL signals under two different magnetic pole spacings, it was observed that, for defect depths ranging from 1 mm to 5 mm, the $B_{p\text{-}v}$ under 40 mm magnetic pole spacing showed an average increase of 380 Gs compared to that under 20 mm. This indicates that, as the distance decreases from 40 mm to 20 mm, the intensity of the MFL signal decreases significantly. In addition, the outer $B_{p\text{-}v}$ at the 20 mm pitch and 5 mm defect depth is very similar to the $B_{p\text{-}v}$ at the 40 mm pitch and 1 mm defect depth. The presence of DPV may result in an underestimation of defect depth and a narrower range of detectable defect depths.

4.2. The Effect of Defect Length on the Characteristics of MFL Signals

A pipe wall thickness of T = 10 mm and a defect depth and width of D = 5 mm and W = 3 mm, respectively, were used for the simulation calculations. The magnetic field B_y was simulated for defect lengths L = 1, 2, 3, 4, and 5 mm at the magnetic pole spacings of 40 mm and 20 mm, as shown in Figure 11a,b, respectively. Figure 11c shows the variation in the $B_{p\text{-}v}$ of the magnetic field B_y concerning the defect length for different magnetic pole spacings.

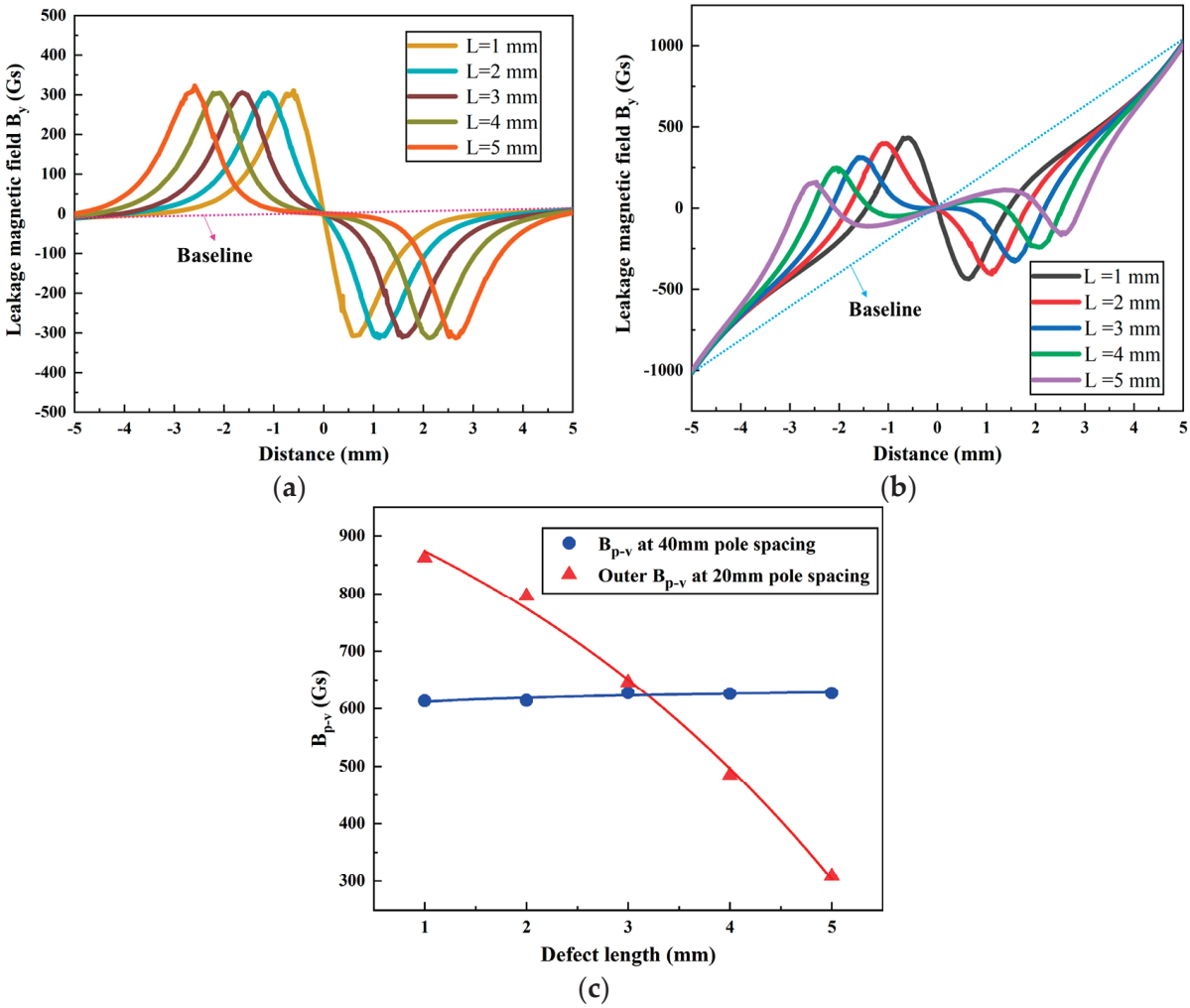

Figure 11. Leakage magnetic field B_y at different defect lengths: magnetic pole spacings of (**a**) 40 mm and (**b**) 20 mm, and (**c**) the variation in $B_{p\text{-}v}$.

Figure 11 show that, at a magnetic pole spacing of 40 mm, increasing the defect length from 1 mm to 5 mm results in an expansion of the horizontal distance between peaks and valleys (corresponding to the defect length), while $B_{p\text{-}v}$ remains relatively constant. For a magnetic pole spacing of 20 mm, the outer $B_{p\text{-}v}$ decreases by 553 Gs as the defect length increases from 1 mm to 5 mm. The baseline of the MFL signal curve changes from horizontal to inclined, as indicated by the dashed lines in the figure. It is evident that, for a magnetic pole spacing of 40 mm, the defect length has a minimal effect on the intensity of the magnetic field, B_y. However, when the magnetic pole spacing is reduced to 20 mm, the intensity of the magnetic field, B_y, decreases rapidly as the defect length increases.

From Figure 11c, it can be seen that, in the range of defect lengths from 1 mm to 3 mm, the outer $B_{p\text{-}v}$ for a magnetic pole spacing of 20 mm is greater than that for 40 mm. However, as the defect length exceeds 3 mm, the $B_{p\text{-}v}$ for a magnetic pole spacing of 40 mm exceeds that for 20 mm. From this, it can be seen that the MFL signal is more stable at a

spacing of 40 mm, allowing a wider range of defect lengths to be detected. Conversely, a spacing of 20 mm is more suitable for detecting smaller defects. Therefore, the presence of DPV facilitates the detection of defects with smaller opening dimensions.

Based on the above discussion, this study also discussed the detection range of small defect sizes using DPV signals. Magnetic field B_y was simulated for defect lengths ranging from 0.1 mm to 1 mm in steps of 0.1 mm, at magnetic pole spacings of 40 mm and 20 mm, illustrated in Figure 12a,b, respectively. Figure 12c demonstrates the variation in $B_{p\text{-}v}$ of magnetic field B_y with respect to the defect length. The results indicate that, within the range of defect lengths from 0.1 mm to 1 mm, the $B_{p\text{-}v}$ of DPV signals at a 20 mm pole spacing consistently exceeds that at a 40 mm pole spacing. Therefore, in conjunction with the findings from Figure 11, this study suggests that DPV signals, compared to conventional MFL signals, are more advantageous in identifying microdefects with lengths smaller than 3 mm. In the future, this specific signal may be utilized for detecting certain unique sizes.

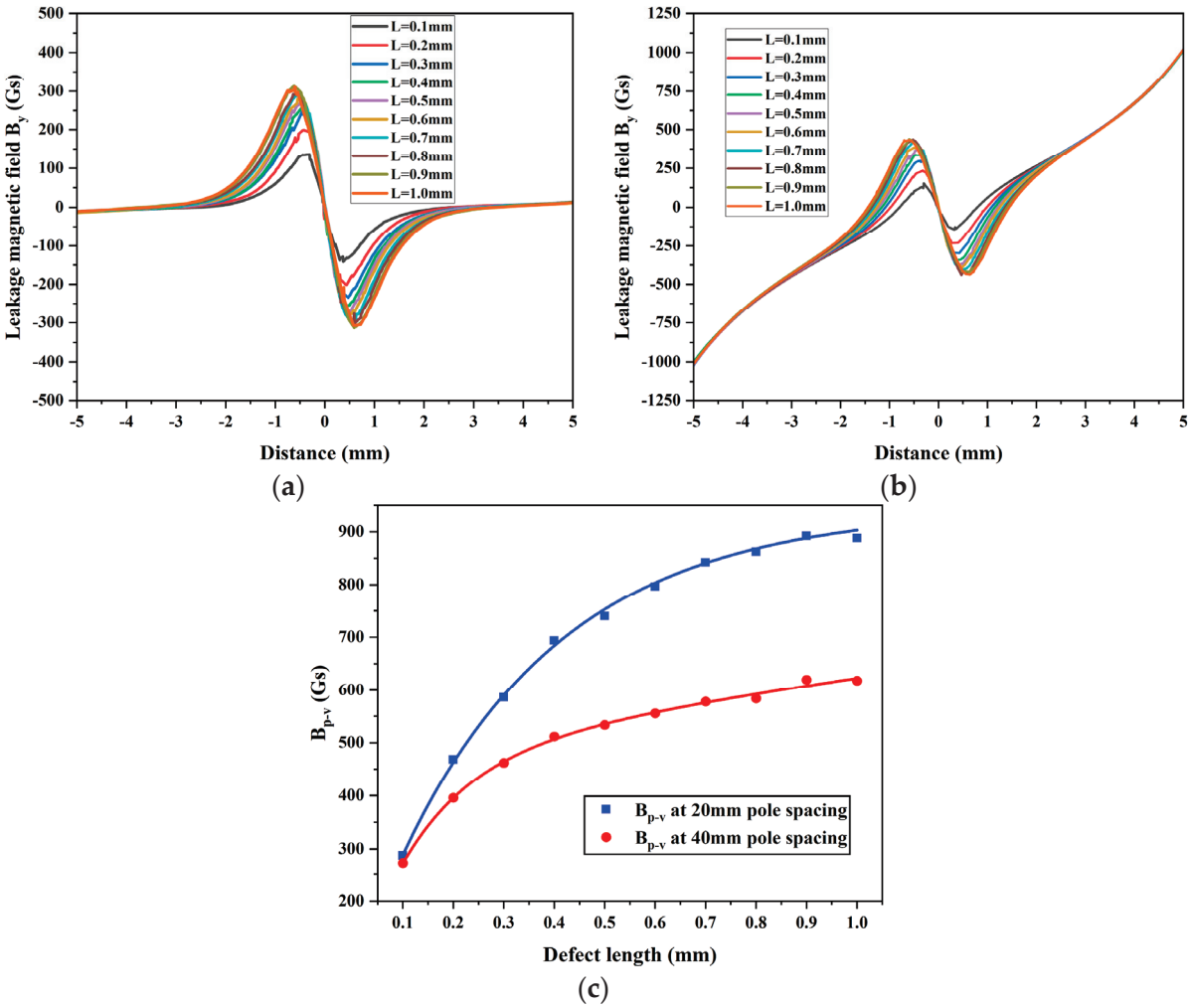

Figure 12. Leakage magnetic field B_y at smaller defect lengths: magnetic pole spacings of (**a**) 40 mm and (**b**) 20 mm, and (**c**) the variation in $B_{p\text{-}v}$.

4.3. The Effect of Wall Thickness on the Characteristics of MFL Signals

For a pipe defect of length L = 5 mm, width W = 3 mm, and depth D = 5 mm, the corresponding magnetic field B_y was simulated and calculated for wall thicknesses T = 6, 7, 8, 9, and 10 mm at magnetic pole spacings of 20 mm and 40 mm. The corresponding results are shown in Figure 13a,b, respectively. In addition, Figure 13c shows the variation in the $B_{p\text{-}v}$ of the magnetic field B_y as a function of the pipe wall thickness for different magnetic pole spacings.

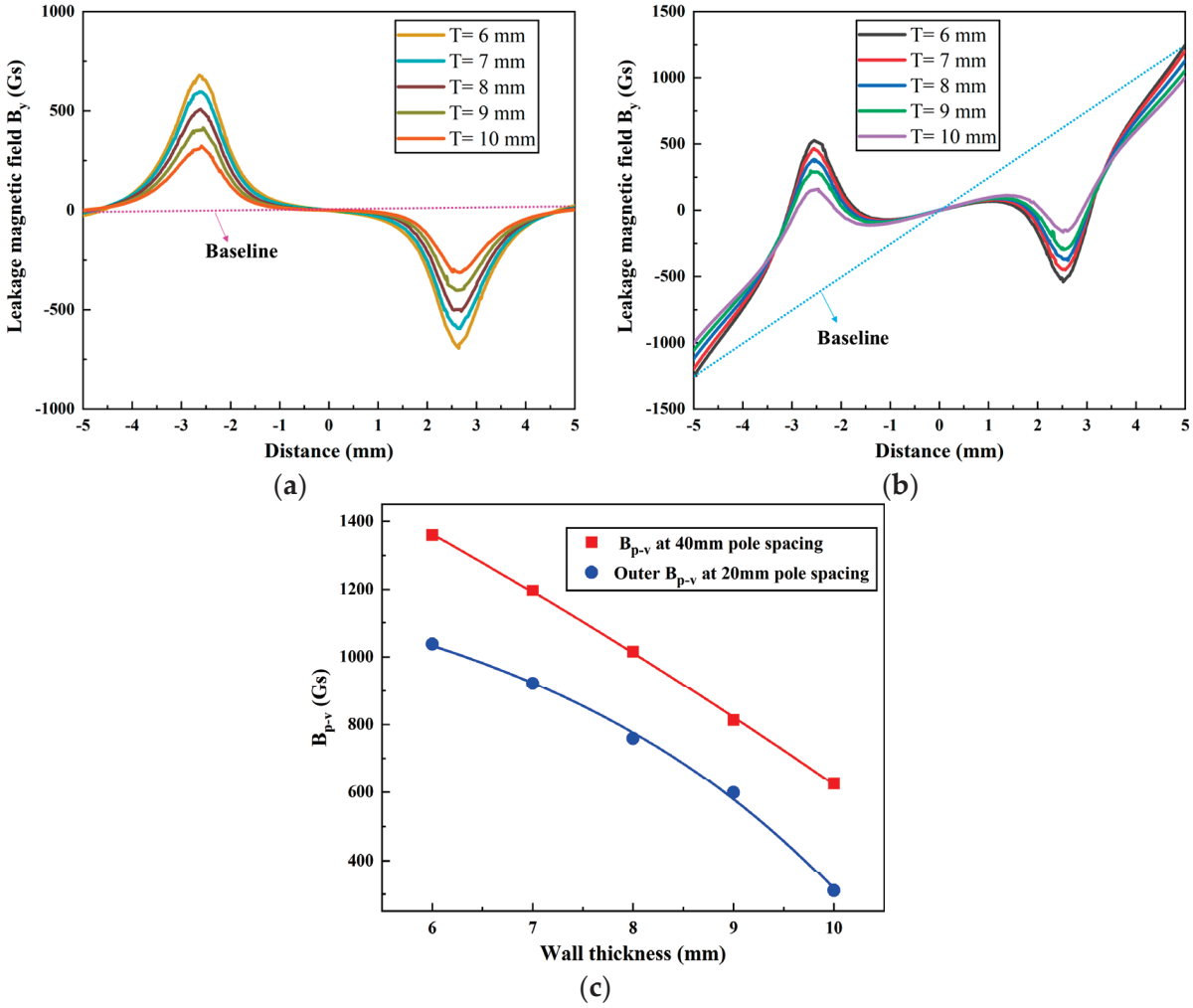

Figure 13. The leakage magnetic field B_y at different wall thicknesses: magnetic pole spacing of (**a**) 40 mm and (**b**) 20 mm, and (**c**) the variation in B_{p-v}.

As shown in Figure 13, when the pipe wall thickness increases from 6 mm to 10 mm, the average B_{p-v} at a spacing of 40 mm is approximately 276 Gs higher than that at 20 mm. Additionally, at 40 mm, B_{p-v} decreases by 734 Gs. At 20 mm, the outer B_{p-v} decreases by 734 Gs. It is noteworthy that the reduction in signal intensity appears to be similar regardless of the magnetic pole spacing used. In conclusion, increasing the wall thickness has a negative effect on MFL detection and has a similar effect on the MFL signal at different pole spacings.

4.4. The Effect of the Geometrical Height of the Magnetic Pole and Rigid Brush on the Characteristics of MFL Signals

In this section, the effects of the height of the magnetic pole (5 mm, 10 mm, 15 mm, 20 mm, 25 mm, and 30 mm) and rigid brush (5 mm, 10 mm, 15 mm, 20 mm, 25 mm, and 30 mm) on the MFL signals with different pole spacings are investigated using FEM simulations. The results are shown in Figures 14 and 15, respectively.

As illustrated in Figure 14a,b, the amplitude of the MFL signal at the two pole spacings appears to increase with the magnetic pole height. This is due to an increase in the size and magnetizing ability of the magnet, which leads to an increase in the strength of the leakage magnetic field. As indicated by the results for the pole spacing of 20 mm, the magnetic pole height does not have a significant effect on the magnitude of the DPV signal.

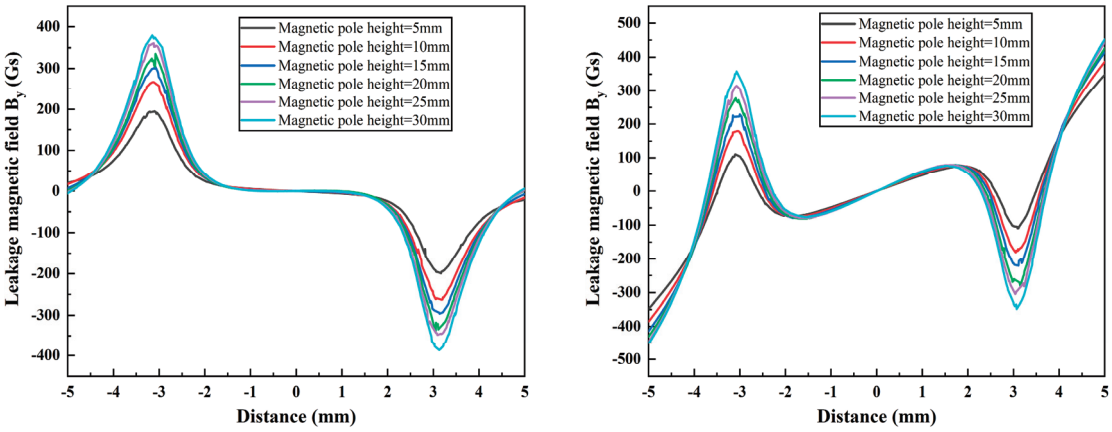

Figure 14. The leakage magnetic field B_y at different magnetic pole heights, with magnetic pole spacings of (**a**) 40 mm and (**b**) 20 mm.

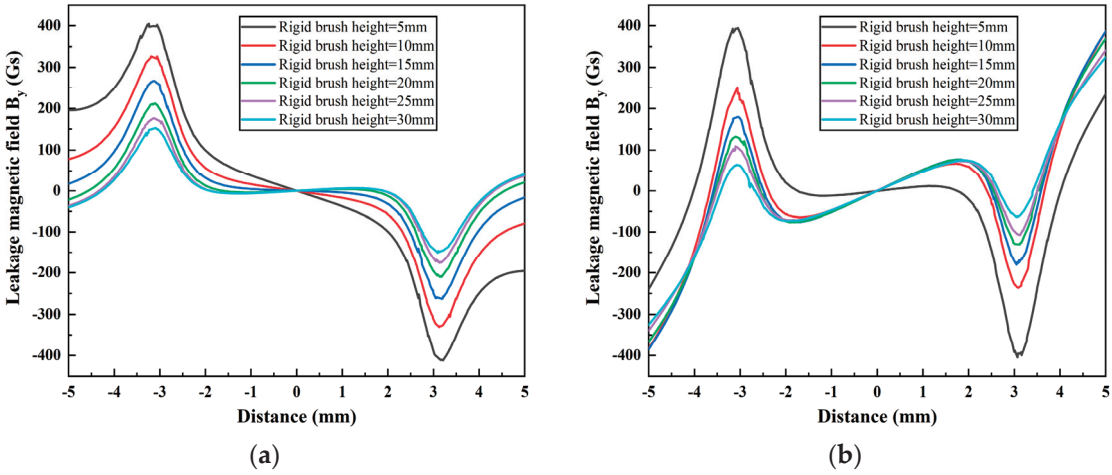

Figure 15. The leakage magnetic field B_y at different rigid brush heights, with magnetic pole spacings of (**a**) 40 mm and (**b**) 20 mm.

Figure 15a,b illustrate that the MFL signal amplitude tends to increase at both pole spacings as the rigid brush height decreases. This is due to the fact that a reduction in the height of the rigid brushes results in a reduction in the magnetic flux required to magnetize the rigid brushes, while simultaneously reducing the leakage flux of the rigid brushes in the magnetic circuit. This, in turn, increases the magnetic flux in the wall of the ferromagnetic tube and enhances the strength of the leakage magnetic field. At a pole spacing of 20 mm, the reduction in the rigid brush height weakens the characteristics of the DPV signal. In particular, when the rigid brush height is reduced to 5 mm, the DPV phenomenon almost disappears, and the degree of sudden change in the signal amplitude at the two ends of the sweep range is also reduced. This indicates that the height of the rigid brush can be reduced to diminish the DPV of the MFL signal. The rationale behind this phenomenon will be elucidated in greater detail in Section 4.5.

4.5. Theoretical Analysis of the Mechanisms of DPV Phenomena

It is worth noting that, in both the experiments and FEM simulations, the magnetic field B_y curves at the ends of the scan range become even steeper as the magnetic pole spacing decreases. In some cases, the difference in signal values between the two ends exceeds the inner and outer $B_{p\text{-}v}$. This can cause the peak-to-valley difference in the MFL signals of the pipe defects to be overshadowed by the MFL signal curves at the ends of the scan range during actual inspection scenarios. As a result, it becomes difficult to distinguish

the MFL signals associated with pipe defects. This scarcity is primarily attributed to the presence of significant background magnetic fields. The interaction between the magnetic poles generates a background magnetic field above the defect [29]. As the magnetic field lines move away from the north pole, they exhibit closed-loop behavior and enter the south pole, causing a change in direction as they leave and enter the poles. See Figure 16a for a detailed illustration of this phenomenon. As the magnetic field lines approach the magnetic pole, they tend to converge towards it, resulting in an increased density of field lines. This ultimately results in a higher magnetic field intensity in the vicinity of the magnetic pole. As shown in Figure 16b, the FEM simulation provides clear evidence of the magnetic field distribution between the two magnetic poles and further confirms the previous conclusions.

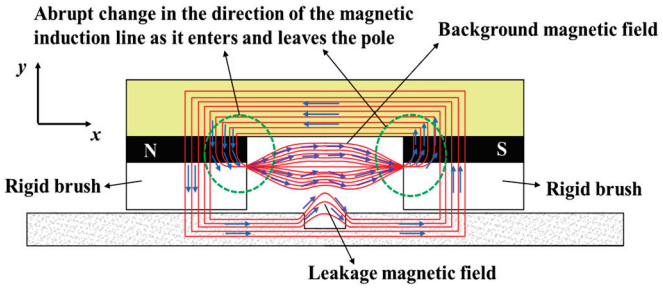

(**a**)

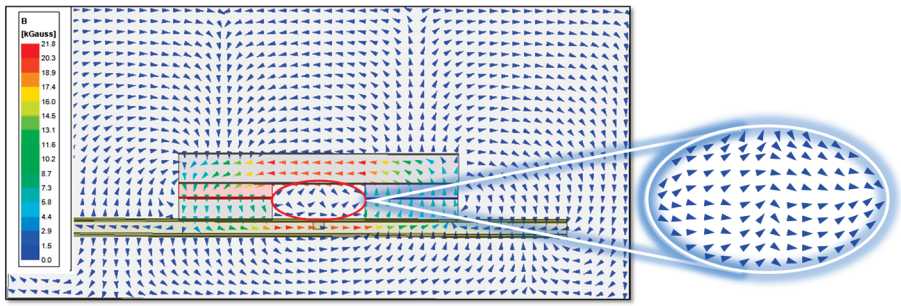

(**b**)

Figure 16. Schematic diagrams of the background magnetic field and defect leakage magnetic field: (**a**) magnetic field line diagram; (**b**) magnetic field vector diagram.

In general, the scanning range selected by the sensor is much smaller than the distance between the magnetic poles, which means that there is only a relatively stable background magnetic field within the scanning range. However, if the distance between the magnetic poles is too small, the detection area above the defect becomes very limited due to the restricted space. As a result, the sensor may collect magnetic field signals from the vicinity of the magnetic pole, where the direction and intensity of the magnetic field lines change abruptly within the background magnetic field.

The DPV phenomenon in the magnetic field B_y is also attributed to the background magnetic field. As the magnetic pole spacing decreases, a narrow detection region is formed due to the presence of a strong background magnetic field. When the background magnetic field is aligned parallel to the leakage magnetic field, their magnetic fields impede each other's diffusion, resulting in a magnetic compression effect [29]. As shown in Figure 17, this effect compresses the leakage field in the air from distribution 'a' to 'b', resulting in a decrease in the intensity of the leakage magnetic field. As the magnetic pole spacing decreases, the detection area encounters an uneven distribution of MFL signals due to the influence of the magnetic compression effect [24]. Consequently, multiple directional MFL signals overlap, ultimately leading to the formation of DPV.

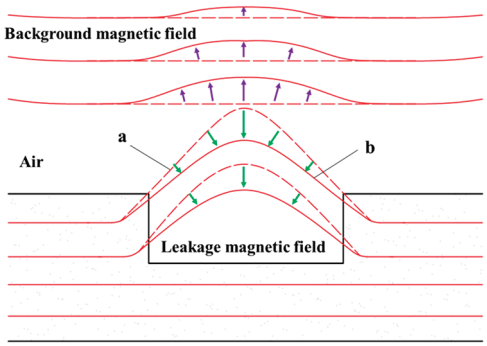

Figure 17. Schematic diagram of the magnetic compression effect.

Based on the above findings, the presence of a background magnetic field significantly influences the DPV phenomenon. Therefore, this paper further investigated the effects of shielding the background magnetic field on this phenomenon. As documented in the literature [30], when a ferromagnetic material is magnetized, a magnetic flux leaks from the ferromagnetic material into the air, which is known as refractive flux. However, this leakage can be mitigated by employing a closed magnetic circuit. The simulation results depicted in Figure 16 illustrate that, within the MFL detection device, the background magnetic field is mainly formed by the refraction of the leakage flux from the rigid brushes on both sides to the air domain above the defect; that is, the magnetic circuit forms an open circuit in the rigid brush part. Building upon this analysis, in this section, the height of the rigid brushes is set to zero and the ferromagnetic pipe wall is magnetized directly using the magnetizing device (yoke and poles) to establish a closed magnetic circuit, thereby eliminating the background magnetic field. The subsequent verification utilizing FEM, as shown in Figure 18a, demonstrates that, upon removing the background magnetic field generated by the rigid brush, the MFL signal's amplitude increases solely with the reduction in magnetic pole spacing, and there is no DPV phenomenon or sharp increase in the signal amplitude at either end of the sweep range. This suggests that the background magnetic field is the direct cause of the DPV phenomenon observed in the MFL signal.

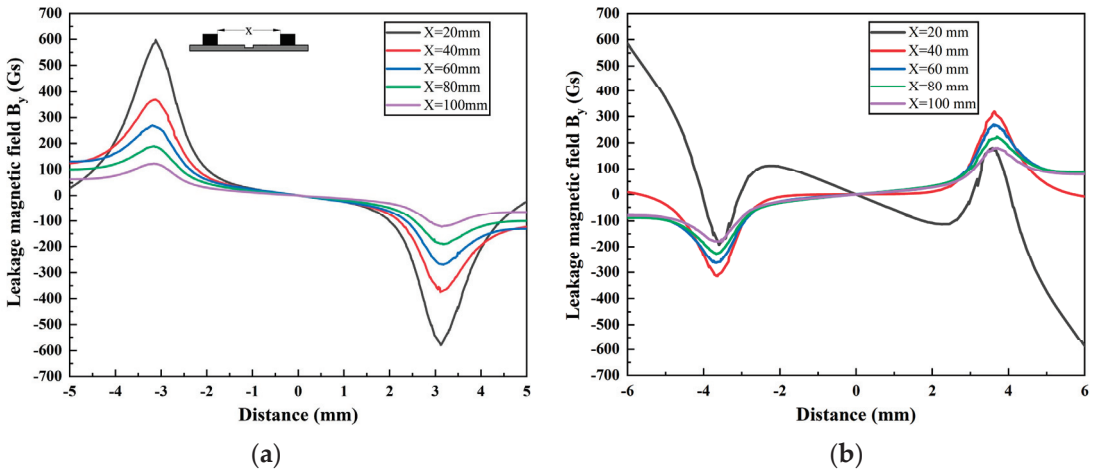

Figure 18. Leakage magnetic field variation at different pole spacings: (**a**) shielded background magnetic field; (**b**) altered pole directions.

Additionally, this paper explores the influence of the direction of the background magnetic field on the DPV phenomenon. We reversed the N and S pole directions of the two magnetic poles in the FEM depicted in Figure 2a and simulated the MFL signals for magnetic pole spacings of 20 mm, 40 mm, 60 mm, 80 mm, and 100 mm. The simulation results are illustrated in Figure 18b. Even when the pole spacing is 20 mm, the MFL signal

exhibits a clear DPV phenomenon. In comparison with Figure 5b, the amplitude of the MFL signal remains largely unchanged; only the signal direction varies.

5. Conclusions

This study delves into the impact of smaller magnetic pole spacings on the propagation characteristics of MFL signals using a leakage magnetic field FEM and a physical experiment. Moreover, the effects of defect size, pipeline wall thickness, and magnetic pole and rigid brush height on the MFL signals are also investigated under smaller pole spacings. The following conclusions are drawn:

With the reduction in magnetic pole spacing, a novel signal phenomenon emerges within the radial MFL signal. This phenomenon, termed the DPV, is distinguished by an outer peak and valley enclosing an inner peak and valley. Moreover, the signal amplitude at both ends of the sweep range also exhibits a sharp increase. The formation of this phenomenon can be attributed to the magnetic diffusion and compression interactions between the background magnetic field and the defect leakage magnetic field. The background magnetic field is primarily generated by the leakage magnetic flux of the rigid brush. By reducing the height of the rigid brush, the leakage magnetic flux from the rigid brushes can be diminished, thereby reducing the intensity of the background magnetic field and ultimately eliminating the DPV phenomenon. However, neither the pipe wall thickness nor the magnetic pole height exhibits a significant influence on the DPV phenomenon within the MFL signal. In comparison to the MFL signal under conventional magnetic pole spacing, the DPV signal at small pole spacing diminishes the detectable depth range of defects but enhances the identification rate of defects with small opening dimensions.

Author Contributions: Conceptualization, W.L. and L.R.; methodology, W.L.; software, W.L.; validation, W.L., L.R., and G.T.; formal analysis, W.L.; investigation, W.L.; resources, G.T.; data curation, W.L.; writing—original draft preparation, W.L.; writing—review and editing, L.R.; visualization, W.L.; supervision, L.R.; project administration, G.T.; funding acquisition, G.T. All authors have read and agreed to the published version of the manuscript.

Funding: This research was funded by the Key R&D Program of Shandong Province, China; grant number 2022SFGC0801.

Institutional Review Board Statement: Not applicable.

Informed Consent Statement: Not applicable.

Data Availability Statement: Due to the confidentiality requirements of the project responsible unit, the data provided in this study should be provided at the request of the corresponding author, because the project has not yet been concluded.

Conflicts of Interest: The authors declare no conflicts of interest.

References

1. Zhang, H.G.; Jiang, L.; Liu, J.H.; Qu, F.M. Data Recovery of Magnetic Flux Leakage Data Gaps Using Multifeature Conditional Risk. *IEEE Trans. Autom. Sci. Eng.* **2021**, *18*, 1064–1073. [CrossRef]
2. Peng, X.; Anyaoha, U.; Liu, Z.; Tsukada, K. Analysis of Magnetic-Flux Leakage (MFL) Data for Pipeline Corrosion Assessment. *IEEE Trans. Magn.* **2020**, *56*, 15. [CrossRef]
3. Kasai, N.; Maeda, T.; Tamura, K.; Kitsukawa, S.; Sekine, K. Application of risk curve for statistical analysis of backside corrosion in the bottom floors of oil storage tanks. *Int. J. Press. Vessel. Pip.* **2016**, *141*, 19–25. [CrossRef]
4. Feng, B.; Wu, J.; Tu, H.; Tang, J.; Kang, Y. A Review of Magnetic Flux Leakage Nondestructive Testing. *Materials* **2022**, *15*, 7362. [CrossRef] [PubMed]
5. Yigzew, F.E.; Kim, H.; Mun, S.; Park, S. Non-destructive damage detection for steel pipe scaffolds using MFL-based 3D defect visualization. *J. Civ. Struct. Health Monit.* **2024**, *14*, 501–509. [CrossRef]
6. Jiang, L.; Zhang, H.G.; Liu, J.H.; Shen, X.K.; Xu, H. THMS-Net: A Two-Stage Heterogeneous Signals Mutual Supervision Network for MFL Weak Defect Detection. *IEEE Trans. Instrum. Meas.* **2022**, *71*, 9. [CrossRef]
7. Kim, H.M.; Park, G.S. A New Sensitive Excitation Technique in Nondestructive Inspection for Underground Pipelines by Using Differential Coils. *IEEE Trans. Magn.* **2017**, *53*, 4. [CrossRef]

8. Kopp, G.; Willems, H. Sizing limits of metal loss anomalies using tri-axial MFL measurements: A model study. *NDT E Int.* **2013**, *55*, 75–81. [CrossRef]
9. Long, Y.; Huang, S.L.; Peng, L.S.; Wang, S.; Zhao, W. A Novel Compensation Method of Probe Gesture for Magnetic Flux Leakage Testing. *IEEE Sens. J.* **2021**, *21*, 10854–10863. [CrossRef]
10. Wu, J.B.; Sun, Y.H.; Kang, Y.H.; Yang, Y. Theoretical Analyses of MFL Signal Affected by Discontinuity Orientation and Sensor-Scanning Direction. *IEEE Trans. Magn.* **2015**, *51*, 7.
11. Wang, Y.J.; Melikhov, Y.; Meydan, T. Dipole modelling of temperature-dependent magnetic flux leakage. *NDT E Int.* **2023**, *133*, 9. [CrossRef]
12. Liu, B.; Luo, N.; Feng, G. Quantitative Study on MFL Signal of Pipeline Composite Defect Based on Improved Magnetic Charge Model. *Sensors* **2021**, *21*, 3412. [CrossRef]
13. Wu, L.B.; Yao, K.; Shi, P.P.; Zhao, B.X.; Wang, Y.S. Influence of inhomogeneous stress on biaxial 3D magnetic flux leakage signals. *NDT E Int.* **2020**, *109*, 17. [CrossRef]
14. Antipov, A.G.; Markov, A.A. Using a Tail Field in High-Speed Magnetic Flux Leakage Testing. *J. Nondestruct. Eval.* **2022**, *41*, 9. [CrossRef]
15. Feng, B.; Deng, K.X.; Wang, S.H.; Chen, S.K.; Kang, Y.H. Theoretical Analysis on the Distribution of Eddy Current in Motion-Induced Eddy Current Testing and High-Speed MFL Testing. *J. Nondestruct. Eval.* **2022**, *41*, 6. [CrossRef]
16. Pullen, A.L.; Charlton, P.C.; Pearson, N.R.; Whitehead, N.J. Magnetic Flux Leakage Scanning Velocities for Tank Floor Inspection. *IEEE Trans. Magn.* **2018**, *54*, 8. [CrossRef]
17. Pullen, A.L.; Charlton, P.C.; Pearson, N.R.; Whitehead, N.J. Practical evaluation of velocity effects on the magnetic flux leakage technique for storage tank inspection. *Insight* **2020**, *62*, 73–80. [CrossRef]
18. Usarek, Z.; Chmielewski, M.; Piotrowski, L. Reduction of the Velocity Impact on the Magnetic Flux Leakage Signal. *J. Nondestruct. Eval.* **2019**, *38*, 7. [CrossRef]
19. Peng, L.; Huang, S.; Wang, S.; Zhao, W. A Simplified Lift-Off Correction for Three Components of the Magnetic Flux Leakage Signal for Defect Detection. *IEEE Trans. Instrum. Meas.* **2021**, *70*, 6005109. [CrossRef]
20. Feng, J.; Lu, S.; Liu, J.; Li, F. A Sensor Liftoff Modification Method of Magnetic Flux Leakage Signal for Defect Profile Estimation. *IEEE Trans. Magn.* **2017**, *53*, 6201813. [CrossRef]
21. Liu, B.; Liang, Y.S.; He, L.Y.; Lian, Z.; Geng, H.; Yang, L.J. Quantitative study on the propagation characteristics of MFL signals of outer surface defects in long-distance oil and gas pipelines. *NDT E Int.* **2023**, *137*, 11. [CrossRef]
22. Deng, Z.Y.; Sun, Y.H.; Yang, Y.; Kang, Y.H. Effects of surface roughness on magnetic flux leakage testing of micro-cracks. *Meas. Sci. Technol.* **2017**, *28*, 13. [CrossRef]
23. Yousaf, J.; Harseno, R.W.; Kee, S.-H.; Yee, J.-J. Evaluation of the Size of a Defect in Reinforcing Steel Using Magnetic Flux Leakage (MFL) Measurements. *Sensors* **2023**, *23*, 5374. [CrossRef]
24. Huang, S.; Wang, S. Magnetic Flux Leakage Testing. In *New Technologies in Electromagnetic Non-Destructive Testing*; Springer Series in Measurement Science and Technology; Springer: Singapore, 2016; pp. 185–222.
25. Haifeng, L.; Xiuyan, W.; Renyang, H.; Tao, M.; Cunfu, H.; Bin, W. Study on simulation and experiment of magnetic flux leakage inspection for inner pipeline. *Transducer Microsyst. Technol.* **2009**, *28*, 61–64.
26. Long, Y.; Huang, S.L.; Peng, L.S.; Wang, S.; Zhao, W. A Characteristic Approximation Approach to Defect Edge Detection in Magnetic Flux Leakage Testing. In Proceedings of the Joint Conference of Conference on Precision Electromagnetic Measurements (CPEM) and Conference of NCSL-International (NCSLI), Electr Network, Denver, CO, USA, 24–28 August 2020.
27. Li, F.M.; Feng, J.; Zhang, H.G.; Liu, J.H.; Lu, S.X.; Ma, D.Z. Quick Reconstruction of Arbitrary Pipeline Defect Profiles from MFL Measurements Employing Modified Harmony Search Algorithm. *IEEE Trans. Instrum. Meas.* **2018**, *67*, 2200–2213. [CrossRef]
28. Ji, F.Z.; Wang, C.L.; Sun, S.Y.; Wang, W.G. Application of 3-D FEM in the simulation analysis for MFL signals. *Insight* **2009**, *51*, 32–35. [CrossRef]
29. Sun, Y.H.; Kang, Y.H. Magnetic compression effect in present MFL testing sensor. *Sens. Actuator A-Phys.* **2010**, *160*, 54–59. [CrossRef]
30. Sun, Y.H.; Kang, Y.H. A new MFL principle and method based on near-zero background magnetic field. *NDT E Int.* **2010**, *43*, 348–353. [CrossRef]

materials

MDPI

Article

Analysis of the Suitability of Ultrasonic Testing for Verification of Nonuniform Welded Joints of Austenitic–Ferritic Sheets

Łukasz Rawicki [1], Ryszard Krawczyk [2], Jacek Słania [1,2], Grzegorz Peruń [3,*], Grzegorz Golański [4] and Katarzyna Łuczak [5]

[1] GIT Łukasiewicz Research Network—Upper Silesian Institute of Technology, K. Miarki 12-14, 44-100 Gliwice, Poland; lukasz.rawicki@git.lukasiewicz.gov.pl (Ł.R.); jacek.slania@git.lukasiewicz.gov.pl (J.S.)
[2] Faculty of Mechanical Engineering and Computer Science, Częstochowa University of Technology, Armii Krajowej 21, 42-201 Częstochowa, Poland; ryszard_krawczyk@wp.pl
[3] Department of Road Transport, Faculty of Transport and Aviation Engineering, Silesian University of Technology, Krasińskiego 8, 40-019 Katowice, Poland
[4] Department of Material Engineering, Częstochowa University of Technology, Armii Krajowej 19, 42-201 Częstochowa, Poland; grzegorz.golanski@pcz.pl
[5] Faculty of Architecture, Civil Engineering and Applied Arts, Academy of Silesia, Rolna 43, 40-555 Katowice, Poland; katarzyna.luczak@wst.com.pl
* Correspondence: grzegorz.perun@polsl.pl

Abstract: The purpose of the presented research was to determine the suitability of using ultrasonic testing (UT) to inspect heterogeneous, from a material point of view, welded joints on the example of the joints of a ferritic steel element with elements made of an austenitic steel. The echo technique with transverse (SEK) and longitudinal wave heads (SEL) addressed this issue. Due to the widespread use of 13CrMo4-5 and X2CrNiMo17-12-2 steel grades in the energy industry, they were selected as the test materials for the study. The objects of the presented research were welded joint specimens with thicknesses of 8, 12, and 16 mm and dimensions of 300 × 300 mm, made using the 135 metal active gas (MAG) process with the use of the Lincoln 309LSi wire—a ferritic–austenitic filler material. The stages of the research task were (1) making distance–amplitude curve (DAC) patterns from the test materials; (2) preparation of specimens of welded joints with artificial discontinuities in the form of through-holes; (3) performing UT tests on welded joints with artificial discontinuities using heads with 60° and 70° angles for the transverse wave and angle heads for longitudinal waves with similar beam insertion angles; (4) selection, by radiographic testing (RT), of welded joint specimens with natural discontinuities in the form of a lack of sidewall fusion; (5) performing UT tests on welded joints with natural discontinuities, using heads as welded joints with artificial discontinuities. It was found that (1) the highest sensitivity of discontinuity detection was obtained by performing tests on the ferritic steel side, which is due to the lower attenuation of the ultrasonic wave propagating in ferritic steel compared to austenitic steel; (2) the best detection of discontinuities could be obtained using a longitudinal ultrasonic wave; (3) there is a relationship between the thickness of the welded elements, the angle of the ultrasonic beam introduction, and the effectiveness of discontinuity detection.

Keywords: ultrasonic inspection; austenitic steel; ferritic steel; DAC; 13CrMo4-5; X2CrNiMo17-12-2 (AISI 316L)

1. Introduction

Welding processes are classified as special processes, that is, processes whose results cannot be predicted while they are in progress and potential imperfections may only become apparent after completion. It is therefore crucial to test welded joints, with the recommended methods being volumetric non-destructive methods, which include ultrasonic testing (UT). In the case of heterogeneous joints, the issue with carrying out ultrasonic testing is the differing physical properties of the various zones of the welded joint, which

are related to the conditions under which these tests are performed. For example, in UT testing of austenitic steels, the problem is wave transformation, limited detection of subsurface weld discontinuities, and abnormal coupling due to surface roughness. These issues are discussed in more detail in [1,2]. The coarse-grained structure causes scattering and attenuation of the wave and changes its direction. Attenuation affects the pressure amplitude of the wave propagating through the material, which decreases with increasing distance from the head [3]. In the case of heterogeneous joints, there are differences in the measured amplitude values in different areas of the joint. The primary factors limiting the detection of discontinuities are beam scattering and divergence, which are influenced by the material's structural properties. These phenomena are particularly pronounced in the assessment of nonuniform welded joints [4].

The necessity to join materials with significantly disparate physical properties by welding methods is a common occurrence in the field of mechanical engineering, including in the construction of power equipment, reactors, and chemical installations. For instance, in power boilers, heat exchanger tubes operating at exceedingly high temperatures are manufactured from austenitic steels and joined with plant components fabricated from ferritic steels. Austenitic–ferritic and duplex steels are employed in the fabrication of chemical tankers. Furthermore, structural elements in joints with tank components made of duplex steels are also examples of joints of heterogeneous materials, in this case usually with high-strength carbon steel [5]. The popularity of these materials in the construction of nuclear power plant installations around the world is due to their high durability and corrosion resistance. In this case, safety considerations require the implementation of tests to determine the correctness of the technical condition of the components, which are carried out by non-destructive testing at specified intervals. One of the main methods of implementing such tests, despite the difficulties outlined earlier, is the ultrasonic technique.

The fundamental principle of ultrasonic testing, assuming a known and constant speed of sound, is to relate the time of the received echo to the location of the reflector. However, in the case of austenitic welded joints, where the microstructure with large oriented austenitic grains induces local velocity differences that deflect the ultrasonic beam, this assumption is not valid [6]. Furthermore, the testing problem is complicated by scattering at grain boundaries, causing structural noise and attenuation. For this reason, a number of solutions have been proposed, including the embedding of material information and the weld structure into imaging algorithms. This usually improves the quality of the images and aids interpretation [7].

One of the research projects at UT that was engaged in the study of the nuclear industry is [8]. The study examined the ultrasonic behavior of beams in relation to the orientation of grains in the weld joint. The study employed both conventional ultrasonic transducers and linear and matrix phase transducers to generate ultrasonic beams. To enhance the efficacy of ultrasonic non-destructive testing within this industry, a methodology for modeling ultrasonic inspection of such welds, which has been successfully applied to arc welding, was presented in Ref. [9]. The paper also presented the results of laboratory tests on the repair of a nickel-based alloy weld made using an automatic tungsten arc welding process, with particular attention paid to ultrasonic propagation interferences, including anisotropic, heterogeneous, and coarse-grained weld structures of austenitic stainless steel.

The primary factors contributing to the difficulty of inspecting austenitic steels and joints of these steels with ferritic steels by degradation of image quality presented in Ref. [10] are time errors, phase errors, and multipath propagation and scattering. They were selected based on experimental studies conducted during the inspection of austenitic welds with high inhomogeneity and anisotropy.

During ultrasonic testing of nonuniform welded joints, measurement parameters are very often chosen experimentally. This is due to the fact that, at present, no standards and regulations specify criteria for evaluating volumetric testing of such joints by ultrasonic methods. This makes it necessary to determine test parameters that will provide the

necessary conditions to detect discontinuities in the analyzed case of welded joints PN-EN ISO 11666:2018-04 [11].

The purpose of this paper is to present the methodology and to learn the cognitive qualities that are the starting point for the study of welded joints of miscellaneous materials. Due to their peculiarities, joints of this type require a different approach to the study of classical ferritic steels. The testing capabilities have been verified on reference specimens made from the test materials. This type of joint is used in the energy, petrochemical, and chemical industries. A heterogeneous welded joint is, among other things, a configuration of two different base materials and the welding of base materials with an additional material with different properties.

2. A Brief Overview of UT Research Directions in the Literature

The testing of ferritic steels with UT generally poses no difficulties. The most common technique for testing ferritic welds is the echo method, which utilizes vibration frequencies of 2–5 MHz in materials with a fine-grained structure. However, the issue of testing austenitic steels is a significant concern for many researchers, with several works, including [12,13], providing detailed descriptions of the problem. The large grain size and high ultrasonic attenuation are identified as the source of the problem. The authors note the difficulty of penetrating deep into the material, since stainless steel is also an anisotropic material, meaning that ultrasonic properties vary depending on the direction of propagation. It has been demonstrated that conventional techniques have shown limited success in inspecting welded joints and that the use of various phase matrix techniques is recommended for the inspection of stainless steel components. Ref. [14] addresses the subject of offline post-processing techniques using the full set of time-domain data from all combinations of transmit and receive elements. The authors define the mathematical and practical implementation of four post-processing algorithms for use with the full matrix of array data: plane B-scan, focused B-scan, sector B-scan, and the total focusing method (TFM). The main advantages of these approaches are increased sensitivity to small defects and increased inspection coverage.

In Ref. [15], the application of mechanized ultrasonic inspection to the examination of austenitic stainless steel test blocks with various types of defects, including intergranular stress corrosion cracking, is described. The results demonstrated that cracks located in the weld's heat-affected zone are relatively easily detected due to the ability to perform inspection from both sides of the weld. However, in the event of restricted accessibility, when the inspection is conducted solely from one side of the weld, the differentiation of signals emanating from the dissipation within the weld and those indicative of cracks presents a significant challenge.

The influence of alloy composition and welding line energy of two Ni-Cr-Fe alloys on the crystallographic structure and the characterization of the effect on ultrasonic propagation was investigated in Ref. [16]. Samples made entirely of weld metal were examined using ultrasonic testing, and then, characterized using large-area backscattered electron diffraction. The pseudo-single-crystal structure exhibited significant variations in the UT scan outcomes when the ultrasonic beam angle was altered in relation to the texture direction. However, the observed discrepancies in the UT scans with regard to the texture direction were less pronounced, attributable to the fact that the fiber texture was predominantly oriented along a single crystallographic axis and tended to be random in other orientations.

Ref. [17] presents a novel phase-matching technique, designated as "reverse phase matching". The technique employs a ray-tracing algorithm to model the propagation of an acoustic wave and calculate the sound propagation time, taking into account the anisotropy and inhomogeneity of the weld structure. According to the researchers, this technique can be used to reconstruct 2D and 3D images in real time. An iterative gradient constant descent method (GECDM) algorithm was implemented, which is essential for studying inhomogeneous anisotropic media with unknown properties.

The difficulties and complications associated with the application of NDT techniques to the peripheral welds of a urea reactor are examined in detail in [18]. The authors conducted a comprehensive review of the theory and advanced aspects of UPA technology and demonstrated that UPA is effective and efficient in solving the safety inspection of circumferential welds. Subsequently, two related test blocks (RB-2/20 and an austenitic stainless steel butt joint test block) with artificial defects were selected to simulate the outer and inner layers.

Ref. [19] presents phased array ultrasonic testing (PAUT) of trimetallic welded joints in a prototype fast breeder reactor (PFBR) using dual matrix array (DMA) probes. The inspection of SS316LN–Alloy 800 welds is challenging due to the anisotropic and inhomogeneous properties of the weld pool, which leads to beam skewing and affects the detection, location, and size of discontinuities. The PAUT test was conducted on an SS316LN to Alloy 800 welded joint section of trimetallic welded joints and verified by RT. A weld specimen (24 mm thick) with an artificial defect such as lack of sidewall fusion (LOF) was produced by metal arc welding and gas tungsten arc welding. The study demonstrated that the DMA probe successfully detected LOF defects and improved the signal-to-noise ratio in the inspection of trimetallic welded joints. This shows that the DMA probe is a promising candidate for the inspection of coarse-grained, anisotropic, and heterogeneous materials.

A specific research objective is presented in Ref. [20]. The authors decided to utilize the laser ultrasonic technique to identify grain size in interstitial steels (IFs). They assert that the ultrasonic technique can be employed online for direct grain size measurements during steel production. The absolute values of the average grain size were calculated directly from the ultrasonic traces. In turn, in [21], UT tests were conducted in order to determine the orientation of the grains in an anisotropic weld. The objective was to facilitate future ultrasonic NDT simulations of these types of welds, with the aim of obtaining more accurate results. A model was introduced, assuming the type of weld, the transmitter model, the receiver model, and the type of two-dimensional ray tracing algorithm.

The coarse-grained, dendritic grain structure of the weld material and its anisotropy are features detailed in numerous works on ultrasonic testing of austenitic welds [22,23]. The influence of these factors on ultrasonic wave propagation and their distortions has led many researchers to conclude that the use of conventional ultrasonic research techniques using constant beam angles is very limited and the use of phased array ultrasonic techniques is desirable. The enhancement of ultrasonic signals for coarse-grained materials through machine learning analysis is described in [24].

Ultrasonic array technology offers significant advantages over conventional ultrasonic technology, mainly due to its ability to focus and direct the beam and its electronic scanning capabilities [25]. Despite its advancement, ultrasound examination using this method still provides results that are difficult to evaluate. In the case of cast stainless steels, UT does not permit the achievement of sufficient measurement accuracy. In order to address this issue, in [26] a comprehensively analyzable phased array ultrasonic testing system (PAUT) was developed. The authors noted that the defect dependence of echo intensity differs from granular noise when PAUT conditions, such as focusing depths and ultrasonic incidence angles, are continuously changed.

3. Testing Techniques for Welded Joints

The efficacy of ultrasonic testing in detecting discontinuities is contingent upon a number of variables, including the characteristics of the ultrasonic beam and the ability of the discontinuities to reflect the wave. As previously demonstrated in [27], if the size of the discontinuity is less than half the wavelength, it will be bypassed and the discontinuity will not be detected, with the ultrasonic wave undergoing only slight scattering. This is related to the roughness of the tested surface. High roughness, characterized by discontinuities, causes strong scattering of the beam. However, it should be noted that part of the ultrasonic beam may reach the head and be analyzed by the flaw detector system. Surfaces characterized by low roughness will reflect the ultrasonic beam well. When performing

ultrasonic tests, the angle at which the ultrasonic wave beam is introduced into the tested material is also important. The largest echo can be obtained when the wave beam falls perpendicularly onto the surface of the discontinuity. This is in accordance with the findings presented in [28]. The angle formed by the direction of the incident wave and the plane of discontinuity is larger at higher frequencies than with head transducers using lower frequencies. At lower frequencies, the beam is more divergent, and part of the reflected wave more easily reaches the head at a specific location of discontinuities in the material.

The most frequently used technique for testing ferritic welds is the echo method. With a fine-grained material structure, vibration frequencies of 2–5 MHz are utilized. In an austenitic weld, a coarse-grained structure is formed as a result of the crystallization of the basic and additional materials. Consequently, a weld pool will be formed whose crystallite direction is parallel to the material thickness [29]. The side edges of the weld may be characterized by the deflection of crystallites in a direction perpendicular to the direction of the base material. In the case of austenitic welds, they are usually 10 mm long and 1 mm wide. The greater length may be the result of the greater thickness of the welding beads. The size of the grains and their exact orientation may depend on the type of material or technology used. The austenitic weld structure may exhibit features that impede the use of volumetric testing methods, such as the ultrasonic method. These features include the presence of elongated grain sizes, their orientation in the direction of thickness, or deviations in the orientation of crystallites near the fusion line.

The ultrasonic testing of various joints between low- and high-alloy steels and nickel alloys is typically more difficult than testing joints made of ferritic steels [30]. The issue of testing various welded joints is considered in terms of the structure influencing the propagation of the ultrasonic wave, the measurement technique, and the evaluation criteria. The factors that play an important role are the test parameters such as the ultrasonic wave used, the transmitting pulse, and the reduction in structural noise. The difficulties associated with conducting ultrasonic tests in welds of various joints may be caused by the coarse-grained or directionally oriented structure of the material, which can result in significant differences in attenuation, reflection, and refraction of waves at the grain boundaries. The lack of significant differences in the structure of the weld and the base material does not alter the procedure under the test conditions. The structure of the native material is usually fine-grained and does not pose any problems for the propagation of the ultrasonic beam. In such a case, the test is carried out similarly to the testing of ferritic steels. The structure of austenitic joints is most often heterogeneous and coarse-grained. The grains are oriented in the direction of heat dissipation, and the sizes of columnar crystallites often exceed several millimeters [31,32].

The structure of welds made of various materials gives rise to the occurrence of apparent indications which should not be taken into account when performing the test. In instances where indications are observed that do not originate from typical welding discontinuities, it has been found that the propagation speeds of ultrasonic waves are different. Furthermore, the acoustic wave resistances (impedance) are also different, and these values are characteristic of the type of wave and medium. High-alloy steels with a high chromium content, above 10%, may be prone to the segregation of components and excessive grain growth. The transition zone is particularly vulnerable to this phenomenon. Such phenomena may result in the appearance of false echoes that are difficult to interpret when performing ultrasound examinations [33].

Appropriate testing methodologies, taking into account sufficient sensitivity, enable the development of testing techniques for these welds. Oblique heads of transverse waves enable the examination of welds up to 25 mm thick. When examining welds whose thickness exceeds 25 mm, it is convenient to use oblique longitudinal wave heads. Testing with transverse waves polarized parallel to the surface where the waves are introduced also gives good results. The testing of welded joints of various materials should be based on the test results of test joints made using the same technological parameters. In this type of testing, an important issue is the possibility of access from both sides of the joint,

knowledge of the grain orientation, and an appropriately processed face surface. In order to test such joints, a detailed test procedure must be developed. This procedure should include provisions related to testing standards and provide possible exceptions. The elimination of difficulties encountered when testing materials with a strongly damping structure can be carried out by using appropriate measurement parameters such as the selection of the ultrasonic wave, frequency, and head angle [34].

The study of various connections, including low-alloy and austenitic steel, encounters difficulties related to the coarse-grained structure. Another issue is anisotropy, which is related to the direction-dependent wave propagation speed [35,36]. When testing diverse joints, another problem is the transformation of the ultrasonic wave occurring at the fusion line between the base material and the austenitic weld. The propagation of the ultrasonic beam is not linear, rather it exhibits a bending behavior in the vicinity of fusion lines and grain boundaries. This phenomenon results in beam splitting and the generation of virtual echoes due to the geometry of the shape [37].

The structural construction of various welded joints differs. Given the absence of a uniform welded joint comprising multiple sheets of steel, it is essential to select a testing technique that considers the properties of the base material, weld material, thickness of the tested element, welding method, and parameters, in accordance with the standards set forth in PN-EN ISO 22825:2017-12 [38].

Heterogeneity and a coarse-grained anisotropic structure result in incorrect localization of indications detected by ultrasound. The speed of wave propagation at various junctions, in addition to beam deflection, is the main source of errors in the location of discontinuities. In cases where ultrasonic testing does not detect unacceptable discontinuities (no echoes are obtained), in terms of size and intensity, these discontinuities do not exist in the welds. Nevertheless, in instances where echoes from discontinuities emerge in ultrasonic tests, indicating an unsatisfactory level of joint quality, and the discontinuities are located primarily in its transition zone, radiographic tests should be performed in accordance with the requirements of PN-EN ISO 22825:2017-12.

4. Purpose of the Study and Research Methodology

The purpose of this study is to determine the applicability of UT testing to the inspection of welded joints of heterogeneous materials—austenitic materials with ferritic materials. The echo technique and transverse and longitudinal wave heads have been used for this purpose. The 13CrMo4-5 and X2CrNiMo17-12-2 (according to the international designation AISI 316L) steels were selected as the test materials for the study due to their properties and widespread use in the power industry. The scope of the work included the testing of 8, 12, and 16 mm thick welded joints, 300 × 300 mm in size, produced by the 135 (MAG) process using Lincoln 309LSi (Lincoln, Poland) filler material (a welded joint between a ferritic steel component and an austenitic steel component using a ferritic–austenitic filler). The shielding gas used was an M12 mixture containing 97.5% Ar and 2.5% CO_2.

The various stages of the research task included:

- Making distance–amplitude curve (DAC) patterns from the test materials;
- Preparation of specimens of welded joints with artificial discontinuities in the form of through-holes;
- Performing UT tests on welded joints with artificial discontinuities using heads with 60° and 70° angles for the transverse wave and angle heads for longitudinal waves with similar beam insertion angles;
- Selection by radiographic testing (RT) of welded joint specimens with natural discontinuities in the form of a lack of sidewall fusion;
- Performing UT tests on welded joints with natural discontinuities using heads for welded joints with artificial discontinuities.

Low-alloy steel 13CrMo4-5 is a ferritic chromium–molybdenum steel with a relatively low carbon content compared to other related grades used for high-temperature work. It is

characterized by good cold and hot formability, very good machinability, and weldability while maintaining high strength properties at both ambient and elevated temperatures. This steel is used to produce parts of fittings for installations—heads, flanges, elbows, tees, profiles, seamless tubes, bars, bushes, forgings, flat bars, and hot-rolled sheets in various thicknesses and cross-sections. The above fittings are used for steam discharge lines and pipelines, as well as for superheater tubes. 13CrMo4-5 steel is mainly supplied in quenched and tempered, softening annealed, and normalized and tempered conditions. The approximate chemical composition of the steel is given in Table 1.

Table 1. Indicative chemical composition of 13CrMo4-5 steel.

C, %	Cr, %	Ni, %	Mn, %	Mo, %	Si, %
0.16	0.8	0.03	0.475	0.471	0.213

X2CrNiMo17-12-2 (316L) steel is an austenitic steel used for the manufacture of components used in the chemical, paper, automotive, and food industries [39]. It is also used for various types of filters and heat exchangers. It is resistant to intergranular corrosion and acetic and sulfuric acid. It is characterized by high ductility and plasticity and does not change its physical properties at elevated temperatures. The chemical composition of the steel, together with heat treatment conditions and tensile strengths, is given in Table 2.

Table 2. Indicative chemical composition of X2CrNiMo17-12-2 (316L) steel.

C, %	Cr, %	Ni, %	Mn, %	Mo, %	N, %
$\leq$0.03	17.5	11.5	$\leq$2	2.3	$\leq$0.11

The most popular welding wire for joining austenitic and ferritic steels is LNM 309LSi, a solid wire with an austenitic–ferritic structure for welding austenitic steels with low-alloy steels. The high Si content improves the wettability. The chemical composition of the wire is given in Table 3, and the mechanical properties are given in Table 4.

Table 3. Indicative chemical composition of LNM 309LSi wire.

C, %	Cr, %	Ni, %	Mn, %	Mo, %	Si, %
0.02	23.3	13.8	1.8	0.14	0.8

Table 4. Selected physical properties of LNM 309LSi wire.

Parameter	Unit	Value
Average coefficient of thermal expansion at 20 ÷ 200 °C	1/K	16.5×10^{-6}
Average coefficient of thermal expansion at 20 ÷ 400 °C	1/K	17.5×10^{-6}
Thermal conductivity at 20 °C	W/(m K)	15
Specific heat capacity at 20 °C	J/(kg K)	500
Specific electrical resistance at 20 °C	Ω mm^2/m	0.75
Density at 20 °C	kg/dm^3	8.0
Modulus of elasticity at 20 °C	MPa	200

www.lincolnelectric.com/en/Products/lincolner309si309lsi_gtaw (accessed on 28 June 2024)

The tests were carried out on prepared welds with artificial and natural discontinuities of 8, 12, and 16 mm thickness. Figure 1 shows the elements of the weld groove and the parameters used. The resulting butt joints used a V-type weld groove bevel, which is the most common practice in industrial applications for the MAG welding method. The bevel angle was 25°. The weld thicknesses used reflect those most commonly used for industrial components.

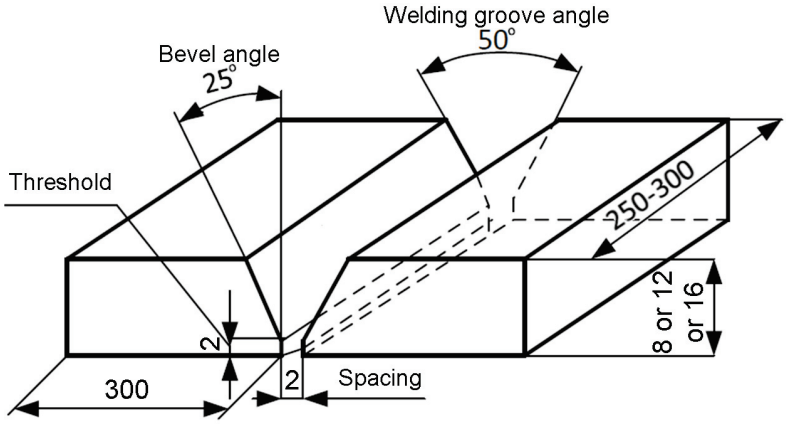

Figure 1. Welding groove components.

Figure 2 shows the patterns prepared for testing with through-holes drilled perpendicular to the surface of the welded joints to provide a reference line on the screen of the ultrasonic defectoscope. The set of standards used in the tests included welded plates and discs made of the materials to be tested. These were required to set the velocity of the transverse waves and the divergence of the longitudinal waves.

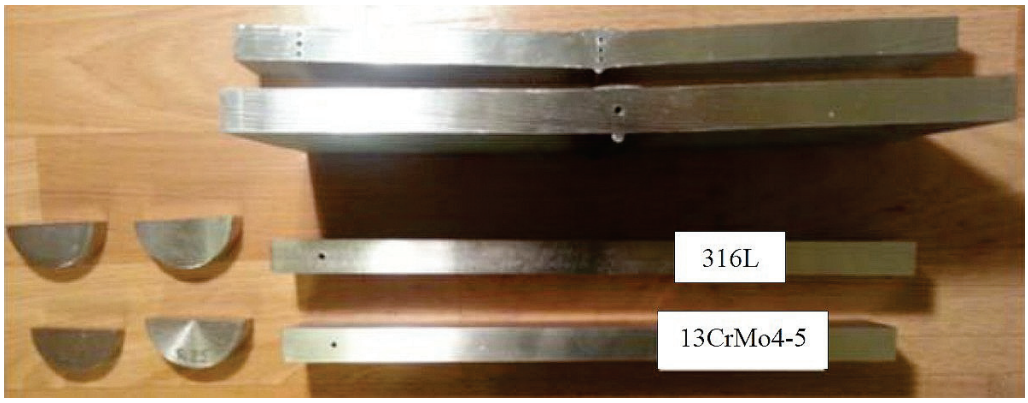

Figure 2. Patterns made from the materials under test.

Reference reflectors in accordance with EN ISO 17640 [40], in the form of through-holes 3 mm in diameter and 30 mm in length, drilled perpendicular to the surface of the specimen at various locations on the welded joints were made on reference specimens of 8, 12, and 16 mm thickness. The reference reflectors were made in the weld axis (at the center of the weld, at the top below the surface) in the fusion line and behind the fusion line on both the 13CrMo4-5 and 316L material sides. The performance of the artificial reference reflectors in different zones of the welded joint was intended to verify the feasibility of ultrasonic testing for the considered test areas.

Figures 3 and 4 show a diagram indicating the location of the artificial reference reflectors and photographs of the reflectors, respectively. For measurement purposes, the test plates located to the left and right sides of the welded joint are marked with the symbols A and B.

Tests on the welded joints with artificial discontinuities were followed by tests on welded joints with natural discontinuities. The tested plates with natural discontinuities were characterized by a lack of a sidewall, which is characteristic of MAG-welded joints. Their distribution is shown in Figure 5.

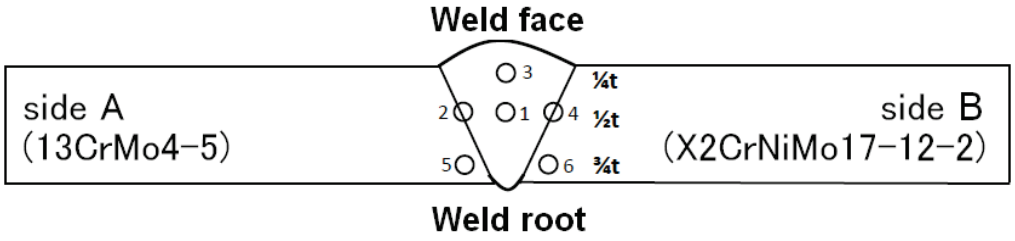

Figure 3. Diagram of the arrangement of artificial gauge reflectors in the form of through-holes for welded joints of dissimilar materials (side A—13CrMo4-5 steel, side B—316L steel); position points: 1—in the center of the weld, 2—on the fusion line on the side of the 13CrMo4-5 material, 3—on the top of the weld under the face, 4—on the fusion line on the side of the 316L material, 5—behind the fusion line on the side of the 13CrMo4-5 material, 6—behind the fusion line on the side of the 316L material.

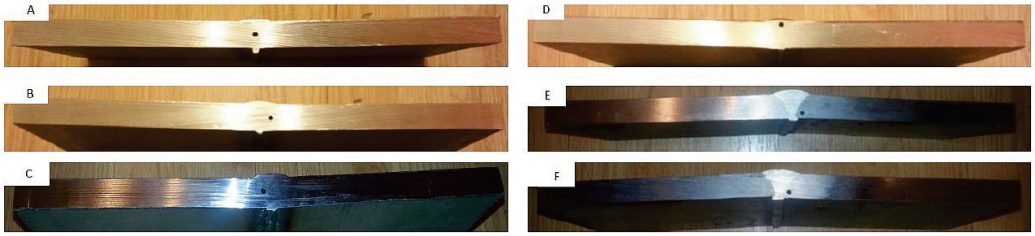

Figure 4. View of the distributed artificial reference reflectors in different zones of the welded joint in the example of a welded joint made of 16 mm thick dissimilar materials: (**A**) in the axis at the center of the weld, (**B**) in the fusion line from the 316L material, (**C**) in the fusion line from the 13CrMo4-5 material, (**D**) in the weld axis at the top of the welded joint, (**E**) behind the fusion line from the 13CrMo4-5 material, (**F**) behind the fusion line from the 316L material.

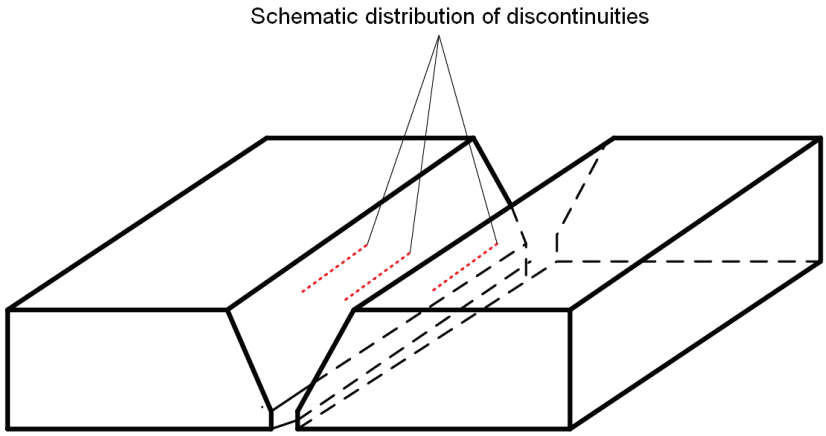

Figure 5. Schematic distribution of discontinuities in fabricated welded joints.

In addition to ultrasonic testing, radiographic and metallographic tests were carried out on weld specimens to confirm that they had been properly prepared. Macroscopic metallographic examinations were carried out to confirm the locations of natural discontinuities detected by UT. The deposits were obtained by cutting the test plates in a vertical plane at the location of the discontinuities using a Bomar saw, shown in Figure 6, at the point where the maximum amplitude value originating from the discontinuity in question was recorded. The surface condition of the metallographic scrap was corrected by milling and grinding. The obtained specimens were then photographed on the bench using an Olympus SZX 10 stereoscopic microscope (Evident /former Olympus/, Tokyo, Japan) equipped with a 0.5 eyepiece and an EP50 camera. The obtained images were graphically processed using the EPview program (Olympus Stream Desktop 2.4) used with the microscope.

Figure 6. Instruments used to prepare samples and perform metallographic tests: (**A**) a Bomar saw model transverse 610.440 DGH used to cut the plates and (**B**) a station for taking photographic images of the scraps taken (Olympus SZX 10 stereoscopic microscope with EP50 camera).

As a result of the tests, the prepared macrographic sections showed natural discontinuities in the form of the lack of a sidewall on the walls of the weld groove. Such discontinuities are characteristic of the MAG method used to produce the specimens. Figure 7 shows an example of images obtained on a deposit of a 316L steel welded joint. The arrows indicate the location of the discontinuities. The figures show a cross-section of the whole specimen with discontinuities and zoom in to show the discontinuities more clearly.

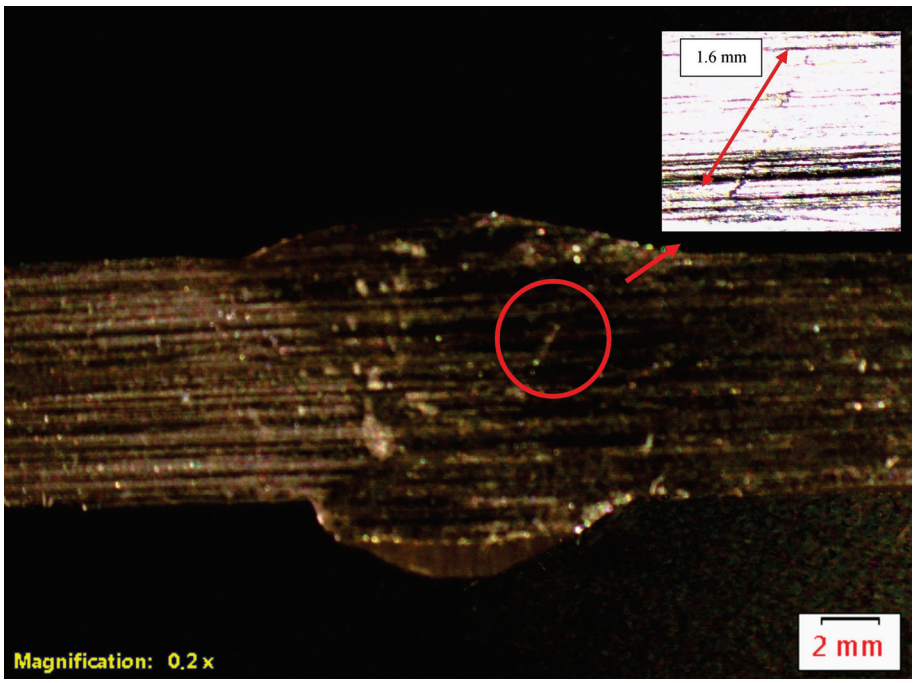

Figure 7. Sample result of macroscopic metallographic examination—welded joint with natural discontinuities; 316L steel with a thickness of 8 mm.

Ultrasonic testing was performed with an Olympus EPOCH 650 ultrasonic defectoscope (Olympus /now Evident/, Westborough, MA, USA) with Type A imaging, using AM4R-8x 9-70-4 MHz, AM4R-8x9-60-4 MHz, 70-4 MHz VSY, and 60-4 MHz VSY ultrasonic

heads. A mixture of FERDOM's CH-1 inhibitor (an agent used to protect central heating systems from deposits) and water in a 1:25 ratio was used as the coupling agent.

The choice of beam angle depends on the thickness of the weld to be inspected. For thicknesses from 8 to 15 mm, the relevant standards (for example, EN ISO 17640:2018 [40]) recommend a basic angle of 70° and an additional angle of 60°, while for thicknesses above 15 mm, they recommend a basic angle of 60° and an additional angle of 70°.

5. Results of the Study

As a result of preliminary activities before the test, the defectoscope and heads were checked according to PN-EN ISO 22232-3 [41], the speed of the wave in the material was determined, the center of the ultrasonic head was measured, the angle of the introduction of the ultrasonic wave beam into the tested material was determined, and the observation range was selected. Transverse and longitudinal transducers with an angle of 70° were used in the tests. For joints that were 16 mm thick, additional longitudinal and transverse wave heads with an angle of 60° were used.

Holes and discontinuities were detected with a direct incident wave from the mid-stroke when longitudinal waves were used. A summary of the results of the baseline and applied reinforcement for 13CrMo4-5–316L steel using transverse ultrasound waves is shown in Table 5.

Table 5. Summary of results of baseline and applied reinforcement for 13CrMo4-5–316L steel using transverse ultrasound waves.

Material Thickness t, mm	Angle, °	Base Gain Value, dB	Base Gain Value, dB	Used Gain Value, dB	Used Gain Value, dB
		13CrMo4-5	316L	13CrMo4-5	316L
8	70	47.1	44.1	52.0	51.0
12	70	47.1	44.1	52.7	50.8
16	70	47.1	44.1	54.5	51.1
16	60	39.7	40.5	49.2	51.5

The transverse wave inspection included the evaluation of discontinuities at the location of the maximum amplitude of the ultrasonic wave. Firstly, the sensitivity of the test was measured using a reference hole drilled in the weld to allow for attenuation in the welded joint being tested. The baseline gain was then set so that the echo from a 3 mm diameter hole made in the base material was at 0.8H of the screen height (SH). A summary of the baseline and applied reinforcement results for 16 mm thick 13CrMo4-5–316L steel using longitudinal ultrasonic waves is shown in Table 6.

Table 6. Summary of results of baseline and applied reinforcement for 16 mm thick 13CrMo4-5–316L steel using longitudinal ultrasound waves.

Angle, °	Base Gain Value, dB 13CrMo4-5	Base Gain Value, dB 316L	Used Gain Value, dB 13CrMo4-5	Used Gain Value, dB 316L
70	69.1	65.6	70.5	67.6
60	67.0	61.6	68.5	63.5

Subsequently, the amplitudes of reflectors, in the form of cylindrical holes located in different zones of the welded joint, were measured, and discontinuities were evaluated using plotted comparison lines. The registration, acceptance, and evaluation levels were determined and the test results were analyzed according to the adopted criteria. According to the accepted evaluation levels, length measurements were carried out for natural discontinuities.

The scanning range during the test was sufficient to cover 100% of the weld volume and the heat-affected zone (HAZ), where a range of 10 mm on each side of the weld is assumed to include this zone. Joints were tested using the same technique—within 1.25 full strokes of the ultrasonic beam for transverse wave heads and 0.5 stroke for longitudinal PN-EN ISO 17640:2019-01 [42]. The tests were performed in accordance with the recommendations of the standard, which required adequate access to both sides of the joint.

The main results of the tests carried out are presented in the following subsections, broken down by type—natural and artificial—and by the transverse and longitudinal test heads used. The following subsections present the values of the changes in decibel gain levels. The results presented were averaged. Each measurement for a given measurement point was taken five times to minimize measurement error. In the case of ultrasonic testing using the echo technique, the assumed accuracy of evaluation that can be assumed in the study is 1 mm. Values in the order of tenths of a millimeter are not possible.

5.1. Artificial Discontinuities—Testing with a Transverse Wave Head

Figure 8 shows the results obtained when artificial discontinuities were tested in an 8 mm thick welded joint of dissimilar materials. For this type of joint, reference reflectors were distributed at six test locations, which were measured from the rim and face area of both the ferritic steel side (Figure 8A) and the austenitic steel side (Figure 8B). From the data presented, it can be seen that in the case of ferritic steel, the value of the recorded amplitude for the discontinuity localized at the measurement point of 3-weld root A did not exceed 20% SH. For 316L steel, such a relationship was obtained for two positions: 3-weld root B and 5-weld face B. However, the highest amplitude values were obtained for the 4-weld face B and 6-weld face B reflectors and amounted to 110% SH. For 13CrMo4-5 steel, the highest amplitude value was 101% and was recorded for reflector 5-weld face A. The lowest values were obtained for positions 3-weld root A (15%) and 5-weld face B (17%). In addition, it can be seen that the reference reflector number 3 is poorly detectable for both the A and B sides of the investigation. In the case of the other discontinuities, a certain correlation can be seen, namely, that the measuring points that are better recorded for ferritic steel are less visible for austenitic steel and vice versa.

The amplitudes recorded for a welded joint of dissimilar materials with a thickness of 12 mm are shown in Figure 9 (A—ferritic steel, B—austenitic steel). For 13CrMo4-5 steel, the amplitude did not exceed 20% SH for the discontinuity located at the 2-weld root A. For 316L steel, values below 20% SH were obtained for two positions: 2-weld root B and 4-weld root B. The highest amplitudes were recorded for discontinuities located in the following measurement areas: 4-gradient A (96% SH) and 1-gradient B (101% SH). On the other hand, the lowest amplitude was obtained for reflector number 2, located in the ridge area, for both ferritic (11%) and austenitic (7%) steels. For 13CrMo4-5 steel, reflector number 4 is the best detectable, and number 2 is the weakest. For 316L steel, discontinuities number 3, 5, and 6 have good detectability, while discontinuities number 4 and 2 are slightly worse. Reference reflector number 1 is well detectable from both sides tested.

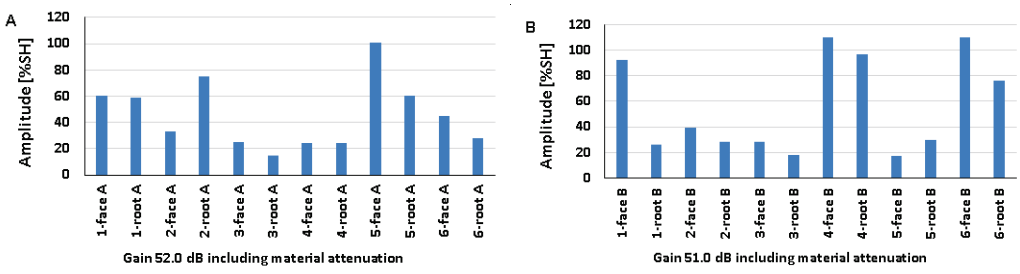

Figure 8. The change in signal amplitude depending on the position of the reference reflectors for (**A**) 13CrMo4-5 and (**B**) 316L materials with a thickness of 8 mm. The test was carried out with a 70°, 4 MHz transverse wave head.

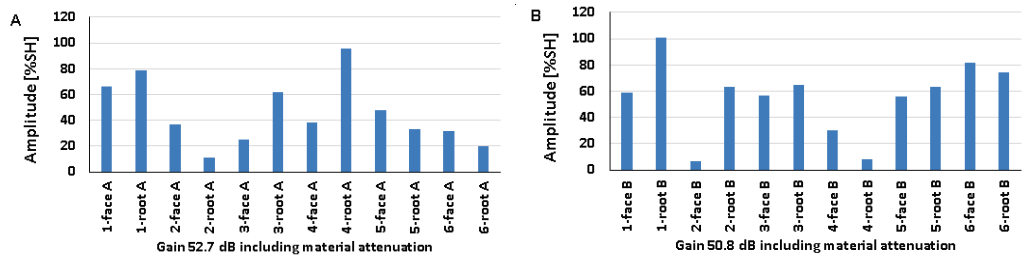

Figure 9. The change in signal amplitude depends on the position of the reference reflectors for (**A**) 13CrMo4-5 and (**B**) 316L materials with a thickness of 12 mm. The test was carried out with a 70°, 4 MHz transverse wave head.

The amplitudes recorded for a welded joint of dissimilar materials with a thickness of 16 mm are shown in Figure 10 (as before: A—ferritic steel, B—austenitic steel). For 13CrMo4-5 steel, the amplitude value did not exceed 20% SH for the discontinuity located in 2-weld root of A. For 316L steel, values below 20% SH were obtained for two positions: 2-weld root B and 4-weld root B. The highest amplitudes were recorded for discontinuities located in the following measurement areas: 4-gradient A (96% SH) and 1-gradient B (101% SH). On the other hand, the lowest values for both ferritic (11% SH) and austenitic (7% SH) steels were obtained for reflector number 2 located in the ridge region. For 13CrMo4-5 steels, reflector number 4 is the best detectable, while number 2 is the weakest. For 316L steels, discontinuities number 3, 5, and 6 have good detectability, while discontinuities number 4 and 2 are slightly worse. Reference reflector number 1 is well detectable from both sides tested.

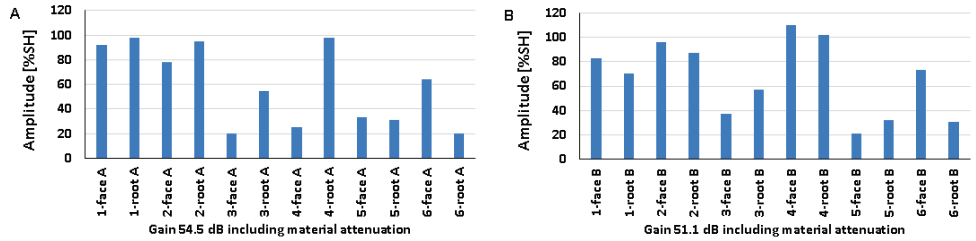

Figure 10. The change in signal amplitude depending on the position of the reference reflectors for (**A**) 13CrMo4-5 and (**B**) 316L materials with a thickness of 16 mm. The test was carried out with a 70°, 4 MHz transverse wave head.

Figure 11 shows the values of amplitudes recorded during the test of a 16 mm welded joint measured with a transverse wave head with a beam insertion angle of 60° (A—ferritic steel, B—austenitic steel).

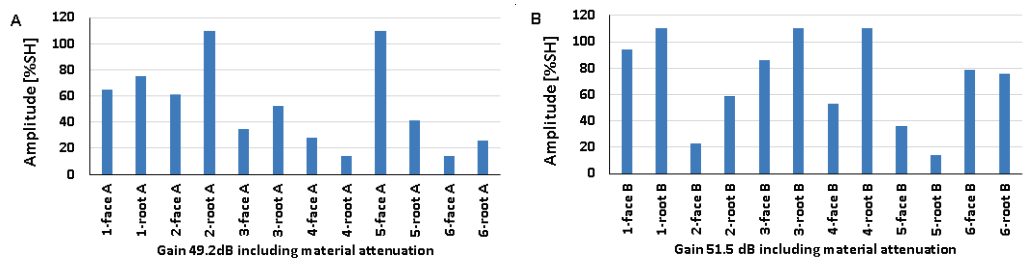

Figure 11. The change in signal amplitude depending on the position of the reference reflectors for (**A**) 13CrMo4-5 and (**B**) 316L materials with a thickness of 16 mm. The test was carried out with a 60°, 4 MHz transverse wave head.

For the two measuring points measured on the side of the 13CrMo4-5 steel, the amplitude value did not exceed 20% SH: 4-weld root A and 6-weld face A. For the 316L

steel, only one measuring point achieved a value below 20% SH —5-weld root B. The highest amplitude values of 110% were recorded for discontinuities located at the following measurement positions: 2-weld root A, 5-weld face A, 1-weld root B, 3-weld root B, and 4-weld root B. On the other hand, the lowest values of 14% were obtained for reflectors located in areas 4-weld root A, 6-weld face A, and 5-weld root B. Artificial discontinuities numbered 1, 3, 4, and 6 are better detectable on the austenitic steel side, while 1 and 5 are better detectable on the ferritic steel side. The results are characterized by slightly lower values of the recorded signals compared to those obtained with the 70° beam angle head.

5.2. Natural Discontinuities—Testing with a Transverse Wave Head

Figures 12–14 show the results obtained for welded joints with natural discontinuities using a transverse wave head with a beam introduction angle of 70° (A—austenitic steel, B—ferritic steel). Compared to the reference reflectors, the amplitudes recorded for natural discontinuities located in welded joints with thicknesses of 8, 12, and 16 mm are lower. From the data obtained for the 8 mm thick plate, it can be seen that in the case of testing discontinuities on the austenitic steel side (Figure 12A), the value of the recorded signal exceeds 20% SH in half of the results. The highest value was recorded for measurement point 2-weld face A (52%), and the lowest for measurement point 3-weld face A (9%). In the case of the tests carried out on the ferritic steel side, only one position recorded an amplitude value above 20% SH (2-weld face B), and this is also the highest value obtained, which is 31% (Figure 12B), while the lowest value was obtained for position 2-weld face B—6%. In addition, no signal was detected for the 1-weld face B and 3-weld face B positions.

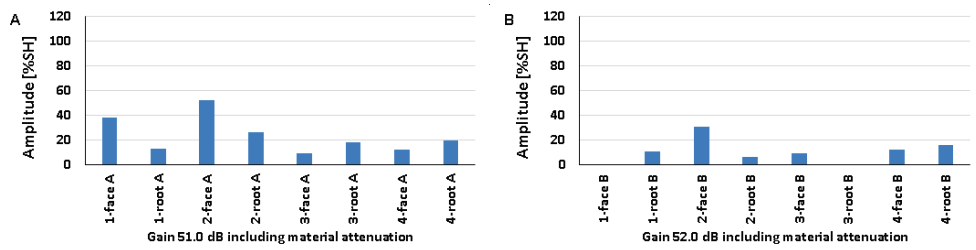

Figure 12. The change in signal amplitude depending on the position of the natural discontinuity for (**A**) 316L and (**B**) 13CrMo4-5 materials with a thickness of 8 mm. The test was carried out with a 70°, 4 MHz transverse wave head.

Comparing the results of the austenitic and ferritic side measurements, it can be seen that the recorded signals from individual discontinuities are higher for the former. In the case of testing a 12 mm thick plate, only three measurement points tested from the 316L steel side (Figure 13A) obtained an amplitude value above 20% SH (1-weld face A, 2-weld root A, and 3-weld face A). On the other hand, from the measurements made on the 13CrMo4-5 steel side (Figure 13B), it can be seen that the amplitude exceeded the value of 20% SH for only two points (2-weld face B and 3-weld face B). The highest amplitude values were recorded for 2-weld face B, 47% SH, and for 1-weld face A and 2-weld face A the values were 22% SH. On the other hand, the lowest signals were obtained for 2-weld face A (13%) and 3-weld face A (13%) for 316L steel, and 4-weld face B (3%) for 13CrMo4-5 steel. Again, better detectability, i.e., higher amplitudes, were obtained for the measurements conducted on the austenitic steel side. The exceptions are the discontinuities measured in the areas 2-weld face B and 3-weld face B, where higher readings were obtained from the ferritic steel side.

The values of the recorded amplitudes for a 16 mm thick plate are shown in Figure 14. For austenitic steel (Figure 14A), three measurement points were characterized by signal values above 20% SH (1-weld face A, 1-weld root A, 3-weld face A). In the case of ferritic steel, half of the recorded amplitudes exceeded 20% SH. The highest values were recorded for 4-weld face B, 47% SH (13CrMo4-5), and 1-weld face A—26% SH (316L). The lowest amplitudes, on the other hand, were obtained for 3-groove A (8%) and 2-groove B (5%).

Natural discontinuities in the measurement areas of 1-weld face B and 3-weld face B were not detected. In addition, as in the case of the study of 8 and 12 mm thick plates, in this case, better detectability was also obtained for discontinuities measured on the austenitic steel side.

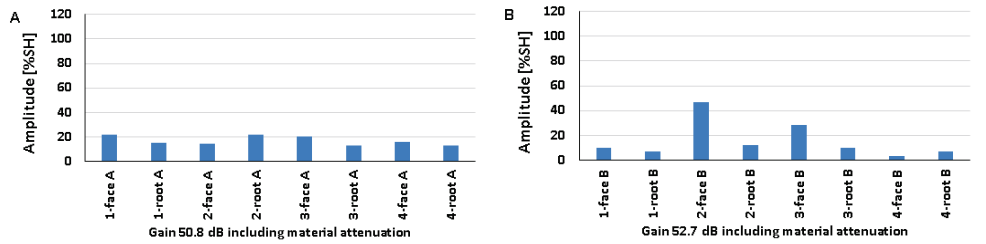

Figure 13. The change in signal amplitude depending on the position of the natural discontinuity for (**A**) 316L and (**B**) 13CrMo4-5 materials with a thickness of 12 mm. The test was carried out with a 70°, 4 MHz transverse wave head.

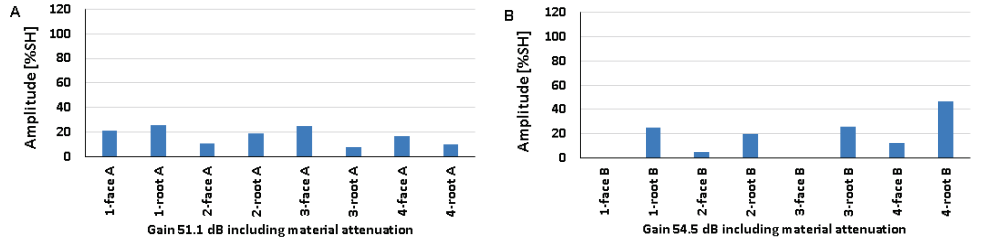

Figure 14. The change in signal amplitude depending on the position of the natural discontinuity for (**A**) 316L and (**B**) 13CrMo4-5 materials with a thickness of 16 mm. The test was carried out with a 70°, 4 MHz transverse wave head.

Figure 15 shows the results of a test carried out on a 16 mm thick welded joint using a transverse wave head with a beam insertion angle of 60° into the material. From the data presented, it can be seen that, as in previous measurements, the amplitudes of the recorded signals are lower than those obtained for reference reflectors. On the other hand, comparing the values with the data obtained when measuring the same plate, but using a 70°, 4 MHz head, it can be observed that tests performed with a smaller angle of beam introduction allow better detection of natural discontinuities. In the case of ferritic steel (Figure 15B), all the values exceeded 20% SH, whereas in the case of austenitic steel (Figure 15A) such a relationship was obtained for only half of the discontinuities. The highest amplitudes were recorded for 4-weld face A (86%) and 3-weld face B (83%). In contrast, the lowest amplitudes were obtained for discontinuities located in the survey areas 3-weld face A (11%) and 2-weld face B (22%). Unlike previous studies, this time better detectability was obtained for natural discontinuities measured from the ferritic steel side.

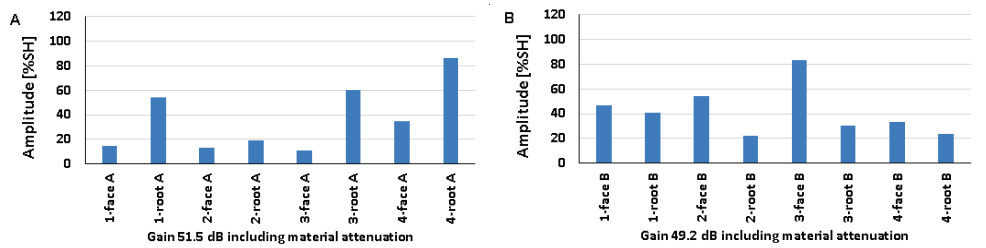

Figure 15. The change in signal amplitude depending on the position of the natural discontinuity for (**A**) 316L and (**B**) 13CrMo4-5 materials with a thickness of 16 mm. The test was carried out with a 60°, 4 MHz transverse wave head.

5.3. Artificial Discontinuities—Tests with a Longitudinal Wave Head

The recorded values of the amplitudes for artificial discontinuities obtained when testing welded joints of various thicknesses of 8, 12, and 16 mm using a longitudinal wave head with a beam introduction angle of 70° are shown in Figures 16–18 (A—ferritic steel, B—austenitic steel).

In the case of an 8 mm thick welded joint and measurements carried out on the side of 316L steel, it can be seen that all the values obtained exceeded 20% SH (Figure 16B), whereas in the case of 13CrMo4-5 steel, the value of the amplitude for measurement point 6-weld root A did not exceed this (Figure 16A). The highest values were recorded for the reflectors located at 2-weld face A (79%) and 6-weld face B (94%), and the lowest for 6-weld face A (13%) and 3-weld face B (23%). When comparing the individual values of the amplitudes recorded for the reflectors during their examination on the ferritic and austenitic steel sides, a slightly better detectability was observed on the 13CrMo4-5 steel side.

From the data obtained for a 12 mm thick plate, it can be seen that the values of the amplitudes obtained from the examination of the discontinuities on both sides of the joint exceed 20% SH (Figure 17). For ferritic steel, the highest value was recorded for the reflector in the point 5-weld face A area (76%), and the lowest value of 27% was obtained at two measurement points: 3-weld face A and 6-weld face A. For austenitic steel, the highest value was 82% (2-weld face B) and the lowest was 20% (3-weld face B). After comparing the amplitudes recorded for individual reflectors on both sides of the joint, no significant differences in their detectability were observed. All the amplitudes obtained during the test of the 16 mm thick plate also exceeded 20% SH (Figure 18). The highest values of 73% and 88% were recorded from the following tested areas 1-weld face A, 2-weld face A, and 4-weld face B. On the other hand, the lowest values were recorded from the points 4-weld face A (20%) and 3-weld face B (40%). Reflector number three was not detected on either side of the face. As in the case of the test of the 8 mm thick plate, there were no significant differences when comparing the values of the amplitudes obtained from the measurements on the ferritic and austenitic steel sides.

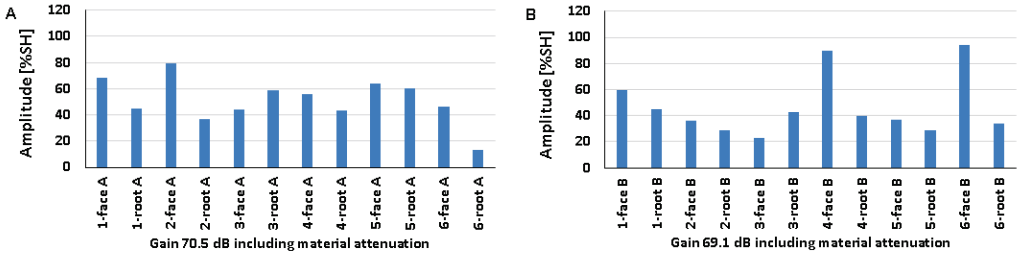

Figure 16. The change in signal amplitude depending on the position of the reference reflectors for (**A**) 13CrMo4-5 and (**B**) 316L materials with a thickness of 8 mm. The test was carried out with a 70°, 4 MHz longitudinal wave head.

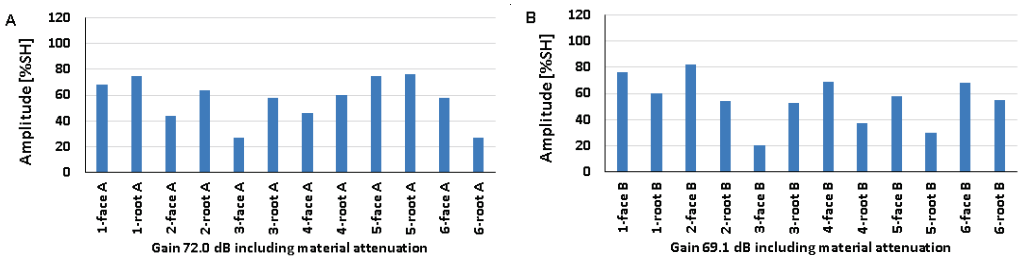

Figure 17. The change in signal amplitude depending on the position of the reference reflectors for (**A**) 13CrMo4-5 and (**B**) 316L materials with a thickness of 12 mm. The test was carried out with a 70°, 4 MHz longitudinal wave head.

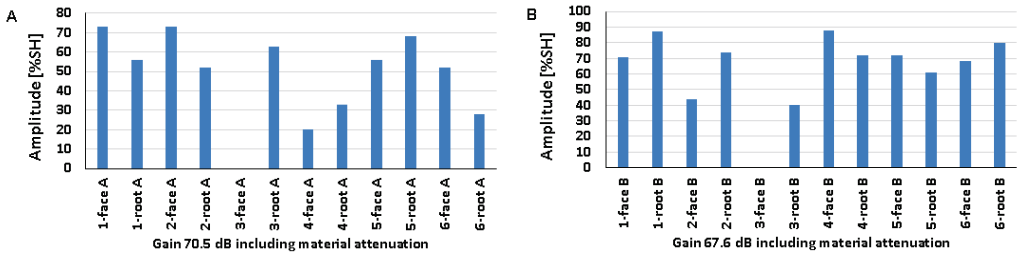

Figure 18. The change in signal amplitude depending on the position of the reference reflectors for (**A**) 13CrMo4-5 and (**B**) 316L materials with a thickness of 16 mm. The test was carried out with a 70°, 4 MHz longitudinal wave head.

On the other hand, when comparing the data obtained from the transverse wave head test with those obtained from the measurements made with the longitudinal wave head, no clear differences could be observed in the amplitudes recorded for each reference reflector. In the case of the 8 and 12 mm plates, a slightly better detection of discontinuities was obtained when testing with the longitudinal wave head, while for the 16 mm plate, with the transverse wave head.

The results recorded for a 16 mm plate with a 60° longitudinal wave head are shown in Figure 19 (consistently: A—ferritic steel, B—austenitic steel). All the amplitudes recorded on the austenitic steel side are above 20% SH, while for ferritic steel only one value is below this level. The highest amplitude value of 110% SH was obtained for the following measurement areas: 1-weld face A, 4-weld face A, 2-weld face B, 3-weld face B, and 3-weld face B. In contrast, the lowest values were obtained for 6-weld face A (18%) and 5-weld face B (20%). Better detectability for most artificial discontinuities was recorded for measurements on the austenitic steel side. However, if the results are compared with those obtained using a 70° head, it is clear that the detection of discontinuities is better at a smaller angle. Measurements made at the same angle but with a transverse wave head gave higher values of recorded amplitude signals when tested with a longitudinal wave head.

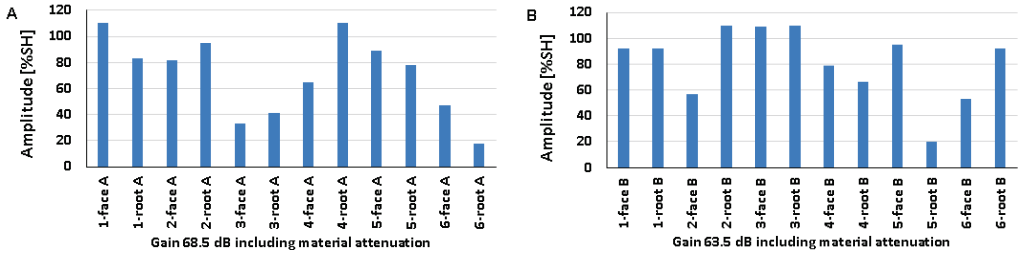

Figure 19. The change in signal amplitude depending on the position of the reference reflectors for (**A**) 13CrMo4-5 and (**B**) 316L materials with a thickness of 16 mm. The test was carried out with a 60°, 4 MHz longitudinal wave head.

5.4. Natural Discontinuities—Tests with a Longitudinal Wave Head

The results obtained from measurements of welded joints containing various natural discontinuities are shown in Figures 20–22 (A—austenitic steel, B—ferritic steel).

Based on the values obtained during the testing of an 8 mm thick welded joint (Figure 20), it was observed that the amplitude values for the discontinuities of 1-weld root A, 3-weld root A, and 4-weld root A tested on the 316L steel side did not exceed 20% SH. However, the highest value was recorded for the position of 1-weld face A (69%), and the lowest value of 16% was recorded for 1-weld root A and 3-weld root A. On the other hand, for the ferritic steel, an amplitude value of less than 20% SH was obtained for 4-weld face B, and this is also the measurement point with the lowest amplitude (18%). The highest signal value of 40% was obtained for discontinuities number 3 and 4 measured from the

ridge area. The detectability of individual discontinuities from both sides of the tested joint was similar; there were no significant differences in the values of the recorded amplitudes.

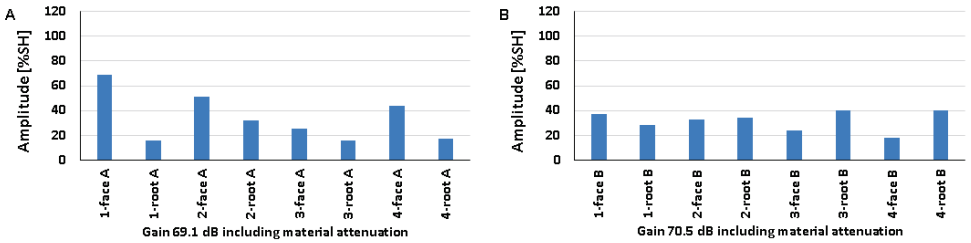

Figure 20. The change in signal amplitude depending on the position of the natural discontinuity for (**A**) 316L and (**B**) 13CrMo4-5 materials with a thickness of 8 mm. The test was carried out with a 70°, 4 MHz longitudinal wave head.

In the case of the data obtained from measurements on a 12 mm thick plate, it was observed that only the signal amplitude of discontinuity number 4 measured from the rim area did not exceed 20% SH from both the 316L and 13CrMo4-5 steel sides (Figure 21). For measurements taken on the austenitic steel side, the highest amplitude value of 38% was obtained for 1-weld face A and 2-weld face A, while on the ferritic steel side it was obtained for 3-weld root B (64%). In contrast, the lowest values were recorded for discontinuities number four from the ridge area, where they were 17% and 15% for 316L and 13CrMo4-5 steels, respectively. As with the 8 mm thick plate, there is no significant difference in the detectability of individual discontinuities depending on the side of the test. The amplitude values recorded during the measurement of a 16 mm thick welded joint are shown in Figure 22.

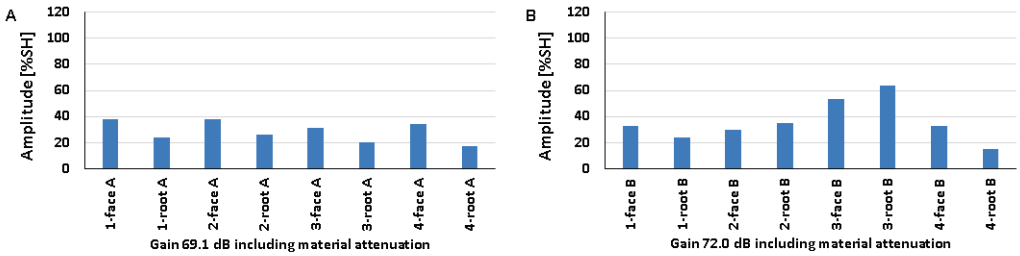

Figure 21. The change in signal amplitude depending on the position of the natural discontinuity for (**A**) 316L and (**B**) 13CrMo4-5 materials with a thickness of 12 mm. The test was carried out with a 70°, 4 MHz longitudinal wave head.

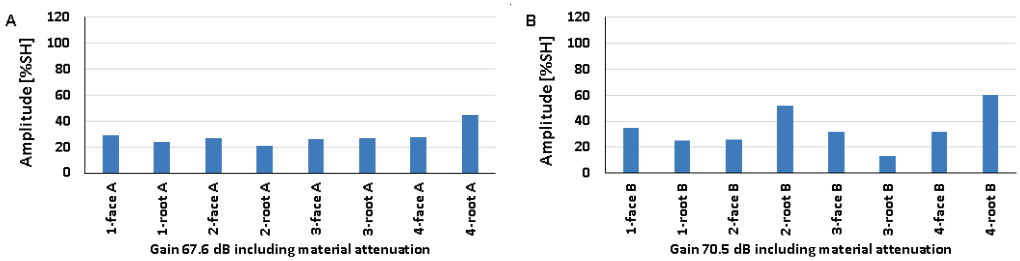

Figure 22. The change in signal amplitude depending on the position of the natural discontinuity for (**A**) 316L and (**B**) 13CrMo4-5 materials with a thickness of 16 mm. The test was carried out with a 70°, 4 MHz longitudinal wave head.

All the amplitude values obtained during the measurement on the 316L steel side were above 20% SH, whereas on the 13CrMo4-5 steel side, for the discontinuity located in the 3-weld root B area, the value was below this at 13%. At the same time, this represents

the least detectable discontinuity for measurements from this side of the joint. On the other hand, for the tests carried out on the austenitic steel side, the lowest value was recorded for 2-weld root A. The highest values were observed for 4-weld root A, 45% (316L), and 4-weld root B, 60% (13CrMo4-5). Comparing the recorded amplitudes obtained during the longitudinal wave head test with those obtained during the transverse wave head measurements, it was observed that in the case of the former, the detection of individual natural discontinuities was better for all the welded joint thicknesses tested.

Figure 23 shows the results obtained when testing a 16 mm thick plate with a 60° beam angle longitudinal wave head (A—austenitic steel, B—ferritic steel). Compared to the tests carried out with the 70° head, a deterioration in the detection of individual discontinuities can be seen, namely, for three of the tested areas on the 316L steel side and for half on the 13CrMo4-5 side, the value of the amplitudes did not exceed 20% SH. The highest signal value of 104% was recorded for 1-weld root A and 4-weld root B, while the lowest values were recorded for 4-weld root A (13%), 2-weld face B (16%), and 2-weld root B (16%). There were no significant differences in the results obtained when testing at the same angle but with a transverse wave head in the detection of individual natural discontinuities.

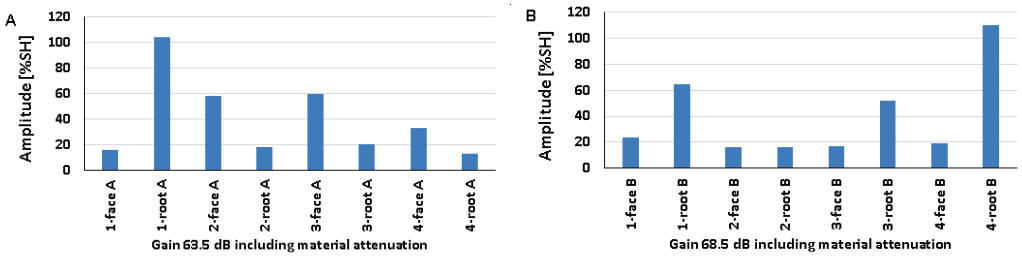

Figure 23. The change in signal amplitude depending on the position of the natural discontinuity for (**A**) 316L and (**B**) 13CrMo4-5 materials with a thickness of 16 mm. The test was carried out with a 60°, 4 MHz longitudinal wave head.

5.5. Values of Changes in Decibel Gain Level—Transverse Wave Head

Tables 7 and 8 show the values of the change in decibel gain level obtained when recording the signal from the discontinuity in relation to the DAC reference line. The results obtained when testing the reference reflectors with the transverse wave head are shown in Table 7. From these data, it can be seen that for the 8 mm thick test welded joint the change in the decibel gain level ranges from −10.4 to 6 dB for ferritic steel, and from −6.4 to 4.5 dB for austenitic steel. For a 12 mm thick plate, the ranges are −9.5 to 1.6 dB and −14.5 to 6.8 dB, respectively. The ranges of change in decibel gain levels obtained when testing a 16 mm thick welded joint are −0.6 to 4.3 dB (13CrMo4-5) and −9.4 to 7.6 dB (316L). For the data obtained when testing a 16 mm plate but at a smaller beam angle, the ranges vary from −15.3 to 6.2 dB and −5.7 to 9.3 dB, respectively.

Tests for artificial reference discontinuities distributed over different areas of the welded joint were carried out on the face and rim sides using transverse wave heads, and the measurement points were then classified according to the acceptance criteria adopted (Table 7).

For the 8 mm thick joint, the results exceed the rating level of −14 dB, and allow the evaluation of all recorded artificial discontinuities for both the 13CrMo4-5 and 316L steel side tests. The lowest result was recorded for test point 4-weld root A (−10 dB). However, this exceeded the registration level of −14 dB and was equal to the acceptance level of −10 dB, so it was unacceptable, as were the other measurements made on the measurement points as artificial reference reflectors. In each case, the −10 dB acceptance level was exceeded.

For the 12 mm thick welded joint, a result below the evaluation level of −14 dB was obtained for the reading from measurement point 4-weld root B (−14.5 dB). According to

the specified criteria, this result from the 316L steel side should not be taken into account. The remaining results were unacceptable and exceeded the acceptance level of −10 dB.

For the tests carried out on the welded joint with a thickness of 16 mm using 70° and 60° beam introduction angles, all the indications from the reference discontinuities exceeded the −14 dB evaluation level. They were simultaneously indications that exceeded the level of registration and acceptance, and were therefore unacceptable in view of the assumptions made.

Table 7. The change in the decibel gain level (ΔH_u) with respect to the DAC comparison line for 316L material considering the path of the ultrasonic wave(s) for artificial discontinuities. The tests were carried out with a transverse ultrasound wave head.

Measurement Point *	8 mm 70° ΔH_u dB	8 mm 70° s mm	12 mm 70° ΔH_u dB	12 mm 70° s mm	16 mm 70° ΔH_u dB	16 mm 70° s mm	16 mm 60° ΔH_u dB	16 mm 60° s mm
1-F-A	0.2	33.8	−1.8	22.2	1.4	24.6	6.2	45.9
1-F-B	3.4	30.2	3.1	44.4	1.0	24.3	7.8	42.0
1-R-A	−6.0	14.9	0.0	18.6	2.2	25.4	−0.2	15.0
1-R-B	−4.5	44.7	6.0	18.2	5.1	23.0	4.3	15.0
2-F-A	−5.3	32.7	0.1	49.7	−0.6	23.8	−1.8	16.0
2-F-B	−4.0	32.4	3.3	42.0	7.6	45.9	0.8	74.6
2-R-A	1.3	31.1	−9.5	54.8	1.6	24.4	4.3	14.8
2-R-B	−2.7	49.3	2.7	40.6	1.2	23.8	4.0	44.0
3-F-A	−5.8	38.8	−0.2	61.8	3.2	91.8	3.6	58.6
3-F-B	−6.4	32.4	4.2	49.8	4.6	74.1	9.3	56.1
3-R-A	−4.7	62.2	−0.9	28.9	1.8	43.0	−0.5	26.3
3-R-B	−4.9	52.4	−1.2	24.0	1.6	39.8	6.9	26.5
4-F-A	−7.5	36.2	−0.8	45.9	2.9	75.6	0.5	78.1
4-F-B	4.5	27.7	−9.1	43.8	3.6	23.0	−2.5	16.1
4-R-A	−10.0	18.7	0.0	24.5	2.4	26.1	−15.3	14.3
4-R-B	3.2	27.8	−14.5	43.2	2.2	22.1	4.2	13.9
5-F-A	6.0	17.0	−4.5	24.1	−0.1	52.7	5.2	19.7
5-F-B	−3.5	64.1	6.8	63.4	−9.4	31.9	−2.2	34.5
5-R-A	0.6	36.9	1.6	58.7	4.3	71.9	4.1	52.9
5-R-B	−2.1	47.4	−4.9	58.7	2.3	66.0	−5.7	60.2
6-F-A	−4.1	28.4	−6.4	29.8	0.3	32.7	−8.3	40.8
6-F-B	4.0	25.6	0.5	21.9	1.9	32.6	7.5	20.6
6-R-A	−3.5	44.8	−1.0	65.4	1.7	81.8	0.5	55.1
6-R-B	1.6	29.6	5.4	48.1	2.0	65.8	9.3	62.8

* 1–6—locations of measurement points according to Figure 3; F/R—face/ridge of the weld; A/B—sides of the welded joint according to Figure 3.

A similar analysis of the data was carried out for the decibel gain level values obtained when natural discontinuities in welded joints were detected using a transverse wave head (Table 8). In this case, the ranges of decibel level changes for ferritic steel were −15.4 to 0 dB for 8 mm, −20.6 to −12.9 dB for 12 mm, −24.8 to 6.8 dB for 16 mm, and −6.8 to 5.7 dB for 16 mm, at a 60° angle. For austenitic steel, the ranges were −14.8 to −1.8 dB, −12 to −4.7 dB, −12.5 to −2.6 dB, and −11.7 to 2.1 dB, respectively. It should also be noted that these values were negative for austenitic steel when tested with a head with a beam introduction angle of 70°. For ferritic steel, such a relationship was only obtained when testing a 12 mm thick joint.

The tests for natural discontinuities carried out with a transverse wave head with the same reinforcement as for artificial reflectors gave the following results according to the adopted evaluation criteria (Table 8).

For a thickness of 8 mm, the measurement points 1-weld root B (−15 dB), 2-weld root B (−15.4 dB), and 3-weld root A (−14.8 dB) were below the −14 dB evaluation level and were not considered. Indications from the measurement points 1-weld face A (−7.8 dB), 2-weld

face A (−1.8 dB), 2-weld face A (−3 dB), and 3-weld face A (−4.3 dB) were unacceptable indications, exceeding the −14 dB registration level and the −10 dB acceptance level. Measurement points below the −14 dB registration level but above the −10 dB acceptance level were recorded and were acceptable according to the imposed criteria.

Table 8. The change in the decibel gain level (ΔH_u) with respect to the DAC comparison line for 316L material considering the path for the ultrasonic wave(s) for natural discontinuities. The tests were carried out with a transverse ultrasound wave head.

Measurement Point *	8 mm 70° ΔH_u dB	8 mm 70° s mm	12 mm 70° ΔH_u dB	12 mm 70° s mm	16 mm 70° ΔH_u dB	16 mm 70° s mm	16 mm 60° ΔH_u dB	16 mm 60° s mm
1-F-A	−7.8	40.2	−7.3	37.9	−2.6	59.0	−4.7	47.3
1-F-B	0.0	0.0	−18.1	25.5	0.0	0.0	2.8	55.5
1-R-A	−13.5	30.8	−5.4	60.6	−9.4	24.3	−0.4	24.8
1-R-B	−15	33.9	−20.0	22.2	−8.7	25.3	−3.3	26.1
2-F-A	−1.8	30.3	−5.9	59.3	−10.2	48.0	−7.3	38.8
2-F-B	−12.2	55.5	−18.9	19.7	−24.8	24.8	2.4	48.8
2-R-A	−3.0	49.5	−8.6	31.6	−12	17.9	−11.7	49.6
2-R-B	−15.4	57.7	−14.9	29.5	−12.2	24.2	−3.7	16.8
3-F-A	−14.8	40.4	−6.1	45.7	−3.2	47.7	−11.2	37.6
3-F-B	−11.5	54.1	−18.9	18.7	0.0	0.0	5.7	44.5
3-R-A	−4.3	57.8	−12.0	34.4	−12.5	53.3	−0.1	20.9
3-R-B	0.0	0.0	−12.9	43.3	6.8	35.9	−6.8	23.2
4-F-A	−11.8	41.6	−4.7	59.8	−5.3	54.3	2.1	39.8
4-F-B	−12	30.1	−14.8	80.5	−4.4	71.7	−1.8	50.1
4-R-A	−12	13.3	−7.0	56.7	−8.8	59.4	1.9	34.8
4-R-B	−13	10.0	−20.6	44.0	−3.1	29.9	−5.8	18.7

* 1–4—location of measurement points according to Figure 3; F/R—face/ridge of the weld; A/B—sides of the welded joint according to Figure 3.

For a welded joint with a thickness of 12 mm, eight measurement points were unclassifiable, exceeding the −14 dB evaluation level. It is noteworthy that all of these locations were on the test side of the 13CrMo4-5 material. The discontinuities detected on the 316L steel side, with the exception of the reading from measurement point 3-weld face A (−12 dB), were unacceptable as they exceeded the −10 dB acceptance level.

Tests carried out on a 16 mm thick welded joint and using an angle of 70°, with the exception of the indication of 2-weld face B (−24.8 dB), were indications considered for evaluation and subject to registration. Indications exceeding the level of registration but not exceeding the level of acceptance were recorded for measurement points 2-weld face A (−10.2 dB), 2-weld root A (−12 dB), 2-weld root B (−12, 2dB), and 3-weld root A (−12.5 dB). Other indications from discontinuities were unacceptable.

The use of a 60° angle resulted in indications exceeding the −14 dB evaluation level. The indications subject to registration and unacceptable discontinuities were those from the measurement points 2-weld root B (−11.7 dB) and 3-weld face B (−11.2 dB). The remaining discontinuities were unacceptable according to the imposed criteria.

The range of the ultrasonic wave path obtained when measuring the 8 mm thick welded joint with artificial reference reflectors using a transverse wave head with 70° beam angle introduction and made of 13CrMo4-5–316L steel was from 14.9 to 62.2 mm for ferritic steel, and from 25.6 to 64.1 mm for austenitic steel (Table 7). For the 12 mm thickness, the range was from 18.6 to 65.4 mm and from 18.2 to 63.4 mm, respectively. For the 16 mm thick welded joint tested with a 70° head, the path ranges were 23.8 to 91.8 mm and 22.1 to 74.1 mm, respectively, and for a 60° head, 14.3 to 78.1 mm and 13.9 to 74.6 mm, respectively.

The path ranges for welded joints with natural discontinuities, measured with the transverse wave head, are shown in Table 8. For the 8 mm thick plate of 13CrMo4-5–316L steel, they ranged from 10.0 to 57.7 mm for ferritic steel, and from 13.3 to 57.8 mm for

austenitic steel; for the thickness of 12 mm, the ranges were from 18.7 to 80.5 mm and from 31.6 to 60.6 mm, respectively. In the case of the 16 mm thick welded joint, tested with a 70° head, the path ranges were from 24.2 to 71.7 mm, and from 22.1 to 74.1 mm, respectively. For the 60° angle head, the values were from 16.8 to 55.5 mm and from 20.9 to 49.6 mm, respectively.

5.6. Values of Changes in Decibel Gain Level—Longitudinal Wave Head

The values of decibel gain level changes obtained by recording the amplitude signal against the DAC curve using the longitudinal wave head are shown in Tables 9 (for artificial discontinuities) and 10 (for natural discontinuities). From the data in Table 9, it can be seen that when testing the 8 mm thick welded joint, the range of decibel gain varied from −15.3 to 0.4 dB for 13CrMo4-5 steel and from −9.2 to 2.5 dB for 316L steel. For the 12 mm joint, the ranges were −8 to 2.2 dB and −8.8 to 2.1 dB, respectively, while for the 16 mm joint, the ranges were −7.5 to 2.6 dB and −1.4 to 3.4 dB, respectively. When the 16 mm plate was tested using a head with a smaller beam angle (60°), the ranges of changes in decibel gain were −10.3 to 9.8 dB (ferritic steel) and −17.3 to 5.5 dB (austenitic steel).

The results obtained during the tests for welded joints with artificial discontinuities with the longitudinal wave head were also verified according to the adopted evaluation criteria (Table 9). For the thickness of 8 mm, the value of the decibel gain recorded for measurement point 6-weld root A (−15.3 dB) was below the evaluation level of −14 dB. The remaining values obtained for individual measurement points were evaluated, as was the case for the 12 mm thick welded joint, where all values met the criteria. When the results were considered in relation to the acceptance level of −10 dB, all indications were unacceptable. For the joint with a thickness of 16 mm and an angle of 70°, all measurement values exceeded the evaluation level of −14 dB while simultaneously exceeding the registration and acceptance levels, and were therefore unacceptable. On the other hand, in the case of measurements carried out for an angle of 60°, measurement point 5-weld root B (−17.3 dB) was not evaluable, and 6-weld root A (−10.3 dB) was a registrable indication and met the acceptance level. The remaining artificial reference discontinuities did not meet the acceptance levels.

For the natural discontinuity test (Table 10), the ranges of change in the decibel gain level of the recorded signal relative to the reference line for ferritic steel were −12 to −3.6 dB (8 mm), −11.5 to 0.9 dB (12 mm), −15.1 to 0.3 dB (16 mm), and −11.8 to 7.4 dB (16 mm and 60° angle). For austenitic steel, the ranges were −11.8 to 7.4 dB, −9.5 to −1.6 dB, −8.3 to −1.8 dB, and −15.7 to 5.5 dB, respectively. As with the study of natural discontinuities using the transverse wave head, negative ranges were also obtained, but only for the austenitic steel specimens with 12 and 16 mm thickness.

As for artificial discontinuities, tests for natural discontinuities were carried out on the side of the 13CrMo4-5 and 316L materials, which were then verified according to the adopted evaluation criteria (Table 10).

All indications of discontinuities for the 8 and 12 mm thicknesses of the heterogeneous joints were subject to evaluation because they exceeded the evaluation level of −14 dB. Discontinuities subject to registration but not exceeding the acceptance level, were indications from measurement points 1-weld face A (−11.8 dB), 4-weld face B (−12 dB), and 4-weld face A (−10.7 dB) for the 8 mm thickness; and 4-weld face B (−11.5 dB) for the 12 mm thickness. The remaining discontinuities did not meet the requirements for the imposed acceptance levels. For tests performed on the 16 mm thick welded joint, only the indication from the 3-weld root B measurement point (−15.1 dB) was below the evaluation level. The remaining discontinuities exceeded the registration and acceptance levels and were classified as unacceptable. For the tests performed on the 16 mm thick specimen using a 60° angle head, only the discontinuity at measurement point 4-weld root A (−15.7 dB) was not evaluated. Measurement points 1-weld face A (−10.7 dB), 2-weld face B (−11.8 dB), 2-weld face A (−11.4 dB), 2-weld face B (−11.8 dB), and 3-weld face B (−10.9 dB) were

above the registration level but below the acceptance level. The remaining discontinuities were below the acceptance level.

Tables 9 and 10 summarize the ultrasonic wave path values obtained from the measurements carried out with the longitudinal wave head on welded joints containing artificial and natural discontinuities.

The path range for the 8 mm thick plate made of 13CrMo4-5–316L steel with reference reflectors was from 19.6 to 29.8 mm for ferritic steel, and from 15.5 to 30.0 mm for austenitic steel. For the 12 mm plate, the ranges were 16.3 to 33.4 mm and 16.7 to 33.8 mm, respectively. For the 16 mm thick welded joint tested with a 70° head, the path ranges were 22.3 to 45.3 mm and 23.0 to 41.6 mm, and for a 60° head, 12.7 to 34.1 mm and 14.9 to 35.2 mm, respectively.

The path range for measuring a welded joint with natural discontinuities using a 70° longitudinal wave head and an 8 mm thickness was from 20.8 to 32.9 mm for ferritic steel, and from 28.5 to 32.2 mm for austenitic steel. For the 12 mm thick plate, the ranges were 26.9 to 32.6 mm and 28.5 to 42.5 mm. For the 16 mm thick joint, the path range was from 23.3 to 40.1 mm and from 20.6 to 38.9 mm, respectively. The results of measuring the same specimen but with a 60° head gave the ranges of 16.0 to 33.0 mm and from 17.0 to 33.8 mm.

Table 9. The change in the decibel gain level (ΔH_u) with respect to the DAC comparison line for 316L material considering the path for the ultrasonic wave(s) for artificial discontinuities. The tests were carried out with a longitudinal ultrasound wave head.

Measurement Point *	8 mm 70° ΔH_u dB	8 mm 70° s mm	12 mm 70° ΔH_u dB	12 mm 70° s mm	16 mm 70° ΔH_u dB	16 mm 70° s mm	16 mm 60° ΔH_u dB	16 mm 60° s mm
1-F-A	0.4	25.4	0.3	25.1	1.6	28.3	5.1	21.8
1-F-B	0.0	23.6	1.7	24.7	1.6	25.5	4.8	32.6
1-R-A	−3.9	22.3	1.1	24.6	−0.2	30.3	8.4	21.4
1-R-B	−3.9	19.6	−1.0	20.6	3.0	23.6	3.6	21.8
2-F-A	−3.9	19.9	−2.3	30.4	0.5	22.3	2.9	26.0
2-F-B	−3.5	30.0	1.6	20.1	−0.7	37.1	0.0	25.9
2-R-A	−4.9	20.8	0.3	27.9	−1.4	28.7	4.2	25.9
2-R-B	−5.1	20.9	−2.6	16.7	2.8	30.4	5.5	16.4
3-F-A	−3.6	24.7	−8.0	24.2	0.0	0.0	−4.7	31.0
3-F-B	−9.2	21.5	−8.8	27.3	0.0	0.0	4.3	19.7
3-R-A	−1.1	24.3	−2.0	23.7	2.6	45.3	−3.3	24.3
3-R-B	−3.1	24.5	−0.9	26.1	−1.4	43.4	5.3	15.3
4-F-A	−1.8	22.9	−4.3	19.3	0.0	34.9	1.5	32.9
4-F-B	2.5	19.2	2.1	29.8	3.0	23.8	3.5	32.6
4-R-A	−3.0	27.8	−2.2	17.6	−4.3	33.4	9.6	33.4
4-R-B	−5.6	15.5	−4.6	22.9	1.7	25.5	−4.7	26.5
5-F-A	−0.9	21.5	2.2	29.5	1.3	39.8	9.8	28.3
5-F-B	−4.0	26.0	1.8	33.8	3.0	33.2	3.9	22.6
5-R-A	−1.9	19.6	−0.4	16.3	0.0	23.6	0.3	12.7
5-R-B	−7.1	23.6	−5.9	26.5	0.1	23.0	−17.3	14.9
6-F-A	−2.3	29.8	0.7	33.4	0.0	35.8	4.6	34.1
6-F-B	2.4	17.7	0.6	24.7	3.4	41.6	2.0	35.2
6-R-A	−15.3	21.9	−2.4	29.4	−7.5	23.5	−10.3	25.7
6-R-B	−7.3	13.2	−3.2	13.1	−0.1	12.7	−4.3	11.6

* 1–6—location of measurement points according to Figure 3; F/R—face/ridge of the weld; A/B—sides of the welded joint according to Figure 3.

Table 10. The change in the decibel gain level (ΔH_u) with respect to the DAC comparison line for 316L material considering the path for the ultrasonic wave(s) for natural discontinuities. The tests were carried out with a longitudinal ultrasound wave head.

Measurement Point *	8 mm 70° ΔH_u dB	8 mm 70° s mm	12 mm 70° ΔH_u dB	12 mm 70° s mm	16 mm 70° ΔH_u dB	16 mm 70° s mm	16 mm 60° ΔH_u dB	16 mm 60° s mm
1-F-A	1.6	26.8	−1.6	40.3	−4.3	38.9	−10.7	26.5
1-F-B	−8.8	22.1	−4.4	32.1	−3.1	38.0	−8.9	18.7
1-R-A	−11.8	23.2	−6.1	37.2	−1.8	25.6	5.5	32.9
1-R-B	−6.0	30.3	−7.4	29.6	−6.5	36.3	0.4	21.6
2-F-A	0.2	30.1	−2.3	35.9	−5.2	37.7	0.3	33.5
2-F-B	−5.7	24.9	−5.4	30.8	−5.3	40.1	−11.8	20.7
2-R-A	−5.6	23.4	−5.2	38.7	−7.1	38.6	−11.4	17.0
2-R-B	−5.2	26.7	−4.9	29.0	0.3	36.8	−11.8	16.0
3-F-A	−7.1	28.0	−3.7	42.5	−5.5	38.0	0.6	33.8
3-F-B	−7.3	32.9	−0.3	32.6	−3.8	38.6	−10.9	26.0
3-R-A	7.4	25.7	−9.0	28.5	−8.3	20.7	−8.9	28.2
3-R-B	−3.6	28.4	0.9	30.4	−15.1	23.3	−0.9	27.9
4-F-A	−1.5	32.2	−2.6	40.9	−4.8	37.7	−4.7	33.0
4-F-B	−12.0	20.8	−5.0	30.4	−4.0	36.5	−9.5	28.1
4-R-A	−10.7	27.3	−9.5	34.0	−3.3	20.6	−15.7	16.2
4-R-B	−4.0	27.0	−11.5	26.9	−1.3	23.5	7.4	33.0

* 1–4—location of measurement points according to Figure 3; F/R—face/ridge of the weld; A/B—sides of the welded joint according to Figure 3.

6. Evaluation of Ultrasonic Test Results for a Heterogeneous Joint in 13CrMo4-5–316L Steel

In order to determine how the angle of beam introduction into the material or the type of wave used affects the results, a comparative analysis was carried out and the values obtained are shown graphically in Figures 24–27. The data are presented for a variety of joints to further analyze the differences in amplitude values recorded from the ferritic and austenitic steel sides. All the amplitude values recorded from the reference holes were divided into three groups, values less than 40% SH, values from 40 to 80% SH inclusive, and values greater than 80% SH, and then, counted and related to their total number. In addition, within each of these ranges it was analyzed how much data was recorded from the face or root area and whether the test was performed from the A side (ferritic steel) or B side (austenitic steel).

Figure 24 shows that the values of the amplitudes increase as the thickness of the tested joint increases. For a joint thickness of 8 mm, the interval containing amplitudes below 40 is more than 50% of all recorded indications, while for a connector thickness of 16 mm, it is only 25%. In the case of this joint, the use of a 60° angle head reduced the number of recorded signals. On the other hand, the use of a longitudinal wave head for testing significantly improved the quality of the signals obtained.

Figure 25 shows that the range of values below 40% SH has been significantly reduced in favor of the range of values between 40 and 80% SH. However, the range of values above 80% SH does not exceed 10% in any of the joints tested. The use of a head with a beam angle of 60° to measure the 16 mm thick specimen improved the quality of the recorded signals, and for more than 50% SH of the amplitudes, the value exceeded 80% SH. From the data presented in the text boxes in Figures 24 and 25, it can be seen that most of the indications characterized by amplitude values above 80% SH were recorded from the face area. This effect is most evident for the longitudinal wave when testing the joints of 8 and 12 mm thickness. However, when analyzing the side from which the highest amplitude values were recorded (Figures 26 and 27), it can be seen that it is the B side, i.e., the austenitic steel side. Furthermore, in the case of the longitudinal wave, except for the beam angle of 60°, all values above 80% SH were recorded from the B side.

Table 11 shows the locations of the measurement points corresponding to different locations of the reference reflectors placed in one of the zones of the welded joint. For each point and all the thicknesses and angles tested, as well as the type of wave, the degree of detection of the artificial discontinuity was determined graphically. On the basis of the results obtained, some correlations were observed. In particular, for the reflector placed in the center of the weld (no. 1), only in the case of the specimen of 8 mm thickness for side B was the area was poorly detectable, and the amplitude was less than 40% SH.

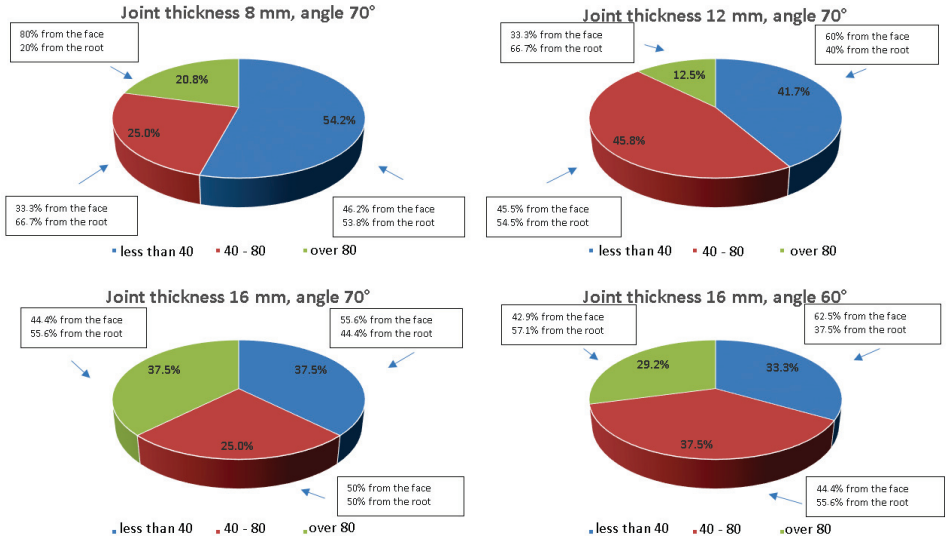

Figure 24. Percentage summary of the results when dividing into three ranges the values of the amplitudes obtained during the registration of the signal coming from the reference holes. Measurement was performed using a transverse wave head. In each interval, the percentage of how many indications were recorded from the boundary area and how many from the face was determined.

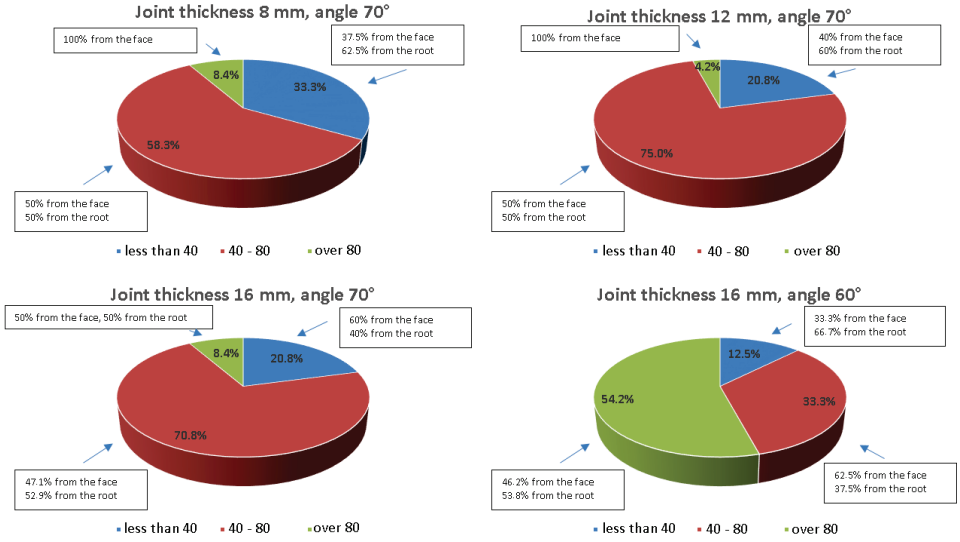

Figure 25. Percentage summary of the results for the diverse joints when divided into three ranges of amplitude values obtained when recording the signal coming from the reference holes. Measurement was performed with a longitudinal wave head. In each interval, the percentage of how many indications were recorded from the boundary area and how many from the face was determined.

This point was best detected for thicker welded joints and measurements with a longitudinal wave head and an angle of 60°. For the reflector located at the top of the weld under the face (no. 3), a deterioration in detectability was observed. This is particularly noticeable at a joint thickness of 8 mm and other joints when examined from the face area.

The reflectors numbered 2 and 4 located on the fusion lines are best detected at a joint thickness of 16 mm using a transverse wave head and an angle of 70° or a longitudinal wave head but an angle of beam insertion into the material of 60°. For reflectors located behind the fusion line on both sides of the tested joint (no. 5 on the ferritic steel side and no. 6 on the austenitic steel side), no improvement in detectability was observed with increasing plate thickness. However, the change in wave type affected the increase in detectability of reflector no. 5, while reflector no. 6 was characterized by significantly higher readings obtained during the test from the face area on the austenitic steel side.

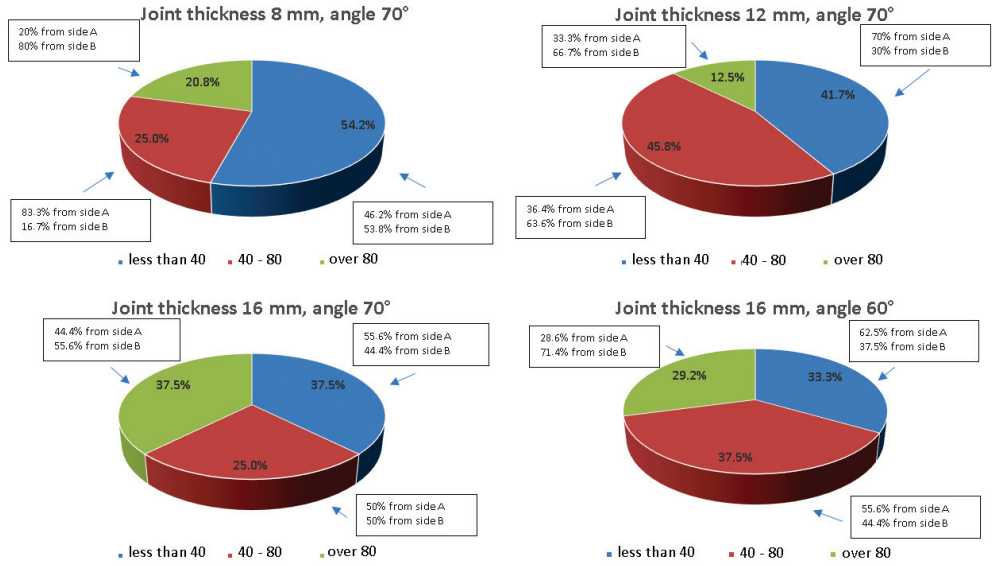

Figure 26. Percentage summary of the results for the diverse joints when divided into three ranges of amplitude values obtained during the recording of the signal coming from the reference holes. Measurement was performed with a transverse wave head. In each interval, the percentage of how many readings were recorded from side A (ferritic steel) and side B (austenitic steel) was determined.

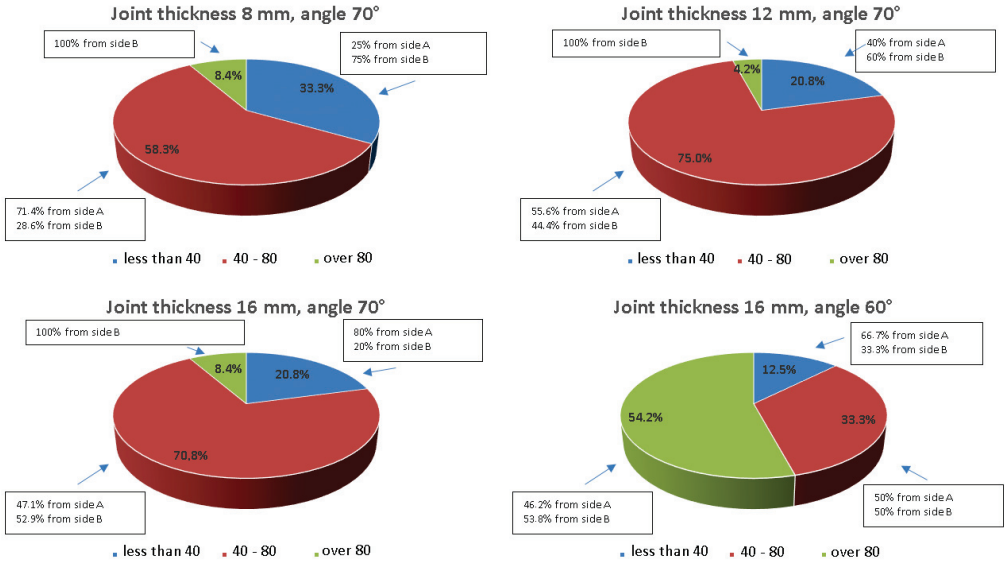

Figure 27. Percentage summary of the results for diverse joints when divided into three ranges of amplitude values obtained when recording the signal coming from the reference holes. Measurement was performed using a longitudinal wave head. In each interval, the percentage of how many readings were recorded from side A (ferritic steel) and side B (austenitic steel) was determined.

Table 11. Summary of measurement points with consideration of their detectability (•—poorly detectable, amplitude below 40% SH; ••—well detectable, amplitude between 40 and 80% SH; •••—very well detectable, amplitude above 80% SH). Data are presented for all tested joint thicknesses and both angles using ultrasonic transverse (T) and longitudinal (L) wave heads.

Measurement point	8, mm 70°, T	12, mm 70°, T	16, mm 70°, T	16, mm 60°, T	8, mm 70°, L	12, mm 70°, L	16, mm 70°, L	16, mm 60°, L	∑ •	∑ ••	∑ •••
1-weld face A	••	••	•••	••	••	••	••	•••	0	6	2
1-weld face B	•••	••	•••	•••	••	••	••	•••	0	4	4
1-weld root A	••	••	•••	••	••	••	••	•••	0	6	2
1-weld root B	•	•••	••	•••	••	••	•••	•••	1	3	4
2-weld face A	•	•	••	••	••	••	••	•••	2	5	1
2-weld face B	•	•	•••	•	•	••	••	••	4	3	1
2-weld root A	••	•••	•••	•••	•	••	••	•••	1	3	4
2-weld root B	•	•	•••	••	•	•	••	•••	4	2	2
3-weld face A	•	•	•	•	••	•	•	•	7	1	0
3-weld face B	•	••	•	•••	•	•	•	•••	5	1	2
3-weld root A	•	••	••	••	••	••	••	••	1	7	0
3-weld root B	•	••	••	•••	••	••	••	•••	1	5	2
4-weld face A	•	•	•	•	••	••	•	••	5	3	0
4-weld face B	•••	•	•••	••	•••	•••	•••	••	1	2	5
4-weld root A	•	•	•••	•	••	••	•	•••	4	2	2
4-weld root B	•••	••	•••	•••	••	••	••	••	0	5	3
5-weld face A	•••	••	•	•••	••	••	••	•••	1	4	3
5-weld face B	•	••	•	•	•	••	••	•••	4	3	1
5-weld root A	••	•	•	••	••	••	••	••	2	6	0
5-weld root B	•	••	•	•	•	•	••	•	6	2	0
6-weld face A	••	•	••	•	••	••	••	••	2	6	0
6-weld face B	•••	•••	••	••	•••	••	••	••	0	5	3
6-weld root A	•	•	•	•	•	•	•	•	8	0	0
6-weld root B	••	••	•	••	•	••	••	•••	2	5	1
∑ •	13	10	9	8	8	5	5	3	-	-	-
∑ ••	6	11	6	9	14	18	17	8	-	-	-
∑ •••	5	3	9	7	2	1	2	13	-	-	-

From the summary of the number of points in a given numerical range shown on the right side of Table 11, the most and least detectable artificial discontinuities were determined. Point 1 is characterized by the lowest number of indications of less than 40% SH, with which it is best detected in all the joint thicknesses tested and at both heads and angles (values are marked in green). On the other hand, discontinuities 3, 5, and 6 are the least detectable, with the highest number of indications detected in the range below 40% SH (values marked in red). In addition, it can be seen that these points have the fewest indications of more than 80% SH. A comparable summary has been made in the bottom rows of Table 11, this time counting the points contained in each column. From these data, it can be seen that the least detectable discontinuities are those located in the 8 mm thick joint when using the transverse wave head. On the other hand, when using the longitudinal wave head, and analyzing the number of indications in each interval, very good detection of discontinuities is observed in all the joint thicknesses tested.

7. Discussion

Tests conducted on artificial discontinuities in the thickness ranges of 8, 12, and 16 mm using a 70° angle of the transverse wave were best detected at the 16 mm thickness both measured from the austenitic and ferritic steel sides. Differences in the detectability of

individual artificial discontinuities depending on the side tested were not as apparent as for other thicknesses. The lowest readings were obtained at a thickness of 12 mm and point 2 face B and 4 root B, where the values of readings did not exceed 10%. Hole 1 was detectable at levels above 50% in all cases from both ferritic and austenitic steels. Hole 3 was the least detectable at the 8 mm thickness on both the ferritic and austenitic steel sides.

The results were similar for each of the materials tested. Reflector 6 face B for each of the thicknesses considered in the 8–16 mm range had higher readings than 6 face A. Reflector 5 face A showed a similar magnitude of recorded amplitude at thicknesses of 8 and 12 mm while for the 16 mm thickness the measured reading indicated a value of 110%. On the B side, the highest values on both the face and border sides were registered at the 12 mm thickness and similar results were registered at the 8 and 16 mm thicknesses and did not exceed the value of 35%.

The use of angle heads for transverse and longitudinal waves gave positive results during the performed tests for artificial discontinuities. In the case of artificial discontinuities, the highest amplitude values were recorded for the 16 mm thick heterogeneous joint using a transverse wave head and an angle of 70° and 60°. For the tests performed on the artificial discontinuities located in the 8 mm thick welded heterogeneous joint with longitudinal waves, higher amplitude values were obtained on the 316L steel side than for the discontinuities measured on the 13CrMo4-5 steel side. For the other thicknesses, of 12 and 16 mm, amplitude values were observed from measurements on both sides of the joint. The highest values of the recorded amplitude were obtained during the measurement for the discontinuities of artificial longitudinal waves and welded joints of different thicknesses of 16 mm and angle of 60°.

Angle heads for transverse waves gave lower amplitude ratios for natural discontinuities than for artificial discontinuities. Not all measurement points could be located. This was the case for point 1 face B with thicknesses of 8 and 16 mm, and 3 root B (thickness 8 mm) and 3 face B with a thickness of 16 mm. For the 16 mm thickness, the readings on each side of the test gave results of more than 10%. No such relationship was observed for the 8 and 12 mm thicknesses. The highest reading rates were obtained for the 16 mm thickness and lower values were registered for the 8 and 12 mm thicknesses.

Tests carried out on representative welded joints in the 8–16 mm range for a longitudinal wave and an angle of 70° with implemented natural discontinuities showed registered amplitude magnitudes higher than for samples with artificial discontinuities. Discontinuities at measurement points 1 face A and 8 mm thick, 3 root B and 12 mm thick, and 4 root B for 16 mm thick gave results of 60% or higher. All other measurement points gave lower results. In the considered thickness interval of 8–16 mm, all measurement points gave a measurement result above 10%. The most similar distribution of amplitudes in the 20–40% range was obtained for measurement points for thicknesses of 12 and 16 mm and tests from test area A. Similar magnitudes were recorded here at a thickness of 8 mm, however, when testing from area B of the welded joint. The use of a 60° angle and a longitudinal wave head gave higher measurement readings for points 3 root B and 4 root B than the use of a 70° longitudinal wave head in this case. The use of the 60° head gave higher magnitudes of measurement readings than the 70° head for points 1 root A and 1 root B, 2 face A, and 3 face A. Point 4 from the root A area gave a higher result for the 70° head than for the 60° angle.

Longitudinal waves propagate at a higher speed than transverse waves. They are less sensitive to deflections at grain boundaries and to obtaining readings derived from apparent occurring indications; i.e., indications that do not originate from natural discontinuities, which are often the result of technological errors in the execution of welded structures.

Normal heads for longitudinal waves are insufficient for ultrasonic testing in heterogeneous joints, so it is necessary to use heads that introduce longitudinal waves at a specific angle. When using dual heads for longitudinal waves, it is important to separate the transmitting and receiving signal paths. This phenomenon does not occur when testing with standard transverse wave heads. The most common use of dual heads is characterized by a

better signal-to-noise ratio and a limited sensitivity zone. The narrowing of the sensitivity zone is the result of a longer dead zone with single-angled longitudinal wave heads than with the same transverse wave heads. This is also due to the higher structural noise when testing welds made of dissimilar materials. Transverse waves propagate at a smaller angle and at a slower speed than longitudinal waves. Echoes obtained from longitudinal waves can be identified by their position in a suitably close range of the time base. Interpretation of the indications is limited to half a pitch. In contrast, indications obtained from transverse waves will always be characterized by longer delays. There is, however, a possibility here to perform half-pitch and multiples of it, which gives the possibility of reading from further ranges of the path of the transducer head.

8. Conclusions

The essence of the article is to determine the reliability of test results using technique no. 1 according to DAC curves and to analyze the size of the error based on the evaluation of the height of the echo amplitude. The tests carried out on heterogeneous welded joints in this study were exploratory in nature. They have made it possible to formulate conclusions that will inform further consideration of the use of ultrasonic testing to measure heterogeneous joints. It is also a starting point for planning the next stages of testing on, among other things, specimens in the form of plates with other combinations of base and filler materials and the use of other welding processes that affect the change in the structure of welded joints.

The following observations can be made from the results of the tests:

1. For artificial discontinuities, the highest amplitude values were recorded for a 16 mm thick heterogeneous joint using a transverse wave head and angles of 70° and 60° (Figures 8–11).
2. For tests performed on natural discontinuities in heterogeneous joints using transverse waves, discontinuities on the side of 316L steel were detected more favorably. On the ferritic 13CrMo4-5 steel side, not all discontinuities were detected (Figures 12 and 15).
3. Testing of a 16 mm thick natural joint using a transverse wave head with a beam insertion angle of 60° had the most favorable detection of natural discontinuities concerning the other measurements made for heterogeneous joints (Figures 12–15).
4. For the tests carried out on the artificial discontinuities located in the 8 mm thick variegated welded joint with longitudinal waves, higher values of amplitudes were obtained on the 316L steel side than for the discontinuities measured on the 13CrMo4-5 steel side—Figure 16. For the other thicknesses of 12 and 16 mm, similar values of amplitudes obtained from measurements on both sides of the joint were observed—Figures 17 and 18.
5. The highest values of the recorded amplitude were obtained during the measurement of artificial discontinuities using longitudinal waves and welded joints of various thicknesses of 16 mm and an angle of 60°—Figure 19.
6. No significant differences were observed for tests conducted using the longitudinal wave head on the ferritic and austenitic steel sides at natural discontinuities for both the thickness and the side from which the test was conducted (Figures 20–23).
7. Similar ranges of decibel gain level change values to the comparison line carried out on artificial discontinuities in heterogeneous joints using both transverse and longitudinal waves were recorded (Tables 7 and 9).
8. Higher values of decibel gain level changes to the determined comparison lines were observed when tested on natural discontinuities on the 13CrMo4-5 side of the material at thicknesses of 8 and 12 mm than on the 316L side (Table 8), while smaller differences were observed for tests conducted using longitudinal waves (Table 10).

Based on the study, it is concluded that, despite the difficulties, ultrasonic testing allows volumetric inspection of welded joints of diverse materials of the type of ferritic steel in the grade 13CrMo4-5 with austenitic steel 316L. In addition:

1. The sensitivity of detection in the testing of heterogeneous joints depends on the type of material and its phase structure, the ultrasonic wave used, and the angle of beam introduction.
2. The highest detection sensitivity was obtained by conducting tests from the ferritic steel side, which is due to the lower attenuation of the ultrasonic wave propagating in ferritic steel compared to austenitic steel.
3. The most favorable conditions for detecting discontinuities were obtained when testing using a longitudinal ultrasonic wave.
4. For testing materials up to 15 mm thick, more favorable detection results were obtained with an ultrasonic beam insertion angle of 70° and above 15 mm with an ultrasonic beam insertion angle of 60°.
5. The ultrasonically tested heterogeneous joints required more sweeps for maximum detection of different areas.

Main test results, stated benefits, and limitations:

1. The DAC technique can be used to evaluate heterogeneous welded joints.
2. The value of the recorded amplitudes depends on the location of the reference reflectors.
3. From the conducted tests, the effect of the test side on the registration of the signal from artificial and natural discontinuities was observed.
4. In ultrasonic testing of welded joints of austenitic steels, due to the structural changes in the tested materials, tests should be carried out from each side.
5. When testing austenitic steel, it is recommended to use longitudinal wave heads. They show lower values of the attenuation coefficient, and therefore, smaller corrections to the amplification used when recording the signal from artificial and natural discontinuities.

Directions for further research:

1. Application of phased array technique—this technique uses multi-transducer mosaic heads for testing and uses a wide angular range of 40–70°. The dual matrix array with transmit–receive longitudinal (DMA-TRL) head, which allows the introduction of creeping L-wave, longitudinal L-wave, and the use of the tandem LLT technique, is also becoming increasingly popular.
2. Testing of welded joints with larger thicknesses, in the range of 20–35 mm—these tests use transverse and longitudinal wave heads with frequencies lower than those used within the framework of this work and with other transducer sizes.
3. Testing of welded joints with thicknesses in the range of 3–8 mm—in the energy industry, tests are also performed on joints with smaller thicknesses in the range of 3 to 8 mm using the Cobra technique. Power blocks on heat exchangers, among others, also include connections in this range.
4. Testing of components with a different configuration—welded joints in different combinations of base and filler materials. The use of other welding processes such as TIG, covered electrode, or powder wire welding can also be considered.

Author Contributions: Conceptualization, Ł.R., and R.K.; methodology, R.K. and J.S.; validation, G.G. and G.P.; formal analysis, Ł.R.; investigation, Ł.R.; writing—original draft preparation, G.P.; writing—review and editing, G.P.; supervision, R.K., J.S. and G.G.; funding acquistion, G.P.; project administration, K.Ł. All authors have read and agreed to the published version of the manuscript.

Funding: This research received no external funding.

Data Availability Statement: The original contributions presented in the study are included in the article, further inquiries can be directed to the corresponding authors.

Conflicts of Interest: The authors declare no conflicts of interest.

Abbreviations

The following abbreviations are used in this manuscript:

DAC	Distance–amplitude curve
DMA	Dual matrix array
DMA-TRL	Dual matrix array with transmit–receive longitudinal
HAZ	Heat-affected zone
L	Longitudinal waves
LA	Linear array
MAG	Metal active gas
NDT	Non-destructive testing
PA	Phased array
PAUT	Phased array ultrasonic testing
RT	Radiographic testing
s	Ultrasonic wave path
SH	Screen height
SEK	Transverse wave heads
SEL	Longitudinal wave heads
t	Material thickness
T	Transverse waves
TFM	Total focusing method
TH	Horizontally polarized transverse waves
UT	Ultrasonic testing
¼t	Reference hole drilled to a depth of ¼ the thickness of the material
½t	Reference hole drilled to a depth of ½ the thickness of the material
¾t	Reference hole drilled to a depth of ¾ the thickness of the material
p	Utrasonic head travel width
Δ Hu	Change in decibel gain level

References

1. Chassignole, B.; Dupond, O.; Fouquet, T.; Brun, A.; Moysan, J.; Benoist, P. Application of modelling for enhanced ultrasonic inspection of stainless steel welds. *Weld. World* **2011**, *55*, 75–82. [CrossRef]
2. Temple, J.; Chapman, R. *Modelling the Ultrasonic Inspection of Ferritic and Austenitic Steel*; Borloo, E., Lemaitre, P., Eds.; Non-Destructive Examination Practice and Results. State of the Art and PISC III Results. EUR 15906; Commission of the European Communities: Brussels, Belgium, 1994; pp. 369–378. Available online: https://www.osti.gov/etdeweb/biblio/21468181 (accessed on 28 April 2024).
3. Apfel, A.; Moysan, J.; Corneloup, G.; Chassignole, B. Simulations of the influence of the grains orientations on ultrasounds propagation; In Proceedings of the World Conference on Nondestructive Testing, Montreal, QC, Canada, 30 August–3 September 2004.
4. Rojek, B.; Gołąbek, P.; Korneta, A. *Laboratorium z Podstaw Badań Ultradźwiękowych*; Ultramet: Radom, Poland, 1994.
5. Słania, J.; Krawczyk, R.; Masłoń, D. Technology of welding joints mixed with duplex steel. *Arch. Metall. Mater.* **2016**, *61*, 159–168.
6. Nageswaran, C.; Carpentier, C.; Tse, Y. Microstructural quantification, modelling and array ultrasonics to improve the inspection of austenitic welds. *Insight–Non-Destr. Test. Cond. Monit.* **2009**, *51*, 660–666. [CrossRef]
7. Kalkowski, M.; Bézi, Z.; Lowe, M.; Schumm, A.; Spisák, B. Supporting Imaging of Austenitic Welds with Finite Element Welding Simulation—Which Parameters Matter? *Appl. Sci.* **2023**, *13*, 7448. [CrossRef]
8. Aizpurua, I.; Ayesta, I.; Castro, I. Characterization of anisotropic weld structure for nuclear industry. In Proceedings of the 11th European Conference on Non-Destructive Testing (ECNDT 2014), Prague, Czech Republic, 6–10 October 2014.
9. Chassignole, B.; Dupond, O.; Quemard, L. Ultrasonic Examination of a Weld Repair in Ni-Based Alloy. In Proceedings of the 9th International Conference on NDE in Relation to Structural Integrity for Nuclear and Pressurized Components, (JRC-NDE 2012), Seattle, WA, USA, 22–24 May 2012.
10. Hunter, A.; Drinkwater, B.; Zhang, J.; Wilcox, P. A study into the effects of an austenitic weld on ultrasonic array imaging performance. *AIP Conf. Proc.* **2011**, *1335*, 1063–1070.
11. *PN-EN ISO 11666:2018-04*; Non-destructive Testing of Welds—Ultrasonic Testing—Acceptance Levels (In Polish: Badania Nieniszczące spoin—Badania Ultradźwiękowe—Poziomy Akceptacji). PKN-Polish Committee for Standardization: Warsaw, Poland, 2019.
12. Lachance, F.; Giguère, D.; Rioux, P. High frequency austenitic stainless steel solution. In Proceedings of the 15th Asia Pacific Conference for Non-Destructive Testing (APCNDT2017), Singapore, 1 March 2018.

13. Lachance, F.; Rioux, P.; Giguere, D.; Turcotte, J. High Frequency Inspection Solution for Austenitic Stainless-Steel Welds. Available online: https://www.cinde.ca/ (accessed on 29 April 2024).
14. Holmes, C.; Drinkwater, B.; Wilcox, P. Post-processing of the full matrix of ultrasonic transmit–receive array data for non-destructive evaluation. *NDT Int.* **2005**, *38*, 701–711. [CrossRef]
15. Dugan, S.; Wagner, S. Ultrasonic inspection of austenitic stainless steel welds with artificially produced stress corrosion cracks. *AIP Conf. Proc.* **2014**, *1581*, 992–998.
16. Capobianco, T.; Young, G., Jr.; Pyle, J.; Khan, F. Effects of microstructure and texture on ultrasonic inspection of austenitic weld metals. *AIP Conf. Proc.* **2012**, *1430*, 1203–1210.
17. Boller, C.; Pudovikov, S.; Bulavinov, A. Quantitative ultrasonic testing of acoustically anisotropic materials with verification on austenitic and dissimilar weld joints. *AIP Conf. Proc.* **2012**, *1430*, 881–888.
18. Hu, D.; Wang, Q.; Xiao, K.; Ma, Y. Ultrasonic phased array for the circumferential welds safety inspection of urea reactor. *Procedia Eng.* **2012**, *43*, 459–463. [CrossRef]
19. Kumar, S.; Menaka, M.; Venkatraman, B. Dual matrix array probe based phased array ultrasonic testing for inspection of trimetallic weld joints. *Trans. Indian Inst. Met.* **2022**, *75*, 1573–1582. [CrossRef]
20. Yin, A.; Yang, Q.; He, F.; Xiao, H. Determination of grain size in deep drawing steel sheet by laser ultrasonics. *Mater. Trans.* **2014**, *55*, 994–997. [CrossRef]
21. Wirdelius, H.; Liu, Q. An ultrasonic methodology to non-destructively estimate the grain orientation in an anisotropic weld. *MATEC Web Conf.* **2014**, *12*, 04008. [CrossRef]
22. Chassignole, B.; Doudet, L.; Dupond, O.; Fouquet, T.; Benoit, R. New developments for the ultrasonic inspection of austenitic stainless steel welds. In Proceedings of the Conference: ENC 2005: European Nuclear Conference. Nuclear Power for the 21 Century: From Basic Research to High-Tech Industry, Versailles, France, 11–14 December 2005.
23. Moysan, J.; Gueudré, C.; Ploix, M.; Corneloup, G.; Guy, P.; Guerjouma, R.; Chassignole, B. Advances in ultrasonic testing of austenitic stainless steel welds. Towards a 3D description of the material including attenuation and optimisation by inversion. In *Ultrasonic Wave Propagation in Non Homogeneous Media*; Springer: Berlin/Heidelberg, Germany, 2009.
24. Xu, W.; Li, X.; Zhang, J.; Xue, Z.; Cao, J. Ultrasonic signal enhancement for coarse grain materials by machine learning analysis. *Ultrasonics* **2021**, *117*, 106550. [CrossRef] [PubMed]
25. Li, C.; Pain, D.; Wilcox, P.; Drinkwater, B. Imaging composite material using ultrasonic arrays. *NDT Int.* **2013**, *53*, 8–17. [CrossRef]
26. Yamamoto, S.; Semboshi, J.; Sugawara, A.; Ochiai, M.; Tsuchihashi, K.; Higuma, K. Phased array ultrasonic inspection technique for cast austenitic stainless steel parts of nuclear power plants. *Int. Conf. Nucl. Eng.* **2016**, *50015*, V001T01A005.
27. Kaczmarek, R.; Krawczyk, R. Badanie zmian amplitudy echa w zależności od kąta padania wiązki ultradźwiękowej na reflektor duży. *Biul. Inst. Spaw.* **2015**, *3*, 63–67.
28. Kaczmarek, R.; Krawczyk, R. Analiza wpływu kąta ukosowania na wykrywalność przyklejeń brzegowych w ultradźwiękowe metodzie badań nieniszczących. *Biul. Inst. Spaw.* **2014**, *6*, 20–26.
29. Śliwowski, M. Case study—The study of austenitic joints for LNG terminal. *Nondestruct. Test. Diagn* **2016**, *1–2*, 19–26.
30. ASME. *ASME V:2015 T-451 Coarse Grain Materials*; ASME: New York, NY, USA, 2015.
31. Pudovikov, S.; Bulavinov, A.; Kröning, M. Ultrasonic inspectability of austenitic stainless steel and dissimilar metal weld joints. In Proceedings of the 34. MPA-Seminar "Werkstoff- Bauteilverhalten in der Energie- Anlagentechnik", Stuttgart, Germany, 9–10 October 2008.
32. Bolotina, I.; Bulavinov, A.; Lider, A.; Sednev, D.; Shtaynbreher, A. Ultrasonic inspection of spent nuclear fuel casks. *IOP Conf. Ser. Mater. Sci. Eng.* **2015**, *81*, 012073. [CrossRef]
33. Olympus. Easy Ultrasonic Phased Array Inspection of Corrosion Resistant Alloys and Disimilar Weld Materials. In *Olympus Industrial Resources. Application Notes.* Available online: https://www.olympus-ims.com/en/easy-ultrasonic-phased-array-inspection-of-corrosion-resistant-alloys-and-dissimilar-weld-materials/ (accessed on 28 April 2024)
34. Szymański, A.; Klimpel, A. *Kontrola i Zapewnienie Jakości w Spawalnictwie. Tom 2*; Silesian University of Technology: Gliwice, Poland, 1998; ISBN 83-85718-09-5. Available online: https://tezeusz.pl/kontrola-i-zapewnienie-jakosci-w-spawalnictwie-tom-2-andrzej-szymanski (accessed on 28 April 2024).
35. Stępiński, T. *Synthethic Aperture Focusing Technique in Ultrasonic Inspection Of Coarse Grained Materials*; SKI, Report; Uppsala University: Uppsala, Sweden, 2008.
36. Braconnier, D. *Synthetic Focusing Aperture for Non-Destructive Testing of Materials*; Raport; KJDT: Osaka, Japan, 2012.
37. Kitze, J.; Brackrock, D.; Brekow, G.; Prager, J.; Gaal, M.; Kreutzbruck, M. SAFT and TOFD-Compared in Ultrasonic Defect Detection. *BAM DGZFP Ger.* **2010**. Available online: https://www.ndt.net/?id=11693 (accessed on 28 April 2024)
38. *ISO 22825:2017-12*; Non-Destructive Testing of Welds—Ultrasonic Testing—Testing of Welds in austenitic Steels and Nickel-Based Alloys. International Organization for Standardization: Geneva, Switzerland, 2017.
39. Kułakowski, M.; Rokosz, K. Alloy austenitic, ferritic and duplex steels used in transport. *Autobusy Tech. Eksploat. Syst. Transp.* **2017**, *18*, 357–362.
40. *EN ISO 17640:2018*; Non-destructive Testing of Welds—Ultrasonic Testing—Techniques, Testing Levels, and Assessment. International Organization for Standardization: Geneva, Switzerland, 2018.

41. *PN-EN ISO 22232-3:2021-03*; Non-destructive Testing—Characterization and Verification of Ultrasonic Test Equipment—Part 3: Combined Equipment (In Polish: Badania Nieniszczące—Charakteryzowanie i Weryfikacja Aparatury Ultradźwiękowej—Część 3: Aparatura Kompletna). PKN-Polish Committee for Standardization: Warsaw, Poland, 2021.
42. *PN-EN ISO 17640:2019-01*; Non-Destructive Testing of Welds—Ultrasonic Testing—Techniques, Testing Levels, and Assessment (In Polish: Badania Nieniszczące Spoin—Badania Ultradźwiękowe—Techniki, Poziomy Badania i Ocena). PKN-Polish Committee for Standardization: Warsaw, Poland, 2019.

applied sciences

MDPI

Article

In-Motion, Non-Contact Detection of Ties and Ballasts on Railroad Tracks

S. Morteza Mirzaei, Ahmad Radmehr, Carvel Holton and Mehdi Ahmadian *

Center for Vehicle Systems and Safety (CVeSS), Virginia Tech, Blacksburg, VA 24060, USA; smhajimirzaei@vt.edu (S.M.M.); radmehr@vt.edu (A.R.); cholton@vt.edu (C.H.)
* Correspondence: ahmadian@vt.edu

Abstract: This study aims to develop a robust and efficient system to identify ties and ballasts in motion using a variety of non-contact sensors mounted on a robotic rail cart. The sensors include distance LiDAR sensors and inductive proximity sensors for ferrous materials to collect data while traversing railroad tracks. Many existing tie/ballast health monitoring devices cannot be mounted on Hyrail vehicles for in-motion inspection due to their inability to filter out unwanted targets (i.e., ties or ballasts). The system studied here addresses that limitation by exploring several approaches based on distance LiDAR sensors. The first approach is based on calculating the running standard deviation of the measured distance from LiDAR sensors to tie or ballast surfaces. The second approach uses machine learning (ML) methods that combine two primary algorithms (Logistic Regression and Decision Tree) and three preprocessing methods (six models in total). The results indicate that the optimal configuration for non-contact, in-motion differentiation of ties and ballasts is integrating two distance LiDAR sensors with a Decision Tree model. This configuration provides rapid, accurate, and robust tie/ballast differentiation. The study also facilitates further sensor and inspection research and development in railroad track maintenance.

Keywords: automated railroad track inspection; non-contact; in motion; LiDAR; machine learning

1. Introduction

Various studies have aimed at identifying, detecting, and assessing the condition of railroad ties and ballasts, mainly using vision systems or ground-penetrating radars [1–5]. The emphasis is often placed on how ballast and tie degradation may increase the likelihood of a derailment [6–10]. Other studies have used alternative technologies for making such assessments, such as the research by Zhao et al. that has developed and fabricated a laser-speckle strain sensor to measure the transfer length of concrete ties [11].

The mentioned techniques are non-contact and have the potential to be mounted onboard Hyrail vehicles or manned and unmanned track geometry cars for autonomous, in-motion assessment of tracks. Their goal is to provide an early warning to track engineers for intervention before any track fault progresses to costly maintenance issues. These studies can be collectively classified as track health condition monitoring research. However, these methods lack the ability to filter out unwanted targets—for example, tie inspection systems often struggle to ignore ballasts, reducing their overall effectiveness.

The primary purpose of our study was to develop an automated method for differentiating between ties and ballasts, allowing health monitoring systems to focus more accurately on their respective targets during in-motion operations. This study was mainly aimed at distinguishing between ties and ballasts as part of a more extensive study to assess the early stages of track instability from tie vibrations. Obviously, to determine tie vibrations, one needs first to differentiate them from ballasts; hence, this study serves as a preliminary step in developing non-contact, in-motion devices for inspecting ties or even ballasts. The purpose of this system is to serve as an auxiliary unit that enhances the performance of other track stability inspection devices. By providing real-time, high-accuracy

differentiation between ties and ballasts, this system helps to narrow the focus of other inspection tools, enabling them to more effectively target specific track components.

The existing methods used to distinguish between ties and ballasts are mainly based on ultrasonic or vision methods. For instance, Datta et al. [12] developed an in-motion method for reconstructing the deflection profile of railroad ties by means of non-contact ultrasonic testing. To demarcate the ties, they use a vision-based image classification approach. Sabato and Niezrecki [13] also used Digital Image Correlation (DIC) for a similar goal. Bojarczak et al. [5] developed an algorithm based on a deep neural network for semantic segmentation of ties and ballasts and eventually detecting ballast unevenness. Despite these methods' effectiveness, a few issues exist, preventing them from being installed on standard track geometry cars. First, their effectiveness for onboard applications is limited because they are mainly intended for stationary or quasi-static implementation. Second, they require significant post-processing, making them unsuitable for real-time or near-real-time measurements.

To further advance tie and ballast detection methods, this study evaluated the application of LiDAR-based methods that can be used at speeds suitable for Hyrail vehicle implementation. The following sections will describe the system, its setup on a robotic track cart for technological feasibility evaluation testing, the assessment of the test results through developing new data analysis methods, and the application of the final system.

2. Setup

The experimental evaluation evaluated various methods and hardware implementations to achieve the study's goal of differentiation between ties and ballasts in motion. A remote-controlled track cart, shown in Figure 1, was constructed and used to house the required sensors and electronics [14]. A rail cart was selected due to its significant advantage over other potential solutions, such as aerial vehicles and legged robots, because of their poor performance in railroad environments and lack of ability to be tested over extensive distances. This rail cart can successfully replicate Hyrail vehicles and track geometry cars that are mainly used for track inspections. It is a stable platform that allows for continuous monitoring of track conditions as the cart moves.

Figure 1. Railway Technologies Laboratory's remotely controlled track cart used for in-motion differentiation of ties and ballasts.

The cart is equipped with a traction-braking system and can run on various railroad tracks. The cart's frame is made of 80/20 extruded aluminum, offering flexibility in mounting multiple sensors and data acquisition units. Its flexibility allows efficient testing

across diverse railroad environments, including branch lines and mainlines. This flexibility is crucial for the research objectives, as the cart can easily navigate various track conditions while ensuring that sensors maintain a stable orientation towards their targets for accurate data collection. Additionally, it features a "kill switch" to enable emergency braking if needed. Its tapered and flanged wheels provide a stable run up to 10 mph (~16 km/h) in both forward and reverse directions. Furthermore, the cart is designed to fit inside the bed of a pickup truck, facilitating easy transportation to various track locations.

3. Methodology

Various sensors, configurations, and data analysis methods were developed and explored to achieve optimal accuracy, efficiency, and robustness, ensuring that the system complies with railroad standards. A set of sensors that exhibit promising potential for this study will be discussed, followed by a series of tests for selecting the most suitable sensors and the required data analysis for tie/ballast differentiation.

3.1. Sensors

The sensors selected for the study are shown in Figure 2. They include an inductive proximity sensor for ferrous materials, distance LiDAR sensors, temperature and humidity sensors, and accelerometers. The inductive proximity sensor is on the far-left side of the cart, right on top of the tie plates. Two distance LiDAR sensors point downward on the right and left sides of the cart. Humidity, temperature, and acceleration are ancillary sensors for possible application of the track cart in other railroad-related system developments, such as evaluating the migration of flange grease on rails and assessing track stability through Doppler LiDAR sensors. Because these studies are outside this paper's scope, these sensors will not be discussed here.

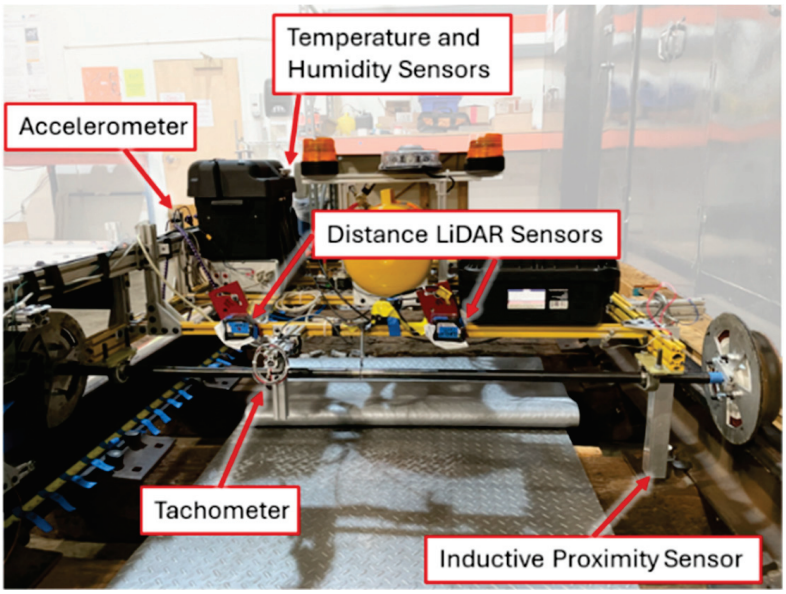

Figure 2. Sensor installation onboard the track cart used for in-motion differentiation of ties and ballasts.

The sensor selection was based on an early evaluation of various sensors, in which some were rejected and others selected because of their promise of yielding satisfactory results. The sensor selection was based on availability, cost-effectiveness, ease of integration, and effectiveness in identifying ties or ballasts. The sensors that were not selected were infrared temperature sensors (or cameras) and time-of-flight LiDAR sensors. They were found to be too slow for in-motion measurements, even at low speeds. Others, such as time-of-flight acoustic sensors, radars, and surface reflectivity/intensity sensors, were proven to provide insufficient functional resolution to capture tie and ballast patterns definitively.

The sensors selected for further integration into the system and track evaluation were an inductive proximity sensor for ferrous materials and distance LiDAR sensors, as will be discussed further next.

3.1.1. Inductive Proximity Sensor for Ferrous Materials

Ties are typically connected to rails with metal fasteners like spikes and tie plates. One way to detect ties and identify their locations is to detect tie plates and possibly spikes using inductive proximity sensors for ferrous materials. Typically, an "inductive proximity sensor" is equipped with a Hall effect probe, which triggers a pulse when it detects a ferrous object in its proximity (Hall effect sensors, named for the physicist Edwin Hall, incorporate one or more Hall elements, generating a voltage proportional to an axial component in a magnetic field. They are commonly used in proximity sensing, positioning, speed detection, and current sensing applications in many industrial devices). For rail applications, the sensor can be positioned above the tie plate and spikes, and the generated pulses can be used to identify tie locations.

3.1.2. Distance LiDAR Sensors

LiDAR, Light Detection and Ranging [15], is a remote sensing method that uses a pulsed laser which can be triangulated to measure the distance from the target point to the lens itself [16]. Ties and ballasts have different surface characteristics to LiDAR, with ties featuring a smoother and ballasts having a rougher pattern. This contrast can be detected in motion using downward-facing vertical LiDAR sensors to identify alternating tie and ballast sections.

Two Keyence IL-600 sensors from Keyence corporation of America (Itasca, IL, USA) were adopted for this study due to their off-the-shelf availability and cost-effectiveness. The Keyence IL-600 is a precise distance sensor with a nominal accuracy of 50 μm and a response time of 0.33, 1.0, 2.0, or 5.0 ms. The fastest response time ensures enough spatial resolution (up to 1.3 cm) for the sensor to record sufficient samples for each tie (about 16 samples) at speeds of up to 40 mph (~65 km/h). A higher number of samples per tie is needed to raise the confidence in the measured data on each tie, with 3–4 samples potentially being the minimum. The required 200–1000 mm installation range provides sufficient standoff distance for most railroad applications.

As shown in Figure 3, two sensors, designated as "right" and "left" sensors, were implemented in line with each other in the lateral direction to enable the collection of data on two parts of the track. Using two sensors allows data to be gathered at two locations on ties and ballasts, reducing the likelihood of false positives and negatives. In addition, having two LiDAR sensors would enable us to develop more sophisticated data analysis methods based on measurements from both sensors. This will be elaborated further in the Analysis section. Although not part of the objectives of this study, the sensors could possibly be used to detect track anomalies, such as sunk, tilted, or bowed ties, by comparing their outputs with each other. For instance, a tilted or bowed tie can be identified from the data by comparing the left and right sensor measurements. If they return different values over a tie, this means that the tie is tilted. The same procedure can be followed for different anomalies.

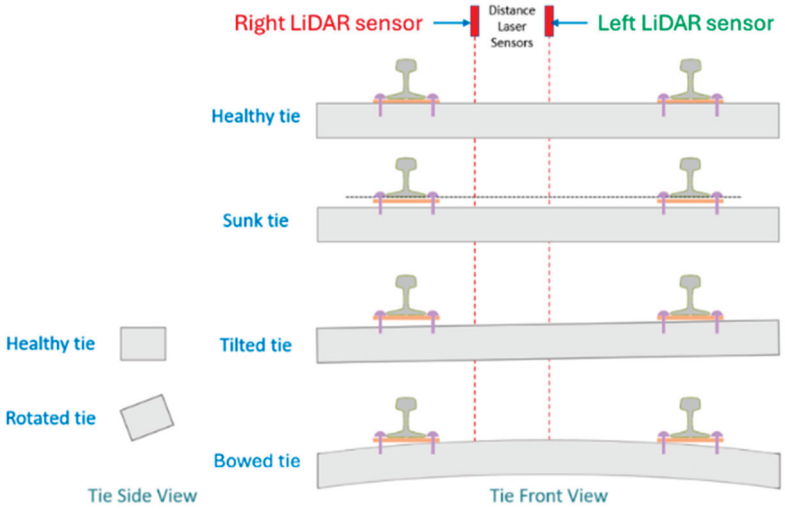

Figure 3. Left and right LiDAR sensor installation for in-motion differentiation of ties and ballasts and their potential application for detecting track anomalies, such as sunk, tilted, or bowed ties.

3.1.3. Tachometer

A tachometer is also employed to monitor the location and speed of the rail cart along the track. This device facilitates the transformation from the time domain to the spatial domain. The tachometer comprises an 18-tooth gear and a Hall effect probe. Along with the cart's wheel diameter of 7.5 inches, a linear resolution of 1.66 cm can be achieved, as derived from Equation (1). The tachometer is attached to the front shaft of the cart, which is a passive (idler) shaft. This configuration was chosen because the active (driver) shaft is directly connected to the DC motor, causing it to experience slippage (rotation without corresponding linear movement) more often, which could result in false information. Thus, using the passive shaft minimizes the occurrence of erroneous readings.

$$Linear\ resolution = \frac{1}{number\ of\ tooth} \times \pi \times \frac{wheel\ diameter}{2} \quad (1)$$

3.2. Data Acquisition Unit

A single data acquisition unit with 16 A/D channels was selected to record the necessary data throughout track tests. The data were sampled at 1000 Hz. The 1000 Hz sampling frequency was selected based on conducting a series of tests in the early stages of the study to assess the most beneficial sampling rate. The sampling frequency provides approximately 11 samples per tie, assuming an 8-inch-wide tie (~20 cm) and a forward speed of 40 mph (~65 km/h), representing the higher range of the intended speed for measurements.

4. Experiments

Three groups of tests were conducted: in the laboratory, on a revenue-service track at walking speeds, and in a simulated track environment at high speeds. These tests aimed to thoroughly investigate the applicability and effectiveness of the proposed system. The laboratory testing focused on evaluating the sensors' ability to capture tie and ballast surface figures in a controlled setting. The revenue-service track testing assessed the system's performance in an uncontrolled environment. Finally, high-speed testing on the simulated track evaluated the system's performance under high-speed conditions resembling those of in-motion inspections. The data collected from these experiments were used to develop robust data analysis methods for distinguishing ties and ballasts based on sensor measurements.

4.1. Laboratory Testing

The system was tested on a 40 ft track panel (~12 m) at the Railway Technologies Laboratory (RTL). The robotic rail cart, equipped with all the mentioned sensors, ran over a small section of the track with ties and ballasts to collect data. As shown in Figure 4, the left distance LiDAR sensor was put on an unballasted section with only ties to establish reference measurements for the ties. These measurements were used as the "ground truth" for another sensor on the right with both ties and ballasts. In parallel with the LiDAR sensors, an inductive proximity sensor was used to detect the ties. This sensor was used for two purposes: first, to evaluate its applicability for differentiating between ties and ballasts; second, to verify the accuracy of the LiDAR measurements in distinguishing between the ties and ballasts.

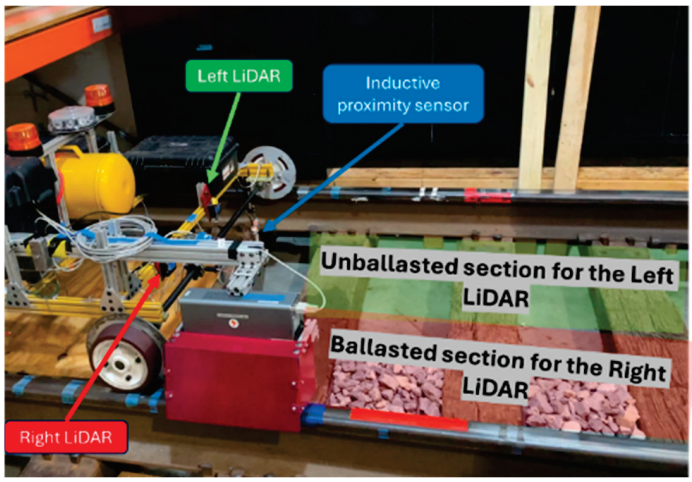

Figure 4. Laboratory evaluation of LiDAR sensors on a 40 ft track panel for differentiating between ties and ballasts.

The tests were intended to evaluate the system's general capability and the applicability of the sensors in tie/ballast detection at low speeds in a controlled environment. Unless the LiDAR's measurements are sufficiently consistent and repeatable, its success for field measurements will be doubtful because of the uncontrolled environment common in track measurements.

Figure 5a shows the measured distances from LiDAR sensors to their target surface (tie, ballast, or ground) and an inductive proximity sensor. Note that the left distance LiDAR measurement is used as the ground truth. The terms "activated" and "null" for the inductive proximity sensor are used to indicate when the sensor is detecting a tie plate (hence, a magnetic field is generated) and when no tie plate is detected and a magnetic field is not generated. As shown in Figure 5a, the system accurately captured the surface profile of the traversed track, down to its finest details. The recorded variations are highly tangible and clear, allowing one to easily visualize the track layout. This level of precision stands in contrast to other similar instruments mentioned before, which often suffer from low resolution or slow sampling rates, whereas the LiDAR sensors used in this system demonstrate superior accuracy and agility. The data in Figure 5a show irregular and noisy measurements over ballast sections (unshaded areas) with more significant and frequent variations. In contrast, the tie sections (orange-shaded areas) exhibit smoother and relatively flat measurements compared to the ballast sections. The measurements also show the surface height differences between ties and ballasts, which agree with a visual inspection of the track. The variations observed in the inductive proximity sensor measurements are attributed to the surface irregulates of the tie plates, as verified by visual observations.

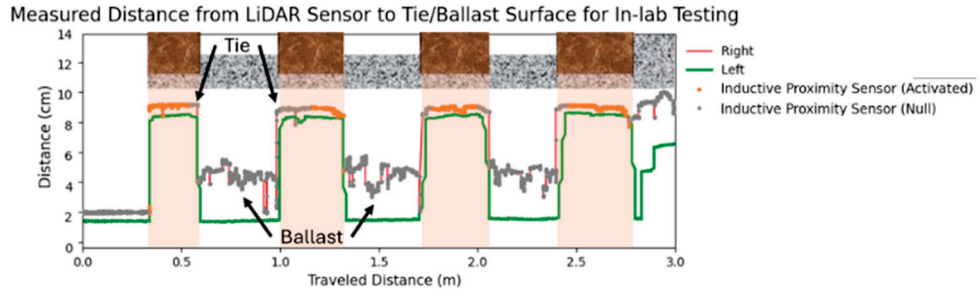

(**a**)

(**b**)

Figure 5. Laboratory system evaluation: (**a**) comparison between LiDAR sensor and inductive proximity sensor measurements. Orange-shaded areas correspond to ties and unshaded areas to ballasts; (**b**) response of the inductive proximity sensor to a sample tie, where gray dots indicate the "null" regions (no Hall effect measurement) or ballasts and orange dots show the "activated" regions (Hall effect measurement) or ties.

Figure 5a shows that the inductive proximity sensor does not detect the first half of the second tie. The reason for this is illustrated in Figure 5b, which shows that the first half of the left tie plate is sunk into the tie, making it out of the inductive proximity sensor's range. In contrast, the right tie plate is not sunk and remains in the sensor's measurement range; therefore, it is detected. Inductive proximity sensors tend to have a small working range that requires putting the sensor as close as possible to the tie plate (maximum: 15 mm), increasing the likelihood of interference with objects that may be present on a track. Although there are inductive proximity sensors with more extensive working ranges, their magnetic fields could get diverted to the rail, significantly increasing the rate of false positives. At the conclusion of the laboratory tests, we deemed the inductive proximity sensors unsuitable for revenue-service testing despite their success in the controlled laboratory tests.

4.2. Track Testing

The track tests were performed in two different settings. First, the rail cart ran and collected data on a branch line with a 115RE rail that is used infrequently and has somewhat degraded tie and ballast conditions. Second, it was set on a main line with a 136RE rail with far better tie and ballast conditions. These tests were conducted to assess the system's performance in recording the necessary data at higher speeds, over more extensive distances, and in more realistic environments, including challenging conditions, such as those encountered on branch lines, which could represent worst-case scenarios.

Figure 6 shows a sample section of the track testing for each setting. The raised and smooth surfaces represent the ties, while the lower and more irregular surfaces are the ballast. The highlighted sections mark the locations of the ties. As the plots indicate, the surface tracks are well-captured by the sensors. Note that the left and right measurements are slightly shifted to enable easier differentiation between the two. Plotting them without the shift would place them nearly on top of each other, making it more difficult to identify

any differences. Additionally, some data drop-ins observed during branch-line track testing (Figure 6a) were caused by sunlight interference with the lasers. This issue was addressed in future tests by adding shade covers to block the sunlight. As shown in Figure 6b, there were no drop-ins during the mainline testing because the covers were installed for this test. Additionally, the mainline testing results in Figure 6b display smoother tie surfaces compared to the branch-line testing. For example, some cracks are visible in Figure 6a but not in Figure 6b.

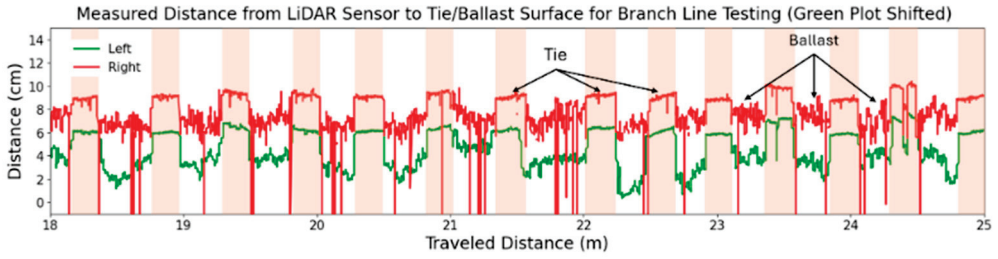

(**a**)

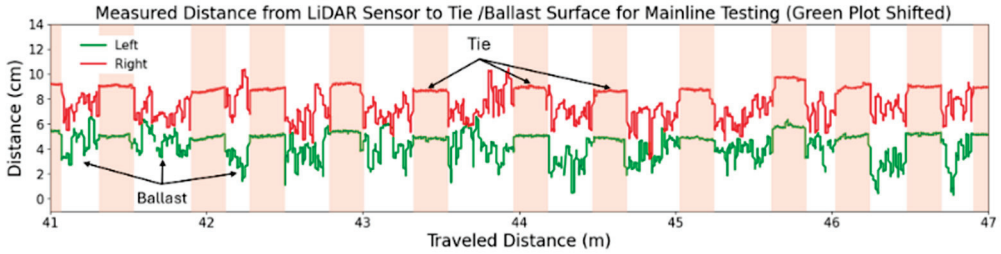

(**b**)

Figure 6. A sample of track testing results performed on a branch track and a mainline: (**a**) measured distances from LiDAR sensors to the tie/ballast surfaces on a branch track, with the left (green) plot shifted for better visualization of the plots; (**b**) measured distances from LiDAR sensors to the tie/ballast surfaces on a mainline, with the left (green) plot shifted. Like the previous plots, orange-shaded areas are associated with the ties, and the unshaded regions are associated with the ballasts.

It must be noted that the track tests in both settings were limited to walking speeds, in the range of approximately 1.5 to 4.0 mph (2.4 to 6.4 km/h). The track cart was remotely controlled by an operator who was following it. Although the cart can move at speeds of up to 10 mph (16 km/h), the test speeds were limited to speeds the operator could walk while safely negotiating the ties and ballasts.

4.3. High-Speed Testing

Although the earlier branch-line track testing indicates that the LiDAR system can successfully differentiate between ties and ballasts, these runs were performed at low speeds, usually less than 4 mph (6.4 km/h). The low speeds were due to the speed limitation of the track cart used for the tests and the need for safe operation while following the cart. Due to lack of access to track time and standard Hyrail vehicles, it was decided to answer the question about how well the system can perform at higher speeds by conducting a series of tests with a road vehicle over a simulated track consisting of alternating wood planks and ballasts. The main concern was the adequacy of the selected sampling rate, specifically, having sufficient data points on the surface of the ties and ballasts to adequately identify them with low numbers of false positives and false negatives.

The simulated track on an asphalt surface outside the RTL facility and the system installation on the rear of a Chevy Silverado pickup truck are shown in Figure 7. Figure 7a displays the simulated track that consisted of 13 planks with the same width as an 8-inch tie (~20 cm) and a length of 2 ft (~0.66 m). The planks were painted to resemble

the tie surface color. The space between the planks was filled with ballast nearly 3 to 4 cm lower than the top surface of the planks to provide a clear distinction between ties and ballasts in the data. Figure 7b shows the left and right LiDAR sensors mounted to an aluminum structure attached to the hitch of a Chevy Silverado pickup truck. This installation proved to be accessible and adequate for the intended tests. This setup was chosen to ensure safe operation while closely replicating real-world conditions during high-speed testing with Hyrail vehicles. A road vehicle, due to its nature, introduces more stochastic vibrations compared to standard Hyrail vehicles, as they have a more flexible suspension system [17,18], presenting a worst-case scenario. However, after initial testing, it was determined that the system effectively mitigated the impact of these unwanted vibrations, still capturing satisfactory data. As shown in Figure 8, despite the vehicle's vibrations, the sensors successfully recorded the surface figure of the simulated track.

(**a**) (**b**)

Figure 7. High-speed test setup: (**a**) a simulated track set up on an asphalt surface with a tie and ballast arrangement like a railroad track; (**b**) distance LiDAR sensor installation on the rear of a Chevy Silverado for the simulated high-speed tests.

Figure 8 shows a segment of the measured distances from the LiDAR sensors to the surface of the ties and ballasts at 19 and 37 mph (30 and 59 km/h). Comparing the measurements with the track's setup indicates that the sensors correctly identified the width of the ties and the gaps between them, which were filled with ballast. Beyond the sample measurements shown in Figure 8, we performed tests at speeds ranging from 4 to 37 mph (6.4 to 59 km/h), specifically at 19, 31, and 34 mph (30, 50, and 55 km/h). Although not included here, for brevity, the results for other speeds are similar to those shown in Figure 8, and they similarly indicate the success of the LiDAR system in sampling the ties and ballast sections.

Interestingly, the results in Figure 8 and other measurements indicate that the LiDAR sensors successfully capture irregularities associated with tie and ballast surfaces, with the ballast exhibiting more significant surface variations than the ties, as expected. Comparing Figure 8a,b shows a notable consistency in measurements. The tie surface features in Figure 8b closely resemble those in Figure 8a, proving the system's repeatability. For example, the irregular surface of the first tie, caused by a piece of tarp on top of it, was detected in both tests. It is worth mentioning that the ballast surface has many associated uncertainties, so data from those sections were not expected to be repeatable. For safety

reasons, shade covers were not used to block sunlight during this series of tests, resulting in some data drop-ins observed during high-speed testing (Figure 8). However, these drop-ins can be neglected, as they comprise less than 1 percent of the data.

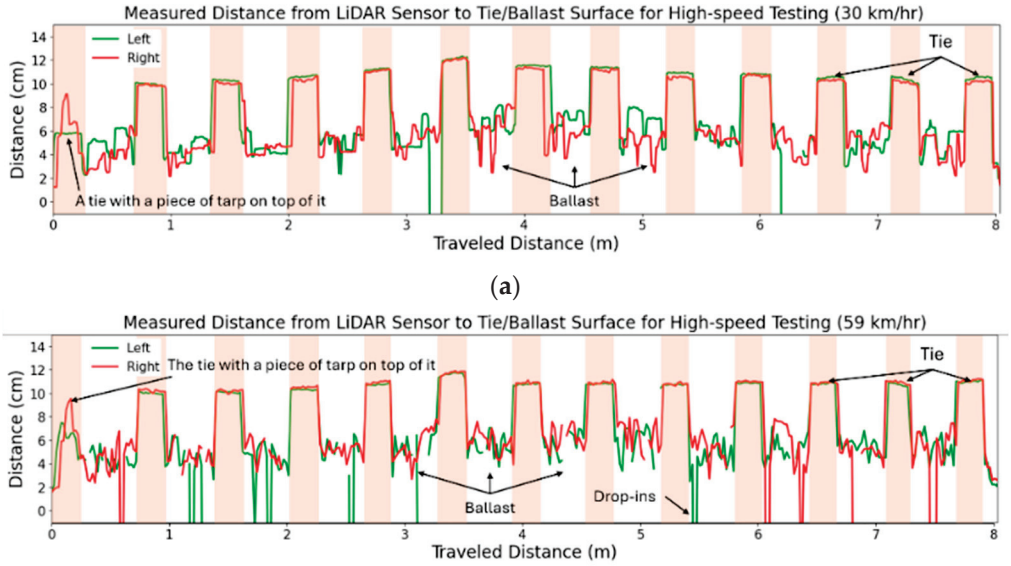

(**a**)

(**b**)

Figure 8. High-speed testing of LiDAR system on a simulated railroad track: (**a**) 19 mph (30 km/h); (**b**) 37 mph (59 km/h). The orange-shaded areas correspond to ties, while the unshaded areas correspond to ballasts.

5. Analysis

Although the unprocessed (raw) LiDAR measurements are distinct enough to the human eye for tie and ballast classification, an automatic differentiation method is needed to process large datasets resulting from track measurements over extended distances. The purpose of this section is to explore various data analytic methods that can process the LiDAR sensor measurements, enabling accurate and efficient differentiation of ties from ballasts in an automated manner.

First, a statistical data analysis method (i.e., moving standard deviation) is evaluated because of its effectiveness in extracting surface variation characteristics. Next, two machine learning (ML) methods, namely Decision Tree and Logistic Regression, are considered to better deal with data uncertainty and ambiguity. Additionally, several preprocessing techniques are investigated to transform the LiDAR measurements into more suitable parameters for training the ML models. The downsides and upsides of each model are elaborated, and the model shown finally to be the best in terms of accuracy and robustness will be selected for analyzing the LiDAR data for tie and ballast differentiation.

5.1. Moving Standard Deviation

As noted earlier, based on visual observation of the track and the measurements, tie surfaces are expected to have fewer variations than ballast surfaces because of their different surface characteristics, irrespective of their height level. This approach uses surface variance to distinguish between ties and ballasts. A moving window over discrete data sections is used to calculate the standard deviation within each window, denoted as "moving standard deviation" here. Equation (2) represents the standard deviation formula. Figure 9 illustrates the process of moving standard deviation. The red bracket with the size

of ws moves along the data and calculates the standard deviation of the data within the "i" data points within the window (i.e., x_i). $\overline{x}$ denotes the average of the data points, x_i.

$$Standard\ deviation = \sqrt{\frac{\sum_{i=1}^{ws}(x_i - \overline{x})^2}{ws - 1}} \quad (2)$$

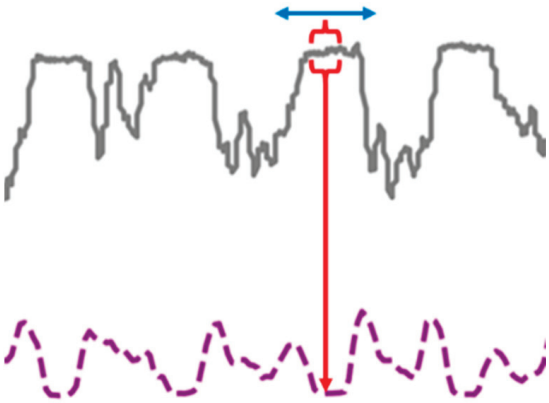

Figure 9. A graphical illustration of moving standard deviation for analyzing the LiDAR sensor measurements used for tie and ballast differentiation.

It is expected that the resulting moving standard deviation would enforce the surface characteristics in the ties and ballasts, leading to more confidence in differentiating between them than would be possible from the individual data points, x_i. The standard deviation over the ties is expected to be lower than over the ballasts, enabling us to identify each.

Figure 10 shows a sample plot for the mainline track testing mentioned earlier. The left axis shows the measured distance from the LiDAR sensor to the tie and ballast surfaces. The right axis shows the moving standard deviation for a spatial window of 4 inches (~10 cm). A spatial window is used because the measurements are made at various speeds that would yield differing numbers of samples on tie and ballast surfaces. Using a spatial window, such as one over 4 inches, would enable a more direct comparison between measurements at different speeds by relating them to a physical reference, such as one-half of the nominal width of a tie. The moving standard deviation (the purple line) exhibits an interesting pattern: it reaches a trough toward the center of the tie and a peak near the boundary between the ties and ballasts. This is because the data near the center of the tie are more consistent and have fewer variations, leading to lower standard deviations. In contrast, the measurements at the interface between the ties and ballasts are highly varied, leading to larger standard deviations.

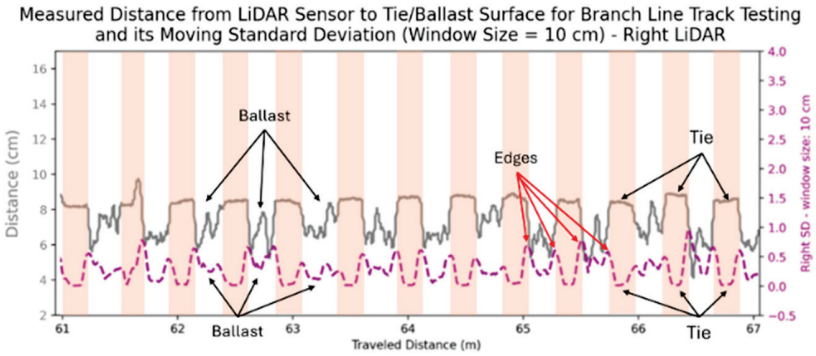

Figure 10. LiDAR system measurements for branch-line track testing at 4 mph showing measured distances from the LiDAR sensor to tie and ballast surfaces (gray line) and the moving standard deviation of the distances for a 4-inch spatial window (purple line). Ties are marked with orange shading, and unshaded areas represent ballasts.

The newly introduced parameter, moving standard deviation, is more interpretable for computers in distinguishing ties and ballasts compared to using measured distances. This method captures surface variations more effectively and enforces new distinct patterns associated with ties and ballasts (local minimums and maximums), enabling easier differentiation between ties and ballasts than before.

Even though this method proved to be successful in differentiating between ties and ballast on the mainline track, it may prove inadequate for branch lines where the variation in data is larger than in the sample data used here. Specifically, large variations in tie surfaces, such as cracks and cuts or displaced and titled ties, can adversely affect the accuracy of the results. Additionally, the ambiguities in correctly identifying the troughs and peaks could lead to errors in autonomously identifying ties and ballasts. A more capable data analysis approach is desired to address these uncertainties.

5.2. Machine Learning Approaches

Another approach for detecting and learning data patterns and better differentiating between ties and ballasts is machine learning (ML). ML models can generally handle highly uncertain tasks, making them well-suited for this task. Due to the high capability of ML models in handling large datasets and automating decision-making processes, the newly developed models are expected to address the challenges previously associated with using the moving standard deviation. With the extensive amount of data collected through our experiments, these models can learn complex patterns and adapt to various conditions, improving the accuracy and reliability of tie and ballast differentiation. The desired ML model will receive the LiDAR data as input and return a classification of tie or ballast as output (prediction).

Like the moving standard deviation method, a moving window is used to process the data at each location. However, unlike the moving standard deviation, which uses a spatial window, this method defines the window size based on the number of surrounding data points required to classify an individual point as tie or ballast. The window size is a tunable parameter that needs to be optimized to achieve the best results. To select the required window size for our model, we evaluated the accuracy that can be achieved for each method for various window sizes, ranging from small to large. This task considers two standard classification "algorithms": Logistic Regression and Decision Tree. Through a series of initial tests, these two algorithms were selected from a larger pool of classification algorithms, including Support Vector Machines (SVMs), k-Nearest Neighbors (k-NN), and neural networks. Logistic Regression and Decision Tree were chosen because they belong to two distinct families—linear and non-linear, respectively—and demonstrated higher accuracy [19].

Logistic Regression uses a linear function to model the relationship between features (i.e., inputs) and a binary outcome. It then applies a sigmoid function to convert this linear output into a 0 or 1 probability, indicating the likelihood of belonging to a specific class [20]. A "0" probability suggests a high likelihood of ballast, and "1" indicates a tie. Equation (3) shows the formula associated with Logistic Regression, where $b_0 + b_1 x$ is the linear function for separating the classes (i.e., ties and ballasts). b_0 and b_1 are the parameters that will be learned through the training process.

$$p = \frac{1}{1 + e^{-(b_0 + b_1 x)}} \tag{3}$$

In contrast, as Breiman et al. (1984) described, the Decision Tree creates a tree-like structure, where each internal node splits the data based on a chosen feature value. This process continues recursively until the data at each leaf node belong predominantly to a single class [21].

These algorithms differ in their interpretability. Logistic Regression provides a single equation representing the entire model, making it relatively straightforward to understand the pattern of each input. On the other hand, a Decision Tree offers a series of branching

rules that often provide a more intuitive understanding of how decisions are made, as the tree visually represents the decision process.

Both Logistic Regression and Decision Tree are supervised learning algorithms, meaning they require training with input data and their respective output labels. In other words, the models need ground-truth labeled data to learn the patterns associated with each label (tie or ballast) and effectively differentiate ties from ballasts. Once trained, these models can predict future unseen data. A small portion of each dataset (approximately 20 percent) is manually labeled as either tie or ballast (i.e., 1 or 0) to construct a ground-truth "labeled dataset" to facilitate this. A portion of the labeled dataset (approximately 60 percent), called here the "training dataset", is used to train the models. The performance of these trained models is then evaluated using the remaining 40 percent of the labeled dataset, referred to as the "test dataset". Various train–test splits, ranging from 50–50 to 90–10, were tested, and the 60–40 split was found to maximize accuracy while minimizing overfitting. Finally, the final trained model was applied to the unlabeled dataset to identify ties and ballasts.

Initially, the measured distances from one of the LiDAR sensors (e.g., the left sensor) to tie or ballast surfaces were used as "input" to train the ML models using both Decision Tree and Logistic Regression algorithms. The difference between the left and right LiDAR sensor measurements was explored as an input for training the models. Finally, to improve the models further, the standard deviation of the difference between the left and right measurements was also evaluated to train the models.

In summary, the measured distance from the LiDAR sensors to the tie or ballast surfaces was considered to be the "input" for training the ML model in the first place and then gradually upgraded to the difference between the left and right LiDAR sensors' measurements, and then the standard deviation of the difference between the left and right measurements was used to achieve higher accuracy and robustness. In Section 5.3, the logic behind these models will be described further, and the most efficient and robust model will be identified. Figure 11 illustrates how six different models were developed based on three different inputs (i.e., preprocessing methods) and two different algorithms.

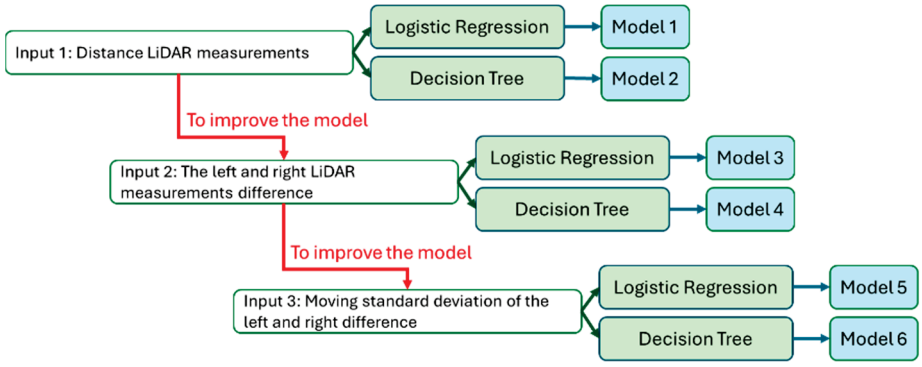

Figure 11. A schematic of six distinct models, developed and investigated to determine the best model for processing LiDAR data to differentiate between ties and ballasts.

5.3. Application of Machine Learning to LiDAR Data

The primary objective of this section is to explore various parameter configurations to develop the most optimal and robust model for analyzing the LiDAR sensors' measurements for tie and ballast differentiation. Three essential parameters have been identified that significantly impact the model's performance: the algorithm, the input for training the ML models, and the window size. As previously mentioned, the two algorithms under consideration are Logistic Regression and Decision Tree, and the three inputs are illustrated in Figure 11. These six models will be evaluated across different window sizes based on their accuracy. Here, "accuracy" is assessed by Equation (4).

$$Accuracy = \frac{Number\ of\ data\ points\ that\ are\ correctly\ classified\ by\ the\ model}{Number\ of\ data\ points\ in\ the\ test\ data\ set} \quad (4)$$

This section is divided into three subsections, each dedicated to analyzing one input. For each input, both algorithms (Logistic Regression and Decision Tree) are considered across a wide range of window sizes.

5.3.1. Measured Distance from LiDAR Sensors to Tie/Ballast Surfaces

First, for simplicity, we used the measured distances from LiDAR sensors to tie/ballast surfaces for training the machine learning models for both Logistic Regression and Decision Tree algorithms. Figure 12 shows a sample of distance LiDAR measurements from the mainline track testing. Distinct patterns for ties (orange-shaded) and ballasts (unshaded) are evident throughout the data, which were explored by the models.

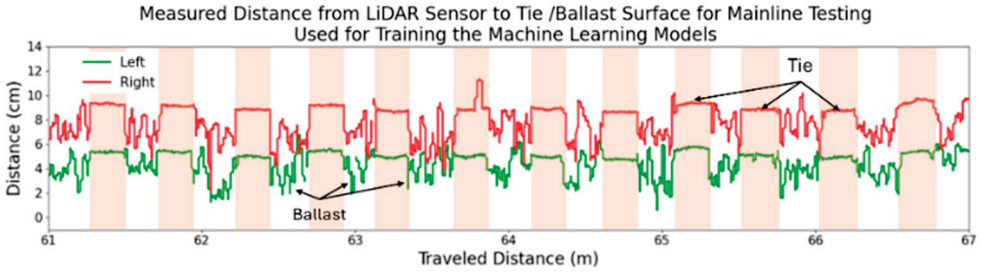

Figure 12. A sample of measured distances from LiDAR sensors to tie/ballast surfaces used for training the ML models for tie/ballast differentiation. Ties are marked with orange shading, and unshaded areas represent ballasts. (Plots are shifted by 3 cm for clarity).

The models were assessed across various window sizes, ranging from 5 to 55 data points. This range was determined to be sufficient after several trial-and-error iterations. Larger window sizes would lead to higher accuracies but require more data points. Therefore, selecting the smallest window size to achieve the necessary accuracy is advantageous. Figure 13 shows the performance of ML models using Decision Tree/Logistic Regression over different window sizes when trained on the measured distances from LiDAR sensors to tie/ballast surfaces. As shown in Figure 13, the Decision Tree algorithm exhibits higher accuracies than Logistic Regression. Additionally, the accuracy for both algorithms increases with the increase in window size. Both algorithms, however, reach a plateau at higher window sizes.

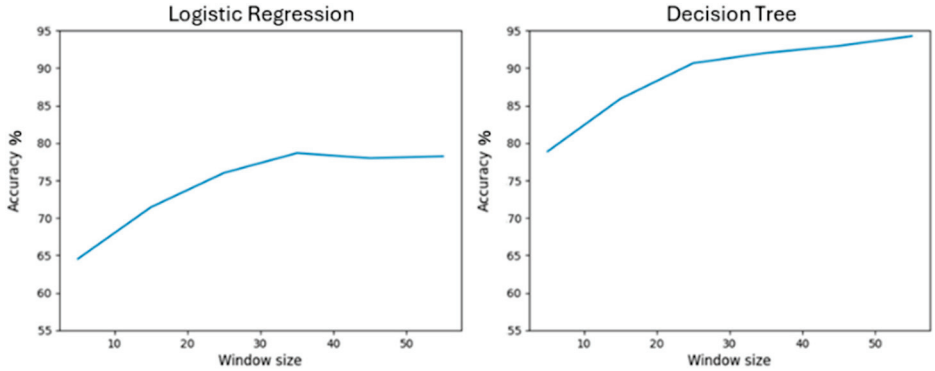

Figure 13. Accuracy of models from Logistic Regression and Decision Tree algorithms for various window sizes trained on the left LiDAR's distance measurements (distance from LiDAR sensor to tie/ballast surfaces).

The analysis shows that the tie/ballast differentiation achieved by both algorithms can be negatively influenced by the condition of ties (e.g., elevated, sunk, tilted, or cracked)

or factors such as their position, elevation, and alignment. To remedy this issue, we evaluated other approaches, such as using the difference between the left and right LiDAR measurements to gauge the two measurements against each other and possibly make the ML models less sensitive to tie conditions.

A model using the Decision Tree algorithm, trained on the measured distances from the LiDAR sensors to tie/ballast surfaces with a window size of 40, was applied to an unseen (unlabeled) section of the data. In Figure 14, the blue line represents the model's predictions, with 1 indicating a tie and 0 indicating ballast. At a specific location in this dataset, two ties with cracks are present, as shown in Figure 14. The model struggles to distinguish between ties and ballasts in these cracked sections.

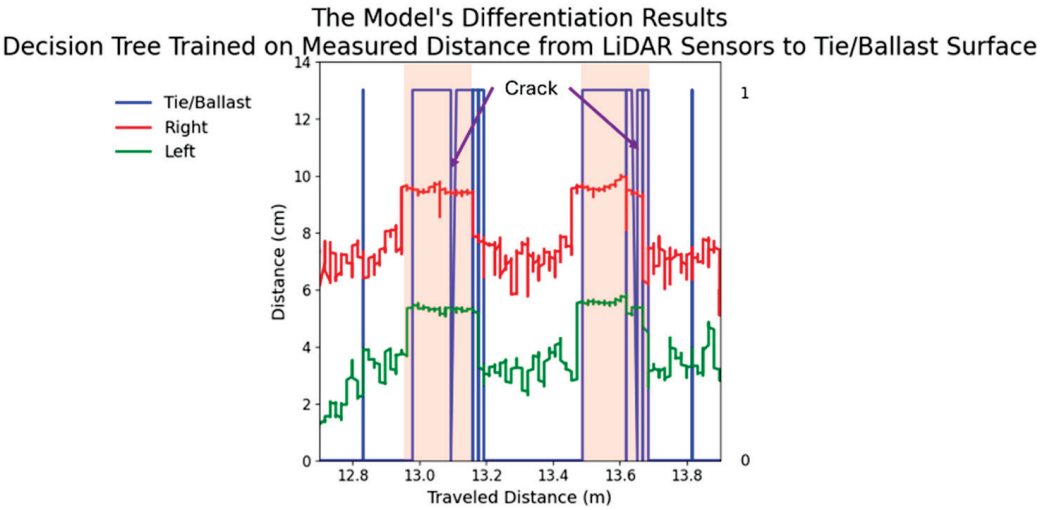

Figure 14. A sample section illustrating the model's performance in differentiating ties and ballasts. The blue line represents the model's predictions, where 1 indicates a tie and 0 indicates ballast. The model is trained on the left LiDAR's distance measurements (distance from the LiDAR sensor to the tie/ballast surface) using the Decision Tree algorithm with a window size of 40. Both ties (highlighted in orange) are cracked.

5.3.2. The Difference between Left and Right LiDAR Sensor Measurements

The difference between the left and right LiDAR sensor measurements could be used as input to train the model. This approach is expected to enhance the signal-to-noise ratio, as ballasts typically exhibit more significant surface irregularities in lateral, longitudinal, and vertical directions. While significant differences in surface figures between a tie's left and right sides (i.e., where the sensors are pointed) are not expected, the ballast sections' left and right sides can vary considerably. Hence, by comparing—or differencing—the left and right LiDAR measurements, more regularities in the tie sections and irregularities in ballast sections can be enforced in the data, facilitating a more accurate distinction between the two.

Figure 15 shows a sample section of the difference between the left and right LiDAR sensor measurements. Comparing Figure 15 with Figure 12, it is evident that the surface figure variation between ties (orange-shaded) and ballasts (unshaded) is now much more pronounced here.

Figure 16 shows the performance of ML models using Decision Tree/Logistic Regression over different window sizes when trained on the difference between the left and right LiDAR sensor measurements. Figure 16 proves that ML models perform better when trained on the difference between the left and right LiDAR sensor measurements than before by showing a slight increase in accuracy based on the Decision Tree algorithm across all window sizes. The improvement is attributed to the improved classification of abnormal ties as ties. However, Logistic Regression could not learn the pattern from these data, since it employs a simple linear classifier; hence, its results are not shown. As expected, using

the difference between the left and right measurements as input to the models could result in a more accurate and reliable model. A similar trend to that observed in Figure 13 can be seen in Figure 16, where accuracy increases with larger window sizes and reaches a plateau at higher values.

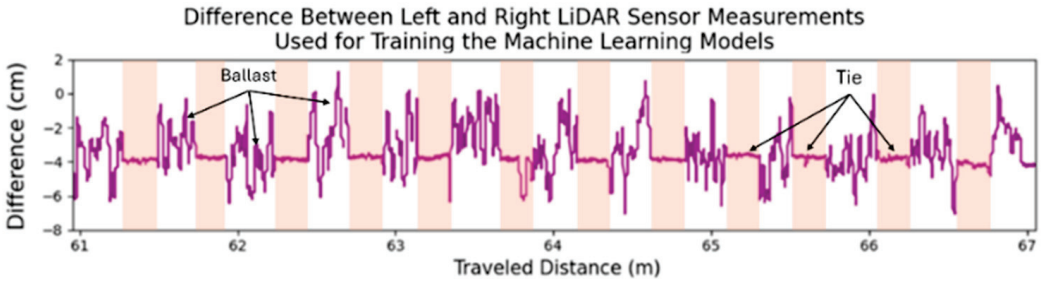

Figure 15. An example of the difference between the left and right LiDAR sensor measurements used for training the ML models for tie/ballast differentiation.

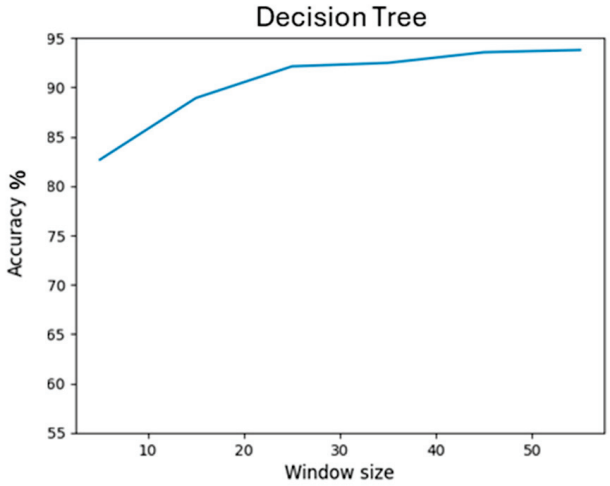

Figure 16. Accuracy of models from the Decision Tree algorithm for various window sizes trained on the differences between the left and right LiDAR sensors' measurements.

5.3.3. Machine Learning on the Standard Deviation of the Difference between the Left and Right Sensor Measurements

Although the previous method demonstrated good performance, there is potential to achieve even higher accuracy. Another approach could be combining standard deviation with machine learning to combine the strengths of both methods. Machine learning excels in classification tasks by learning patterns from different classes to distinguish them. Meanwhile, the standard deviation method reveals more precise and more distinct patterns in a dataset. Integrating these two approaches may achieve better classification performance. The idea is to apply the "moving standard deviation" mentioned earlier to the difference between the left and right sensor measurements.

Figure 17 shows the standard deviation of the difference between the left and right sensor measurements from the previous subsection. The data have clear and distinct patterns over ties (orange-shaded) and ballasts (unshaded).

Figure 18 shows the performance of ML models using Decision Tree/Logistic Regression over different window sizes when trained on the standard deviation of the difference between the left and right sensor measurements. Figure 18 reveals that the Decision Tree algorithm achieves accuracies comparable to those obtained using the difference between the left and right sensors. Additionally, it performs more consistently across various window sizes, demonstrating robust performance at different speeds. This is because the Decision Tree algorithm does not rely on the number of data points, which can vary at

higher speeds due to a constant data acquisition rate, resulting in fewer recorded data points. Logistic Regression, which previously performed poorly, now exhibits behavior similar to the Decision Tree algorithm, demonstrating improved and consistent accuracy across different window sizes.

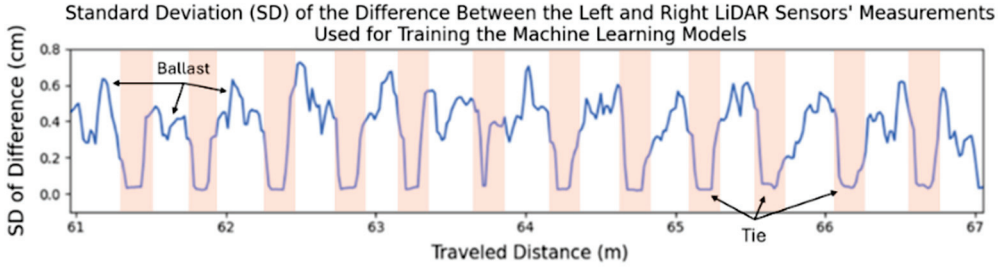

Figure 17. A sample standard deviation of left and right difference LiDAR measurements used in training the ML models for tie/ballast differentiation.

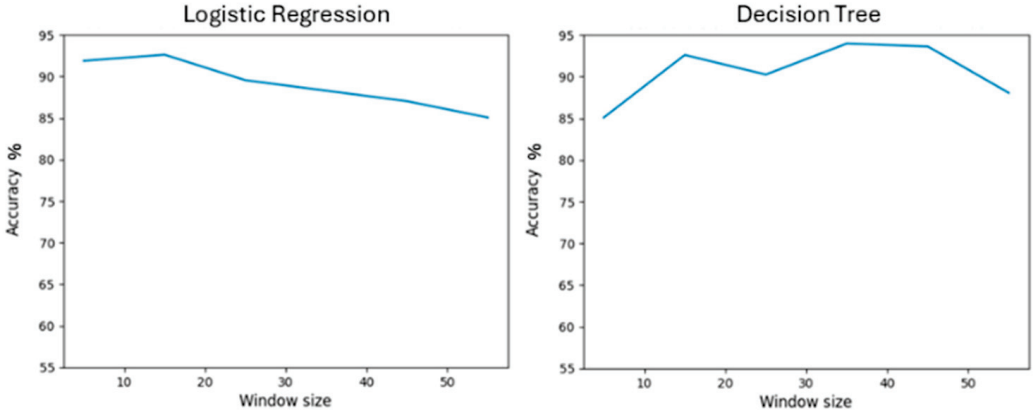

Figure 18. Accuracy of models from Decision Tree and Logistic Regression algorithms for various window sizes trained on the standard deviation of the differences between the left and right LiDAR sensors' measurements.

Training the machine learning model using the Decision Tree algorithm on the standard deviation of the difference between the left and right LiDAR sensor measurements yields the highest possible accuracy, regardless of the window size. The final model, identified as Model 6 in Figure 11, with a window size of 35, was selected for its excellent performance in tie/ballast differentiation compared to the others. Figure 19a shows the model's predictions over an unseen section of the data in a blue line, with 1 indicating a tie and 0 indicating ballast. The high accuracy and precision of the model in distinguishing ties and ballasts are visually evident in this figure. In the entire sampled section, all the ties and ballasts are successfully identified, and the boundaries of each are marked with high precision. The two ties marked with black stars are the same ties shown in Figure 14. The model now performs significantly better than the previous version.

Figure 19b presents the confusion matrix for the model, where 95.2% of the ballast data points are classified as ballast, and 92.4% of the ties are classified as ties. The high and closely matched percentages demonstrate the model's effectiveness in accurately classifying both ties and ballasts. The total accuracy of this model is approximately 93.8%. Note that all the accuracies and percentages are calculated for the test dataset.

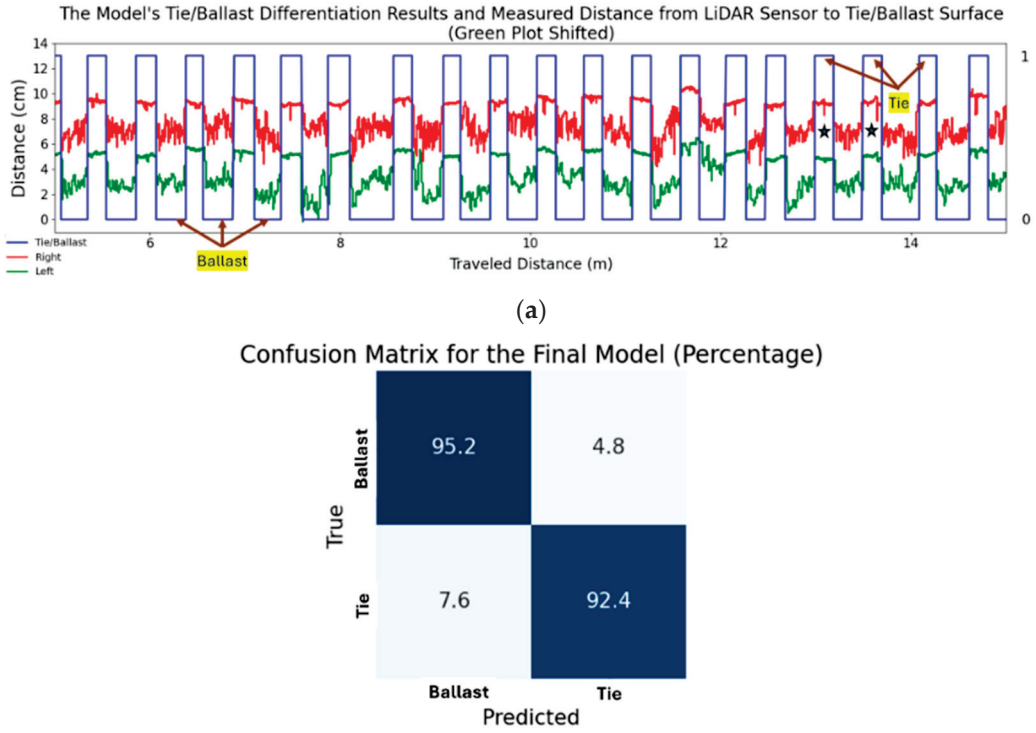

Figure 19. The final model's performance: (**a**) The left and right LiDAR sensor measurements, along with the model's output, in distinguishing between the ties and ballasts over a segment of unseen (i.e., unlabeled) data. The blue line indicates ties (marked as 1) and ballasts (marked as 0). The two ties marked with stars are the same ties shown in Figure 14. (**b**) The confusion matrix shows the percentage of ties and ballasts correctly predicted by the model.

6. Application

The final developed system is capable of accurately distinguishing ties and ballasts in real time while mounted on moving platforms such as Hyrail vehicles and track geometry cars. It operates at speeds of up to 40 mph (65 km/h), which aligns with the operating speed of Class I railroads and performs successfully across various track conditions. This system can be integrated with other track inspection technologies, including ground-penetrating radar, infrared sensors, ultrasonic sensors, and Doppler LiDARs, to focus on their respective targets more effectively. Many of these devices, currently limited to stationary or quasi-stationary applications due to their inability to differentiate between targets, can now perform in-motion analysis over extended distances with the help of this system, facilitating railroad maintenance, reducing costs, and enhancing safety.

7. Conclusions

The goal of this research was to develop a robust, accurate, and effective method for identifying ties and ballasts—a crucial step before implementing inspection approaches that rely on differentiating between ties and ballasts in motion. The system studied here uses two downward-facing distance LiDAR sensors on a moving rail cart. The LiDAR sensors measure the differing Doppler effects caused by ties and ballasts.

Seven techniques were proposed to process the distance of the LiDAR sensors' measurements, starting with the moving standard deviation method aimed at extracting surface figure variations of the track. Despite its simplicity, this method proved unreliable and unsuitable for automated detection. Subsequently, two machine learning algorithms—Logistic Regression and Decision Tree—and three preprocessing methods (inputs) were explored to automatically differentiate between ties and ballasts. Among these six ML models, the one with the Decision Tree algorithm exhibited exceptional accuracy, robustness,

and efficiency, even at high speeds, mainly when applied to the standard deviation of the difference between the left and right LiDAR sensors' measurements; furthermore, unlike computer vision systems designed for similar purposes, this system requires significantly fewer computational resources, making it more feasible for real-time implementation.

In conclusion, the developed system integrates two distance LiDAR sensors (left and right) with Decision Tree algorithms applied to the standard deviation of the difference between the sensors' measurements, providing an effective and practical solution for non-contact, in-motion differentiation of ties and ballasts. This system holds the potential to be used onboard Hyrail vehicles, offering a valuable tool for differentiating between ties and ballasts during track inspection or health monitoring, facilitating more targeted and efficient maintenance interventions.

Author Contributions: Methodology, S.M.M., A.R. and C.H.; experiments, S.M.M. and A.R.; analysis, S.M.M. and A.R.; writing—original draft preparation, S.M.M. and M.A.; writing—review and editing, S.M.M., A.R., C.H. and M.A.; supervision, M.A.; project administration, M.A.; funding acquisition, M.A. All authors have read and agreed to the published version of the manuscript.

Funding: This research was funded by the U.S. Department of Transportation, grant number 693JJ622C000024.

Institutional Review Board Statement: Not applicable.

Informed Consent Statement: Not applicable.

Data Availability Statement: The data presented in this study are available on request from the corresponding author due to privacy.

Acknowledgments: The financial support of the U.S. Department of Transportation and the Federal Railroad Administration's Research, Development and Technology (FRA RD&T) throughout this study is greatly acknowledged. The technical support provided by Robert Wilson (FRA), Wesley Mui (Volpe), and Shaun Eshraghi (Volpe) is also greatly appreciated. We are grateful for Norfolk Southern railroad's support for accommodating the track testing of the LiDAR system.

Conflicts of Interest: The authors declare no conflicts of interest. The funders had no role in the design of the study; in the collection, analyses, or interpretation of data; in the writing of the manuscript; or in the decision to publish the results.

References

1. Artagan, S.S.; Borecky, V. Advances in the nondestructive condition assessment of railway ballast: A focus on GPR. *Ndt E Int.* **2020**, *115*, 102290. [CrossRef]
2. Benedetto, A.; Tosti, F.; Ciampoli, L.B.; Calvi, A.; Brancadoro, M.G.; Alani, A.M. Railway ballast condition assessment using ground-penetrating radar–An experimental, numerical simulation and modelling development. *Constr. Build. Mater.* **2017**, *140*, 508–520. [CrossRef]
3. Silvast, M.; Nurmikolu, A.; Wiljanen, B.; Levomaki, M. An inspection of railway ballast quality using ground penetrating radar in Finland. *Proc. Inst. Mech. Eng. Part F J. Rail Rapid Transit* **2010**, *224*, 345–351. [CrossRef]
4. Wang, S.; Liu, G.; Jing, G.; Feng, Q.; Liu, H.; Guo, Y. State-of-the-art review of ground penetrating radar (GPR) applications for railway ballast inspection. *Sensors* **2022**, *22*, 2450. [CrossRef] [PubMed]
5. Bojarczak, P.; Lesiak, P.; Nowakowski, W. Automatic Detection of Ballast Unevenness Using Deep Neural Network. *Appl. Sci.* **2024**, *14*, 2811. [CrossRef]
6. Yu, H.; Marquis, B.P.; Jeong, D.Y. Failure analysis of railroad concrete crossties in the center negative flexural mode using finite element method. *Proc. Inst. Mech. Eng. Part F J. Rail Rapid Transit* **2017**, *231*, 610–619. [CrossRef]
7. Yu, H. Estimating Deterioration in the Concrete Tie-Ballast Interface Based on Vertical Tie Deflection Profile: A Numerical Study. In Proceedings of the 2016 Joint Rail Conference, Columbia, SC, USA, 12–15 April 2016.
8. Abadi, T.; Pen, L.L.; Zervos, A.; Powrie, W. Effect of Sleeper Interventions on Railway Track Performance. *J. Geotech. Geoenviron. Eng.* **2019**, *145*, 04019009. [CrossRef]
9. Czyczuła, W.; Błaszkiewicz-Juszczęć, D. Influence of Non-Uniform Rail Loads on the Rotation of Railway Sleepers. *Appl. Sci.* **2024**, *14*, 2746. [CrossRef]
10. Esmaeili, M.; Arbabi, B. Stabilising railway embankments using an integrated tied back-to-back strengthening system. *Proc. Inst. Civ. Eng. Ground Improv.* **2017**, *170*, 26–34. [CrossRef]
11. Zhao, W.; Murphy, R.L.; Peterman, R.J.; Beck, B.T.; Wu, C.-H.J.; Duong, P.N. Noncontact Inspection Method to Determine the Transfer Length in Pretensioned Concrete Railroad Ties. *J. Eng. Mech.* **2013**, *139*, 256–263. [CrossRef]

12. Datta, D.; Hosseinzadeh, A.Z.; Cui, R.; di Scalea, F.L. Railroad Sleeper Condition Monitoring Using Non-Contact in Motion Ultrasonic Ranging and Machine Learning-Based Image Processing. *Sensors* **2023**, *23*, 3105. [CrossRef] [PubMed]
13. Alessandro Sabato, C.N. Feasibility of Digital Image Correlation for railroad tie inspection and ballast support assessment. *Measurement* **2017**, *103*, 93–105. [CrossRef]
14. Chen, Y.; Mirzaei, S.M.H.; Holton, C.; Ahmadian, M. Development of an optical sensing system for the detection of lubricity conditions on the rail gage face. *Int. J. Rail Transp.* **2024**, 1–17. [CrossRef]
15. Wandinger, U. Introduction to lidar. In *Lidar: Range-Resolved Optical Remote Sensing of the Atmosphere*; Springer: Berlin/Heidelberg, Germany, 2005; pp. 1–18.
16. Dorsch, R.G.; Häusler, G.; Herrmann, J.M. Laser triangulation: Fundamental uncertainty in distance measurement. *Appl. Opt.* **1994**, *33*, 1306–1314. [CrossRef] [PubMed]
17. Gonçalves, J.P.C.; Ambrósio, J.A.C. Road Vehicle Modeling Requirements for Optimization of Ride and Handling. *Multibody Syst. Dyn.* **2005**, *13*, 3–23. [CrossRef]
18. Sharma, S.K.; Sharma, R.C.; Choi, Y.; Lee, J. Experimental and Mathematical Study of Flexible–Rigid Rail Vehicle Riding Comfort and Safety. *Appl. Sci.* **2023**, *13*, 5252. [CrossRef]
19. Koturwar, P.; Girase, S.; Mukhopadhyay, D. A survey of classification techniques in the area of big data. *arXiv* **2015**, arXiv:1503.07477.
20. Murphy, K.P. *Machine Learning: A Probabilistic Perspective*; MIT Press: Cambridge, MA, USA, 2012.
21. Breiman, L. *Classification and Regression Trees*; Routledge: London, UK, 2017.

sensors

MDPI

Article

Indirect Thermographic Measurement of the Temperature of a Transistor Die during Pulse Operation

Arkadiusz Hulewicz [1,*], Krzysztof Dziarski [2] and Łukasz Drużyński [2]

[1] Institute of Electrical Engineering and Electronics, Poznan University of Technology, Piotrowo 3A, 60-965 Poznan, Poland
[2] Institute of Electric Power Engineering, Poznan University of Technology, Piotrowo 3A, 60-965 Poznan, Poland; krzysztof.dziarski@put.poznan.pl (K.D.); lukasz.druzynski@put.poznan.pl (Ł.D.)
* Correspondence: arkadiusz.hulewicz@put.poznan.pl

Abstract: This paper presents aspects related to the indirect thermographic measurement of a C2M0280120D transistor in pulse mode. The tested transistor was made on the basis of silicon carbide and is commonly used in many applications. During the research, the pulse frequency was varied from 1 kHz to 800 kHz. The transistor case temperature was measured using a Flir E50 thermographic camera and a Pt1000 sensor. The transistor die temperature was determined based on the voltage drop on the body diode and the known characteristics between the voltage drop on the diode and the temperature of the die. The research was carried out in accordance with the presented measuring standards and maintaining the described conditions. The differences between the transistor case temperature and the transistor die temperature were also determined based on simulation work performed in Solidworks 2020 SP05. For this purpose, a three-dimensional model of the C2M0280120D transistor was created and the materials used in this model were selected; the methodology for selecting the model parameters is discussed. The largest recorded difference between the case temperature and the junction temperature was 27.3 °C. The use of a thermographic camera allows the transistor's temperature to be determined without the risk of electric shock. As a result, it will be possible to control the C2M0280120D transistor in such a way so as not to damage it and to optimally select its operating point.

Keywords: thermography; C2M0280120D; transistor; switching; thermal modelling; solidworks

1. Introduction

Transistors are among the electronic components from which electronic devices are built [1]. They consist of a die placed on a base plate made of a well-conducting metal, which, in many cases, is copper. The die is encapsulated inside epoxy resin, and connections to die are possible using leads, commonly called "legs", which are often made of the same material as the base plate. Only one of the leads is directly attached to the base plate. The remaining two leads are placed in the epoxy resin and connected to the die using thin bond wires. The parts of the base plate and leads that are not placed under the epoxy resin layer are covered with a thin layer of tin [2,3]. The dimensions of the base plate, leads, and the epoxy resin layer depend on the type of case used; the most commonly used cases are TO 220 and TO 247. The dimensions of the electronic cases are standardized [4]. In the remainder of this article, the term "transistor" should be understood together with the case in which it is placed.

The most popular materials from which transistor dies are made include silicon (Si), silicon carbide (SiC), and gallium nitride (GaN). Transistors made of these materials differ in their properties [5]. Electronic components made on the basis of silicon reach the limit operating parameters resulting from the theoretical limitations of the material used. For this reason, electronic components based on SiC and GaN materials, called wide band gap

(WBG) semiconductors, are becoming more and more popular. They feature better electrical, mechanical, and thermal properties than the electronic components made on the basis of Si. Replacing Si with WBG semiconductors increases the breakdown voltages, operating temperatures, and switching frequency and reduces switching losses [6]. Elements made on the basis of SiC deserve special attention. Compared to Si elements, those made on the basis of SiC have higher breakdown voltage values and higher thermal conductivity [7]. Another feature of this type of semiconductor is low ON-resistance [8].

Metal oxide semiconductor field effect transistors (MOSFETs) made on the basis of SiC are used in the construction of high conversion ratio converters (HCRCs) [9], traction converters [10], wind turbine converters [11], motor drives for electric vehicles [12], and DC–DC step-up converters [13]. The operational reliability of these devices is related to the operational reliability of the SiC MOSFETs placed inside them [14]. Due to the construction of the die area and the width of the gate oxide, they are susceptible to transient-overloading or short-circuit events [15]. Other examples of SiC MOSFET damage are related to long-term exposure to high temperature, which can cause interlayer dielectric erosion, electrode delamination, gate-oxide breakdown [16], and bond-wire lift-off and solder cracks [17,18].

The temperature value of SiC MOSFETs depends, among other things, on their switching frequency [19]. In turn, the switching frequency depends on the operating characteristics of the device in which the transistor is placed and on its energy efficiency [20]. A good example is the converter. In high-power converters, lower switching frequencies are often used to minimize switching losses and increase energy efficiency [21]. In turn, in low-power converters, higher switching frequencies are usually used, which may lead to smaller converter sizes and better regulation [22]. The higher the switching frequency is, the shorter is the switching time of SiC-based MOSFETs. During switching, rapid changes in voltage and current occur, which leads to power losses and heat generation. Therefore, the switching frequency has a direct impact on heat generation in the transistor [23].

The switching frequency of a SiC MOSFET affects the temperature of its die. In turn, the operation of the die at excessively high temperature may damage the transistor. For this reason, it is necessary to monitor the die temperature of the transistor, T_j. In the literature, is possible to find three groups of methods that make this possible: electrical, contact, and non-contact methods [24].

Electrical methods use a selected parameter whose value depends on T_j. This parameter is called the temperature-sensitive parameter (TSP) [25]. An example of a TSP that is used to determine the die temperature of a transistor is the drop voltage across the body diode. Knowing the relationship between TSP and T_j, it is possible to determine the T_j value based on the measured TSP value. The relationship between TSP and T_j is individual for each transistor. Additionally, its determination requires removing the transistor from the device in which it was installed and placing it in the measurement system. For this reason, this method is not suitable for real-time monitoring of T_j values [26].

Contact methods involve applying a temperature sensor to the transistor package (also called a 'case' in the literature) or directly to the die transistor. There is thermal resistance of an unknown value between the temperature sensor case and the transistor case (or die). Additionally, touching the transistor (or die) case with the temperature sensor causes a local disturbance of the temperature distribution. Part of the transistor case is made of metal; therefore, incorrect application of the temperature sensor (especially when placed in a metal case) may cause electric shock [27].

Non-contact methods are based on the absorption of infrared radiation emitted from the surface of the transistor case (indirect non-contact method) or through the transistor die (direct non-contact method). One of these methods is infrared thermography, which is considered safe, as it poses no risk of electric shock (e.g., as a result of touching a metal temperature sensor based on a plate or a radiator to which a transistor is attached). The direct method requires opening the transistor case. It is difficult to close the opened case. For this reason, it is not suitable for real-time application. The use of the indirect non-contact method consists of two steps: measuring the temperature of the transistor case (T_c) and

determining the difference between T_c and T_j. T_c can be measured using a pyrometer and a thermographic camera. The use of a thermographic camera makes it possible to determine the temperature distribution on the surface of the transistor case. The differences between T_c and T_j can be determined using the finite element method. Knowing the value of the thermographic measurement of the temperature of the transistor case and the relationship between T_c and T_j, it is possible to determine the value of T_j in real time [28,29].

After analyzing the available sources, no studies were found on the indirect thermographic temperature measurement of a SiC MOSFET, the temperature of which increases due to the increase in the switching frequency. For this reason, it was decided to undertake research that would result in the development of a method enabling the indirect thermographic measurement of the SiC MOSFET die temperature and monitoring that temperature at variable switching frequencies.

Section 2 describes the tested SiC MOSFET, the methodology, and the measurement system; Section 3 describes the obtained results of the work; Section 4 contains a discussion; and Section 5 presents conclusions.

2. Tested Transistor, Methodology, and Measurement System

The indirect thermographic measurement of the transistor temperature die consists of two parts. The first part consists of performing a thermographic measurement of the transistor case temperature, T_c. The second part consists of determining the transistor die value T_j using simulation work. The method of performing a thermographic measurement of T_c is described in Section 2.1. The value of T_{Pt1000}, which is used to verify the T_c value, is also determined and described in Section 2.1. The method used to determine the T_j value based on simulation work is described in Section 2.2. The method for determining the T_{jd} value, which is used to verify the T_j value (determined based on simulation work), is also described in Section 2.2. The algorithm for the procedure is presented in Figure 1.

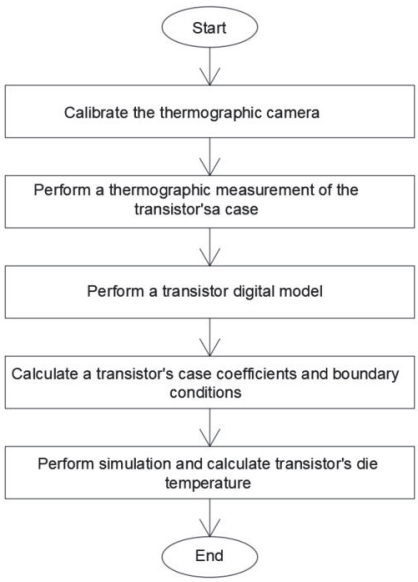

Figure 1. Algorithm for performing indirect thermographic temperature measurements of a transistor.

2.1. Tested Transistor and Measurement System

The model C2M0280120D (Cree Inc., Durham, NC, USA) transistor was selected for testing. This transistor is described by the following parameters: V_{DSmax} = 1200 V (for V_{GS} = 0 V, I_D = 100 µA), V_{GSmax} = −10/+25 V, I_D = 10 A (for V_{GS} = 20 V, T_c = 25 °C), I_D = 6 A (for V_{GS} = 20 V, T_c = 100 °C), and I_{Dpulse} = 20A. The external dimensions of the transistor and schematics are shown in Figure 2. Three randomly selected C2M0280120D transistors from the same series were selected to carry out the work.

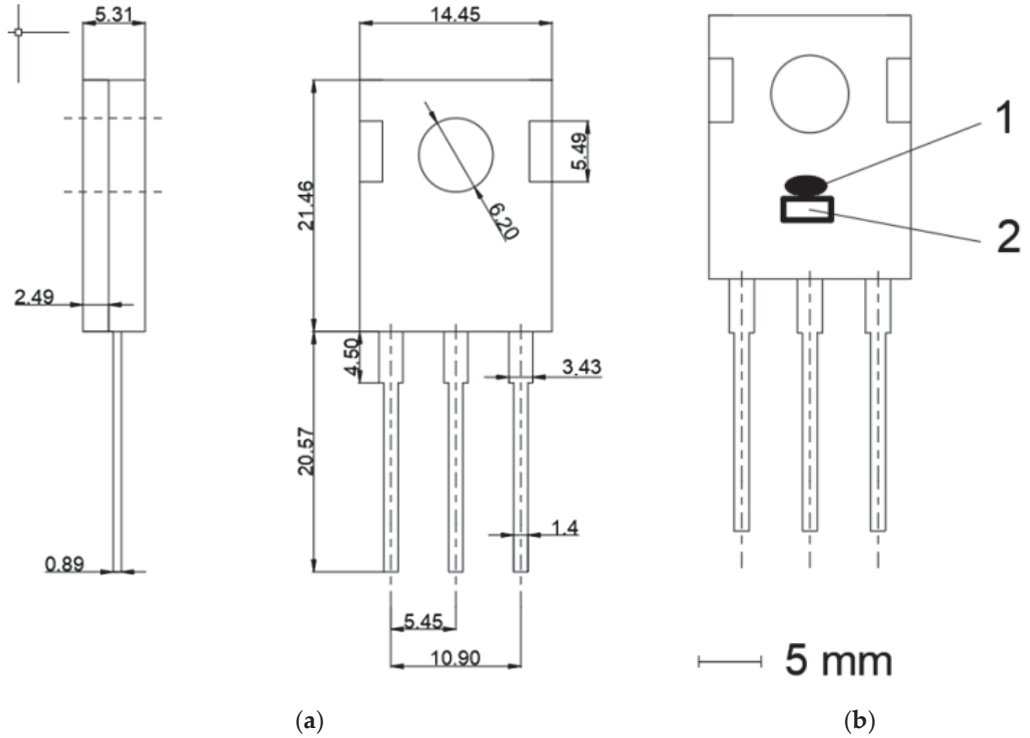

Figure 2. (**a**) External dimensions of transistor model C2M0280120D in a TO 247 case. (**b**) Schematic of C2M0280120D in a TO 247 case. A marker was painted on the case using Velvet Coating 811-21 paint (1) and a Pt1000 sensor was glued onto the case (2).

Pt1000 sensors in an SMD 6203 case (Reichelt electronics GmbH & Co. KG, Sande, Germany) were glued to the case of each transistor [30]. For this purpose, WLK 5 glue with a known thermal conductivity value of k = 0.836 W/mK (Fischer Elektronik GmbH & Co. KG, Lüdenscheid, Germany) was used [31]. Additionally, next to the Pt1000 sensor, a measurement marker was painted on the transistor case. Velvet Coating 811-21 (Nextel, Hamburg, Germany) paint was used for this purpose with a known emissivity coefficient value ε ranging from 0.970 to 0.975 for temperatures within the range from –36 °C to 82 °C. The uncertainty with which the emissivity coefficient value was determined was 0.004 [32].

The transistor prepared in this way was placed in a station where the measuring device was a Flir E50 Thermographic Camera (Flir, Wilsonville, OR, USA) [33]. The selected Flir E50 thermographic camera was equipped with a matrix from an uncooled IR detector (7.5–13 μm) with a resolution of 240 × 180 pixels and an instantaneous field of view (IFOV) value of 1.82 mrad. The noise equivalent differential temperature (NEDT) value of this camera was 50 mK. An additional Close-up 2× lens (T197214, Flir, Wilsonville, OR, USA) was attached to the camera lens [34]. As a consequence, it was possible to obtain an IFOV value of 67 μm for the above-mentioned detector array (240 × 180 pixels) (thermographic camera with the additional lens). Before starting the work, the correctness of the indications of the camera used was verified using the IRS Calilux thermographic camera calibration standard (AT—Automation Technology GmbH, Bad Oldesloe, Germany) [35].

The thermographic camera prepared in this way was placed together with the tested C2M0280120D transistor in a chamber made of plexiglass. The external dimensions of the chamber were 45 cm × 35 cm × 35 cm. The internal dimensions of the chamber were 40 cm × 30 cm × 30 cm. The difference resulted from two reasons: the thickness of the plexiglass used (3 mm) and the thickness of the material (black foam made of polyurethane) lining the internal walls of the chamber. The foam used is characterized by porous structure, and every single pore of the foam resembles the black body cavity model. As a consequence, the material used was characterized by having a high emissivity factor ε = 0.95 [36].

The distance d between the tested transistor and the additional lens was adjusted using a stepper motor. In turn, the stepper motor was controlled using a Siemens S7-1200 PLC controller (Siemens AG, Munich, Germany) [37]. A block diagram of the constructed stand is shown in Figure 3.

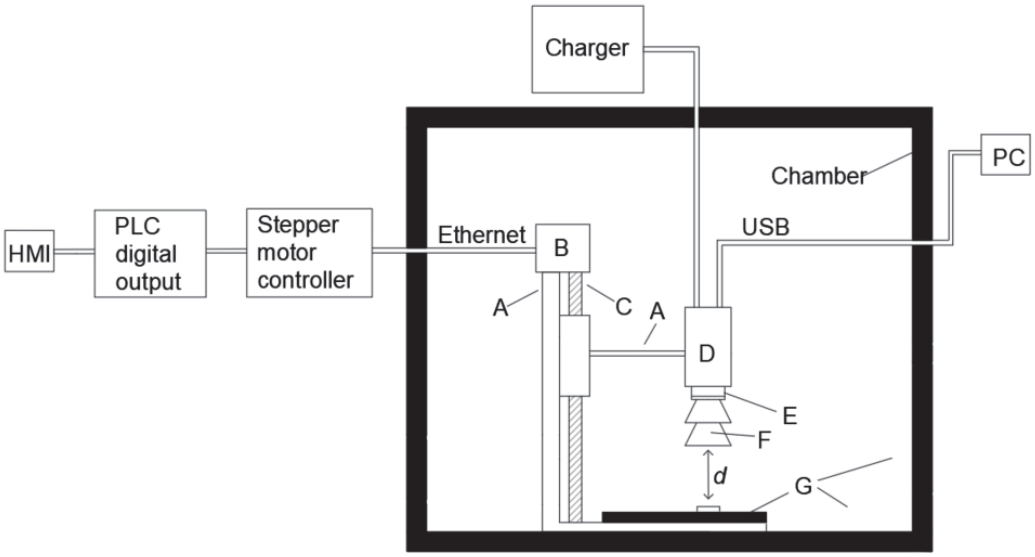

Figure 3. Thermographic camera and observed transistor placed in the prepared chamber. A—stand, B—stepper motor, C—screw, D—thermographic camera, E—thermographic camera lens, F—additional thermographic camera lens, G—polyurethane foam, d—distance between the tested transistor and the additional lens.

The observed transistor was connected to a circuit that allowed its switching frequency to be changed. The circuit diagram is shown in Figure 4. In this circuit, the transistor *T1* was turned on by the generator *G1* for 20 s. As a result, the load current I_{DS} flowed through the tested transistor. During this time, the voltage drop between the drain and the source V_{DS} was measured using an Agilent 34401A voltmeter. In the next step, the same generator *G1* turned on transistor *T2*, allowing the flow of the measuring current I_{di} for 200 ms. This operation allowed estimating the die temperature based on the automatic measurement of the drop voltage V_{fd} on the diode and the known characteristic between the drop voltage value and the die temperature. During the entire testing process, the tested transistor (DUT) was pulse-controlled using the *G2* generator with a PWM waveform with a duty cycle of 50% and a frequency in the range from 1 kHz to 50 kHz.

The case of the tested transistor, in which the switching frequency was changed, was observed using a thermographic camera. During the tests, first, for a given value of the current I_{DS} flowing through the die and a given switching frequency f_T, the temperature of the case (T_c) was measured using a thermographic camera. We then waited until its value increased and stabilized at a specified level. When it was found that the T_c value had stabilized, its thermographic measurement was performed. At the same time, T_c was measured using a Pt1000 sensor, which was glued to the case near the thermographic measurement point (Figure 2). After the measurement was performed, the switching frequency f_T of the transistor was changed for the same I_D current value. The f_T setting was changed for selected values, ranging from 1 kHz to 800 kHz.

2.2. Finite Element Analysis and Measurement of Die Temperature

The relationship between T_c and T_j was determined using finite element analysis (FEA), which is a numerical method used to solve problems in engineering and mathematical physics [38]. The software applied in the work performed was Solidworks 2020 SP05 (Dassault Systèmes, Vélizy-Villacoublay, France), which uses FEA, and the simulation was completed with the use of this software.

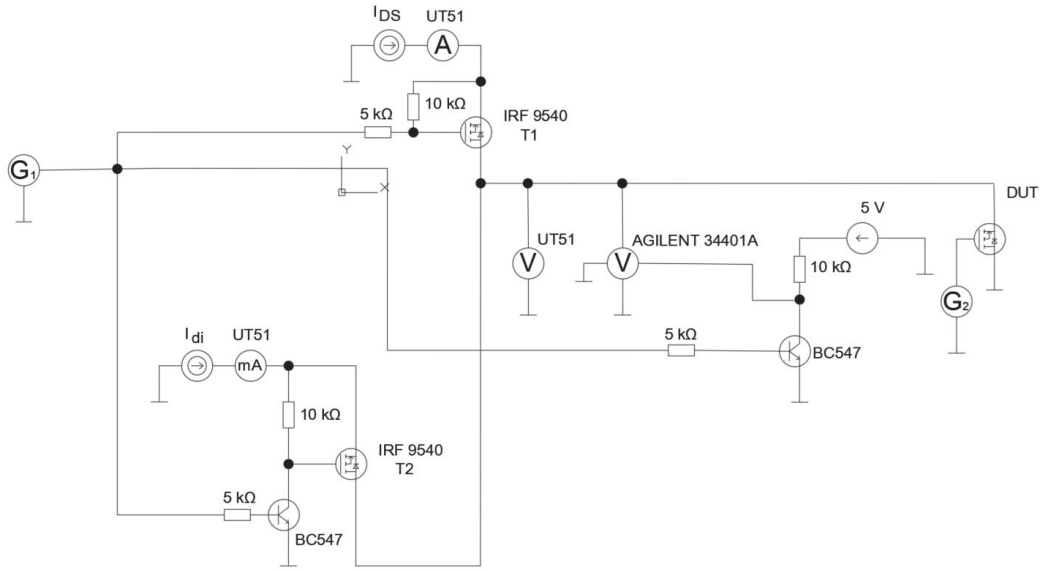

Figure 4. Diagram of the circuit enabling the evaluation of the influence of the switching frequency changes of the transistor on the temperature of its die. DUT—device under test, i.e., the tested transistor.

The simulation could be carried out after the transistor model had been constructed. Making the model required knowledge of its structure and internal dimensions. In order to determine these, the case of the tested transistor was opened and its interior was measured. For this purpose, a microscope equipped with a Cam 3.3 MP camera (Motic, Xiamen, China) was used. The microscope with the camera was calibrated using a special calibration glass. Based on the measurements taken, a three-dimensional model of the tested transistor was created. The model was created in Solidworks 2020 SP05 software. The created model and internal dimensions of the tested transistor C2M0280120D are shown in Figure 5.

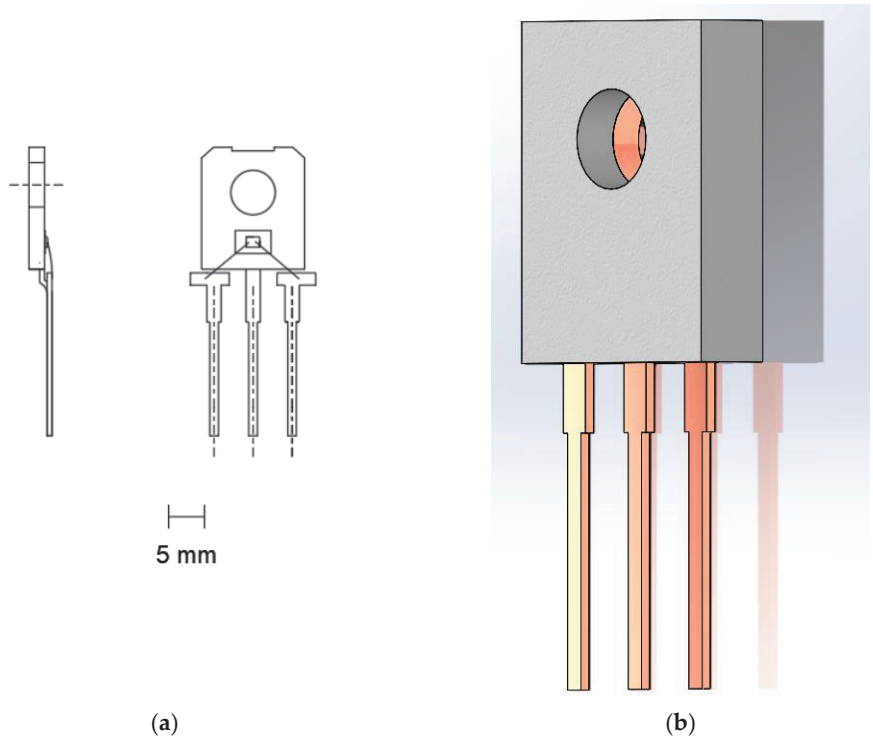

(**a**) (**b**)

Figure 5. (**a**) Internal dimensions (see Figure 2 for details) and (**b**) three-dimensional model of the C2M0280120D transistor.

After creating the model, all of its elements were assigned the material from which it was made, along with the thermal conductivity values *k*. Next, the simulation was started in the Solidworks 2020 SP05 environment. In the initial stage, we checked whether the temperature distribution (measured at the surface) changes after removing individual parts of the model (e.g., leads). The temperature distribution was also checked, depending on the given mesh size. After simplifying the model and selecting the mesh size, it was possible to determine the T_j value based on the simulation work.

The die temperature (T_j) of the tested transistors obtained as a result of simulation work was verified for the same conditions using the electrical method. In order to perform a reliable temperature measurement of the die using the electrical method, it was necessary to select the appropriate temperature-sensitive parameter (TSP). The voltage drop V_{fd} across the body diode was chosen as the TSP. In order to use the TSP to determine the T_j value, the relationship $T_j = f(V_{fd})$ had to be determined. For this reason, a measuring system was designed, the main element of which was a climatic chamber. The chamber used allowed for changing the temperature T_a inside it. The T_a value was changed in the range from 20 °C to 180 °C. Additionally, a Pt1000 sensor was placed inside the chamber, which was used to measure the temperature there. The sensor was connected in a four-wire circuit for measuring resistance using the technical method. A current of 100 μA flowed through the sensor.

In order to determine the relationship $T_j = f(V_{fd})$, three tested transistors were placed inside the described chamber. They were connected in such a way that the current I_{di} (I_{di} = 100 mA) forcing the voltage drop V_{fd} on the body diode flowed through all diodes of the tested transistors (the body diodes of the three transistors were connected in series). The measurement setup is shown in Figure 6. The V_{fd} values of all tested transistors were measured using an Agilent 34401A multimeter (Agilent, Santa Clara, CA, USA) [39]. The measurement was performed for a given temperature T_a at the moment when the V_{fd} voltage value stabilized. The constant values of the V_{fd} voltage in time indicated that the temperature T_a set in the chamber was equal to the die temperature T_j of the transistors located in this chamber. In turn, the voltage drop V_{Pt1000} on the Pt1000 sensor was measured using a UT51 multimeter (UNI-T, Dongguan City, China) [40].

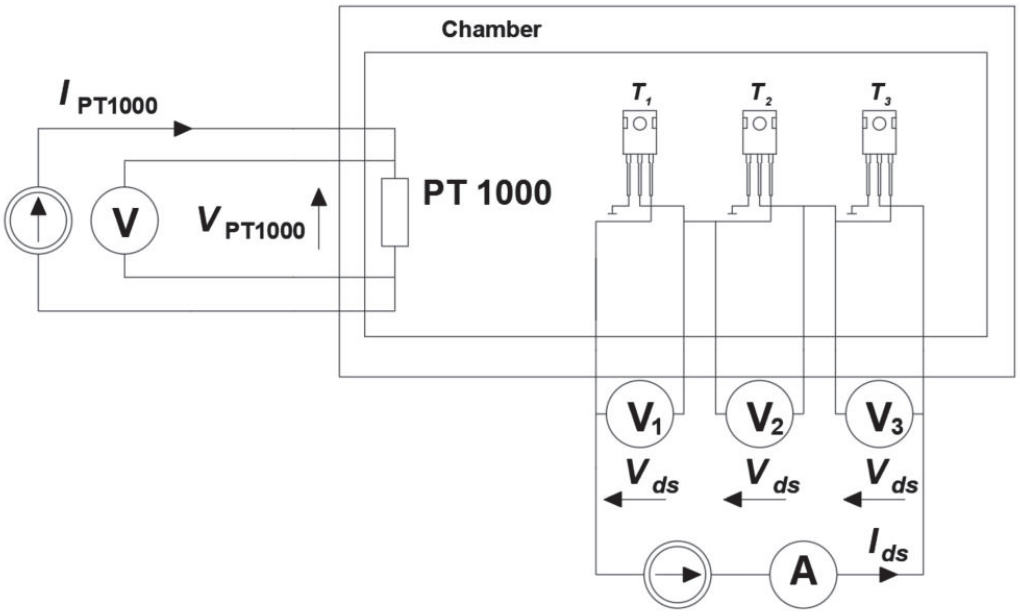

Figure 6. Measurement system enabling determination of the relationship $T_j = f(V_{fd})$.

2.3. Power Dissipated in Die and Ambient Conditions

The correct simulation work using Solidworks 2020 SP05 requires determining the power P that has been released in the die and defining the boundary condition. The power released in the die can be determined using Equation (1):

$$P = V_{DS} \cdot I_{DS} \tag{1}$$

where: P—power (in W) dissipated in the die, V_{DS}—drop voltage (in V) between drain and source, I_{DS}—current (in A) flowing between drain and source.

The V_{DS} and I_{DS} values were measured with measurement errors, which can be determined using the UT51 multimeter documentation (UNI-T, Dongguan City, China). Therefore, the p value will also be within the range defined by the measurement error limit ΔP, which can be determined from Equation (2):

$$\Delta P = V_{DS} \cdot \Delta I_{DS} + I_{DS} \cdot \Delta V_{DS} \tag{2}$$

where: ΔV_{DS}—limiting error of the V_{DS} value (in V), ΔI_{DS}—limiting error of the I_{DS} value (in A). The ΔI_{DS} and ΔV_{DS} values can be determined using the formulas in the UT51 user manual [40].

The increase in die temperature is related to the distribution of effective power, P_{RMS}, in the die. For this reason, the Equation (3) should be used:

$$P_{RMS} = \sqrt{\frac{1}{T_k} \int_{t_0}^{t_0+T_k} P^2(t) dt} \tag{3}$$

where: t_0—beginning of the period, T_k—duration of the period.

The P_{RMS} value is also within the range that is determined by the limiting error ΔP_{RMS}. The limits of the range determined by ΔP_{RMS} can be determined using Equation (2).

The temperature gradient in the radiative heat flux path between the transistor's die and the transistor's case can be determined using Equation (4):

$$J = -k \cdot \nabla \cdot T \tag{4}$$

where: J—radiative heat flux ($\mathrm{W \cdot m^{-2}}$), ∇—Nabla operator.

Equation (4) can be written as Equation (5):

$$J = -k \cdot \frac{dT}{dx} \tag{5}$$

where: x—distance between the points where the temperature values of the die and diode case were measured (m), J—radiative heat flux ($\mathrm{W \cdot m^{-2}}$).

In order to solve Equation (5), we need to separate the differentials that are on the right-hand side of the equation. Consequently, it is possible to integrate the equation on both sides. The constant of integration can be found using Equation (6):

$$\begin{array}{c} \text{for } x = 0 \rightarrow T = T_1 \\ \text{for } x = x_k \rightarrow T = T_2 \end{array} \tag{6}$$

where: x_k—end point of the analyzed heat flow path (m), T_1—temperature at the starting point of the analyzed heat flow path (K), T_2—temperature at the end point of the analyzed heat flow path (K).

Consequently, it is possible to determine Equation (7):

$$T_1 - T_2 = -\frac{P_C}{S \cdot k} \cdot x_k \tag{7}$$

where: P_c—total power (in W) applied to the wall, S—area (m^2) of the wall penetrated by J ($W \cdot m^{-2}$).

Determining the correct temperature distribution in the transistor's case (using Solidworks 2020 SP05 Software) requires determining the radiation coefficient h_r. The h_r coefficient defines the amount of thermal energy transferred to the environment by radiation per unit time, per unit area, and per unit temperature difference between the body radiating energy and the environment. The value of h_r can be determined using Equation (8):

$$h_r = \varepsilon \cdot \sigma \cdot (T_S \cdot T_a) \cdot \left(T_S^2 \cdot T_a^2 \right) \tag{8}$$

where: σ—Stefan–Boltzmann constant equal to 5.67×10^{-8} ($W \cdot m^{-2} \cdot K^{-4}$), T_S—surface temperature (K), T_a—air temperature (K).

It is also necessary to determine the value of the convection coefficient h_{cf}, which defines the amount of thermal energy transferred to the environment by convection per unit time, per unit area, and per unit temperature difference between the body emitting the energy and the environment. To determine the h_{cf} value for a flat surface, Equation (9) can be used:

$$h_{cf} = \frac{Nu \cdot k}{L} \tag{9}$$

where: h_{cf}—convection coefficient of flat surfaces, Nu—Nusselt number (-), L—characteristic length in meters (for a vertical wall, this value represents height).

The Nusselt number can be determined using Equation (10).

$$Nu = a \cdot (Pr \cdot Gr)^b \tag{10}$$

where: Gr—Grashof number (-), Pr—Prandtl number (-), a and b—dimensionless coefficients. The values of coefficients a and b are provided in Table 1.

Table 1. Values of coefficients a and b in Equation (10). lam—value for laminar flow, turb—value for turbulent flow.

Shape	$Gr \cdot Pr$	a_{lam}	b_{lam}	a_{turb}	b_{turb}
Vertical flat wall	10^9	0.59	0.25	0.129	0.33
Upper flat wall	10^8	0.54	0.25	0.14	0.33
Lower flat wall	10^5	0.25	0.25	NA	NA

The Grashof number can be obtained from Equation (11):

$$Gr = \frac{\alpha \cdot g \cdot (T_s - T_a) \cdot \rho^2 \cdot L^3}{\eta^2} \tag{11}$$

where: g—gravitational acceleration ($9.8\ m \cdot s^{-2}$), α—coefficient of expansion ($0.0034\ K^{-1}$), ρ—air density ($1.21\ kg \cdot m^{-3}$) at 273.15 K, η—dynamic air viscosity ($1.75 \times 10^{-5}\ kg \cdot m^{-1} \cdot s^{-1}$) at 273.15 K.

Prandtl's number is determined from Equation (12):

$$Pr = \frac{c \cdot \eta}{k} \tag{12}$$

where: Pr—Prandtl's number, c—specific heat of air ($1005\ J \cdot kg^{-1} \cdot K^{-1}$) at 293.15 K.

When the value of the average linear velocity of the fluid flow is greater than 0 m/s, the Reynolds number must also be taken into account, which can be obtained using Equation (13):

$$Re = \frac{V \cdot \rho \cdot L}{\eta} \tag{13}$$

where: V—average linear velocity of the fluid flow (m/s).

In order to enable a better understanding of the boundary condition, the analyzed heat flow path and its emission by the observed surface (by convection h_{cf} and radiation h_r) are shown in Figure 7.

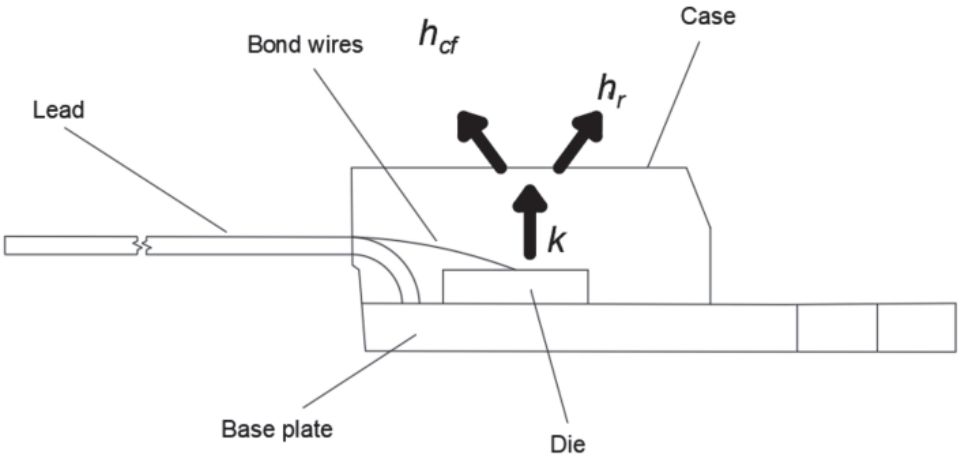

Figure 7. Analyzed heat flow path and its emission from the observed surface (by convection h_{cf} and radiation h_r). Thermal conductivity is designated as k.

2.4. Uncertainties

The method by which the uncertainty of the thermographic temperature measurement T_c can be determined is described in the document *Evaluation of the Uncertainty of Measurement in calibration* (EA-4/02 M: 2022) [41]. This is a method for determining the uncertainty of type B. In order to use this method, all input quantities X_i that affect the result of the T_c measurement and the range of their variability must be determined. This can be done based on experience and the literature. In this work, the thermographic camera processing equation from publication [42] was used (Equation (14)):

$$T_c = \sqrt[4]{\frac{T_{cam}^4 \cdot \varepsilon \cdot \sigma - (1-\varepsilon) \cdot \tau_a \cdot \sigma \cdot T_{refl}^4 \cdot \tau_l - (1-\tau_a) \cdot \sigma_c \cdot T_a^4 \cdot \tau_l - (1-\tau_l) \cdot \sigma_c \cdot T_l^4}{\varepsilon \cdot \tau_a \cdot \sigma_c \cdot \tau_l}} \quad (14)$$

where: T_{cam}—temperature indicated by the thermographic camera without taking into account the influence of other factors, σ_c—Stefan-Boltzmann constant equal to 5.67×10^{-8} ($W \cdot m^{-2} \cdot K^{-4}$), τ_a—atmosphere transmittance coefficient, τ_1—transmittance of the thermographic camera lens, T_a—air temperature, T_{refl}—reflected temperature, T_l—thermographic camera lens temperature.

The next step is to determine the sensitivity coefficient c_s for all input quantities from Equation (14). This is a derivative described in Equation (15):

$$c_s(y) = \frac{\partial f}{\partial X_i} \quad (15)$$

where: f_i—all input quantities from Equation (14).

In order to determine the uncertainty of the T_c value, estimates of x_i of the input quantities X_i (for all above input quantities) must be determined. This is possible using Equation (16) (rectangular probability distribution):

$$x_i = \frac{1}{2}(a_+ + a_-) \quad (16)$$

where: a_+—upper limit of the input quantity range, a_-—lower limit of the input quantity range.

Then, for each X_i, the uncertainty standard $u(x_i)$ should be determined as per Equation (17):

$$u^2(x_i) = \frac{1}{12}(a_+ - a_-)^2 \tag{17}$$

By multiplying the values of $u(x_i)$ and c_s, we can obtain the uncertainty contribution $u(y)$. The standard uncertainty $u(T_c)$ of the T_c value can be obtained as the square root of the sum of squares of the values of $u(y)$ as per Equation (18):

$$u^2(T_c) = \sum_{i=1}^{N} u(y) \tag{18}$$

In order to determine the expanded uncertainty $U(T_c)$, the value of $u(T_c)$ should be multiplied by the coverage factor k.

To determine $\Delta T_{\mathrm{Pt1000}}$, Equations (19)–(23) can be used:

$$\delta V_{\mathrm{Pt1000}} = \frac{\Delta V_{\mathrm{Pt1000}}}{V_{\mathrm{Pt1000}}} \cdot 100 \tag{19}$$

$$\delta I_{\mathrm{Pt1000}} = \frac{\Delta I_{\mathrm{Pt1000}}}{I_{\mathrm{Pt1000}}} \cdot 100 \tag{20}$$

$$\delta R_{\mathrm{Pt1000}} = \delta V_{\mathrm{Pt1000}} + \delta I_{\mathrm{Pt1000}} \tag{21}$$

$$\Delta R_{\mathrm{Pt1000}} = \frac{R_{\mathrm{Pt1000}} \cdot \delta R_{\mathrm{Pt1000}}}{100} \tag{22}$$

where: $\Delta V_{\mathrm{Pt1000}}$—limit error of V_{Pt1000}, $\delta V_{\mathrm{Pt1000}}$—relative error of V_{Pt1000}, $\Delta I_{\mathrm{Pt1000}}$—limit error of I_{Pt1000}, $\delta I_{\mathrm{Pt1000}}$—relative error of I_{Pt1000}, $\delta R_{\mathrm{Pt1000}}$—relative error of R_{Pt1000}, $\Delta R_{\mathrm{Pt1000}}$—limit error of R_{Pt1000}, R_{Pt1000}—resistance of Pt1000 [42].

Then, by inserting the upper and lower range of $\Delta R_{\mathrm{Pt1000}}$ into Equation (23), it is possible to obtain the upper and lower range of $\Delta T_{\mathrm{Pt1000}}$ values:

$$T_{\mathrm{Pt1000}} = 10^{-5} \cdot R_{\mathrm{Pt1000}}^2 + 0.235 \cdot R_{\mathrm{Pt1000}} - 245.35 + R_{\mathrm{Pt1000}}^2 \cdot 4 \cdot 10^{-7} - R_{\mathrm{Pt1000}} \cdot 2 \cdot 10^{-5} + 0.0011 \tag{23}$$

To determine the $\Delta V_{\mathrm{Pt1000}}$ and $\Delta I_{\mathrm{Pt1000}}$ values, the documentation of the multimeter describe in reference [40] can be used.

3. Results

Using the measurement system shown in Figure 6, the relationship $T_{jd} = f(V_{fd})$ was determined. This relationship was approximated by the linear equation $y = e \cdot x + f$. As a result, the individual equations $T_{jd} = T_C + e \cdot V_{fd} + f$ were obtained for each transistor. The values of the coefficients for each transistor are given in Table 2.

Table 2. Values of the coefficients e and f of the curves $T_{jd} = T_C + e \cdot V_{fd} + f$ of the tested transistors.

No	*Transistor*	*e*	*f*
1	C2M0280120D	8.9582	1.6507
2	C2M0280120D	8.9684	1.6012
3	C2M0280120D	8.9549	1.6577

Then, each of the tested transistors was connected according to the diagram shown in Figure 4. The black part of the transistor case was observed with a thermographic camera. In order to minimize the factors disturbing the thermographic measurements, the observed transistors and the thermographic camera were placed in a chamber whose connection layout is shown in Figure 3. Additionally, V_{fd} values were measured using a voltmeter. Using these values, the junction temperature T_{jd} values were determined based on the previously determined relationship $T_{jd} = f(V_{fd})$ (Table 2). The T_{jd} values determined in this way are given in Table 2, and sample recorded thermograms are shown in Figure 8.

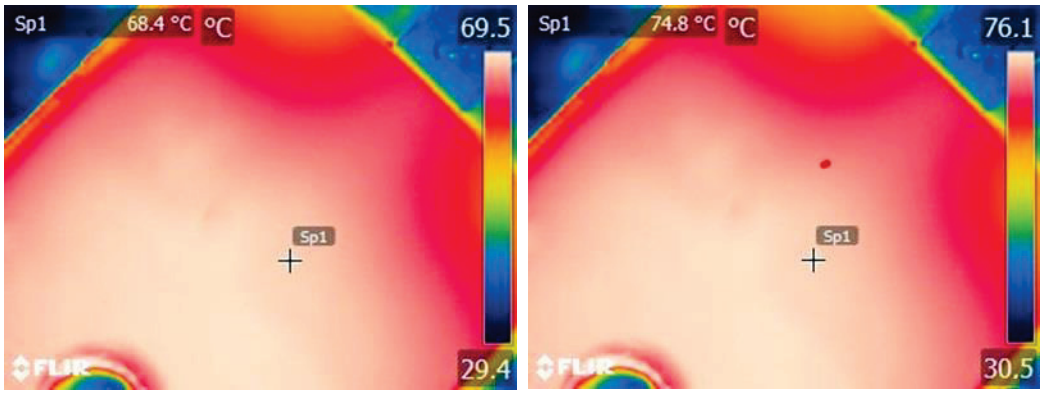

(**a**) (**b**)

Figure 8. Examples of recorded thermograms: (**a**) I_{DS} = 1 A; f_T = 1 kHz, (**b**) I_{DS} = 1 A; f_T = 10 kHz. The thermograms were taken before gluing the Pt1000.

In the next stage of the research, simulations were carried out using the FEM method. In the first step, a model of the tested transistor was designed. Materials and thermal conductivity values *k* are given in Table 3.

Table 3. Materials specified in the 3D model and their thermal conductivity values *k*.

Internal Structure Component	Material	*k* [W/m·K]
Black part of the case	EME 590	0.25
Back part of the case	Copper	400
Semiconductor element	Silicon carbide	150
Left lead	Copper	400
Internal lead	Copper	400
Right lead	Copper	400
Internal connections	Copper	400
Grease	Melamine resin	0.20

The selected values of the convection coefficients h_{cf} of the observed surface (black part of the case) were in the range of 15.3 W/m^2 K to 24.8 W/m^2 K for the tested temperature ranges.

Additionally, the relationship between the mesh size *l* specified in the simulation parameters, the duration of a single simulation t_s, and the accuracy of the determined temperature values DT_S was checked. The obtained results are presented in Table 4.

Table 4. Mesh size *l*, simulation duration t_s, and temperature values T_S obtained during FEM simulation defined in the simulation parameters.

No.	t_s [s]	*l* [mm]	ΔT_S [°C]
1	3	4.0	1.9
2	5	3.0	1.4
3	8	2.0	0.6
4	15	1.5	0.4
5	41	1.0	0.1
6	499	0.5	0.1

Based on the data presented in Table 4, a mesh size was selected at which the simulation duration was sufficiently short and the accuracy of the ΔT_S temperature value obtained as a result of the simulation work was 0.1 °C (Table 4, No. 5). As a result, the T_S temperature values obtained from the simulation work were close to the temperature

T_c recorded in the thermographic measurement for a given value of the power dissipated in the P_{RMS} transistor. The selected mesh size was l = 1.0 mm. The example temperature distributions obtained from the simulation are shown in Figure 9.

Tables 5–8 present the values of T_c and T_j recorded during measurements and the values of T_S (transistor case) obtained as a result of simulation work, depending on the set value of the switching frequency f_T of the transistor. The measurements were carried out for four current values.

In order to determine the uncertainty of the T_c value, the range of all variables was determined from Equation (14). The adopted ranges of values and the determined x_i are given in Table 9.

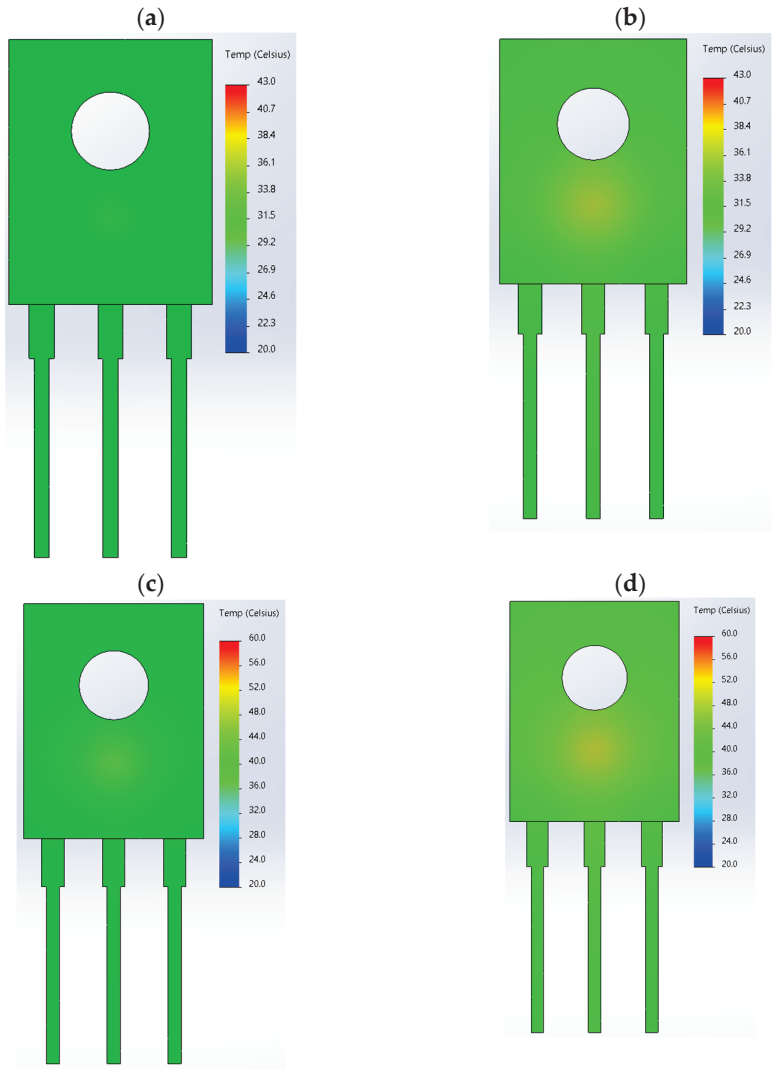

Figure 9. *Cont.*

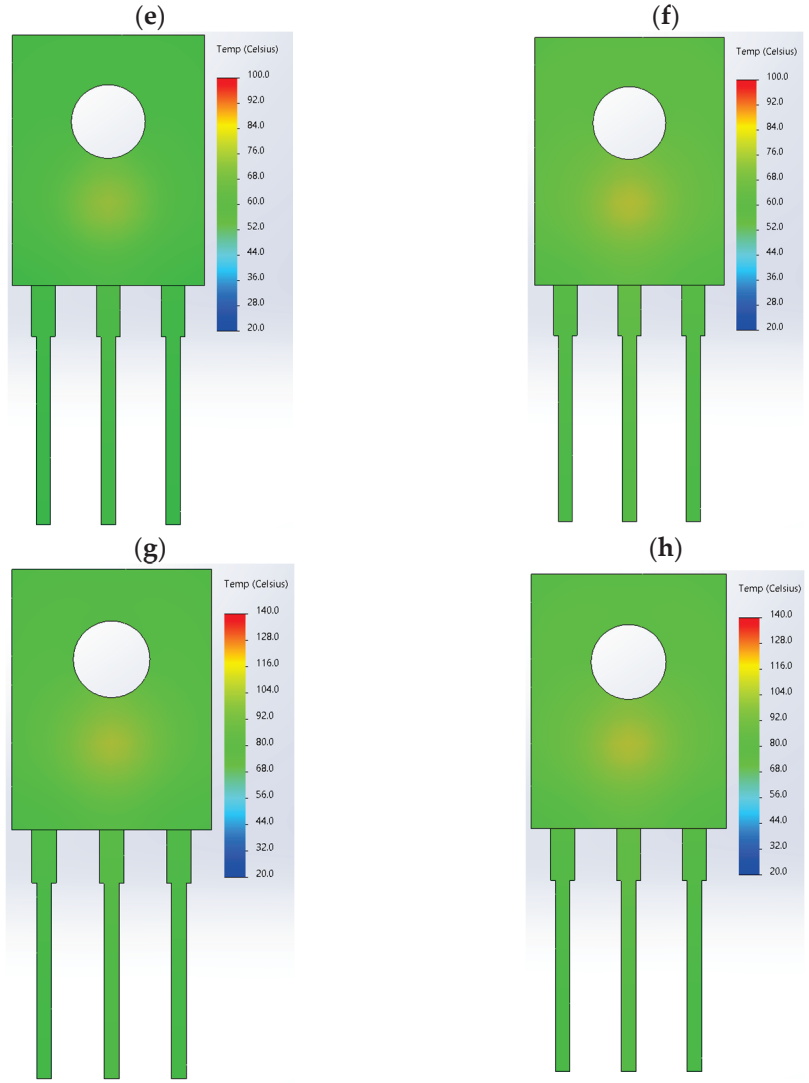

Figure 9. Examples of temperature distributions obtained from FEM simulations. (**a**) I_{DS} = 0.25 A, f_T = 1 kHz, (**b**) I_{DS} = 0.25 A, f_T = 500 kHz, (**c**) I_{DS} = 0.5 A, f_T = 1 kHz, (**d**) I_{DS} = 0.5 A, f_T = 500 kHz, (**e**) I_{DS} = 1 A, f_T = 1 kHz, (**f**) I_{DS} = 1 A, f_T = 500 kHz, (**g**) I_{DS} = 1.5A, f_T = 1 kHz, (**h**) I_{DS} = 1.5A, f_T = 500 kHz.

Table 5. Transistor case temperature T_c determined from thermographic measurements, junction temperature T_{jd} determined from the relationship $T_{jd} = f(V_{fd})$, and transistor case temperature T_S and junction temperature T_j determined from simulations, depending on the set switching frequency f_T. The results were obtained for the current I_{DSmax} = 0.25 A. T_{c1} is the T_c value measured for the first transistor, T_{c2} is the T_c value measured for the second transistor, and T_{c3} is the T_c value measured for the third transistor.

No.	f_T [kHz]	I_{DS} [A]	P [W]	T_{c1} [°C]	T_{c2} [°C]	T_{c3} [°C]	T_{jd} [°C]	T_S [°C]	T_j [°C]	T_{Pt1000} [°C]
1	1	0.25	0.52	33.1	33.3	32.6	53.4	33.0	49.4	31.1
2	5	0.25	0.52	33.4	33.6	32.9	53.7	33.3	49.8	31.4
3	10	0.25	0.52	33.6	33.8	33.1	53.9	33.5	50.1	31.6
4	50	0.25	0.52	33.9	34.2	33.3	54.2	33.8	50.5	31.9
5	100	0.25	0.52	34.3	34.6	33.7	54.6	34.2	51.1	32.3
6	150	0.25	0.52	35.0	35.3	34.4	55.3	34.9	52.1	32.9
7	200	0.25	0.52	35.6	35.9	35.0	55.9	35.5	53.1	33.6
8	300	0.25	0.52	36.6	36.9	36.0	56.9	36.5	54.2	34.6
9	400	0.25	0.52	36.9	37.2	36.3	57.2	36.8	54.9	34.9

Table 5. *Cont.*

No.	f_T [kHz]	I_{DS} [A]	P [W]	T_{c1} [°C]	T_{c2} [°C]	T_{c3} [°C]	T_{jd} [°C]	T_S [°C]	T_j [°C]	T_{Pt1000} [°C]
10	500	0.25	0.52	37.3	37.6	36.7	57.5	37.2	55.5	35.3
11	600	0.25	0.52	37.1	37.4	36.5	57.3	37.0	55.1	35.1
12	700	0.25	0.52	37.3	37.6	36.7	57.5	37.2	55.3	35.3
13	800	0.25	0.52	37.6	37.9	37.0	57.8	37.5	55.7	35.6

Table 6. Transistor case temperature T_c determined from the thermographic measurements, junction temperature T_{jd} determined from the relationship $T_{jd} = f(V_{fd})$, and the transistor case temperature T_S and junction temperature T_j determined from simulations, depending on the set switching frequency f_T. The results were obtained for the current I_{DSmax} = 0.5 A. T_{c1} is the T_c value measured for the first transistor, T_{c2} is the T_c value measured for the second transistor, T_{c3} is the T_c value measured for the third transistor.

No.	f_T [kHz]	I_{DS} [A]	P [W]	T_{c1} [°C]	T_{c2} [°C]	T_{c3} [°C]	T_{jd} [°C]	T_S [°C]	T_j [°C]	T_{Pt1000} [°C]
1	1	0.5	1.20	45.7	46.1	45.3	68.8	45.7	66.3	43.7
2	5	0.5	1.19	45.7	46.1	45.3	68.7	45.7	66.3	43.7
3	10	0.5	1.19	46.0	46.4	45.6	69.0	46.0	66.7	44.0
4	50	0.5	1.18	47.0	47.4	46.6	69.8	47.0	67.2	45.0
5	100	0.5	1.18	48.1	48.5	47.7	70.8	48.1	68.7	46.1
6	150	0.5	1.17	49.2	49.6	48.8	71.8	49.2	69.3	47.2
7	200	0.5	1.17	50.1	50.5	49.7	72.7	50.1	70.7	48.0
8	300	0.5	1.17	50.9	51.3	50.5	73.5	50.9	71.9	48.8
9	400	0.5	1.17	50.7	51.1	50.3	73.3	50.7	71.6	48.6
10	500	0.5	1.17	51.0	51.4	50.6	73.5	51.0	71.1	48.9
11	600	0.5	1.17	51.6	52.0	51.2	74.1	51.6	72.0	49.5
12	700	0.5	1.17	51.5	51.9	51.1	74.0	51.5	71.8	49.4
13	800	0.5	1.16	51.3	51.7	50.9	73.8	51.3	71.5	49.2

Table 7. Transistor case temperature T_c determined from thermographic measurements, junction temperature T_{jd} determined from the relationship $T_{jd} = f(V_{fd})$, and transistor case temperature T_S and junction temperature T_j determined from simulations, depending on the set switching frequency f_T. The results were obtained for the current I_{DSmax} = 1 A. T_{c1} is the Tc value measured for the first transistor, T_{c2} is the Tc value measured for the second transistor, T_{c3} is the T_c value measured for the third transistor.

No.	f_T [kHz]	I_{DS} [A]	P [W]	T_{c1} [°C]	T_{c2} [°C]	T_{c3} [°C]	T_{jd} [°C]	T_S [°C]	T_j [°C]	T_{Pt1000} [°C]
1	1	1	2.90	80.0	80.6	79.7	107.7	80.1	106.1	77.8
2	5	1	2.90	80.4	81.0	80.1	108.1	80.5	106.3	78.2
3	10	1	2.89	79.9	80.5	79.6	107.6	80.0	106.1	77.7
4	50	1	2.88	81.6	82.2	81.3	109.1	81.7	106.6	79.4
5	100	1	2.87	81.9	82.5	81.6	109.4	82.0	106.8	79.7
6	150	1	2.86	81.7	82.3	81.4	109.1	81.8	106.5	79.5
7	200	1	2.86	82.4	83.0	82.1	109.8	82.5	106.8	80.1
8	300	1	2.85	83.0	83.6	82.7	110.3	83.1	106.8	80.7
9	400	1	2.85	83.1	83.7	82.8	110.4	83.2	106.9	80.8
10	500	1	2.85	83.1	83.7	82.8	110.4	83.2	106.9	80.8
11	600	1	2.85	82.9	83.5	82.6	110.1	83.0	106.7	80.6
12	700	1	2.85	83.1	83.7	82.8	110.3	83.2	106.7	80.8
13	800	1	2.85	83.0	83.6	82.7	110.2	83.1	106.6	80.7

Table 8. Transistor case temperature T_c determined from thermographic measurements, junction temperature T_{jd} determined from the relationship $T_{jd} = f(V_{fd})$, and transistor case temperature T_S and junction temperature T_j determined from simulations, depending on the set switching frequency f_T. The results were obtained for the current I_{DSmax} = 1.5 A. T_{c1} is the T_c value measured for the first transistor, T_{c2} is the T_c value measured for the second transistor, T_{c3} is the T_c value measured for the third transistor.

No.	f_T [kHz]	I_{DS} [A]	P [W]	T_{c1} [°C]	T_{c2} [°C]	T_{c3} [°C]	T_{jd} [°C]	T_S [°C]	T_j [°C]	T_{Pt1000} [°C]
1	1	1.5	3.30	111.9	112.6	111.8	141.9	112.1	140.0	109.5
2	5	1.5	3.29	113.3	114.0	113.2	143.2	113.5	140.7	110.8
3	10	1.5	3.28	113.4	114.1	113.3	143.2	113.6	140.9	110.9
4	50	1.5	3.27	113.2	113.9	113.1	142.9	113.4	140.5	110.7
5	100	1.5	3.26	113.3	114.0	113.2	142.9	113.5	140.7	110.8
6	150	1.5	3.25	113.4	114.1	113.3	143.0	113.6	140.9	110.9
7	200	1.5	3.24	113.3	114.0	113.2	142.8	113.5	140.7	110.8
8	300	1.5	3.22	113.4	114.1	113.3	142.7	113.6	140.9	110.9
9	400	1.5	3.22	113.4	114.1	113.3	142.7	113.6	140.9	110.9
10	500	1.5	3.22	113.4	114.1	113.3	142.7	113.6	140.9	110.9
11	600	1.5	3.22	113.3	114.0	113.2	142.6	113.5	140.7	110.8
12	700	1.5	3.22	113.4	114.1	113.3	142.7	113.6	140.9	110.9
13	800	1.5	3.22	113.4	114.1	113.3	142.7	113.6	140.9	110.9

Table 9. Values of the variables from Equation (14) and the determined x_i.

No	Value	Unit	a_+	a_-	x_i
1	ε	-	0.98	0.96	0.97
2	τ_a	-	1.00	0.98	0.99
3	T_{refl}	°C	5.00	0.00	2.50
4	τ_l	-	1.00	0.98	0.99
5	T_a	°C	30.00	16.00	22.5
6	T_l	°C	30.00	16.00	22.5

The T_{cam} value was also taken into account. The T_{cam} value limits were selected individually for each case ($T_{cam} \pm 2$ °C).

Then, using equations from Section 2.4, the standard uncertainty $u(x_i)$ and sensitivity coefficient c_s (for all input quantities from Equation (14)) were determined. For each X_i, the uncertainty contribution $u(y)$ was determined. The T_{cam} value was added to the budget with c_s equal to 1. After constructing the uncertainty budget, the standard uncertainty $u(T_c)$ was determined. An example uncertainty budget for f_t = 1 kHz and I_{DS} = 0.25 A. T_{cc} = 304.3 °C is shown in Table 10.

The value of $U(T_c)$ = 2.36 °C was obtained by multiplying the value of 1.18 by k = 2. Using the formulas presented in Section 2.4, the maximum value of ΔT_{Pt1000} of 1.73 °C was also determined.

Table 10. Example uncertainty budget for f_t = 1 kHz and I_{DS} = 1.5 A T_{c1} = 112.1 °C.

Symbol	Unit	x_i	$u(x_i)$	Probability Distribution	c_s	$u_i(y)$
τ_a	-	0.99	0.01	normal	0.45	0.01
ε	-	0.95	0.03	rectangular	−7.65	−0.22
T_{refl}	°C	20.85	1.44	rectangular	0.01	0.02
τ_l	-	0.99	0.01	rectangular	−10.32	−0.06
T_a	°C	20.85	4.04	rectangular	−0.02	−0.06
T_l	°C	20.85	4.04	rectangular	−0.02	−0.06
T_{cam}	°C	20.85	1.15	rectangular	1.00	1.15
T_c	°C	112.1				1.18

4. Discussion

During the experimental work, an additional lens (Close-up 2×) was used with the thermographic camera. This enabled the thermographic camera used during the measurements (equipped with a 240 × 180 pixels detector matrix) to obtain such spatial resolution for which the edge of the field of view of a single detector was 67 µm. This value, taking into account the dimensions of the transistor shown in Figure 2, guaranteed that 25 fields of the view of a single detector of the thermographic camera (fields of the view placed in a rectangle of 5 × 5 pixels) were placed on the transistor case during the measurement. For this reason, the result of the thermographic temperature measurement can be considered reliable.

Before starting the measurements, the performance of the thermographic camera was compared with to the IRS Calilux radiation standard (Automation Technology, Bad Oldesloe, Germany). The results were compared in the range of 30–90 °C with a step of 5 °C. The largest difference between the standard and the camera was 0.72 °C (the camera error was ±2 °C or ±2%, whichever is greater). For this reason, the output from the thermographic camera can be considered reliable.

The results of the thermographic temperature measurements were comparable to those obtained using the Pt1000 sensor and to the results obtained during simulation work using the FEM method. During the work carried out, three transistor specimens were tested. Similar measurement results were obtained for each. Brand new Pt1000 sensors were used.

Analyzing the data from Tables 5–8 (and especially comparing the die temperature (T_j) determined based on the simulation and the voltage drop T_{jd}) it can be seen that the largest difference was 4 °C. The conducted studies prove that the use of the transistor body diode during measurements allows for obtaining reliable results. They also prove that the results obtained by simulation work are confirmed in real conditions. Comparing the case temperature determined by simulation work (T_S) with the temperature measured by means of a thermographic camera (T_c), it can be seen that these values are the same. This proves that the model created is reliable.

Analyzing the data from Tables 5–8, it can be seen that the difference between all results for T_{c1}–T_{c3} are within the limit defined by the uncertainty $U(T_c)$. It can also be seen that the values of T_{c1}–T_{c3} and T_S and T_{Pt1000} are within the range defined by $\Delta T_{\mathrm{Pt1000}}$ and $U(T_c)$. For this reason, it can be assumed that the thermographic temperature measurement is reliable.

5. Conclusions

The aim of this research was to develop a method for performing indirect thermographic measurement of a SiC MOSFET and monitoring the SiC MOSFET temperature at variable switching frequencies.

Analyzing the transistor case temperatures measured with a thermographic camera (T_c) at a frequency f_t, it can be seen that despite the constant value of the I_{DS} current, the T_c value increases. The increase in the T_c value depends on the I_{DS} value. For the value of I_{DS} = 0.25 A and f_t in the range of 1 kHz–800 kHz, the T_c value increased by 4.5 °C. For the value of I_{DS} = 0.5 A and f_t in the range of 1 kHz–800 kHz, the T_c value increased by 5.6 °C. For the value of I_{DS} = 1 A and f_t in the range of 1 kHz–800 kHz, the T_c value increased by 3 °C. For the value of I_{DS} = 1.5 A and f_t in the range of 1 kHz–800 kHz, the T_c value increased by 1.5 °C. The T_c value depends on the value of I_{DS} and f_t. With the increase in I_{DS}, the T_c value is set at increasingly lower values of f_T.

The largest recorded difference between the case temperature and the die temperature was 27.3 °C. The use of a thermographic camera allows determining the temperature of the transistor die, which allows selecting the optimal control of the C2M0280120D transistor.

Due to the use of thermographic, there is no risk of electric shock as a result of touching the base plate or radiator, and the measurement result is obtained immediately. Based on a properly performed thermographic measurement of the temperature of the black part

of the case (made of epoxy mold compound), it is possible to determine the temperature of the transistor die. As a result, its optimal operating point can be selected even more precisely. It is also possible to capture the operating point at which the transistor begins to operate incorrectly. This will prevent damage and save funds that would have to be spent in the event of a failure.

Author Contributions: Conceptualization, K.D.; methodology, K.D. and A.H.; formal analysis, K.D., A.H. and Ł.D.; investigation, K.D. and A.H.; resources, K.D.; writing—original draft preparation, K.D., A.H. and Ł.D.; writing—review and editing, K.D., A.H. and Ł.D.; visualization, K.D.; supervision, K.D. and A.H. All authors have read and agreed to the published version of the manuscript.

Funding: This research was funded by the Ministry of Science and Higher Education, grant numbers 0212/SBAD/0617 and 0212/SBAD/0618.

Institutional Review Board Statement: Not applicable.

Informed Consent Statement: Not applicable.

Data Availability Statement: Data are contained within the article.

Conflicts of Interest: The authors declare no conflicts of interest.

Nomenclature

a and b	dimensionless coefficients
a_+	upper limit of the input quantity range
a_-	lower limit of the input quantity range
a_{lam}	value of coefficient a for laminar flow
b_{lam}	value of coefficient b for laminar flow
a_{turb}	value of coefficient a for turbulent flow
b_{turb}	value of coefficient b for turbulent flow
c	specific heat of air equal to 1005 $J \cdot kg^{-1} \cdot K^{-1}$ at 293.15 K
c_s	sensitivity coefficient
d	distance between the tested transistor and the additional lens
DUT	device under test
e	slope of the equation $T_{jd} = f(V_{fd})$ of the transistor
f	free term of the equation $T_{jd} = f(V_{fd})$ of the transistor
FEM	finite element method
f_i	all input quantities from Equation (14)
f_T	switching frequency
g	gravitational acceleration (9.8 $m \cdot s^{-2}$)
Gr	Grashof number
h_{cf}	convection coefficient of flat surfaces
h_r	radiation coefficient
I_D	drain current
I_{DS}	drain—source current (in A)
I_{Dpulse}	pulse current
I_{Pt1000}	current flowing through Pt1000
IFOV	instantaneous field of view
IR	infrared radiation
J	radiative heat flux
K	thermal conductivity
k	coverage factor
L	characteristic length in meters (for a vertical wall, this value represents height)
Nu	Nusselt number
P_{RMS}	power supplied to the transistor
P	power dissipated in the die (in W)
P_c	total power applied to the wall
Pr	Prandtl number
Re	Reynolds number
R_{Pt1000}	resistance of Pt1000

S	area of the wall penetrated by J
T_a	ambient temperature
T_c	case temperature
T_{c1}	T_c value measured for the first transistor
T_{c2}	T_c value measured for the second transistor
T_{c3}	T_c value measured for the third transistor
T_{cam}	temperature indicated by the thermographic camera
T_k	duration of the period
T_j	junction temperature
T_d	junction temperature determined electrically
T_l	thermographic camera lens temperature
T_{Pt1000}	temperature value measured with Pt1000
T_{refl}	reflected temperature
T_1	temperature at the starting point of the analyzed heat flow path (K)
T_2	temperature at the end point of the analyzed heat flow path (K)
t_0	beginning of the period
$u(x_i)$	standard uncertainty of each X_i,
$u(y)$	uncertainty contribution
$u(T_c)$	standard uncertainty of T_c values
$U(T_c)$	expanded uncertainty of T_c values
V	average linear velocity of the fluid flow
V_{DS}	drop voltage between drain and source (in V)
V_{Dsmax}	maximum drain—source voltage
V_{fd}	diode forward voltage
V_{GS}	gate—source voltage
V_{GSmax}	maximum gate—source voltage
V_{Pt1000}	voltage drop on Pt1000
x	distance between the points where the temperature values of the die and diode case were measured, and J is the radiative heat flux
x_k	end point of the analyzed heat flow path
X_i	input quantities
x_i	estimates of the input quantities X_i
∇	Nabla operator
α	coefficient of expansion equal to 0.0034 K^{-1}
ε	emissivity factor
ΔI_{DS}	limiting error of the I_{DS} value (in A)
ΔV_{DS}	limiting error of the V_{DS} value (in V)
$\Delta I_{\mathrm{Pt1000}}$	limit error of I_{Pt1000}
$\delta I_{\mathrm{Pt1000}}$	relative error of I_{Pt1000}
ΔP	limiting error of the P value in W
$\delta R_{\mathrm{Pt1000}}$	relative error of R_{Pt1000}
$\Delta R_{\mathrm{Pt1000}}$	limit error of R_{Pt1000}
$\Delta T_{\mathrm{Pt1000}}$	limit error of $\Delta T_{\mathrm{Pt1000}}$ of measurement T_{Pt1000}
$\Delta V_{\mathrm{Pt1000}}$	limit error of V_{Pt1000}
$\delta V_{\mathrm{Pt1000}}$	relative error of V_{Pt1000}
η	dynamic air viscosity equal to 1.75×10^{-5} $\mathrm{kg{\cdot}m^{-1}{\cdot}s^{-1}}$ at 273.15 K
ρ	density equal to 1.21 ($\mathrm{kg{\cdot}m^{-3}}$) in 273.15 (K)
σ_c	Stefan–Boltzmann constant
τ_a	atmosphere transmittance coefficient
τ_l	transmittance of the thermographic camera lens

References

1. Božanić, M.; Sinha, S. Emerging Transistor Technologies Capable of Terahertz Amplification: A Way to Re-Engineer Terahertz Radar Sensors. *Sensors* **2019**, *19*, 2454. [CrossRef]
2. Ibrahim, M.S.; Abbas, W.; Waseem, M.; Lu, C.; Lee, H.H.; Fan, J.; Loo, K.-H. Long-Term Lifetime Prediction of Power MOSFET Devices Based on LSTM and GRU Algorithms. *Mathematics* **2023**, *11*, 3283. [CrossRef]
3. Dziarski, K.; Hulewicz, A.; Kuwałek, P.; Wiczyński, G. Methods of Measurement of Die Temperature of Semiconductor Elements: A Review. *Energies* **2023**, *16*, 2559. [CrossRef]

4. Ulrich, R.K.; Brown, W.D. *Advanced Electronic Packaging*; Wiley-IEEE Press: Hoboken, NJ, USA, 2006.
5. Wang, Y.; Ding, Y.; Yin, Y. Reliability of Wide Band Gap Power Electronic Semiconductor and Packaging: A Review. *Energies* **2022**, *15*, 6670. [CrossRef]
6. Millan, J. Wide band-gap power semiconductor devices. *IET Circuits Devices Syst.* **2007**, *1*, 372–379. [CrossRef]
7. Roussel, P. SiC Market and Industry Update. In Proceedings of the International SiC Power Electronics Application Workshop, Birmingham, UK, 1–2 September 2011; pp. 3–4.
8. Yang, X.; Xu, M.; Li, Q.; Wang, Z.; He, M. Analytical method for RC snubber optimization design to eliminate switching oscillations of SiC MOSFET. *IEEE Trans. Power Electron.* **2022**, *37*, 4672–4684. [CrossRef]
9. Gupta, A.; Ayyanar, R.; Chakraborty, S. Novel electric vehicle traction architecture with 48 V Battery and multi-input, high conversion ratio converter for high and variable DC-link voltage. *IEEE Open J. Veh. Technol.* **2021**, *2*, 448–470. [CrossRef]
10. Fabre, J.; Ladoux, P. Parallel connection of SiC MOSFET modules for future use in traction converters. In Proceedings of the 2015 International Conference on Electrical Systems for Aircraft, Railway, Ship Propulsion and Road Vehicles (ESARS), Aachen, Germany, 3–5 March 2015; pp. 1–6. [CrossRef]
11. Lagier, T.; Ladoux, P.; Dworakowski, P. Potential of silicon carbide MOSFETs in the DC/DC converters for future HVDC offshore wind farms. *High Volt.* **2017**, *2*, 233–243. [CrossRef]
12. Ding, X.; Lu, P.; Shan, Z. A high-accuracy switching loss model of SiC MOSFETs in a motor drive for electric vehicles. *Appl. Energy* **2021**, *291*, 116827. [CrossRef]
13. Scognamillo, C.; Catalano, A.P.; Riccio, M.; d'Alessandro, V.; Codecasa, L.; Borghese, A.; Tripathi, R.N.; Castellazzi, A.; Breglio, G.; Irace, A. Compact Modeling of a 3.3 kV SiC MOSFET Power Module for Detailed Circuit-Level Electrothermal Simulations Including Parasitics. *Energies* **2021**, *14*, 4683. [CrossRef]
14. Chen, M.; Wang, H.; Pan, D.; Wang, X.; Blaabjerg, F. Thermal characterization of silicon carbide MOSFET module suitable for high-temperature computationally efficient thermal-profile prediction. *IEEE J. Emerg. Sel. Top. Power Electron.* **2020**, *9*, 3947–3958. [CrossRef]
15. Du, H.; Reigosa, P.; Ceccarelli, L.; Iannuzzo, F. Impact of repetitive short-circuit tests on the normal operation of SiC MOSFETs considering case temperature influence. *IEEE J. Emerg. Sel. Topics Power Electron.* **2020**, *8*, 195–205. [CrossRef]
16. Tanimoto, S.; Ohashi, H. Reliability issues of SiC power MOSFETs toward high junction temperature operation. *Phys. Status Solidi A* **2019**, *206*, 2417–2430. [CrossRef]
17. Wang, H. Transitioning to physics-of-failure as a reliability driver in power electronics. *IEEE J. Emerg. Sel. Top. Power Electron.* **2014**, *2*, 97–114. [CrossRef]
18. Wang, H.; Liserre, M.; Blaabjerg, F. Toward reliable power electronics: Challenges design tools and opportunities. *IEEE Ind. Electron. Mag.* **2013**, *7*, 17–26. [CrossRef]
19. Li, H.; Liao, X.; Hu, Y.; Zeng, Z.; Song, E.; Xiao, H. Analysis of SiC MOSFET dI/dt and its temperature dependence. *IET Power Electron.* **2017**, *11*, 491–500. [CrossRef]
20. Yodwong, B.; Guilbert, D.; Kaewmanee, W.; Phattanasak, M. Energy Efficiency Based Control Strategy of a Three-Level Interleaved DC-DC Buck Converter Supplying a Proton Exchange Membrane Electrolyzer. *Electronics* **2019**, *8*, 933. [CrossRef]
21. Faizan, M.; Wang, X.; Yousaf, M.Z. Design and Comparative Analysis of an Ultra-Highly Efficient, Compact Half-Bridge LLC Resonant GaN Converter for Low-Power Applications. *Electronics* **2023**, *12*, 2850. [CrossRef]
22. Urkin, T.; Peretz, M.M. Asymmetrically Driven HB-LLC Resonant Converter Integrated in Low-Power IoT Devices. In Proceedings of the 2023 IEEE Applied Power Electronics Conference and Exposition (APEC), Orlando, FL, USA, 19–23 March 2023; pp. 2105–2110. [CrossRef]
23. Li, X.; Zhang, L.; Guo, S.; Lei, Y.; Huang, A.; Zhang, B. Understanding switching losses in SiC MOSFET: Toward lossless switching. In Proceedings of the 2015 IEEE 3rd Workshop on Wide Bandgap Power Devices and Applications (WiPDA), Blacksburg, VA, USA, 2–4 November 2015; pp. 257–262. [CrossRef]
24. Dziarski, K.; Hulewicz, A.; Drużyński, Ł.; Dombek, G. Indirect Thermographic Temperature Measurement of a Power-Rectifying Diode Die Based on a Heat Sink Thermogram. *Energies* **2023**, *16*, 332. [CrossRef]
25. JESD 51-53. Available online: https://www.jedec.org (accessed on 3 February 2024).
26. Bercu, N.; Lazar, M.; Simonetti, O.; Adam, P.M.; Brouillard, M.; Giraudet, L. KPFM-Raman Spectroscopy Coupled Technique for the Characterization of Wide Bandgap Semiconductor Devices. *Mater. Sci. Forum* **2022**, *1062*, 330–334. [CrossRef]
27. Avenas, Y.; Dupont, L.; Khatir, Z. Temperature measurement of power semiconductor devices by thermo-sensitive electrical parameters—A review. *IEEE Trans. Power Electron.* **2011**, *27*, 3081–3092. [CrossRef]
28. Abad, B.; Borca-Tasciuc, D.A.; Martin-Gonzalez, M.S. Non-contact methods for thermal properties measurement. *Renew. Sustain. Energy Rev.* **2017**, *76*, 1348–1370. [CrossRef]
29. Hulewicz, A.; Dziarski, K.; Drużyński, Ł.; Dombek, G. Thermogram Based Indirect Thermographic Temperature Measurement of Reactive Power Compensation Capacitors. *Energies* **2023**, *16*, 2164. [CrossRef]
30. Pt_1000. Available online: https://www.reichelt.com/ch/pl/czujnik-temperatury-p-lstrok-ytek-smd-0603-1000-om-oacute-w-smd-0603-pt1000-p151239.html?CCOUNTRY=459&LANGUAGE=fr&GROUPID=9145&START=0&OFFSET=16&SID=964d99ec818539c8448982376b9e52e375c224e23ed7359cb8a59&LANGUAGE=PL&&r=1 (accessed on 15 February 2024).
31. WLK 5. Available online: https://www.tme.eu/en/details/wlk_5/heatsinks-equipment/fischer-elektronik/wlk-5/ (accessed on 15 February 2024).

32. Kawor, E.T.; Mattei, S. Emissivity measurements for nexel velvet coating 811-21 between—36 °C and 82 °C. *High Temp.—High Press.* **2001**, *33*, 551–556. [CrossRef]
33. Flir E50. Available online: https://docs.rs-online.com/ca3e/0900766b81371810.pdf (accessed on 15 February 2024).
34. Close-up 2x (50 μm) T197214. Available online: https://www.ideadigitalcontent.com/files/12228/T197214-en-US_A4.pdf (accessed on 15 February 2024).
35. IRS Calilux. Available online: https://www.ndt.net/news/files/AT_Newsletter_3._Quarter_2020_ENG.pdf (accessed on 15 February 2024).
36. Krawiec, P.; Różański, L.; Czarnecka-Komorowska, D.; Warguła, Ł. Evaluation of the Thermal Stability and Surface Characteristics of Thermoplastic Polyurethane V-Belt. *Materials* **2020**, *13*, 1502. [CrossRef] [PubMed]
37. Siemens s71200 PLC. Available online: https://support.industry.siemens.com/cs/mdm/91696622?c=60698891275&dl=sk&lc=pl-pl (accessed on 15 February 2024).
38. Dziarski, K.; Hulewicz, A.; Drużyński, Ł.; Dombek, G. Indirect Thermographic Temperature Measurement of a Power Rectifying Diode Die under Forced Convection Conditions. *Appl. Sci.* **2023**, *13*, 4440. [CrossRef]
39. Agilent. Available online: https://www.agilent.com/?gad_source=1&gclid=CjwKCAjwm_SzBhAsEiwAXE2CvxfrIFaUKFw_i-uOUtxsLtOrH-DNMHQtVQQRM37HcCh6fHAZMqL4qxoCYOQQAvD_BwE&gclsrc=aw.ds (accessed on 16 March 2024).
40. UT55. Available online: https://www.uni-trend.com/ (accessed on 16 March 2024).
41. Available online: https://www.enac.es/documents/7020/635abf3f-262a-4b3b-952f-10336cdfae9e (accessed on 30 July 2024).
42. Dziarski, K.; Hulewicz, A.; Dombek, G. Lack of thermogram sharpness as component of thermographic temperature measurement uncertainty budget. *Sensors* **2021**, *21*, 4013. [CrossRef]

sensors

MDPI

Article

A Novel Defect Quantification Method Utilizing Multi-Sensor Magnetic Flux Leakage Signal Fusion

Wenlong Liu, Lemei Ren * and Guansan Tian

School of Thermal Engineering, Shandong Jianzhu University, Jinan 250100, China; 19861806215@163.com (W.L.); tgs4170@sdjzu.edu.cn (G.T.)

* Correspondence: 24332@sdjzu.edu.cn

Abstract: In the assessment of pipeline integrity using magnetic flux leakage (MFL) detection, it is crucial to quantify defects accurately and efficiently using MFL signals. However, in complex detection environments, traditional defect inversion methods exhibit low quantification accuracy and efficiency due to the complexity of their algorithms or excessive reliance on a priori knowledge and expert experience. To address these issues, this study presents a novel defect quantification method based on multi-sensor signal fusion (MSSF). The method employs a multi-sensor probe to fuse the MFL signals under multiple lift-off values, enhancing the diversity of defect information. This enables defect-opening profile recognition using the characteristic approximation approach (CAA). Subsequently, the MSSF method is based on a 3D magnetic dipole model and integrates the structural features of multi-sensor probes to develop an algorithm. This algorithm iteratively determines the defect depth at multiple data acquisition points within the defect region to obtain the maximum defect depth. The feasibility of the MSSF quantification method is validated through finite element simulation and physical experiments. The results demonstrate that the proposed method achieves accurate defect quantification while enhancing efficiency, with the number of iterations for each defect depth calculation point consistently requiring fewer than 15 iterations. For rectangular metal loss, perforation, and conical defects, quantification errors are less than 10%, meeting practical inspection requirements.

Keywords: magnetic flux leakage (MFL); multi-sensor signal fusion (MSSF); characteristic approximation approach (CAA); defect depth calculation point

1. Introduction

As vital national strategic energy sources, oil and natural gas play a significant role in the national economy. Pipeline transportation serves as their primary mode of transportation. Currently, the combined length of oil and gas pipelines in different countries or regions has surpassed 2 million kilometers [1,2]. Due to the aging of pipelines and the harsh operating conditions they face, they are highly susceptible to various types of damage defects, such as metal loss, local pitting, cracks, dents, and corrosion, which increases the risk of oil and gas leakage [3]. Consequently, the integrity evaluation of pipeline structure is crucial for safe production and economic development [4–6]. As one of the most popular non-destructive testing technologies, magnetic flux leakage (MFL) detection technology is widely used in the detection of ferromagnetic materials like oil and gas pipelines [7,8], steel rails [9], steel wire ropes [10,11], steel belts [12], and other materials for automatic detection and evaluation.

Defect quantification is an essential part of pipeline MFL detection, with the most prevalent approach involving the construction of a robust model for determining defect size [13]. The key challenge lies in accurately and efficiently utilizing MFL signals to determine defect sizes, making it the focal point and primary difficulty in the defect quantification process [14]. In general, there are two main technical routes: (1) data-driven method and (2) model-driven method.

The data-driven method based on intelligent algorithms is constructed to describe the relationship between the signal and defect size. The majority of the method is based on machine-learning models. Initially, researchers could only quantify defects using shallow-learning methods due to limitations in computing capability. K. Hwang et al. [15] used a wavelet basis function (WBF) neural network to transform the MFL signal into a 3D defect profile, and the WBF approximated the defect profile by adjusting the resolution of the network. K.MR et al. [16] employed a neural network to extract the contour features of the MFL signal to identify the length and width dimensions of the defect and to estimate the depth of the defect using the peaks of the signal. B. Liu et al. [17] proposed a method for the reconstruction of 2D profiles based on a kernelized extreme learning machine (ELM) and used a quantum genetic algorithm (QGA) to optimize the parameters. However, shallow-learning methods can usually only obtain limited defect information due to the weak feature extraction capability [16]. In recent years, with the development of computer technology, deep learning methods have been widely applied to defect quantification. S.Lu et al. [18] proposed a new visual transform convolutional neural network (VT-CNN) for defect quantification, which uses a visual transform layer to transform the original MFL signal into a 3D image, improving quantification accuracy. Y.Ren et al. [19] designed a task-based bias DA network (TBDA-net) based on an adaptive dimension alignment subnet and task-based distribution-matching subnet to realize the quantification of defect size in small samples. M. Zhang et al. [20] proposed a visual deep transfer learning neural network to convert 1D MFL signals into 2D images, extending defect information and improving quantification accuracy. The above methods have made significant advances in defect quantification, but there are still some limiting factors: 1. Deep-learning models require a large number of labeled data for training, while in real industrial production, the limited availability of labeled samples and high production costs limit the performance of the models. 2. Deep-learning models are difficult to integrate with the underlying MFL theory, resulting in unclear physical meaning of the models.

The model-driven method leverages the uniqueness of the forward model, mapping defect size to defect MFL signals, to estimate defect size through iterative optimization of model parameters [21]. J. Feng et al. [22] considered the impact of detector vibration on the MFL detection in pipelines, and proposed a sensor lift-off modification method to correct the original MFL signal for accurate fault quantification. However, this correction process is time-consuming. G.Yu et al. [23] proposed a pipeline defect inversion method based on Stacking Learning, which enhances the generalization ability for different sample sets of defect inversion issues. Nevertheless, the quantification process requires the intervention of expert experience in the field of leakage detection, which reduces the quantification efficiency. R.Priewald et al. [24] used Gauss-Newton optimization to reconstruct the defect profile based on a nonlinear orthogonal model, but it is difficult to quantify the actual defects. Z. Wu et al. [25] proposed an algorithm based on an actor-critic structure for sizing defect profiles, aiming to mitigate the impact of signal noise on quantification and improve robustness. F.Li et al. [26] introduced a rapid approach to reconstruct defect profiles from MFL signals employing a modified harmony search (MHS) algorithm. Despite the increased computational speed, the quantification accuracy is compromised. D Zhang et al. [27] proposed a defect profile reconstruction method based on modified cuckoo search (MCS), employing a FEM as a forward model. The method successfully reconstructs 2D defect contours while enhancing computational speed by filtering and updating the primary error information between the predicted and reference signals, thereby minimizing interference from cluttered data in other dimensions. K.C. Hari et al. [28] proposed a novel scheme for the rapid forward simulation of MFL signals through a reduced nonlinear FEM method. This model facilitates the reconstruction of internal surface defect shapes using genetic algorithms (GAs), thereby improving the speed of defect quantification by decreasing the computational volume associated with FEM. S Zhang et al. [29] utilized an improved discrete magnetic dipole model (DMDM) as a forward model to estimate the depth of complex defects. Notably, the MFL signals obtained through the DMDM

method exhibited minimal differences when compared with those derived from FEM and experimental results. Moreover, the computational efficiency of the DMDM approach was significantly greater than that of traditional FEM simulations. These methods provide theoretical support for defect quantification. Nevertheless, the complexity of the iterative inversion model results in low quantification efficiency, making their practical application in inspections challenging.

In addition to the two mainstream quantification methods, the data-driven method and model-driven method, recent research has explored the use of multiple sensor probes rather than the traditional single sensor. Scholars have investigated the use of specialized multi-sensor probe structures to develop defect size estimation equations. P.Shi et al. [30] analyzed the quantification errors associated with traditional single-sensor systems, particularly those arising from the lift-off effect and proposed a dual-sensor strategy that incorporates an uncertain lift-off value to enhance depth quantification accuracy. However, this method has not yet been validated through physical experiments. Y.Long et al. [31] introduced a detection topology for crack defects and, based on this, developed an MFL probe with double lift-off magnetic field sensors in the radial direction. This approach enhanced the quantification of crack defect depth and partially overcame the limitations of conventional magnetic flux leakage (MFL) detection methods in identifying and quantifying crack defects. Additionally, Y.Long et al. [32] proposed a new type of probe with dual diagonal distributed magnetic sensors. This design aims to compensate for probe attitude shifts caused by mechanical vibrations when the detector moves in the pipeline, thereby improving the signal-to-noise ratio and quantification accuracy. In conclusion, the use of multiple sensor probes enables the acquisition of MFL signals at varying lift-off values, facilitating lift-off compensation and enhancing defect quantification accuracy.

Based on the aforementioned analysis, this study proposes a novel defect quantification method based on multi-sensor signal fusion (MSSF), utilizing a configuration of four alternately staggered sensors. The multi-sensor probes enhance defect information diversity by integrating MFL signals from multiple lift-off values, significantly reducing the tedious iterative quantification process. This advancement markedly improves efficiency. Building on the fused signals, the MSSF method establishes a computational model for iteratively estimating defect depth, combining a three-dimensional magnetic dipole model (MDM) with the structural characteristics of the multi-sensor probe. Furthermore, this method identifies defect-opening profiles employing the characteristic approximation approach (CAA), leveraging MFL signals acquired by multi-sensor probes across various lift-off values. The proposed method represents a significant improvement in defect quantification efficiency and also improves the accuracy of MFL detection.

This paper is organized as follows: Section 2 elaborates on the defect quantification method based on the multi-sensor probe. Section 3 describes the finite element model (FEM) and physical experiments used to obtain the MFL signal of defects. Section 4 discusses and verifies the feasibility and robustness of the proposed method under simulation and experimental conditions. Finally, Section 5 presents the conclusions of this paper.

2. Methods

2.1. The Principle of the MFL Detection

Figure 1 illustrates the principle of internally detecting pipeline leakage magnetic field. The MFL detection model consists mainly of permanent magnets, magnetic sensors, and yoke irons. The principle is based on the high magnetic permeability characteristics of ferromagnetic materials. The pipe wall is fully magnetized using a permanent magnet and a rigid brush, achieving a saturated or near-saturated state. In the absence of any defects, the magnetic field lines run parallel to the inner surface of the pipe. However, the presence of defects, such as surface or near-surface imperfections, disrupts the magnetic field lines, leading to leakage from the pipe surface [33]. The characteristics of the leakage magnetic field distribution are closely correlated with the size of the defect. Detection and

characterization of defects can be accomplished through the use of a magnetic sensor to detect the MFL signal.

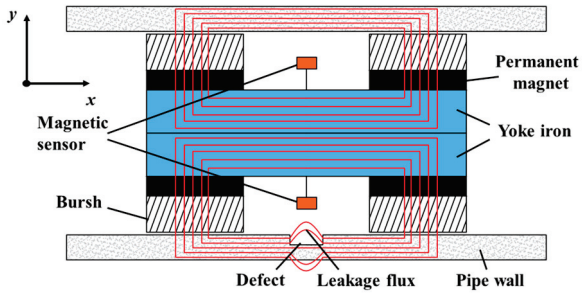

Figure 1. Principle of the MFL inspection.

2.2. The MSSF Method for Defect-Opening Profile Identification

Defect-opening profile identification is the initial step in defect quantification. This step significantly influences the accuracy of the quantification process. This section discusses the characteristic approximation approach (CAA) proposed by Yue Long for achieving accurate recognition of defect-opening profiles [34]. The CAA is based on the characteristic that the extreme value of the MFL signal approaches the edge of the defect as the lift-off value decreases. It calculates the signal pole value at the time when the lift-off value is 0 by numerically fitting the relationship between the pole value and lift-off value. Figure 2 shows that the extreme value point coordinates move closer to the defect edge (green dotted line) as B_x and B_y decrease with the lift-off value. Therefore, the CAA method is advantageous in identifying the defect profile compared to assuming that the peak width of the MFL signal is equal to the width of the defect. The CAA method determines the axial length of the defect using B_x, B_y, and B_z in the axial detection direction. It identifies the circumferential length of the defect using B_y and B_z in the circumferential detection direction.

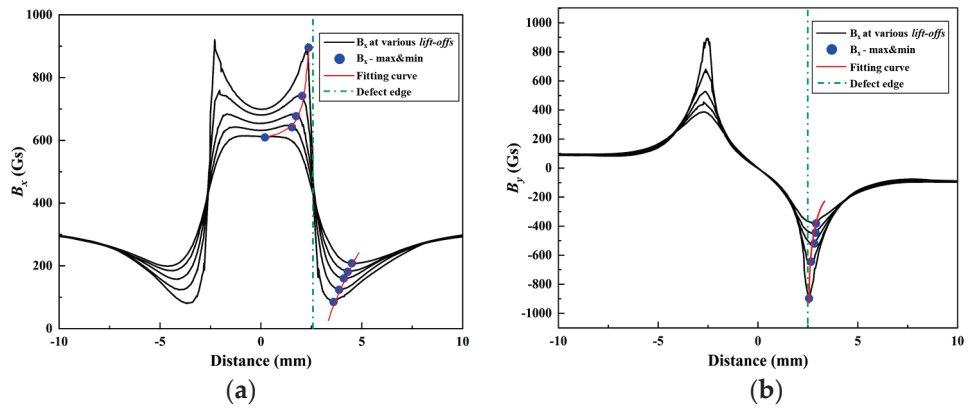

Figure 2. Defect-opening profile recognition: (**a**) B_x in the x-detection, (**b**) B_y in the x-detection.

2.3. The MSSF Method for Defect Depth Quantification

In this section, the MSSF quantification method is accomplished by deriving a 3D MDM and utilizing a multi-sensor probe.

Three-dimensional MDM: It is assumed that the two surfaces of a rectangular defect perpendicular to the applied magnetic field are uniformly distributed with magnetically opposite surface charges whose density is $\pm\sigma_s$. The interaction between the two produces a leakage magnetic field [35], as shown in Figure 3. A coordinate system with right angles is established on the inner surface of the pipe. The x-axis is defined as the axial direction of the pipe, the y-axis as the radial direction, and the z-axis as the circumferential direction. The dimensions of the defect are $2l$ for length, $2w$ for width, and h for depth. Equations (1)–(3)

can be used to solve for the axial component H_x, radial component H_y, and circumferential component H_z at the field point $P(x, y, z)$ according to the Biot–Savart law [36,37].

$$\begin{aligned} H_x(x,y,z) = \tfrac{\sigma_s}{4\pi} \times \{ & \arctan\left[\frac{y(x+l)}{(z-w)\sqrt{(x+l)^2+(z-w)^2+y^2}}\right] - \arctan\left[\frac{y(x+l)}{(z+w)\sqrt{(x+l)^2+(z+w)^2+y^2}}\right] \\ & + \arctan\left[\frac{y(x-l)}{(z+w)\sqrt{(x-l)^2+(z+w)^2+y^2}}\right] - \arctan\left[\frac{y(x-l)}{(z-w)\sqrt{(x-l)^2+(z-w)^2+y^2}}\right] \\ & + \arctan\left[\frac{(y+h)(x+l)}{(z+w)\sqrt{(x+l)^2+(z+w)^2+(y+h)^2}}\right] - \arctan\left[\frac{(y+h)(x-l)}{(z+w)\sqrt{(x-l)^2+(z+w)^2+(y+h)^2}}\right] \\ & + \arctan\left[\frac{(y+h)(x-l)}{(z-w)\sqrt{(x-l)^2+(z-w)^2+(y+h)^2}}\right] - \arctan\left[\frac{(y+h)(x+l)}{(z-w)\sqrt{(x+l)^2+(z-w)^2+(y+h)^2}}\right] \} \end{aligned} \tag{1}$$

$$H_y(x,y,z) = \tfrac{\sigma_s}{4\pi} \times \{\ln\left[\frac{\left[z+w+\sqrt{(x-l)^2+(z+w)^2+(y+h)^2}\right]\times\left[z+w+\sqrt{(x+l)^2+(z+w)^2+y^2}\right]}{\left[z-w+\sqrt{(x+l)^2+(z-w)^2+y^2}\right]\times\left[z+w+\sqrt{(x+l)^2+(z+w)^2+(y+h)^2}\right]}\right] + \ln\left[\frac{\left[z-w+\sqrt{(x-l)^2+(z-w)^2+y^2}\right]\times\left[z-w+\sqrt{(x+l)^2+(z-w)^2+(y+h)^2}\right]}{\left[z-w+\sqrt{(x-l)^2+(z-w)^2+(y+h)^2}\right]\times\left[z+w+\sqrt{(x-l)^2+(z+w)^2+y^2}\right]}\right]\} \tag{2}$$

$$H_z(x,y,z) = \tfrac{\sigma_s}{4\pi} \times \{\ln\left[\frac{\left[y+h+\sqrt{(x+l)^2+(z-w)^2+(y+h)^2}\right]\times\left[y+\sqrt{(x+l)^2+(z+w)^2+y^2}\right]}{\left[y+\sqrt{(x+l)^2+(z-w)^2+y^2}\right]\times\left[y+h+\sqrt{(x+l)^2+(z+w)^2+(y+h)^2}\right]}\right] + \ln\left[\frac{\left[y+\sqrt{(x-l)^2+(z-w)^2+y^2}\right]\times\left[y+h+\sqrt{(x-l)^2+(z+w)^2+(y+h)^2}\right]}{\left[y+h+\sqrt{(x-l)^2+(z-w)^2+(y+h)^2}\right]\times\left[y+\sqrt{(x-l)^2+(z+w)^2+y^2}\right]}\right]\} \tag{3}$$

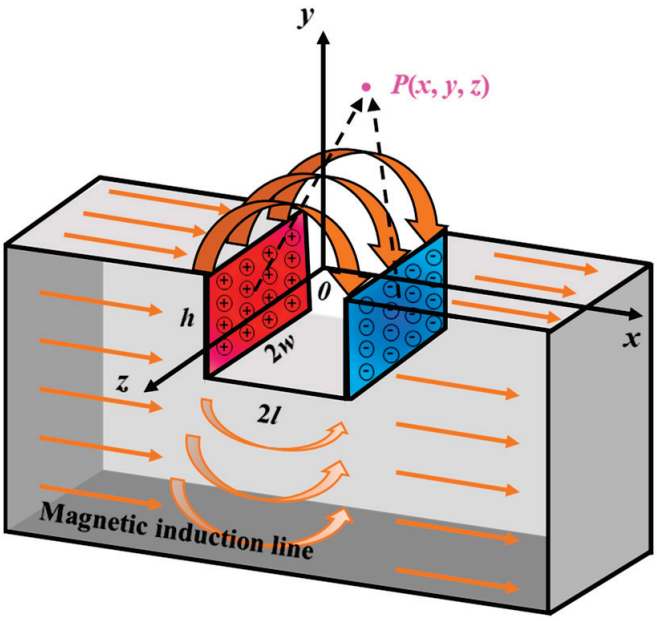

Figure 3. Three-dimensional MDM of the MFL detection.

Figure 4 shows the structure of the multi-sensor probe, which consists of four Hall sensors arranged in staggered rows above and below. The lift-off values are denoted as r_1, r_2, r_3, and r_4, respectively, where $r_2 - r_1 = d$ and $r_4 - r_3 = d$. The CAA method can fit the MFL signals at a lift-off value of 0 from the MFL signals under the four different lift-off values. This enables the quantification of the defect length $2l$ and the defect width $2w$.

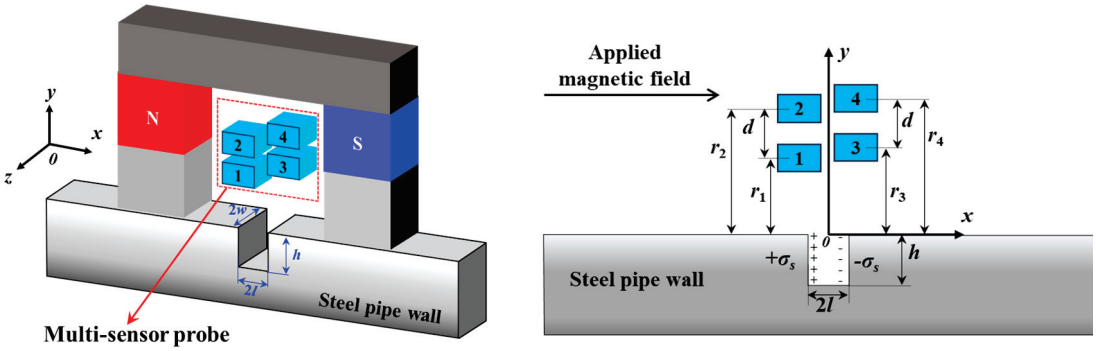

(**a**) (**b**)

Figure 4. Multi−sensor probe detection system: (**a**) schematic of the spatial layout, (**b**) 2D dimensional display, blue squares represent sensors; 1, 2, 3, 4 represent sensor numbers.

When analyzing the MFL signals, particular attention should be paid to the signals in the vicinity of defects, as the magnetic field in regions far from the defect is very weak and exhibits negligible differences [29]. In this study, a square signal area with a side length of 20 mm is chosen as an example, with its center coinciding with the defect center. This area adequately covers the leakage magnetic field generated by the defect. As shown in Figure 5a, the Region of Interest (ROI) is delineated by blue dashed lines, representing detection channels along the x and z directions, spaced 1 mm apart. The defect-opening profile identified by CAA is depicted by the red box in Figure 5b, encompassing $2m + 1$ channels in the x direction and $2n + 1$ channels in the z direction. There are $c = (2m + 1) \times (2n + 1)$ data acquisition points, $P_{-n,\,-m}$, $P_{-n,\,m}$, $P_{n,\,[-m}$, $P_{n,\,m}$, $\cdots\cdots P_{i,j}$, $i \in [-\mathrm{n}, \mathrm{n}]$, $j \in [-\mathrm{m}, \mathrm{m}]$. The magnetic field at point $P_{i\,j}$ $(\frac{i}{n}l,\ y,\ \frac{j}{m}w)$ is given by

$$H_{P\,i\,j}(\frac{i}{n}l,\ y,\ \frac{j}{m}w) = (H_x(\frac{i}{n}l,\ y,\ \frac{j}{m}w), H_y(\frac{i}{n}l,\ y,\ \frac{j}{m}w), H_z(\frac{i}{n}l,\ y,\ \frac{j}{m}w)) \tag{4}$$

where y represents the lift-off value of data acquisition points, $y > 0$. By calculating the defect depth at each data acquisition point, the maximum defect depth can be determined using Equation (5), providing insights into the extent of pipeline damage.

$$h_{max} = max\{h_{1,1},\ h_{1,2} \cdots\cdots h_{i,j}\}_{-n<i<n,\ -m<j<m} \tag{5}$$

Taking point $P_{n,0}$ $(l,y,0)$ at the center of the defect edge in Figure 5b as an example, we derive the algorithm for solving defect depth using the MSSF based on the 3D MDM. By substituting point $P_{n,0}$ $(l,y,0)$ into Equations (1)–(3), expressions for H_x, H_y, and H_z at this point are obtained as (6)–(8).

$$H_x(l,y,0) = \frac{\sigma_s}{4\pi} \times \left\{ arctan\left[\frac{4l(y+h)}{w\sqrt{4l^2+w^2+(y+h)^2}}\right] - arctan\left[\frac{4ly}{w\sqrt{4l^2+w^2+y^2}}\right]\right\} \tag{6}$$

$$H_y(l,y,0) = \frac{\sigma_s}{4\pi} \times \left\{ ln\left[\frac{\left[w+\sqrt{w^2+(y+h)^2}\right]\times\left[w+\sqrt{4l^2+w^2+y^2}\right]\times\left[\sqrt{w^2+y^2}-w\right]\times\left[\sqrt{4l^2+w^2+(y+h)^2}-w\right]}{\left[\sqrt{4l^2+w^2+y^2}-w\right]\times\left[w+\sqrt{4l^2+w^2+(y+h)^2}\right]\times\left[\sqrt{w^2+(y+h)^2}-w\right]\times\left[w+\sqrt{w^2+y^2}\right]}\right]\right\} \tag{7}$$

$$H_z(l,y,0) = \frac{\sigma_s}{4\pi} \times \left\{ ln\left[\frac{\left[y+h+\sqrt{4l^2+w^2+(y+h)^2}\right]\times\left[y+\sqrt{4l^2+w^2+y^2}\right]}{\left[y+\sqrt{4l^2+w^2+y^2}\right]\times\left[y+h+\sqrt{4l^2+w^2+(y+h)^2}\right]}\right]\right\} = 0 \tag{8}$$

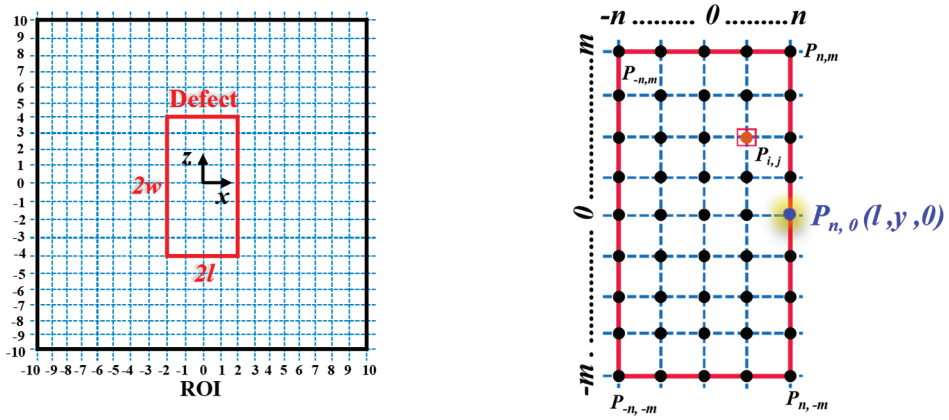

(**a**) (**b**)

Figure 5. Detection region of the multi-sensor probe: (**a**) Region of interest (ROI) selected, (**b**) Defect-opening profile area.

During the derivation of the formula, it was found that the signal value of the circumferential signal H_z at the point $P_{n,0}$ $(l, y, 0)$ is zero. This is because the circumferential signal is insensitive to defect edges perpendicular to the direction of magnetization. However, it is more sensitive to defect edges parallel to the direction of magnetization and to defect right-angled features [38]. Thus, the significance of the circumferential signal H_z at this point is not relevant. Therefore, subsequent calculations mainly utilize the axial signal H_x and radial signal H_y. The intermediate variables $P_x(y)$, $M_y(y)$, and $N_Z(y)$ are defined as follows:

$$P_x(y) = tan\left(H_x \times \frac{4\pi}{\sigma_s}\right) \tag{9}$$

$$M_y(y) = e^{H_y \times \frac{4\pi}{\sigma_s}} \tag{10}$$

$$N_z(y) = e^{H_z \times \frac{4\pi}{\sigma_s}} = 1 \tag{11}$$

In Equations (9) and (10), we observe that the numerator and denominator of $P_x(y)$ and $M_y(y)$ are of the same order. Inspired by [32], we divide the numerator and denominator of $P_x(y)$ by y^2 and the numerator and denominator of $M_y(y)$ by y^4. Additionally, we define the intermediate variables $u(y)$, $v(y)$, and $\eta(y)$.

$$u(y) = l/y \tag{12}$$

$$v(y) = w/y \tag{13}$$

$$\eta(y) = h/y \tag{14}$$

Therefore, Equations (9) and (10) can be expressed as (15) and (16), respectively.

$$P_x(y) = \frac{4u(y)(1+\eta(y))}{v(y)\left(4u(y)^2 + v(y)^2 + 1 + 2\eta(y) + \eta(y)^2\right)^{\frac{1}{2}}} - \frac{4u(y)}{v(y)\left(4u(y)^2 + v(y)^2 + 1\right)^{\frac{1}{2}}} \tag{15}$$

$$\begin{aligned} M_y(y) \quad = & \frac{v(y)+\left(1+2\eta(y)+\eta(y)^2+v(y)^2\right)^{\frac{1}{2}}}{\left(4u(y)^2+v(y)^2+1\right)^{\frac{1}{2}}-v(y)} \times \frac{v(y)+\left(4u(y)^2+v(y)^2+1\right)^{\frac{1}{2}}}{v(y)+\left(4u(y)^2+v(y)^2+1+2\eta(y)+\eta(y)^2\right)^{\frac{1}{2}}} \\ & \times \frac{\left(v(y)^2+1\right)^{\frac{1}{2}}-v(y)}{\left(v(y)^2+1+2\eta(y)+\eta(y)^2\right)^{\frac{1}{2}}-v(y)} \times \frac{\left(4u(y)^2+v(y)^2+1+2\eta(y)+\eta(y)^2\right)^{\frac{1}{2}}-v(y)}{v(y)+\left(v(y)^2+1\right)^{\frac{1}{2}}} \end{aligned} \tag{16}$$

The Equations (15) and (16) can be solved iteratively to determine the value of $\eta(y)$. For sensors 1, 2, 3, and 4, the relation $r_2 = r_1 + d$ and $r_4 = r_3 + d$ holds. Therefore, h can be

denoted by $\eta(r_1)$, $\eta(r_2)$, $\eta(r_3)$, $\eta(r_4)$, and d, thereby enabling multi-sensor signal fusion to quantify the defects. Please refer to Equations (17) and (18) for further details:

$$\begin{cases} h_1 = \frac{\eta(r_1)\eta(r_2)d}{\eta(r_1)-\eta(r_2)} \\ h_2 = \frac{\eta(r_3)\eta(r_4)d}{\eta(r_3)-\eta(r_4)} \end{cases} \tag{17}$$

$$h = \alpha h_1 + \beta h_2 \tag{18}$$

where α and β are the weighting coefficients for h_1 and h_2, weighted average solution h.

The solution map and block diagram of the MSSF quantification are shown in Figure 6a,b respectively. In the solution map, for sensor 1 with a lift-off value of r_1, the obtained values of H_x (r_1), H_y (r_1), H_z (r_1) and the dimensions of the defect length $2l$ and width $2w$ are substituted into Equations (9), (10), and (11) to solve for $P_x(y)$, $M_y(y)$, and $N_Z(y)$. Subsequently, iterative computation of Equations (15) and (16) are used to obtain $\eta(r_1)$. Similarly, $\eta(r_2)$, $\eta(r_3)$, and $\eta(r_4)$ are obtained for sensors 2, 3, and 4. Finally, Equations (17) and (18) are used to estimate the defect depth h.

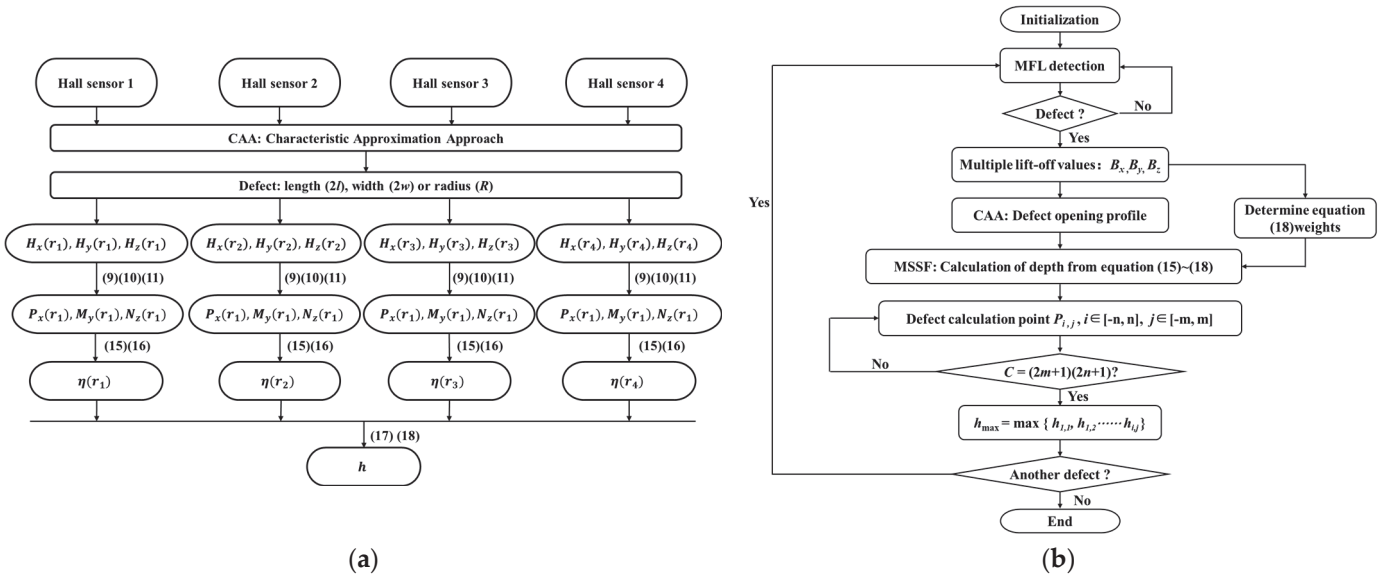

Figure 6. The MSSF quantification algorithm: (**a**) the solution map, (**b**) the block diagram.

The block diagram illustrates the complete procedure for defect quantification, as follows:

Step 1: Conduct an MFL detection on the component to detect the presence of defects. If a defect is identified, the region surrounding the defect is designated as the ROI, and Step 2 is initiated. If no defects are found, the process is completed.

Step 2: Use multi-sensor probes to extract MFL signals at various lift-off values. Apply CAA to identify defect-opening profiles. These profiles are then substituted into Equations (15)–(18) to iteratively determine the depth of each point $P_{i,j}$ within the computational domain.

Step 3: After computing the depth h at all calculation points within the domain, where $c = (2m+1) \times (2n+1)$, output the maximum depth h_{max} from all calculated values. If the depth calculations for all points are not yet completed, proceed to compute the depth for the next point.

Step 4: Check for additional defects. If no further defects are detected, conclude the quantification process. If other defects are present, continue with the quantification process for the next defect.

For defect depths at other data acquisition points, the derivation process is identical to the above, allowing computation of defect depths at all sampling points within the

defect-opening region to ultimately obtain the maximum depth h_{max}. Similarly, for cylindrical [35] and conical [39] defects, the MSSF quantification method can be utilized for depth calculation. The derivation process parallels that of rectangular defects, with the defect-opening dimensions $2l$ and $2w$ replaced by the radius R. The specific transformations are as follows:

$$\text{Defect-opening dimensions: length } 2l\text{, width } 2w \rightarrow \text{radius } R$$

$$\text{Data sampling points : } P_{i,j}\left(\frac{i}{n}l,\ y,\ \frac{j}{m}w\right) \rightarrow P_{i,j}\left(\frac{i}{n}R,\ y,\ \frac{j}{m}R\right)$$

$$\text{Intermediate variables : } \begin{cases} u(y) = l/y \\ v(y) = w/y \\ \eta(y) = h/y \end{cases} \rightarrow \begin{cases} u(y) = R/y \\ \eta(y) = h/y \end{cases}$$

3. Simulation and Experiment

3.1. Design of the Finite Element Model

FEM is based on Maxwell equations when solving MFL fields. MFL problems can be effectively treated as magnetostatic problems using a scalar magnetic potential method. These magnetostatic problems can be expressed by the following equation [40]:

$$\nabla \times \frac{1}{\mu} \nabla \times A = J \tag{19}$$

where ∇ is the Hami operator, A is the magnetic vector potential, J is the current density, and μ is a function of the magnetic flux density B, given by $\mu = \mu(B)$, which exhibits nonlinearity as depicted in Figure 7, corresponding to the material's *B-H* curve.

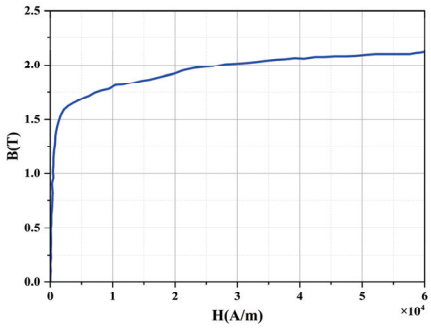

Figure 7. Magnetostatic characteristics of nonlinear *B-H* curves.

The integration by parts in (19) gives the following [41]:

$$\iiint \frac{1}{\mu}\left(\frac{\partial W}{\partial x} \times \frac{\partial A}{\partial x} + \frac{\partial W}{\partial y} \times \frac{\partial A}{\partial y} + \frac{\partial W}{\partial z} \times \frac{\partial A}{\partial z}\right) da - \iiint w \times J\, da = 0 \tag{20}$$

where w and a denote the weight function and volume of the space, respectively. As the shape functions are equal to the weighting functions [42], Equation (20) could be represented in a matrix from Equation (21):

$$\sum_e [\frac{1}{\mu}[S]_e A_e - [Q]_e J] = [0] \tag{21}$$

$$S_{e,ij} = \iiint \frac{\partial N_i}{\partial x}\frac{\partial N_j}{\partial x} + \frac{\partial N_i}{\partial y}\frac{\partial N_j}{\partial y} + \frac{\partial N_i}{\partial z}\frac{\partial N_j}{\partial z} da \tag{22}$$

$$Q_{e,ij} = \iiint N_i da \tag{23}$$

where e represents that the matrices pertain to a specific element, and $S_{e,ij}$, and $Q_{e,ij}$ are the typical entries in these matrices in (21). After calculating the magnetic vector potential A_e at each vertex of the element in the magnetic field from (21), then the magnetic field strength B can be calculated from $B = \nabla \times A$.

To accurately obtain the distribution characteristics of the leakage magnetic field of defects and verify the feasibility of the MSSF quantification method, the research team established a 3D FEM using a ANSYS 2021 software, as shown in Figure 8a. To reduce computational complexity, only 1/18th of the entire circumference is selected for the simulation study, due to the cylindrical symmetry of both the leakage detector and the inspected pipeline. The ferromagnetic specimen in the model is made of Q235 steel. Its magnetic permeability adheres to the *B-H* curve illustrated in Figure 6. The magnetization device comprises a yoke and two permanent magnets made of neodymium with a remanent magnetic strength of 1.3 T. A layer of rigid brushes is placed on the surface of the permanent magnets, which are in direct contact with the ferromagnetic specimen. The entire MFL detection device is enclosed by the air domain, where the relative magnetic permeability is set to 1. The detailed structural and material parameters of the detector are illustrated in Figure 8b and Table 1, respectively.

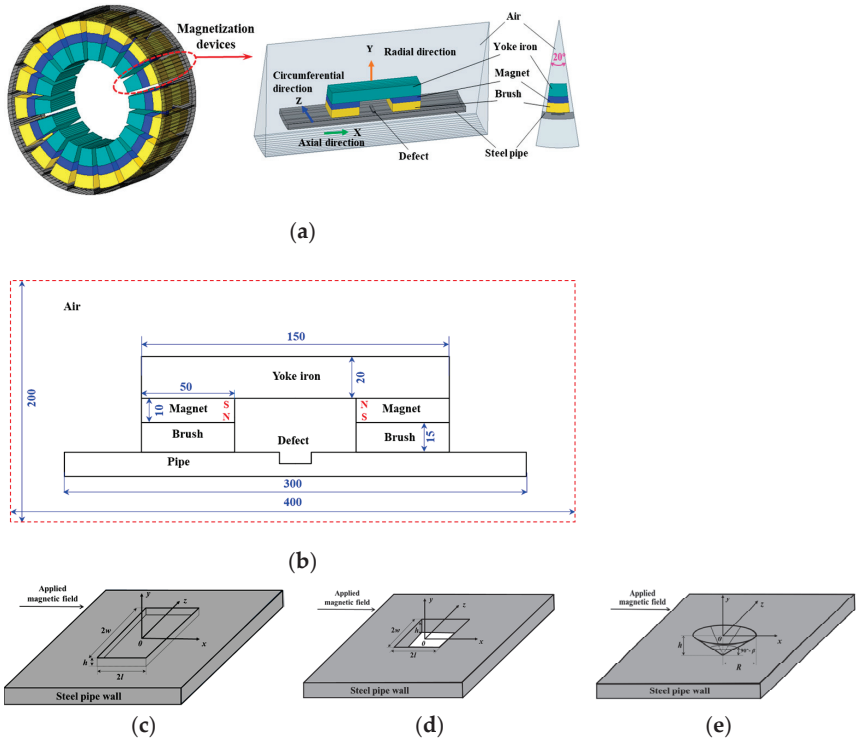

Figure 8. The FEM of MFL detection: (**a**) MFL detection system, (**b**) structural dimensions of the MFL detection system, (**c**) rectangular metal loss defect, (**d**) square perforation defect, (**e**) conical defect.

Table 1. Material parameters for each component.

Part	Relative Magnetic Permeability	Remanent Magnetization
Magnet	1	1.3 T
Air	1	-
Brush	3000	-
Yoke iron	5000	-
Steel pipe	shown in the *B-H* curve	-

Given the variability in actual pipe defect profiles, this section analyzes the MFL signals of rectangular defect, square perforation defect, and conical defect using FEM, as

illustrated in Figure 8c–e. The model does not account for velocity effects, so the leakage magnetic field can be treated as static. Therefore, the 3D static magnetic field solver is used. To resolve the contradiction between the large specimen volume and the same defect volume, we implemented varying grid sizes in different regions [43]. The computational domain was divided into unstructured grids, and the air domain over the defects was locally encrypted.

3.2. Results of the FEM Simulation

The rectangular metal loss defect dimensions chosen for this study are length $2l$ = 4 mm, width $2w$ = 10 mm, depth h = 3 mm, and wall thickness t = 10 mm. MFL signals were simulated across lift-off values ranging from 0.1 mm to 5 mm, incremented by 0.1 mm. Figure 9 shows the relationship between the leakage magnetic field and the lift-off value in the x and z detection directions, as simulated by the FEM. It is evident that as the lift-off value increases, the amplitude of each signal component decreases sharply, causing the characteristic information, such as extreme and inflection points, to become gradually submerged, and the signal-to-noise ratio (SNR) to decrease. B_x in the x-detection direction and B_y in the z-detection direction show axisymmetric single-peak features, while B_y in the x-detection direction and B_z in the z-detection direction show centrosymmetric double-peak features. The signal components in the x-detection direction have a peak spacing that corresponds to the length of the defect $2l$. Similarly, the signal components in the z-detection direction have a peak spacing that corresponds to the width of the defect $2w$. This is a prerequisite for implementing the CAA method.

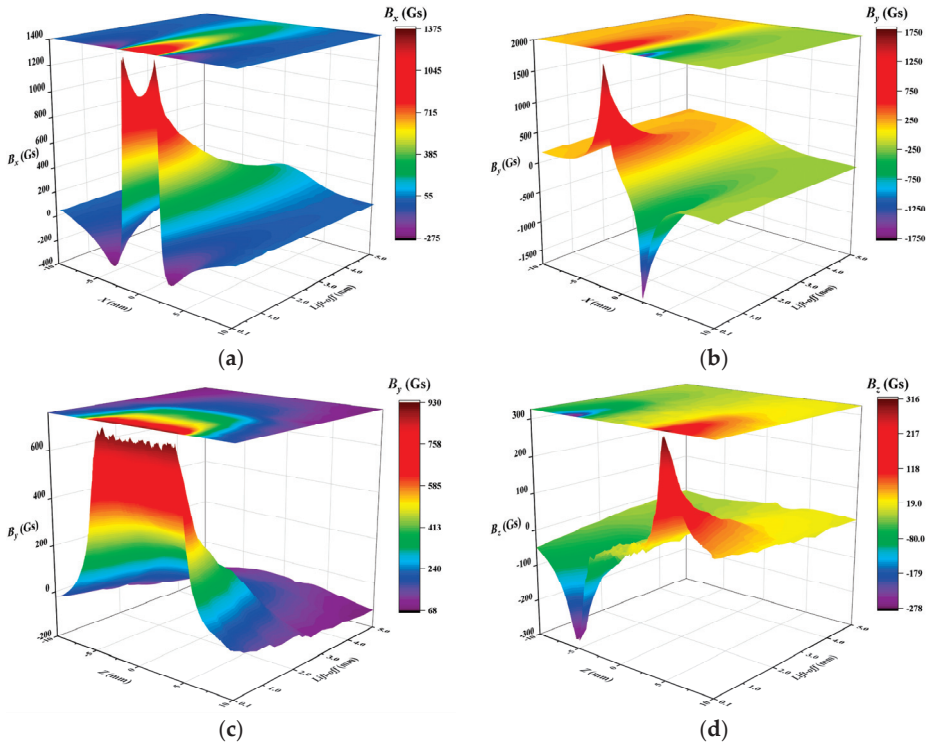

Figure 9. The correlation between rectangular metal loss defect leakage magnetic field and the lift-off value: (**a**) B_x in the x-detection, (**b**) B_y in the x-detection, (**c**) B_y in the z-detection, (**d**) B_z in the z-detection.

Similarly, the square perforation defect measures $2l$ = 6 mm and $2w$ = 6 mm, with a defect depth h = wall thickness t = 3 mm. The conical defect has dimensions R = 3 mm, h = 3 mm, $\beta = 45°$, and wall thickness t = 10 mm. MFL signals are simulated across a range of lift-off values from 0.1 mm to 5 mm. Figure 10 illustrates the axial signal B_x and radial signal B_y in the x-detection direction for both of these defects.

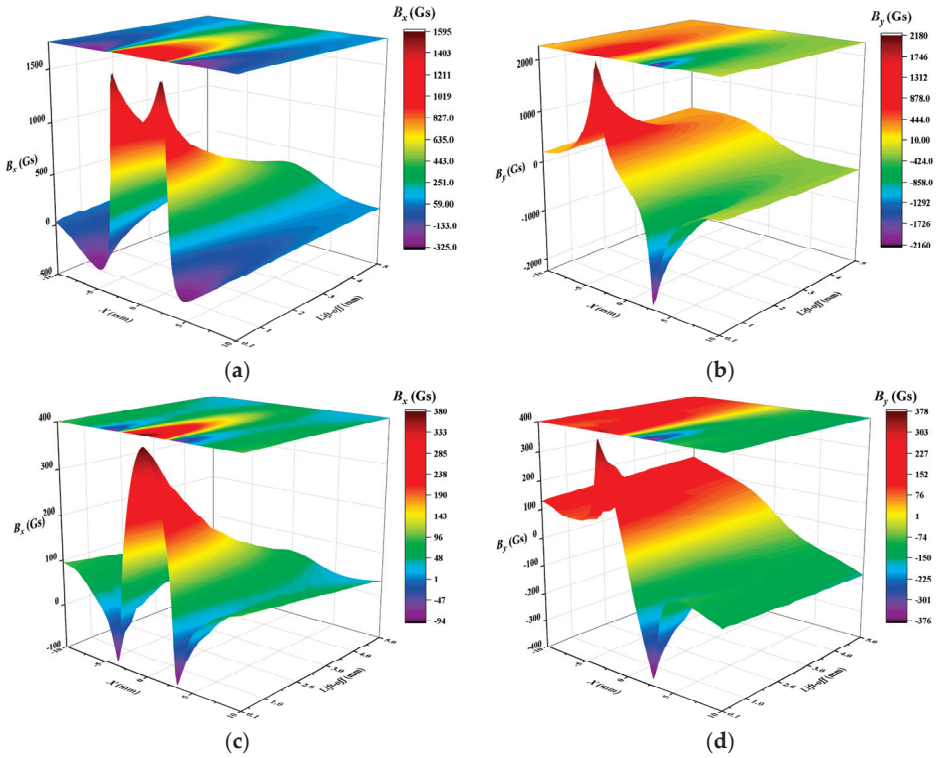

Figure 10. The correlation between the leakage magnetic field in the x-detection and the lift-off value: (**a**) B_x for square perforation defect, (**b**) B_y for square perforation defect, (**c**) B_x for conical defect, (**d**) B_y for conical defect.

3.3. Design of the Physical Experiments

To evaluate the practicality of the MSSF quantification method in practical inspection, the research team developed an MFL detection device and a ferromagnetic specimen with surface defects, as shown in Figure 11. The steel plate specimen measures 440 mm in length and has a wall thickness t of 6.00 mm. It contains a circumferential rectangular groove defect with an axial length $2l$ of 6.00 mm, a circumferential width $2w$ of 30.00 mm, and a depth h of 2.40 mm, an axial rectangular groove defect with an axial length $2l$ of 30.00 mm, a circumferential width $2w$ of 6.00 mm, and a depth h of 2.40 mm, as well as a circular perforation defect with a radius R of 2.50 mm and a depth h of 6.00mm. The specimen was magnetized by a permanent magnet with a remanent magnetic strength of 1.3 T.

The MFL signal collection probe consists of four Hall sensors. These sensors maintain an axial sampling interval of 0.05 mm, while the detection device moves at a speed of 0.1 m/s along the slide guide. The sensor lift-off value is adjusted using a fixing bolt. Upon completion of detection, the collected MFL signal is stored in the storage unit and subsequently transmitted to the data analysis and processing system.

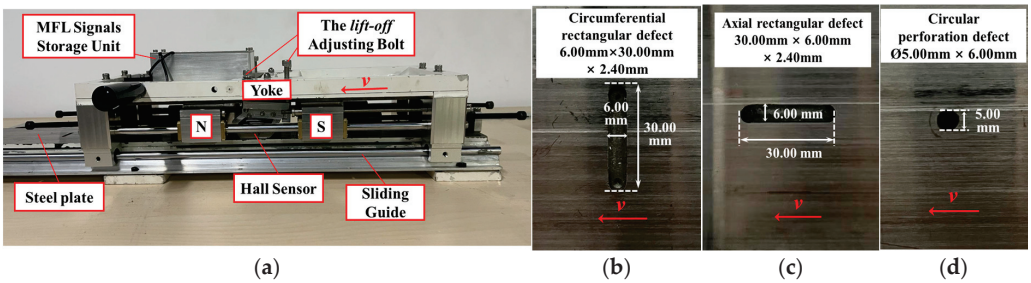

Figure 11. Experiment site: (**a**) MFL detection system, (**b**) circumferential rectangular groove defect, (**c**) axial rectangular groove defect, (**d**) circular perforation defect.

3.4. Results of the Physical Experiments

During the experiment, the adjusting bolts were used to set four different lift-off values: r_1 = 1.5 mm, r_2 = 2.5 mm, r_3 = 2.0 mm, and r_4 = 3.0 mm, with a sensor spacing d of 1 mm. Several experiments were conducted, and the results are presented in Figure 12, illustrating the measured MFL signals of rectangular grooves and perforation defects in the x-direction detection. It becomes evident that as the lift-off value increases, the MFL signal exhibits a consistent trend with the FEM results, demonstrating a decrease in signal amplitude and SNR. It is noteworthy that the amplitude of the MFL signal obtained experimentally may not match exactly with that obtained by the FEM due to differences in material properties and dimensional setup parameters. However, the signals' characteristics and distribution trends exhibit a high degree of consistency.

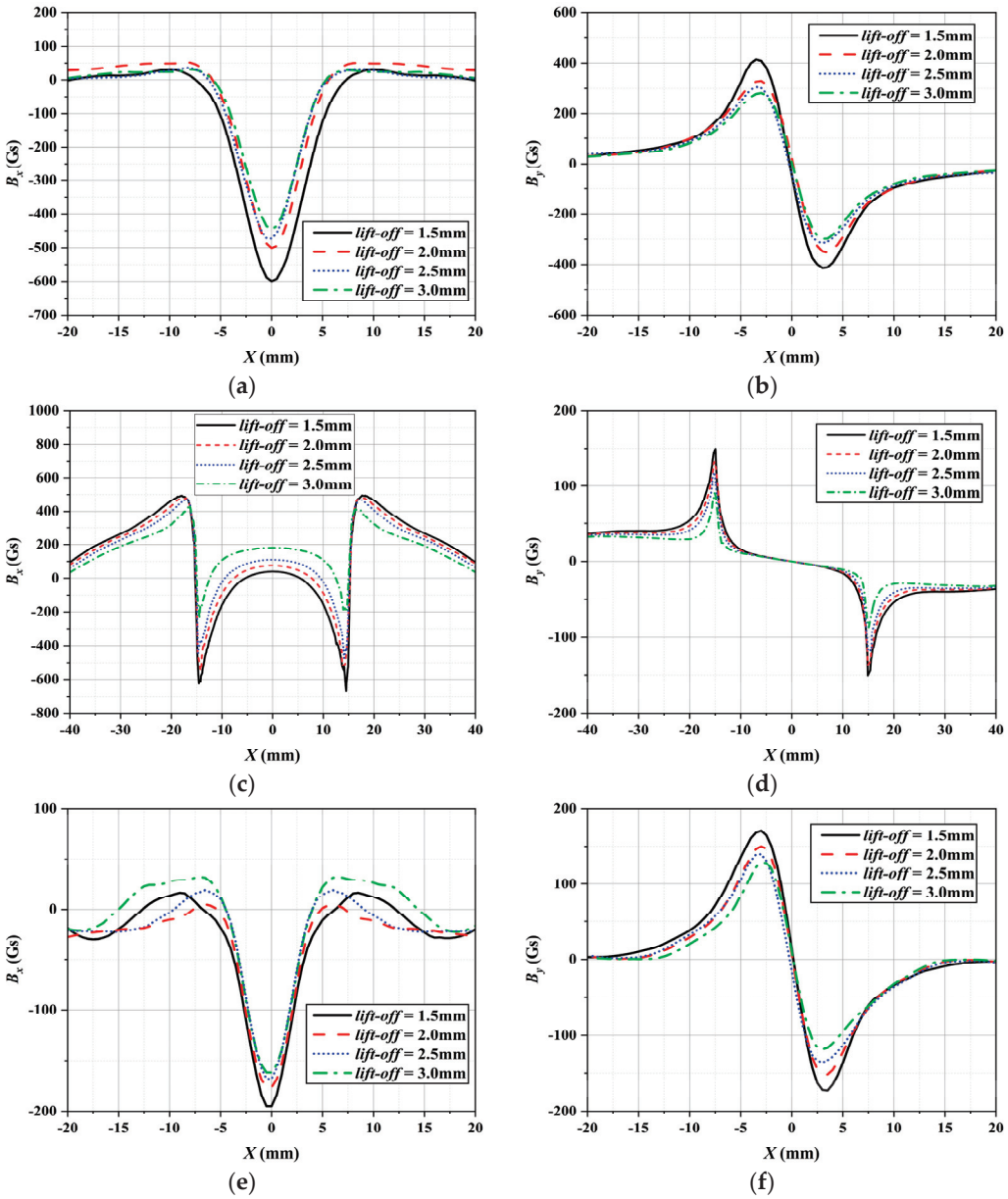

Figure 12. The MFL signals obtained from the experiments: (**a**) B_x of the circumferential rectangular groove defect, (**b**) B_y of the circumferential rectangular groove defect, (**c**) B_x of the axial rectangular groove defect, (**d**) B_y of the axial rectangular groove defect, (**e**) B_x of the circular perforation defect, (**f**) B_y of the circular perforation defect.

4. Results and Discussion

In this section, the functions and robustness of the MSSF quantification method will be discussed based on the simulation data obtained from the FEM and the experimental data collected from the MFL detection experiment.

4.1. The Solution of the Size of Rectangular Defect

Based on the rectangular metal loss defect MFL signals presented in Figure 9, the lift-off values for the multi-sensor probe are selected as follows: r_1 = 1 mm, r_2 = 2 mm, r_3 = 1.5 mm, r_4 = 2.5 mm, with a sensor spacing d of 1 mm. The CAA method was used to estimate the length and width dimensions of defects based on the MFL signals under the different lift-off values. Within the defect-opening region, there are 11 channels in the x-detection direction and 5 channels in the y-detection direction, and the total number of data acquisition points c is 55. The defect depth h at each data acquisition point was estimated using $H_x(r)$, $H_y(r)$, $H_z(r)$, and d, following the algorithm outlined in Figure 6. The specific calculation results are shown in Table 2.

Table 2. Quantification results and relative errors for the rectangular metal loss defect using simulation data.

	Defect Dimension (mm)			Computing Time (s)
	l	w	h_{max}	
True values	2.00	5.00	3.00	4.12
Calculated values	2.08	5.06	2.88	
Relative error	4.00%	1.20%	3.83%	

Similarly, the dimensions of the circumferential and axial rectangular groove defects were estimated using the MSSF quantification method, based on the experimental data shown in Figure 12a–d. The specific calculation results are shown in Tables 3 and 4.

Table 3. Quantification results and relative errors for the circumferential rectangular groove defect using experimental data.

	Defect Dimension (mm)			Computing Time (s)
	l	w	h_{max}	
True values	3.00	15.00	2.40	16.10
Calculated values	3.26	16.10	2.22	
Relative error	8.67%	7.33%	7.58%	

Table 4. Quantification results and relative errors for the axial rectangular groove defect using experimental data.

	Defect Dimension (mm)			Computing Time (s)
	l	w	h_{max}	
True values	15.00	3.00	2.40	14.31
Calculated values	15.30	3.22	2.30	
Relative error	2.00%	7.33%	4.17%	

Tables 2–4 demonstrate that the error between the estimated and actual defect size derived from the MSSF quantification method is below 10% for both simulated and experimental cases. Notably, the axial and circumferential sampling intervals of the sensors were notably larger in the physical experiments compared to the FEM simulation. Consequently, this reduces the accuracy of defect-opening profile recognition by CAA, which in turn increases the depth quantification error. However, the error remains within acceptable

thresholds. Regarding computation time, due to larger defect sizes observed in experiments compared to simulations, there is an increase in data acquisition points, resulting in longer computing times for quantifying experimental defects.

4.2. The Solution of the Size of Perforation Defect

To investigate the proposed method's versatility in dealing with various types of defects, this study also examined perforation defects through quantitative analysis. The axial signal B_x and radial signal B_y in the x-detection direction are illustrated in Figure 10a,b, respectively, for the simulated signals of the square perforation defect. The lift-off values for the multi-sensor probe were selected as follows: r_1 = 1 mm, r_2 = 2 mm, r_3 = 1.5 mm, and r_4 = 2.5 mm. The specific calculation results are shown in Table 5. Table 5 quantification results and relative errors for the square perforation defect using simulation data

Table 5. Quantification results and relative errors for the square perforation defect using simulation data.

	Defect Dimension (mm)			Computing Time (s)
	l	w	h_{max}	
True values	3.00	3.00	3.00	3.76
Calculated values	3.12	3.07	2.89	
Relative error	4.00%	2.33%	3.78%	

The experiment estimated the defect size utilizing the MSSF quantification method that relied on the MFL signals of the circular perforation defect shown in Figure 12e,f. The calculation results are presented in Table 6.

Table 6. Quantification results and relative errors for the circular perforation defect using experimental data.

	Defect Dimension (mm)		Computing Time (s)
	R	h_{max}	
True values	2.50	6.00	1.04
Calculated values	2.27	5.72	
Relative Error	8.80%	4.63%	

Tables 5 and 6 demonstrate the high accuracy and efficiency of the MSSF quantification method in handling various shapes of perforation defects. The size quantification errors for the square perforation defect in the FEM simulation are below 5%. In the physical experiment, the size quantification errors for the circular perforation defect are below 10%, and the calculation time of both is less than 5 s.

4.3. The Solution of the Size of Conical Defect

For the conical defect, the axial signal B_x and radial signal B_y in the x-detection direction are illustrated in Figure 10c,d, respectively. The lift-off values for the multi-sensor probe were selected as follows: r_1 = 1 mm, r_2 = 2 mm, r_3 = 1.5 mm, and r_4 = 2.5 mm. In the defect region depicted in Figure 13, the red line is the profile of the defect opening. there are 7 channels in the x-detection direction and 7 channels in the y-detection direction, and the total number of data acquisition points c is 29. Calculate the defect depth at each acquisition point, identifying the maximum defect depth h_{max} at point $h_{0,0}$ (the vertex position of the cone). The calculation results are presented in Table 7.

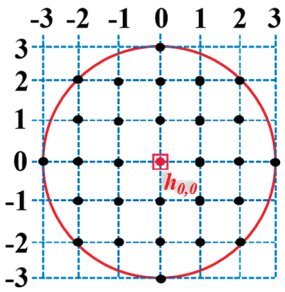

Figure 13. Layout of data acquisition points in the conical defect-opening region.

Table 7. Quantification results and relative errors for the conical defect using simulation data.

	Defect Dimension (mm)		Computing Time (s)
	R	h_{max}	
True values	3.00	3.00	2.01
Calculated values	2.96	2.81	
Relative Error	1.33%	6.33%	

According to the calculation results in Table 7, under simulated conditions, the MSSF quantification model maintains a fast computation speed, requiring only 2.01 s even when the base of the conical defect is uneven. Furthermore, it exhibits a quantification error of only 6.33% for the maximum defect depth, which meets the requirements for ultra-high-definition MFL detection. This demonstrates that the MSSF quantification model excels in both computation speed and quantification accuracy.

4.4. Comparison of the Quantification Accuracy and Efficiency

To compare the performance of the MSSF quantification method with other quantification methods, additional comparative experiments are conducted. This study selects the test defect depicted in Figure 14, representing a rectangular defect with dimensions of $2l$ = 21.20 mm, $2w$ = 20.60 mm, and h = 3.00 mm. The MFL signals of the test defect are acquired using the MFL detection setup depicted in Figure 11a. Subsequently, the quantification accuracy and iteration speed of the MSSF method were compared with those of the single sensor quantification method, the genetic algorithm (GA) [28], the particle swarm optimization (PSO) [44], and the radial basis function neural network (RBFNN)-based error adjustment (EA) methodology [45]. The specific calculation results are presented in Table 8.

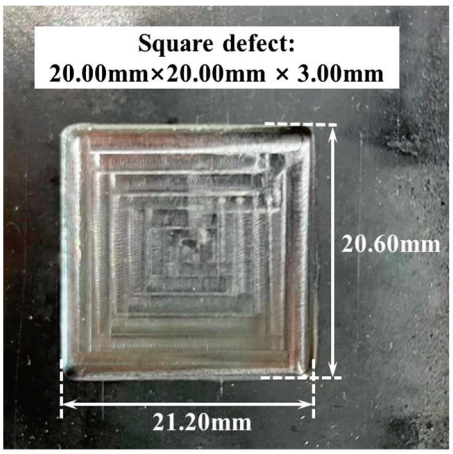

Figure 14. Example of the test defect.

Table 8. Comparative analysis of the results of different quantification methods.

Quantification Method	Estimated Dimension (mm)						Computing Time (s)
	l	Error	w	Error	h	Error	
True values	10.60	-	10.30	-	3.00	-	-
Single-sensor	8.93	15.75%	8.67	15.83%	2.44	18.67%	84
GA	11.32	6.79%	10.50	1.94%	3.30	10.00%	186
PSO	11.50	8.49%	10.00	2.91%	3.20	6.67%	164
RBFNN-EA	9.87	6.89%	10.00	2.91%	3.20	6.67%	97
MSSF	**10.00**	**5.66%**	**9.85**	**4.37%**	**2.91**	**3.00%**	**32**

Computer hardware configurations are as follows: CPU-Inter Core i7-12700K CPU @ 3.60 GHz, Memory-32 GB, GPU-NVIDIA GeForce RTX 3060, and hard disk-1 TB. All the computations are implemented in MATLAB R2021(b).

The computational results demonstrate that the quantification accuracies of most methods are satisfactory, except those using single-sensor probes, which exhibit relatively higher quantification errors. Moreover, the computation time of the MSSF method is notably shorter than that of other models. This is attributed to the fact that the MSSF quantification method does not necessitate the iterative optimization of the forward model parameters in the traditional defect inversion method. Instead, it directly incorporates defect information obtained from multi-sensor probes into the derived forward model (MDM), allowing for direct iterative determination of defect size. Furthermore, the solution equation for the MSSF method is simplified, requiring only a single equation to be solved for each element. In a series of experiments, the MSSF quantification method typically required fewer than 15 iterations to calculate the defect depth at each acquisition point. This notably reduces computational complexity, highlighting that the method substantially improves efficiency without compromising accuracy.

4.5. Robustness of MSSF Quantification Method

This section examines the robustness of the MSSF quantification method in various application scenarios. These scenarios include rectangular defects with varying extension directions: axial defect ($2l$ = 10 mm, $2w$ = 4 mm) and circumferential rectangular defect ($2l$ = 4 mm, $2w$ = 10 mm), anomalous lift-off values including ultra-high lift-off values of r_1 = 3 mm, r_2 = 4 mm, r_3 = 3.5 mm, r_4 = 4.5 mm, and MFL signals with 5% and 10% noise levels. The relative error of the proposed method for defect depth quantification in the above cases was analyzed and calculated. The specimen thickness t is 10 mm, and the defect depth ranges from 10%t to 70%t in steps of 10%t. The results are presented in Figure 15.

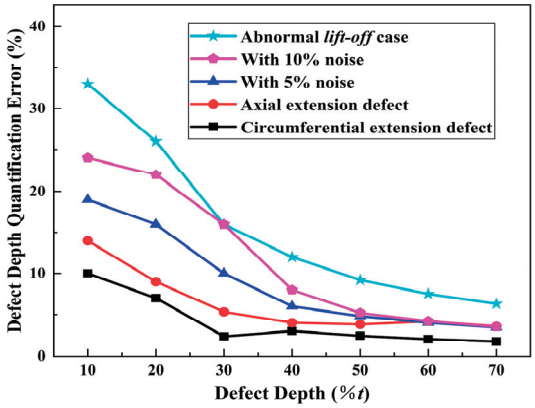

Figure 15. Quantification error of MSSF method for different defect depths.

As illustrated in Figure 15, there is a negative correlation between the relative error and the overall defect depth. For defects with a depth of less than 20%t, the amplitude and SNR of the MFL signal are low, resulting in a substantial relative error in quantification. Nevertheless, the quantification error of the defects under different extension directions consistently remains below 15%. When the defect depth exceeds 20%t, the quantification error remains within 10%. Regarding conditions involving noise and anomalous lift-off values, the reduction in SNR results in diminished characteristic information such as extreme and inflection points. Consequently, this adversely affects the quantification accuracy. However, when the defect depth is increased to 40%t, the relative error of the depth quantification for both 5% and 10% noise remains below 10%. Even under conditions of abnormal lift-off values, the relative error remains below 15%.

Furthermore, the figure illustrates that anomalous lift-off values have the most significant impact on the quantification accuracy. Specifically, when the defect depth is only 10%t, the relative error in depth quantification is 33.4%, with an absolute error of 3.3%t. Conversely, when the defect depth reaches 70%t, the relative error decreases to 6.3%, and the absolute error is 4.4%t. These results are within the acceptable range for ultra-high-definition MFL detection. Additionally, the MSSF quantization method demonstrates notable robustness even under complex detection conditions.

5. Conclusions

In this article, an MSSF quantification method is proposed to achieve a fast estimation of defect size in MFL detection. The method constructs a multi-sensor probe system that can acquire a variety of lift-off value MFL signals, which increases the diversity of defect information and thus reduces the complex iterative process. Subsequently, a method for iteratively solving the defect dimensions is derived based on a 3D MDM combined with the structural characteristics of the multi-sensor probe. The proposed method is validated by FEM simulations and physical experiments. The results demonstrate that the method accurately and efficiently estimates defect sizes, typically requiring fewer than 15 iterations per depth calculation point within the defective region. Rectangular metal loss, circular perforation, square perforation, and conical metal loss defects are quantified with an error rate of less than 10%. In comparison to other prevalent quantification methodologies, this approach not only guarantees accuracy but also enhances efficiency.

Author Contributions: Conceptualization, W.L. and L.R.; methodology, W.L.; software, W.L.; validation, W.L., L.R. and G.T.; formal analysis, W.L.; investigation, W.L.; resources, G.T.; data curation, W.L.; writing—original draft preparation, W.L.; writing—review and editing, L.R.; visualization, W.L.; supervision, L.R.; project administration, G.T.; funding acquisition, G.T. All authors have read and agreed to the published version of the manuscript.

Funding: This research was funded by the Key R&D Program of Shandong Province, China; grant number 2022SFGC0801.

Institutional Review Board Statement: Not applicable.

Informed Consent Statement: Not applicable.

Data Availability Statement: Due to the confidentiality requirements of the project responsible unit, the data provided in this study should be provided at the request of the corresponding author, because the project has not yet been concluded.

Conflicts of Interest: The authors declare no conflicts of interest.

References

1. Maruschak, P.; Prentkovskis, O.; Bishchak, R. Defectiveness of external and internal surfaces of the main oil and gas pipelines after long-term operation. *J. Civ. Eng. Manag.* **2016**, *22*, 279–286. [CrossRef]
2. Chen, X.F.; Wu, Z.Z.; Chen, W.T.; Kang, R.X.; He, X.Z.; Miao, Y.C. Selection of key indicators for reputation loss in oil and gas pipeline failure event. *Eng. Fail. Anal.* **2019**, *99*, 69–84. [CrossRef]

3. Skovhus, T.L.; Eckert, R.B.; Rodrigues, E. Management and control of microbiologically influenced corrosion (MIC) in the oil and gas industry-Overview and a North Sea case study. *J. Biotechnol.* **2017**, *256*, 31–45. [CrossRef] [PubMed]
4. Joshi, A.; Udpa, L.; Udpa, S.; Tamburrino, A.J.I.T.o.M. Adaptive Wavelets for Characterizing Magnetic Flux Leakage Signals From Pipeline Inspection. *IEEE Trans. Magn.* **2006**, *42*, 3168–3170. [CrossRef]
5. Li, Y.; Wilson, J.; Tian, G.Y. Experiment and simulation study of 3D magnetic field sensing for magnetic flux leakage defect characterisation. *NDT E Int.* **2007**, *40*, 179–184. [CrossRef]
6. Amineh, R.K.; Koziel, S.; Nikolova, N.K.; Bandler, J.W.; Reilly, J.P. A Space Mapping Methodology for Defect Characterization From Magnetic Flux Leakage Measurements. *IEEE Trans. Magn.* **2008**, *44*, 2058–2065. [CrossRef]
7. Katragadda, G.; Lord, W.; Sun, Y.S.; Udpa, S.; Udpa, L.J.I.T.o.M. Alternative magnetic flux leakage modalities for pipeline inspection. *IEEE Trans. Magn.* **1996**, *32*, 1581–1584. [CrossRef]
8. Hu, B.; Yu, R.Q. Magnetic testing for inter-granular crack defect of tubing coupling. Nondestruct. *Test. Eval.* **2018**, *33*, 119–129. [CrossRef]
9. Chen, W.C.; Liu, W.B.; Li, K.Y.; Wang, P.; Zhu, H.X.; Zhang, Y.Y.; Hang, C. Rail crack recognition based on Adaptive Weighting Multi-classifier Fusion Decision. *Measurement* **2018**, *123*, 102–114. [CrossRef]
10. Yan, X.L.; Zhang, D.L.; Zhao, F. Improve the signal to noise ratio and installation convenience of the inductive coil for wire rope nondestructive testing. *NDT E Int.* **2017**, *92*, 221–227. [CrossRef]
11. Liu, S.W.; Hua, X.; Liu, Y.; Shan, L.X.; Wang, D.Q.; Wang, Q.H.; Sun, Y.H. Accurate wire rope defect MFL detection using improved Hilbert transform and LSTM neural network. *Nondestruct. Test. Eval.* **2024**, *30*, 1–30. [CrossRef]
12. Liu, Z.T.; Liu, Y.L.; Shen, C.; Wei, L.M.; Wu, J.B.; Yang, W.H.; Huang, K.W.; Miao, P.Y. Influence of tensile stress on the magnetic flux leakage signal of the coated steel belt. *Nondestruct. Test. Eval.* **2023**, *21*, 1–21. [CrossRef]
13. Feng, B.; Wu, J.; Tu, H.; Tang, J.; Kang, Y. A Review of Magnetic Flux Leakage Nondestructive Testing. *Materials* **2022**, *15*, 7362. [CrossRef] [PubMed]
14. Feng, J.; Yao, Y.; Lu, S.X.; Liu, Y. Domain Knowledge-Based Deep-Broad Learning Framework for Fault Diagnosis. *IEEE Trans. Ind. Electron.* **2021**, *68*, 3454–3464. [CrossRef]
15. Hwang, K.; Mandayam, S.; Udpa, S.S.; Udpa, L.; Lord, W.; Atzal, M.J.N.; International, E. Characterization of gas pipeline inspection signals using wavelet basis function neural networks. *NDT E Int.* **2000**, *33*, 531–545. [CrossRef]
16. Kandroodi, M.R.; Araabi, B.N.; Bassiri, M.M.; Ahmadabadi, M.N. Estimation of Depth and Length of Defects from Magnetic Flux Leakage Measurements: Verification with Simulations, Experiments, and Pigging Data. *IEEE Trans. Magn.* **2017**, *53*, 6200310. [CrossRef]
17. Liu, B.; Tang, L.W.; Wang, J.B.; Li, A.H.; Hao, Y.L. 2-D defect profile reconstruction from ultrasonic guided wave signals based on QGA-kernelized ELM. *Neurocomputing* **2014**, *128*, 217–223. [CrossRef]
18. Lu, S.X.; Feng, J.; Zhang, H.G.; Liu, J.H.; Wu, Z.N. An Estimation Method of Defect Size from MFL Image Using Visual Transformation Convolutional Neural Network. *IEEE Trans. Ind. Inform.* **2019**, *15*, 213–224. [CrossRef]
19. Ren, Y.F.; Liu, J.H.; Zhang, H.G.; Wang, J.F. TBDA-Net: A Task-Based Bias Domain Adaptation Network Under Industrial Small Samples. *IEEE Trans. Ind. Inform.* **2022**, *18*, 6109–6119. [CrossRef]
20. Zhang, M.; Guo, Y.B.; Xie, Q.J.; Zhang, Y.S.; Wang, D.G.; Chen, J.Z. Estimation of Defect Size and Cross-Sectional Profile for the Oil and Gas Pipeline Using Visual Deep Transfer Learning Neural Network. *IEEE Trans. Instrum. Meas.* **2023**, *72*, 2501613. [CrossRef]
21. Deif, S.; Daneshmand, M. Multiresonant Chipless RFID Array System for Coating Defect Detection and Corrosion Prediction. *IEEE Trans. Ind. Electron.* **2020**, *67*, 8868–8877. [CrossRef]
22. Feng, J.; Lu, S.X.; Liu, J.H.; Li, F.M. A Sensor Liftoff Modification Method of Magnetic Flux Leakage Signal for Defect Profile Estimation. *IEEE Trans. Magn.* **2017**, *53*, 6201813. [CrossRef]
23. Yu, G.; Liu, J.H.; Zhang, H.G.; Liu, C. An Iterative Stacking Method for Pipeline Defect Inversion with Complex MFL Signals. *IEEE Trans. Instrum. Meas.* **2020**, *69*, 3780–3788. [CrossRef]
24. Priewald, R.H.; Magele, C.; Ledger, P.D.; Pearson, N.R.; Mason, J.S.D. Fast Magnetic Flux Leakage Signal Inversion for the Reconstruction of Arbitrary Defect Profiles in Steel Using Finite Elements. *IEEE Trans. Magn.* **2013**, *49*, 506–516. [CrossRef]
25. Wu, Z.N.; Deng, Y.M.; Wang, L.X. A Pinning Actor-Critic Structure-Based Algorithm for Sizing Complex-Shaped Depth Profiles in MFL Inspection with High Degree of Freedom. *Complexity* **2021**, *2021*, 995033. [CrossRef]
26. Li, F.M.; Feng, J.; Zhang, H.G.; Liu, J.H.; Lu, S.X.; Ma, D.Z. Quick Reconstruction of Arbitrary Pipeline Defect Profiles from MFL Measurements Employing Modified Harmony Search Algorithm. *IEEE Trans. Instrum. Meas.* **2018**, *67*, 2200–2213. [CrossRef]
27. Zhang, D.; Huang, C.; Fei, J. Defect reconstruction from magnetic flux leakage measurements employing modified cuckoo search algorithm. *Math. Biosci. Eng.* **2021**, *18*, 1898–1925. [CrossRef]
28. Hari, K.C.; Nabi, M.; Kulkarni, S.V. Improved FEM model for defect-shape construction from MFL signal by using genetic algorithm. *IET Sci. Meas. Technol.* **2007**, *1*, 196–200. [CrossRef]
29. Zhang, S.Z.; Li, H.M.; Zhao, C.T. Defect-depth-field algorithm for simulating magnetic flux leakage signals based on discrete magnetic dipole model. *NDT E Int.* **2023**, *139*, 8. [CrossRef]
30. Shi, P.-P.; Hao, S.; Liang, T.-S.J.J.o.M.; Materials, M. The defect depth evaluation based on the dual-sensor strategy: Resisting the lift-off disturbance in magnetic flux leakage testing. *J. Magn. Magn. Mater.* **2023**, *582*, 171039. [CrossRef]
31. Long, Y.; Zhang, J.; Huang, S.; Peng, L.; Wang, W.; Wang, S.; Zhao, W. A Novel Crack Quantification Method for Ultra-High-Definition Magnetic Flux Leakage Detection in Pipeline Inspection. *IEEE Sens. J.* **2022**, *22*, 16402–16413. [CrossRef]

32. Long, Y.; Huang, S.L.; Peng, L.S.; Wang, S.; Zhao, W. A Novel Compensation Method of Probe Gesture for Magnetic Flux Leakage Testing. *IEEE Sens. J.* **2021**, *21*, 10854–10863. [CrossRef]
33. Sun, Y.H.; Kang, Y.H. A new MFL principle and method based on near-zero background magnetic field. *NDT E Int.* **2010**, *43*, 348–353. [CrossRef]
34. Long, Y.; Huang, S.L.; Peng, L.S.; Wang, S.; Zhao, W. A Characteristic Approximation Approach to Defect Edge Detection in Magnetic Flux Leakage Testing. In Proceedings of the 2020 Conference on Precision Electromagnetic Measurements (CPEM), Aurora, CO, USA, 24–28 August 2020.
35. Dutta, S.M.; Ghorbel, F.H.; Stanley, R.K. Dipole Modeling of Magnetic Flux Leakage. *IEEE Trans. Magn.* **2009**, *45*, 1959–1965. [CrossRef]
36. Wu, D.H.; Liu, Z.T.; Wang, X.H.; Su, L.X. Mechanism analysis of influence of surface-breaking orientation on magnetic leakage field distribution. *Acta Phys. Sin.* **2017**, *66*, 048102.
37. Hosseingholizadeh, S.; Filleter, T.; Sinclair, A.N. Evaluation of a Magnetic Dipole Model in a DC Magnetic Flux Leakage System. *IEEE Trans. Magn.* **2019**, *55*, 6200407. [CrossRef]
38. Huang, S.L.; Peng, L.S.; Wang, Q.; Wang, S.; Zhao, W. An Opening Profile Recognition Method for Magnetic Flux Leakage Signals of Defect. *IEEE Trans. Instrum. Meas.* **2019**, *68*, 2229–2236. [CrossRef]
39. Trevino, D.A.G.; Dutta, S.M.; Ghorbel, F.H.; Karkoub, M. An Improved Dipole Model of 3-D Magnetic Flux Leakage. *IEEE Trans. Magn.* **2016**, *52*, 1–7. [CrossRef]
40. Zuoying, H.; Peiwen, Q.; Liang, C.J.N.; International, E. 3D FEM analysis in magnetic flux leakage method. *NDT E Int.* **2006**, *39*, 61–66. [CrossRef]
41. Park, G.S.; Park, S.H.J.I.T.o.M. Analysis of the velocity-induced eddy current in MFL type NDT. *IEEE Trans. Magn.* **2004**, *40*, 663–666. [CrossRef]
42. Xue, T.; Lord, W.; Udpa, S.J.I.T.o.U.F.; Control, F. Finite element simulation and visualization of leaky Rayleigh waves for ultrasonic NDE. *IEEE Trans. Ultrason. Ferroelectr. Freq. Control.* **1997**, *44*, 557–564. [CrossRef]
43. Long, Y.; Huang, S.L.; Peng, L.S.; Wang, S.; Zhao, W. A Characteristic Approximation Approach to Defect Opening Profile Recognition in Magnetic Flux Leakage Detection. *IEEE Trans. Instrum. Meas.* **2021**, *70*, 6003912. [CrossRef]
44. Han, W.H.; Xu, J.; Wang, P.; Tian, G.Y. Defect Profile Estimation from Magnetic Flux Leakage Signal via Efficient Managing Particle Swarm Optimization. *Sensors* **2014**, *14*, 10361–10380. [CrossRef] [PubMed]
45. Feng, J.; Li, F.M.; Lu, S.X.; Liu, J.H. Fast reconstruction of defect profiles from magnetic flux leakage measurements using a RBFNN based error adjustment methodology. *IET Sci. Meas. Technol.* **2017**, *11*, 262–269. [CrossRef]

sensors

MDPI

Article

^{1}H NMR Sensor for Nondestructive Characterization of Organic and Inorganic Materials

Floriberto Díaz-Díaz [1,2], Prisciliano F. de J. Cano-Barrita [1,*], Frank M. León-Martínez [1] and Víktor Acevedo-Arzola [3]

[1] Instituto Politécnico Nacional/CIIDIR Unidad Oaxaca, Calle Hornos No. 1003, Col. Noche Buena, Santa Cruz Xoxocotlán, Oaxaca 71230, Mexico; fdiazd@ipn.mx (F.D.-D.); fmleonm@ipn.mx (F.M.L.-M.)
[2] Conahcyt-Instituto Politécnico Nacional/CIIDIR Unidad Oaxaca, Calle Hornos No. 1003, Col. Noche Buena, Santa Cruz Xoxocotlán, Oaxaca 71230, Mexico
[3] School of Engineering and Architecture, Universidad La Salle Oaxaca, Camino a San Agustín No. 407, Santa Cruz Xoxocotlán, Oaxaca 71230, Mexico; 014405021@ulsaoaxaca.edu.mx
* Correspondence: pcano@ipn.mx

Abstract: Nuclear magnetic resonance relaxation of the proton spins of liquid molecules and their evolution during processes such as drying, fluid flow, and phase change of a sample can be monitored in a nondestructive way. A unilateral ^{1}H NMR sensor made with a permanent magnet array, inspired by the NMR MOUSE, with an RF coil tuned to 11.71 MHz was developed. This creates a sensitive homogeneous measuring volume parallel to the sensor surface and located 14 mm from its surface, allowing contactless measurements from the sample's interior. As this sensitive volume is moved across the sample using a semi-automatic linear displacement mechanism with millimetric precision, spatial T_2 lifetime and signal intensity 1D profiles can be obtained. To characterize the sensor's sensitive volume, eraser samples were used. To evaluate the sensor's ability to characterize different materials, cement paste samples containing ordinary and white Portland cement were prepared and measured at seven days of age. In addition, measurements were made on organic samples such as a Hass avocado and beef steak. Based on the results, a 1 mm spatial resolution of the sensor was achieved. The sensor was able to detect differences in T_2 lifetimes in eraser specimens composed of layers of three different erasers. Also, a clear difference in T_2 lifetimes and signal intensities was observed in cement pastes composed of white and ordinary Portland cement. On the other hand, it was possible to obtain signals from the peel and pulp of the avocado fruit, as well as from the fat and meat in a beef steak in a nondestructive way. The T_2 lifetimes of the different materials agreed with those obtained using a commercial NMR spectrometer.

Keywords: relaxometry; nondestructive testing; profile

1. Introduction

Nuclear magnetic resonance (NMR) is a nondestructive and non-invasive technique that enables the observation of changes in the microstructure of materials without the need for sample extraction or causing damage to the object of study. This technique is based on the absorption and emission of electromagnetic radiation by the nuclei of specific atoms subjected to a strong magnetic field and excited by radiofrequency pulses [1–3]. By measuring the NMR signal, information about the structure and composition of the sample is obtained.

In the context of cement-based materials, NMR has been used to study hydration [4], moisture content, pore refinement, compressive strength [5], carbonation depth [6], and moisture content profiles during capillary water absorption [7]. In the agri-food industry, NMR has also proven to be a valuable tool. For example, NMR spectroscopy has been used to detect adulterations in vegetable oils, determine the composition of fatty acids, the presence of trans fats, and other parameters important for quality and health [8], as well as

in the identification of contaminants, pesticide residues, additives, and other unwanted compounds in food [9].

Relaxometry, another NMR tool, allows the study of food components through relaxation times and signal intensity [10]. In this context, unilateral NMR emerges as a promising technique derived from traditional NMR, allowing the application of these relaxometry principles to study a specific region of the sample without the need to place the entire object within a homogeneous magnetic field. This technique benefits from low-field unilateral sensors, which are mainly classified into two types: those that generate a gradient B_0 magnetic field and those that create a B_0 magnetic field sweet spot [11].

Sensors that generate a gradient B_0 magnetic field are used to obtain spatial information about the interior of the sample, which allows the creation of depth profiles of the studied material. The simplest design of this type is the single bar magnet, which produces a B_0 field perpendicular to its surface [12]. For its operation, a coil is required that generates a transverse B_1 field, for which a "figure 8" coil is generally used. However, the low homogeneity of this coil limits the penetration of the field into the sample [11], which presents difficulties in applications that demand exploring deeper volumes or require a more uniform excitation. One of the most used geometries is the "U" shaped magnet, which generates a B_0 field parallel to the surface. The first version of the NMR MOUSE [13] was developed with this geometry, consisting of two semicylindrical shape magnets separated by a gap on an iron plate. This sensor allowed profiles to be obtained by varying the frequency according to the desired depth. Subsequently, improvements were introduced to the design, which mainly consisted of dividing the U-shaped magnet into two parts, introducing a small additional gap between these divisions to adjust the uniformity of the magnetic field laterally [14,15]. These improvements made the NMR MOUSE evolve into an advanced sensor capable of making profiles with microscopic resolution.

On the other hand, sensors that generate an optimal magnetic field point B_0 are used to maximize the size of the sensitive volume and obtain homogeneous measurements without considering spatial information. Such sensors have proven helpful in agri-food and industrial applications, such as assessing intramuscular fat content in live cattle [16], quantifying fat and water in fresh tuna meat [17,18], and measuring moisture in low-grade pulverized coal [19]. Among the most representative examples of this category are the barrel magnet [20], the NMR MOLE [21], and the three-magnet array [22,23].

The aim of the present work was to develop a unilateral NMR sensor, based on the NMR MOUSE [14], that allows measurements from the surface to the interior of the sample with a millimetric resolution. This allows a significant cost reduction when measuring samples that do not require microscopic resolution like the NMR MOUSE. A design based on an optimal point would not be suitable since it generates a sensitive volume that is too large, which would reduce the resolution and make it difficult to obtain profiles. Therefore, the design will be based on a modified U-shaped geometry, which will allow adequate control of the magnetic field, ensuring that the sensitive area is far from the surface, allowing the use of more efficient antennas such as the surface spiral type and the possibility of obtaining profiles with sufficient resolution without compromising cost. In addition, semi-automation of measurements is incorporated, which will allow the sensor to make horizontal and vertical millimetric movements.

2. Materials and Methods

2.1. Sensor Design and Construction

The unilateral NMR sensor mainly consists of an array of NdFeB permanent magnets and a radiofrequency antenna. Four N35 grade NdFeB rectangular magnets (Magnetika Saiffe, Guadalajara, Mexico) measuring 50 mm × 50 mm × 25 mm were used. The magnetic field strengths on their surfaces were 368 mT, 377 mT, 370 mT, and 377 mT for magnets 1, 2, 3, and 4, respectively, which were measured using a gaussmeter HT-20 (Hangzhou Best Magnet Co. Ltd., Hangzhou, China). The COMSOL Multiphysics® version 3.4 finite element software (COMSOL, Burlington, MA, USA) was used to perform static magnetic

field simulations of the magnet array based on a modified U-shaped geometry by varying the separation distance d and t between the magnets (Figure 1a). To achieve the best configuration that permitted reaching a homogeneous volume of the magnetic field away from the surface, like the NMR MOUSE magnet array [14,15,24]. Based on the simulation results, the array was constructed by placing the magnets on a mild steel plate measuring 105 mm × 130 mm × 15 mm, arranged as shown in Figure 1a. A 3D-printed case was used to hold the magnets in place (Figure 1b). Because the four magnets were not perfectly matched in the magnetic field strength across their surface, it was demonstrated both in simulation and construction to place the magnets in the order shown in Figure 1b.

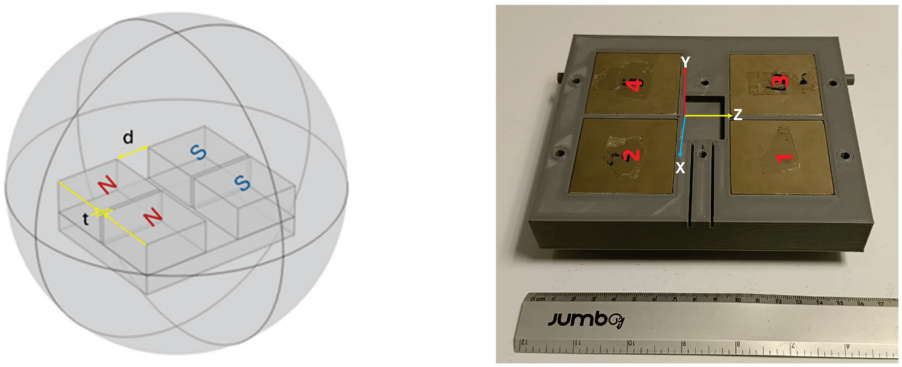

(**a**) (**b**)

Figure 1. (**a**) Configuration of the magnet array optimized by simulation, where the distances d and t were 28 mm and 3 mm respectively, (**b**) Constructed magnet array, the magnets were placed inside a 3D-printed case to keep them in place according to the simulation. The numbers in red refer to each specific magnet whose magnetic field was measured.

Subsequently, a surface RF antenna was designed, constructed, and tuned to a frequency of 11.71 MHz for ^{1}H resonance frequency, according to the Larmor Equation (1), using fixed and variable non-magnetic capacitors. A rectangular spiral antenna measuring 20 mm × 30 mm (Figure 2a), was constructed with 21 AWG copper wire and coated with epoxy resin. It comprises ten turns, with a bandwidth Δf = 100.5 kHz and a quality factor Q = 116. The S11 parameter (scattering parameter) was evaluated to ensure proper antenna matching to the system and minimize reflected power. This parameter measures the level of reflected energy at the antenna input port; a low S11 indicates that the antenna is well-matched to the system, allowing most of the power to be transferred without significant losses. In the case of the built antenna, the minimum of S11 occurs at the frequency of 11.71 MHz (Figure 2b), confirming proper matching for signal transmission at this frequency. The antenna was installed on a 1.5 mm-thick printed circuit board, covering the magnet array's surface to minimize the effects of eddy currents. When combined, the antenna and the board have a total thickness of 2.9 mm, reducing the available measurement distance to 11.1 mm. This distance represents the space between the antenna surface and the magnetic field's homogeneous zone.

$$\omega = \gamma * B_0 \quad (1)$$

where ω is the Larmor frequency in MHz, γ is the gyromagnetic ratio in MHz/T, and B_0 is the strength of the static magnetic field in T.

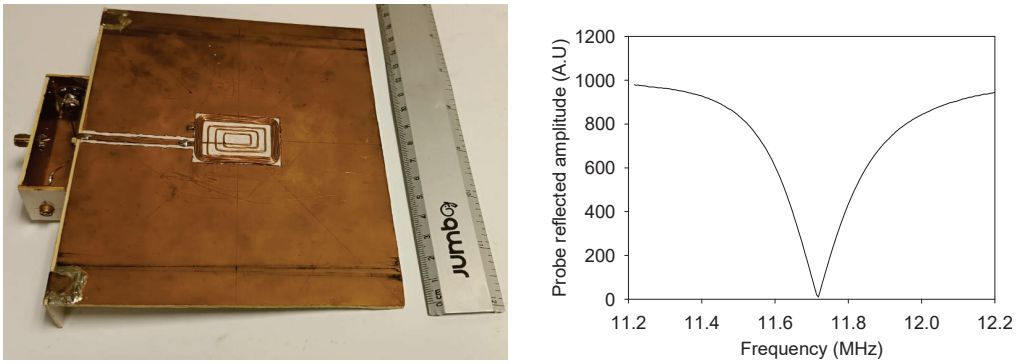

(**a**) (**b**)

Figure 2. (**a**) A photograph of the constructed RF antenna and (**b**) Reflected signal from the transmitter as a function of frequency, where the minimum value indicates the optimal tuning corresponding to 11.71 MHz.

2.2. Linear Movement Mechanism for Sensor Displacement

A semi-automatic CNC displacement mechanism was designed and built to carry out NMR measurements at precise sample positions. The mechanism is 110 cm tall and has a base measuring 53 cm × 35 cm (Figure 3). It utilizes structural aluminum profiles of various cross-sectional dimensions (40 mm × 40 mm, 40 mm × 20 mm, and 20 mm × 20 mm) to ensure strength and rigidity. Additionally, it incorporates smooth 12-mm diameter stainless steel rods, a 16-mm diameter spindle with corresponding nuts, and various parts manufactured via 3D printing.

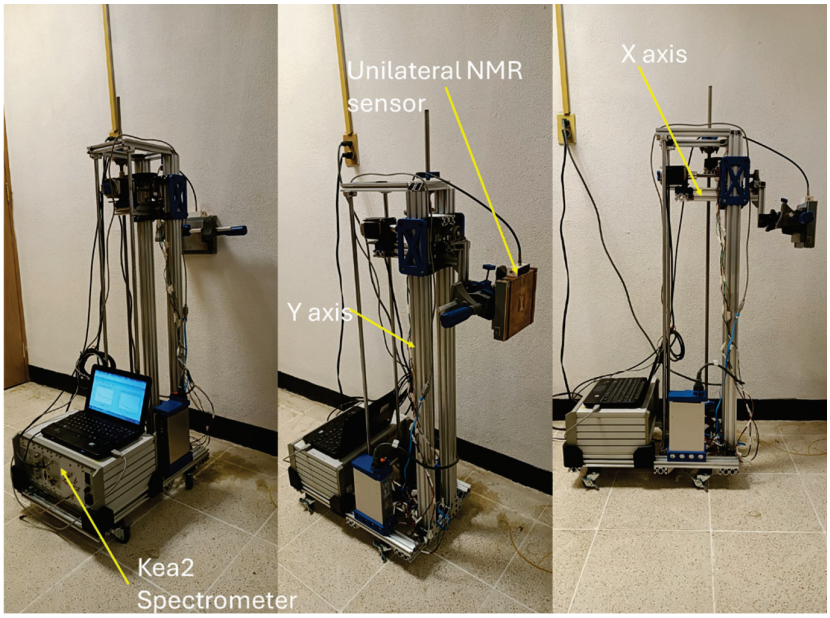

Figure 3. Photograph of automatic mechanism for displacement of the unilateral NMR sensor.

The mechanism comprises two primary axes: the longitudinal *X*-axis and the vertical *Y*-axis. The *X*-axis controls longitudinal movement, allowing the sensor to approach or retract from the sample's surface within a maximum displacement of 10 cm. The *Y*-axis permits the vertical movement of the sensor, with a maximum displacement of 75 cm. These displacements are driven by NEMA 23 OK57H18112A 4.2A 3 Nm (Oukeda Electric Appliance Co., Ltd., Changzhou, China) stepper motors and drivers DM556 (Leadshine Technology Co., Ltd., Shenzhen, China), which offer precise and reliable positioning control. The movement instructions are transmitted to the motors from an ESP32-WROOM-32U

(Espressif Systems, Shanghai, China) development board, which manages and coordinates axis movements along with controlling other system functions.

2.3. NMR Measurements

To characterize the sensor, we used different types of erasers for the NMR measurements (Figure 4a). These materials were used to conduct tests to determine parameters for the CPMG technique, such as the amplitude and the 90° and 180° pulse widths.

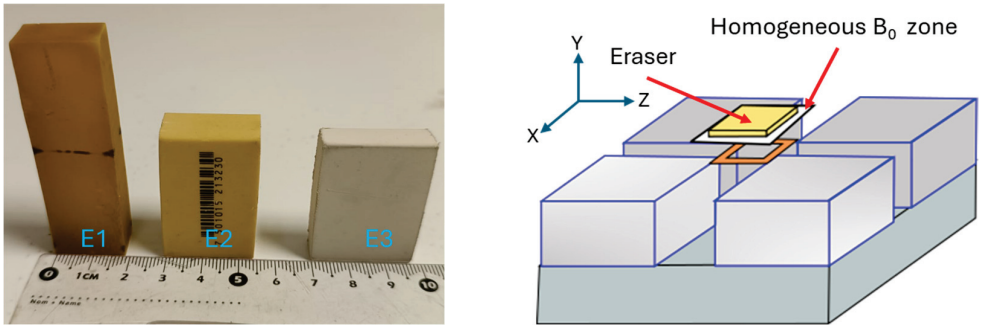

(**a**) (**b**)

Figure 4. Materials used in sensor characterization. (**a**) Samples of three types of erasers. (**b**) The 2 mm thick eraser slice was moved to different positions within the homogeneous magnetic field zone B_0 along the *Y*-axis.

We measured the thickness of the region excited by the RF antenna using a 2-mm-thick slice of an eraser. The eraser was displaced in 0.2 mm increments upward and downward along the vertical axis of the homogeneous zone of the magnetic field generated by the magnet array (Figure 4b). An NMR signal was acquired at each position using the CPMG technique [25]. Based on the signal intensity, two profiles were obtained to determine the thickness of the region that can be excited by the sensor antenna. To establish the sensor's upper and lower sensitive limits, we identified the position where the signal intensity became relatively constant in the downward profile, aligning with the last position where the signal intensity was still zero in the upward profile. The upper limit was determined by finding the position where the signal intensity became relatively constant in the upward profile and coincided with the last position where the signal intensity was still zero in the downward profile.

Subsequently, an eraser sample composed of the three layers of each type of eraser was made. Each eraser layer measured 2 mm × 23.6 mm × 19.6 mm, resulting in a total thickness of 6 mm (Figure 5). The specimen was then measured in 10 vertical positions by moving the sensor, which consequently moved the sensitive volume from top to bottom in 1 mm steps. At each position, a CPMG NMR signal acquisition was performed.

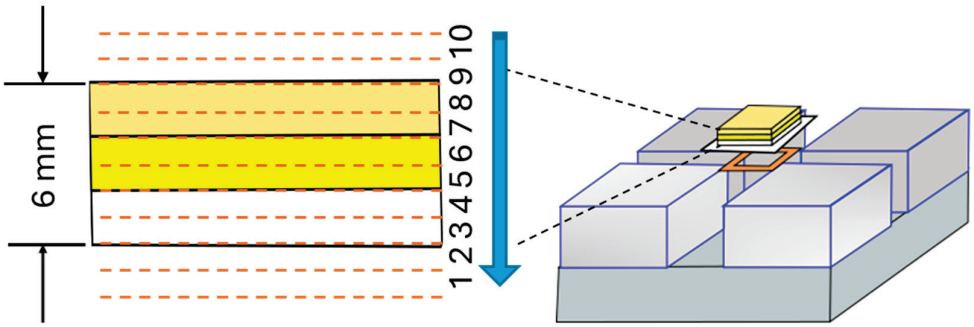

Figure 5. On the left, a representation of the specimen made with layers of three different types of erasers is shown. The dashed red lines indicate the positions where signal measurements were taken, with the sensor moved in 1 mm steps from top to bottom, as indicated by the blue arrow.

2.4. Testing the Applicability of the Sensor

Two cylindrical (∅ = 4 cm and h = 4 cm) specimens of white Portland cement (WPC) and ordinary Portland cement (OPC) at a water-to-cement ratio (w/c) of 0.60 were prepared. Also, one additional WPC sample was prepared with a w/c ratio of 0.70. These were measured with the CPMG technique at the age of 14 days.

For organic material, measurements were performed on Hass avocado samples at their final ripening stage and on beef steak, as shown in Figure 6. NMR measurements using the unilateral sensor were performed on the avocado's pulp and skin without cutting. Then the pulp and skin were extracted and measured separately using a Maran DRX HF 12/50 system (Oxford Instruments Ltd., Abingdon, Oxford, UK) operating at 12.9 MHz. These last measurements were used to compare with those obtained using the sensor.

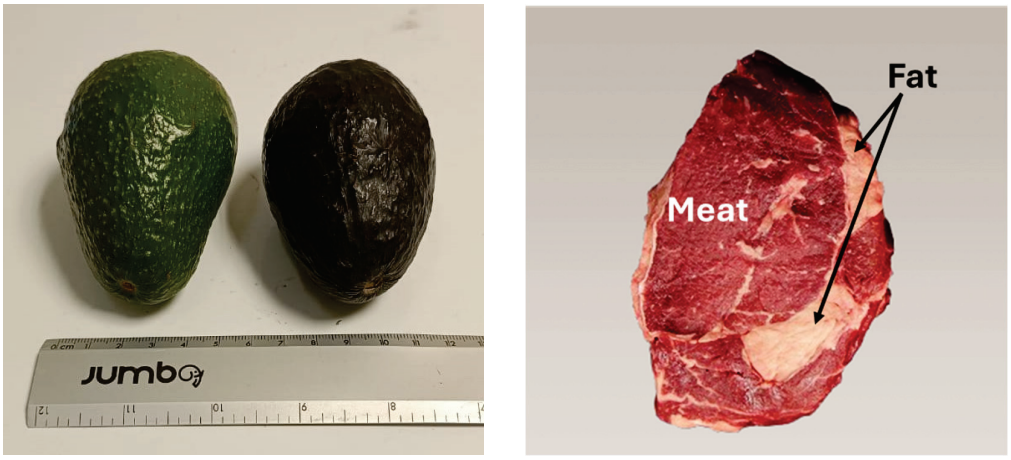

(**a**) (**b**)

Figure 6. Organic material for the NMR measurements with the sensor (**a**) Hass avocado samples and (**b**) Beef steak.

For the beef steak, measurements with the unilateral sensor were performed separately on the part containing only fat and on the part containing only meat.

All NMR experiments with the sensor were performed using a Kea^2 spectrometer (Magritek Limited, Wellington, New Zealand). Table 1 provides the parameters for the CPMG NMR measurements using the unilateral sensor and the Maran DRX HF 12/50 instrument for the different materials.

Table 1. Parameters of the CPMG sequence used in the measurements with the unilateral sensor and the Maran DRX HF 12/50 instrument.

	Sensor					Maran DRX	
Parameters	**Eraser**	**Cement Paste**	**Avocado**	**Meat**	**Fat**	**Eraser**	**Avocado**
90° pulse width (μs)	21	21	21	21	21	15.45	15.45
Number of echoes	512	32	512	512	512	512	512
Echo time (μs)	150	105	300	300	300	150	300
Number of scans	16,384	16,384	2048	2048	2048	1024	256
Acquisition time (min)	48	110	56	56	56	4.8	5.2

For each material analyzed, the T_2 values and the amplitude associated with each component were determined by fitting the CPMG echo train to the exponential decay model described by Equation (2).

$$S(t) = \sum_{i=1}^{n} A_i e^{-t/T_{2,i}} \quad (2)$$

where S(t) is the NMR signal measured as a function of time t, A_i is the amplitude associated with component i. This term reflects the relative contribution of that component to the total signal and is related to the number of protons in that population. $e^{-t/T2,1}$ is the exponential term describing the signal decay associated with component i. $T_{2,i}$ is the transverse relaxation time for component i. This parameter indicates how quickly magnetization is lost due to interactions between protons and their environment. n is the number of components detected in the signal decay.

3. Results and Discussion

In Figure 7, the measured magnetic field generated by the unilateral magnet array is compared with the simulated field. A good agreement of the magnetic field was obtained through simulation compared to the measurement of the built sensor. Notably, a relatively uniform zone of the magnetic field B_0, with an intensity of 274 mT at a height of 14 mm above the magnet surface, is present. This is significant because it ensures the homogeneous zone is inside the samples, allowing for NMR measurements at different depths. Furthermore, this homogeneous zone extends over a rectangular area measuring approximately 14 mm × 30 mm.

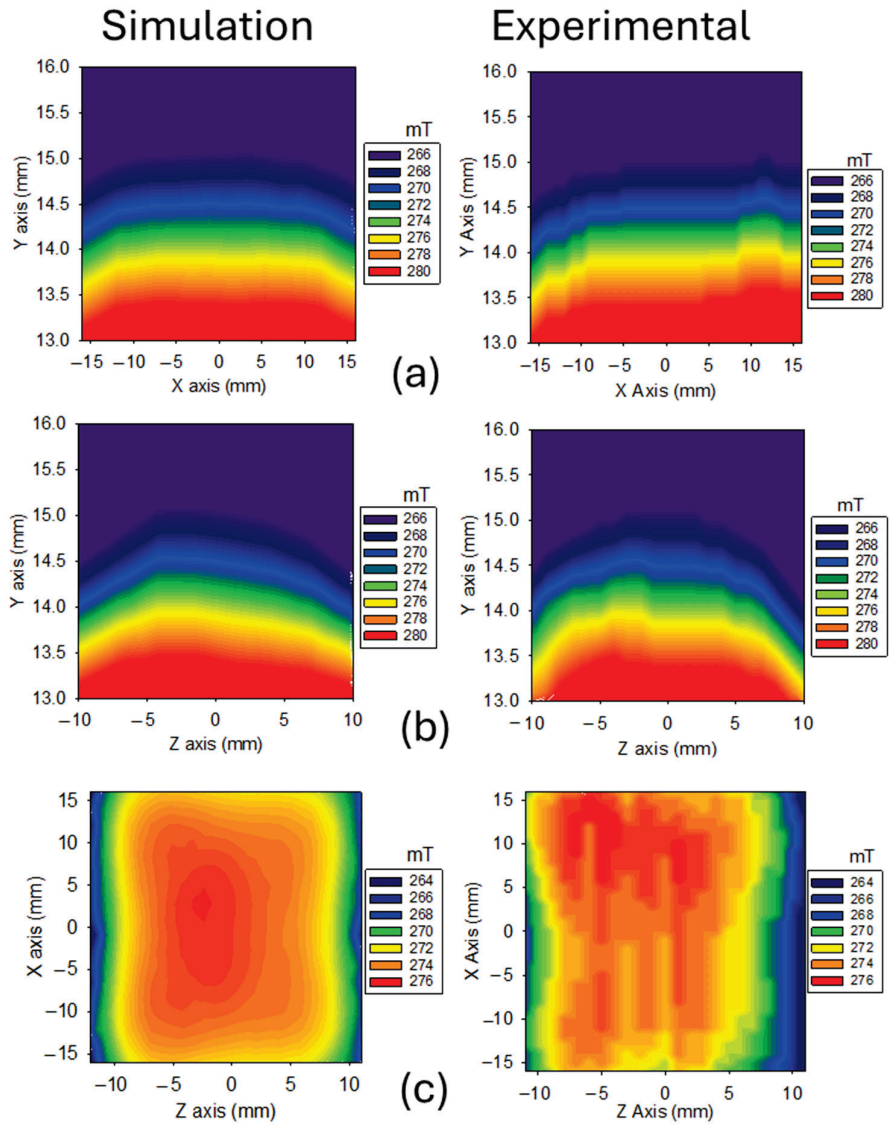

Figure 7. 2D plots of the magnetic field generated by the magnet array: (**a**) YX plane, (**b**) ZX plane, and (**c**) ZY plane at a height of 14 mm above the surface of the array.

Figure 8 displays the signal intensity of an eraser sample 2 mm thick. It was moved parallel to the vertical axis, up and down between the uniform field zone (B_0). Based on the downward profile (circles and red lines), signal intensity equals zero for the first two measurements because the sample is outside the sensitive zone. However, at 11.7 mm, the NMR signal becomes detectable, and its intensity increases as the sample is moved downward, indicating that most of the sample is entering the sensor's sensitive zone. The upward profile (circles and blue lines) shows the same trend. The sensitive zone of the sensor spans from 11.1 mm to 12.1 mm, demonstrating that the RF antenna can excite a slice of approximately 1.0 mm thick, which is considered the maximum sensor resolution. To profile different depths in a sample, the sensor must be moved in steps of 1.0 mm.

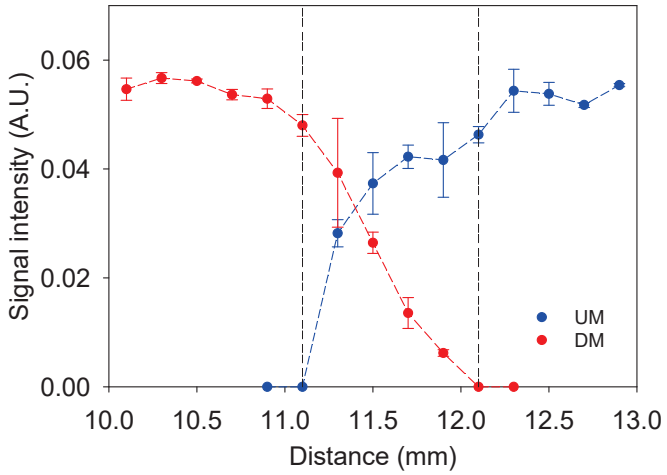

Figure 8. Profiles of signal intensity were obtained, with vertical indicating the thickness of the sensitive zone, approximately 1 mm: upward measurements (UM) and Downward measurements (DM).

Figure 9a shows the CPMG signals obtained from measurements of three different types of erasers. Despite the low signal-to-noise ratio (SNR) of 7, 19, and 22 for E1, E2, and E3, respectively, each material's signal lifetimes can be observed. This is further supported by measurements taken with the Maran DRX system, as shown in Figure 9b.

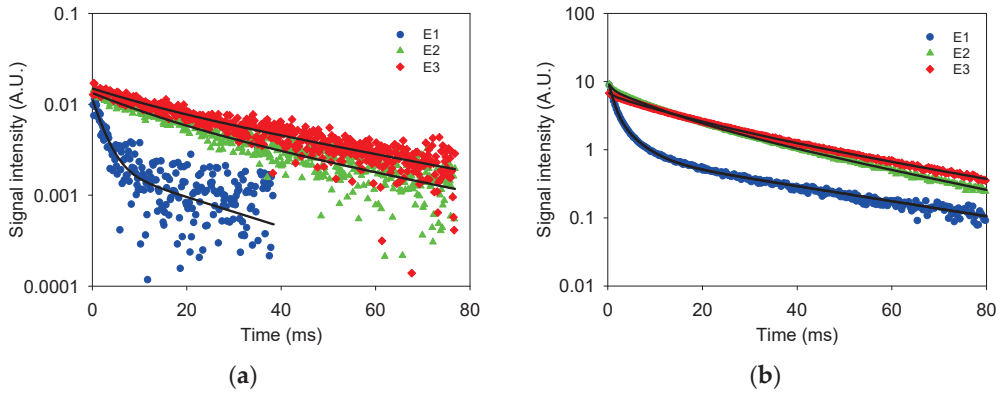

Figure 9. Transverse magnetization decay signals measured in each type of eraser: (**a**) with the constructed unilateral NMR sensor and (**b**) with the Maran DRX system.

Figure 10 compares the T_2 (Figure 10a) and amplitude values (Figure 10b) obtained by fitting the data from Figure 9 to exponential decay functions with two and three components. For all erasers, the short (2–10 ms) and long (27–40 ms) T_2 lifetime components obtained with the sensor were like those obtained with the Maran DRX named medium and long T_2 components. Intensity and T_2 time obtained with the sensor showed similar behavior to those obtained with the Maran DRX. However, the shortest component ($T_2 < 1$ ms) was

undetectable for the sensor because the signal-to-noise ratio of the signals is low compared to the SNR of the signals obtained with the Maran DRX system. A higher quality of the CPMG decays acquired with the Maran system (SNR of 237, 301, and 219 for E1, E2, and E3, respectively) allowed the fitting of signal with a higher number of components, compared to the SNR of the CPMG decays obtained with the sensor (SNR of 7, 19, and 22 for E1, E2, and E3, respectively). This is because, being a unilateral sensor, several factors affect the signal quality; for example, lower B_0 homogeneity, B_1 homogeneity, and intensity are dramatically reduced with distance and smaller volume of the excited sample.

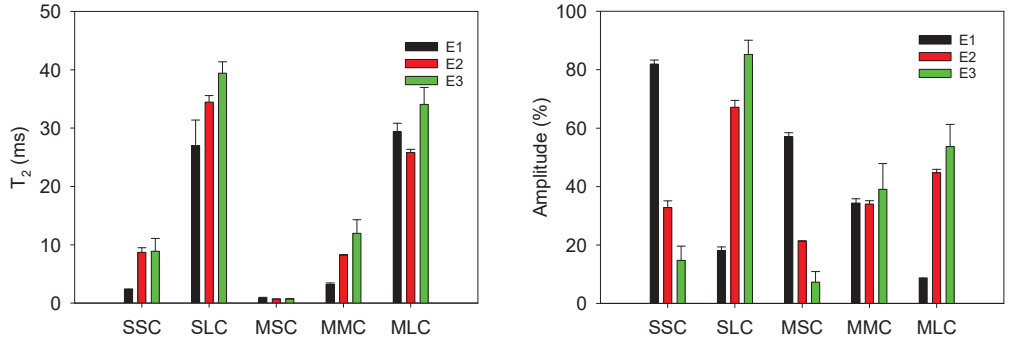

Figure 10. (**a**) T_2 and (**b**) amplitude values obtained for each eraser. The abbreviations correspond to: Sensor short component (SSC), Sensor long component (SLC), Maran DRX short component (MSC), Maran DRX medium component (MMC), and Maran DRX long component (MLC). The error bars represent ± one standard deviation.

The signals obtained from different positions of the layered specimen, using slices of three types of erasers, exhibited biexponential decay behavior. The T_2 lifetime components and their corresponding signal intensities were determined and labeled as short and long T_2 components and are presented in Figure 11. Differences in T_2 lifetimes and intensity can be noted between the material type at the position corresponding to the material localization. Notice that the T_2 lifetime values agree with those measured in each eraser sample individually (horizontal lines in Figure 11a). This demonstrates the ability of the sensor to detect changes due to sample heterogeneity.

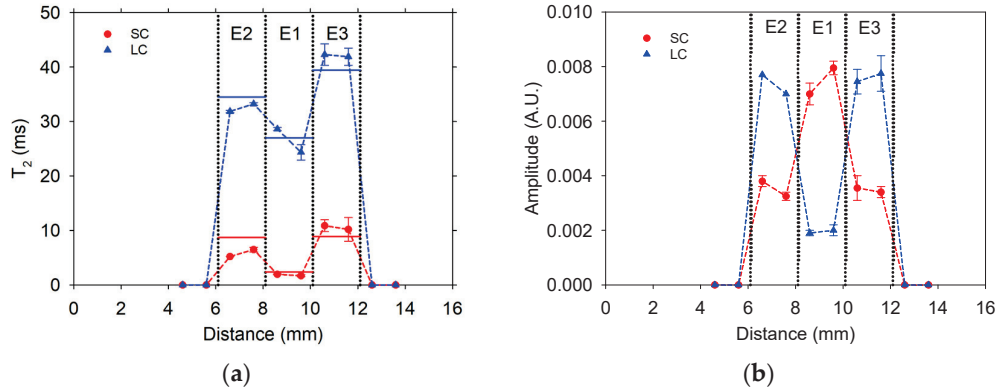

Figure 11. Profiles obtained from specimen measurements composed of slices of three types of erasers: (**a**) T_2 lifetime and (**b**) signal intensity. The solid horizontal lines represent the measured T_2 lifetime value for each type of eraser individually.

Figure 12a presents the CPMG decays in WPC and OPC paste specimens, resulting in an SNR of ≈30 for both signals. These signals were analyzed using a biexponential decay function, which resulted in a short T_2 lifetime of 0.07 ms (I = 0.073 A.U.) and a long T_2

lifetime of 1.53 ms (I = 0.0014 A.U.) for WPC paste and 0.11 ms (I = 0.0023 A.U.) and 1.11 ms (I = 0.0009 A.U.) for the OPC paste. The shorter T_2 values are for water in gel pores, and the longer T_2 are for water in capillary pores, both present in the hydrated cement paste. The reduction in the long T_2 lifetime component in the OPC paste compared with WPC, is caused by the iron present in the OPC that enhances the T_2 relaxation. On the other hand, if the two w/c ratios of OPC pastes are compared (Figure 12b), there is a higher intensity in the 0.70 w/c ratio paste, as expected. The SNR ratios were 26 and 28 for 0.60 and 0.70 w/c pastes, respectively. For the 0.70 w/c ratio, the T_2 lifetimes were 0.12 ms (I = 0.0026 A.U.) and 1.64 ms (I = 0.0014 A.U.), whereas for the 0.60 w/c ratio, the T_2 lifetimes were 0.107 ms (I = 0.0037 A.U.) and 1.67 ms (I = 0.0008 A.U.).

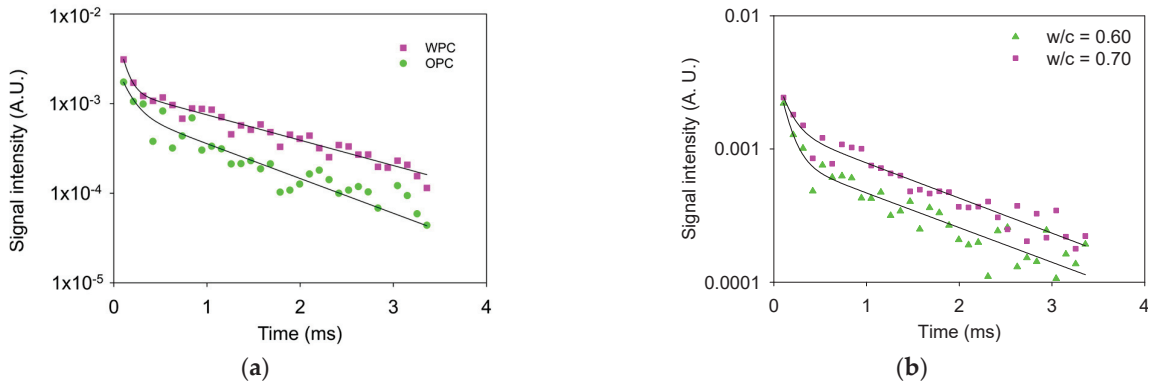

Figure 12. CPMG decays are measured in (**a**) specimens of WPC and OPC pastes with a w/c ratio of 0.60 and (**b**) OPC paste with 0.60 and 0.70 w/c ratios.

Figure 13 presents the CPMG signal decays measured in the Hass avocado samples. It shows significant differences between the signals obtained for the peel, seed, and pulp, both with the unilateral sensor and with the Maran DRX system.

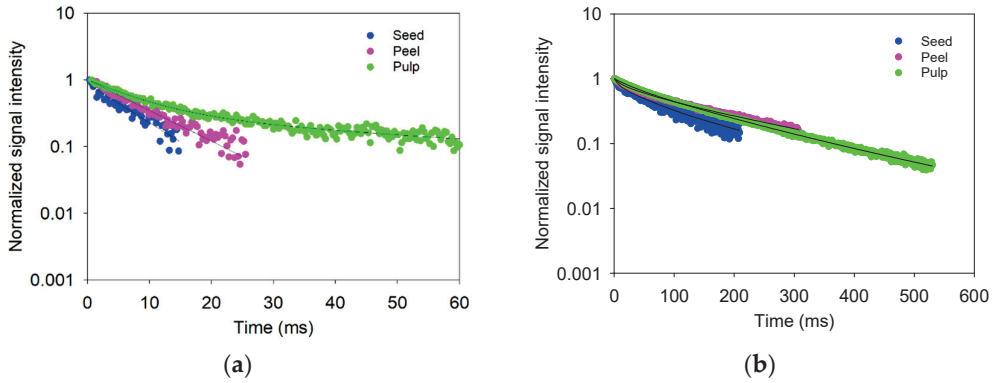

Figure 13. Transverse magnetization decay signals measured from Hass avocado: (**a**) with the built unilateral NMR sensor and (**b**) with the Maran DRX system.

When analyzing the T_2 values of the signals (Figure 14), three components were determined with the Maran DRX system, which was expected given that the SNR values obtained were higher than 100 (137 for the seed, 104 for the peel, and 104 for the pulp). This allowed for a better determination of the T_2 relaxation times. In contrast, with the unilateral sensor, the presence of a B_0 field gradient across the sensitive zone accelerates the CPMG signal decays. This effect causes a low SNR in the signal (15 for the seed, 25 for the peel, and 27 for the pulp), making resolving three components difficult compared with the Maran DRX system. In this case, only one component was obtained for the seed and peel, while two components were determined for the pulp.

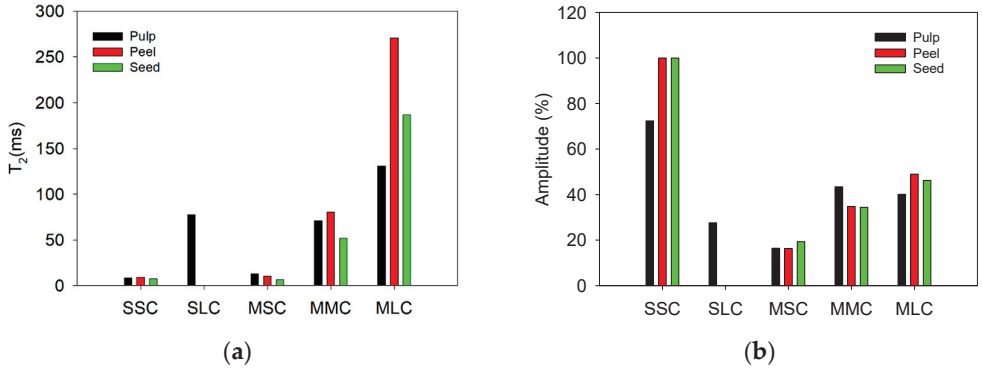

Figure 14. (**a**) T_2 and (**b**) amplitude values obtained from measurements conducted on a Hass avocado sample.

While the Maran DRX system offers a superior quality of the signals, it is limited by sample size and lack of portability. Because of its size, the need to cut the avocado to perform measurements is an explicit limitation, which puts the unilateral sensor at a clear advantage in applications requiring portability and in situ measurements of large samples.

Figure 15 presents the echo train decay measured in a beef steak's meat (red) and fat (blue) regions using the unilateral sensor. It is evident that the signal corresponding to the meat decays significantly faster compared to the fat, which is reflected in the relaxation times T_2 and the associated amplitudes. The values obtained for the meat were component 1 (T_2 = 8.46 ms, 89% of the total amplitude) and component 2 (T_2 = 59.17 ms, 11% of the total amplitude). For the fat, the results were component 1 (T_2 = 18.72 ms, 48% of the total amplitude) and component 2 (T_2 = 90.09 ms, 52% of the total amplitude). In this case, the unilateral sensor demonstrates its ability to distinguish between fat and meat, opening up opportunities for its use in industrial applications, such as food quality control.

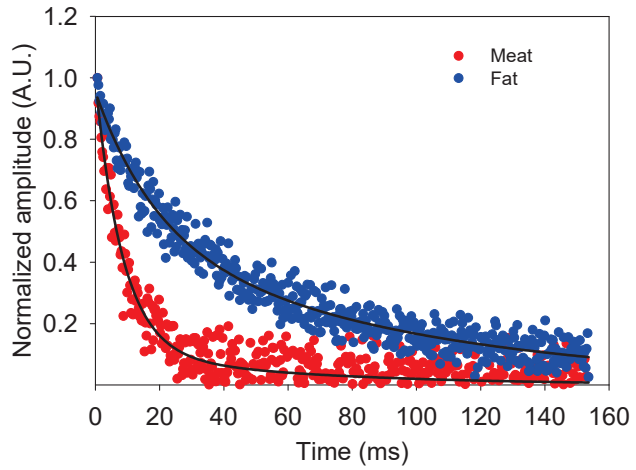

Figure 15. Normalized amplitude decay curves obtained by CPMG measurements on a beef steak performed with the unilateral sensor. The signal corresponding to meat (red) exhibits a faster decay than fat (blue), reflecting each component's molecular dynamics properties. T_2 values and associated amplitudes for the fitted components are detailed in the text.

4. Conclusions

A unilateral ^{1}H NMR sensor mounted on a millimetric precision semi-automatic linear displacement mechanism was developed, permitting the measurement of CPMG decay signals in a sensitive volume parallel to the sensor surface. The sensor was used to characterize both organic and inorganic materials. The following conclusions were drawn:

- Simulations of magnetic fields performed using the COMSOL Multiphysics® version 3.4 software resulted yielded similar results to experimentally measured fields. The

software facilitated the determination of magnet spacing to generate a relatively homogeneous magnetic field zone. The resulting array yielded a 274 mT zone in a rectangular area measuring approximately 14 mm × 30 mm at 14 mm away from the surface of the magnets.

- Operating at a frequency of 11.71 MHz for ^{1}H with a spatial resolution of 1 mm, the sensor was successfully used to acquire NMR signals at different internal depths in both organic and inorganic materials that exhibited relatively short- and long-lived signals. T_2 lifetime and signal intensity profiles were obtained that showed differences in three types of erasers, as well as differences in signals from white and ordinary Portland cement pastes, in the peel and pulp of Hass avocado samples, and in the fat and meat of a beef steak.

Author Contributions: Conceptualization, P.F.d.J.C.-B. and F.D.-D.; methodology, F.D.-D. and P.F.d.J.C.-B.; software, F.D.-D. and V.A.-A.; validation, P.F.d.J.C.-B., F.D.-D. and F.M.L.-M.; formal analysis, P.F.d.J.C.-B.; investigation, F.D.-D.; data curation, F.D.-D.; writing—original draft preparation, F.D.-D.; writing—review and editing, P.F.d.J.C.-B.; visualization, F.M.L.-M.; supervision, P.F.d.J.C.-B.; project administration, P.F.d.J.C.-B.; funding acquisition, P.F.d.J.C.-B. All authors have read and agreed to the published version of the manuscript.

Funding: This research received funding from SIP at the Instituto Politécnico Nacional for the innovation project ID code SIP 20232772.

Institutional Review Board Statement: Not applicable.

Informed Consent Statement: Not applicable.

Data Availability Statement: The data substantiating the conclusions of this study can be obtained from the corresponding author upon a reasonable request.

Acknowledgments: Priscililano Cano acknowledges SIP from Instituto Politécnico Nacional for financial support of the innovation project with ID code 20232772. Floriberto Díaz acknowledges CONAHCYT for the postdoctoral stay: Estancias Posdoctorales por México 2022 (3).

Conflicts of Interest: The author declares no conflicts of interest.

References

1. Blümich, B.; Haber-Pohlmeier, S.; Zia, W. *Compact NMR*; Walter de Gruyter GmbH: Berlin, Germany; Boston, MA, USA, 2014; ISBN 978-3-11-026628-3.
2. Fukushima, E.; Roeder, S.B.W. *Experimental Pulse NMR: A Nuts and Bolts Approach*; Addison-Wesley: Reading, MA, USA, 1981.
3. Macomber, R.S.; Harbison, G.S. *A Complete Introduction to Modern NMR Spectroscopy*; John Wiley & Sons: New York, NY, USA, 1997.
4. Apih, T.; Lahajnar, G.; Sepe, A.; Blinc, R.; Milia, F.; Cvelbar, R. Proton Spin—Lattice Relaxation Study of the Hydration of Self-Stressed Expansive Cement. *Cem. Concr. Res.* **2001**, *31*, 263–269. [CrossRef]
5. Díaz-Díaz, F.; Cano-Barrita, P.F.d.J.; Balcom, B.J.; Solís-Nájera, S.E.; Rodríguez, A.O. Embedded NMR Sensor to Monitor Compressive Strength Development and Pore Size Distribution in Hydrating Concrete. *Sensors* **2013**, *13*, 15985–15999. [CrossRef]
6. Díaz-Díaz, F.; Cano-Barrita, P.F.d.J.; León-Martínez, F.M.; Castellanos, F. Unilateral Low-Field Magnetic Resonance Measurements of Carbonation Depth in Unsaturated and Saturated Portland Cement Mortars. *Cem. Concr. Res.* **2020**, *138*, 106237. [CrossRef]
7. Cano-Barrita, P.F.d.J.; Díaz-Díaz, F. Moisture Distribution during Water Absorption of Ordinary Portland Cement Mortars Obtained with Low-Field Unilateral Magnetic Resonance. *Materials* **2021**, *14*, 4279. [CrossRef] [PubMed]
8. Hatzakis, E. Nuclear Magnetic Resonance (NMR) Spectroscopy in Food Science: A Comprehensive Review. *Compr. Rev. Food Sci. Food Saf.* **2019**, *18*, 189–220. [CrossRef] [PubMed]
9. Koskela, H. Use of NMR Techniques for Toxic Organophosphorus Compound Profiling. *J. Chromatogr. B* **2010**, *878*, 1365–1381. [CrossRef] [PubMed]
10. Capitani, D.; Sobolev, A.P.; Di Tullio, V.; Mannina, L.; Proietti, N. Portable NMR in Food Analysis. *Chem. Biol. Technol. Agric.* **2017**, *4*, 17. [CrossRef]
11. Perlo, J. Magnets and Coils for Single-Sided NMR. In *Single-Sided NMR*; Springer: Berlin/Heidelberg, Germany, 2011; pp. 87–110, ISBN 9783642163067.
12. Blümich, B.; Anferov, V.; Anferova, S.; Klein, M.; Fechete, R.; Adams, M.; Casanova, F. Simple NMR-MOUSE with a Bar Magnet. *Concepts Magn. Reson. Educ. J.* **2002**, *15*, 255–261. [CrossRef]
13. Eidmann, G.; Savelsberg, R.; Blümler, P.; Blümich, B. The NMR MOUSE, a Mobile Universal Surface Explorer. *J. Magn. Reson. Ser. A* **1996**, *122*, 104–109. [CrossRef]

14. Perlo, J.; Casanova, F.; Blümich, B. Profiles with Microscopic Resolution by Single-Sided NMR. *J. Magn. Reson.* **2005**, *176*, 64–70. [CrossRef] [PubMed]
15. Oligschläger, D.; Glöggler, S.; Watzlaw, J.; Brendel, K.; Jaschtschuk, D.; Colell, J.; Zia, W.; Vossel, M.; Schnakenberg, U.; Blümich, B. A Miniaturized NMR-MOUSE with a High Magnetic Field Gradient (Mini-Mouse). *Appl. Magn. Reson.* **2015**, *1*, 181–202. [CrossRef]
16. Nakashima, Y.; Shiba, N. Nondestructive Measurement of Intramuscular Fat Content of Fresh Beef Meat by a Hand-Held Magnetic Resonance Sensor. *Int. J. Food Prop.* **2021**, *24*, 1722–1736. [CrossRef]
17. Nakashima, Y. Non-Destructive Quantification of Lipid and Water in Fresh Tuna Meat by a Single-Sided Nuclear Magnetic Resonance Scanner. *J. Aquat. Food Prod. Technol.* **2019**, *28*, 241–252. [CrossRef]
18. Nakashima, Y. Development of a Hand-Held Magnetic Resonance Sensor for the Nondestructive Quantification of Fat and Lean Meat of Fresh Tuna. *J. Food Meas. Charact.* **2020**, *14*, 2947–2955. [CrossRef]
19. Nakashima, Y.; Sawatsubashi, T.; Fujii, S. Nondestructive Quantification of Moisture in Powdered Low-Rank Coal by a Unilateral Nuclear Magnetic Resonance Scanner. *Int. J. Coal Prep. Util.* **2022**, *42*, 1421–1434. [CrossRef]
20. Utsuzawa, S.; Fukushima, E. Unilateral NMR with a Barrel Magnet. *J. Magn. Reson.* **2017**, *282*, 104–113. [CrossRef] [PubMed]
21. Manz, B.; Coy, A.; Dykstra, R.; Eccles, C.D.; Hunter, M.W.; Parkinson, B.J.; Callaghan, P.T. A Mobile One-Sided NMR Sensor with a Homogeneous Magnetic Field: The NMR-MOLE. *J. Magn. Reson.* **2006**, *183*, 25–31. [CrossRef] [PubMed]
22. Marble, A.E.; Mastikhin, I.V.; Colpitts, B.G.; Balcom, B.J. A Compact Permanent Magnet Array with a Remote Homogeneous Field. *J. Magn. Reson.* **2007**, *186*, 100–104. [CrossRef] [PubMed]
23. Garcia-Naranjo, J.C. Three-Magnet Arrays for Unilateral Magnetic Resonance. Ph.D. Thesis, University of New Brunswick, New Brunswick, Canada, 2012.
24. Blümich, B.; Blümler, P.; Eidmann, G.; Guthausen, A.; Haken, R.; Schmitz, U.; Saito, K.; Zimmer, G. The NMR-MOUSE: Construction, Excitation, and Applications. *Magn. Reson. Imaging* **1998**, *16*, 479–484. [CrossRef] [PubMed]
25. Meiboom, S.; Gill, D. Modified Spin-Echo Method for Measuring Nuclear Relaxation Times. *Rev. Sci. Instrum.* **1958**, *29*, 688–691. [CrossRef]

sensors

MDPI

Article

Modeling of a Novel T-Core Sensor with an Air Gap for Applications in Eddy Current Nondestructive Evaluation

Siquan Zhang

Department of Electrical and Automation, Shanghai Maritime University, Shanghai 201306, China; sqzhang@shmtu.edu.cn

Abstract: Multi-layer conductive structures, especially those with features like bolt holes, are vulnerable to hidden corrosion and cracking, posing a serious threat to equipment integrity. Early defect detection is vital for implementing effective maintenance strategies. However, the subtle signals produced by these defects necessitate highly sensitive non-destructive testing (NDT) techniques. Analytical modeling plays a critical role in both enhancing defect-detection capabilities and guiding the design of highly sensitive sensors for these complex structures. Compared to the finite element method (FEM), analytical approaches offer advantages, such as faster computation and high accuracy, enabling a comprehensive analysis of how sensor and material parameters influence defect detection outcomes. This paper introduces a novel T-core eddy current sensor featuring a central air gap. Utilizing the vector magnetic potential method and a truncated region eigenfunction expansion (TREE) method, an analytical model was developed to investigate the sensor's interaction with multi-layer conductive materials containing a hidden hole. The model yielded closed-form expressions for the induced eddy current density and coil impedance. A comparative study, implemented in Matlab, analyzed the eddy current distribution generated by T-core, E-core, I-core, and air core sensors under identical conditions. Furthermore, the study examined how the impedance of the T-core sensor changed at different excitation frequencies between 100 Hz and 10 kHz when positioned over a multi-layer conductor with a hidden air hole. These findings were then compared to those obtained from E-core, I-core, and air-core sensors. The analytical results were validated through finite element simulations and experimental measurements, exhibiting excellent agreement. The study further explored the influence of T-core design parameters, including the air gap radius, dome radius, core column height, and relative permeability of the T-core material, on the inspection sensitivity. Finally, the proposed T-core sensor was used to evaluate crack and hole defects in conductors, demonstrating its superior sensitivity compared to I-core and air core sensors. Although slightly less sensitive than the E-core sensor, the T-core sensor offers advantages, including a more compact design and reduced material requirements, making it well-suited for inspecting intricate and confined surfaces of the target object. This analytical model provides a valuable tool for designing advanced eddy current sensors, particularly for applications like detecting bolt hole defects or measuring the thickness of non-conductive coatings in multi-layer conductor structures.

Keywords: eddy current testing; ferrite-core coil; T-core coil sensor; analytical model; truncated region eigenfunction expansion method

1. Introduction

Multi-layer metal structures, crucial for equipment like aircraft skins, oil pipelines, and nuclear power plant heat exchangers, are susceptible to safety hazards posed by cracks, corrosion, and other hidden defects [1]. Over time, these structures inevitably develop corrosion and fatigue cracks, leading to thinning and compromised structural integrity [2,3]. These defects can negatively impact equipment performance and safety, highlighting the need for early detection to prevent catastrophic consequences.

To ensure safety, crucial equipment components are regularly inspected using NDT methods. Common NDT methods include liquid penetrant testing, magnetic particle testing, ultrasonic inspection, eddy current testing (ECT), radiography, and infrared thermography [4,5]. While liquid penetrant testing is fast and easy, it only detects surface defects and requires extensive surface cleaning. Magnetic particle testing is limited to ferromagnetic materials and necessitates demagnetization. Ultrasonic flaw detection is effective for identifying deep defects in thick conductors and can also reveal internal flaws in multi-layer conductor configurations [6,7]. However, it typically requires a uniform and well-filled adhesive or sealant layer between these multi-layer conductors. Traditional ultrasonic testing methods struggle when it comes to detecting multi-layer structures that have air gaps between the conductor layers [8–10]. Infrared thermography, while useful, relies on complex equipment and trained operators. ECT, a widely used and effective technique, is particularly well-suited for detecting defects in multi-layer conductive structures, especially surface and subsurface micro-cracks and corrosion [11]. This non-contact method offers high sensitivity due to its ability to detect changes in eddy currents induced within the conductor by an alternating current excitation. These eddy currents generate a secondary magnetic field, which is influenced by factors like the sensor–conductor distance, material properties, and the presence of defects. Any change in the magnetic field, resulting from defect-induced variations in the eddy currents, alters the impedance of the excitation coil or the induced voltage in a receiving coil. This sensitivity makes ECT applicable to a wide range of applications, including distance measurements, material property assessments, and coating thickness determinations.

While effective, traditional ECT suffers from limitations, such as the shallow penetration depth of high-frequency eddy currents. While lower frequencies improve penetration, they compromise sensitivity. To address this, emerging magnetic sensing technologies, including Hall sensors, Giant Magnetoresistive (GMR) sensors, and Tunnel Magnetoresistive (TMR) sensors [12–14], are increasingly integrated with traditional ECT excitation coils. These advanced sensors greatly enhance ECT's sensitivity and accuracy. GMR sensors leverage the giant magnetoresistance effect to detect minute variations in magnetic fields [15,16], providing high sensitivity and resolution. For example, Joseph utilized a high-current, low-frequency excitation coil and a GMR sensor array to quantify corrosion defects in a pipe without removing the insulation [17]. TMR sensors, employing quantum tunneling phenomena, demonstrate even greater sensitivity than GMR, making them ideal for high-performance applications. Betta developed a novel ECT probe with a double coil excitation and a triaxial TMR sensor array, achieving high signal-to-noise ratios for thin defect detection [18]. Fei Yang et al. designed a flexible eddy current TMR (FEC-TMR) sensor and successfully detected internal cracks in metal joints [19].

Dodd and Deeds pioneered the use of Bessel functions to model electromagnetic fields generated by coils interacting with conductive materials [20]. This approach, employing Bessel function series, enabled the analysis of various coil geometries and material configurations, such as coil–plane, coil–tube, and coil–rod systems. It allowed for the accurate prediction of ECT signals by expressing electromagnetic fields and impedance changes as Bessel function series, ultimately resulting in an integral solution. Subsequently, Theodoulidis developed the TREE method [21]. This technique employs domain truncation, eigenfunction expansion, and the matching of boundary and surface conditions, providing a flexible and efficient solution for problems involving intricate geometries and boundary conditions [22]. In contrast to conventional ECT methods, the TREE method yields a series solution, resulting in faster computation and the ability to control accuracy by adjusting the number of series terms included.

Improving defect detection sensitivity in multi-layer conductors involves directing the excitation sensor's magnetic flux along low-resistance paths [5,23,24]. This increases magnetic flux penetration into the conductor, enabling deeper eddy current penetration and the enhanced detection of deeper defects. Ferrite cores, composed of iron oxide and metallic additives, exhibit tunable magnetic properties [25,26]. Their high permeability

and low loss at high frequencies make them ideal for coil sensors that operate through electromagnetic induction. The TREE method [27,28], initially applied to model simple sensor–conductor interactions in ferrite core ECT sensors, has evolved to address more complex scenarios. This includes analyzing eddy current problems involving intricate conductor defect geometries and various core configurations, such as the E-core, C-core, I-core, and T-core [22,29]. Extensive research has focused on E-core and I-core sensors with air gaps [30,31], as well as T-core sensors without air gaps [32]. Ferrite cores, owing to their flux concentration and shielding properties, enhance the flux density and sensor sensitivity compared to the air-core. The sensitivity of an ECT sensor varies depending on the specific ferrite core configuration and size, highlighting the importance of considering both sensitivity and core characteristics during sensor selection. Despite these advancements, accurately locating hidden defects within multilayer structures using ECT sensors remains a significant challenge.

This paper presents the first application of the TREE method to analyze a novel T-core ECT sensor. The sensor features a circular air gap positioned above a conductive layer containing a hidden hole. A homogeneous Dirichlet boundary condition is applied to the truncated surface, with the azimuthal component of the magnetic vector potential (A_φ) expressed as a series of orthogonal eigenfunctions. By carefully selecting eigenfunctions and applying field continuity conditions at boundaries and interfaces, the series coefficients and eigenvalues are determined. Truncating the infinite solution domain to a finite space allows for a series solution instead of an integral, resulting in a faster numerical calculation and easier error control. The analysis begins with a filamentary coil encircling the T-core column, deriving expressions for the magnetic vector potential. This analysis is then extended to coils with rectangular cross-sections using the superposition method to obtain the magnetic vector potential in each region. Finally, closed-form expressions for the induced eddy current density and coil impedance of the T-core ECT sensor are derived. The analytical model provides a valuable tool for evaluating the ECT sensor, allowing for the analysis of individual parameters. The T-core sensor's coil impedance variation is calculated for frequencies ranging from 100 Hz to 10 kHz. These results are compared with those from E-core, I-core, and air-core sensors. Further validation is achieved through a comparison with FEM simulations and experimental results, showing good agreement. The results highlight the significantly higher sensitivity of the T-core ECT sensor compared to I-core and air-core sensors when detecting hidden defects in a multi-layer conductor. Analytical and simulation methods are used to analyze the eddy current distribution produced by different core sensors (E, T, I, and air) under identical excitation conditions, providing insights into the T-core's superior sensitivity. The influence of key T-core parameters on sensor sensitivity is also assessed, leading to the determination of optimal sensor dimensions.

2. Analysis

Figure 1 illustrates three ferrite core ECT sensor types: I-core, T-core, and E-core. These sensors share a common structural feature, a circular air gap within the core column, and display structural similarities. Notably, the E-core can be derived from the T-core by adding a cylindrical shield, while the I-core results from removing the T-core's upper ring plane [33].

However, the T-core sensor with its air gap (Figure 1b) has not yet been subjected to theoretical or experimental analysis. Consequently, its sensitivity and other performance characteristics require investigation and a comparison with the E-core and I-core ECT sensors [34].

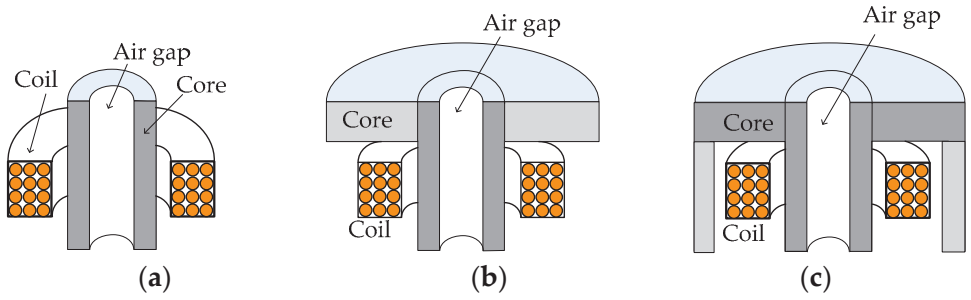

Figure 1. Cross-sectional illustrations of (**a**) an I-core, (**b**) a T-core, and (**c**) an E-core ECT sensors, each featuring an air gap within the ferrite core.

Figure 2a illustrates the initial configuration for analysis, featuring a filamentary coil driven by a harmonic current, $Ie^{j\omega t}$. This configuration involves a sensor positioned above a non-magnetic, conducting half-space comprised of three layers with conductivities σ_6, σ_7, and σ_8. The second layer contains an air hole. The $z = 0$ plane corresponds to the upper surface of this multi-layered conductor, resulting in a problem domain with eight distinct regions. The method of variable separation is employed, and the resulting expressions for each region depicted in Figure 2a are presented in matrix form below.

$$A_1(r,z) = J_1(\mathbf{q}^T r)\mathbf{q}^{-1}e^{-\mathbf{q}z}\mathbf{C}_1 \tag{1}$$

$$A_2(r,z) = \begin{cases} J_1(\mathbf{m}^T r) & 0 \le r \le a_0 \\ R_1(\mathbf{m}^T r)\mathbf{m}^{-1}(e^{-\mathbf{m}z}\mathbf{C}_2 - e^{\mathbf{m}z}\mathbf{B}_2) & a_0 \le r \le a_3 \\ R_1'(\mathbf{m}^T r) & a_3 \le r \le b \end{cases} \tag{2}$$

$$A_3(r,z) = \begin{cases} J_1(\mathbf{p}^T r) & 0 \le r \le a_0 \\ L_1(\mathbf{p}^T r)\mathbf{p}^{-1}(e^{-\mathbf{p}z}\mathbf{C}_3 - e^{\mathbf{p}z}\mathbf{B}_3) & a_0 \le r \le a_1 \\ L_1'(\mathbf{p}^T r) & a_1 \le r \le b \end{cases} \tag{3}$$

$$A_4(r,z) = \begin{cases} J_1(\mathbf{p}^T r) & 0 \le r \le a_0 \\ L_1(\mathbf{p}^T r)\mathbf{p}^{-1}(e^{-\mathbf{p}z}\mathbf{C}_4 - e^{\mathbf{p}z}\mathbf{B}_4) & a_0 \le r \le a_1 \\ L_1'(\mathbf{p}^T r) & a_1 \le r \le b \end{cases} \tag{4}$$

$$A_5(r,z) = J_1(\mathbf{q}^T r)\mathbf{q}^{-1}(e^{-\mathbf{q}z}\mathbf{C}_5 - e^{\mathbf{q}z}\mathbf{B}_5) \tag{5}$$

$$A_6(r,z) = J_1(\mathbf{q}^T r)\mathbf{s}_6^{-1}(e^{-\mathbf{s}_6 z}\mathbf{C}_6 - e^{\mathbf{s}_6 z}\mathbf{B}_6) \tag{6}$$

$$A_7 = \begin{matrix} F_1(\mathbf{v}c)J_1(\mathbf{u}^T r) \\ F_1(\mathbf{v}^T r)J_1(\mathbf{u}c) \end{matrix} \mathbf{u}^{-1}(e^{-\mathbf{u}z}\mathbf{C}_7 - e^{\mathbf{u}z}\mathbf{B}_7) \quad \begin{matrix} 0 \le r \le c \\ c \le r \le b \end{matrix} \tag{7}$$

$$A_8(r,z) = -J_1(\mathbf{q}^T r)\mathbf{s}_8^{-1}e^{\mathbf{s}_8 z}\mathbf{B}_8 \tag{8}$$

where $\mathbf{s}_6 = \sqrt{\mathbf{q}^2 + j\omega\mu_0\mu_{r6}\sigma_6}$, $\mathbf{s}_8 = \sqrt{\mathbf{q}^2 + j\omega\mu_0\mu_{r8}\sigma_8}$.

The analytical solution is derived using Bessel functions of the first and second kind, denoted by J_n and Y_n, respectively, where n represents the order of the function. The parameters $J_1(\mathbf{q}^T r)$, $J_1(\mathbf{m}^T r)$, $R_1(\mathbf{m}^T r)$, $R_1'(\mathbf{m}^T r)$, $J_1(\mathbf{p}^T r)$, $L_1(\mathbf{p}^T r)$, $L_1'(\mathbf{p}^T r)$, $J_1(\mathbf{u}^T r)$, and $F_1(\mathbf{v}^T r)$ are represented by row vectors. Additionally, $\mathbf{q}^{-1}$, $\mathbf{m}^{-1}$, $\mathbf{p}^{-1}$, $\mathbf{u}^{-1}$, $\mathbf{v}^{-1}$, $\mathbf{s}_6^{-1}$, $\mathbf{s}_8^{-1}$, and the exponential functions are expressed as diagonal matrices. Finally, $\mathbf{C}_k$ and $\mathbf{B}_k$ (where k ranges from 1 to 8, representing different regions) are column vectors of unknown coefficients.

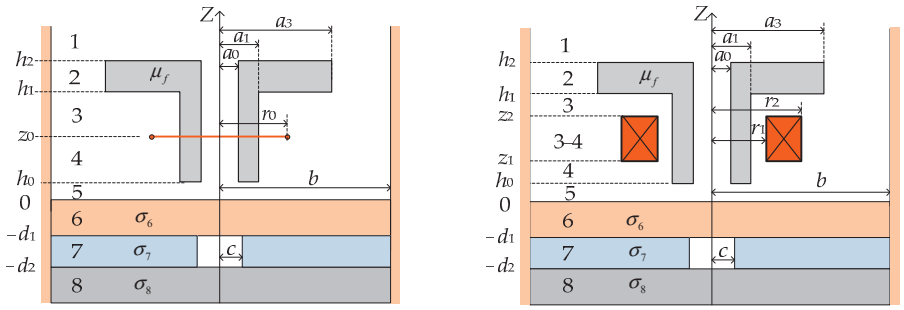

Figure 2. T-core ECT sensors consisting of (**a**) a filamentary coil and (**b**) a multi-turn coil positioned above a layered conductor with a hole in its second layer. Numbers 1–8 represent different regions.

Figure 2's regions 1, 5, 6, and 8 have eigenvalues (q_i) that are the positive real roots of Equation (9), where i represents the root number.

$$J_1(q_i b) = 0 \tag{9}$$

Region 2 is further divided into three subregions. Subregions I ($0 \le r \le a_0$) and III ($a_3 \le r \le$ b) are filled with air, while subregion II ($a_0 \le r \le a_3$) contains a ferrite core. The positive real roots of Equation (10) yield the discrete eigenvalues (m_i).

$$R_1'(m_i b) = 0 \tag{10}$$

where

$$R_n'(m_i r) = B_{3F} J_n(m_i r) + C_{3F} Y_n(m_i r) \tag{11}$$

$$C_{3F} = \frac{\pi m_i a_3}{2}\left[\frac{J_1(m_i a_3) R_0(m_i a_3)}{\mu_f} - J_0(m_i a_3) R_1(m_i a_3)\right] \tag{12}$$

$$B_{3F} = \frac{\pi m_i a_3}{2}\left[Y_0(m_i a_3) R_1(m_i a_3) - \frac{Y_1(m_i a_3) R_0(m_i a_3)}{\mu_f}\right] \tag{13}$$

$$R_n(m_i r) = B_{2F} J_n(m_i r) + C_{2F} Y_n(m_i r) \tag{14}$$

$$C_{2F} = \frac{\pi m_i a_0}{2} J_0(m_i a_0) J_1(m_i a_0)(\mu_f - 1) \tag{15}$$

$$B_{2F} = \frac{\pi m_i a_0}{2}\left[J_1(m_i a_0) Y_0(m_i a_0) - J_0(m_i a_0) Y_1(m_i a_0)\mu_f\right] \tag{16}$$

Regions 3 and 4 are subdivided into three subregions: Subregion I ($0 \le r \le a_0$), Subregion II ($a_0 \le r \le a_1$), and Subregion III ($a_1 \le r \le b$). Subregions I and III represent air, while Subregion II encompasses the ferrite core. The discrete eigenvalues, denoted by p_i, are positive real roots of Equation (17):

$$L_1'(p_i b) = 0 \tag{17}$$

where

$$L_n'(p_i r) = B_{3F}' J_n(p_i r) + C_{3F}' Y_n(p_i r) \tag{18}$$

$$C_{3F}' = \frac{\pi p_i a_1}{2}\left[\frac{J_1(p_i a_1) L_0(p_i a_1)}{\mu_f} - J_0(p_i a_1) L_1(p_i a_1)\right] \tag{19}$$

$$B_{3F}' = \frac{\pi p_i a_1}{2}\left[Y_0(p_i a_1) L_1(p_i a_1) - \frac{Y_1(p_i a_1) L_0(p_i a_1)}{\mu_f}\right] \tag{20}$$

$$L_n(p_i r) = B_{2F}' J_n(p_i r) + C_{2F}' Y_n(p_i r) \tag{21}$$

$$C_{2F}' = \frac{\pi p_i a_0}{2} J_0(p_i a_0) J_1(p_i a_0)(\mu_f - 1) \tag{22}$$

$$B'_{2F} = \frac{\pi p_i a_0}{2}[J_1(p_i a_0)Y_0(p_i a_0) - J_0(p_i a_0)Y_1(p_i a_0)\mu_f] \tag{23}$$

Region 7 comprises two subregions: an air space ($0 \le r \le c$) and a conductive material ($c \le r \le b$). Applying the interface condition in the radial direction at $r = c$ yields the following equation. The eigenvalues, u_i, are then determined as the positive real roots of Equation (24):

$$u_i F_1(v_i c)J_0(u_i c) = \mu_{r7}^{-1} v_i F_0(v_i c)J_1(u_i c) \tag{24}$$

where

$$F_n(v_i r) = J_n(v_i r)Y_1(v_i b) - J_1(v_i b)Y_n(v_i r) \tag{25}$$

The relationship between eigenvalues (u_i) and their corresponding eigenvectors (v_i) is as follows:

$$u_i = \sqrt{v_i^2 + j\omega\sigma_7\mu_0\mu_{r7}} \tag{26}$$

The eigenvalues (u_i), which are the complex roots of Equation (24), can be determined using the Newton–Raphson method [35–37]. While this method is effective, more efficient algorithms have been developed in recent years to ensure the identification of all roots [38,39].

To solve the problem, the interface conditions between the eight regions must be satisfied, specifically the continuity of B_z and H_r. Determining the magnetic vector potential $A_{(k)filamentary}(r,z)$ in each region, excited by the T-core filamentary coil (Figure 2a), requires solving for the discrete eigenvalues and unknown coefficients through these continuity conditions at various boundaries and interfaces. Subsequently, the magnetic vector potential of each region excited by a coil with a rectangular cross-section can be derived using the superposition method.

$$A_k^{coil}(r,z) = \int_{r_1}^{r_2}\int_{z1}^{z_2} A_{(k)filamentary}(r,z,r_0,z_0)dr_0dz_0, k = 1,2,\ldots,8 \tag{27}$$

The eddy current density within the layered conductive material can be determined using the method outlined in [21].

$$J_L^{eddy}(r,z) = -j\omega\sigma_L A_L^{coil}(r,z); \quad L = 6,7,8 \tag{28}$$

The final expression for the eddy current density within the first-layer conductor (region 6) can be derived as follows.

$$\begin{array}{l} J_6^{eddy}(r,z) = -j\omega\sigma_6 A_6^{coil}(r,z) \\ = \frac{-j\omega\sigma_6\mu NI}{2(r_2-r_1)(z_2-z_1)} J_1(\mathbf{q}r)\mathbf{s}_6^{-1}\mathbf{W}_4\mathbf{W}_2^{-1}\mathbf{W}_3\mathbf{p}^{-3}\mathbf{D}^{-1}\chi(\mathbf{p}r_1,\mathbf{p}r_2) \end{array} \tag{29}$$

Following the derivation of magnetic vector potentials A_3^{coil} and A_4^{coil} for regions 3 and 4 in Figure 2b, the potential A_{3-4}^{coil} within the region between these two regions can be determined by substituting z for z_2 in A_3^{coil} and z for z_1 in A_4^{coil} and summing the results. The final impedance expressions for the T-core coil sensor are then derived as follows:

$$\begin{array}{l} Z = \frac{j\omega 2\pi N}{I(z_2-z_1)(r_2-r_1)}\int_{r_1}^{r_2}\int_{z_1}^{z_2} rA_{3-4}^{coil}(r,z)drdz \\ = \frac{j\omega\mu\pi N^2}{(r_2-r_1)^2(z_2-z_1)^2}\chi(\mathbf{p}r_1,\mathbf{p}r_2)\mathbf{p}^{-4} \\ \cdot[2(z_2-z_1)\mathbf{p} + e^{\mathbf{p}(z_1-z_2)} - e^{\mathbf{p}(z_2-z_1)} + \mathbf{W}_1\mathbf{W}_2^{-1}\mathbf{W}_3]\mathbf{p}^{-3}\mathbf{D}^{-1}\chi(\mathbf{p}r_1,\mathbf{p}r_2) \end{array} \tag{30}$$

where

$$\chi(\mathbf{p}r_1,\mathbf{p}r_2) = \int_{\mathbf{p}r_1}^{\mathbf{p}r_2}(\mathbf{p}r)L_1'(\mathbf{p}r)d(\mathbf{p}r)] \tag{31}$$

$$\mathbf{W}_1 = (e^{-\mathbf{p}z_1} - e^{-\mathbf{p}z_2})\mathbf{C}_{48} - (e^{\mathbf{p}z_2} - e^{\mathbf{p}z_1})\mathbf{B}_{48} \tag{32}$$

$$\mathbf{W}_2 = (\boldsymbol{\lambda}_1\mathbf{F}^{-1}\mathbf{G} + \boldsymbol{\lambda}_2\mathbf{F}^{-1}\mathbf{H})e^{-\mathbf{p}h_1}\mathbf{C}_{48} - (\boldsymbol{\lambda}_1\mathbf{F}^{-1}\mathbf{G} - \boldsymbol{\lambda}_2\mathbf{F}^{-1}\mathbf{H})e^{\mathbf{p}h_1}\mathbf{B}_{48} \tag{33}$$

$$\mathbf{W}_3 = (\boldsymbol{\lambda}_1\mathbf{F}^{-1}\mathbf{G} - \boldsymbol{\lambda}_2\mathbf{F}^{-1}\mathbf{H})(e^{\mathbf{p}(h_1-z_1)} - e^{\mathbf{p}(h_1-z_2)}) - (\boldsymbol{\lambda}_1\mathbf{F}^{-1}\mathbf{G} + \boldsymbol{\lambda}_2\mathbf{F}^{-1}\mathbf{H})(e^{\mathbf{p}(z_2-h_1)} - e^{\mathbf{p}(z_1-h_1)}) \tag{34}$$

$$\mathbf{W}_4 = e^{-\mathbf{s}_6 z}\mathbf{C}_{68} - e^{\mathbf{s}_6 z}\mathbf{B}_{68} \tag{35}$$

$$\boldsymbol{\lambda}_1 = (\mathbf{T} - \mathbf{U})e^{\mathbf{m}(h_1-h_2)} + (\mathbf{T} + \mathbf{U})e^{\mathbf{m}(h_2-h_1)} \tag{36}$$

$$\boldsymbol{\lambda}_2 = (\mathbf{T} - \mathbf{U})e^{\mathbf{m}(h_1-h_2)} - (\mathbf{T} + \mathbf{U})e^{\mathbf{m}(h_2-h_1)} \tag{37}$$

$$\mathbf{C}_{48} = \frac{1}{2}e^{\mathbf{p}h_0}\mathbf{D}^{-1}[(\mathbf{H}^* + \mathbf{G}^*)e^{-\mathbf{q}h_0}\mathbf{C}_{58} + (\mathbf{H}^* - \mathbf{G}^*)e^{\mathbf{q}h_0}\mathbf{B}_{58}] \tag{38}$$

$$\mathbf{B}_{48} = \frac{1}{2}e^{-\mathbf{p}h_0}\mathbf{D}^{-1}[(\mathbf{H}^* - \mathbf{G}^*)e^{-\mathbf{q}h_0}\mathbf{C}_{58} + (\mathbf{H}^* + \mathbf{G}^*)e^{\mathbf{q}h_0}\mathbf{B}_{58}] \tag{39}$$

$$\mathbf{C}_{58} = \frac{1}{2}[(\mu_6^{-1} + \mathbf{q}\mathbf{s}_6^{-1})\mathbf{C}_{68} + (\mu_6^{-1} - \mathbf{q}\mathbf{s}_6^{-1})\mathbf{B}_{68}] \tag{40}$$

$$\mathbf{B}_{58} = \frac{1}{2}[(\mu_6^{-1} - \mathbf{q}\mathbf{s}_6^{-1})\mathbf{C}_{68} + (\mu_6^{-1} + \mathbf{q}\mathbf{s}_6^{-1})\mathbf{B}_{68}] \tag{41}$$

$$\mathbf{C}_{68} = \frac{1}{2}e^{-\mathbf{s}_6 d_1}[(\mathbf{E}^{-1}\mathbf{N} + \mathbf{s}_6\mathbf{q}^{-1}\mathbf{E}^{-1}\mathbf{V})e^{\mathbf{u}d_1}\mathbf{C}_{78} + (\mathbf{E}^{-1}\mathbf{N} - \mathbf{s}_6\mathbf{q}^{-1}\mathbf{E}^{-1}\mathbf{V})e^{-\mathbf{u}d_1}\mathbf{B}_{78}] \tag{42}$$

$$\mathbf{B}_{68} = \frac{1}{2}e^{\mathbf{s}_6 d_1}[(\mathbf{E}^{-1}\mathbf{N} - \mathbf{s}_6\mathbf{q}^{-1}\mathbf{E}^{-1}\mathbf{V})e^{\mathbf{u}d_1}\mathbf{C}_{78} + (\mathbf{E}^{-1}\mathbf{N} + \mathbf{s}_6\mathbf{q}^{-1}\mathbf{E}^{-1}\mathbf{V})e^{-\mathbf{u}d_1}\mathbf{B}_{78}] \tag{43}$$

$$\mathbf{C}_{78} = \frac{1}{2}e^{-\mathbf{u}d_2}(\mathbf{N}^{-1}\mathbf{E} - \mathbf{V}^{-1}\mathbf{E}\mathbf{q}\mathbf{s}_8^{-1})e^{-\mathbf{s}_8 d_2} \tag{44}$$

$$\mathbf{B}_{78} = \frac{1}{2}e^{\mathbf{u}d_2}(\mathbf{N}^{-1}\mathbf{E} + \mathbf{V}^{-1}\mathbf{E}\mathbf{q}\mathbf{s}_8^{-1})e^{-\mathbf{s}_8 d_2} \tag{45}$$

where

$$\mathbf{C}_{n7} = \frac{\mathbf{C}_n}{\mathbf{B}_7} \tag{46}$$

$$\mathbf{B}_{n7} = \frac{\mathbf{B}_n}{\mathbf{B}_7} \tag{47}$$

The matrices **T**, **U**, **F**, **G**, **G***, **H**, **H***, **N**, **V**, **D**, and **E** are detailed in Appendix A.

3. Numerical Implementation

The eddy current density in the first layer conductor and the impedance of the T-core coil were calculated using the Matlab software package version 7.0, based on Equations (29) and (30). The main steps of the numerical calculation procedure are shown in Figure 3. Employing the same derivation method used for the T-core sensor, expressions for the coil impedance of E-core and I-core sensors, along with the eddy current density in the conductor (as depicted in Figure 4), were derived. Subsequently, the coil impedances of the E-core, I-core (with relative permeability μ_r = 2500), and air-core (μ_r = 1) sensors and the corresponding eddy current densities at the same conductor depth were determined using analytical methods.

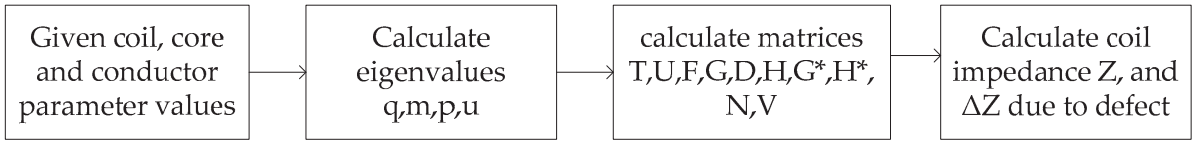

Figure 3. Numerical calculation scheme of the analytical model.

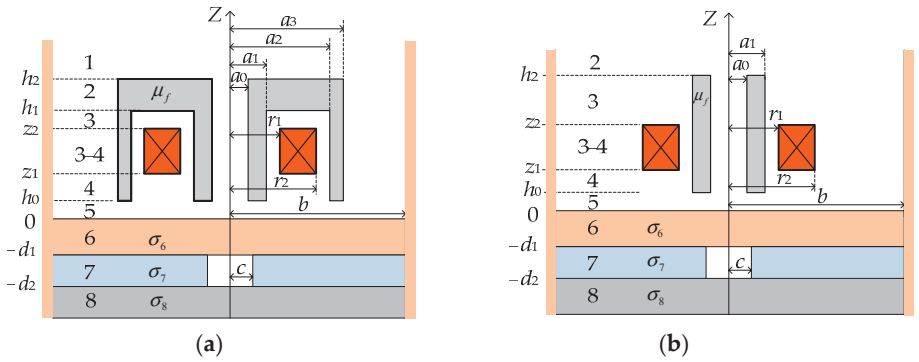

Figure 4. Axially symmetric (**a**) E-core and (**b**) I-core ECT sensors positioned above a layered conductor with a hidden hole in the second layer. Numbers 1–8 represent different regions.

The analytical calculations utilize parameters derived from measurements of the cored sensors and conductors employed in the experiments, as detailed in Table 1. For all analytical calculations, the solution domain was truncated at b = 90 mm (nine times the coil's outer radius, r_2), and the number of summation terms was set to N_s = 60. A comparative analysis was then conducted, comparing the analytical results with those obtained from finite element analysis and experimental measurements.

Table 1. The parameters of the coil, T-core, E-core, I-core, and conductor used in experiments, analytical calculation, and FEM.

Core	Air gap radius of core	a_0	2.7 mm
	Inner core radius	a_1	5.7 mm
	Parameter	a_2	10.85 mm
	Outer core radius	a_3	12.85 mm
	Offset	h_0	0.1 mm
	Inner core height	h_1	5.8 mm
	Outer core height	h_2	8.2 mm
	Core relative permeability	μ_f	2500
Coil	Inner coil radius	r_1	6.4 mm
	Outer coil radius	r_2	9.8 mm
	Parameter	z_1	0.7 mm
	Parameter	z_2	4.8 mm
	Number of turns	N	400
Conductor	Liftoff	d_1	0.5 mm
	Parameter	d_2	4.5 mm
	Relative permeability	μ_6, μ_7, μ_8	1
	Conductivity	σ_6, σ_7, σ_8	36 MS/m
	Hole radius	c	4 mm
	Radius of the domain	b	90 mm

4. Experimental Confirmation

The proposed analytical model was validated through experimental verification. The experimental setup, shown in Figure 5, comprised a T-core sensor, a layered conductor, and a Gwinstek LCR meter. Figure 6 displays the E-core, T-core, I-core, and air coil used in the experiments. The parameters detailed in Table 1 also served as inputs for these experimental investigations, which involved measuring impedance changes across a frequency range of 100 Hz to 10 kHz. These impedance changes were observed in each core sensor due to the presence of a layered conductor containing a hidden hole.

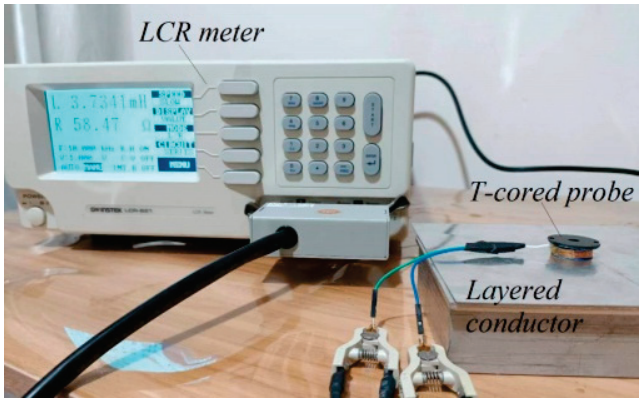

Figure 5. Configuration for the experiment.

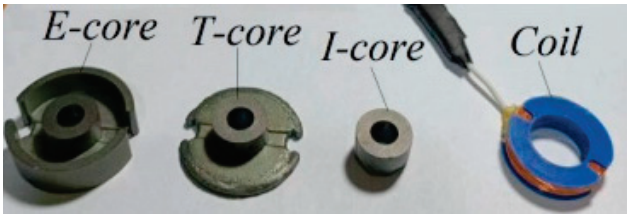

Figure 6. E-core, T-core, I-core, and coil used in the experiments.

5. Comparison with FEM

To validate the proposed analytical model, Ansoft Maxwell software version 5.0 is employed for finite element analysis and verification. Experimental measurements are restricted by available equipment and materials. For instance, the type and precision of measurement apparatuses, the type and dimensions of sensors, and the type and size of multilayer conductor materials all govern the experimental type and measurement accuracy. In contrast, finite element simulation offers the advantage of freely adjusting the sensor size and the thickness and material parameters of multilayer conductors.

Initially, to confirm the efficacy of the proposed analytical model for multilayer conductors composed of diverse materials, the conductivities of the first- and third-layer conductors in the experimental parameters (as shown in Table 1) were modified to σ_6 = 15 MS/m and σ_8 = 5 MS/m respectively, while the other parameters remained unaltered. The coil impedance of the T-core coil sensor positioned above three distinct layers of conductors with a hidden hole in the second layer, calculated using Equation (30), is presented in Table 2. Here, the values in the corresponding columns of ε_R and ε_X represent the relative errors between the analytical calculation outcomes and the finite element simulation results, with the relative errors defined by Equations (48) and (49).

$$\varepsilon_R = \left| \frac{R^{analytical} - R^{FEM}}{R^{FEM}} \right| \times 100\% \tag{48}$$

$$\varepsilon_X = \left| \frac{X^{analytical} - X^{FEM}}{X^{FEM}} \right| \times 100\% \tag{49}$$

Table 2. Analytical results of the resistance and reactance of the T-core coil sensor and the relative error with the FEM ones.

f [kHz]	R [Ω]	ε_R	X [Ω]	ε_X
0.2	1.57413	0.64%	8.08502	0.024%
1	6.29085	0.94%	31.2587	0.028%
5	19.48457	0.84%	131.7659	−0.12%
10	31.33254	0.82%	249.4438	−0.17%

Furthermore, the analytical calculation and finite element analysis of the eddy current density of the conductor were carried out according to the experimental parameters shown in Table 1.

Figure 7 illustrates the real component of eddy current densities at varying distances from the coil's central axis. These results were taken at a depth of 0.2 mm below the surface of the layered conductor and are shown for different types of ferrite core sensors. Specifically, the eddy current produced by a T-core sensor within the conductor can be calculated using Equation (29). These computational results demonstrate good agreement with the finite element analysis results.

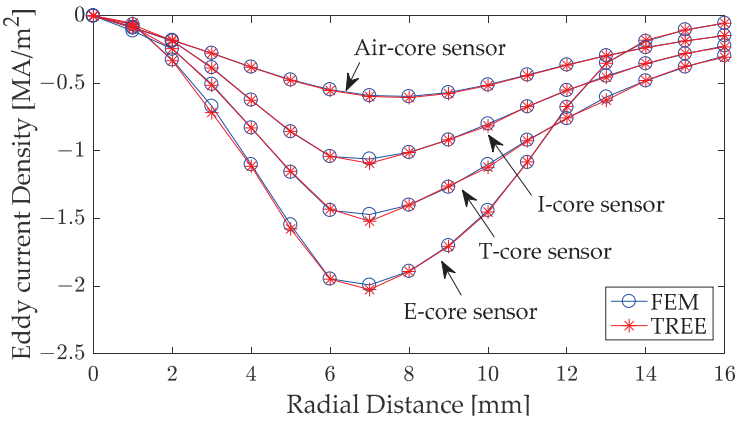

Figure 7. Real component of the eddy current density at a depth of 0.2 mm beneath the surface of the layered conductor, across varying distances from the coil's central axis.

An analysis of Figure 7 reveals that all core sensor configurations produce the highest eddy current density in the conductor beneath the coil's inner radius. Furthermore, under identical excitation conditions, the E-core sensor generates the strongest eddy current density within the conductor. The T-core sensor induces a smaller, yet still significant, eddy current density compared to the E-core sensor, but larger than that produced by the I-core sensor. The air-core sensor generates the weakest eddy current density among all sensor configurations.

The magnetic flux distribution generated by each coil type was simulated using Ansoft software version 5.0. Figure 8 depicts the magnetic flux density distributions for the E-core, T-core, I-core, and air-core sensors within the ferrite core, coil, and layered conductor with the embedded hole. The figure highlights a higher concentration of magnetic flux lines within the ferrite core, facilitating the propagation of magnetic flux into the conductor. The E-core configuration exhibits the most efficient magnetic flux transfer path, followed by the T-core and then the I-core. The simulated eddy current density results are consistent with the analytical calculations, providing a rationale for the varying eddy current densities observed in Figure 7 across the different core sensor types.

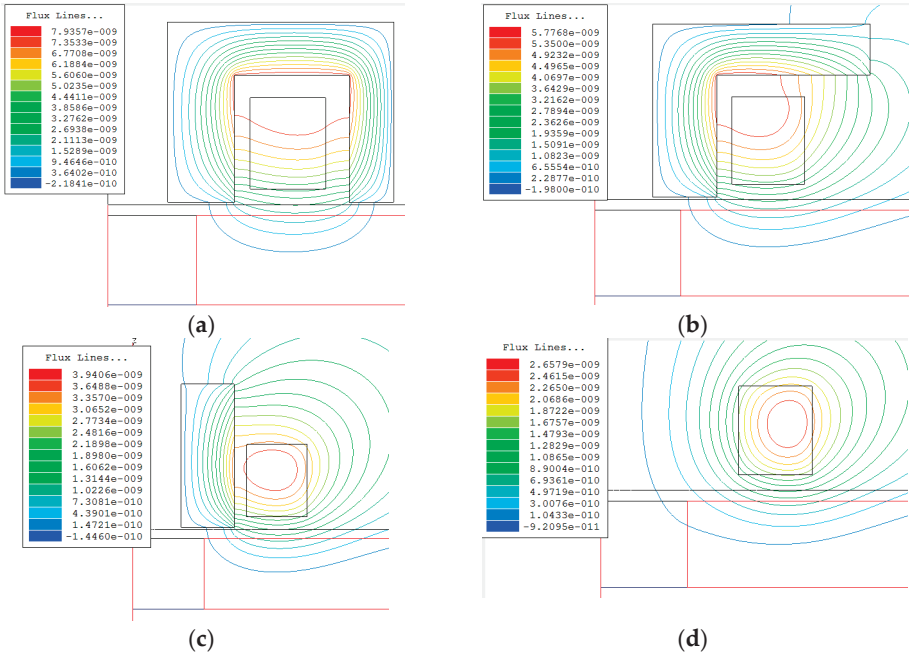

Figure 8. Magnetic flux density distributions generated by sensors of four different core types: (**a**) E-core, (**b**) T-core, (**c**) I-core, and (**d**) air-core. All sensors were positioned above the same layered conductor and subjected to the same excitation.

6. Results

Initially, the multilayer conductor's conductivities were set to $\sigma_6 = \sigma_7 = \sigma_8 = 36$ MS/m, and coil impedances ($Z = R + jX$) were calculated using derived analytical formulas. Subsequently, coil impedances ($Z_0 = R_0 + jX_0$) were calculated in the absence of conductive material ($\sigma_6 = \sigma_7 = \sigma_8 = 0$), along with the coil inductance (L_0) of air-core (2.75 mH), I-core (4.93 mH), T-core (7.633 mH), and E-core (10.02 mH) sensors. The changes in coil resistance ($\Delta R = R - R_0$) and reactance ($\Delta X = X - X_0$) due to the multilayer conductor were then determined. Figure 9a,b illustrate the normalized changes in coil resistance and reactance, respectively, for different core sensors caused by the layered conductor. Notably, the relative difference between the TREE method and the finite element method remained below 1% in all cases.

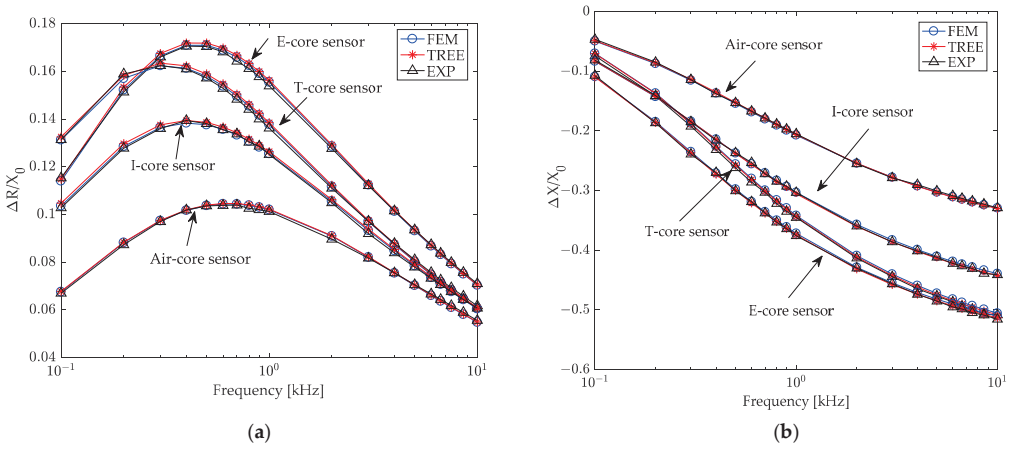

Figure 9. Normalized changes in (**a**) resistance and (**b**) reactance caused by the layered conductor of E-core, T-core, I-core (with a relative permeability of 2500), and air-core (with a relative permeability of 1) sensors, as a function of frequency.

Following the calculation of eigenvalues for m_i, p_i, u_i, etc., the impedance of a T-core coil above a multilayer conductor with a hidden defect was determined using a Matlab program based on Equation (30). This computation, performed on a desktop computer (AMD Ryzen 5 5600 G 3.9 GHz CPU (Santa Clara, CA, USA), 24 GB RAM, Windows 10), required approximately 3.869 s under single-frequency excitation. Calculating the impedance for a defect-free multilayer conductor under the same conditions took about 2.535 s. The numerical results achieved a precision of 15 decimal places.

As a verification method, this problem can also be solved using Ansys Ansoft 2D finite element software version 5.0. This involves modeling the multilayer conductor with the defect and the T-core coil sensor, defining excitation and material parameters, and meshing the solution area with 41,714 triangles. The impedance calculation using this method took approximately 15 s. Simulating the defect-free scenario with the finite element method under the same conditions required about 10 s. However, increasing the mesh density or employing a 3D solver would significantly increase the computation time.

When a large number of frequency points need to be calculated, the analytical model offers a substantial advantage over the FEM in terms of computational efficiency. This advantage hinges on the prior calculation of the eigenvalues required for the analytical solution.

Figure 9 reveals that the normalized changes in coil impedance due to the layered conductor vary significantly across different core sensors. This variation primarily depends on the presence and shape of the core. Under identical coil and excitation conditions, the E-core sensor exhibited the highest sensitivity, followed by the T-core sensor, and then the I-core sensor. The air-core sensor demonstrated the lowest sensitivity.

The impact of an air hole in the second layer conductor on the normalized change in coil impedance was further investigated across varying excitation frequencies, with the results presented in Figure 10.

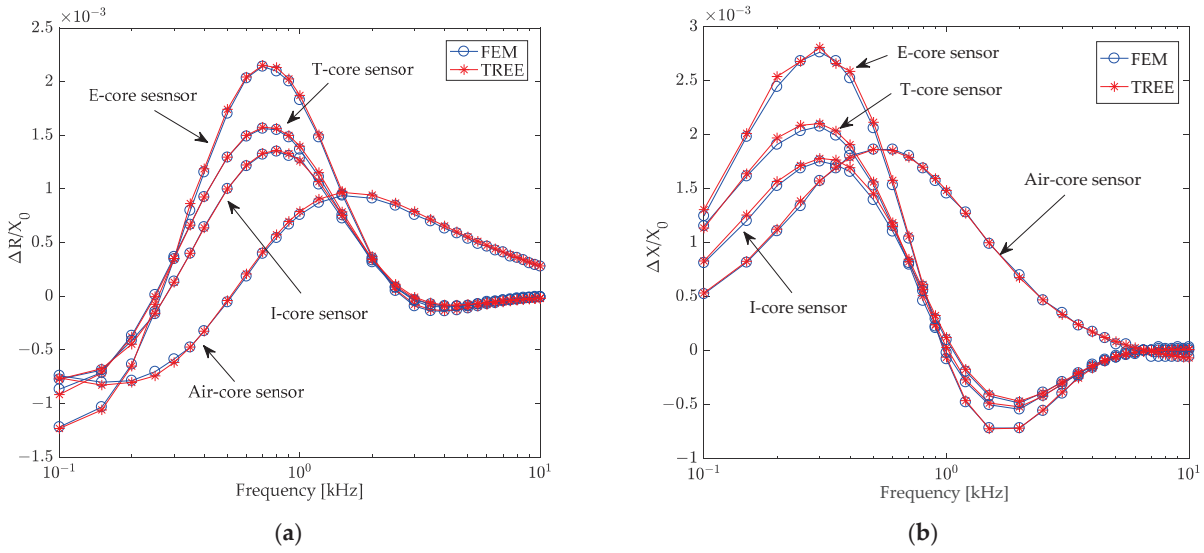

Figure 10. Normalized changes in (**a**) resistance and (**b**) reactance caused by an air hole in the second-layer conductor of E-core, T-core, I-core (with a relative permeability of 2500), and air-core (with a relative permeability of 1) sensors, as a function of frequency.

Figure 10 shows that, due to the small size and location of the air hole within the second conductor layer, the normalized impedance changes for coils with different cores were relatively small and exhibited minimal differences. However, within the excitation frequency range below 1 kHz, the normalized impedance changes decreased in the following order: E-core sensor, T-core sensor, I-core sensor, and air-core sensor.

7. The Influence of T-Core Parameters on Coil Impedance Changes

To optimize the design of the T-core sensor for detecting hidden defects in a multi-layer conductor, it is crucial to understand how key T-core parameters, including the air gap radius, upper circular plate radius, column height, and core permeability affect coil impedance. This study employed both an analytical model and finite element simulation to investigate the impact of these parameters on coil impedance. The analysis yielded optimal values for the key T-core parameters, paving the way for the design of a highly sensitive T-core sensor.

7.1. Air Gap Radius of T-Core

A T-core sensor with excitation frequencies of 0.6 kHz, 1 kHz, and 5 kHz and an outer column radius (a_1) of 5.7 mm was investigated. The study focused on the impact of varying the T-core's air gap radius (a_0) from 0.1 mm to 5 mm on coil impedance, specifically considering the presence of a second-layer conductor hole. Results indicate that while the air gap radius minimally affects coil reactance, it significantly influences the coil resistance. Figure 11 illustrates this relationship, showcasing the change in coil resistance due to the second-layer conductor hole as a function of the T-core's air gap radius. Figure 11 reveals that, with a constant outer column radius (a_1), a smaller air gap radius leads to a greater absolute value of the change in coil resistance caused by the presence of the hole in the second-layer conductor. Within a constant air gap, the variation in coil resistance attributed to the concealed air hole exhibits a dependence on the excitation frequency. The resistance change is most pronounced at 1 kHz, followed by 0.6 kHz, while the least change occurs at 5 kHz.

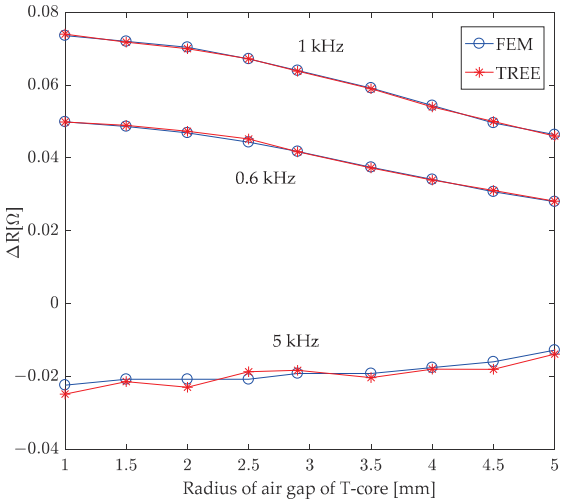

Figure 11. Investigating the correlation between variations in T-core coil resistance caused by a hole in the second-layer conductor and the radius of the T-core air gap.

7.2. The Radius of Upper Circular Plate of T-Core

A T-core sensor, operating at excitation frequencies of 0.6 kHz, 1 kHz, and 5 kHz, was analyzed using the derived analytical model. The radius of the upper circular plate (a_3) was incrementally increased from 6 mm to 17 mm, while other T-core sensor parameters remained constant (as detailed in Table 1). The study focused on determining the impact of this radius variation on the coil impedance, specifically in the presence of a hole in the second-layer conductor. Calculations revealed that the coil reactance remained relatively unaffected by changes in the upper circular plate radius. Conversely, coil resistance exhibited a more pronounced response, as depicted in Figure 12. This figure shows that the absolute value of the change in coil resistance due to the hole gradually increases with the radius until it reaches 14 mm, after which it stabilizes.

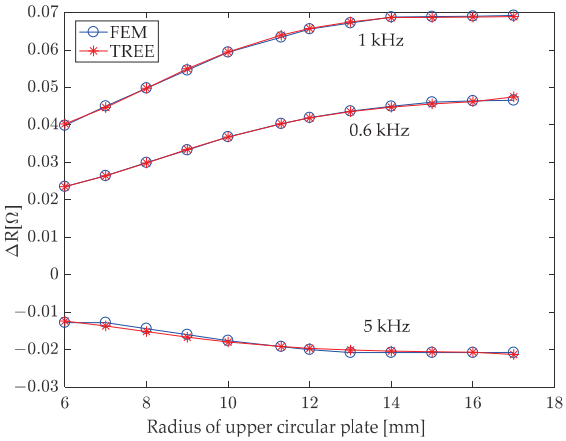

Figure 12. Investigation of the correlation between the variation in resistance of the T-core coil, caused by the presence of a hole in the second-layer conductor, and the radius of the T-core's upper circular plate.

For a constant upper circular plate radius, the variation in coil resistance induced by the hidden hole exhibits a dependence on the excitation frequency. As illustrated in Figure 12, the absolute value of the coil resistance change, caused by the three frequencies, decreases in the order of 1 kHz, 0.6 kHz, and 5 kHz.

7.3. Height of T-Core Column

A T-core sensor was excited at frequencies of 0.6 kHz, 1 kHz, and 5 kHz. The T-core's parameters remained consistent with Table 1, with the exception of the column height (h_1, as depicted in Figure 2), which was incrementally increased from 5.8 mm to 15.8 mm. Figure 13 illustrates the correlation between the T-core coil's resistance change and the column height, specifically resulting from a hole in the second-layer conductor. This figure reveals that an increase in the T-core column height leads to a decrease in the absolute value of the coil's resistance change attributed to the presence of this hole.

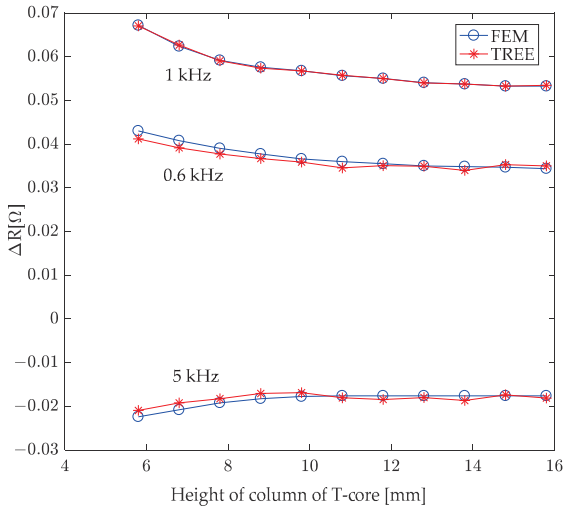

Figure 13. Investigating the correlation between variation in T-core coil resistance caused by a hole in the second-layer conductor and the T-core's column height.

While maintaining a constant T-core column height, the variation in coil resistance induced by the hidden hole also exhibits a dependence on the excitation frequency. Notably, the maximum absolute change in coil resistance remains at 1 kHz.

7.4. Permeability of T-Core

Additionally, the research assessed the effect of the T-core's relative permeability on the sensor's sensitivity. The T-core coil sensor was driven by 0.6 kHz, 1 kHz, and 5 kHz sinusoidal currents, respectively. Varying the T-core's relative permeability from 1 to 2500, the analytical formula (30) was utilized to predict changes in coil resistance and reactance resulting from an air hole in the second-layer conductor. These analytical results were then validated against simulation data obtained using Ansoft Maxwell software, with the findings presented in Figure 14.

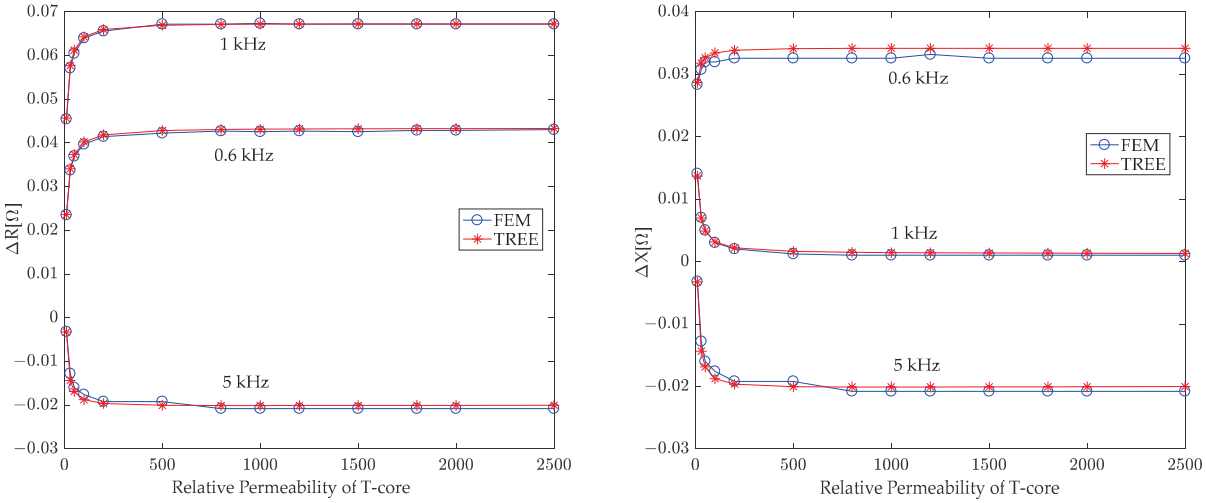

Figure 14. Investigating the correlation between variations in coil (**a**) resistance and (**b**) reactance caused by a hole in the second-layer conductor and the T-core's relative permeability.

Figure 14a demonstrates that as the T-core's relative permeability increases from 10, the resulting change in the absolute value of coil resistance due to the hole gradually rises, reaching a maximum at a permeability of 500. Further increases in permeability did not lead to a corresponding increase in resistance change. Figure 14b illustrates that increasing the magnetic permeability of the T-core from 10 initially leads to a fluctuating effect on the absolute change in coil reactance due to the hidden hole across various excitation frequencies. Specifically, the absolute change in coil reactance at 0.6 kHz and 5 kHz increases, while it decreases at 1 kHz. Nevertheless, as the permeability rises to 500, these changes in reactance stabilize.

The above study investigated the impact of a hidden hole within a multilayer conductor on coil impedance across three excitation frequencies (0.6 kHz, 1 kHz, and 5 kHz). The analysis explored how variations in key T-core parameters, including the air gap radius, upper plate radius, column height, and relative permeability, influence these impedance changes. Results indicate that, under consistent conditions, the coil resistance change is most pronounced at 1 kHz. Regarding the T-core air gap, minimizing or eliminating the air gap radius is optimal. For the upper circular plate, a radius of 14 mm maximizes the coil impedance change. Regarding the T-core column height, shorter heights are preferable within the constraints of accommodating the coil and ensuring proper contact with the measured conductor, with 5.8 mm identified as optimal in this study. Finally, concerning the T-core material's relative permeability, a value around 500 was found to be sufficient for achieving the maximum coil impedance change, suggesting that higher permeability does not necessarily translate to better performance.

8. T-Core Sensor for Conductor Defect Detection

8.1. Crack Detection

An aluminum plate (30 mm thick) was machined with a 2 mm wide and 10 mm deep rectangular groove to simulate a crack. This simulated crack was then investigated using finite element simulations employing four different ECT core sensors: E-core, T-core, I-core, and air-core. The characteristics of each sensor are detailed in Table 1. The study focused on the changes in coil impedance as the sensors scanned across the crack perpendicular to its direction. Figure 15a,b illustrate the variations in the real (resistance) and imaginary (reactance) components of coil impedance, respectively.

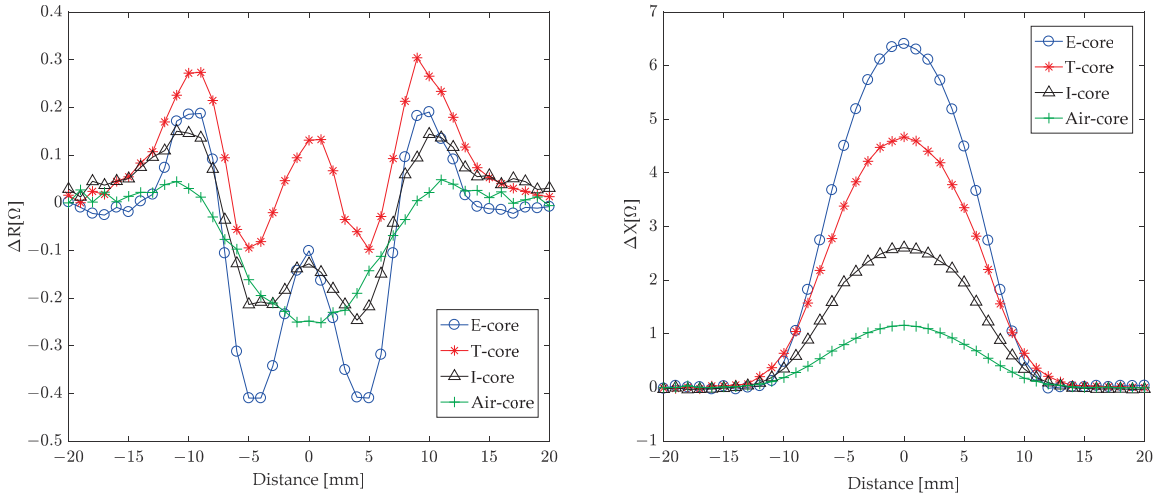

Figure 15. The correlation between variations in coil (**a**) resistance and (**b**) reactance and the distance from the crack's center line during scanning with various core sensors.

An analysis of the coil resistance changes (Figure 15a) reveals a gradual increase from zero as the sensors approach the crack from 20 mm away from its center line. This increase culminates in peak values at ±10 mm, ±5 mm, and directly above the crack's center. The resistance changes exhibit symmetry, with values mirroring those observed during the approach when the sensors are moved further away from the crack. Notably, at two of these peak positions (±10 mm), the T-core sensor demonstrated larger resistance changes compared to the E-core, I-core, and air-core coils.

An examination of the coil reactance changes (Figure 15b) shows a minimal initial change as the sensors approach the crack from ±20 mm away from its center line. A significant increase in reactance begins at ±10 mm from the center line, reaching maximum values directly above the crack's center. Similar to the resistance changes, the reactance variations exhibit symmetry when the sensors are moved away from the crack. While the T-core coil's reactance changes were smaller than those of the E-core coil, they were larger than those observed for the I-core and air-core coils.

8.2. Hole Defect Detection

An ECT method, simulated using the FEM, was employed to evaluate a hole with a 10 mm depth and 4 mm radius in a 30 mm thick aluminum plate. The simulation investigated the impact of scanning various core sensors (E-core, T-core, I-core, and air-core) through the hole on coil impedance. The core sensor parameters are detailed in Table 1. Figure 16a,b illustrate the changes in coil resistance and reactance, respectively, as the sensors are scanned across different positions relative to the hole center.

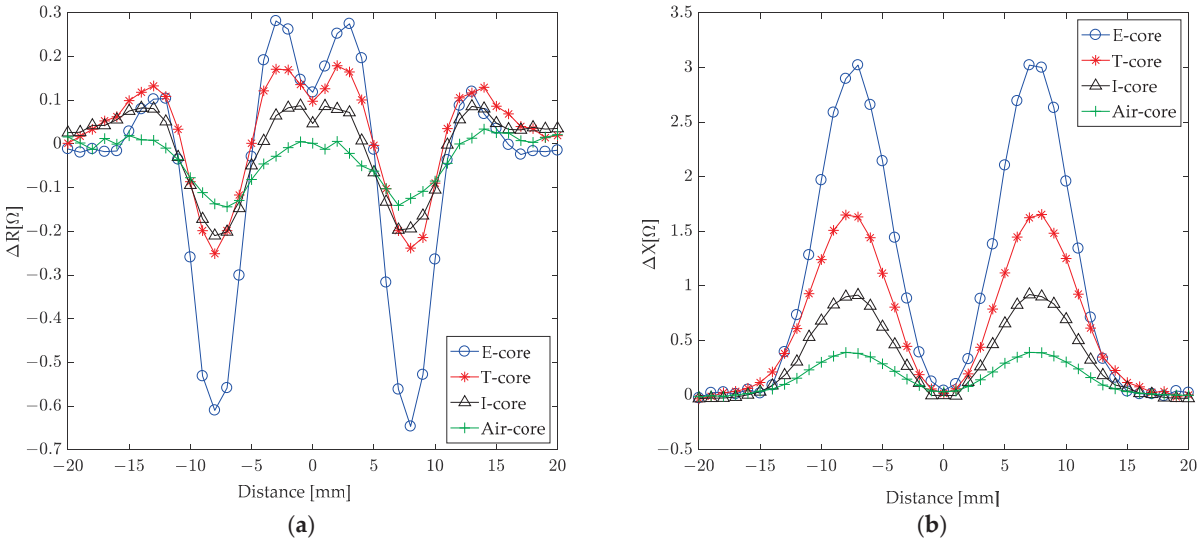

Figure 16. The correlation between variations in coil (**a**) resistance and (**b**) reactance and the distance from the hole's center during the scanning process of various core sensors through the hole.

An analysis of the coil resistance changes (Figure 16a) reveals that as sensors approach the hole from a distance of ±20 mm, resistance gradually increases from zero, reaching peak values at ±13 mm, ±8 mm, and ±3 mm from the hole center. The resistance changes exhibit symmetry when the sensors move away from the hole. While the T-core coil experiences smaller resistance changes compared to the E-core coil at these peak positions, they are larger than those observed for the I-core and air-core coils.

Figure 16b depicts the changes in coil reactance. As sensors approach the hole from ±20 mm, reactance increases until reaching a maximum at ±7 mm from the hole center, after which it decreases. Directly above the hole, the reactance change is zero. Similar to the resistance changes, reactance changes are symmetrical when the sensors move away from the hole. Though the T-core coil exhibits smaller reactance changes compared to the E-core coil, they remain larger than those of the I-core and air-core coils.

8.3. Relationship Between Defect Depth and Frequency Selection

To effectively detect conductor flaws, it is essential to take into account the impact of skin depth on the detection of defects at various depths under different excitation frequencies. A T-core coil sensor was used at various excitation frequencies to examine surface and subsurface cracks (1 mm, 2 mm, 3 mm, and 4 mm below the surface) in a conductor, with the coil axis situated 10 mm away from the crack's centerline. The finite element method was used to study the changes in resistance and reactance of the T-core coil caused by the cracks at different excitation frequencies.

Figure 17 displays the results of this study. To better visualize the low-frequency band changes in coil impedance, Figure 18 show a detailed view of the changes in coil resistance and reactance at excitation frequencies below 1.6 kHz.

According to Figure 17, for a surface crack, the changes in coil resistance and reactance increase as the frequency rises. However, for subsurface cracks, the change in coil resistance decreases as the excitation frequency rises. Although the change in coil reactance increases with frequency, there is little difference between cracks of different depths. As illustrated in Figure 18, in the low-frequency excitation range below 1.6 kHz, the coil impedance change decreases as the depth of subsurface cracks rises. However, the distinction between defects of different depths is clearer. Therefore, when detecting subsurface defects, low-frequency excitation should be used to achieve a larger skin depth.

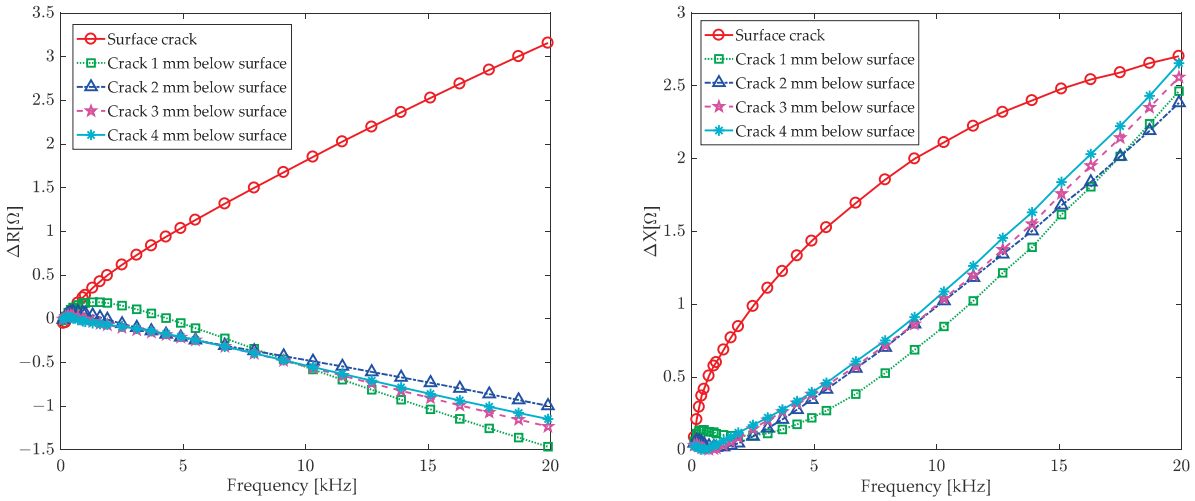

Figure 17. The relationship between the change in (**a**) resistance and (**b**) reactance of the T-core coil and the excitation frequency; the distance between the coil axis and the crack centerline is 10 mm.

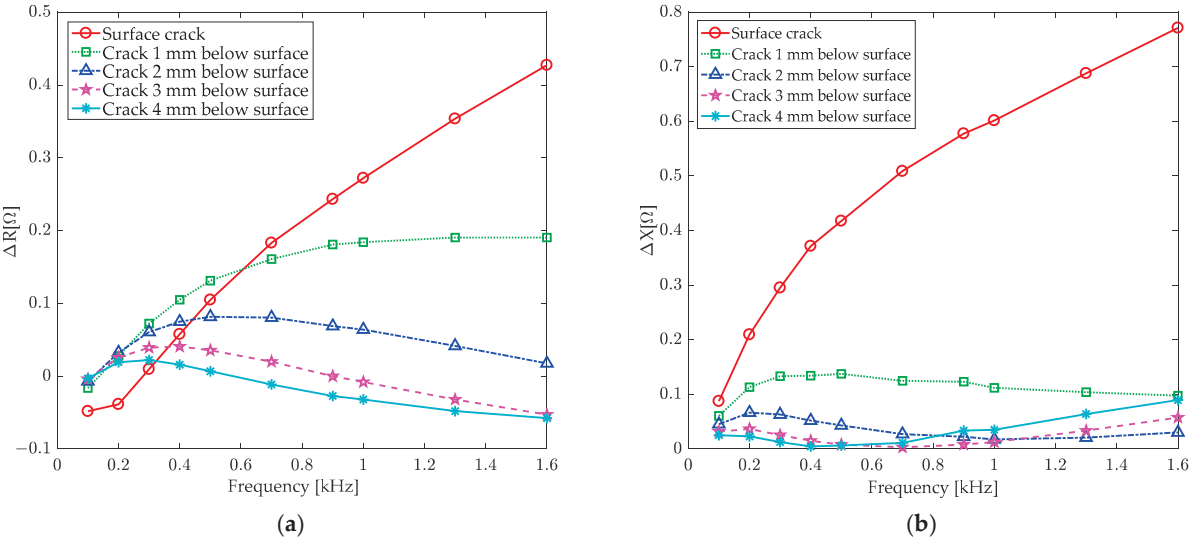

Figure 18. Refinement of the low-frequency area of Figure 17: (**a**) resistance and (**b**) reactance.

It is worth noting that, as shown in Figure 18, the changes in coil resistance and reactance are more sensitive to deep subsurface cracks at lower excitation frequencies. This suggests that low-frequency excitation is more effective at detecting deep subsurface cracks using the T-core coil sensor.

9. Conclusions

This paper presents an analytical model for a novel T-core sensor featuring an air gap positioned above a layered, conductive half-space containing a concealed defect. The TREE method is employed to derive analytical expressions for the eddy current density within the multilayered conductor and the impedance of the T-core coil. These expressions are readily implementable in mathematical software, like Mathematica or Matlab. Validation of the analytical model is achieved through a comparison with FEM simulations and experimental results, demonstrating strong agreement. A comparative analysis reveals that the proposed T-core sensor exhibits a superior flux concentration and shielding compared to an I-core and an air-core sensor, while maintaining a smaller size than an E-core sensor.

The study further explores the relationships between various T-core parameters and the alterations in coil impedance caused by a hidden defect, leading to the identification of optimal values for the primary parameters of the T-core. The advantages of the T-core coil sensor in detecting crack and air hole defects are assessed against other magnetic core and air-core sensors. Additionally, the principles governing frequency selection in the T-core coil sensor and their capability of detecting defects at different depths are discussed.

This analytical model facilitates computer simulations, enables optimized eddy current sensor design, and provides a direct application for conductor defect detection. Future work could extend this solution to analyze more complex conductor geometries and defect shapes.

Funding: This research received no external funding.

Institutional Review Board Statement: Not applicable.

Informed Consent Statement: Not applicable.

Data Availability Statement: Data is contained within the article.

Conflicts of Interest: The author declares no conflicts of interest.

Appendix A

The matrices T, U, F, G, H, D, G*, H*, V, N, and E were defined in the following form:

$$\begin{aligned}\mathbf{T} = [t_{ij}] \quad &= \int_0^{a_0} rJ_0(\mathbf{q}r)J_0(\mathbf{m^T}r)dr + \int_{a_0}^{a_3} rJ_0(\mathbf{q}r)R_0(\mathbf{m^T}r)dr \\ &+ \int_{a_3}^{b} rJ_0(\mathbf{q}r)R_0'(\mathbf{m^T}r)dr\end{aligned} \tag{A1}$$

$$\begin{aligned}\mathbf{U} = [u_{ij}] \quad &= \int_0^{a_0} rJ_1(\mathbf{q}r)J_1(\mathbf{m^T}r)dr + \frac{1}{\mu_f}\int_{a_0}^{a_3} rJ_1(\mathbf{q}r)R_1(\mathbf{m^T}r)dr \\ &+ \int_{a_3}^{b} rJ_1(\mathbf{q}r)R_1(\mathbf{m^T}r)dr\end{aligned} \tag{A2}$$

$$\begin{aligned}\mathbf{F} = [f_{ij}] \quad &= \int_0^{a_0} rJ_0(\mathbf{m}r)J_0(\mathbf{m^T}r) + \frac{1}{\mu_f}\int_{a_0}^{a_3} rR_0(\mathbf{m}r)R_0(\mathbf{m^T}r)dr) \\ &+ \int_{a_3}^{b} rR_0'(\mathbf{m}r)R_0'(\mathbf{m^T}r)dr\end{aligned} \tag{A3}$$

$$\begin{aligned}\mathbf{G} = [g_{ij}] \quad &= \int_0^{a_0} rJ_0(\mathbf{m}r)J_0(\mathbf{p^T}r)dr + \frac{1}{\mu_f}\int_{a_0}^{a_1} rR_0(\mathbf{m}r)L_0(\mathbf{p^T}r)dr \\ &+ \frac{1}{\mu_f}\int_{a_1}^{a_3} rR_0(\mathbf{m}r)L_0'(\mathbf{p^T}r)dr + \int_{a_3}^{b} rR_0'(\mathbf{m}r)L_0'(\mathbf{p^T}r)dr\end{aligned} \tag{A4}$$

$$\begin{aligned}\mathbf{H} = [h_{ij}] \quad &= \int_0^{a_0} rJ_1(\mathbf{m}r)J_1(\mathbf{p^T}r)dr + \frac{1}{\mu_f}\int_{a_0}^{a_1} rR_1(\mathbf{m}r)L_1(\mathbf{p^T}r)dr \\ &+ \int_{a_1}^{a_3} rR_1(\mathbf{m}r)L_1'(\mathbf{p^T}r)dr + \int_{a_3}^{b} rR_1'(\mathbf{m}r)L_1'(\mathbf{p^T}r)dr\end{aligned} \tag{A5}$$

$$\begin{aligned}\mathbf{D} = [d_{ij}] \quad &= \int_0^{a_0} rJ_1(\mathbf{p}r)J_1(\mathbf{p^T}r)dr + \frac{1}{\mu_f}\int_{a_0}^{a_1} rL_1(\mathbf{p}r)L_1(\mathbf{p^T}r) \\ &+ \int_{a_1}^{b} rL_1'(\mathbf{p}r)L_1'(\mathbf{p^T}r)dr\end{aligned} \tag{A6}$$

$$\begin{aligned}\mathbf{G}* = [g*_{ij}] \quad &= \int_0^{a_0} rJ_0(\mathbf{p}r)J_0(\mathbf{q^T}r)dr + \int_{a_0}^{a_1} rL_0(\mathbf{p}r)J_0(\mathbf{q^T}r)dr \\ &+ \int_{a_1}^{b} rL_0'(\mathbf{p}r)J_0(\mathbf{q^T}r)dr\end{aligned} \tag{A7}$$

$$\begin{aligned}\mathbf{H}* = [h*_{ij}] \quad &= \int_0^{a_0} rJ_1(\mathbf{p}r)J_1(\mathbf{q^T}r)dr + \int_{a_0}^{a_1} rL_1(\mathbf{p}r)J_1(\mathbf{q^T}r)dr \\ &+ \int_{a_1}^{b} rL_1'(\mathbf{p}r)J_1(\mathbf{q^T}r)dr\end{aligned} \tag{A8}$$

$$\begin{aligned}\mathbf{V} = [v_{ij}] \quad &= F_1(\mathbf{v}c)\int_0^{c} J_0(\mathbf{u}r)J_0(\mathbf{q^T}r)dr \\ &+ J_1(\mathbf{u}c)\mathbf{v}\mathbf{u}^{-1}\int_c^{b} rF_0(\mathbf{v}r)J_0(\mathbf{q^T}r)dr\end{aligned} \tag{A9}$$

$$\mathbf{N} = [n_{ij}] \quad = F_1(\mathbf{v}c)\int_0^c rJ_1(\mathbf{u}r)J_1(\mathbf{q}^{\mathbf{T}}r)dr \\ +\mu_7^{-1}J_1(\mathbf{u}c)\int_c^b rF_1(\mathbf{v}r)J_1(\mathbf{q}^{\mathbf{T}}r)dr \tag{A10}$$

$$\mathbf{E} = [e_{ij}] = \int_0^b rJ_0(\mathbf{q}r)J_0(\mathbf{q}^{\mathbf{T}}r)dr = \int_0^b rJ_1(\mathbf{q}r)J_1(\mathbf{q}^{\mathbf{T}}r)dr \tag{A11}$$

References

1. Aamir, M.; Giasin, K.; Tolouei-Rad, M.; Vafadar, A. A review: Drilling performance and hole quality of aluminium alloys for aerospace applications. *J. Mater. Res. Technol.* **2020**, *9*, 12484–12500. [CrossRef]
2. Ye, C.; Udpa, L.; Udpa, S. Optimization and Validation of Rotating Current Excitation with GMR Array Sensors for Riveted Structures Inspection. *Sensors* **2016**, *16*, 1512. [CrossRef]
3. Gupta, M.; Khan, M.A.; Butola, R.; Singari, R.M. Advances in applications of Non-Destructive Testing (NDT): A review. *Adv. Mater. Process. Technol.* **2022**, *8*, 2286–2307. [CrossRef]
4. Mevissen, F.; Meo, M. Nonlinear Ultrasound Crack Detection with Multi-Frequency Excitation—A Comparison. *Sensors* **2021**, *21*, 5368. [CrossRef]
5. Xie, L.; Gao, B.; Tian, G.Y.; Tan, J.; Feng, B.; Yin, Y. Coupling pulse eddy current sensor for deeper defects NDT. *Sens. Actuators A Phys.* **2019**, *293*, 189–199. [CrossRef]
6. Chen, X.; Ye, Z.; Xia, J.Y.; Wang, J.X.; Ji, B.H. Double-probe ultrasonic detection method for cracks in steel structure. *Appl. Sci.* **2020**, *23*, 8436. [CrossRef]
7. Le, M.; Le, D.V.; Le, T.D.; Lee, J. Ultrasonic testing of rivet in multilayer structure using a convolutional neural network on edge device. *Sci. Prog.* **2023**, *106*, 368504231177551. [CrossRef]
8. Chan, H.; Masserey, B.; Fromme, P. High frequency guided ultrasonic waves for hidden fatigue crack growth monitoring in multi-layer model aerospace structures. *Smart Mater. Struct.* **2015**, *24*, 025037. [CrossRef]
9. Lindgren, E.; Aldrin, J.C.; Jata, K.; Scholes, B.; Knopp, J. Ultrasonic plate waves for fatigue crack detection in multi-layered metallic structures. In Proceedings of the 14th International Symposium on Smart Structures and Materials & Nondestructive Evaluation and Health Monitoring, San Diego, CA, USA, 19–22 March 2007; International Society for Optics and Photonics: Bellingham, WA, USA, 2007; Volume 6532, p. 53207.
10. Najarre, I.; Kostson, E.; Fromme, P. Guided ultrasonic waves for the monitoring of hidden fatigue crack growth in multi-layer aerospace structures. In Proceedings of the Health Monitoring of Structural and Biological Systems 2014, San Diego, CA, USA, 9–13 March 2014; International Society for Optics and Photonics: Bellingham, WA, USA, 2014; Volume 9064, pp. 634–640.
11. Yang, Q.; Xie, S.; He, K.; Chen, Y.-E.; Chen, Z.; Uchimoto, T.; Takagi, T. A novel circumferential eccentric eddy current probe and its application for defect detection of small-diameter tubes. *Sens. Actuators A Phys.* **2021**, *331*, 113023. [CrossRef]
12. Wang, Z.D.; Gu, Y.; Wang, Y.S. A review of three magnetic NDT technologies. *J. Magn. Magn. Mater.* **2012**, *324*, 382–388. [CrossRef]
13. Rifai, D.; Abdalla, A.N.; Ali, K.; Razali, R. Giant magnetoresistance sensors: A review on structures and non-destructive eddy current testing applications. *Sensors* **2016**, *16*, 298. [CrossRef]
14. Faraj, M.A.; Samsuri, F.; AbdAlla, A.N.; Rifai, D.; Ali, K.; Al-Douri, Y. Hybrid GMR/IR probe to reduce the effects of lift-off. *Meas. Control* **2019**, *52*, 588–598. [CrossRef]
15. Bernieri, A.; Ferrigno, L.; Laracca, M.; Rasile, A. Eddy current testing probe based on double-coil excitation and GMR sensor. *IEEE Trans. Instrum. Meas.* **2019**, *68*, 1533–1542. [CrossRef]
16. Nguyen, H.-T.; Jeng, J.-T.; Doan, V.-D.; Dinh, C.-H.; Trinh, X.T.; Dao, D.-V. Detection of Surface and Subsurface Flaws with Miniature GMR-Based Gradiometer. *Sensors* **2022**, *22*, 3097. [CrossRef]
17. Bailey, J.; Long, N.; Hunze, A. Eddy current testing with giant magnetoresistance (GMR) sensors and a pipe-encircling excitation for evaluation of corrosion under insulation. *Sensors* **2017**, *17*, 2229. [CrossRef]
18. Betta, G.; Ferrigno, L.; Laracca, M.; Rasile, A.; Sangiovanni, S. A novel TMR based triaxial eddy current test probe for any orientation crack detection. *Meas. J. Int. Meas. Confed.* **2021**, *181*, 109617. [CrossRef]
19. Yang, F.; He, Y.; Fan, X.; Chen, T.; Zhang, T.; Ma, B. A flexible eddy current TMR sensor for monitoring internal fatigue crack. *Sensors* **2023**, *23*, 9507. [CrossRef]
20. Dodd, C.V.; Deeds, W.E. Analytical solutions to eddy-current probe-coil problems. *J. Appl. Phys.* **1968**, *39*, 2829–2838. [CrossRef]
21. Theodoulidis, T.P.; Kriezis, E.E. *Eddy Current Canonical Problems (with Applications to Nondestructive Evaluation)*; Tech Science Press: Forsyth, GA, USA, 2006.
22. Sakkaki, F.; Bayani, H. Solution to the problem of E-cored coil above a layered half-space using the method of truncated region eigenfunction expansion. *J. Appl. Phys.* **2012**, *111*, 07E717. [CrossRef]
23. Li, Y.; Liu, Z.; Yan, B.; Wang, Y.; Zainal Abidin, I.M.; Chen, Z. A funnel-shaped probe for sensitivity enhancement in pulse-modulation eddy current inspection of subsurface flaws in conductors. *Sens. Actuators A Phys.* **2020**, *307*, 111991. [CrossRef]
24. Smetana, M.; Gombarska, D.; Psenakova, Z. Progress in evaluation of deep artificial defects from sweep-frequency eddy-current testing signals. *Sensors* **2023**, *23*, 6085. [CrossRef] [PubMed]
25. Lee, K.H.; Baek, M.K.; Park, I.H. Estimation of deep defect in ferromagnetic material by low frequency eddy current method. *IEEE Trans. Magn.* **2012**, *48*, 3965–3968. [CrossRef]

26. Zhang, S.; Ye, C. Model of ferrite-cored driver-pickup coil probe application of TREE method for eddy current nondestructive evaluation. *Appl. Comput. Electromagn. Soc. J.* **2022**, *37*, 632–638. [CrossRef]
27. Yu, Y.; Gao, K.; Liu, B.; Li, L. Semi-analytical method for characterization slit defects in conducting metal by Eddy current nondestructive technique. *Sens. Actuators A Phys.* **2020**, *301*, 111739. [CrossRef]
28. Lu, Y.; Bowler, J.R.; Theodoulidis, T.P. An analytical model of a ferrite-cored inductor used as an eddy current probe. *J. Appl. Phys.* **2012**, *111*, 103907. [CrossRef]
29. Zhang, S. Analytical model of a T-core coil above a multi-layer conductor with hidden hole using the TREE method for nondestructive evaluation. *COMPEL Int. J. Comput. Math. Electr. Electron. Eng.* **2021**, *40*, 1104–1117. [CrossRef]
30. Tytko, G.; Dziczkowski, L. An analytical model of an I-cored coil with a circular air gap. *IEEE Trans. Magn.* **2017**, *53*, 1–4. [CrossRef]
31. Tytko, G.; Dziczkowski, L. E-cored coil with a circular air gap inside the core column used in eddy current testing. *IEEE Trans. Magn.* **2015**, *51*, 1–4. [CrossRef]
32. Zhang, S. An analytical model of a new T-cored coil used for eddy current nondestructive evaluation. *Appl. Comput. Electromagn. Soc. J.* **2020**, *35*, 1099–1104. [CrossRef]
33. Yan, S.; Chen, X. Time-domain analytical solutions to pulsed eddy current model of moving cylindrical conductor. *NDT E Int.* **2023**, *137*, 102863. [CrossRef]
34. Tytko, G.; Yin, W.; Luo, Y.; Adamczyk-Habrajska, M. Eddy current testing of conductive tubes with the employment of the I-core sensor. *IEEE Access* **2024**, *12*, 25525–25535. [CrossRef]
35. Dellnitz, M.; Schütze, O.; Zheng, Q. Locating all the zeros of an analytic function in one complex variable. *J. Comput. Appl. Math.* **2002**, *138*, 325–333. [CrossRef]
36. Vasic, D.; Ambrus, D.; Bilas, V. Computation of the eigenvalues for bounded domain eddy-current models with coupled regions. *IEEE Trans. Magn.* **2016**, *52*, 1–10. [CrossRef]
37. Mehtre, V.V. Root finding methods: Newton raphson method. *Int. J. Res. Appl. Sci. Eng. Technol.* **2019**, *7*, 411–414. [CrossRef]
38. Tytko, G.; Dawidowski, Ł. Locating complex eigenvalues for analytical eddy-current models used to detect flaws. *COMPEL Int. J. Comput. Math. Electr. Electron. Eng.* **2019**, *38*, 1800–1809. [CrossRef]
39. Theodoulidis, T.; Skarlatos, A.; Tytko, G. Computation of eigenvalues and eigenfunctions in the solution of eddy current problems. *Sensors* **2023**, *23*, 3055. [CrossRef]

energies

MDPI

Article

A Two-Stage Corrosion Defect Detection Method for Substation Equipment Based on Object Detection and Semantic Segmentation

Zhigao Wang [1], Xinsheng Lan [1] , Yong Zhou [2] , Fangqiang Wang [1], Mei Wang [2,*], Yang Chen [3], Guoliang Zhou [3] and Qing Hu [3]

[1] State Grid Sichuan Electric Power Research Institute, Chengdu 610041, China; wzg33@163.com (Z.W.); zjocean123@163.com (X.L.); chrisscu@163.com (F.W.)
[2] College of Mechanical Engineering, Sichuan University, Chengdu 610065, China; zhouyong0905@stu.scu.edu.cn
[3] State Grid Yibin Power Supply Company, Yibin 644000, China; chenyanggg123@126.com (Y.C.); guoliangzhou1010@163.com (G.Z.); qinghuu5566@163.com (Q.H.)
* Correspondence: wangmei@scu.edu.cn

Abstract: Corrosion defects will increase the risk of power equipment failure, which will directly affect the stable operation of power systems. Although existing methods can detect the corrosion of equipment, these methods are often poor in real-time. This study presents a two-stage detection approach that combines YOLOv8 and DDRNet to achieve real-time and precise corrosion area localization. In the first stage, the YOLOv8 network is used to identify and locate substation equipment, and the detected ROI areas are passed to the DDRNet network in the second stage for semantic segmentation. To enhance the performance of both YOLOv8 and DDRNet, a multi-head attention block is integrated into their algorithms. Additionally, to address the challenge posed by the scarcity of corrosion defect samples, this study augmented the dataset using the cut-copy-paste method. Experimental results indicate that the improved YOLOv8 and DDRNet, incorporating the multi-head attention block, boost the mAP and mIoU by 5.8 and 9.7, respectively, when compared to the original method on our self-built dataset. These findings also validate the effectiveness of our data augmentation technique in enhancing the model's detection accuracy for corrosion categories. Ultimately, the effectiveness of the proposed two-stage detection method in the real-time detection of substation equipment corrosion defects is verified, and it is 48.7% faster than the one-stage method.

Keywords: substation equipment; corrosion defect detection; object detection; semantic segmentation

1. Introduction

With the increasing number of substations, ensuring the continuous and stable operation of substation equipment has become the key to maintaining the stability of the power system. These devices are exposed to the changing climate and environment for a long time, and they are affected by humidity, temperature changes, rainfall, and pollutants, which will gradually corrode, thereby reducing the performance and reliability of the equipment. Currently, the supervision and maintenance of substations mainly rely on manual inspection, although this process has been relatively perfect, but there are still problems of low efficiency and high cost. Therefore, there is an urgent need to develop an intelligent, automated corrosion area detection technology to improve inspection efficiency and quality, as well as ensure the smooth operation of the power system.

Currently, research on the corrosion detection of substation equipment mainly focuses on the corrosion detection of grounding networks [1–3]. Common methods include the ultrasonic method [4], electromagnetic method [5], and electrochemical method [6]. However, there are fewer studies on the corrosion detection of other equipment in substations

(e.g., transformers, capacitors, mutual inductors, disconnect switches and circuit breakers). Therefore, this paper aims to explore a corrosion detection algorithm with wider applicability. In recent years, machine vision inspection algorithms have made significant progress in the field of surface defect detection [7–12] and have received widespread attention due to their non-contact detection means and low cost. Therefore, this paper attempts to solve the problem of detecting corroded areas in substations using vision sensor-based artificial intelligence algorithms. Object detection [7,13] and semantic segmentation [14,15] are the two most common types of algorithms in the field of machine vision.

Object detection algorithms are now widely used in industrial production, which can be divided into two categories: one-stage networks and two-stage networks. The representative networks of two-stage networks are the RCNN series [16,17]. The task of two-stage networks is usually divided into two steps: first using the region proposal algorithm to generate candidate regions that may contain objects and then carrying out accurate coordinate regression and classification of these candidate regions. In contrast, one-stage object detection networks directly perform dense prediction of the entire image without an intermediate step of generating candidate regions, thus allowing direct determination of the location, size, and class of the detected target. Representative models of such networks are the YOLO series [18–20] and the SSD series [21], among others. Since one-stage object detection networks do not need to generate candidate regions, detection time is saved. This method can achieve real-time detection while ensuring detection accuracy, thus becoming an important research direction for the current defect detection of substation equipment. In this paper, the latest YOLOv8 network is selected as the object detection network.

Semantic segmentation is able to classify each pixel in an image and therefore accurately identify the boundaries and shape of corroded areas. This is important for determining the extent and location of corrosion on metal surfaces. The current mainstream semantic segmentation algorithms can be categorized as encoder–decoder structure, image pyramid structure, and two-branch structure. The encoder–decoder structure is represented by U-Net [22], which tends to be symmetric, connects the encoder and decoder parts through jump connections to improve the ability to capture details, and is widely used in medical image segmentation. The image-pyramid-based structure is represented by the DeepLab family [23,24], which uses dilated convolution and null-space pyramid pooling to capture contextual information at multiple scales, thus improving the accuracy of segmentation. Semantic segmentation algorithms with a two-branch structure, represented by DDRNet [25], usually include a main branch for extracting high-level semantic information, which focuses on global contextual information. And a secondary branch for extracting detailed features is used to ensure that the detailed parts of the segmentation results are accurately processed. The two-branch design allows the network to balance segmentation accuracy and real-time performance, which is suitable for scenarios that require fast processing. The timely detection and treatment of corrosion problems can avoid further deterioration of the corrosion problem, thus reducing the cost of large-scale repair or replacement.

Although the two-branch semantic segmentation network already has good real-time performance, the substation monitoring image contains a lot of noise information other than the equipment to be detected, such as the sky, the road, some equipment that does not corrode, etc. In order to solve the problem, this paper tries to use a two-stage detection method. Detecting these regions will consume a certain amount of time, which affects the real-time performance of the detection system. In order to solve this problem, this paper tries to adopt a two-stage detection method, i.e., firstly, we use the target detection algorithm to find out the region of interest (ROI) in the monitoring image and the pixel regions of the equipment to be detected, and then we feed the ROI into the semantic segmentation network for local detection. Since the computational complexity of the object detection algorithm is much lower than that of the semantic segmentation algorithm, the two-stage detection method will save a lot of time compared to the pixel-by-pixel detection of the whole image using only the semantic segmentation algorithm. The

object detection and semantic segmentation networks used in this paper are YOLOv8 and DDRNet [25], respectively.

In substation environments, the background is complex and diverse, and a variety of disturbing factors may be present. Meanwhile, corrosion defects may have different scales and shapes. In order to improve the performance of the algorithm in this situation, this paper introduces multi-head attention block in YOLOv8 and DDRNet, which helps the models to distinguish between corrosion defects and background noise and improves the performance of the detection system in complex environments. Adaptively handling features of different scales makes the model performance more robust and stable when facing different types of defects. In addition, in order to solve the difficult problem of collecting samples of corrosion defects, we intercepted the corroded areas from devices with corrosion and pasted them on uncorroded devices, thus expanding the samples of corrosion defects. Through experimental validation on the self-constructed dataset, the proposed two-stage detection method yielded better real-time performance and higher accuracy than the semantic segmentation algorithm alone in locating the corroded areas in substations. Meanwhile, the improved versions of YOLOv8 and DDRNet were found to be more suitable for substation scenarios compared to the original networks. Finally, we determined that the designed data enhancement method can effectively improve the accuracy of the model for corrosion detection.

The main contributions of this paper can be summarized in the following three points:

1. A two-stage detection method that fuses target detection and semantic segmentation is proposed to measure real-time substation corrosion regions.
2. A multi-head attention block is used to optimize the original YOLOv8 and DDRNet networks to make them more suitable for substation scenarios.
3. A cut-copy-paste data enhancement method is designed to expand the samples of corrosion defects.

2. Related Work

In recent years, the You Only Look Once (YOLO) family and two-branch semantic segmentation network have been widely used in many fields. This section will review the representative achievements.

2.1. You Only Look Once

The YOLO model has high detection speed and can detect objects in real-time video streams. This is because unlike traditional object detection methods such as the R-CNN family, YOLO uses an end-to-end training approach that treats object detection as a regression problem, mapping directly from image pixels to bounding boxes and class probabilities, thus simplifying the training and reasoning process. This makes YOLO particularly suitable for application scenarios that require fast response. In addition, compared to some other advanced target detection methods, YOLO's models are typically smaller and can be more easily deployed on resource-constrained devices, such as mobile devices and embedded systems.

Due to the powerful performance of YOLO, it is used in many fields. The work in [26] presented an improved YOLOv4-Tiny algorithm for surface crack detection. The work in [27] integrated YOLOv5 into inflated 3D models that can be used for human activity recognition. In [26], a lightweight infrared object detection model G-YOLO-based on UAV was proposed. YOLO has also emerged in power inspection work, such as transmission line corridor external damage risk detection [28], insulator defect detection [29–31], and wind turbine blade damage detection [32]. In particular, YOLOv8, as a relatively new framework of the YOLO series, is relatively more efficient in terms of computing resources and memory consumption, so a large number of studies have begun to try to apply it to real-world scenarios. The work in [33] utilized the improved YOLOv8 algorithm in conjunction with an infrared image slicing-assisted hyper-inference technique to automatically detect Inter-Turn Short Circuit fault traces in dry-type transformers. The work in [34] presented an improved

YOLOv8-based object detection algorithm for infrared images of substation equipment. The work in [35] introduced a road indicator detection model using the advanced features of YOLOv8. The work in [36] proposed an efficient small-target YOLO detection model based on YOLOv8 for Unmanned Aerial Vehicle object detection.

2.2. Two-Branch Semantic Segmentation Network

The two-branch semantic segmentation network is a deep learning model architecture that shows significant advantages in semantic segmentation tasks. A two-branch network usually contains a low-level feature branch and a high-level feature branch, where the high-level feature branch usually contains rich contextual information, while the low-level feature branch contains more detailed local information. The model uses a two-branch structure, which is able to find a balance between details and global context. Moreover, the design can effectively integrate multi-scale features so as to improve the recognition ability of the model to different scale targets.

Because of its good real-time performance, the two-branch network has been applied in the fields of automatic driving [37,38], remote sensing image analysis [39,40], and medical impact analysis [41,42]. Specifically, in autonomous vehicles, the two-branch network is used to identify roads, pedestrians, vehicles, traffic signs, etc., to help the vehicle understand the surrounding environment and make safe driving decisions. The application of two-branch semantic segmentation network in remote sensing image analysis can significantly improve the semantic segmentation accuracy of high-resolution images. Through the fusion of multi-scale features, the network can better cope with complex scenes and diversified task requirements. In the medical field, the two-branch network is used to analyze images to help doctors quickly and accurately identify and segment lesions, organs, etc., to assist diagnosis and treatment. DDRNet is a relatively new two-branch semantic segmentation network, which has been adapted by many researchers to better suit their specific tasks. In [43] DDRNet was used for real-time segmentation in unstructured environments to enable autonomous navigation for off-road robots. The use of DDRNet in [44] was used for automated driving assistance to cope with the complexity of road scenarios and the real-time requirements of segmentation algorithms in application scenarios. The work of [45,46] used DDRNet to sense the environment for the automatic unloading of outdoor forklifts.

Through a review of the above work, we can see that YOLOv8 and DDRNet stand out in many fields with their high-precision computation, compact network model, and excellent high-resolution image processing capabilities. In the particular scenario of substation inspection, in addition to high precision, the real-time performance of the algorithm is also very high. At the same time, in order to ensure refined inspection, an on-board camera and monitoring probe equipped with the substation inspection robot offer relatively high resolution.

Because YOLOv8 and DDRNet can effectively address these challenges, we chose them as the benchmark models for this work.

3. Materials and Methods

In this section, we first describe the dataset in the experiment and the corresponding data enhancement method. Then, the proposed two-stage substation corrosion defect detection method is presented, where each stage is described in a subsection. Finally, the multi-head attention mechanism block used to improve the semantic segmentation algorithm is presented.

3.1. Dataset and Data Enhancement Strategies

The image dataset used in this paper is composed of 7215 corrosion images taken by substation staff, intelligent inspection robots, and light-load head. The maximum resolution of the image is 4032 $\times$ 3024, the minimum is 2048 $\times$ 1024, and the image data were divided into a training set (5050 images), a verification set (722 images), and a test set

(1443 images) in a ratio of 7:1:2. Labelme was used to mark the equipment to be tested in each picture in the form of a rectangle. In this work, there were five types of equipment that we tested, namely, cooling fin (CF), oil storage tank (OST), disconnecting switch (ds), circuit breaker (CB), and flange. Then, based on the boundary box of each marked object in the annotation file, it was cut out from the picture, and then labelme was used to carry out pixel-level boundary annotation. The semantic segmentation employed one more category, i.e., corrosion and then object detection.

We counted the number of instances of each type of marked object and the proportion of pixels occupied by each type of object. The statistical results are shown in Figure 1. As can be seen from Figure 1b, the corrosion area accounts for 0.9% of the whole dataset, accounting for the smallest proportion and 29.9% lower than the OST, having the highest proportion. Serious data imbalance will inevitably bring difficulty to the training of the model. To solve this problem, we proposed to use the cut-copy-paste method to expand the corroded sample. That is, a corrosion area is cut from the corroded equipment and then pasted onto the non-corroded equipment. In the process of capturing, the input original image and the corresponding label are captured at the same time, which can save the time of relabeling. It should be noted that only similar devices can cut and paste each other, which is done to maintain the fidelity of the corroded area. The sample augmented by this method is shown in Figure 2.

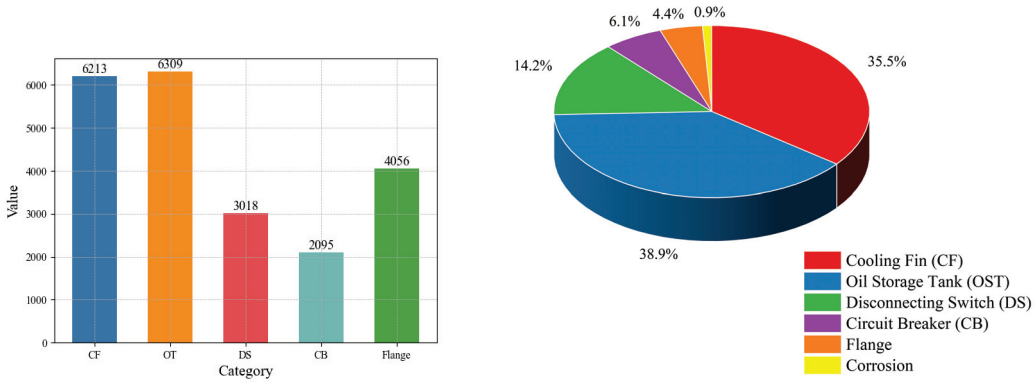

(**a**) (**b**)

Figure 1. Dataset statistics for each category. (**a**) Number of instances per category. (**b**) The proportion of pixels occupied by each category.

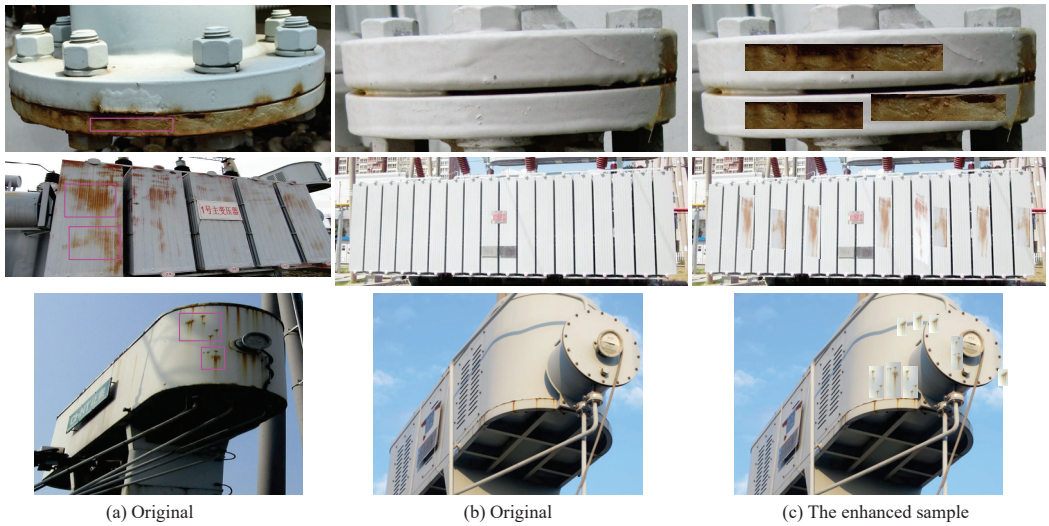

(a) Original (b) Original (c) The enhanced sample

Figure 2. Diagram of corrosion sample enhancement. (**c**) is from the fusion of (**a**,**b**).

3.2. YOLOv8 Model Structure

In the first stage, we adopted the object detection algorithm YOLOv8. As the latest one-stage object detection algorithm, YOLOv8 has the advantages of high real-time performance, multi-scale detection, and global context information utilization, which is suitable for substation equipment corrosion defect detection task. YOLOv8 uses a lightweight backbone network and a series of optimization strategies to achieve fast and accurate target detection. The architecture of YOLOv8 can be divided into three key components: backbone, neck, and head, as shown in Figure 3. In the backbone stage, YOLOv8 integrates depthwise separable convolutions to improve computational efficiency and feature extraction capabilities. In the neck part, path aggregation network structure is used to improve feature fusion and capture spatial context information, which help the model better detect targets at different scales. In terms of the head, the anchor-free method is introduced to directly predict the bounding box of the target without relying on a predefined anchor, and the decoupling head structure is adopted so that the classification task and the regression task can be processed independently. The network structure of YOLOv8 is shown in Figure 3.

In this paper, in order to further improve the detection performance of YOLOv8 in the substation environment, we added a multi-head attention block (MHAB) in front of the YOLOv8 decoupling head. This improvement aims to provide a finer focus on different features, allowing the model to better capture complex features and details in the substation environment. This mechanism helps to enhance the adaptability of the model in the face of multiple substation equipment and their different states, and it ultimately improves the accuracy and robustness of the detection. The addition of MHAB to YOLOv8 is shown in Figure 3.

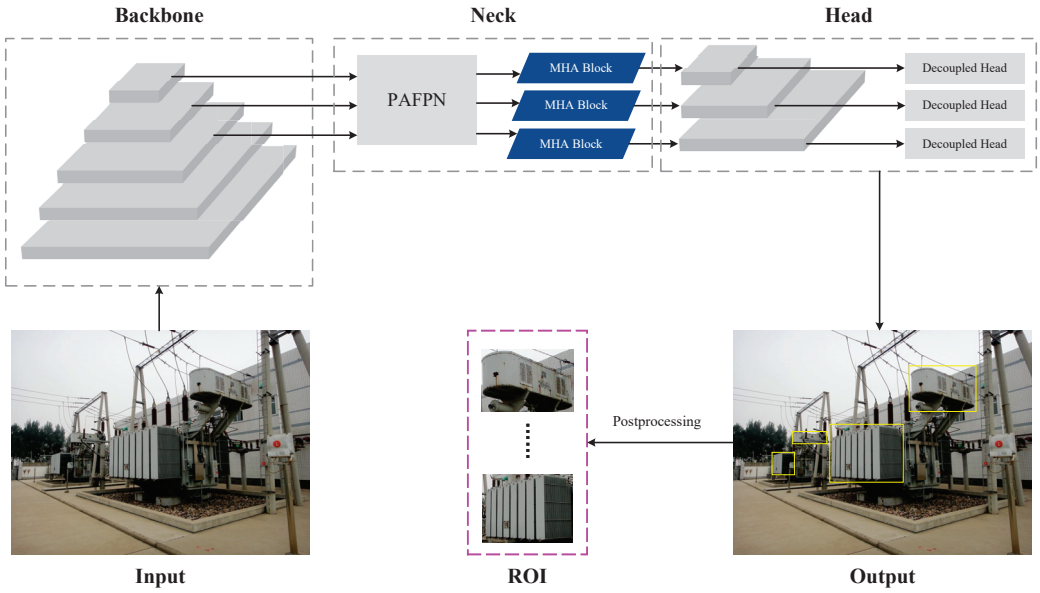

Figure 3. The improved YOLOv8 network structure, in which the gray part is the original YOLOv8, and the module filled in blue is the newly added multi-head attention block (MHAB).

3.3. DDRNet Model Structure

The semantic segmentation network used in this work is DDRNet, which is composed of one high-resolution branch and one low-resolution branch, and it aims to extract high-resolution global feature information and high-level semantic details simultaneously. Suppose the output feature graph of a high-resolution branch is F_p, which can be expressed as

$$F_p = f_p(I; \theta_p), \tag{1}$$

where f_p is the network function of the main branch, θ_p is the parameter of the high-resolution branch, $I \in \mathbb{R}^{H \times W \times C}$ is the input image, H is the image height, W is the image width, and C is the number of channels of the image. Suppose that the output feature chart of a low-resolution branch is F_a, which can be expressed as

$$F_a = f_a(I; \theta_a), \tag{2}$$

where f_a is the network function of the main branch, and θ_a is the parameter of the high-resolution branch. The feature graph of the two branches is fused directly using addition. The fused feature graph F_f can be expressed as

$$F_f = Add(F_p, F_a) \tag{3}$$

Finally, the fused feature map is mapped to the category label of each pixel through a segmentation head. Assuming that the output segmentation result is S, it can be expressed as

$$S = h(F_f; \theta_s) \tag{4}$$

where h is a function of segmentation head, and θ_s is parameter of segmentation head.

The design of two-branch semantic segmentation network makes it have both strong performance and excellent real-time performance. Therefore, this work used DDRNet as the benchmark network. However, the surveillance video and image of substation contain a lot of information, involving equipment, environment, personnel, and other aspects, so background noise and interference may affect the detection effect. To solve this problem, we added a multi-head attention block (MHAB) to DDRNet to form our improved version of DDRNet. An overview of the improved DDRNet and its parameter details are shown in Figure 4 and Table 1.

The original DDRNet is mainly composed of resdidual blocks and resdidual bottleneck blocks. We only inserted the MHAB in the high-resolution branch, because the feature map in the high-resolution branch contains more information and is more conducive to extracting the contour information of the target. The precise location of the MHAB in the improved version of DDRNet is shown in Figure 4. In addition, the space pyramid pool (SPP) uses DDRNet's original deep aggregation pyramid pool module.

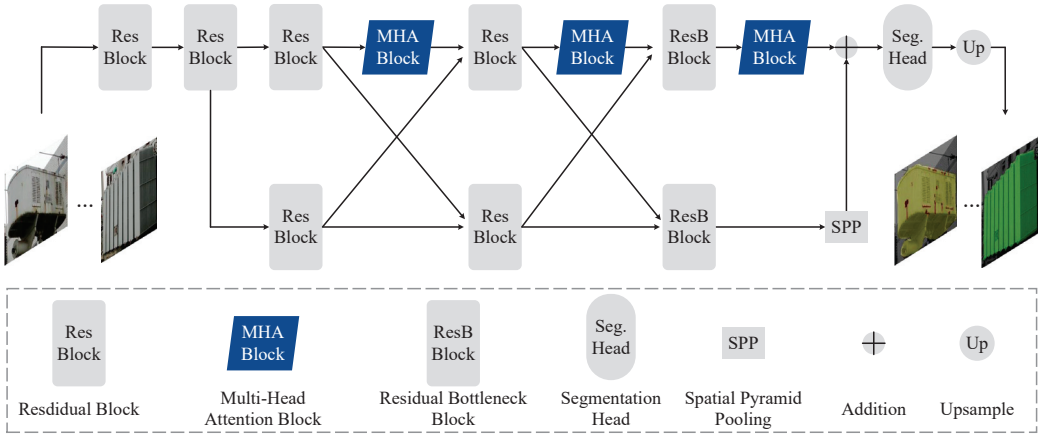

Figure 4. An overview of the proposed improved version of DDRNet. These different shaped markers are used to represent individual modules, where the blue filled module is the newly added attention mechanism module. Explanations of these shapes are found in the dashed box below this figure.

Table 1. Details the architecture of the improved DDRNet. The improved version of DDRNet in this table assumes an image size of 896 × 896 × 3 as input. *N* in the table indicates the number of types of objects to be detected.

Stage	Output	DDRNet	
1	448 × 448	3 × 3, 32, stride 2	
	224 × 224	3 × 3, 32, stride 2	
	224 × 224	$\begin{bmatrix} 3\times3, 32 \\ 1\times1, 32 \end{bmatrix} \times 2$	
	112 × 112	$\begin{bmatrix} 3\times3, 64 \\ 1\times1, 64 \end{bmatrix} \times 2$	
2	112 × 112, 56 × 56	$\begin{bmatrix} 3\times3, 64 \\ 1\times1, 64 \end{bmatrix} \times 2$	$\begin{bmatrix} 3\times3, 128 \\ 1\times1, 128 \end{bmatrix} \times 2$
		MHAB	–
3	112 × 112, 28 × 28	$\begin{bmatrix} 3\times3, 64 \\ 1\times1, 64 \end{bmatrix} \times 2$	$\begin{bmatrix} 3\times3, 256 \\ 1\times1, 256 \end{bmatrix} \times 2$
		MHAB	–
4	112 × 112, 14 × 14	$\begin{bmatrix} 1\times1, 64 \\ 3\times3, 64 \\ 1\times1, 128 \end{bmatrix} \times 2$	$\begin{bmatrix} 1\times1, 256 \\ 3\times3, 256 \\ 1\times1, 512 \end{bmatrix} \times 2$
		MHAB	SPP
5	112 × 112	Addition	
	112 × 112	$\begin{bmatrix} 3\times3, 64 \\ 1\times1, N \end{bmatrix}$	
	896 × 896	Bilinear Upsampling	

3.4. Multi-Head Attention Block

The structure of the Muti-Head Attention Block is shown in Figure 5. The central idea of the multi-head attention mechanism is that multiple "attention heads" process different parts of information in parallel to capture different features and relationships. Each "head" can be thought of as an independent attention mechanism that learns and focuses on different aspects of the input data in different subspaces. First, for the input, we map it to different Query, Key, and Value vectors through linear transformations. For the ith attention head, we have the query vector $Q_i = XW_i^Q$, the key vector $K_i = XW_i^K$, and the value vector $V_i = XW_i^V$, where W_i^Q, W_i^K, and W_i^V define the weight matrix corresponding to each attention head. For each attention head i, we calculate the attention weight. The dot product of the query vector and the key vector are first calculated; they are then scaled and converted to a probability distribution by the softmax function. The formula is

$$Attention\_Scores_i = \frac{Q_i K_i^T}{\sqrt{d_k}}, \tag{5}$$

where d_k is the dimension of the key vector (usually $d_k = d_{\mathrm{model}}/h$, where h is the number of attention heads). Then, we apply the softmax function:

$$Attention\_Weights_i = soft\max(Attention\_Scores_i) \tag{6}$$

Next, we use the calculated attention weight to weight the value vector:

$$Output_i = Attention\_Weights_i V_i \tag{7}$$

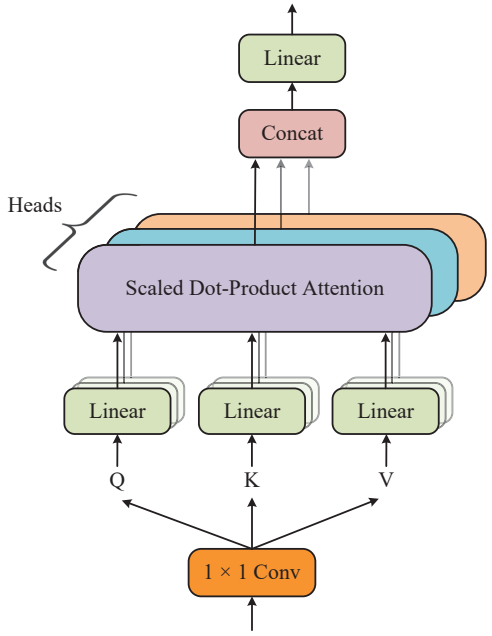

Figure 5. Schematic diagram of the multi-head attention mechanism.

4. Experiments and Analyses

4.1. Implementation Details

The operating system used for the experiments was Windows 10, and Pytorch 2.1 and GPU acceleration were used for training and testing. The GPU model was NVIDIA GeForce RTX 4060 (8 G); the software environments were Anaconda3, Cuda12.2, and Python 3.9; and the development tool was PyCharm Community Edition 2022.2.2.

In the proposed method, the training processes of the target detection and semantic segmentation were independent of each other, and the loss functions involved in the training process of both are described below. In the training process of target detection, the loss function was divided into two types: a classification loss function and a bounding box loss function. In YOLOv8, the classification loss function uses the cross-entropy loss. The bounding box loss function uses a combination of a Distribution Focal Loss (DFL) loss function and a CIOU loss function, where the DFL calculates the offsets from the center of the anchor point to the upper-left and lower-right corners, and the CIOU calculates the localization loss of the positive samples only.

To ensure that the training can be carried out smoothly, the initial learning rate for substation equipment type identification using the YOLOv8 network in the first stage was set to 0.005, while in the second stage, the initial learning rate for equipment and corrosion defect segmentation using the DDRNet network was set to 0.0005. In both stages, the number of epochs was set to 500. The Adam function was used as the optimization function in both stages. The image size for training and testing was uniformly reduced to 1500×1500.

4.2. Evaluation Indicators

This section introduces the evaluation indicators used in the experiment, which are defined as follows:

Mean Average Precision (mAP) is a common evaluation index used in object detection tasks to measure the performance of a model in detecting different types of objects. For each category of targets, we first need to calculate the Precision and Recall of that category. The accuracy rate represents the proportion of correctly predicted positive samples to all predicted positive samples, and the recall rate is the proportion of correctly predicted positive samples to all true positive samples. By changing the confidence threshold of the detection model, different Precision rates and Recall rates can be obtained to form a

precision–recall (PR) Curve. AP is the area under the entire PR curve, and the PR curve is generally integrated to calculate the area. After calculating the AP in all categories, the AP of all categories is averaged to obtain mAP. The formula is

$$mAP = \frac{1}{N}\sum_{i=1}^{N} AP_i \tag{8}$$

where N is the total number of categories, and AP_i is the AP value of the i-th category.

Mean pixel accuracy ($mAcc$) is the ratio between the number of pixels correctly classified by the model and the total number of pixels, which is defined as follows:

$$Acc = \frac{T_p + T_n}{T_p + T_n + F_p + F_n} \tag{9}$$

$$mAcc = \sum Acc/N \tag{10}$$

In this equation, N represents the number of categories in the semantic segmentation task, T_p means true positive, T_n means true negative, F_p means false positive, and F_n means false negative.

Mean Intersection over Union ($mIoU$) measures the degree of overlap between the predicted and true regions, while ($mIoU$) is the average of all categories of (IoU). For each category, the (IoU) is calculated as follows:

$$IoU = \frac{T_p}{T_p + F_p + F_n} \tag{11}$$

where the meanings of T_p, F_p, and F_n are the same as above. After calculating the (IoU) for each category, we take the average of these IoU values to obtain the ($mIoU$):

$$mIoU = \sum IoU/N \tag{12}$$

4.3. Comparison with Existing Methods

In order to verify the effectiveness and advantages of the proposed method, we compared it with existing target detection and semantic segmentation algorithms. The mainstream object detection algorithms Sparse R-CNN [47], Faster RCNN, and YOLOX [18], as well as the semantic segmentation algorithms DeepLabV3 [48], Mask2Former [49], UNet [22], and DDRNet, were selected for comparison. All algorithms were fully trained on self-built datasets. Due to space constraints, only the variation in the loss function of our methods (i.e., YOLOv8 and DDRNet with MHAB inserted) during the training process is shown here, as shown in Figure 6. The final experimental results are shown in Tables 2 and 3. The results show that the performance of YOLOv8 and DDRNet improved by MHAB was the best. Specifically, YOLOv8 with MHAB improvement performed 4.6% better on the mAP than the YOLOv8 without improvement, as shown in Table 2; DDRNet with MHAB improvements performed 4.3% better on mIoU and 6.3% better on mACC than DDRNet without improvements, as shown in Table 3.

Table 2. Comparative experiments with existing object detection algorithms.

Method	mAP
Sparse R-CNN	53.46
YOLOX	48.97
Faster R-CNN	37.25
YOLOv8	56.53
YOLOv8 & MHAB	59.18

Table 3. Comparative experiments with existing semantic segmentation algorithms.

Method	mIoU	mACC
DeepLabV3	70.83	75.76
UNet	65.48	67.62
Mask2Former	73.94	74.28
DDRNet	72.24	73.95
DDRNet & MHAB	75.36	78.64

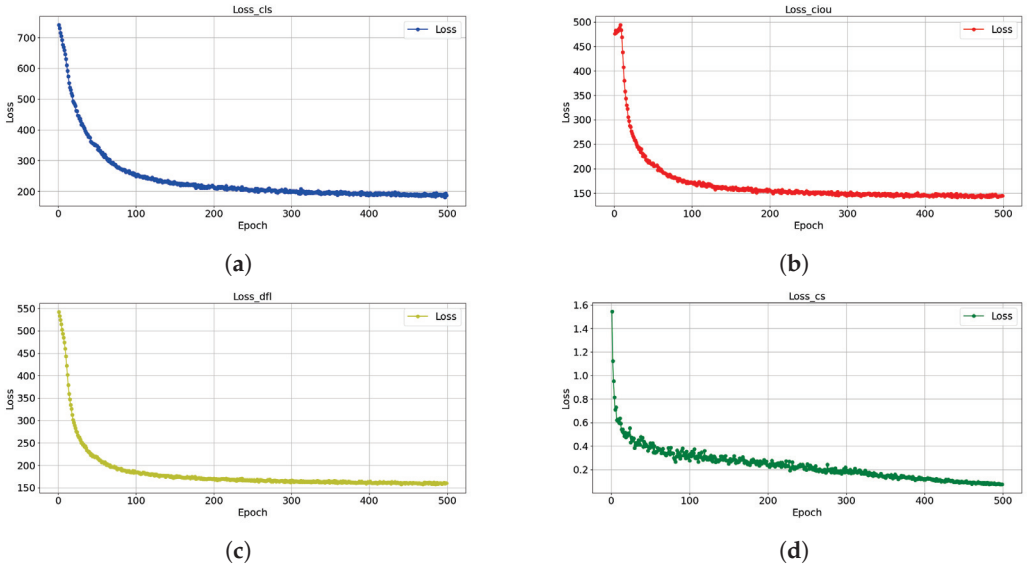

Figure 6. Variation trend of the loss function involved in the experiment. (**a**) Loss of object detection classification. (**b**) Loss of object detection CIOU. (**c**) Object detection DFL loss function. (**d**) Semantic segmentation cross entropy loss function.

4.4. Ablation Experiment

The purpose of this part was to verify the validity of the proposed data enhancement method. We first trained with the unenhanced dataset and then retrained the model with the enhanced dataset. The algorithm used was DDRNet modified by MHAB. The results of the two training sessions are shown in Table 4. It can be seen that although the algorithm improvement after data enhancement training was not obvious in the non-corrosive category of IoU (CF, OST, DS, CB, and flange), the performance of the network after data enhancement training was 23.37% and 24.24% higher than that of the network without data enhancement training in the Corrosion category of IoU and ACC, respectively. Therefore, the experiment shows that the cut-copy-paste enhancement strategy can significantly improve the model accuracy under unbalanced sample conditions.

Table 4. Experimental results of DDRNet modified by MHAB under data enhancement and without data enhancement.

Enhancement	Corrosion		CF		OST		DS		CB		Flange	
	IoU	ACC	IoU	ACC	IoU	ACC	IoU	ACC	IoU	ACC	IoU	ACC
✗	45.65	46.37	86.29	87.16	79.85	81.67	72.45	76.32	63.63	66.58	60.24	61.29
✓	56.32	57.61	85.97	86.19	80.62	82.49	75.89	77.93	65.98	67.46	61.65	65.81

4.5. Real-Time Comparison of Algorithms

The purpose of the proposed two-stage method was to reduce the time consumed by the model during inference. Therefore, this part of the experiment proved the real-time performance of this method. The final experimental results are shown in Table 5. It can be seen that although DDRNet had a faster inference speed, it was still not as good

as the well-designed two-stage detection method, because DDRNet performs pixel-level calculation on the whole image, while the two-stage method uses a YOLOv8 to filter part of the background first.

Table 5. Comparison of calculation time of different methods.

Method	Algorithm	Time (ms)
One stage	DDRNet	11.28
Two stage	YOLOv8	1.35
	Postprocessing	0.86
	DDRNet	3.58

4.6. Visual Result Discussion

In order to verify the accuracy of the experimental results more intuitively, we carried out a visual display of the experimental results. Meanwhile, in order to comprehensively compare the performance of different methods, we have presented the results of all existing methods involved in the experiment, including Sparse R-CNN, Faster R-CNN, YOLOX, YOLOv8, DeepLabV3, Mask2Former, UNet, and DDRNet. The results also include our improved YOLOv8 and DDRNet with MHAB.

The results of various object detection methods in stage 1 are shown in Figure 7. It can be seen that although the bounding boxes predicted by these methods were relatively close to the labels, our proposed YOLOv8 and MHAB had the highest confidence. In the semantic segmentation results of stage 2 (as shown in Figure 8), although the methods performed similarly in the overall segmentation of the device, DDRNet and MHAB performed better in the segmentation of finer corrosion areas. This is because the attention mechanism it introduces allows the algorithm to focus on the target area more efficiently. Through visualization comparison of the methods involved in the experiment, not only the effectiveness of the proposed method is verified, but also its superiority is further highlighted.

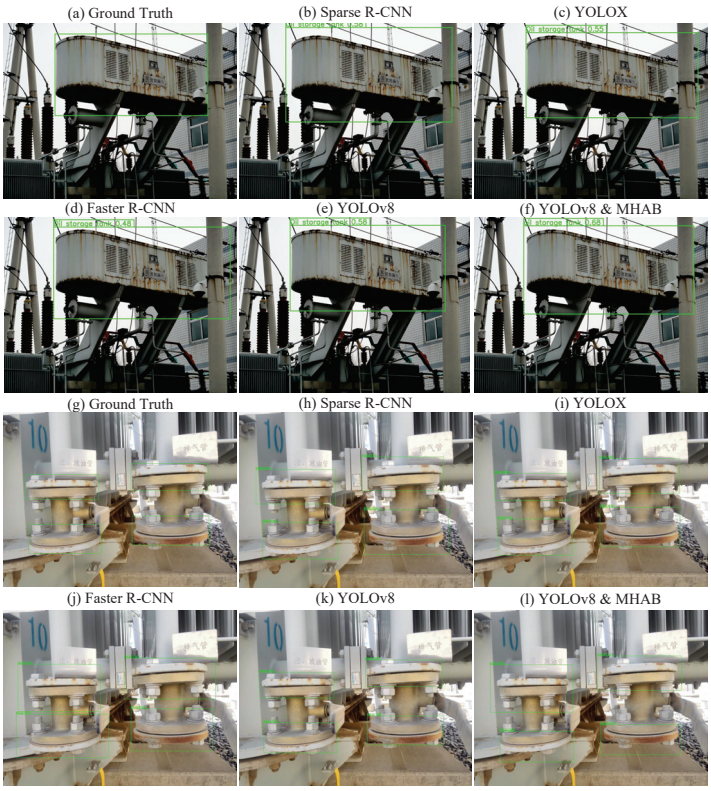

Figure 7. Object detection results in stage 1, where (**a**–**i**) belong to the same image and (**j**–**l**) belong to the same image.

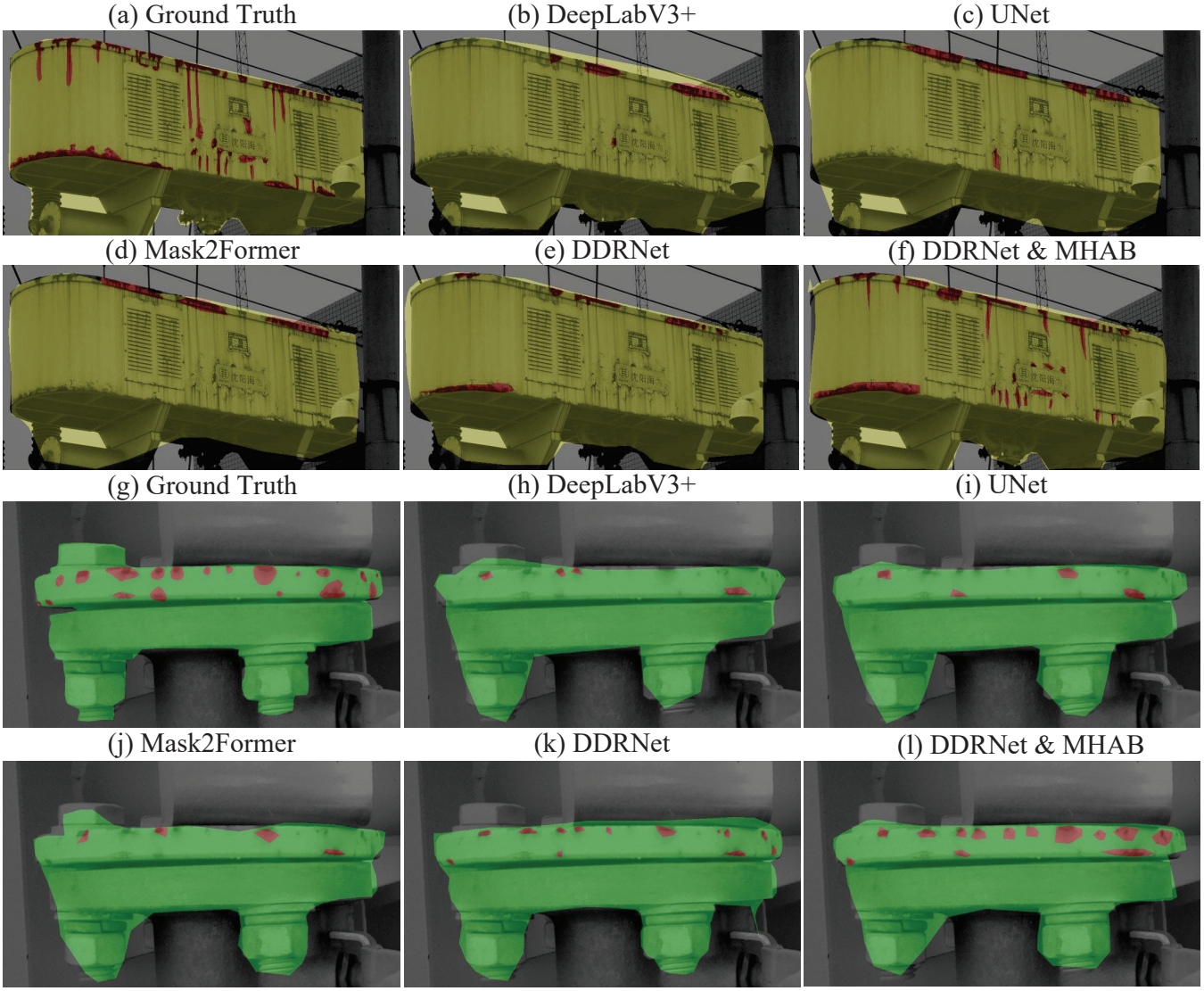

Figure 8. Semantic segmentation results in stage 2, where (**a**–**i**) belong to the same image, and (**j**–**l**) belong to the same image.

4.7. Failure Case Discussion

Although our method has been effective to a certain extent, it still has some shortcomings. Especially in the case of semantic segmentation in backlight, the shadow region may be misjudged as a corrosive region (as shown in Figure 9), which is undoubtedly a key point that needs to be improved. To effectively address this issue, we plan to first collect a large amount of data under various lighting conditions (especially in backlit scenes) to ensure that the model is exposed to a sufficient number of backlit and shadowed samples during training. Subsequently, we will annotate the shadows and eroded regions more finely, so as to ensure that the model can accurately distinguish the difference between the two during training.

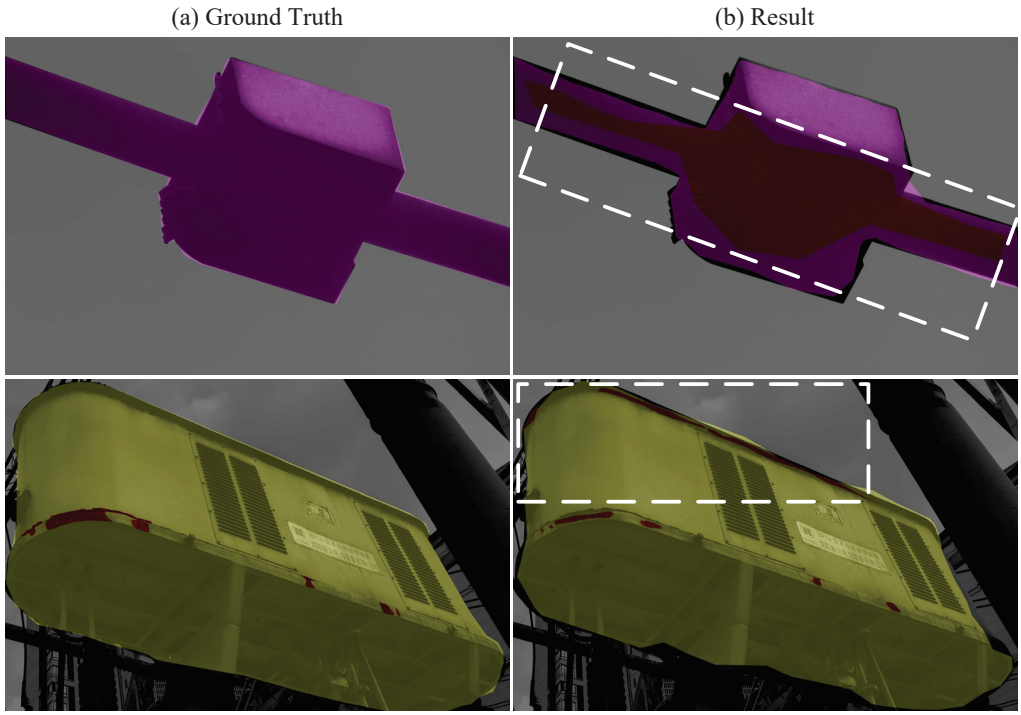

Figure 9. Demonstration of failure cases of the proposed method. The white dashed box shows the area of the failure case.

5. Conclusions

This work has proposed a two-stage method based on YOLOv8 and DDRNet to detect the corrosion defects of substation equipment. In the first stage, the improved target detection network YOLOv8 was used to conduct object detection on the equipment in the substation. In the second stage, a DDRNet semantic segmentation network was used to accurately segment substation equipment and its corrosion defects. In addition, multi-head attention block (MHAB) was used in YOLOv8 and DDRNet, effectively improving the detection capabilities of both in substation environments. Finally, a clip-copy-paste method was used to expand the corrosion sample. Experimental results show that the proposed two-stage substation corrosion location method can meet good real-time performance, and the effectiveness of MHAB and data enhancement was also verified. However, the proposed method is prone to misidentify the shaded area as a corroded area under backlight conditions. Therefore, it is planned that the shadows and erosion areas will be labeled in future work to ensure that the model can accurately distinguish the difference between the two when trained.

Author Contributions: Conceptualization, Z.W.; methodology, X.L. and Y.Z.; validation, F.W.; software, Y.C.; formal analysis, Z.W.; investigation, Z.W.; resources, Z.W.; data curation, Y.Z.; writing—original draft preparation, Y.Z.; writing—review and editing, Z.W.; visualization, Z.W. and Q.H.; supervision, Z.W. and G.Z.; project administration, M.W.; funding acquisition, Z.W. All authors have read and agreed to the published version of the manuscript.

Funding: This research was funded by the State Grid Sichuan Electric Power Company Science and Technology Project (521997230012).

Data Availability Statement: Due to lab policy, we do not have the authority to release the data.

Conflicts of Interest: The authors declare that this study received funding from State Grid Sichuan Electric Power Company. The funder was not involved in the study design, collection, analysis, interpretation of data, the writing of this article or the decision to submit it for publication. Authors Zhigao Wang, Xinsheng Lan and Fangqiang Wang were employed by the company State Grid Sichuan Electric Power Research Institute. Authors Yang Chen, Guoliang Zhou and Qing Hu were employed by the company State Grid Yibin Power Supply Company. The remaining authors declare that the

research was conducted in the absence of any commercial or financial relationships that could be construed as a potential conflict of interest.

References

1. Zhou, B. Design of Corrosion Detection Device for Grounding Network Based on Magnetic Resistivity Method. Master's Thesis, Jilin University, Changchun, China, 2024.
2. Meng, X. Design of Distributed Corrosion Detection Device of Grounding Grids Based on Electric Network Theory. Master's Thesis, Jilin University, Changchun, China, 2022.
3. Fu, X. Influence of Grounding Conductor on Grounding Performance and Its Defect Detection Method. Master's Thesis, North China Electric Power University, Beijing, China, 2022.
4. Wei, W. Design of Ground Grid Corrosion Diagnosis System Based on Ultrasonic Guided Wave. Master's Thesis, Chongqing University, Chongqing, China, 2020.
5. Wu, M. Research on the Corrosion Diagnosis Method of Grounding Grids by Transient Electromagnetic Imaging. Master's Thesis, Chongqing University, Chongqing, China, 2019.
6. Gao, Y. Grounding Grid Corrosion Detection and Prediction Method and Its Realization. Master's Thesis, Hunan University, Changsha, China, 2021.
7. Li, J.; Wu, J.; Shao, Y. FSNB-YOLOV8: Improvement of Object Detection Model for Surface Defects Inspection in Online Industrial Systems. *Appl. Sci.* **2024**, *14*, 7913. [CrossRef]
8. Ma, S.; Liu, Y.; Zhang, Y. Fabric Defect Detection Based on Improved Lightweight YOLOv8n. *Appl. Sci.* **2024**, *14*, 8000. [CrossRef]
9. Lei, Z.; Zhang, Y.; Wang, J.; Zhou, M. Cloud-Edge Collaborative Defect Detection Based on Efficient Yolo Networks and Incremental Learning. *Sensors* **2024**, *24*, 5921. [CrossRef] [PubMed]
10. Zhang, T.; Zhong, S.; Xu, W.; Yan, L.; Zou, X. Catenary Insulator Defect Detection: A Dataset and an Unsupervised Baseline. *IEEE Trans. Instrum. Meas.* **2024**, *73*, 1–15. [CrossRef]
11. Luo, J.; Yang, Z.; Li, S.; Wu, Y. FPCB Surface Defect Detection: A Decoupled Two-Stage Object Detection Framework. *IEEE Trans. Instrum. Meas.* **2021**, *70*, 1–11. [CrossRef]
12. Davari, N.; Akbarizadeh, G.; Mashhour, E. Corona Detection and Power Equipment Classification Based on GoogleNet-AlexNet: An Accurate and Intelligent Defect Detection Model Based on Deep Learning for Power Distribution Lines. *IEEE Trans. Power Deliv.* **2022**, *37*, 2766–2774. [CrossRef]
13. Ling, H.; Zhao, T.; Zhang, Y.; Lei, M. Engineering Vehicle Detection Based on Improved YOLOv6. *Appl. Sci.* **2024**, *14*, 8054. [CrossRef]
14. Zhang, Q.; Xu, B.; Liu, H.; Zhang, Y.; Yu, Z. A Multi-Organ Segmentation Network Based on Densely Connected RL-Unet. *Appl. Sci.* **2024**, *14*, 7953. [CrossRef]
15. Wang, J.; Zhao, X.; Peng, L.; Wang, H. A Method for Detecting the Yarn Roll's Margin Based on VGG-UNet. *Appl. Sci.* **2024**, *14*, 7928. [CrossRef]
16. He, K.; Zhang, X.; Ren, S.; Sun, J. Spatial Pyramid Pooling in Deep Convolutional Networks for Visual Recognition. *IEEE Trans. Pattern Anal. Mach. Intell.* **2015**, *37*, 1904–1916. [CrossRef]
17. Ren, S.; He, K.; Girshick, R.; Sun, J. Faster R-CNN: Towards Real-Time Object Detection with Region Proposal Networks. *IEEE Trans. Pattern Anal. Mach. Intell.* **2017**, *39*, 1137–1149. [CrossRef] [PubMed]
18. Ge, Z.; Liu, S.; Wang, F.; Li, Z.; Sun, J. YOLOX: Exceeding YOLO Series in 2021. *arXiv* **2021**, arXiv:2107.08430.
19. Li, C.; Li, L.; Jiang, H.; Weng, K.; Geng, Y.; Li, L.; Ke, Z.; Li, Q.; Cheng, M.; Nie, W.; et al. YOLOv6: A Single-Stage Object Detection Framework for Industrial Applications. *arXiv* **2022**, arXiv:2209.02976.
20. Wang, C.Y.; Bochkovskiy, A.; Liao, H.Y.M. YOLOv7: Trainable bag-of-freebies sets new state-of-the-art for real-time object detectors. *arXiv* **2022**, arXiv:2207.02696.
21. Liu, W.; Anguelov, D.; Erhan, D.; Szegedy, C.; Reed, S.; Fu, C.Y.; Berg, A.C. SSD: Single Shot MultiBox Detector. In *Computer Vision–ECCV 2016: Proceedings of the 14th European Conference, Amsterdam, The Netherlands, 11–14 October 2016*; Proceedings, Part I 14; Springer International Publishing: Berlin/Heidelberg, Germany, 2016.
22. Ronneberger, O.; Fischer, P.; Brox, T. U-net: Convolutional networks for biomedical image segmentation. In *Proceedings of the International Conference on Medical Image Computing and Computer-Assisted Intervention*; Springer: Berlin/Heidelberg, Germany, 2015; pp. 234–241.
23. Chen, L.C.; Papandreou, G.; Schroff, F.; Adam, H. Rethinking atrous convolution for semantic image segmentation. *arXiv* **2017**, arXiv:1706.05587.
24. Chen, L.C.; Zhu, Y.; Papandreou, G.; Schroff, F.; Adam, H. Encoder-Decoder with Atrous Separable Convolution for Semantic Image Segmentation. In Proceedings of the European Conference on Computer Vision, Munich, Germany, 8–14 September 2018.
25. Pan, H.; Hong, Y.; Sun, W.; Jia, Y. Deep Dual-Resolution Networks for Real-Time and Accurate Semantic Segmentation of Traffic Scenes. *IEEE Trans. Intell. Transp. Syst.* **2022**, *24*, 3448–3460. [CrossRef]
26. Rajesh, S.; Jinesh Babu, K.S.; Chengathir Selvi, M.; Chellapandian, M. Automated Surface Crack Identification of Reinforced Concrete Members Using an Improved YOLOv4-Tiny-Based Crack Detection Model. *Buildings* **2024**, *14*, 3402. [CrossRef]
27. Luo, R.; Anand, A.; Zulkernine, F.; Rivest, F. YOLO-I3D: Optimizing Inflated 3D Models for Real-Time Human Activity Recognition. *J. Imaging* **2024**, *10*, 269. [CrossRef]

28. Zou, H.; Yang, J.; Sun, J.; Yang, C.; Luo, Y.; Chen, J. Detection Method of External Damage Hazards in Transmission Line Corridors Based on YOLO-LSDW. *Energies* **2024**, *17*, 4483. [CrossRef]
29. Liu, J.; Liu, C.; Wu, Y.; Xu, H.; Sun, Z. An Improved Method Based on Deep Learning for Insulator Fault Detection in Diverse Aerial Images. *Energies* **2021**, *14*, 4365. [CrossRef]
30. Liu, C.; Wu, Y.; Liu, J.; Han, J. MTI-YOLO: A Light-Weight and Real-Time Deep Neural Network for Insulator Detection in Complex Aerial Images. *Energies* **2021**, *14*, 1426. [CrossRef]
31. Han, J.; Yang, Z.; Xu, H.; Hu, G.; Zhang, C.; Li, H.; Lai, S.; Zeng, H. Search Like an Eagle: A Cascaded Model for Insulator Missing Faults Detection in Aerial Images. *Energies* **2020**, *13*, 713. [CrossRef]
32. Zou, L.; Chen, A.; Li, C.; Yang, X.; Sun, Y. DCW-YOLO: An Improved Method for Surface Damage Detection of Wind Turbine Blades. *Appl. Sci.* **2024**, *14*, 8763. [CrossRef]
33. Zhang, Z.; Xia, J.; Wen, Y.; Weng, L.; Ma, Z.; Yang, H.; Yang, H.; Dou, J.; Wang, J.; Zhao, P. Detection Method for Inter-Turn Short Circuit Faults in Dry-Type Transformers Based on an Improved YOLOv8 Infrared Image Slicing-Aided Hyper-Inference Algorithm. *Energies* **2024**, *17*, 4559. [CrossRef]
34. Xiang, S.; Chang, Z.; Liu, X.; Luo, L.; Mao, Y.; Du, X.; Li, B.; Zhao, Z. Infrared Image Object Detection Algorithm for Substation Equipment Based on Improved YOLOv8. *Energies* **2024**, *17*, 4359. [CrossRef]
35. Yao, Z.; Hu, Z.; Tian, P.; Sun, J. Adaptation of Object Detection Algorithms for Road Indicator Lights in Complex Scenes. *Appl. Sci.* **2024**, *14*, 10012. [CrossRef]
36. Luo, J.; Liu, Z.; Wang, Y.; Tang, A.; Zuo, H.; Han, P. Efficient Small Object Detection You Only Look Once: A Small Object Detection Algorithm for Aerial Images. *Sensors* **2024**, *24*, 7067. [CrossRef]
37. Miao, S.; Du, Y.; Lu, X.; Guan, H. Semantic segmentation of vehicle vision based on two-branch Enet network. In Proceedings of the 2023 IEEE 3rd International Conference on Power, Electronics and Computer Applications (ICPECA), Shenyang, China, 29–31 January 2023; pp. 477–481. [CrossRef]
38. Lin, H.; Qiu, J.; Tong, Y.; Tang, Y. Trilateral dual-resolution real-time semantic segmentation network for road scenes. In Proceedings of the 2023 IEEE 18th Conference on Industrial Electronics and Applications (ICIEA), Ningbo, China, 18–22 August 2023; pp. 135–140. [CrossRef]
39. Gao, Y.; Zhang, S.; Zuo, D.; Yan, W.; Pan, X. TMNet: A Two-Branch Multi-Scale Semantic Segmentation Network for Remote Sensing Images. *Sensors* **2023**, *23*, 5909. [CrossRef]
40. Zhao, C.; Guo, H.; Guo, Y.; Zhong, S.; Luo, H.; Fan, J. TBNet: Two-Branch Cloud Detection Network for Remote Sensing Imagery. In Proceedings of the 2022 2nd International Conference on Frontiers of Electronics, Information and Computation Technologies (ICFEICT), Wuhan, China, 19–21 August 2022 2022; pp. 477–82.
41. Chen, J.; Gao, J.; Yang, W.; Sun, H.; Chen, B.; Yang, M.; Ma, J. MedFPNet: A Medical Image Segmentation Network Based on Fourier Transform. In *Artificial Intelligence in China: Proceedings of the 5th International Conference on Artificial Intelligence in China. Lecture Notes in Electrical Engineering (1043), Changbaishan, China, 22 July 2023*; Wang, W., Mu, J., Liu, X., Na, Z., Eds.; Springer: Berlin/Heidelberg, Germany, 2024; pp. 223–30.
42. Niu, Y.; Li, Z.; Li, S. Cross Attention with Transformer for Few-shot Medical Image Segmentation. In Proceedings of the 2022 12th International Conference on Information Technology in Medicine and Education (ITME), Xiamen, China, 18–20 November 2022; pp. 644–648. [CrossRef]
43. Lin, N.; Zhao, W.; Liang, S.; Zhong, M. Real-Time Segmentation of Unstructured Environments by Combining Domain Generalization and Attention Mechanisms. *Sensors* **2023**, *23*, 6008. [CrossRef]
44. Ni, H.; Jiang, S. Deep Dual-Resolution Road Scene Segmentation Networks Based on Decoupled Dynamic Filter and Squeeze-Excitation Module. *Sensors* **2023**, *23*, 7140. [CrossRef]
45. Yu, X.; Ren, Y.; Yin, X.; Meng, D.; Zhang, H. High Precision Positioning and Rotation Angle Estimation of a Flatbed Truck Based on BDS and Vision. *Sensors* **2024**, *24*, 1826. [CrossRef] [PubMed]
46. Meng, D.; Ren, Y.; Yu, X.; Yin, X.; Wang, W.; Men, J. High-Precision Positioning and Rotation Angle Estimation for a Target Pallet Based on BeiDou Navigation Satellite System and Vision. *Sensors* **2024**, *24*, 5330. [CrossRef] [PubMed]
47. Sun, P.; Zhang, R.; Jiang, Y.; Kong, T.; Xu, C.; Zhan, W.; Tomizuka, M.; Li, L.; Yuan, Z.; Wang, C.; et al. SparseR-CNN: End-to-End Object Detection with Learnable Proposals. *arXiv* **2020**, arXiv:2011.12450.
48. He, K.; Gkioxari, G.; Dollar, P.; Girshick, R. Mask R-CNN. In Proceedings of the 2017 IEEE International Conference on Computer Vision (ICCV), Venice, Italy, 22–29 October 2017.
49. Cheng, B.; Misra, I.; Schwing, A.G.; Kirillov, A.; Girdhar, R. Masked-attention Mask Transformer for Universal Image Segmentation. *arXiv* **2021**, arXiv:2112.01527.

designs

MDPI

Article

Experimental Analysis and Modeling of an Impact Response Along Sets of Steel Sheets Joined with Rivets

Víctor Martínez-Calzada, Felipe de Jesús Tapia-Pérez, Adriana Rodríguez-Torres and Alonso Saldaña-Heredia *

Ingeniería en Aeronáutica, Universidad Politécnica Metropolitana de Hidalgo, Boulevard Acceso a Tolcayuca 1009, Ex Hacienda San Javier, Tolcayuca C.P. 43860, Hidalgo, Mexico; vmartinez@upmh.edu.mx (V.M.-C.); 223220001@upmh.edu.mx (F.d.J.T.-P.); adrodriguez@upmh.edu.mx (A.R.-T.)
* Correspondence: aheredia@upmh.edu.mx

Abstract: This paper is focused on understanding how a wave was transmitted along arrays joined with rivets. The arrays were made of steel plates, and each section was joined to the other with five rivets. A total of three arrays were studied, which were compounded by one, two and three steel plates. To determine the wave transmission, a laser, a lens and a camera were set up in the experiment to calculate the in-plane motion both while the structure was still and during the indirect collisions. Results were studied by means of the general theory of elasticity coupled with spectral analysis from a general mathematical model; the latter fitted all the responses with a mean of 98% accuracy.

Keywords: wave propagation; amplitude; velocity; oscillation; steel array; impact; analytical response; modeling response

1. Introduction

This section is divided into five parts, starting with non-destructive testings (NDTs), as our research deals with a different type of NDT; followed by interferometry, which is the most used optical system for measurements; the recent developments of digital image correlation, which is the technique used in this research; some reports on wave transmission; and finally, recent developments on rivets.

1.1. Applications of Non-Destructive Testings (NDTs) Among Industries

Non-destructive testings (NDTs) are widely used in different industries, such as the implementation of the double pass retroreflection for corrosion detection in aircraft structures. One group of researchers developed their tests by using a scanning system and a spatial resolution for images of 640 × 480 pixels; after adding a solvent to the specimens, gray-scale images were acquired. To achieve their results, the authors assumed a degree of corrosion on the surface establishing a percentage of the thickness of the sheet, which demonstrates that this technique is cable of detecting hidden corrosion [1].

NDTs have been also tested to evaluate the integrity of critical aerospace composites. Tests such as ultrasound, acoustic emission, eddy currents, infrared thermography, laser shearography, and X-ray radiography were compared between them. The comparison revealed that ultrasound is an effective tool for detecting porosity, acoustic is a superior technique for finding cracks in the matrix, eddy currents are most often used to identify impact damage, infrared is effective for observing microcracks in the matrix, shearography is most effective when used for imaging disbonds, and X-ray can be combined with computerized thermography and laminography [2].

In addition, NDTs were used to test aerospace composites; in this research, the authors declared a sum of tests for each procedure time during the fabrication of face sheet consolidation, the bonds and the core inclusions; the composites should be inspected with visual, tap, ultrasound, X-ray, thermography and shearography tests [3].

Following aerospace application, NDTs were used to determine the behavior of carbon fiber composites; some of the tests were ultrasound, thermography, vibration and shearography. Ultrasound and radiography were found to be the most successful methods for the evaluation of composite materials; additionally hologropahy is a non-conventional inspection method that demonstrated great potential in revealing delaminations in composites [4].

NDTs were applied for the inspection of aircraft; in this article, the authors stated that signal processing for determining phase characteristics in the time domain was developed to obtain information parameters and signal characteristics for the industry. To achieve this, the research focused on the application of signal processing to eddy currents and ultrasonic testing for thickness measurement and pulse acoustic inspection [5].

A review about NDTs discussed different methodologies, such as visual, magnetic particles, dye penetration, ultrasonic, radiographic, acoustic and Eddy current testing. Here, the authors outline the limitations and capabilities as well as a description of each test. Furthermore, they present some of the applications and challenges, concluding that the tests are simple, but a single technique is not enough for total satisfaction. However, coupling two or more ensures the effectiveness of the measurement [6].

NDTs are also present in the automotive industry for oil sump inspection: in particular, visual, dye penetration, ultrasound and X-ray tests were used. The discrepancies in the oil sump detected by these tests were 7.9%, 1.9%, 21.9% and 45.1%, respectively. The results revealed that visual inspection was the technique that contributed the most to the detection of nonconformities, while X-ray was the best technique to observe them [7].

Finally, an unusual technique was established: the use of high-frequency (Terahertz) as a measurement system for different applications such as the detection of weapons, substances, and explosives for thickness and current measurements. Terahertz technology proved to be useful for measuring thickness in aeronautical and automotive industries [8].

1.2. Interferometry as a Non-Destructive Testing Technique

Optical techniques are also applied as non-destructive methods; this group of researchers used the sampling Moiré method to measure deformation, particularly to monitor structural health and elucidate material damage mechanisms. They focused on two of the application examples: the measurement of dynamic deflection for large-scale concrete bridges and the measurement of residual thermal strain for small-scale flip packages [9].

An experimental set-up was reported that determined displacements through interferometry, in which a reference signal was obtained by fixing the still position, and Fourier transform and its inverse were performed. These allowed the system to recover the time-varying offset in each modulation period [10].

The ultrasonic technique was used along with optical interferometry to determine diameter and depth measurements. The experiment verified the measurements obtained by ultrasonic methods; measurements were performed ten times with each technique to quantify the error. These techniques ensured the use of materials in a variety of applications [11].

Interferometry has also been used to analyze and identify structural health in buildings, demonstrating that it can monitor systems for environmental effects on the spatial distribution of wave velocities using operational modal analysis and ambient noise deconvolution interferometry [12].

Interferometry has also been applied for 3D modeling by scanning 2D surfaces, it was assessed with rigorous simulation, and the results were compared between experimental and simulation, reproducing the image formation [13].

Following the application of interferometry, an experimental set-up of self-mixing was created; here, authors declared the use of a convolutional neural network to reconstruct the displacement of a target by training it with periodic displacements [14].

In addition, an interferometry function was established using the multiple aperture technique, based on the spectral diversity method, which consists of splitting the azymuth synthetic aperture signal spectrum into separate subbands to estimate the surface displacement [15].

Finally, structural health was also assessed using differential synthetic aperture radar interferometry. This technique allowed the authors to identify possible critical situations for buildings; also, the active deformation process and related damages were studied [16].

1.3. Digital Image Correlation in Different Applications

Digital image correlation (DIC) is considered an optical technique, as it is based on comparing images acquired with a digital camera. One of their approaches was to characterize a fracture process in which wood composites were subjected to loading, and the results showed that experimental displacement measurements from DIC were as accurate as the numerical simulation [17]. A typical application of DIC is displacement measurement; the authors declared the acquisition of full-field time history of vibrating components [18].

The authors developed an accurate methodology to measure external systems in structural parts of aircraft: the experimental set-up obtained satellite information in real time, and in addition, a camera acquired it and displayed it as an image. They stated that the accuracy of the system has a relative error of less than 1% [19]. DIC has also been used to measure complex deformations in aircraft; the methodology is based on detecting movement, vibration, warping and the distortion of aircraft wheels [20].

Following aircraft application, the authors developed DIC measurements for the deformation of rotor blades under load and their vibration due to aeroelastic phenomena. By setting up a high-speed camera, the authors were able to measure frequency vibrations up to 1 kHz with an exposure time below 210 ns [21].

Another study using DIC in the structural field attempted to measure the mechanical properties of concrete; this was accomplished by coupling fiber optical strain on bars plus DIC measurements on concrete surfaces. After testing the concrete samples, the optical fibers demonstrated that the polyimide-coated one adequately captured high strain gradients; furthermore, the authors presented a procedure to quantify DIC uncertainty in large-scale structural tests [22].

Finally, a review was presented talking about the importance of DIC in large-scale tests; the authors' objective was to study the recent advances of the technique and its application to composite structures. One of the most used is in the wind energy and aerospace sector, measuring strains under static loading and modal analysis during dynamic structural tests [23].

1.4. Wave Propagation

On the other hand, there are studies focused on understanding the propagation of waves. An example is the development of neural networks based on physics: this methodology has been applied to solve direct and inverse problems in science and engineering [24].

Research was developed on the importance of studying the propagation of waves in porous media, since it is the main cause of the anelasticity of waves. To solve this,

the authors worked on a theory for saturated fluids containing inclusions at multiple scales [25].

Another application was presented by coupling experimental and modeling approaches to monitor the structural health using guided wave propagation; the result of this methodology was the understanding of the structural integrity of primary and secondary structures as well as the detection of damage and alterations due to environmental and operational conditions [26].

In addition, the analysis of wave propagation in composites was developed; the authors studied the size-dependent behavior of a spinning composite reinforced with graphene nanoplatelets in which the small-scale effect was analyzed using strain gradient theory. One of the results was established by increasing the radius; the phase velocity values were presented at the lowest values of the wave number [27].

Following with wave propagation in composites, the authors stated the use of a size-dependent laminated composite nanostructure together with a piezoelectric actuator to understand the importance of the angle ply on phase velocity changes in the composite when increasing the wave number [28].

1.5. The Use of Riveting Joints

Rivets are very important as structural joints; for the inspection of riveted joints, a non-destructive test was used, in which damage around the surface, subsurface and corrosion were simulated with eddy current excitation [29].

Another study presented the effects of the riveting process on the residual and clamping stress, in which variables such as riveting force, sheet thickness, sheet and rivet material, rivet hole and diameter tolerances were taken into account. The authors evidenced that the crack initiation depends on the residual hoop compression stress zone [30].

An investigation was carried out on the influences of cutting positions on the measurement accuracy of riveted joints, in which the authors developed evaluation and correction methods to estimate and compare the interlocking error caused by these cuts [31].

Additionally, the authors explored the advantages and disadvantages of riveting, comparing procedural quality measures such as the failure mode, joint strength, fatigue lifetime, corrosion strength, and vibration, among others. During this comparison, they demonstrated that numerical equation models focus on the interactions at the rivet–material level and can more quickly build a prediction model [32].

A study was carried out on the fatigue behavior of rivets, in which the authors evidenced that the stress concentration in riveted lap joints of various diameter and rivet pitches was optimized; this was evaluated by adjusting the rivets to the stress distribution analysis under tensile loads and modeling a theoretical model with finite element [33].

Another study presented the effects of ultrasonic vibration on the riveting process, in which the authors declared that this experimental technique can reduce the forming force, decrease the friction in the metal-forming process, and serve to improve the quality of the workpiece surface. Thus, application to the riveting process showed that the technique reduced the riveting force and decreased friction; as a consequence, the flow of the rivet material improved [34].

An optical technique was used for the inspection of rivets: the experimental technique, multi-intensity high dynamic range fringe projection profilometry, was evaluated for 2D and 3D data acquisition, in which it was demonstrated that a riveted metal workpiece was detected with high precision [35].

Finally, the aim of the present article is to characterize the impact reaction on metallic sheets joined by rivets in three different configurations and to understand how the wave travels along them by means of digital image correlation. The experimental results were

evaluated analytically and following a numerical procedure, in which it was demonstrated that both curves achieved more than 95% and in some results, and the approach reached 99% of accuracy according to the registered movement.

2. Materials and Methods

The experimental set-up was built combining a sum of three elements: beginning with a metallic box (B), with dimensions of 40 × 40 × 40 cm, it was made with galvanized steel sheet caliber 12 (3.4 mm thickness) [36,37]. This box was filled with G 0/3 sand, with a density between 1.5 and 1.55 kg/m^3 [36,37], approximately at 90% of its capacity. Finally, the steel arrays were joined with rivets. Each section was assembled with five rivets using the following equation:

$$N_R = \frac{51.71 * LT}{S} \tag{1}$$

where 51.71 is a tensile resistance constant (in daN/mm^2), and L, T and S are the sheet metal length, the plate thickness (both in millimeters), and the flattening resistance (in daN), respectively [38]. Setting the parameters on the equation, a value of 5.73 was obtained as the number of rivets (N_R); however, it was important to take into account two mechanical design parameters: there must be a space of 2.5 times the *diameter* between the borders of the sheet and the distance between each rivet taken from its center must be 2.65 times the *diameter* as a minimum. The rivets used had 3.175 mm of diameter; as a consecuence, five rivets were joining each sheet, as shown in Figure 1.

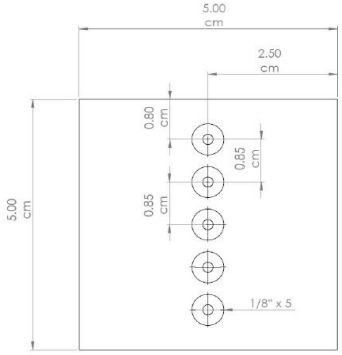

Figure 1. Mechanical design of riveting the sheet metal.

Figure 2 depicts the experimental way in which the correlation technique was performed: a laser (L), a lens (l) and a camera (C) were used: the laser was a diode-pumped solid state with 220 mW power [39], a converging lens with f = 7 cm and the camera sensor of the iPhone 13 pro [40] were set to capture the specular reflection of the laser on a screen (S).

The experimental methodology consisted of giving soft impacts assessed with a hammer with 0.575 kg of mass; each hit was exactly at the midpoint of the transversal face of the box, and all impacts were carried out in the longitudinal direction with an initial angle of 30° according to the transversal face plane [36,37]. The impacts were propagated along the box (Figure 3A), sand and the sets of steel sheets arrays, following the next order: a set of three impacts were measured after the rivets and another set of three collisions before them (Figure 3B). This procedure was repeated for two and three splices joined by rivets.

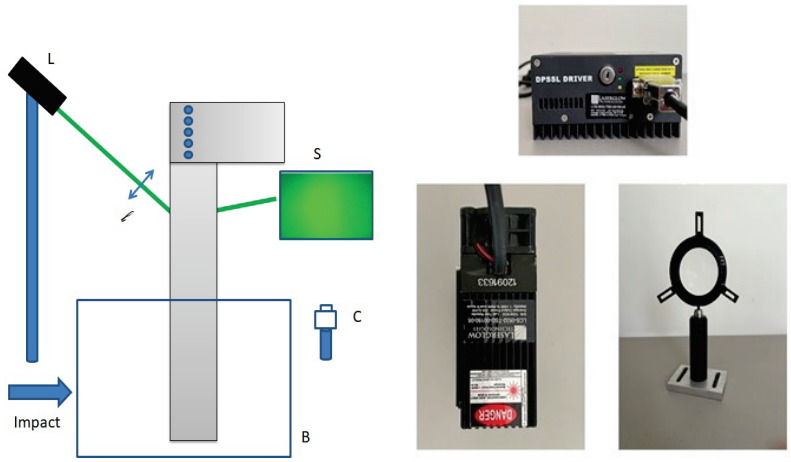

Figure 2. Experimental set-up (**a**); laser and lens (**b**).

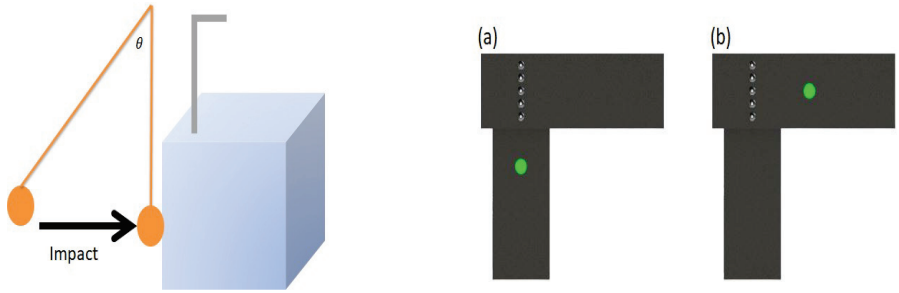

Figure 3. Impact action (**A**) and optical measurement (**B**): before (**a**) and after (**b**) the rivets.

2.1. Wave Propagation Modeling

The theoretical modeling of the wave propagation part of the equation of motion is shown below [41]:

$$\frac{\partial F}{\partial x} = \rho A \frac{\partial^2 u}{\partial t^2} + \eta A \frac{\partial u}{\partial t} - q \tag{2}$$

where $A\rho$ is the mass density per unit length, η is the damping per unit volume, and q is the externally applied axial force per unit length. But in the particular case of uniform properties and no damping, all dependent variables have an equation of the following form:

$$C_0{}^2 \frac{\partial^2 u}{\partial x^2} - \frac{\partial^2 u}{\partial t^2} = 0 \tag{3}$$

In this case, the waves are governed by the simple wave equation, and the D'Alembert is the general solution. However, it is needed to study its spectral representation, making the assumption that modulus and area will not vary; hence, the Fourier coefficients can be obtained from the following:

$$EA \frac{d^2 \hat{u}}{dx^2} + (\omega^2 \rho A - i\omega\eta A)\hat{u} = 0 \tag{4}$$

in which its general solution can be in the form of

$$\hat{u}(x) = \hat{A} e^{-ik_1 x} + \hat{B} e^{+ik_1 x} \tag{5}$$

with k_1 as

$$k_1 = \sqrt{\frac{\omega^2 \rho A - i\omega\eta A}{EA}} \tag{6}$$

This solution can be used for the statement of a bar subjected to a force P [41]

$$EA\frac{d\hat{u}_n}{dx} = -\hat{P}_n \tag{7}$$

Thus, it is possible to establish the transfer function $G_v(x, \omega)$ for the velocity as

$$\hat{G}_v(x, \omega) = \frac{\omega}{\sqrt{(\omega^2 \rho A - i\omega\eta A)EA}} e^{-ik_1 x} \tag{8}$$

2.2. Laser Metrology and Image Processing

A solid-state laser as a source to measure was used. The laser properties that serve to fulfill the measurements are the Gaussian distribution and that it is monochromatic; when such a source of light is reflected form a rough surface, the optical wave resulting at any moderate distance consists of many coherent components [42]. These physical phenomena can be studied through the probability density function of intensity $P_{(I)}$:

$$P_{(I)} = \frac{1}{4\pi\sigma^2} exp^{\left(\frac{-I}{2\sigma^2}\right)} \tag{9}$$

where σ is the average intensity I of the speckles in the field. The speckles have a very large number of random variables; thus, the central limit theorem is followed, as real and imaginary parts of the field are asymptotically Gaussian [42].

The image-processing procedure consists of recording the specklegram in slow motion (240 fps) by means of the sensor incorporated to (C), which is followed by obtaining each frame helped by a free software: *free video-to-jpg converter* (version 5.2.3.112). Then, a code was written in Octave® v. 9.3; it loads each image and correlates them in the Fourier domain iteratively [36,37]. Finally, the displacement field is calculated using the following equation:

$$D_f = \frac{Re(C_c)}{(s_1 * s_2)^2 M} \tag{10}$$

where C_c is the mathematical correlation and the denominator, formed by the standards deviation and the image size, s and M respectively, which helped to normalize the result. To obtain the displacement field, an iteration by code was completed, in which the distance between each peak amplitude intensity was plotted as a scalar value measured in millimeters according to [36,37]. Once this result was obtained, a low-pass filter was performed to observe the main impact and to delete the high frequencies [43]; the impact was approached by means of damped and harmonic oscillations as well as a numerical solution taken from rod propagation theory. It obtained more than 95% accuracy with the analytical fitting model, and in some cases, using the rod theory, it reached more than 99% accuracy.

3. Results

This category is subdivided into three items: first, the analysis of a single lamina coupled with rivets, measuring before and after the structural joints, which was followed by two and three laminae, respectively. In each experimental set-up, results were obtained evaluating the in-plane displacement between joints.

3.1. One Sheet Analysis: Before and After the Riveted Section

Figure 4 showed the behavior of six impacts; each graph plots the experimental displacement obtained by digital image correlation (black), the analytical approximation

(red) following [43] and the rod theory model (blue) by solving Equation (8). In Table 1, the damped waveform of the analytical and modeled results measured before the structural joints is displayed.

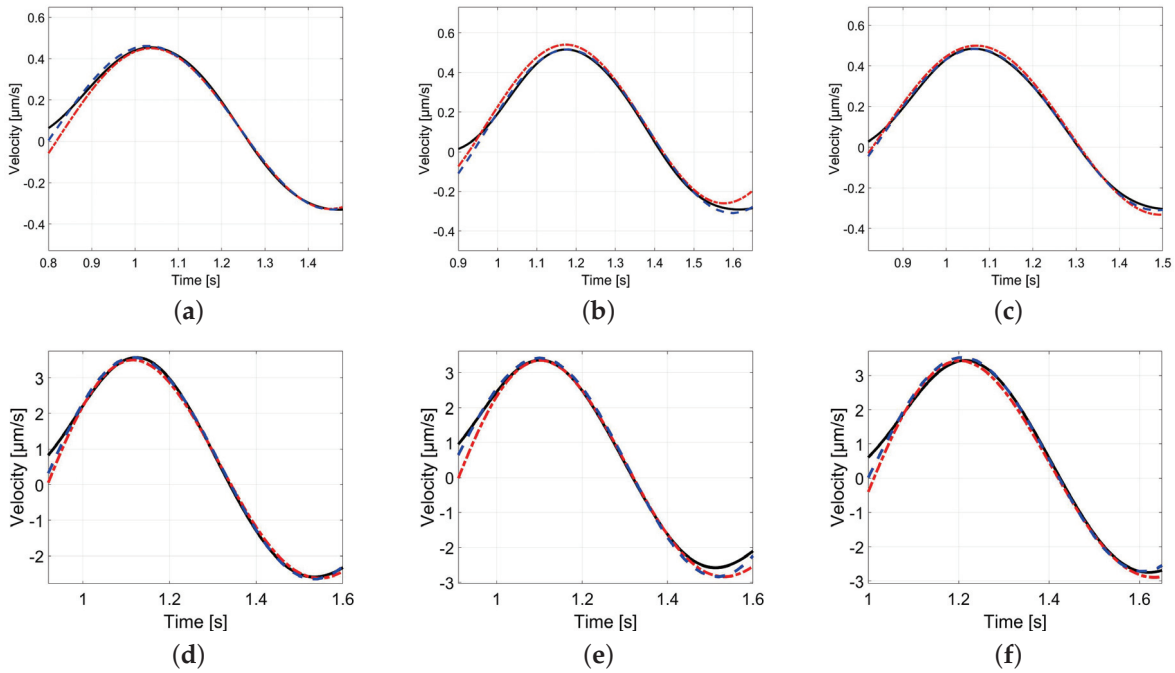

Figure 4. One sheet array graphs: (**a**–**c**) analysis before the rivets; (**d**–**f**) solution after the rivets.

In Table 1, it can be seen that the analytical and modeled solutions are similar. Both have a damped behaviour, and it is evident that the frequencies have higher values in the modeled solution. This suggests that the collision came with an amount of energy which was dissipated by the box and sand; then, when propagated to the lamina, a reduction was sensed in each case. The mean accuracy for the analytical approximation was 96.3%; however, modeling followed by the rod propagation theory gave 98.1%.

Table 1. Analytical and modeling solutions for one steel sheet; measurement before the rivets.

Figure		Function Type	Accuracy
a_r	Analytical	$f(x) = 0.4 * \sin(7.5x + 1.49) * \exp(-0.09x) + 0.018$	96.2%
a_b	Modeled	$f(x) = 0.49 * \sin(28x - 3.45) * \exp(-0.235x) - 0.0206$	98.6%
b_r	Analytical	$f(x) = 0.395 * \sin(7.9x - 3.6) * \exp(-0.087x) + 0.05$	95.9%
b_b	Modeled	$f(x) = 0.49 * \sin(28x - 1.9) * \exp(-0.19x) - 0.04$	97.1%
c_r	Analytical	$f(x) = -0.42 * \sin(7.4x - 3.2) * \exp(-0.1) + 0.084$	96.8%
c_b	Modeled	$f(x) = 0.5 * \sin(27.8x - 1) * \exp(-0.269x) - 0.0801$	98.8%

Table 2 expresses the solutions for the measurements taken after the joints. These are congruent with Table 1, as the modeled response had higher values of frequency again. However, in this case, the rod propagation theory reached 99.9% accuracy; it is appreciated that its amplitude has a lower value than the analytical solution.

Table 2. Analytical and modeling solutions for one steel sheet; measurement after the rivets.

Figure		Function Type	Accuracy
d_r	Analytical	$f(x) = 8.8 * \sin(7.3 * x - 0.4) * \exp(-0.8 * x) - 0.086$	95.2%
d_b	Modeled	$f(x) = 3.8 * \sin(28 * x + 1.87) * \exp(-1.4 * x) - 0.214$	99.6%
e_r	Analytical	$f(x) = 8.8 * \sin(7.3 * x - 0.3) * \exp(-0.8 * x) - 0.273$	96.8%
e_b	Modeled	$f(x) = 4.08 * \sin(28 * x + 2.32) * \exp(-0.2 * x) - 0.2554$	99.4%
f_r	Analytical	$f(x) = 9 * \sin(7.3 * x - 1.04) * \exp(-0.84 * x) - 0.3$	96.7%
f_b	Modeled	$f(x) = 4.1 * \sin(29.12 * x - 2.51) * \exp(-0.6 * x) - 0.3$	99.9%

3.2. Two Riveted Sections Analysis

A total of six graphs are depicted in Figure 5. The first three correspond to the measurements after a set of five rivets, and the other three were obtained next to the second set of joints. The analytical and modeled solutions are shown in Table 3.

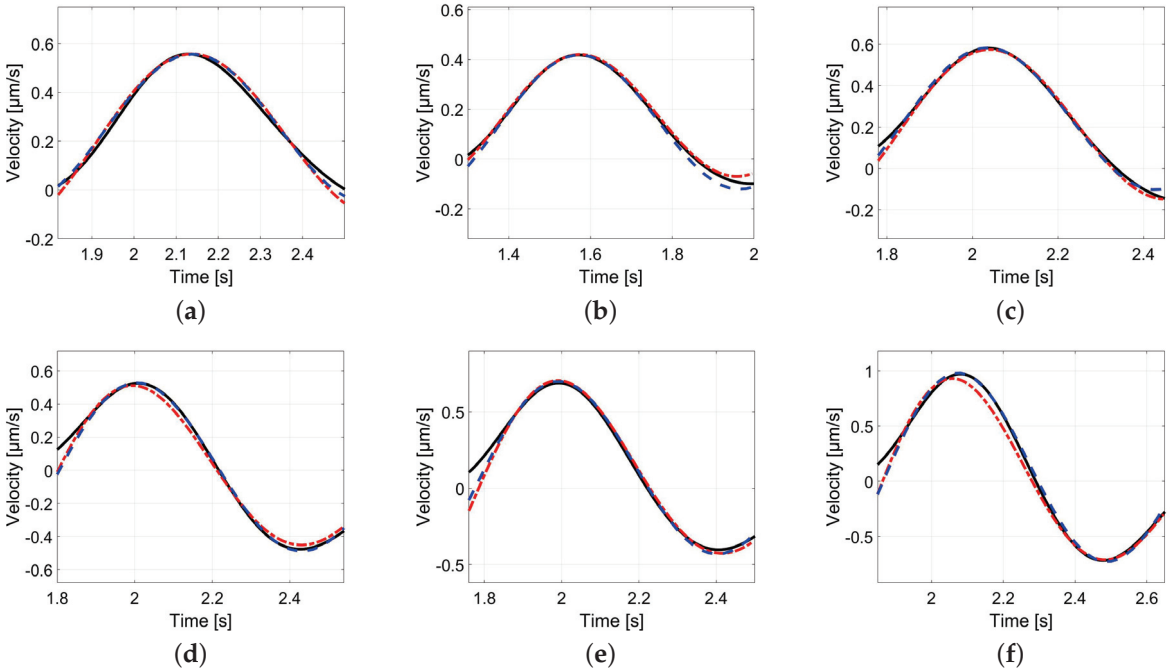

Figure 5. Two sheets array graphs: (**a**–**c**) analysis after the first section of four rivets; (**d**–**f**) solution after the second section.

Table 3. Analytical and modeling solutions measured after the first section of five rivets.

Figure		Function Type	Accuracy
a_r	Analytical	$f(x) = 0.5 * \sin(7 * x - 0.85) * \exp(-0.17 * x) + 0.21$	98.5%
a_b	Modeled	$f(x) = 0.5 * \sin(28 * x + 0.3) * \exp(-0.2 * x) - 0.25$	99.1%
b_r	Analytical	$f(x) = 0.51 * \sin(7.4 * x + 1.205) * \exp(-0.17 * x) + 0.167$	96.4%
b_b	Modeled	$f(x) = 0.49 * \sin(29.5 * x + 4) * \exp(-0.5 * x) - 0.14$	99.2%
c_r	Analytical	$f(x) = -0.53 * \sin(7.6 * x + 1.75) * \exp(-0.17 * x) + 0.2$	96.4%
c_b	Modeled	$f(x) = 0.51 * \sin(29.5 * x - 1.3) * \exp(-0.4 * x) - 0.2325$	98.9%

Table 3 exposed again a damped oscillation; in this set, the analytical approximation reached a maximum of 98.5%, but rod theory obtained a greater accuracy again of more than 99%. It can be observed that the behavior is congruent with Tables 1 and 2, and the frequency is greater, demonstrating that the physical phenomena was reproduced for a

set of two laminae. Additionally, Table 4 shows the results for the measurements after the second set of rivets; in this case, the analytical approximation has a mean accuracy of 96.7% and rod theory reached 99.8%. It is important to declare that the oscillatory movement was reproduced again and the amplitude increased in the modeled section.

Table 4. Analytical and modeling solutions measured after the second section of rivets.

Figure		Function Type	Accuracy
d_r	Analytical	$f(x) = 2.8 * \sin(7.2 * x - 0.33) * \exp(-0.8 * x) - 0.053$	97.2%
d_b	Modeled	$f(x) = 18.5 * \sin(27.3 * x - 2.75) * \exp(-1.5 * x) + 0.024$	99.6%
e_r	Analytical	$f(x) = 3.27 * \sin(7.4 * x - 0.7) * \exp(-0.8 * x) + 0.044$	96.7%
e_b	Modeled	$f(x) = 18.4 * \sin(28.3 * x - 3.85) * \exp(-1.4 * x) - 0.0901$	98.9%
f_r	Analytical	$f(x) = 3 * \sin(7.4 * x - 1.2) * \exp(-0.8 * x) - 0.028$	96.3%
f_b	Modeled	$f(x) = 18.3 * \sin(28 * x - 6.32) * \exp(-1.4 * x) - 0.0591$	99.8%

3.3. Three Riveted Sections Analysis

Finally, nine plots are shown in Figure 6. They are collocated in the following order: after the first set of five rivets; next to the other set and at the end of the lamina. The modeling and analytical solutions are presented in Table 5.

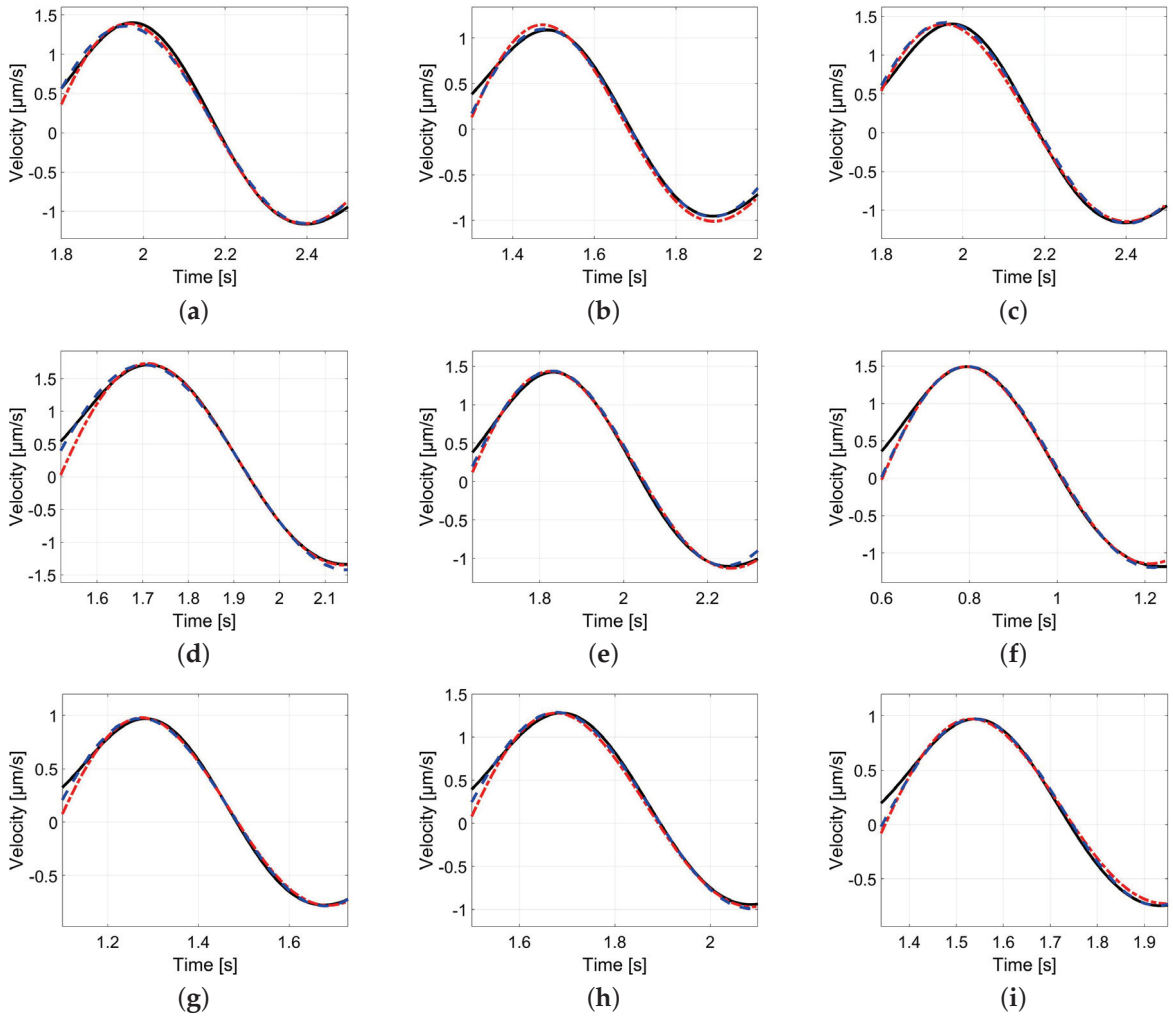

Figure 6. Three sheets array graphs: (**a**–**c**) analysis after the first section of four rivets; (**d**–**f**) solution after the second section; (**g**–**i**) solution of the third one.

Table 5. Analytical and modeling solutions for three sheets; measurement after the first section of five rivets.

Figure		Function Type	Accuracy
a_r	Analytical	$f(x) = 7.2 * \sin(7.3 * x - 0.3) * \exp(-0.8 * x) - 0.1$	95.6%
a_b	Modeled	$f(x) = 36 * \sin(26.26 * x) * \exp(-1.4 * x) + 0.005$	98.6%
b_r	Analytical	$f(x) = 7.1 * \sin(7.5 * x - 3.3) * \exp(-0.8 * x) - 0.11$	95%
b_b	Modeled	$f(x) = 36.5 * \sin(26.2 * x - 5.61) * \exp(-1.42 * x) + 0.01$	99%
c_r	Analytical	$f(x) = 7.2 * \sin(7 * x + 0.35) * \exp(-0.8 * x) - 0.1$	96.3%
c_b	Modeled	$f(x) = 37.2 * \sin(26 * x + 0.6) * \exp(-1.4 * x) - 0.016$	98.5%

It can be appreciated that Table 5 shows similar results to Table 4. In this set, the analytical approximation decreased to 95% compared with results obtained with one and two riveted sections; however, the accuracy obtained using the rod theory remained greater than 98%. The damped oscillation is consistent, while the amplitude and frequency are greater in the modeled equation, evidencing the repetition of the phenomena in a set of three laminae. Table 6 shows the numerical results for the measurements obtained after the second section of rivets; again the oscillation is congruent with the other results, analytical approximation reached a maximum accuracy of 97%, and the rod theory obtained a maximum of 98.4%.

Table 6. Analytical and modeling solutions for three sheets; measurement after the second section of rivets.

Figure		Function Type	Accuracy
d_r	Analytical	$f(x) = 8.6 * \sin(7.3 * x + 1.53) * \exp(-0.9 * x) - 0.104$	95.9%
d_b	Modeled	$f(x) = 26.5 * \sin(26 * x + 3.38) * \exp(-1.6 * x) + 0.005$	98.4%
e_r	Analytical	$f(x) = 8.5 * \sin(7.3 * x + 0.7) * \exp(-0.8 * x) - 0.066$	97.1%
e_b	Modeled	$f(x) = 27.6 * \sin(28 * x - 4.89) * \exp(-1.4 * x) - 0.071$	98.2%
f_r	Analytical	$f(x) = 8 * \sin(7.5 * x + 1.8) * \exp(-0.83 * x) - 0.0533$	96.4%
f_b	Modeled	$f(x) = 27 * \sin(27.5 * x + 1.04) * \exp(-2.4 * x) + 0.0321$	97.3%

Finally, Table 7 shows how the wave behaved in the third lamina; it is seen that the oscillation behavior continued, for the last case, the analytical approximation reached a mean accuracy of 96% while the rod theory 98.5%. It can be appreciated that the amplitude decreased from Tables 5–7. It seems that part of the wave was stopped by the structural joints; however, the waveform remained.

Table 7. Analytical and modeling solutions while studying the impact transmission after the third one.

Figure		Function Type	Accuracy
g_r	Analytical	$f(x) = 4.5 * \sin(7.65 * x - 2.02) * \exp(-0.9 * x) - 0.062$	96.3%
g_b	Modeled	$f(x) = 9.6 * \sin(28.5 * x + 1.16) * \exp(-1.43 * x) - 0.024$	98.9%
h_r	Analytical	$f(x) = 4.3 * \sin(7.62 * x + 1.23) * \exp(-1 * x) - 0.0745$	96%
h_b	Modeled	$f(x) = 10.2 * \sin(28.5 * x - 0.8) * \exp(-1.4 * x) - 0.062$	98.1%
i_r	Analytical	$f(x) = 4.77 * \sin(7.62 * x + 2.33) * \exp(-1 * x) - 0.05$	96.2%
i_b	Modeled	$f(x) = 10 * \sin(29.7 * x - 3.53) * \exp(-1.35 * x) - 0.052$	98.5%

4. Discussion

The authors declared in [43] that the pendular motion generated sometimes a harmonic reaction, and some others generated a damped reaction. The structural rigidity

given by the screws may provoke those changes, making the incoming wave travel in a different waveform.

In this article, the results evidenced that a physical phenomena was reproduced; all the solutions were damped, and the incoming wave (modeled) had greater values of frequency compared with the analytical ones. Along the three sets of sheets joined with rivets, the rod theory demonstrated a better approximation, reaching a maximum of 99.9% accuracy. Consequently, the results evidenced that the methodology shown in [43] agreed with the approximation obtained using the rod theory.

5. Conclusions

This article demonstrated that the laser system methodology can sense the behavior of an indirect impact with a maximum accuracy of 99.9%; this result was reached by means of the rod propagation theory.

Also, the results evidenced that a physical phenomena was reproduced; the wave motion always was damped, and the frequency values were greater in the modeled solution compared with the analytical ones. It is assumed that this behavior could be attributed to an energy absorption due to the sand; however, the waveform remains.

Wave transmission sensing might be used in seismic, civil, mechanic and aeronautic engineering, to mention some of the options. Also, the present system is a cheap solution, as it only requires a laser source and a camera.

Author Contributions: V.M.-C. helped with coding the formulation of the wave propagation according to James Doyle. A.R.-T. supervised the methodology of joining the sheets with rivets as well as the experiment execution. F.d.J.T.-P. conducted the experiment and obtained all the results. A.S.-H. supervised the research, revised the results and wrote the article. All authors have read and agreed to the published version of the manuscript.

Funding: This research received no external funding.

Institutional Review Board Statement: Not applicable.

Informed Consent Statement: Not applicable.

Data Availability Statement: All data are available in the article.

Acknowledgments: Felipe de Jesús Tapia-Pérez thanks CONAHCYT, as they gave him a grant to study his Master's degree. The authors thank the Universidad Politécnica Metropolitana de Hidalgo for all the administrative support. Also, special thanks to Antonio Pérez Jiménez for all the English advice.

Conflicts of Interest: The authors declare no conflicts of interest.

References

1. Katunin, A.; Lis, K.; Joszko, K.; Żak, P.; Dragan, K. Quantification of hidden corrosion in aircraft structures using enhanced D-Sight NDT technique. *Measurement* **2023**, *216*, 112977. [CrossRef]
2. Towsyfyan, H.; Biguri, A.; Boardman, R.; Blumensath, T. Successes and challenges in non-destructive testing of aircraft composite structures. *Chin. J. Aeronaut.* **2020**, *33*, 771–791. [CrossRef]
3. Bossi, R.H.; Georgeson, G.E. Nondestructive testing of aerospace composites. In *Woodhead Publishing Series in Composites Science and Engineering, Polymer Composites in the Aerospace Industry*, 2nd ed.; Irving, P., Soutis, C., Eds.; Woodhead Publishing: Sawston, UK, 2020; pp. 461–489, ISBN 9780081026793.
4. Gholizadeh S. Impact behaviours and Non-Destructive Testing (NDT) methods in Carbon Fiber Composites in Aerospace Industry: A Review. *Authorea* **2022** . [CrossRef]
5. Iuliia, L. Advanced Signal Processing Methods for Inspection of Aircraft Structural Materials. *Trans. Aerosp. Res.* **2020**, *2020*, 27–35. [CrossRef]
6. Mridul, G.; Khan, M.A.; Butola, R.; Singari, R.M. Advances in applications of Non-Destructive Testing (NDT): A review. *Adv. Mater. Process. Technol.* **2021**, *8*, 1–22. [CrossRef]

7. Pacana, A.; Czerwińska, K.; Dwornicka, R. Analysis of quality control efficiency in the automotive industry. *Transp. Res. Procedia* **2021**, *55*, 691–698. [CrossRef]
8. Nüßler, D.; Jonuscheit, J. Terahertz based non-destructive testing (NDT): Making the invisible visible. *tm-Tech. Mess.* **2021**, *88*, 199–210. [CrossRef]
9. Wang, Q.; Ri, S. Sampling Moiré method for full-field deformation measurement: A brief review. *Theor. Appl. Mech. Lett.* **2022**, *12*, 100327. [CrossRef]
10. Wang, H.; Ruan, Y.; Yu, Y.; Guo, Q.; Xi, J.; Tong, J. A New Algorithm for Displacement Measurement Using Self-Mixing Interferometry With Modulated Injection Current. *IEEE Access* **2020**, *8*, 123253–123261. [CrossRef]
11. Barakat, M.A.Y.; Abdelwahab, M.; Abdallah, A.W. Evaluation of new designed reference blocks for calibration and NDT by optical and ultrasonic techniques. *Metrol. Meas. Syst.* **2022**, *29*, 719–736. [CrossRef]
12. García-Macías, E.; Ubertini, F. Automated operational modal analysis and ambient noise deconvolution interferometry for the full structural identification of historic towers: A case study of the Sciri Tower in Perugia, Italy. *Eng. Struct.* **2020**, *215*, 110615. [CrossRef]
13. Pahl, T.; Hagemeier, S.; Künne, M.; Yang, D.; Lehmann, P. 3D modeling of coherence scanning interferometry on 2D surfaces using FEM. *Opt. Express* **2020**, *28*, 39807–39826. [CrossRef] [PubMed]
14. Barland, S.; Gustave, F. Convolutional neural network for self-mixing interferometric displacement sensing. *Opt. Express* **2021**, *29*, 11433–11444. [CrossRef] [PubMed]
15. Pietro, M.; Serio, C.; Masiello, G.; Pepe, A. The Multiple Aperture SAR Interferometry (MAI) Technique for the Detection of Large Ground Displacement Dynamics: An Overview. *Remote Sens.* **2020**, *12*, 1189. [CrossRef]
16. Di Carlo, F.; Miano, A.; Giannetti, I.; Mele, A.; Bonano, M.; Lanari, R.; Prota, A.M.A. On the integration of multi-temporal synthetic aperture radar interferometry products and historical surveys data for buildings structural monitoring. *J. Civ. Struct. Health Monit.* **2021**, *11*, 1429–1447. [CrossRef]
17. Ostapska, K.; Malo, K.A. Calibration of a combined XFEM and mode I cohesive zone model based on DIC measurements of cracks in structural scale wood composites. *Compos. Sci. Technol.* **2021**, *201*, 108503. [CrossRef]
18. Bhowmick, S.; Nagarajaiah, S.; Lai, Z. Measurement of full-field displacement time history of a vibrating continuous edge from video. *Mech. Syst. Signal Process.* **2020**, *144*, 106847. [CrossRef]
19. Cai, Y.; Liu, Y.; Yang, C.; Zhu, K.; Liu, W.; Huang, J.; Zheng, P.; Zhang, K. External Measurement System for Aircraft Structural Parts Based on Digital Image Correlation in Signal-limited Spaces. *J. Phys. Conf. Ser.* **2023**, *2468*, 012121. [CrossRef]
20. Shi, X.; Guo, X.; Suo, T.; Yuan, Y.; He, H.; Ren, Z. A novel subset assignment and matching method for DIC measurement of complex deformation in aircraft braking process. *Chin. J. Aeronaut.* **2024**, *37*, 373–387. [CrossRef]
21. Goessling, J.; Seume, J.R. High-speed Digital Image Correlation (DIC) for measuring deformation and vibration of fast rotating fan blades. *J. Phys. Conf. Ser.* **2023**, *2526*, 012075. [CrossRef]
22. Mata-Falcón, J.; Haefliger, S.; Lee, M.; Galkovski, T.; Gehri, N. Combined application of distributed fibre optical and digital image correlation measurements to structural concrete experiments. *Eng. Struct.* **2020**, *225*, 111309. [CrossRef]
23. Janeliukstis, R.; Chen, X. Review of digital image correlation application to large-scale composite structure testing. *Compos. Struct.* **2021**, *271*, 114143. [CrossRef]
24. Majid, R.-B.; Huber, C.; Shukla, K.; Karniadakis, G.E. Physics-informed Neural Networks (PINNs) for Wave Propagation and Full Waveform Inversions. *ESS Open Arch.* **2021**, *127*, e2021JB023120. [CrossRef]
25. Abbas, R.M.; Jorshari, T.D.; Lü, C.; Ansari, R.; Kouzani, A.Z.; Amabili, M. A review of size-dependent continuum mechanics models for micro- and nano-structures. *Thin-Walled Struct.* **2021**, *170*, 108562. [CrossRef]
26. De Luca, A.; Perfetto, D.; Polverino, A.; Aversano, A.; Caputo, F. Finite Element Modeling Approaches, Experimentally Assessed, for the Simulation of Guided Wave Propagation in Composites. *Sustainability* **2022**, *14*, 6924. [CrossRef]
27. Ebrahimi, F.; Mohammadi, K.; Barouti, M.M.; Habibi, M. Wave propagation analysis of a spinning porous graphene nanoplatelet-reinforced nanoshell. *Waves Random Complex Media* **2019**, *31*, 1655–1681. [CrossRef]
28. Habibi, M.; Mohammadi, A.; Safarpour, H.; Shavalipour, A.; Ghadiri, M. Wave propagation analysis of the laminated cylindrical nanoshell coupled with a piezoelectric actuator. *Mech. Based Des. Struct. Mach.* **2021**, *49*, 640–658. [CrossRef]
29. Janovec, M.; Bugaj, M.; Smetana, M. Eddy Current Array Inspection of Riveted Joints. *Transp. Res. Procedia* **2019**, *43*, 48–56. [CrossRef]
30. Korbel, A. Effect of aircraft rivet installation process and production variables on residual stress, clamping force and fatigue behaviour of thin sheet riveted lap joints. *Thin-Walled Struct.* **2022**, *181*, 110041. [CrossRef]
31. Liu, Y.; Han, L.; Zhao, H.; Liu, X. Evaluation and correction of cutting position's effects on quality indicator measurement of self-piercing riveted joint. *Mater. Design* **2021**, *202*, 109583. [CrossRef]
32. Kim, K.-Y.; Sim, J.; Jannat, N.-E.; Ahmed, F.; Ameri, S. Challenges in riveting quality prediction: A literature survey. *Procedia Manuf.* **2019**, *38*, 1143–1150. [CrossRef]

33. Liu, J.; Zhao, A.; Ke, Z.; Zhu, Z.; Bi, Y. Influence of Rivet Diameter and Pitch on the Fatigue Performance of Riveted Lap Joints Based on Stress Distribution Analysis. *Materials* **2020**, *13*, 3625. [CrossRef]
34. Xie, Z.; Chen, F.; He, W. The effects of ultrasonic vibration on riveting quality. *Sci. Rep.* **2022**, *12*, 12948. [CrossRef] [PubMed]
35. Wang, Y.; Zhao, H.; Li, X.; Jiang, H. High-Accuracy 3-D Sensor for Rivet Inspection Using Fringe Projection Profilometry with Texture Constraint. *Sensors* **2020**, *20*, 7270. [CrossRef] [PubMed] [PubMed Central]
36. Saldaña-Heredia, A.; Martínez-Calzada, V.; Márquez-Aguilar, P.A.; Hernández-Cruz, D. Optical Characterization of a Pendular Impact. *Front. Phys.* **2020**, *8*, 329. [CrossRef]
37. Saldaña-Heredia, A.; Martínez-Calzada, V.; Villar-Ramírez, V.U.D.; Rodríguez-Torres, A. Optical measurement of an impact reaction in a modeled wing. *Front. Phys.* **2022**, *10*, 770536. [CrossRef]
38. Khurmi, R.S.; Gupta, J.K. *A Textbook of Machine Design*; Eurasia Publishing House Pvt. Ltd.: Ram Nagar, India, 2005.
39. Laserglow Technologies. *LCS-0532 Low-Cost DPSS Laser System Laserglow Part Number: C53200XSX, Laser Product Datasheet Generated on (2015)*; Laserglow Technologies: North York, ON, Canada, 2015.
40. iPhone 13 Pro Data Sheet. Available online: https://support.apple.com/en-us/111871 (accessed on 3 October 2024).
41. Doyle, J.F. *Wave Propagation in Structures: Spectral Analysis Using Fast Discrete Fourier Transforms*, 2nd ed.; Mechanical Engineering Series; Springer: Berlin/Heidelberg, Germany; New York, NY, USA, 1997.
42. Dainty, J.C. *Laser Speckle and Related Phenomena*; Springer: Berlin/Heidelberg, Germany; New York, NY, USA, 1975.
43. Martínez-Calzada, V.; Tapia-Pérez, F.d.J.; Rodríguez-Torres, A.; Saldaña-Heredia, A. Optical Analysis of the Impact Transmission in Steel Sheet Arrays with Bolted-Type Joints. *Appl. Sci.* **2023**, *13*, 9275. [CrossRef]

MDPI AG
Grosspeteranlage 5
4052 Basel
Switzerland
Tel.: +41 61 683 77 34

MDPI Books Editorial Office
E-mail: books@mdpi.com
www.mdpi.com/books

Academic Open
Access Publishing

mdpi.com

ISBN 978-3-7258-4294-0